MODELLING OF TSUNAMI GENERATED BY SUBMARINE LANDSLIDES

A thesis

submitted in partial fulfilment

of the requirements for the Degree

of

Doctor of Philosophy in Civil Engineering

in the

University of Canterbury

by

Langford Phillip Sue

University of Canterbury

Christchurch, New Zealand

2007

Abstract

Tsunami are a fascinating but potentially devastating natural phenomena that have occurred regularly throughout history along New Zealand's shorelines, and around the world. With increasing population and the construction of infrastructure in coastal zones, the effect of these large waves has become a major concern. Many natural phenomena are capable of creating tsunami. Of particular concern is the underwater landslide-induced tsunami, due to the potentially short warning before waves reach the shore.

The aims of this research are to generate a quality benchmark dataset suitable for comprehensive comparisons with numerical model results and to increase our understanding of the physical processes involved in tsunami generation. The two-dimensional experimental configuration is based on a benchmark configuration described in the scientific literature, consisting of a semi-elliptical prism sliding down a submerged 15° slope. A unique feature of these experiments is the method developed to measure water surface variation continuously in both space and time. Water levels are obtained using an optical technique based on laser induced fluorescence, which is shown to be comparable in accuracy and resolution to traditional electrical point wave gauges. In the experiments, the landslide density and initial submergence are varied and detailed measurements of wave heights, lengths, propagation speeds, and shore run-up are made. Particle tracking velocimetry is used to record the landslide kinematics and sub-surface water velocities. Particular attention is paid to maintaining a high level of test repeatability throughout the experimental process.

The experimental results show that a region of high pressure ahead of the landslide forces up the water over the front half of the landslide to form the leading wave crest, which propagates ahead of the landslide. The accelerating fluid above, and the turbulent wake behind, the moving landslide create a region of low pressure, which draws down the water surface above the rear half of the landslide to form the leading trough. Differences in the phase and group velocities of the components in the wave packet cause waves to be continually generated on the trailing end of the wave train. The downstream position that these waves form continually moves downstream with time and the wave packet is found to be highly dispersive.

The interaction of the landslide pressure field with the free surface wave pressure field is important, as the location of the low pressure around the landslide relative to the wave field acts to reinforce or suppress the waves above. This has a substantial effect on the increase or decrease in wave potential energy. When the low pressure acts to draw down a wave trough, the wave potential energy increases. When the low pressure is below a wave crest, it acts to suppress the crest amplitude, leading to an overall decrease in wave potential energy.

Measurements of the efficiency of energy transfer from the landslide to the wave field show that the ratio of maximum wave potential energy to maximum landslide kinetic energy is between 0.028 and 0.138, and

tends to increase for shallower initial landslide submergences and heavier specific gravities. The ratio of maximum wave potential energy to maximum landslide potential energy ranges between 0.011 and 0.059 and tends to be greater for shallower initial submergences. For two experimental configurations the ratio of maximum wave potential energy to maximum fluid kinetic energy is estimated to be 0.435 and 0.588.

The wave trough initially generated above the rear end of the landslide propagates in both onshore and offshore directions. The onshore-propagating trough causes a large initial draw-down at the shore. The magnitude of the maximum draw-down is related to the maximum amplitude of the offshore-propagating first wave trough. A wave crest generated by the landslide as it decelerates at the bottom of the slope causes the maximum wave run-up observed at the shore.

A semi-analytical model, based on inviscid and irrotational theory, is used to investigate the wave generation process of a moving submerged object in a constant depth channel. The simplified geometry allows a variety of phenomena, observed during the experimental tests, to be investigated further in a more controlled setting. The variations in the growth, magnitude, and decay of energy as a function of time is due the interaction of the pressure distribution surrounding the moving slider with the wave field, in particular, the leading crest and trough. The largest energy transfer between slider kinetic energy and wave potential energy occurs when there is prolonged interaction between the slider's low pressure region and the leading wave trough. The generation of onshore propagating waves by a decelerating landslide is confirmed, and the magnitude of the maximum wave run-up is found to be dependent on the magnitude of the slider deceleration. The model also shows that slides with Froude number close to unity convert substantial amounts of energy into offshore propagating waves. The onshore propagating wave potential energy is not as sensitive to Froude number. A further result from the model simulations is that the specific shape of the slider has only a minor influence on the wave response, provided the slider's length and area are known.

A boundary element model, based on inviscid and irrotational theory, is used to simulate the laboratory experiments. Model predictions of the wave field are generally accurate, particularly the magnitude and range of wave amplitudes within the wave packet, the arrival time of the wave group, the amplitude of the run-up and run-down at the shore, the time the maximum run-down occurs, and the form and magnitude of the wave potential energy time history. The ratios of maximum wave potential energy to maximum slider kinetic energy are predicted to within ± 29%. The model predictions of the crest arrival times are within 3.6% of the measured times. The inability of the inviscid and irrotational model to simulate the flow separation and wake motions lead to a 45% under prediction of the maximum fluid kinetic energy.

Both the semi-analytical and BEM models highlight the need for the correct specification of initial slider accelerations in numerical simulations in order to accurately predict the wave energy.

Acknowledgements

This research was made possible by the support provided by the New Zealand Earthquake Commission (EQC) Research Foundation. The H. J. Hopkins Postgraduate Scholarship in Civil Engineering, the Institute of Professional Engineers New Zealand (IPENZ) Craven Scholarship for Postgraduate Research in Engineering, and the University Research Awards also provided valuable financial support.

A big thank you goes out to my supervisors, Dr Roger Nokes, Dr Mark Davidson, and Dr Roy Walters. Without your insightfulness, continual guidance, advice, suggestions, and general critiquing, this thesis would not be possible. It has been an honour, a privilege, and a pleasure working among such talented people. I would also like to thank Dr Willem de Lange and Dr Robert Labeur for their review of the thesis, Des Bull for his encouragement in doing this PhD, and Dr Pedro Lee for his advice.

My gratitude also goes out to the technical staff at the University of Canterbury's Department of Civil Engineering. Without the skill and lateral thinking of Ian Sheppard, Kevin Wines, Ray Allen, Colin Bliss, and David MacPherson, the laboratory work would not have been successful. A big thank you also goes out to Melody Callihan for her expertise and help.

I would also like to thank the staff at the National Institute of Water and Atmospheric Research (NIWA), particularly Jason Fleming for the preliminary laboratory work, and Fraser Callaghan for the preliminary numerical modelling.

My conversations with fellow post-graduate students, Caroline, Dave, Bill, Cameron, Gustaaf, and James, allowed me to overcome so many problems. Also the support of my friends provided humour and perspective throughout my research.

To my wife, Hae-Ryun, your calming influence and understanding have made an immeasurable difference. I struggle to think how I would have done this without your unwavering love, humour, patience, and encouragement.

Lastly, but firstly, I want to thank my parents and family. Mum and Dad, I would not be the person I am without the belief, encouragement, and support you have given me throughout my life. Words cannot express my gratitude for everything you have done for me. This thesis is for you guys!

Table of Contents

List of Figures

List of Tables

Nomenclature

Upper Case Latin

B	Slide length parallel to the slope
C	Constant
C_d	Drag coefficient
C_g	Wave group velocity
C_m	Added mass coefficient
C_n	Coulomb friction coefficient
C_p	Wave phase speed
C_{12}	PTV cost (between frames 1 and 2)
ΔC	Abe's source region correction factor
D	Constant water depth
E	Energy, Wave potential energy
E_k	Kinetic energy
$E_{k,max}$	Maximum kinetic energy
E_p	Potential energy
$E_{p,max}$	Maximum potential energy
Fr	Froude number
H	Wave Height, standard tsunami wave height, Horizontal distance of camera from laser light sheet, Bottom boundary amplitude function
Ha	Hammack number
Ha_0	Hammack number at t=0
$\overline{H}_r$	Mean tsunami run-up height
$H_{r\,max}$	Maximum tsunami run-up height
IS	Initial Submergence
K	Forcing function
L_b	Landslide length
L_{crest}	Distance from camera to positive water level
L_o	Distance from camera to still water level
L_{trough}	Distance from camera to negative water level
M_t	Abe's tsunami magnitude scale
N_b	Number of bottom boundary elements
N_{fs}	Number of free surface elements
N_r	Number of right end boundary elements
N_s	Number of slider elements
R	Run up height

S_g	Submergence number
SG	Specific Gravity
T	Wave period
V	Output voltage, Vertical distance of camera above still water level, Landslide volume
WL	Refraction-corrected water level (positive and negative)
$WL_{corrected}$	Water level corrected for camera angle-induced scaling errors

Lower Case Latin

a	Wave amplitude, Acceleration
a, b, c	Coefficient
a_{const}	Constant acceleration
$\mathbf{a}_{est}$	Estimated acceleration
a_0	Initial acceleration
$\mathbf{a}_{pred}$	Predicted acceleration
area	Area of water viewed in PTV experiments
b	Horizontal length of landslide
block	Block, Landslide, Slider
c	Soil cohesion, Height of vertical front face of landslide, barrel correction coefficient
d	Initial water depth directly above the landslide centre of mass, Water depth
d_{b0}	Initial water depth directly above the landslide centre of mass
dv	Vertical displacement relative to initial RWG submergence
e	Conversion of maximum landslide E_k into wave E_p
f	Slider shape function
g	Acceleration of gravity
h	Constant water depth
h_b	Slider thickness
h_{b0}	Initial slider thickness
h_1	Final slider thickness
i_s	Soloviev's tsunami intensity
k	Wave number
m_b	Unsubmerged mass of landslide
m_m	Imamura-Iida's tsunami magnitude scale
m_o	Mass of water displaced by the landslide
n	Number of particles, Outward normal
$\underline{n}_i$	Unit inward normal at *i*th node

p	Fourier coefficient, Pressure
r	Magnitude of $\mathbf{r}_d$
$\mathbf{r}$	Pixel location
$\mathbf{r}_d$	Destination image pixel location
$\mathbf{r}_s$	Source image pixel location
r_x	Horizontal run-up distance
r_y	Vertical run-up height
r^2	Coefficient of determination
s	Landslide position, Arc length coordinate
s_0	Characteristic distance of motion, Slider position in arc length coordinates
t	Time
t_{max}	Time to maximum velocity
t_0	Characteristic time of motion, time=0
t_{peak}	Time to peak velocity
t_{zero}	Time to zero velocity
u	Horizontal landslide velocity, Local coordinates relative to slider centre of
$\underline{u}$	Velocity vector
u_t	Terminal velocity
v	Vertical landslide velocity
vel	Total landslide velocity
vel_{area}	Area below velocity time history
vel_{max}	Maximum slider velocity
v_b	Landslide volume
v_{nb}	Normal velocity of the boundary
w	Unit mass of water, Landslide or flume width
$wave$	Wave, Water, Fluid
x	Horizontal coordinate, Horizontal landslide position
x_{inset}	Inset in horizontal domain
x_0	Horizontal position of slider, initial horizontal position of slider
x_r	Right extent of horizontal domain
y	Vertical coordinate, Vertical landslide position
y_b	Bottom boundary

Greek

α, β	Coefficient
Δ	Submergence, increment
ε	Slider thickness decay parameter
ϕ	Internal friction angle, Velocity potential
γ	Specific density, Specific gravity, Slider thickness decay parameter
η	Water level, Amplitude
η_{airy}	Far-field characteristic wave amplitude
η_{max}	Maximum water level, Near-field characteristic wave amplitude
λ	Wavelength, $(a_0/g)^{0.5}$
λ_0	Characteristic wavelength
Λ	Non-dimensional wavelength
θ	Slope angle
ρ	Density, Ratio of initial slider thickness to water depth, Ratio of initial slider thickness to its half-length
ρ_0	Density of water
σ	Normal stresses on the slope
τ	Ratio of water depth to slider half-length
τ_s	Soil shear strength
ω	Angular frequency
ξ	Pore water pressure
ζ	Ratio of wave potential energy to slider kinetic energy

Superscripts

ι	Imaginary
r	Real
$'$	Non-dimensional form
$\overline{\quad}$	Depth average
$\overline{\overline{\quad}}$	Area average

Subscripts

0	Initial, water, characteristic, position
area	area
b	Block, Landslide, Slider
backward	Backward propagating
d	Destination image
est	Estimated
forward	Forward propagating
i	Frame, integer, node
inset	Inset
max	Maximum
min	Minimum
pred	Predicted
P1	Particle in frame 1
P2	Particle in frame 2
r	Right
s	Source image
zero	Zero
α	Closest

Chapter 1: Introduction

Unlike tidal waves, tsunami are not a phenomena associated with the tides, but instead are water waves generated by seismic events in and around the oceans. The word 'tsunami' originates from the Japanese word that means 'harbour wave', and has been adopted by the western world to differentiate between waves generated seismically and those related to tidal effects. Many natural phenomena are capable of creating tsunami, including earthquakes, marine volcanic eruptions, meteorite splashdowns, and sub-aerial and underwater landslides.

There are several reasons tsunami are hazardous. Firstly it is their size, with waves several hundred metres in height known to have occurred in the past (Murty 2003; New Scientist 2004). Secondly, tsunami can travel at considerable speeds, upwards of many hundreds of kilometres per hour. Lastly, tsunami occurrences are unpredictable. Seismic events such as earthquakes and landslides, the generation mechanisms of tsunami, occur sporadically in time and space, and not all seismic events have generated significant waves.

After the events in the Indian Ocean on the 26th of December 2004, the existence of powerful tsunami cannot be disputed. Studies of historical records and forensic analysis of coastal geology have shown significant wave events occur frequently across the world. With the increasing population in communities and the development of infrastructure around the coastal fringes, the possible impact of these large waves is becoming a major concern.

Of great concern is the underwater landslide-induced tsunami, typically triggered by seismic activity, as there will often only be a few minutes warning before the wave washes up the shore, providing little time for evacuation. This research focuses on this class of tsunami, in which sections of sediment or rock on the seabed slide into deeper water, translating into a disturbance on the water surface above. Regions of potential inundation need to be identified to allow communities to locate their population and property outside these hazardous areas.

New Zealand is especially at risk from landslide-induced tsunami as it has a long coastline and the majority of the country's population lives in close proximity to the ocean. Continual erosion of New Zealand's steep mountainous terrain supplies vast quantities of unconsolidated sediment, which deposit on the continental slopes offshore. Along the east coast of New Zealand is the boundary of the Pacific and Indo-Australian Plates and its associated subduction zone. The active seismicity of this highly faulted region acts as a possible trigger for these loose sediments to slide, potentially creating a significant tsunami.

1.1 Motivation and Objectives

The focus of this research is the experimental, analytical, and numerical modelling of the generation, initial propagation, and shore run-up of waves generated by underwater landslides. The primary aim is to perform laboratory experiments to generate a high quality and comprehensive dataset that can be used for comparisons with numerical models. The secondary aim of this work is to enhance our understanding of the fluid dynamics involved in the generation of underwater landslide-induced tsunami. This includes an understanding of how the motion of the slide material manifests itself as a water wave, and the fluid dynamical mechanisms involved in the generation and propagation processes.

Wave height, propagation speed, and run up depend on a range of key physical parameters including the mass of the landslide and the distance below the free surface from which the landslide begins its descent. This project explores this parameter space seeking a deeper and more fundamental understanding of the behaviour of the tsunami wave and velocity-fields and their dependence on these key parameters.

One of the key benefits of this research is the generation of significant experimental data sets against which numerical models can be calibrated. Accurate numerical models are important in predicting the expected hazards to coastal and lakeside communities. They have the ability to model a broad range of water body geometries and landslide parameters that would prove extremely challenging to model physically in the laboratory. However these computational models require high quality data against which they can be calibrated and assessed. This study will provide such benchmark data.

Numerical modelling can provide valuable insights into the wave generation process. Within such models, a multitude of physical parameters can be varied in a controlled manner, so the effects of each can be observed and investigated. Comparisons between numerical results and the experimental data can provide insights into the validity, accuracy, and limitations of the model. It also proof-tests the quality and range of the experimental data.

1.2 Thesis Outline

Chapter 2 presents background information on the characteristics of tsunami and landslides, and details some of the historical events. Chapter 3 summarizes the literature associated with underwater landslides and the water waves that they create in the laboratory. The numerical models previously developed to simulate these waves are also presented. Chapter 4 contains information pertaining to the laboratory experiments conducted at the University of Canterbury. Details of the experimental set-up are given, along with information on the methods developed to measure the wave phenomena and the equipment and computer software required. The key results are given and discussed in Chapter 5.

Chapter 6 describes the semi-analytical spectral model and the results from an investigation into several key physical wave generation parameters. A numerical model, based on the boundary element method, is described in Chapter 7. This includes comparisons between the numerical data and the experimental results. This is followed by some concluding remarks in Chapter 8.

Chapter 2: Literature Review I: Tsunami and Landslides

With the recent events around the Indian Ocean in December 2004 and Indonesia in July 2006, the perceived danger from tsunami has escalated significantly. Also, as more detailed mapping and accurate prediction methods become available, the number of locations identified as being potentially threatened by these large waves is greater than initially thought. This has led to a renewed effort in tsunami prediction, analysis, mitigation, and public awareness at these locations.

This chapter begins in Section 2.1 with a review of basic tsunami characteristics. The major historical underwater landslide-induced tsunami events from around the world and New Zealand are then presented in Section 2.2, followed in Section 2.3 by a brief discussion of the soil mechanics of slope failures and natural sediments and their importance in the understanding of terrestrial and underwater landslides and their causes. This chapter closes in Section 2.4 with a review of the triggering mechanisms, classification, and characteristics of underwater landslides, and details of some historical landslide events. A review of laboratory and numerical modelling of underwater landslides is presented in Chapter 3.

2.1 Tsunami Characteristics

Even though there are several mechanisms that are capable of generating tsunami, the majority occur as a result of undersea earthquakes and landslides. The rupture of underwater faults disturbs a large area of the ocean along the length of the fault rupture, generating a set of waves that propagate away perpendicular to the fault line. As such, tsunami generated by fault ruptures along a substantial length of fault line can be considered a line source. Landslides displace or disturb the water when they slide into or through the water column generating waves that radiate away from the landslide, and can be considered a point source. Landslides often occur in conjunction with seismic events as the ground shaking agitates the soil mass and initiates sliding. Other landslide triggering mechanisms are listed in Section 2.4.1. Marine volcanic eruptions, such as Krakatau, Indonesia, in 1883, and meteorite splashdowns, are capable of generating the largest tsunami. Fortunately, these very rarely occur.

Earthquake generated tsunami can produce large wave heights and have far-reaching effects. They are strongly related to the magnitude of the seismic event and attempts have been made to derive equations that relate tsunami wave heights to the size of the earthquake (De Lange and Moon 2004). These waves have long wavelengths, typically several hundred kilometres, and long periods, in excess of several tens of minutes. As such, they exhibit little wave height decay due to weak energy attenuation. Waves lose energy inversely proportional to their period, with longer periods having less attenuation. Earthquake induced tsunami exhibit less radiation attenuation compared to landslide tsunami, as the wave energy from a line source does not spread as quickly as that from a point source.

For landslide-induced events, large waves are produced along areas of coast close to the source, typically 10-15 km either side of the slide area (Papadopoulos and Kortekaas 2003). Tsunami may be observed over a considerably greater distance if the landslide is exceptionally large or if it is combined with seismic sources. The effects of landslide tsunami are geographically constrained, but their danger lies in the short travel times compared to seismically generated waves and their higher amplitudes in the near field. Tsunami from landslide sources have minimal far-reaching effects because wave energy is spread over a wider-and-wider area as the waves move away from what is essentially a point source.

There are several indicators that a tsunami is possibly landslide-generated as opposed to earthquake-generated. Landslide-tsunami have a more localised effect and greater dissipation, such that damage is generally isolated to small areas close to the origin, and far field effects may be negligible. However, this near field damage may be more severe than from seismically generated tsunami. Damage may also be more intense in certain areas due to directivity associated with radiation away from a point source. Tsunami with landslide origins often have fewer waves in the wave train, and attenuate more rapidly due to their shorter periods. Underwater landslide tsunami can often be distinguished from the earthquake-generated tsunami in a co-seismic event by their arrival times being inconsistent with that expected from a purely fault rupture-type scenario. Also, the magnitude of the waves may be larger than expected from an earthquake of that magnitude.

During the initial stages of an underwater landslide, the motion of the failure mass downwards pulls the water surface down. The surrounding water will be driven into this depression due to the horizontal pressure gradients. Waves then propagate due to gravitational forces, given the initial perturbation of the water surface. Wave trains travel both upslope and forward in the direction of the slide and are therefore, more focussed than those created by earthquakes. While there is still no consensus as to the characteristics of these waves with regard to wavelength components, linearity, and dispersion, it is clear that tsunami waves are affected significantly by the local bathymetry as they approach the shore.

The danger of tsunami to society occurs when these waves interact with coastal land used for human activity. On the open ocean tsunami wave amplitudes are small, noticeable only as a slight swell, but as they approach the shore amplitudes increase due to shoaling effects. Quoted tsunami wave amplitudes are usually measured close to the shore, where their heights are at a maximum. The momentum of the water within the waves can carry the water mass onshore for a considerable distance. The extent of wave inundation, often referred to as wave run-up, is usually measured from the still water level preceding the arrival of the tsunami. Run-up height is the vertical elevation

reached by the wave and run-up length is the horizontal distance the tsunami propagates inland, relative to the original beach location.

Tsunami are often quantified by means of a magnitude or intensity scale. A common measure for characterising tsunami is the Imamura-Iida scale, as shown in Equation 2.1, developed in tsunami-prone Japan from approximately 100 Japanese tsunami records between 1700 and 1960 (Shuto 1991).

$$m_m = \log_2(H_{r\max} / H) \tag{2.1}$$

where m_m = Imamura-Iida's tsunami magnitude scale

$H_{r\max}$ = maximum tsunami run-up height (m)

H = standard tsunami height of 1 metre

Imamura-Iida's magnitude scale is now commonly used globally. However, maximum wave run-up heights were considered too variable, so Soloviev proposed a more general scale, shown in Equation 2.2 (Horikawa and Shuto 1981).

$$i_s = \log_2(\sqrt{2}\overline{H}_r / H) \tag{2.2}$$

where i_s = Soloviev's tsunami intensity

$\overline{H}_r$ = mean tsunami run-up height along a stretch of coast (m)

Both of these scales peak around a value of 4 and can produce magnitudes with negative values. Abe (1981) suggests a remedy to this with the following scale in Equation 2.3, which has become widely used.

$$M_t = \log_{10}\left(H_{r\max} / H\right) + 9.1 + \Delta C \tag{2.3}$$

where M_t = Abe's tsunami magnitude scale

ΔC = source region correction factor (eg. Hilo, -0.3; California, 0.2; Japan, 0.0)

2.2 Historical Underwater Landslide-Induced Tsunami

Tsunami waves have been recorded throughout history, with the earliest accounts from as long ago as 4000 years in China, 2500 years in the Mediterranean, and 1300 years in Japan (Bryant 2001). Recent underwater landslide-induced events often quoted in the literature are those at Grand Banks in 1929, Alaska in 1964 and 1994, and Papua New Guinea in 1998. These caused widespread damage and loss of life. Tsunami created by landslides are responsible for most of Alaska's tsunami fatalities, unlike

the rest of the USA. These local waves arrive in a few minutes and give little or no opportunity for warning or evacuation. New Zealand experiences a similar frequency of tsunami (seismically- and landslide-induced) with amplitudes greater than one metre as Hawaii and Indonesia, and about a third of the number experienced by Japan.

One of the most recent underwater landslide events occurred in Izmit Bay, Turkey, in 1999. Even though this event is still under ongoing investigation, reports of tsunami generation due to slope movements along the coast after the magnitude 7.4 Kocaeli earthquake illustrates the close association between landslide-generated tsunami and seismic activity (Watts, Grilli, Tappin and Fryer 2005; Wright and Rathje 2003). A computer recreation of the landslide is shown in Figure 2.1.

The most recent of the large tsunami occurred in 1998 along the shores of the Sissano Lagoon in Papua New Guinea. Shortly after a magnitude 7.1 earthquake, wave run-up heights of 15 m were observed along an isolated stretch of coastline. A photo of the tsunami inundation is shown in Figure 2.2. The arrival time and wave heights were inconsistent with the magnitude of the seismic event itself, spurring further investigations as to the cause. Due to the scale of devastation, a comprehensive investigation was initiated, starting with survivors' accounts, on and off shore surveys, seabed imaging, geological interpretation, seismic interpretation, and computer simulations.

The earthquake originated along Northern Papua New Guinea on the boundary of the Australian and Pacific Plates. Numerical simulations indicated that this was the source of a far-reaching tsunami recorded as far away as Japan. However, further simulations showed that the fault dislocation was unable to produce the time and wave height distribution observed in the near field. An underwater slump source was proposed and evidence was found to support this (Tappin, Watts, McMurtry, Lafoy and Matsumoto 2001).

From the detailed offshore surveys that were conducted, evidence was found of a large amphitheatre-shaped rotational slump, along with evidence of recent seabed disturbance (fissures, angular blocks, vertical slopes). The slide material was thought to be 750 m thick and contain 5 to 10 million m^3 of cohesive sediment (Tappin et al. 2001). This provided investigators with a possible cause for the disaster that destroyed 3 villages, badly damaged 4 others, killed 2,200 people and left 12,000 homeless.

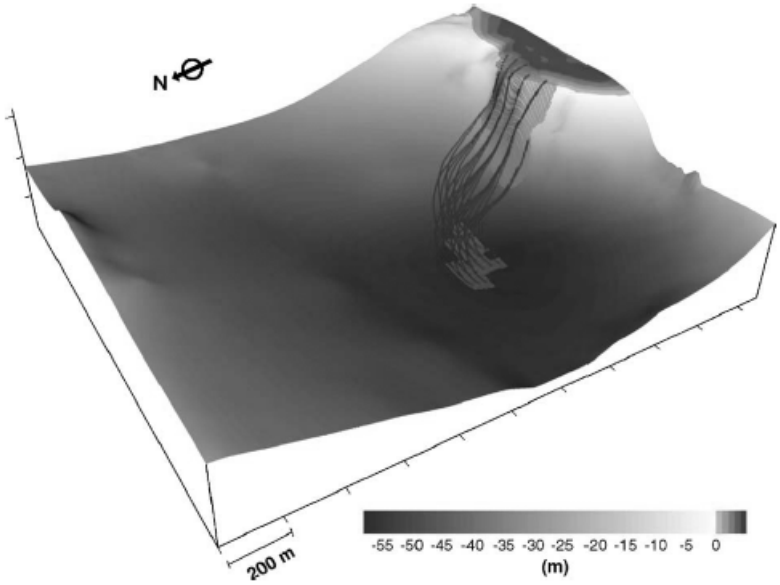

Figure 2.1. 3D computer recreation of the Izmit Bay underwater landslide (Tinti, Armigliato, Manucci, Pagnoni, Zaniboni, Yalciner and Altinok 2006).

Figure 2.2. Looking towards Arop Community School, this photograph of the aftermath of the Papua New Guinea tsunami shows mature trees uprooted for a distance of 500 m inland (Davies, Davies, Perembo and Lus 2003).

Further evidence was found through the analysis of records from surrounding hydrophone stations. An event was recorded 13 minutes after the main shock and found to have originated within the amphitheatre structure. The exceptionally long duration and the frequency content recorded by the

hydrophone indicated a slump was the source of the signal, not a fault dislocation of the seabed (Okal 2003).

The tsunami, consisting of three large waves, arrived approximately 20 minutes after the main shock. Interviews with survivors determined that all three waves, spaced about 500 m to 600 m apart, were approximately 4 m in height as they approached the shore near Sissano. Shoaling effects and coastal topography amplified this height considerably, with wave run-up heights consistently higher than 10 m along a 15 km to 20 km stretch of coastline (Imamura and Hashi 2003; Lynett, Borrero, Liu and Synolakis 2003). Observers of the tsunami wave train stated that the maximum run-up height of 15 m was due to the second of the waves, which surged up the beach atop the first wave that had not yet receded fully (Davies et al. 2003).

The port of Swagway, Alaska, experienced landslide-generated tsunami in November 1994. Waves with heights of 8-11 m were observed at the shoreline after approximately 16 km^3 of material slid down the harbour, with the death of one worker and damage to the port facilities (Murty 2003; Papadopoulos and Kortekaas 2003; Rzadkiewicz, Mariotti and Heinrich 1997; Watts et al. 2005).

Another example of a seismically induced tsunami occurred on December 1992 when an earthquake with a surface magnitude of 7.5 struck the Indonesian island of Flores (Bardet, Synolakis, Davies, Imamura and Okal 2003; Tinti and Bortolucci 2000b). A detailed survey followed the earthquake and tsunami. Measurements of wave run-up and penetration were found to be up to four times higher than the mean value of the area surrounding Riangkroko on the eastern flanks of the island. The maximum run-up height of 26 m, higher than that caused by the earthquake itself, was due to what was assumed to be localised underwater landslides offshore from this area, and direct evidence of coastal slumping and land sliding was consequently found. The death toll from the combined seismic and underwater landslide-generated tsunami was approximately 2,000, of which 122 were directly associated with the localised event offshore of Riangkroko.

An event at Nice, France, in 1979 is an example of how the disturbance of an initial underwater landslide can initiate subsequent larger landslides. An underwater slide with an initial volume of 10 million m^3 situated 15 km offshore evolved into a turbidity current, with a volume of 100 million m^3, and severed several submarine cables off Nice (Hampton, Lee and Locat 1996; Papadopoulos and Kortekaas 2003; Rzadkiewicz et al. 1997). The small tsunami created a 3m draw-down along the previously stable Port of Nice, increasing shear stresses in the slope by only 1.5% to 2% (Wright and Rathje 2003). However, this small increase was enough to induce flow liquefaction in a sand layer and progressive failure of the slope.

A large underwater landslide involving between 10 million m^3 and 55 million m^3 of material occurred on the 27th April, 1975 in Kitimat Inlet, British Columbia, Canada (Jiang and Leblond 1992; Murty 2003). This generated at least two large waves, the height of the first was estimated to be roughly 8 m (Rzadkiewicz et al. 1997). The cause of this landslide was thought to be a combination of a low tide, the loading of man-made structures, and the expansive pressure of gas within the sediment (Hampton et al. 1996).

On Good Friday, 27 March 1964, one of the largest measured earthquakes in North America struck the Prince William Sound region of Alaska. The southward movement of Alaska over the Pacific Plate created a shallow dip fault rupture displacing 115-120 km^3 of crust. This displaced 25,000 km^3 of water, forming a large trans-Pacific tsunami. However, this was only one of the three major causes of tsunami to affect Prince William Sound during that time. The second was due to the numerous local landslides, and the third occurred much later and was due to resonance effects in the Port of Valdez region.

Large landslide-generated wave run-up was experienced at several communities along the coast of Prince William Sound. Waves were created immediately at Seward and Valdez following the failure of the steep submerged slopes of Resurrection Bay and Port Valdez respectively. These slides were peculiar in that they originated underwater but retrogressed back up the shore, sinking sections of coastal land and port facilities (Finn 2003; Hampton et al. 1996).

At Seward, the initial smaller slides created waves that initially drew down the water level at the coast, as observed by the rapid drop of ships at their berths at the Standard Oil Dock. The increase in pore water pressure due to the removal of water triggered a flow (shear or liquefaction) failure along a 1 km long section of waterfront containing the docks, rail yard, and oil tanks. This coastal land slid into Resurrection Bay approximately 40 seconds after the start of the strong shaking. This generated several 9 m to 10 m-high localised tsunami that struck the shore moments later bringing back with it burning oil from the damaged oil tanks. All this damage was due to the local slope failures, and it wasn't until 30 minutes later that the earthquake-generated tsunami arrived at Seward, causing further damage. In all, 13 people died at Seward.

The town of Seward was situated on the fan-delta of Lowell Creek, and it was the face of this that failed, destroying much of the town's infrastructure. The southern end of the port's breakwater was originally standing in 3 m of water, but was in 40 m of water after the landslide. The landslide material consisted of loose sediments, deposited at the angle of repose, and rocky debris. It also contained 10 m to 15 m high blocks of soil. This material extended for 500 m offshore at a slope of 25°, tapering to 5° at the toe of the slope (Lee, Kayen, Gardner and Locat 2003). The loose sediments

were severely stirred up and carried a great distance, and finally settled out as a thin layer on the floor of Resurrection Bay.

At Valdez, a similar underwater landslide was generated at the entrance to the port by a collapse of Shoup Glacier's terminal moraine. The tsunami generated carried debris as high as 67 m above sea level. Like Seward, Valdez itself was situated on a steep-fronted outwash delta. A 180 m wide and 1.2 km long stretch of coast slid into the fjord, causing a 9 m high tsunami to surge through the remains of the town only minutes later. In all, 32 people were lost at Valdez.

Of the 106 lives taken by the various tsunami related to the Good Friday earthquake, 82 were attributed to the localised landslide events (Bryant 2001).

It was in the aftermath of the tsunami generated near Unimak Island along the Aleutian Trench in 1946 that the Pacific Tsunami Warning Centre was established to give coastal communities warning of trans-Pacific tsunami. This tsunami was created by a very large underwater landslide involving approximately 200 million m^3 that was triggered by an earthquake with a surface magnitude of 7.1. The head of the slide originated on the continental shelf in 150 m of water and came to rest at a depth of 6000 m in the Aleutian Trench, having slid over a mean slope of 4°. The tsunami wave ran up to a height of 35 m at the Scotch Cap lighthouse, directly onshore from the slide location (Enet, Grilli and Watts 2003; Grilli, Vogelmann and Watts 2002; Watts et al. 2005).

An earthquake, with a surface magnitude of 7.2, off the coast of Newfoundland and Nova Scotia, Canada, in 1929 induced many underwater landslides along Grand Banks. The slides, with a variety of slump depths ranging from 2 m thick to 30 m thick, occurred in 600 m of water along a 260 km width of the continental slope, which culminated over several hours into a large debris flow and turbidity current. This slide was famous as it was the first observation of a debris flow and turbidity current, detected as it severed several submarine Trans-Atlantic cables lying in its path. Later analysis of the sequence and times the cables were severed indicate the slide moved at an average velocity of 3 m/s, a maximum velocity of 20 m/s, and involved up to 500,000 million m^3 of material, with the turbidity current having travelled down slope at least 700 km from the source. After 11 hours of evolution the turbidity current reached its terminus having grown to a thickness of several hundred metres, eventually covering an area of 160,000 km^2 of seabed in a turbidite layer several metres thick (Fine, Rabinovich, Bornhold, Thomson and Kulikov 2005; Jiang and Leblond 1992; Ruff 2003; Rzadkiewicz et al. 1997; Tinti and Bortolucci 2000b).

The Grand Banks slides initiated a tsunami that caused damage and loss of life along Newfoundland and Nova Scotia's shores. Forty isolated fishing communities on the Burin Peninsula on the south

coast of Newfoundland, directly opposite the headwall of the larger slides, were inundated by a 3 m high wave approximately two and a half hours after the earthquake. Run-up heights of 2 m to 7 m were observed, with a maximum value of 27 m at Taylors Bay. Diagrams of the Grand Banks area affected by the tsunami are presented in Figure 2.3. The waves approached the shore at 140 km/hr with two further waves following the first. The death toll from this event was 28 in Newfoundland, and due to the isolation of these villages news of the disaster did not reach the world until two days later. The damage to the communities was compounded as the tsunami surged in on top of a high spring tide. Nova Scotia felt a less devastating effect of the tsunami, with the death of only one person, as the wave had dissipated as it radiated out from the source area. A 0.5 m high wave was measured in Halifax, and was detected as far away as South Carolina and Portugal (Bryant 2001). The tsunami wave travel times are shown in Figure 2.4.

New Zealand is not immune from underwater landslides and associated tsunami generation. The 1931 Napier earthquake caused a rotational slump in the Waikare estuary sweeping water onshore to a height of 15 m above sea level (Bryant 2001; De Lange and Moon 2004; Peacock 2002). A co-seismic tsunami was also generated, with a maximum height of 3 m to 5.5 m.

The events in March and May of 1947 off the coast of Gisborne, New Zealand, generated tsunami with maximum wave heights of 10m and 6 m respectively. These wave heights were considered too large to have been generated by the magnitude of their associated earthquakes, and appeared to be aperiodic and few in number, with successive waves arriving before the complete withdrawal of the previous wave. Also, the wave height distribution decayed more rapidly with distance from the source than was expected for an earthquake-generated tsunami. Later numerical modelling determined an underwater landslide with a thickness of 125 m, total length of 6000 m, and source area of 9 km^2 located at the head of the continental slope best replicated the observed 10 m tsunami on March 1947 (De Lange and Moon 2004; Peacock 2002).

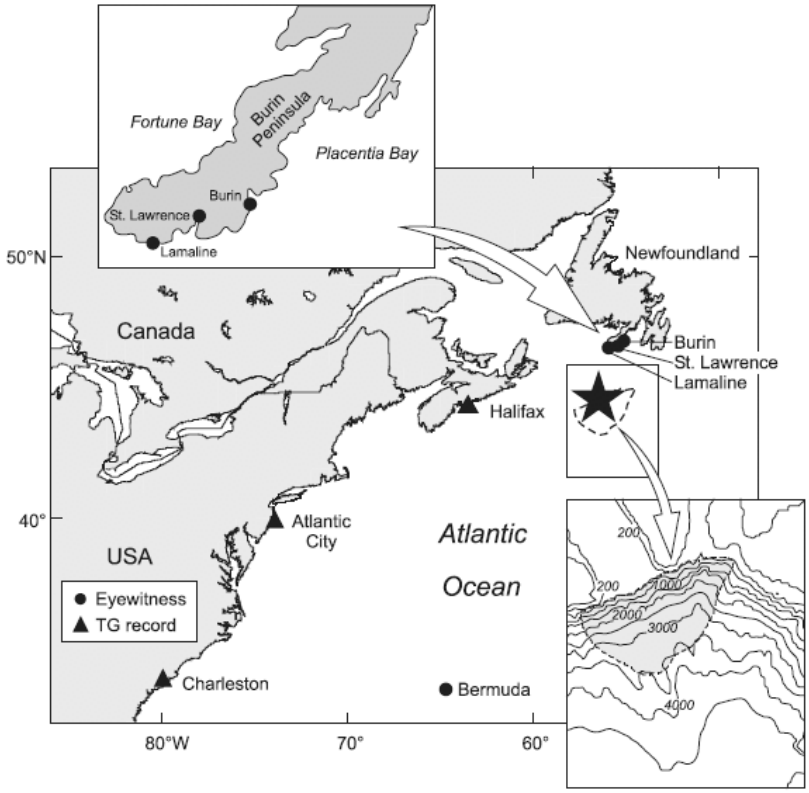

Figure 2.3. The earthquake, with the epicenter indicated by the star, initiates a landslide with an initial outline approximated by the shaded area in the lower-right inset (Fine et al. 2005).

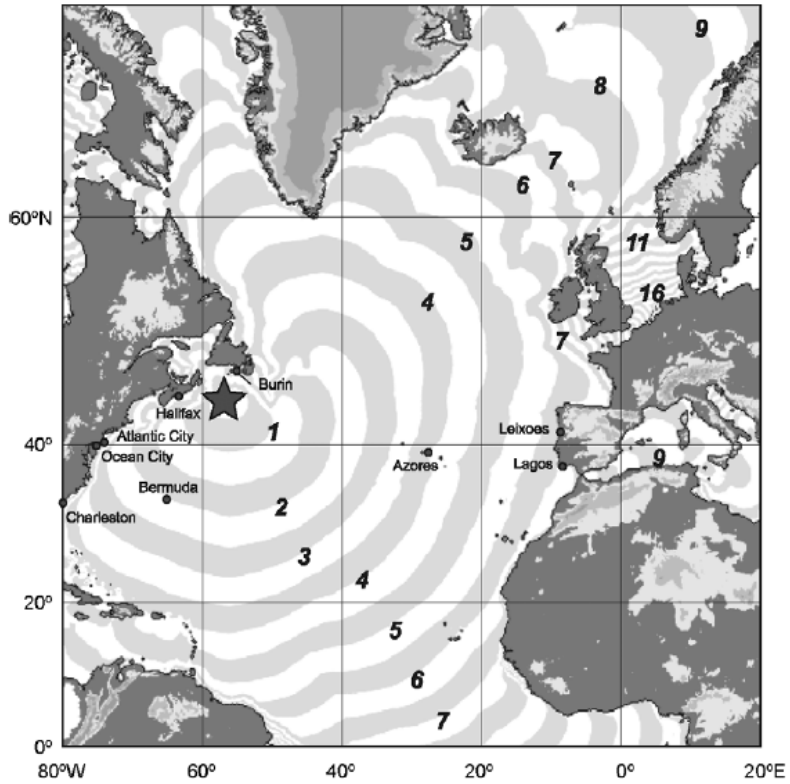

Figure 2.4. Map of estimated travel times (in hours) in the North Atlantic Ocean of the waves generated by the 1929 Grand Banks event (Fine et al. 2005).

2.3 Characteristics of Soils and Landslides

Soils are a natural substance, and as such, have a wide variety of characteristics and exhibit an equally wide range of behaviours. Some basic soil and slope mechanics are presented to detail the generation mechanism of underwater landslide-induced tsunami. How and why slopes fail is dependent on the characteristics of the soil within, and how they respond to external stimulation.

Naturally occurring soils fall into two categories, those that are formed in situ and those that have been transported to their current location. In situ soils are further divided into two categories, weathered rocks and peat. Weathered rocks consist of portions of rock fragmented by mechanical and chemical weathering, whereas peat consists of an amalgamation of organic material such as wood fibres and plant remnants. Transported soils are predominantly moved by water, wind, and ice, under the effects of gravity.

Soils are classified depending on their grain size. Based on the British Soil Classification System (BSCS) soils with grain sizes smaller than 2 μm are classed as clays, soils between 2 μm and 60 μm are silts, sands have grain sizes of between 60 μm and 2 mm, gravels between 2 mm and 60 mm, and cobbles between 60 mm and 200 mm (Barnes 2000). Soils found anywhere on the earth are made of different proportions of clays, silts, sands, gravels, and cobbles.

Soils can be further defined by particle density, shapes of the particles that compose it, distribution of particle sizes, density of the materials, cohesion, and moisture content. Even slight variations in these properties can cause soils to exhibit significantly different behaviour. A peculiar behaviour of sands and cohesionless silts is that when in the presence of water, they tend to dilate and liquify when subject to external loading.

Slope failure can be modelled by the Mohr-Coulomb failure criterion as follows (Barnes 2000; Bryant 2001):

$$\tau_s = c + (\sigma - \xi)\tan\phi \qquad \textbf{(2.4)}$$

where τ_s = soil shear strength

c = soil cohesion

σ = normal stresses on the slope

ξ = pore water pressure

ϕ = internal friction angle

The key factor in this equation is pore water pressure. The greater the saturation of the soil, the more prone it is to failure. Changes in pore water pressure can reduce the $(\sigma - \xi)$ term to zero. This may come about in the very short term by the passage of seismic waves, in the medium term by changes in water level and air pressure associated with large atmospheric depressions, and in the very long term with changes in sea levels (Bryant 2001). With the normal stress negated by the pore water pressure, the soil strength is reliant solely on the cohesion of the soil or rock. Cohesion within the soil structure arises from the attraction between the clay and fine silt particles. Soils devoid of these, especially sands, are at greater risk of failure due to the lack of cohesion and a phenomenon known as liquefaction.

Large landslides tend to occur in materials susceptible to liquefaction (Finn 2003). When saturated pockets of loose sands and cohesionless silts encounter sufficient ground motions, they can exhibit a flowing tendency. Ground-shaking tends to compress these loose soils, but they are unable to do so due to the inability of the pore-fluid to escape from the soil void spaces in the relatively short time of shaking. Earthquake-induced liquefaction is even more likely in offshore environments as the soils are always saturated. It is interesting to note that failure is also possible some time after an event due to changes in soil strength through the redistribution of pore water (Wright and Rathje 2003).

If the driving stress is larger than the post-liquefaction strength, then a liquefaction flow failure develops resulting in large displacements. Sometimes, the liquefied soil may have enough residual strength to resist the static forces applied to it, but with the momentary addition of dynamic stresses with the passage of seismic waves may no longer have adequate strength. Limited displacement, or cyclic mobility, may then occur where movement only occurs when the combination of static and dynamic stresses momentarily exceed the soil strength.

The extent of deformation can range from minor cracking, to slumping, to full mobility where the slide material is essentially unimpeded until the retarding force on the slide finally exceeds the driving (gravitational) force (Ishihara 2002). Liquefaction of sands and cohesionless silts in a saturated state exhibit this peculiar type of behaviour clearly. Figure 2.5 illustrates the stress-strain behaviour of these soils. The external stresses imposed on the soil induce strains, and the soil deforms to a limited extent. The stresses can increase further until some value of maximum undrained strength is reached after which the structure collapses. The resistance drops to a low level that can be maintained for large values of strain, called residual strength, and is the controlling factor in determining the extent of post-liquefaction stability. If the driving gravitational shear stresses are considerably higher than the residual strength, then very large deformations and displacements can result. The initiation and continuance of liquefaction is controlled by the intensity and duration of the loading.

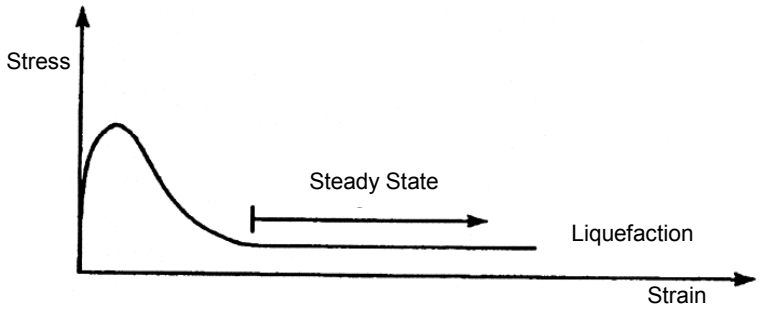

Figure 2.5. Stress-strain behaviour of soils (Finn 2003)

Triggering mechanisms of landslides vary widely. The most common cause is acceleration-induced sliding in which the inertial forces associated with earthquakes cause the driving forces to momentarily exceed the resistance of the soil, initiating movement. If the accelerations are strong, or continue for long enough, the slope may deform excessively or fail completely (Wright and Rathje 2003). Earthquakes also serve as triggers for initiating the movements that combine with other mechanisms, such as liquefaction, to cause the slope to fail.

2.4 Underwater Landslides

The marine and fresh water environments essentially experience the same mass failures as those found on land. As such, most of the underwater landslide geological theory has come from traditional terrestrial slope stability analysis. Much has been published on terrestrial landslides and is generally very well understood. Existing turbidity current mechanics comes from that of avalanches, as both are forms of gravity current, with solid particles suspended in a fluid.

Tsunamigenic landslides fall under three categories depending on the origin of the landslide relative to the water. As shown in Figure 2.6, these are sub-aerial, partially submerged, and submarine or underwater landslides. The initial position of the landslide determines the key physical characteristics of the interaction of the sliding mass and the fluid, and in particular the entrainment of air. Sub-aerial events are considered to be three-phase flows as they contain solid slide material, liquid water, and gaseous air. Underwater landslides are two-phase flows involving only slide material and water.

2.4.1 Landslide Initiation

The advent of detailed side-scan sonar and other recent improvements in underwater survey and mapping techniques have helped to identify which tsunami were most likely created by underwater land sliding instead of earthquakes. However, earthquakes are often the mechanism for triggering the landslide initially. Other causes of underwater landslides are; storm wave loading, oversteepening, changes in sea levels, rapid accumulation and under-consolidation, gas charging, gas hydrate disassociation, low tides, seepage, glacial loading, and volcanic island processes (Locat and Lee

2002). Geological evidence of underwater slides includes headscarp features, large cracks, amphitheatre structures, and hummocky or blocky topography.

Acceleration, liquefaction, and fault rupture-induced landslides occur in both terrestrial and underwater environments. Some landslide triggering mechanisms are limited only to offshore situations, such as water wave-induced sliding. The seafloor in water depths less than 100m are at particular risk to disturbance from the large changes in stress caused by large ocean waves, such as those generated by severe low-pressure weather systems or by the passage of tsunami. The rapid draw-down of water levels at the shore as a tsunami approaches is also capable of removing the resisting force on the slope and could induce a slope failure leading to further tsunami generation mechanisms. Though widely accepted as a mechanism for potential instability in earth dams, any slope comprised of fine-grained soil that is marginally statically stable is susceptible to slope failure triggered by rapid water draw-down.

Surface fault ruptures can significantly change the surface profile of slopes, triggering sliding. Slopes that are marginally stable before the rupture can be more susceptible, and many offshore processes, such as sediment deposition on active river deltas and continental slopes, leave the soil in marginally stable states. Such landslides may only be small, affecting the local area around the rupture, but could be a prompt for a much larger slide.

A process known as under-consolidation can also increase pressures within the soil as natural gases, such as methane, are formed when organic matter in the soil decays anaerobically. Methane on the lower slopes of the deep ocean can often be locked into the sediment as a solid gas hydrate due to the extremely cold temperatures and pressures. As the hydrate decomposes back into methane, it can further increase the pressure with the release of gas, or form voids in the sediment to become planes of weakness.

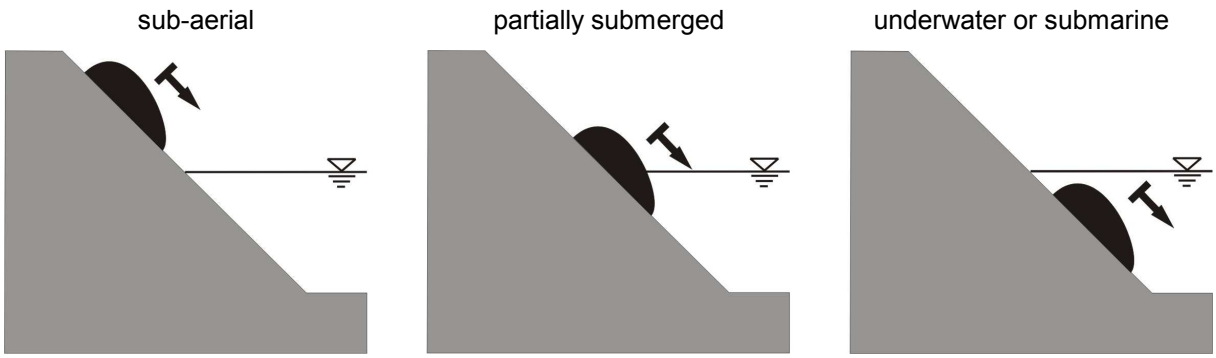

Figure 2.6. Sub-aerial, partially submerged, and underwater and submarine classification of landslides.

2.4.2 Classification and Characteristics of Underwater Landslides

There are many types of underwater mass movements. These are summarised in Figure 2.7, and include rotational and translational slides, debris and mud flows, and turbidity currents. Each event consists of several distinct phases, starting with slide initiation, triggering mechanisms some of which were discussed earlier. Often, slides then transition into a debris flow regime, with subsequent generation of a turbidity current and its motion along the sea floor until final deposition.

There is an extensive literature on landslide morphology and the papers of Hampton et al (1996), Locat and Lee (2002), and Finn (2003), are typical works dealing with the theory of the interaction of soil and fluid. After the initial slope failure, some landslides can evolve from the limited displacement of slides and slumps into more mobile flow structures. This transition is currently not well understood. The final density of the slide material will depend in its flow behaviour. Similar to snow avalanches, the flowing material separates into two layers, the suspension flow over-riding the dense flow. Dense flows can take the form of rock avalanches, debris flows, and mudflows. Suspension flows are generated by the drag forces on the upper interface of the dense flow and can become turbidity currents if they overtake the bottom denser layer. At some critical speed, thought to be approximately 5 m/s, hydroplaning can cause the nose of the dense flow to lift, reducing the shearing resistance along the sliding surface, and adding mobility to the flow. A continual regime of erosion and sedimentation will occur at the interface of the dense flow and the rigid base. These processes can occur on slopes as small as fractions of a degree, and are illustrated in Figure 2.8.

Underwater landslides are often found to occur on slopes less than 10 degrees (McAdoo, Pratson and Orange 2000). This indicates that although the vertical component of the landslide motion may be small, it is enough to create the initial disturbance of the water surface, causing a large wave to develop with the continuing motion of the failure mass. Landslides have a wide range of run-out distances, from short rockfalls and rotational slumps, to long run-out associated with debris flows and turbidity currents. The steepness of the slope adjacent to the failure has been found to be inversely proportional to the length of landslide run-out, indicating failures on steep slopes tend to have less run-out than failures on shallow slopes. Such long run-out lengths along shallow slopes, sometimes of the order of hundreds of kilometres, is only beginning to be understood but the main reason is thought to be hydroplaning of the failed mass (Locat and Lee 2002). Run-out length may well be influential in tsunami generation, but is currently not well researched.

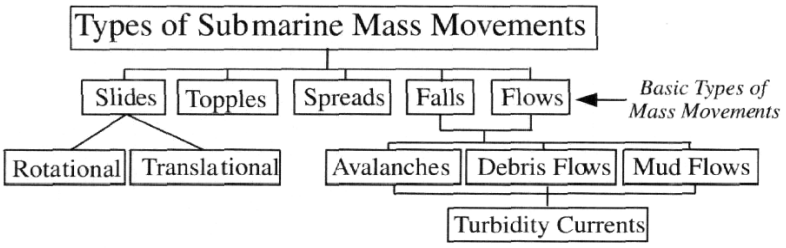

Figure 2.7. Classification of submarine mass movements (Locat and Lee 2002).

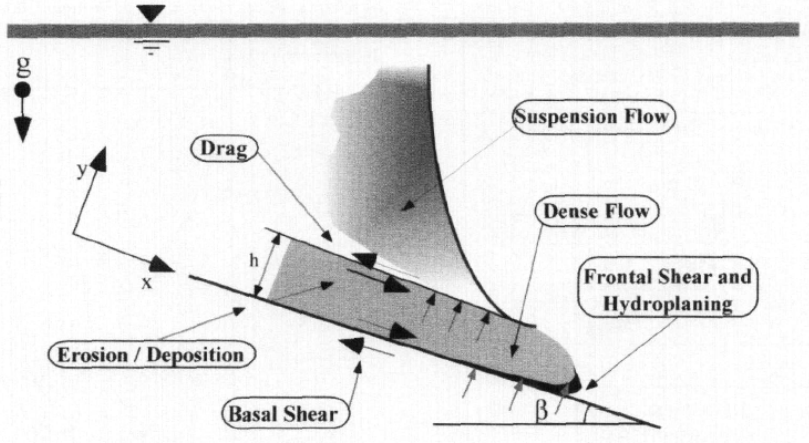

Figure 2.8. Schematic view showing the different flow structures for a hydroplaning dense flow (Locat and Lee 2002).

Observations and computer modelling of both sub-aerial and underwater landslides show they tend, in plan, to have elliptical shapes, width-to-length ratios of 0.5-1 (Martel 2004), and mean thickness to length ratios of approximately 0.01 (Watts and Grilli 2003). Slide material from a rotational slump generally does not move far from its original position, whereas sheet slides can transport slide blocks considerable distances. This sustained movement of a sheet slide allows the material to disintegrate into a debris avalanche and possibly into a turbidity current if the landslide occurs in water.

2.4.3 Historical and Prehistorical Underwater Landslides

One of the largest known underwater landslides occurred 200,000 years ago on the northern flanks of the island of Oahu, Hawaii (Bryant 2001). Known as the Nuuanu landslide, it involved the mobilisation of 5000 billion m^3 of material across a slide scar of 23,000 km^2. This slide ran down 220 km into the 4,600 m deep Hawaii Trough and back up the other side of the underwater canyon to a final water depth of less than 4,300 m. Calculations using the analogy of a frictionless roller coaster, the speed of the slide must have been approximately 80 m/s to be able to run up a height of 350 m (Ward 2001). 140 km offshore of Oahu is the Tuscaloosa Seamount, which with a size of 30 km in length, 17 km in width, and with a 1.8 km thickness, is actually a detached block from the Nuuanu debris avalanche (Hampton et al. 1996). A side-scan sonar mosaic of the Nuuanu landslide is shown

in Figure 2.9. Numerical models of this landslide predict waves of up to 60 m in height striking the beaches of the Hawaiian Islands, and waves of 20 m along the North-west Pacific coastline.

Three massive underwater landslides, with a combined volume of 5580 billion m^3, occurred off the west coast of Norway. The largest of these slides occurred 30,000 years ago at Storegga involving 3880 billion m^3 running 500 km down the continental slope from a water depth of 500 m to over 3000 m (Hampton et al. 1996; Ward 2001). Computations indicate 12 m and 6 m high wave run-ups would have reached Norway and Iceland within two hours of the start of the event respectively. A set of waves up to 15 m in height spread out across the Atlantic Ocean.

Figure 2.9. Side-scan sonar image of the Nuuanu (off Ohau) and Wailau (off Molokai) debris avalanches, Hawaii. Individual displaced blocks, the largest being the Tuscaloosa Seamount, appear as distinct light areas, generally becoming smaller away from the islands (Hampton et al. 1996).

The natural mass-wasting processes are continually moving surface soil offshore into the deep ocean. Along New Zealand's eastern coast, terrestrial erosion is occurring rapidly due to the rapid uplift of the land mass and the large networks of rivers delivering the sediment to the coast. It has been estimated that 1% of all sediment input into the worlds oceans originate from New Zealand (Andrew and Francis 2003). This rich and continual supply of sediment to the continental shelf and high seismicity, associated with the proximity to the plate boundary, provides an environment conductive to underwater landslides. A complex of sheet slides and rotational slumps, ranging from 20 m to 140 m thick and covering a total area of 720 km^2, has been found on the shallow slopes off the coast of Cape Kidnappers on the North Island's east coast (Barnes, Cheung, Smits, Almagor, Read, Barker and Froggatt 1991). Even though it is not known if these slides were tsunamigenic, it highlights that the processes necessary for underwater landslides exist around New Zealand.

2.5 Summary

In Sections 2.1 and 2.2 of this chapter a review of the English language literature illustrated the characteristics, and chronological and global extent of underwater landslide-induced tsunami events. Compared to earthquake-induced tsunami, underwater landslide tsunami essentially can be considered as a point source mechanism. As such the extent of damage of underwater landslide tsunami are generally more constrained than those with earthquake origins. The danger of landslide tsunami is the short travel times. Details of the characteristics of soils were given in Section 2.3 along with how these soils behave under external loading. Particular attention was given to the liquefaction of saturated sands and cohesionless silts, especially in marine environments where these soils are abundant. Typically triggered by seismic events, movement of underwater sediments often occur in liquefiable sands. The tendency for saturated sands to compress when shaken increases the pore water pressures, reducing the shear strength of the soil. Section 2.4 on initiation and morphology of underwater landslides highlighted the variety of forms an underwater landslide can take. The run-out length of underwater landslides was found to be inversely proportional to the slope angle.

Chapter 3: Literature Review II: Tsunami Modelling

This chapter reviews the literature pertaining to laboratory and numerical modelling of underwater landslide induced waves, beginning with a presentation of previous experimental work on the generation of landslide tsunami waves in Section 3.1. Scaled-down experiments are one of the few avenues in which to explore the phenomena of tsunami. The laboratory environment is ideal for the controlled and repeatable generation of water waves, and allows the use of an array of measurement techniques. However, there are many difficulties facing laboratory tests, the main one being the reproduction of real scale dynamics and configurations at small laboratory scales. The experimental work reviewed in this chapter includes two- and three-dimensional tests, benchmark tests, and tests to measure sub-surface velocities.

Section 3.2 follows with some background into the numerical simulation of these phenomena. It is difficult to allow for the complexities in nature, such as varying bathymetry, bottom roughness, and landslide geometry, in laboratory experiments. Due to surface tension issues, it also becomes difficult to scale up laboratory results to apply them in the field. Therefore, modelling of actual events is left to numerical models. Laboratory experimental results and field measurements of actual events provide the only means with which to calibrate and verify the numerical models. To some extent validated models possess some predictive qualities. Model complexity varies from simple empirically based relationships to those capable of modelling wave run-up and sub-surface quantities. This section also includes some examples of the use of these models in the simulation of actual events.

3.1 Experimental Modelling of Underwater Landslide Tsunami

Experimental research into underwater landslide-induced tsunami began in 1955 to dispel the belief of many at the time that disturbances such as underwater landslides were unlikely to cause tsunami. As previously discussed, the type of underwater mass failure is based on the landslide geometry and on the characteristics of the failure material, such as chemical composition, grain size, and density. Due to the inherent difficulties with the scaling of these factors, the landslide failure mass is often approximated experimentally by a solid mass, either triangular or semi-elliptical in shape.

3.1.1 Two-dimensional Experiments

Due to the difficulties with using granular materials, Wiegel (1955) preferred to experiment with sliding and falling blocks of various shapes, sizes, and densities. Some exploratory work (Sauer and Wiegel 1946) was conducted to try to generate underwater landslides with granular material, but ended with little success. Coarse gravel was piled steeply on a sheet of metal at one end of a channel. The sheet was pulled and the disruption to the sand pile caused it to collapse. However, it was found that this tended to result in a slump failure of the sand rather than a true slide. Another attempt to

generate granular landslides was made by piling sand behind a vertical gate, and pulling the gate vertically out of the water. However, the removal of the gate generated waves of the same magnitude as those produced by the movement of the sand. This led Sauer and Wiegel (1946) to suggest the use of a box sliding down an incline as a model for an underwater landslide.

Wiegel's (1955) two-dimensional tests were performed in a 60 ft long, 3 ft deep by 1 ft wide channel. The first set of experiments used a submerged wooden box sliding down an incline with a 45° slope in water 2.5 ft deep. The box was triangular in cross-section (12 in x 12 in) and extended across the entire width of the channel. Six different weights at three initial landslide elevations were investigated. Wave recorders were used to measure the water surface time histories at 8 ft and 25.5 feet downstream from the original intersection of the free surface and the incline. An inclined beach was installed at the far end of the wave channel to reduce wave reflections, with limited success. The second set of tests utilized wooden rectangular boxes and lead plates of various dimensions to model an underwater landslide. Factors such as initial submergence, slope angle, and water depth were varied, and the wave characteristics were measured using parallel-wire resistance wave gauges at both near and far field locations.

Surface time histories downstream of the disturbance showed a crest formed first, followed by a trough with amplitude one to three times that of the first crest, and followed by a crest with a similar magnitude to the trough. It was found that dispersive waves were generated, as crests and troughs continued to be generated with increasing distance, and the amplitudes of the waves diminished as they propagated. The magnitude of the wave heights were found to depend primarily on the block weight, initial submergence, and water depth. For the second set of experiments specifically, the amplitudes of the initial crests and troughs were smaller for the flatter slopes, and increased rapidly as the slope increased. The amplitude tended to a maximum value as the slope approached the vertical.

The period of the waves was found to be independent of water depth, initial landslide submergence, weight, and duration of movement. It was, however, found to increase with increasing block length and decreasing incline angle. The period between slide initiation and the first crest, measured using a wave gauge at the near field location, was found to be less sensitive to slope than the period between the first two crests. Computations, using Equation 3.1, indicated approximately 1% of the initial net submerged potential energy of the sliding block was transferred into wave energy, with this percentage increasing with reduced initial submergence and decreasing water depth. As the waves were found to be dispersive, it was convenient to calculate the energy from measurements close to the origin, when the energy was concentrated in one wave. As such, the wave height, H, was approximated by the combination of the amplitudes of the first trough and second crest.

$$E_p = gwH^2T^2/16\pi \quad \textbf{(3.1)}$$

where g = gravitational acceleration
w = unit mass of water
H = wave height
T = wave period

Other experimentalists have chosen to simulate an underwater landslide with a right-triangular prism sliding down a 45° slope (Rzadkiewicz et al. 1997; Watts 1997; Watts 1998; Watts 2000; Watts and Grilli 2003).

The two-dimensional experiments of Rzadkiewicz, Mariotti, and Heinrich (1997) were a short series of tests to produce data to compare directly with some of their numerical models. These tests involved right-triangular simulated landslide masses, consisting of solid blocks sliding down a 45° slope, and granular sand and gravel sliding down 30° and 45° slopes. The tests were performed in a channel 4.0 m long, 0.3 m wide, and 2.0 m deep.

For the rigid block tests a triangular box, with cross-section 0.5 m by 0.5 m, spanned the width of the channel. Only one landslide specific gravity, equal to 2.0, was used. The top surface of the landslide was initially 0.01 m below the free surface in water 1 m deep. Side-on photographs were captured at 0.5 s and 1.0 s after slide release, and from these landslide shape and water level profiles were coarsely digitised. Instead of direct measurements, their numerical model estimated the landslide velocities.

For the granular tests a triangular landslide, with cross-section 0.65 m by 0.65 m, spanning the width of the channel, and with a specific gravity of 1.95, was used. The top surface of the landslide was initially 0.1 m below the free surface in water 1.6 m deep. Granular materials with three grain-size ranges were used. The first had grain diameters in the range of 50 μm to 250 μm, the second from 0.8 mm to 2 mm, and the third from 2 mm to 7 mm. The granular material was held in place by a vertical gate, which was lifted up to release the landslide mass. It took approximately 0.1 s for the gate to be lifted clear of the water surface, and generated waves of the order of 5 mm when there was no landslide present. For experiments on the 30° slope or with grain sizes less than 250 μm, the landslide generated waves were of similar magnitude to those generated by the gate retraction. For coarse material sliding on a 45° slope, side-on photographs were captured at 0.4 s and 0.8 s after slide release, and from these landslide material shape and position, and water level profiles were digitised.

Watts' (1997) experiments were similar, consisting of solid and granular slides along a 45° slope, as illustrated in Figure 3.1. However, a wider parameter space was investigated, with slide material, initial submergence, porosity, and density varied. The experiments were performed in a 9.14 m long, 0.66 m high, and 0.10 m wide wave tank. The planar incline and half of the length of the wave tank was constructed of Lucite, allowing video capture of parts of the experiments.

For the solid block tests, four right-angle triangular blocks with various volumes were constructed. A hole was drilled horizontally through each of the blocks' center of mass to provide a cavity in which cylindrical pieces of brass or lead could be inserted to vary the weight. A micro-accelerometer screwed to the top surface of the blocks recorded the landslide's acceleration time history. For the solid block tests a 0.62 mm thick nylon sheet was placed over the incline surface to cover over slots cut into the incline for a retractable gate. The block was held in place by a length of nylon string, and was released by manually letting go of the nylon. The timing of landslide release was determined by shining a low-powered laser partially across the front of the solid block and partially onto a photodiode. A systematic change in the photodiode voltage indicated the release of the block.

The landslides accelerated almost instantaneously to a maximum, after which the accelerations decayed as the landslides approached terminal velocity. The initial acceleration was measured directly from the accelerometer or from analyzing movie clips of the slide. Initial acceleration estimates from the accelerometer were up to three times more accurate than accelerations estimated from the movie clips. Initial accelerations measured during the experiments ranged between 0.83 m/s^2 and 2.41 m/s^2, with a maximum absolute error or ± 0.27 m/s^2. Estimates of the landslide terminal velocity were determined by letting the block slide 0.80 m down the incline and measuring the time taken for it to traverse two laser beams spaced slightly apart at the lower end of the incline. This was repeated at least 13 times to provide error estimates. Terminal velocities of the solid block experiments ranged between 0.34 m/s and 0.8 m/s, with maximum absolute errors of ± 0.024 m/s. Even though the laser beams were near the base of the slope the true terminal velocity was not reached, as the accelerations were still positive before the landslide reached the bottom of the incline.

Watts (1997) also gave theoretical expressions to calculate the initial acceleration, a_o, and terminal velocity, u_t, as given by Equations 3.2 and 3.3. Terminal velocity may not be a suitable parameter in all situations, as not all landslides reach terminal velocity. The theoretical values of initial acceleration and terminal velocity may be difficult to estimate as the Coulomb friction, added mass, and drag coefficients are not well defined for all landslide geometries and configurations.

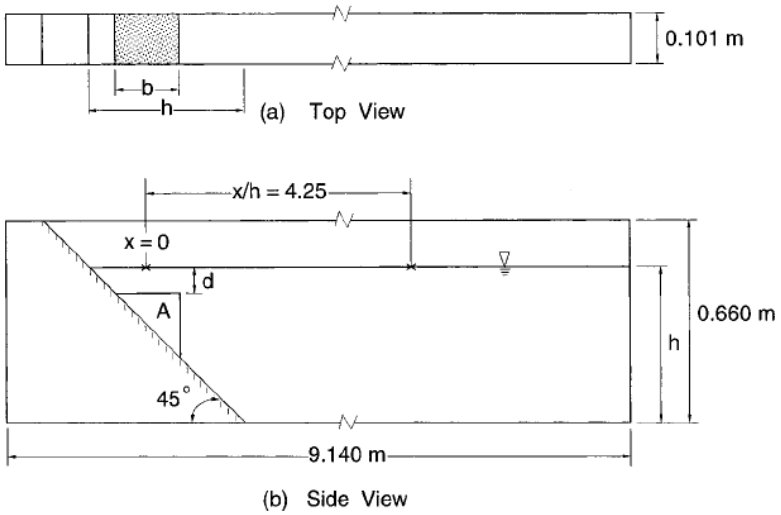

Figure 3.1. Diagram showing the test arrangement of Watts' (1997) 2-dimensional laboratory experiments with sliding triangular masses. The positions of the resistance wave gauges used are shown at the top of the side view (Watts 2000).

$$a_o = \frac{g(\gamma - 1)(\sin\theta - C_n \cos\theta)}{\gamma + C_m} \tag{3.2}$$

$$u_t = \sqrt{\frac{4Bg(\gamma - 1)(\sin\theta - C_n \cos\theta)}{3C_d}} \tag{3.3}$$

where g = gravitational acceleration

γ = specific density

θ = incline angle

B = slide length parallel to the slope

C_n = Coulomb friction coefficient

C_m = added mass coefficient

C_d = drag coefficient

Watts (1997) calculated a characteristic distance of motion, s_o, and a characteristic time of motion, t_o, as given by Equations 3.4 and 3.5. Physically, s_o and t_o correspond to the distance and duration during which significant wave generation processes are taking place. The uncertainty surrounding the calculated values of initial acceleration and terminal velocity may lead to significant ambiguity in s_o and t_o.

$$s_o = \frac{u_t^{\,2}}{a_o} \tag{3.4}$$

$$t_o = \frac{u_t}{a_o} \tag{3.5}$$

The expression derived to characterize the landslide position time history, s(t), is given by Equation 3.6. An example of a comparison of landslide centre of mass position data measured directly from high speed movie clips (dots) to the position calculated using Equation 3.6 (solid line) is shown in Figure 3.2. The effect of errors in the calculation of characteristic distance and time result in the dashed lines.

$$s(t) = s_o \ln[\cosh(t / t_o)] \tag{3.6}$$

Resistance wave gauges were used to measure water level time-histories at two locations. The first gauge was positioned above the middle of the initial landslide location, to measure the near-field wave characteristics, and the other was placed 4.25 channel depths, h, downstream to measure the far-field characteristics. Examples of the near and far field waves measured for solid block landslides of various mass, with initial submergence, d = 74 mm, are plotted in Figure 3.3. Examples of the repeatability of the water level measurements at the far-field wave gauge are shown in Figure 3.4. The two trials represented in Figure 3.4a used a block with horizontal length, b, of 85.2 mm, a mass, m_b, of 0.359 kg, and an initial submergence, d, of 40 mm. The repeatability of these two trials was considered exceptional (Watts 1997). The two trials represented in Figure 3.4b used a block with b = 61.2 mm, m_b = 0.3399 kg, and d = 81.5 mm. The repeatability of these two trials was considered very poor (Watts 1997). Even for the experiments considered repeatable, there was still considerable variation in wave amplitude and timing. As the far-field wave gauges were considered accurate to within 0.25 mm, the differences in wave field generated can most likely be attributed to variations in the sliding dynamics of the landslide between the two repeats.

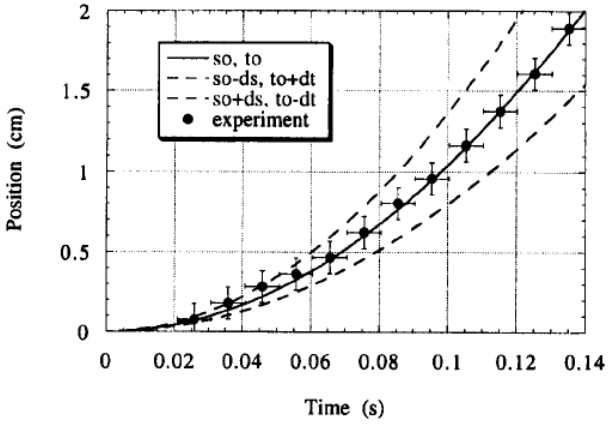

Figure 3.2. An example of a comparison of measured landslide centre of mass position data (dots) to position calculated using Equation 3.6 (solid line). The effect of errors in characteristic distance and time result in the dashed lines (Watts 1997).

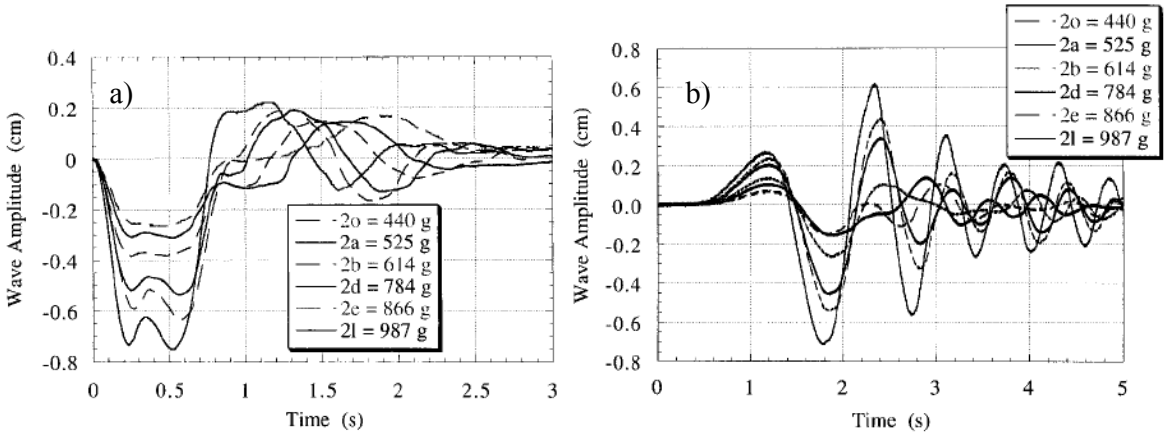

Figure 3.3. Water level time histories, from Watts' (1997) experimental tests, measured at the a) near field wave gauge, and b) far field wave gauge for six block masses. The initial submergence of these solid blocks was 74 mm.

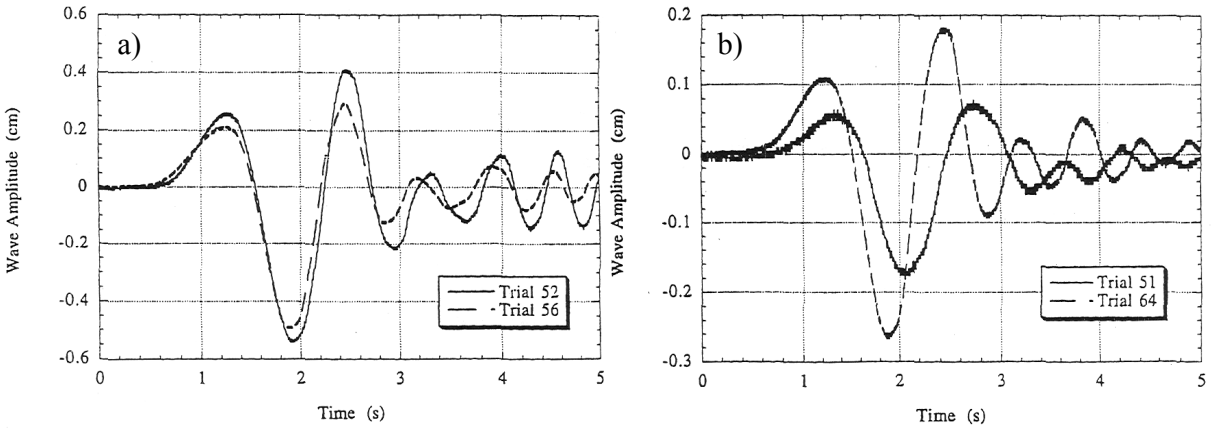

Figure 3.4. Examples of the repeatability of water level measurements considered a) exceptional, and b) poor (Watts 1997).

Watts' study also developed a non-dimensional framework in which to predict maximum wave amplitudes (wave troughs) from specific solid block landslide parameters. It was assumed that landslide motion was governed by only one characteristic distance, s_0, and one characteristic time, t_0. The Hammack number, as shown in Equation 3.7, governed the characteristic wave amplitudes. Figure 3.5 plots a wavemaker curve generated by Watts (1997) in which the near-field characteristic wave amplitude , η_{max}, has been non-dimensionalised by the landslide initial acceleration, a_0, and terminal velocity, u_t.

$$\frac{\eta}{s_o \sin\theta} = \frac{1}{Ha_0} f\left(\frac{b}{d}, \theta, Sg, Ha_0\right) \tag{3.7}$$

where η = free surface amplitude

θ = slope angle

$Ha_0 = t_0\sqrt{(gd)}/b$ = Hammack number at $t=t_0$

g = gravitational acceleration

b = horizontal length of landslide

d = initial submergence

$Sg = s_0 \sin\theta / d$ = submergence number

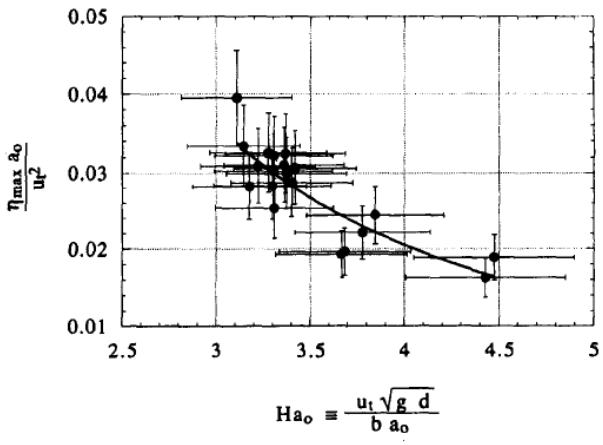

Figure 3.5. An example of a wavemaker plot from Watts' experiments with solid block landslides on a 45° slope (Watts 1997).

The solid line in Figure 3.5 is a power law curve fit to the experimental data, and is given by Equation 3.8.

$$\frac{\eta_{\max} a_o}{u_t^2} = \frac{0.33}{Ha_o^{2.01}} \tag{3.8}$$

η_{max} is the absolute value of the largest near-field wave amplitude, measured above the initial landslide position, and was always found to correspond to a wave trough. It was also found that the near-field wave amplitude was proportional to the expression given in Equation 3.9.

$$\eta_{\max} \propto \frac{c^{1.75}}{d^{0.75}} \tag{3.9}$$

where c is the height of the vertical front face of the landslide and d is the initial submergence. The author stated that the vertical front face of the landslide generated a positive wave in front of the landslide, while the horizontal face of a landslide generated a negative wave above the landslide. The shoreward side of the negative wave propagating away from the incline was found to be highly dispersive and gave rise to higher frequency water waves. Following the trough, a rebound was observed forming a smaller positive wave. This rebound occurred earlier for more massive blocks although the amplitude of the rebound was nearly constant. This dispersion was noted by earlier researchers, including Weigel (1955).

The wavemaker curve incorporates the key physical processes present in solid block landslides. For a given landslide geometry, the maximum amplitude of a wave trough in the near-field can be estimated using Equation 3.8, provided the landslide initial acceleration and terminal velocity can be estimated. Reductions in initial submergence and increases in landslide volume result in a decrease in Ha_o and hence an increase in the amplitude of the maximum near-field trough. The effects of landslide mass and shape, slope angle, and sliding friction are incorporated in the expressions or measurements of terminal velocity and initial acceleration.

The far-field characteristic wave amplitude, η_{airy}, is the maximum amplitude of the leading wave in the wave train measured at the far-field wave gauge. η_{airy} was always a wave crest. The correlation between η_{airy} and η_{max} is given by the expression in Equation 3.10, and is plotted in Figure 3.6. The constant corresponds well with the observations of Weigel (1955) in which the leading crest was followed by a trough with amplitude one to three times that of the crest.

$$\eta_{airy} \approx 0.30\eta_{\max} \tag{3.10}$$

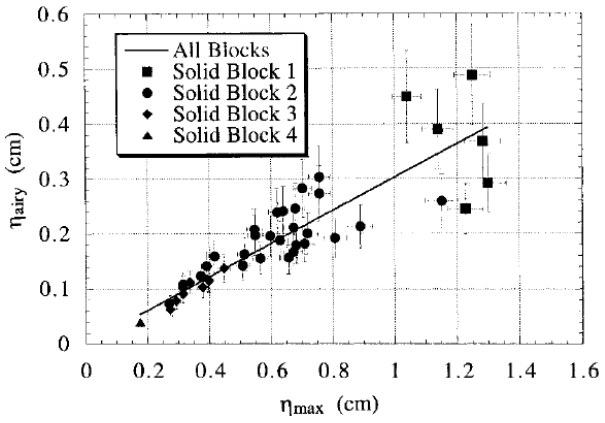

Figure 3.6. Characteristic near-field wave amplitude, η_{max}, correlation with the characteristic far-field wave amplitude, η_{airy} (Watts 1997).

Watts (1997) also considered the wave energies. The limitations of point wave gauges meant the energy estimates were a measure of the total wave potential energy passing a particular downstream location, x/h, where x is the downstream distance relative to the initial landslide centre of mass horizontal position and h is the water depth. The potential energy passing a wave gauge location at x/h was shown to be proportional to the expression in Equation 3.11.

$$E_p(x/h) = \int_0^\infty \eta^2(t, x/h)dt \tag{3.11}$$

The shortcoming of this approach was that the upper limit of integration was not physically possible. In reality the energy integral was evaluated for between 5.5 s and 6 s, or until waves reflecting off the far end of the wave tank reached the wave gauges. The waves that had not passed the wave gauges were not included in the calculation of total wave potential energy. This was particularly problematic for the gauges furthermost downstream as the wave train was still passing the gauge location when the reflections off the end of the tank had returned to the gauge. This resulted in standard errors for the energy integral in excess of ±34%. The non-dimensional energy integral at x/h = 0 as a function of non-dimensional initial submergence is shown in Figure 3.7. A power law curve fit through the origin provides the expression shown in Equation 3.12.

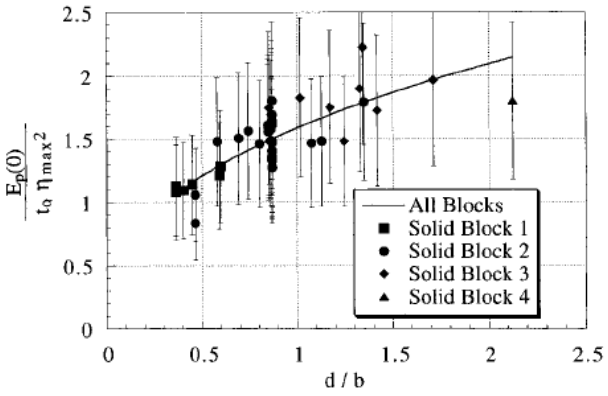

Figure 3.7. Non-dimensional energy integral calculated at the near-field wave gauge as a function of non-dimensional initial submergence (Watts 2000).

$$\frac{E_p(0)}{t_o \eta_{\max}^2} \approx 1.59\left(\frac{d}{b}\right)^{0.40} \tag{3.12}$$

Figure 3.8 shows an example of the variation of energy integral as a function of downstream location for a trial with initial submergence d = 59 mm and water depth h = 359.5 mm. The trial was repeated three times with three wave gauge records per repeat. The base of the incline was at x/h = 0.72. At x/h = 0, the energy integral had a value of $E_p(0) = 0.19$ cm^{2}s. At approximately x/h = 0.5, the energy integral peaked at a value of almost twice that at the origin, and more than twice the value of energy at the far-field asymptote at x/h = 4.2. Watts (2000) stated that as the total energy propagating out of the generation region could be no more than two times the far-field potential energy, at least 20% of the wave energy at x/h = 0.5 must have been derived from a standing wave, presumably standing relative to the moving landslide. However, the validity of this is unclear due to the inaccuracy of the measured energy integrals. The trough that was always observed above the moving landslide accounted for the standing wave. This trough was considered to be due to the low pressure region caused by flow separation on the horizontal face of the landslide. In the near-field region, all the wave energy was invested in wave potential energy. Beyond x/h = 0.5 the potential energy was steadily transferred into kinetic energy, until equipartitioning was achieved as x/h $\rightarrow\infty$.

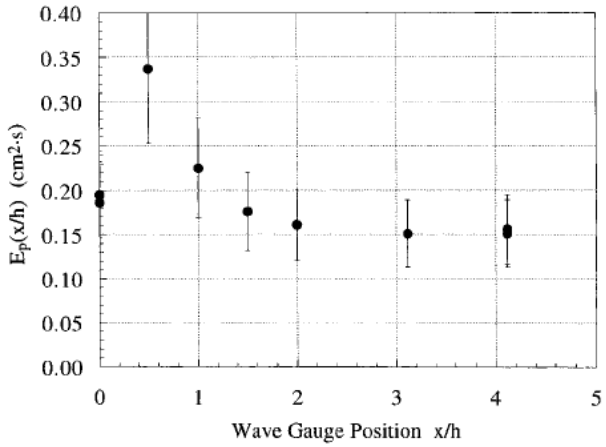

Figure 3.8. Variation of energy integral, Ep, with downstream distance, x/h (Watts 1997).

The conversion of landslide kinetic energy into wave potential energy was also considered. Watts (1997) used Equation 3.13, the energy per unit width for one wavelength of an infinite train of sinusoidal waves, as an estimate of the wave potential energy.

$$E \equiv \frac{\rho_o g \eta_{\max}^2 \lambda_o}{2} \tag{3.13}$$

where ρ_o is the water density and λ_o is a characteristic near-field wavelength. The conversion of maximum landslide kinetic energy into wave potential energy, e, was calculated by Equation 3.14.

$$e = \frac{2 m_o g \eta_{\max}^2 \sqrt{gd}}{m_b a_o u_t b^2} \tag{3.14}$$

where m_o and m_b are the displaced mass of tap water and landslide mass respectively. Figure 3.9 plots the energy conversion percentages as a function of non-dimensional initial submergence. Most of the experiments converted between 2% and 8% of the maximum landslide kinetic energy into wave potential energy. The energy conversion increased for shallower initial submergences. Equation 3.15 gives a power law curve fit to the data. The standard error of energy conversion is ±19.5%.

$$e \approx 3.82 \left(\frac{d}{b} \right)^{-0.62} \tag{3.15}$$

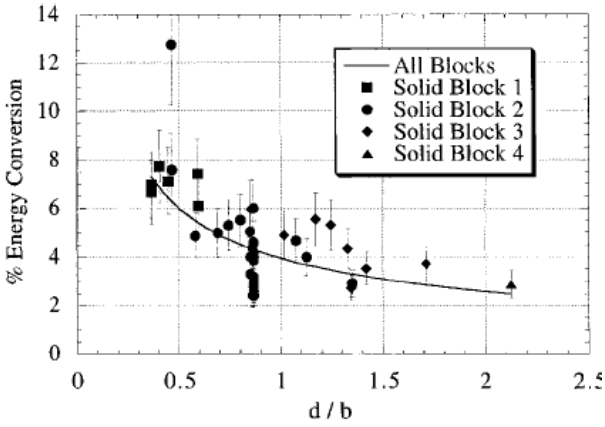

Figure 3.9. Characteristic conversion of solid block kinetic energy into wave potential energy (Watts 1997).

For the granular slide experiments, a thin metal gate was used to support the granular material impounded behind it. The vertical gate was retracted down through the incline in about 40 ms by a length of nylon string connected by a pulley system to a falling weight. Granular material landslides consisting of crushed calcite, glass beads, marbles, steel shot, lead shot, and garnet sand, with various grain diameters, were trailed. All the landslides had a similar total volume (material volume + interstitial volume) of approximately 370 ±15 mL. Movie clips of the material landslide experiments were recorded at 400 Hz. From every third or fourth frame, the outline of the landslide mass was traced and digitized. From these, image processing calculated the landslide centroid position and deformation.

It proved difficult to estimate the initial acceleration and terminal velocity of the slides from the movie clips directly. Instead, the landslide centroid position time history, s(t), was plotted and the characteristic distance and time of motion in Equation 3.6 were found through curve fitting techniques. Characteristic distances for the granular landslide experiments ranged between 11.6 cm and 38.4 cm, with maximum errors of ±5.4 cm. The characteristic time of landslide motion ranged between 0.252 s and 0.531 s, with a maximum error of ±0.029 s.

A comparison of the motions of granular slide material with the motions of a solid block, by using a variety of granular materials to simulate the landslide failure mass, found that the centre of mass motion of a granular slide was similar to that of a solid block slider.

The manner in which the landslide stops at the base of the slope is important in fully understanding the wave field, as will be discussed in Chapter 4. It should be noted that the author did not state the stopping mechanism for the solid and granular landslides. The wave amplitudes from experiments

with granular landslide material were 50% to 90% smaller than those from solid block landslides with identical initial geometries and centre of mass motions.

3.1.2 Three-dimensional Experiments

Much of the latest experimental research appears to be in three-dimensional wave experiments with both angular, semi-hemispherical (Liu, Wu, Raichlen, Synolakis and Borrero 2005; Raichlen and Synolakis 2003), and streamlined solid block slider shapes (Enet et al. 2003).

Raichlen and Synolakis (2003) conducted small and large scale tests using triangular wedge-shaped blocks. The small-scale exploratory work used a lead block with horizontal length of 180 mm, vertical height of 90 mm, and a width of 50 mm. An aluminium plate, at a slope of 1:2.08 (V:H), created a plane beach in a 380 mm wide wave tank. A Teflon membrane was affixed to the base of the slider block to reduce friction. The horizontal surface of the slider was initially positioned 14 mm above the still water level to represent a partially aerial landslide, or 15 mm below the surface to represent an underwater landslide. The waves, generated by the release and motion of the landslide, were recorded downstream and to one side of the landslide. Due to the small scales, wave run-up at the beach was not measured. Even though the submerged portion of the vertical face of the landslide was smaller for the partially aerial case, the first crest was approximately 50% larger than the underwater case, as shown in Figure 3.10. This was due to higher initial accelerations from the reduction in initial form drag and added hydrodynamic mass for the partially submerged slider.

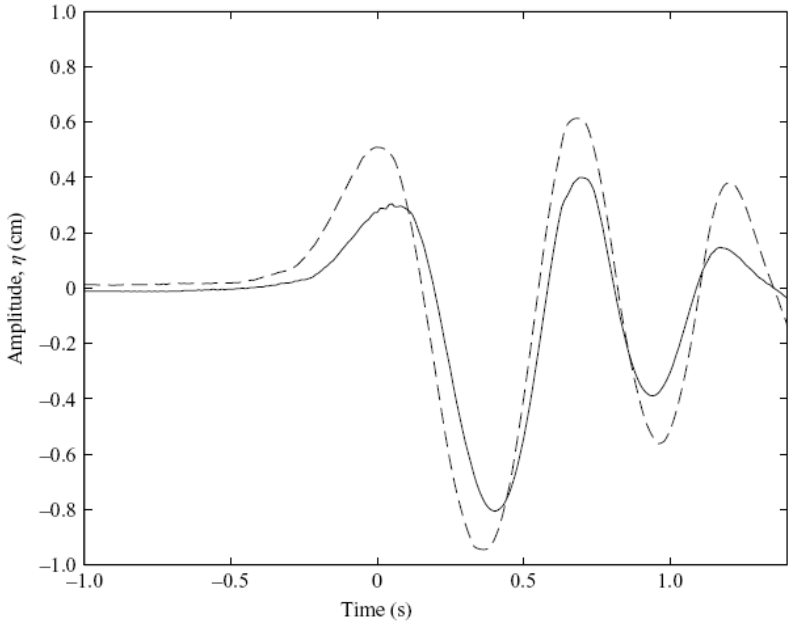

Figure 3.10. Centreline water surface time histories from Raichlen and Synolakis' (2003) small-scale tests for submerged (solid) and partially aerial (dotted) landslides. The times on the horizontal axis are relative to the first crest of the partially aerial trial (Liu et al. 2005).

The large-scale tests, conducted in a 104 m long, 4.6 m deep, and 3.7 m wide wave tank, attempted to minimise the effects of viscosity and capillary action. The landslide models consisted of a 910 mm long, 460 mm high, and 610 mm wide triangular wedge-shaped block and a 914 mm diameter hemisphere sliding down a planar (1 V:2 H) slope, as shown in the photographs in Figure 3.11. Each of the two landslide blocks, constructed from welded 12.7 mm thick aluminium plate, started its slide at various submergences from fully submerged to partially aerial. For a given initial landslide position, the mass of the wedge was varied with lead ballast. Data from a micro-accelerometer and position indicator were used to calculate the block location time-histories, and an array of resistance wave gauges recorded the propagating wave amplitudes, in front of, above, and to the side of the landslide, and run-up heights on the beach behind the sliding mass.

For the wedge, two landslide orientations were used. The first had the front face of the landslide vertical, and the second had the landslide turned end-for-end such that neither face was horizontal or vertical. Two sections of 3 mm diameter steel cable, connected with a wire loop, held the landslide in place before each test. The wire loop was cut to release the slider. A second line connected the slider with a rotary potentiometer, which was used to measure the landslide position and velocity. The wave run-up on the slope was measured in two ways. Firstly, video images of the shoreline were recorded and the run-up position estimated visually. Secondly, three resistance wave gauges were mounted parallel with the slope, approximately 1 mm above the surface. A basket filled with rubberised horse hair stopped the slider before it could run-out along the horizontal bottom of the wave tank.

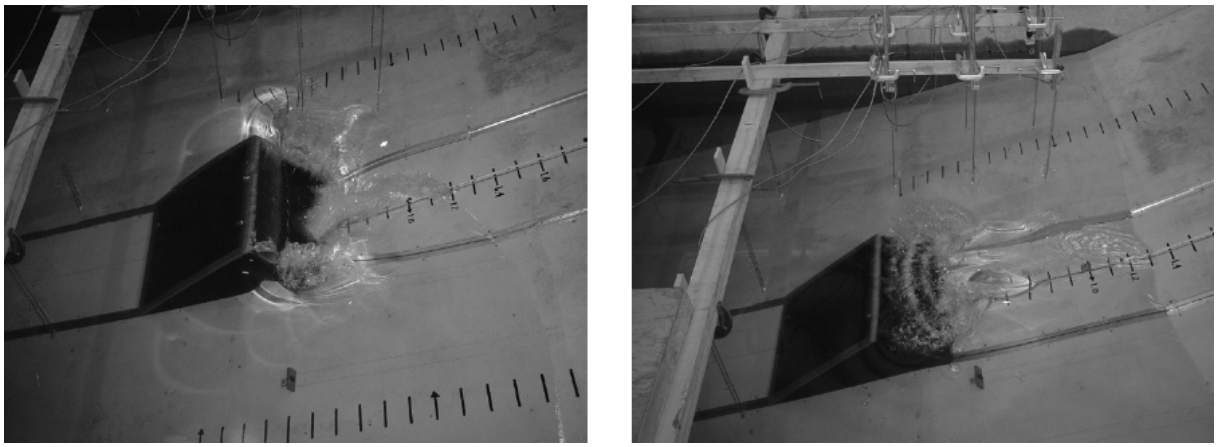

Figure 3.11. Photographs from Raichlen and Synolakis' (2003) 3-dimensional tests. The photo on the left shows the draw-down of the shore as the block begins to slide to the left. The photo on the right shows the same wedge moments later when the wave runs back up the shore. The array of resistance wave gauges used to measure wave heights can be seen hanging above the block.

The relationship between relative initial landslide acceleration and specific gravity for the fully submerged slider tests is shown in Figure 3.12. For a given landslide orientation the relative initial acceleration increased with increasing specific gravity.

Examples of the measured wave run-up height, R, and water level, η, time histories are plotted in Figure 3.13. It was found that as the initial submergence increased, the amplitude of the first trough and second crest decreased. This was observed along both the centreline of the tank and slider, and to the sides of the centreline. A three-dimensional depression formed over the wedge as it began sliding, as illustrated by the photographs in Figure 3.11. This depression was considered to be the leading portion of an N-wave (dipole) propagating towards the shore. The maximum run-down observed at the shore developed before the landslide had moved one body length. Figure 3.14 plots wave run-up height, non-dimensionalised by the landslide length, b, against the submergence parameter $(\Delta/b)\gamma^{-1}$, where Δ is the submergence measured positive above still water level, and γ is the specific gravity of the landslide. This plot combines the experimental results of Raichlen and Synolakis (2003) with the numerical simulations of Liu, Wu, Raichlen, Synolakis, and Borrero (2005). It is clear from this plot that as the initial submergence increases, the run-up height decreases. With the landslide orientated in the end-for-end configuration, the measured run-up heights were smaller, as this orientation effectively streamlined the shape and reduced its wave-making ability.

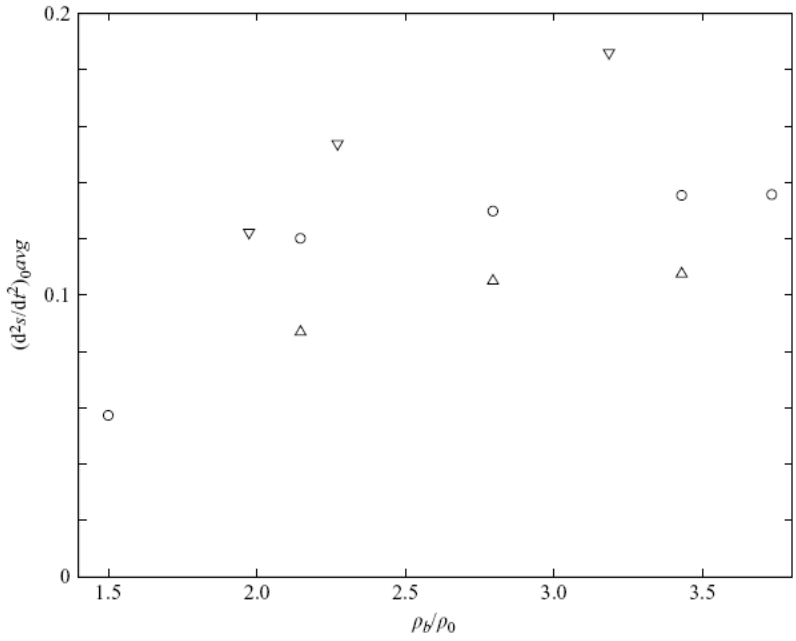

Figure 3.12. Initial acceleration, non-dimensionalised by dividing by gravitational acceleration, shown here as $(d^2s/dt^2)_o avg$, plotted as a function of landslide specific gravity, ρ_b/ρ_o. The downward pointing triangles correspond to the hemisphere, the circles correspond to the wedge with vertical front face, and the upward pointing triangles correspond to the wedge orientated end-for-end (Liu et al. 2005).

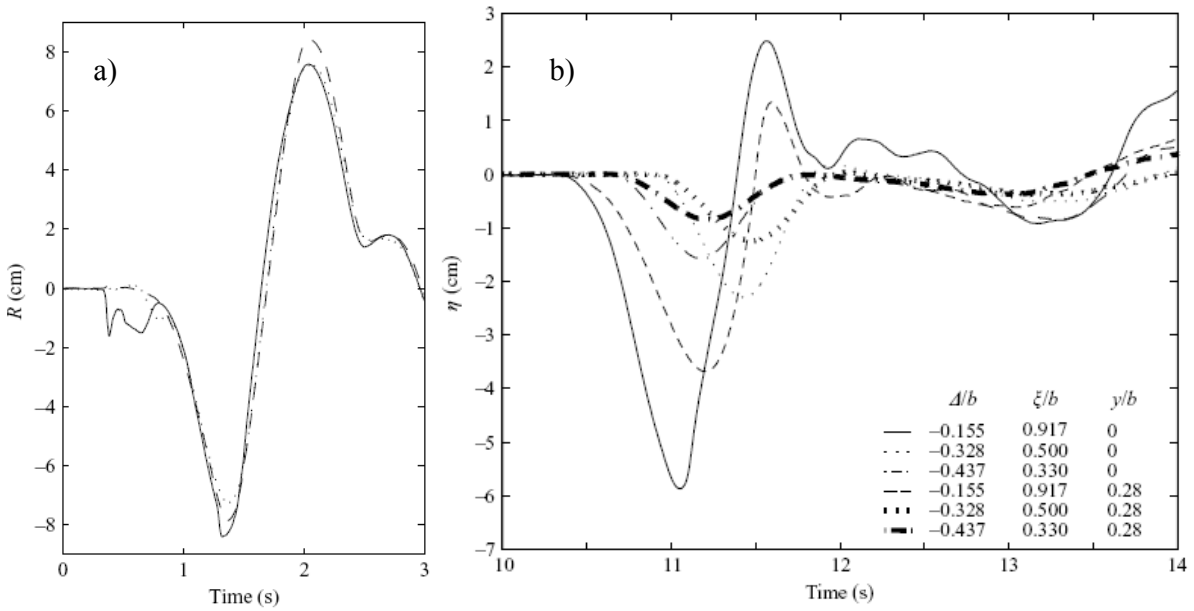

Figure 3.13. Some typical a) run-up time histories and b) water level time histories at different locations for three initial submergences, from Raichlen and Synolakis' (2003) 3-dimensional tests (Liu et al. 2005).

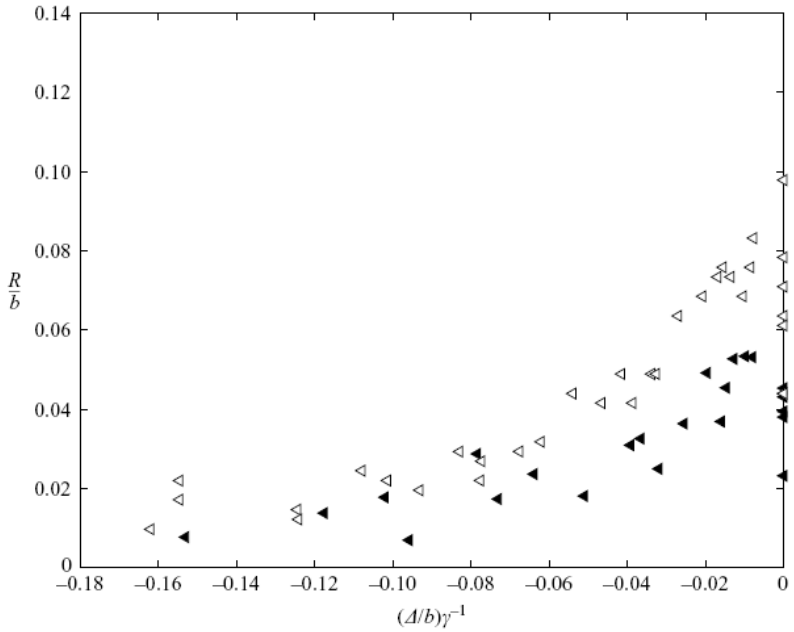

Figure 3.14. Non-dimensional maximum wave run-up from experiments (open triangles) and numerical simulations (solid triangles) plotted against submergence parameter, $(\Delta/b)\gamma^{-1}$ (Liu et al. 2005).

The three-dimensional simulated underwater landslide tests of Enet, Grilli, and Watts (2003) were developed to produce experimental data suitable for comparison with their numerical model results. The flattened dome-like slider block, as shown by the photographs in Figure 3.15, had a thickness of 80 mm, a length of 400 mm, a width of 700 mm, and a bulk density of 2,700 kg/m^3. The wave tank was 3.7 m wide, 1.8 m deep, and 30 m long. The landslide was guided along the slope by a rail, and a

fishing reel was used to position the landslide. The quick-release mechanism of the reel was used to release the slider. The landslide was stopped at the base of the slope with a foam cushion.

The initial submergence was varied (70 mm, 150 mm, and 220 mm) and its motions as it slid down the 15° slope were recorded with a micro-accelerometer located at the block's centre-of-mass. The propagating wave field generated was measured at 100 Hz with an array of four capacitance wave gauges. Photographs of the sliding block and wave gauge array are shown in Figure 3.15.

The micro-accelerometer at the landslide's centre of mass recorded the slider's acceleration parallel to the slope. This was time integrated to produce the velocity time history, and twice time integrated to generate the landslide centre of mass motion. From these, the initial acceleration and terminal velocity were estimated using the approach of Watts (1997). For one of the landslide configurations, the calculated initial acceleration and terminal velocity were used to describe the landslide law of motion in the specification of boundary conditions in a numerical model comparison.

Water level time histories for repeats of the same landslide configuration at two positions within the wave tank are shown by dots in Figure 3.16. The circles are the averages of the repeated runs. The water levels of the large wave trough, measured at a wave gauge located along the centreline of the slider and tank, is shown in Figure 3.16a to be repeatable. However, the water levels following this exhibit significant variation. Figure 3.16b shows the water levels for a wave gauge located off the centreline. The repeatability shown here is significantly worse, with the first trough amplitude ranging between 1.5 mm and 4.5 mm. The second crest amplitude ranges between 1.5 mm and 4 mm. However, the timing of troughs and crests seems repeatable. A comparison of the water level time histories from the experiments with numerical model results is also shown in these plots as the solid lines. The author concludes that the measured surface elevations for repeated runs are repeatable enough such that their average is a good source of data for comparisons with, and validation of, numerical models. The author further concludes the agreement between the average of the measured surface elevations with the numerical results is quite good, and continues with further numerical modelling, including sub-surface velocity distributions.

Figure 3.15. Photographs from the 3-dimensional tests of Enet et al (2003). The photo on the left shows the flattened dome-like model landslide mounted to a guiding rail. The photo on the right shows the array of capacitance wave gauges, used to measure wave heights, placed over the wave tank.

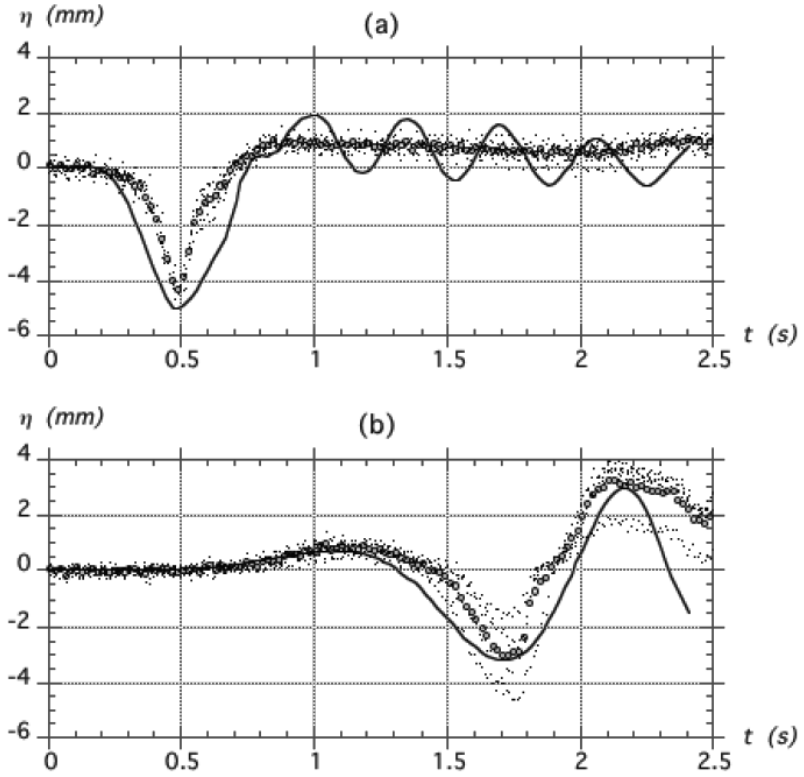

Figure 3.16. Example of water surface time histories. The circles are the average of the experimental values, shown as dots. The solid line is the corresponding numerical model result (Enet et al. 2003).

3.1.3 Benchmark Configuration

In an effort to produce comparable results for their numerical models, the international tsunami research community defined a benchmark configuration for studying the generation of tsunami by underwater landslides. This was deemed necessary due to the difficulties in interpreting the results from the various experimental and numerical models incorporating a wide range of constitutive behaviours (Grilli, Kirby, Liu, Brandes and Fryer 2003; Watts, Imamura, Bengston and Grilli 2001). It was also noted that the sharp edges of the triangular sliding blocks used in previous experimental studies were difficult to model computationally due to the strong flow separation at the vertices. Apart from reef platform failures, this shape was considered to be unrepresentative of the geometry of most underwater mass failures. The tsunami community's recommendation was for a smoother, more streamlined shape which, despite its idealisation, would represent the majority of real events (Grilli et al. 2003).

Two-dimensional tests were recommended as they presented fewer difficulties than three-dimensional tests for numerical modelling. The benchmark configuration consisted of a semi-elliptical block sliding down a planar slope at 15° from the horizontal. The landslide had a thickness:length ratio of 1:20 and a specific gravity of 1.85. It was completely submerged, with the centre of the top surface initially submerged 0.259 times the length of the landslide. Note that the current specification of the benchmark configuration does not uniquely define the sliding characteristics. The specification of the landslide specific gravity does not take into account the sliding friction, which will be dependent on the choice of landslide and slope materials. The landslide deceleration, which will have a significant effect of the wave generation, is also not specified. The acceleration profile of the landslide would have been more appropriate in the specification for a benchmark experiment. The specification of a 15° slope angle in the benchmark is not necessarily realistic of all landslides. As indicated in Chapter 2, a range of slope angles occurs in nature, ranging from steep slopes at 45° or greater to shallow slopes at fractions of a degree.

A basic set of experiments utilising this arrangement was performed by Watts, Imamura, Bengston and Grilli (2001) to compare with numerical model results. These tests were performed in a 30 m long, 3.7 m wide, and 1.8 m deep wave tank. A 15° planar aluminium slope was placed in water 1.05 m deep. The landslide model, 1.0 m long, 0.20 m wide, and 0.052 m thick, was made from plywood and mylar sheeting. A photograph of the landslide block is shown in Figure 3.17. To simulate a 2D situation, two plywood sidewalls, 0.20 m apart, were placed in the central portion of the tank. The block slid down the ramp, between the two sidewalls, on plastic wheels. Lead was placed in the central cavity of the slider to achieve the benchmark density.

The landslide initial submergence, measured from the surface of the landslide above its centre of mass, was 0.259 m. A micro-accelerometer at the landslide centre of mass recorded the landslide motions. The recorded acceleration time history was time integrated once and twice to obtain the velocity and position time histories respectively. From these the initial acceleration, approximately 0.75 m/s^2, and terminal velocity, approximately 1.26 m/s, were estimated. Four capacitance wave gauges were used to measure the wave heights between the two sidewalls. The first gauge was centred directly above the landslide's initial centre of mass, and the remaining three gauges placed at 0.30 m intervals downstream. Measurements from these are shown as circles in Figure 3.18. The solid lines are results from a numerical model comparison.

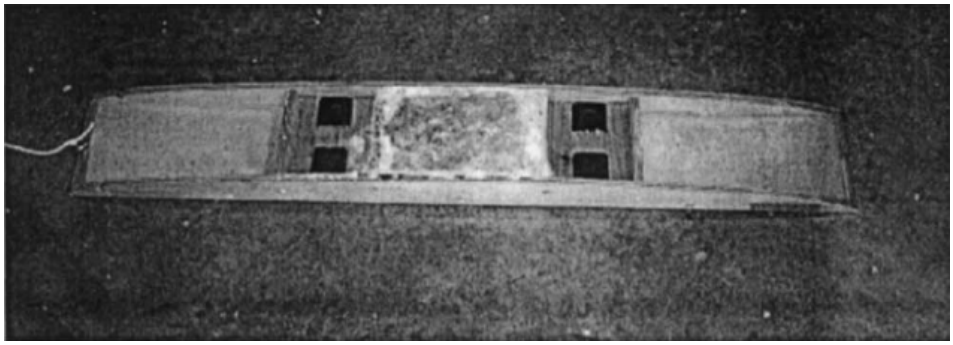

Figure 3.17. The plywood construction of the semi-elliptical model landslide used in the benchmark configuration experiments (Grilli and Watts 2005; Watts et al. 2001). It is 1.0 m long, 0.2 m wide, and has a thickness of 0.052 m.

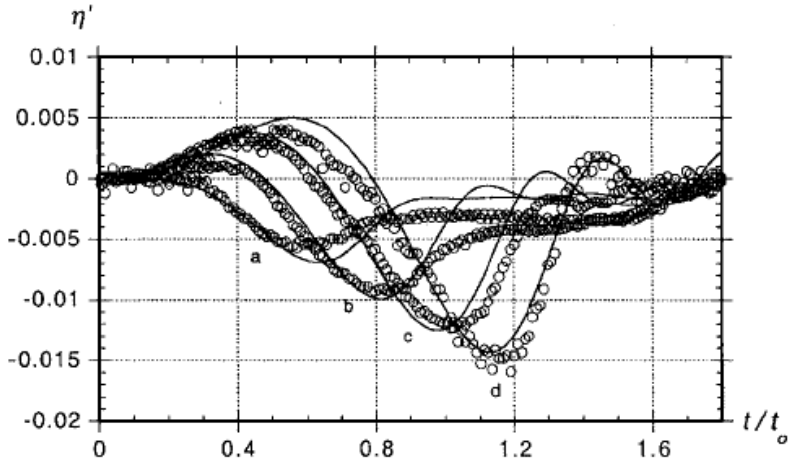

Figure 3.18. Non-dimensionalised water level time histories at four wave gauge locations for the semi-elliptical benchmark experiment (Grilli and Watts 2005). The measured values, represented by circles, are compared with numerical results, shown as solid lines.

The work of Fleming, Walters, Sue, and Nokes (2005) also experimented with a semi-elliptical solid block similar to the benchmark configuration. Sets of experiments were performed with a semi-elliptical block that was 500 mm long, 250 mm wide, 50 mm thick, and constructed using plywood and aluminium sheeting. The block was hollow to allow lead ballast to be added to achieve the desired density of 1900 kg/m^3. Teflon buttons on the bottom and sides minimised the effects of friction against the ramp and sidewalls. Blue circles were affixed to the side of the landslide for later use in particle tracking software to determine the position, velocity, and acceleration time history. The 15 m long, 0.25 m wide, and 0.55 m deep flume, and the 15° planar slope were constructed from acrylic sheet. The initial submergence of the surface of the landslide above its center of mass was 130 mm. A length of cord was tied to the landslide to hold it at the correct position. This cord was released to begin the slide. The other end of the cord was tied to a rigid object and the length of the cord was just long enough to allow the slider to stop at the base of the slope. Water levels were recorded with three resistance wave gauges, with the first above the initial landslide centre of mass position and the second and third 150 mm and 300 mm downstream. The data generated was to be compared with the results of Watts et al (2001), but is currently unpublished.

3.1.4 Sub-surface Velocities

The wave generation from sub-aerial landslides was characterised by Fritz (2002) using Particle Image Velocimetry (PIV) . PIV provided instantaneous velocity vector fields of the generation region of landslide generated impulse waves, as shown in Figure 3.19. The hydrodynamic impact craters that were produced were separated into craters that collapsed in the up-slope and down-slope directions. The water displacement caused by the landslide generated the first wave crest and the collapse of the impact crater generated the second crest. The volume of the impact crater was an order of magnitude larger than the landslide volume.

Capacitance wave gauges were used to measure water surface time histories. Sub-aerial landslides generated four wave types: weakly non-linear oscillatory waves, non-linear transition waves, solitary-like waves, and dissipative transient bores. Examples of these wave types for his experiments are shown in Figure 3.20. Most of the generated waves were classed as intermediate-depth waves. However, the leading crest propagated at close to the theoretical approximation for a solitary wave. It was also found that between 5% and 50% of the slide kinetic energy propagated out in the wave train. Fritz (2002) notes that a large amount of kinetic energy of the landslide is removed from the system when solid block models are abruptly stopped at the bottom of the incline, preventing energy conversion into wave energy, friction, drag, or turbulence. The amount of energy taken out of the system by the block hitting the base of the slope relative to the potential energy of the landslide increases with increasing slide Froude number. Therefore, the small coefficients of conversion of landslide potential energy into wave energy found by previous researchers (Watts 1997; Wiegel 1955)

need to be carefully interpreted. Laboratory block model configurations currently used are not able to recreate the long run-out lengths observed in nature.

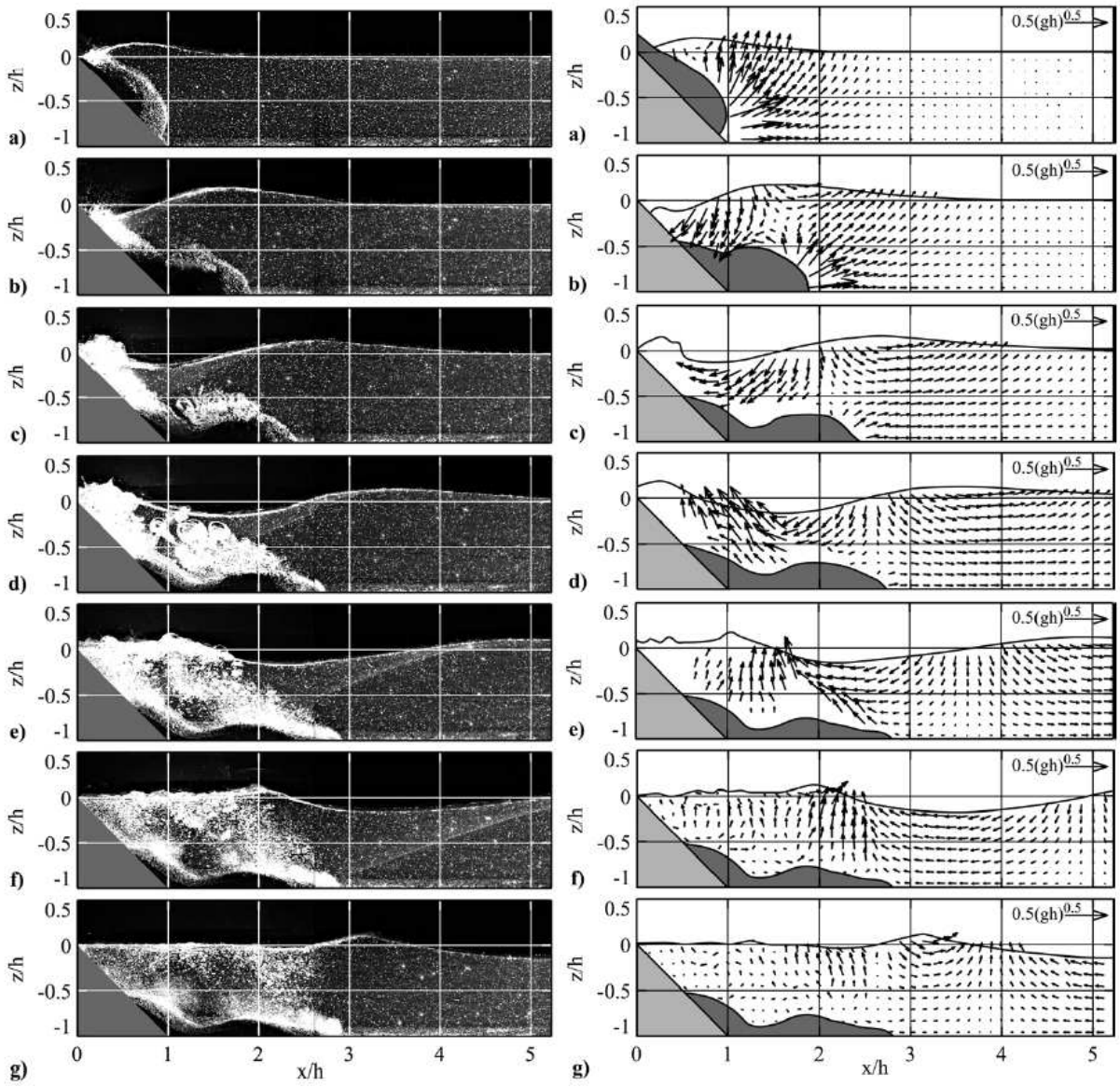

Figure 3.19. PIV images and corresponding velocity vector fields from Fritz' (2002) study into sub-aerial landslide generated impulse waves.

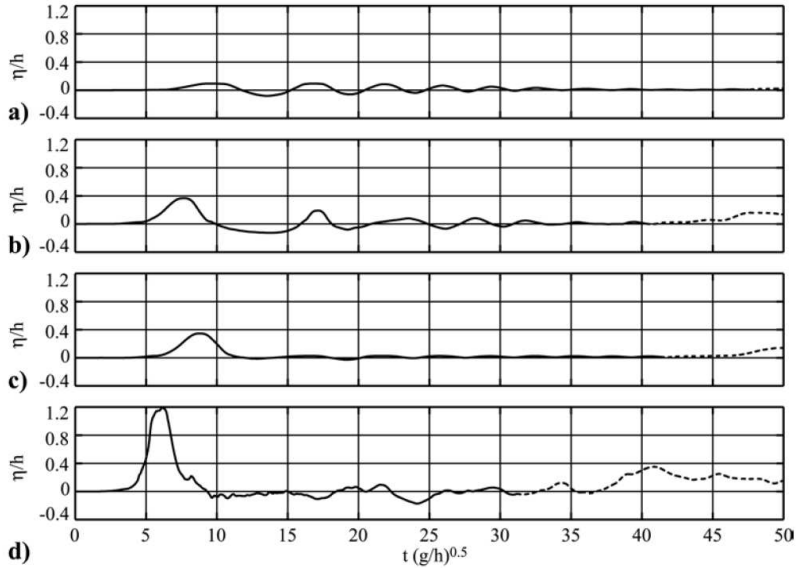

Figure 3.20. Wave types observed during Fritz' (2002) experiments: a) non-linear oscillatory wave, b) non-linear transition wave, c) solitary-like wave, and d) dissipative transient bore. The dotted portions of the lines indicate regions affected by wave reflections.

3.1.5 Experimental Modelling Summary

The laboratory experiments presented in this section utilise a very idealised configuration, that is, solid block and granular materials sliding down planar slopes. No attempts have been made to model the offshore bathymetry with anything other than a constant depth channel. A variety of landslide shapes have been used, including triangular, hemispherical, streamlined, and semi-elliptical shapes. A range of landslide densities, materials, and initial submergences has also been used. Previous researchers have examined the effect of various slope angles on the wave field, but were limited to slopes greater than at least 10°, to overcome sliding friction. The use of solid blocks than slide down the slope and run out gradually along the channel floor has not been attempted.

The key quantities of interest in previous research have been landslide position, velocity, and acceleration time histories, granular landslide shape, max wave amplitudes, wave periods, wave potential energy integrals, and energy conversion ratios. Few investigations have measured the wave run-up behind the landslide due to surface tension effects and the difficulty in accurate measurement techniques. The measurement of sub-surface velocities during laboratory underwater landslide experiments is also deficient.

All previous research efforts have measured wave heights as time histories at specific locations in the channel. There have been no attempts to quantitatively measure the wavelengths and spatial extent of the wave field. As such, it is difficult to ascertain the spatial and temporal development and evolution of the waves as they are generated and propagate offshore. Also, the earlier works make few attempts

to connect the time-dependent motion of the landslide with the wave field, as only representative values of each are used. In particular, the use of initial acceleration and terminal velocity ignores the effect of temporal variations in acceleration and velocity on the generated wave field.

The tsunami research community highlighted the desirability of a benchmark configuration, to allow easier comparison between different sets of experimental and numerical results. As yet, a quality benchmark dataset is still unavailable. The research contained herein attempts to remedy some of these shortcomings.

3.2 Numerical Modelling of Underwater Landslide Tsunami

The deformation that accompanies underwater fault ruptures tends to occur rapidly relative to the propagation speeds of long water waves. This allows the initial condition of the free surface elevation to be a direct outcome of the permanent seafloor displacement. Wave propagation models are then able to calculate how the displaced water surface propagates as a series of gravity waves. However, underwater landslides move significantly slower than a fault rupture, and hence the time-dependence of the seafloor deformation is important. This adds a great deal more complexity to the wave model as additional source terms are required in the equations of motion (Liu et al. 2005). This section reviews the models dealing with the generation and initial propagation of waves induced by the sustained motion of a bottom boundary.

3.2.1 Simple Empirical Models

The simplest models predict gross wave properties, such as maximum expected wave heights and total energy content. Murty (2003) used information available in the literature to find a simple empirical linear relationship between landslide volume and the maximum wave amplitudes. From eleven events, linear regression gave the expression in Equation 3.16, relating maximum wave amplitude (in m), H, to slide volume (in 10^6 m^3), V. The results from numerical simulations were also found. However, the agreement between observed and numerical model results was very poor. No explanation as to why this may be was given.

$$H=0.3945\ V \tag{3.16}$$

Another simple approach was to determine the amount of energy transferred from the block's initial gravitational potential or kinetic energy to the potential energy of the waves. From laboratory experiments this is found to be of the order of 2% - 10% (Jiang and Leblond 1992; Ruff 2003; Watts 1997).

3.2.2 Coupling of Bottom Boundary Motion to the Wave Field

Landslide tsunami models are complex due to the requirement of coupling between the landslide and the water. Jiang and Leblond (1992) developed a numerical model to investigate the coupling of an underwater mudslide and the waves which it generated. The landslide was modelled as the laminar flow of an incompressible viscous fluid. The long wave approximation was invoked and the water motions were considered irrotational and non-dispersive. The resulting differential equations were solved using a finite difference method. Three cases with varying levels of coupling were examined. The first was to observe the behaviour of the mudflow under a fixed surface. The second case incorporated one-way coupling, in which the motion and deformation of the mudflow disturbed the free surface. Thirdly, full two-way coupling was investigated, in which the surface pressure gradients affected the mudflow.

The wave fields generated by the un-restrained free surface models showed that three main waves were generated by the mudslide as it started sliding from a standstill down a gentle slope. The first wave was a crest that propagated into deeper water ahead of the mudslide. This was followed by a trough in the form of a trapped wave that propagated at the same speed as the mudslide. The amplitude of the forced trough was similar to that of the maximum crest amplitude. The third wave was a relatively small trough that propagated back towards the shore behind the mudslide. This agrees with similar observations in laboratory underwater landslide experiments (Watts 1997; Wiegel 1955). The wave amplitudes were found to depend primarily on slide density, initial submergence, landslide volume, and the viscosity of the mud. Mudslides with large densities and volumes, and small submergences and viscosity generated the largest waves.

It was found that the density and initial submergence of the mudslide were the two dominating factors in determining the interaction between the slide and the waves it generated. Two-way interaction appeared most significant for mudslides with lower densities in shallow water. For cases with high mudslide densities and shallow water, the two-way interactions were small, but the wave heights were very large. For deep initial submergences, the interaction was also weak and the waves were small. The interaction of the waves with the mudflow tended to slow the slide speed slightly. The mudflow moved fastest for the case with a fixed water surface. As the surface was fixed, no energy was transferred from the slide to the wave field, and hence the slide motion was slightly faster than when the water surface was free to move. The transfer of energy from the mudslide to the waves was most significant when the interaction between the slide and the waves was strongest. The transfer of energy was not constant, as it was maximised at the beginning of the slide and decreased to approximately 2% - 4% when the waves propagated away from the slide site. The numerical results also indicated that resonance was not expected in most practical situations.

Using an energy balance approach, Ruff (2003) calculated that the conversion of landslide gravitational potential energy into wave energy, for underwater landslides, ranged between 0% for slow velocity slides in deep water to 50% for high velocity slides in shallow water and abruptly truncated landslide motions. In contrast, an earthquake was found to convert no more than 1% of the earthquake energy into wave energy.

Ruff (2003) found that abruptly truncating the motion of the landslide, especially when it was travelling at close to the wave propagation speed, generated large transient waves. These truncation transients had maximum amplitudes similar to the waves generated by the initial acceleration of the landslide, though with opposite polarity. The largest amplitudes were generated when the landslide had moved one slider length, was travelling at the wave propagation speed, and the motion abruptly truncated so that all landslide energy went into the truncation waves and not lost to friction. This abrupt truncation behaviour could convert up to approximately 45% of the net gravitational landslide energy into wave energy. It was found that the more gradual the deceleration of the slider, the smaller the amplitude and the longer the wavelength of the transient. The conversion of gravitational energy into wave energy also decreased, as more energy was lost in sliding friction and water drag. The final energy conversion ratio was highly dependent on slide distance, as longer slides had more time to impart more of its energy to the wave field. The greater the duration of sliding, the smaller the significance of the truncation-induced energy compared to the total energy supplied by the landslide. So a case in which an abrupt truncation of motion created the largest transients, the energy conversion from gravitational potential energy into wave energy could be less than 10% if the slide continued for a great distance. Therefore, the author considers the maximum wave amplitude to be a more robust parameter at describing the landslide waves than the final energy conversion efficiency.

The findings of Ruff (2003) are contrary to the comments of Fritz (2002), in Section 3.1.4, that abruptly stopping the landslide results in small ratios of conversion between landslide potential energy and wave energy. There is not enough information in the literature to determine exactly why previous researchers (Watts 1997; Wiegel 1955) have found low energy conversions. Possible reasons include the landslide speed being dramatically different from the wave propagation speed, long slide distances, landslide decelerations being too gradual, or the measurement techniques and energy formulations do not capture the truncation waves.

3.2.3 Computational Models

Enet et al (2003) used a three-dimensional numerical wave tank to computationally simulate the underwater landslide geometry outlined in Section 3.1.2 (Grilli et al. 2002; Grilli and Watts 1999). Fully non-linear potential flow theory was solved using a high-order boundary element method. The boundaries at the head and toe of the slope were modelled slightly differently from the experimental

configuration, as two shelves were placed at these locations. Due to the finite length of the slope, the landslide was decelerated at some point, such that it came to a smooth stop before the bottom of the slope. A comparison between numerical model results and experimental data for one of the simulations is shown in Figure 3.16. The extent of agreement between the numerical and experimental data led the authors to conclude adequate validation of the numerical model. The sub-surface velocity distribution through the water column at various positions in the numerical wave tank indicated that the horizontal velocities were quite non-uniform over the depth. This highlighted the inappropriateness of the use of long wave models in landslide tsunami generation models. No experimental measurements of sub-surface velocity profiles were attempted.

The same non-linear potential flow theory boundary element model was used in a sensitivity analysis, to observe the effect of domain depth, landslide deformation, and landslide failure type (Grilli and Watts 2005). It was found that by increasing the depth of the domain by a factor of two, and thereby increasing the length of slope and time before the landslide decelerated, there was only a slight increase in the observed maximum run-down at the shore. Meanwhile, observed maximum wave run-up decreased. As the initial draw down at the shore was directly related to the initial motion, and not the final kinetics of the landslide, the small effect on run-down height resulting from a longer slide distance was not unexpected. The smaller run-up height was due to the landslide decelerating in deeper water, which decreased the magnitude of the shoreward-propagating crest that it created. Realistic levels of landslide deformation had more significant effects on far-field wave features compared to near-field features. Typical slump failures generated waves with smaller amplitudes and wavelengths compared to slides.

The landslide motions used in the boundary element method model simulations (Enet et al. 2003; Grilli and Watts 2005) were characterised using the formalism developed by Watts (1997; 1998; 2000). This is described in Section 3.1.1.

Heinrich (1992) used the two-dimensional hydrodynamics package, Nasa-Vof2D, to model waves generated by sliding solid triangular blocks. This numerical model used a non-linear code to solve the complete Navier-Stokes equations using a finite difference method. The fluid was assumed incompressible. The fluid domain boundaries were time dependent to allow the movement of the landslide to be modelled provided its kinematics were known. Close agreement between experimental data and numerical model results were achieved, except when free-surface turbulence occurred. Details of the experimental configuration are given in Section 3.1.1.

Rzadkiewicz, Mariotti, and Heinrich (1997) and Mariotti and Heinrich (1999) modified the Nasa-Vof2D package to model deformable underwater landslides. These landslides were assumed to

separate into two distinct layers, a dense flow just above the slope surface, and a dispersive layer that mixed with the ambient water at the landslide-water interface under the control of a diffusion model. The dense layer was modelled as a visco-plastic fluid, and the dispersive part as an ideal fluid. Interstitial pressure within the landslide and a sediment erosion-diffusion law at the soil-water interface were also introduced. This allowed for different permeability of various granular materials to be modelled. Comparisons with experimental data, created using failing masses of sand and gravel (see Section 3.1.1), produced acceptable agreement between the two.

Tinti and Bortolucci (2000a) described an analytical method to model tsunami generation from underwater landslides that underwent negligible deformation. The linear and long wave assumptions were invoked, and the water surface height varied in the slide direction only. The relationship between landslide motion, prescribed as a slide Froude number, and wave pattern and amplitude were studied in dimensionless space. Both subcritical and supercritical regimes were investigated, although it was noted that natural events were almost exclusively subcritical. The subcritical landslide was found to produce two systems of waves, both characterised by leading waveforms travelling at the free-wave phase speed. The set of waves moving in the direction of slide was led by a crest, whereas the backward propagating set was led by a trough. Another wave trough was observed to move with the landslide as a trapped, or forced, wave. The profile of the trough was a mirror-image of the landslide profile. The landslide motions were characterised using the formalism developed by Watts (1997; 1998; 2000), as described in Section 3.1.1.

Ward (2001) used the assumption of wave linearity to allow the principle of superposition to be valid for modelling waves generated by underwater landslides in an incompressible, homogeneous, and inviscid ocean. Spectrally decomposing, independently propagating, and reconstructing simple waveforms allowed complex tsunami waveforms to be generated.

A variety of complex slides were generated by the summation of several simple slides. A simple slide consisted of a rectangular block of seafloor that was uplifted. One of the lateral dimensions of this rectangular block then increased with time. However, this resulted in a net volume change in the seafloor. This was neutralised by the addition of another simple slide in which the corresponding volume of seafloor was excavated from the seafloor. Through linearity, the wave field generated by each of the uplifted and excavated blocks were then superimposed. The velocity of the landslide was controlled by the rate of expansion of each of the simple slides. To get around the obvious limitation of cumbersome and unnatural rectangular blocks, a Green's function approach was used to produce even more complicated slides. The tsunami was computed by the summation of many small simple slides of different thickness, length, width, velocity, orientation, and initiation time, placed under an ocean of non-uniform depth. This formulation became very computationally demanding, so the entire

wave field was not calculated. Instead, waves were only propagated along ray paths to the location in which the tsunami properties were of importance, and the wave field everywhere else was ignored.

The tsunami from the massive Nuuanu, Hawaii, and Storrega, Norway, slides, as described in Section 2.4.3, where modelled using the superposition approach. 95 simple slides were used to model the Nuuanu slide, resulting in 50 m to 60 m high waves reaching the beaches of Oahu and Molokai within 18 minutes of slide initiation. After 2 ½ hours the wave train extended for over 1500 km, with the leading wave amplitudes reaching 20 m. Waves reached the west coast of North America after 4 ½ hours with amplitudes of 10 m, producing waves at least twice that after shoaling affects at the shore. The Storrega landslide was modelled using 91 simple blocks. Within 2 hours, waves with heights of 12 m, 8 m, and 6 m, reach the coasts of Norway, the Shetland Islands, and Iceland respectively.

3.2.4 Wave Run-up Modelling

Wave run-up on planar beaches has been studied in significant detail in the past (Kanoglu 2003; Kennedy, Chen, Kirby and Dalrymple 2000; Synolakis 1987; Tarman and Kanoglu 2003; Walters 2003). These models studied run-up from waves generated from distant sources and looked at their transformation, breaking, and run-up as they approached the shore. No work was undertaken to model the source mechanism. However, few have examined the wave run-up at the beach above an aerial or underwater landslide, as this is of immediate danger to communities in the slide proximity.

In an underwater landslide, the motion of the failure mass is down slope, generating waves that also move offshore. Liu et al (2005) numerically modelled the wave run-up above underwater and aerial landslides, the results from which were compared with results from laboratory experiments (see Section 3.1.2). The modelling used a large eddy simulation approach to solve the Navier-Stokes equations, and the volume of fluid method was used to track the movements of the free surface. Good agreement between experimental results and numerical simulations was shown for the wave run-up and water level time histories for one sub-aerial case, as shown in Figure 3.21. The large eddy simulation results illustrated the highly transient, rotational, and turbulent nature of the complex three-dimensional flows of sub-aerial landslides. The maximum run-up was a result of the convergence of the flows around either side of the landslide. Through looking at the velocity fields, the authors concluded that the effectiveness of wave generation diminished when the depth of submergence was greater than three times the height of the landslide. The non-dimensionalised experimental and numerical run-up data for submerged landslide cases are presented in Figure 3.14. Generally, the agreement between the experimental and numerical data was reasonably good. However, the numerical model tended to under-predict the maximum run-up height when initial submergence approached zero.

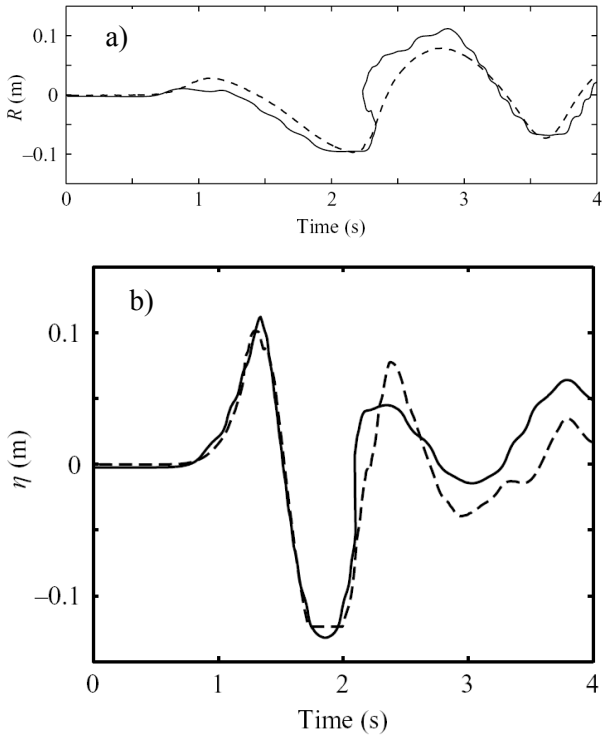

Figure 3.21. Comparison between numerical (solid) and experimental (dotted) results for the time histories of a) run-up and b) water level (Liu et al. 2005).

3.2.5 Simulation of Events

Due to the inherent difficulties with scaling up experimental results to full scale, the modelling of tsunami at real scale is left to numerical models. It is ideal if the models have been adequately validated before their results are used to make any predictions of actual or hypothetical events. Numerical models are often used to 'back-predict' the tsunami characteristics from given geological evidence of a landslide, or to determine the extent of the underwater failure from the observed wave run-up height distributions (Day, Watts, Grilli and Kirby 2005; Fine et al. 2005; Lynett et al. 2003; Tinti et al. 2006; Tinti, Bortolucci and Romagnoli 2000; Ward 2001). There is vast literature on the numerical modelling of physical events, a selection of which will be briefly described here.

Lynett, Borrero, Liu, and Synolakis (2003) describe the use of a Boussinesq model and a non-linear shallow water model to simulate and compare with post-event field data of the 1998 Papua New Guinea tsunami. The landslide motions were not recreated in the models, as there was no information to accurately infer the motion of the landslide. Instead, the initial displaced shape of the ocean's surface was assumed, and the numerical models simulated the evolution of the initial condition. The sensitivity of the wave propagation was investigated as the Boussinesq model included weak frequency dispersion effects and the non-linear shallow water model was a non-dispersive one. In this case, due to the unique bathymetry of the tsunami-affected zone, frequency dispersion was not

important. In normal cases, the non-linear shallow water model would not have been well suited to the short wavelengths of the Papua New Guinea tsunami. It was noted that the uncertainty in tsunami generation dynamics represented a much larger error when compared to that due to the neglect of frequency dispersion. Comparison of computed flow depths over the sand spit at Sissano Lagoon with field survey data showed differences of 50%. However, the errors in the comparison were compounded by the uncertainty in the field measurements and the tsunami source conditions.

Tinti, Bortolucci, and Romagnoli (2000) numerically modelled a hypothetical collapse of a flank of the volcanic island of Stromboli, Italy. Two separate models were used; a Lagrangian model for the sub-aerial landslide collapse and a shallow water model to simulate the resultant tsunami as it propagated over present day bathymetry. The landslide was divided into a series of deformable blocks and the motion of each block was calculated by applying the principle of momentum conservation. The waves were computed by solving a system of shallow water equations with the forcing term dependent on the motion of the sliding blocks. A finite element method was used, as it was considered capable of accounting for the highly irregular bathymetry and shoreline. The modelling predicted wave heights of up to 50 metres in height striking the coast. Due to strong refraction, waves were observed to wrap around the island and strike the opposite coast. The largest waves struck within 300 seconds of landslide initiation.

Walters et al (2003) numerically modelled the generation of tsunami by possible earthquake fault rupture and underwater landslides off New Zealand's Kaikoura coast. The model was based on the Reynolds-averaged Navier-Stokes equations that were time-averaged over turbulent length scales. The equations were also depth-averaged and the pressure distribution was assumed to be hydrostatic. An unstructured grid of triangular finite elements was used to discretize the offshore bathymetry. For an extreme underwater landslide event, the model predicted wave crest amplitudes of approximately 10 m arriving at the nearby coast within 1 minute, running up to a height of 20 m above the tide level. The estimates of flow depth and velocity indicated that all buildings, roads, and rail networks would be swept away during the modelled scenario. If a nearby fault ruptured with maximum displacement, then waves would be expected to run up to a maximum height of 8 m above mean sea level within 10 minutes of the earthquake.

Horrillo, Kowalik, and Shigihara (2006) used three numerical models to determine the importance of wave dispersion on the initial wave propagation of the December 2004 Indian Ocean tsunami. The results from a non-dispersive non-linear shallow water model, a non-linear Boussinesq model, and a full Navier-Stokes model, aided by the volume of fluid method to track the free surface, were compared with each other. The authors considered the last of these to produce the most accurate results due to its use of vertical fluid kinematics and a non-depth integrated approach, and was used as

a frame of reference for the other two models. All three models exhibited the same general features. However, the effect of the lack of dispersion in the shallow water model became evident, as this model could not replicate the trailing train of waves behind the leading waves. The leading wave crest was slightly larger in amplitude and shifted forward in time compared to the other two models. The leading edge of the wave, however, matched well with the other models, so all three models predicted similar tsunami arrival times. Overall, the author concluded the reliable results, conservative wave height estimates, accurate wave arrival times, and low computational cost made the shallow water model attractive for preliminary hazard assessment.

3.2.6 Benchmark Configuration

The numerical models described so far in this section simulate vastly different landslide geometries and motions, which make comparisons between models difficult. As a possible remedy to this, a benchmark configuration was devised. Details and some experimental results from the benchmark configuration were given in Section 3.1.3.

Watts at al (2001) described the application of two numerical models to the benchmark case. The first was a model for a two-layer flow above a non-horizontal bottom, developed by Imamura and Imteaz (1995), in which the continuity and momentum equations were depth-averaged in each layer. The equations were solved using a staggered finite difference scheme. Both fluid layers were considered homogeneous and immiscible. The second model, developed by Grilli and Subramanya (1996), used a boundary element method approach to simulate inviscid and irrotational free surface flows. The boundary was discretized using cubic elements.

The experimental results showed a slightly better agreement with the boundary element model, as shown in Figure 3.22. The depth-averaged model tended to under-predict tsunami amplitude. Characteristic wave amplitudes of the two models differed by up to 13%, possibly due to the boundary element model solving a full set of governing equations compared to the depth-averaging involved in the two-layer model.

Numerical results were also generated using a two-dimensional boundary element method model, solving fully non-linear potential flow theory (Grilli and Watts 2005). For computational efficiency and accuracy, the semi-elliptical landslide shape was replaced with a Gaussian shape. A comparison with experimental data is shown in Figure 3.18.

The benchmark tsunami generation problem was also modelled by Walters (2003). Several versions of the numerical model were used, including a hydrostatic and a non-hydrostatic model, both based on the Reynolds-averaged Navier-Stokes equations. The results showed the surface response consisted of

a bow wake ahead of the landslide, a trough, a trailing wake, and draw down at the shore. A frame from the simulation is shown in Figure 3.23. The results showed that the hydrostatic version tended to overestimate the amplitude of the wave trough and the draw down at the shore, and the trough position predicted as too far downstream. These effects were attributed to the direct coupling of the free surface to the landslide movement due to the hydrostatic assumption.

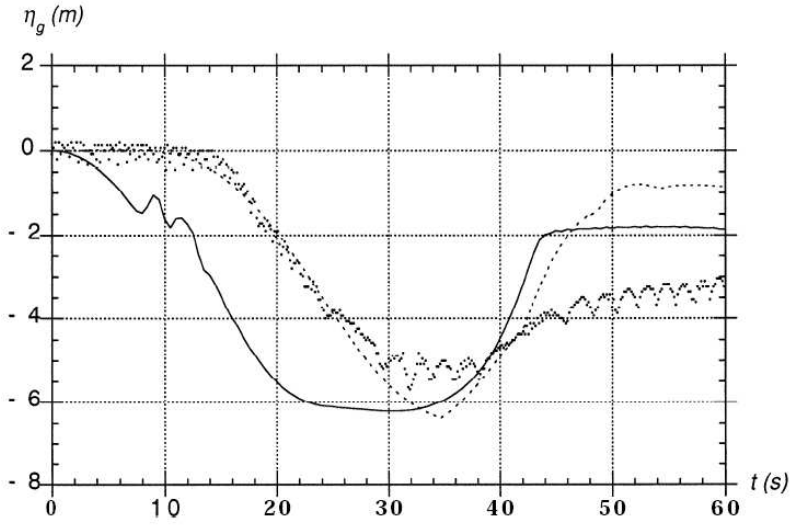

Figure 3.22. Point water level time histories, for the benchmark case, for the two-layer model (solid), boundary element model (dashed), and scaled up experimental data (dots) (Watts, Imamura and Grilli 2000).

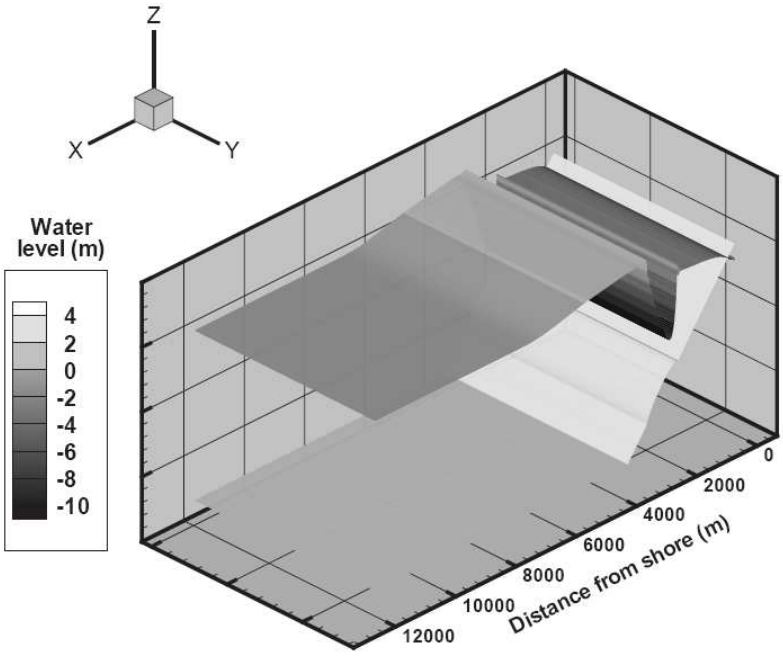

Figure 3.23. Surface wave generated by the benchmark configuration. A semi-elliptical solid block is sliding down a 15° slope. A wave crest and trough are propagating out from right to left (Walters 2003).

3.2.7 Numerical Modelling Summary

Previous researchers have taken a variety of approaches to numerically model tsunami generation, propagation and run-up. Each model made assumptions in order to simplify the governing equations. These assumptions were associated with fluid viscosity and compressibility, landslide kinematics, initial conditions, wavelength-to-water depth ratio, and wave linearity. Model complexity ranged from simple empirical relationships capable of estimating bulk wave parameters, to full three-dimensional models. The expense of computational time associated with complex finite and boundary element models were offset by the comprehensive generation of fluid parameters such as water level, wave run-up, and sub-surface velocities and pressures, varying in three spatial dimensions and over time.

The time saving of simplified model approaches will always have a negative impact on the accuracy and applicability of the results. For instance, the use of depth averaged non-linear shallow water wave equations ignores any vertical accelerations that may be present, and can seriously affect the accuracy in the wave generation zone (Fritz 2002). Also, the shallow water assumption may not always be applicable, as the wavelengths and water depths are changing rapidly during the generation and initial propagation process. Wave dispersion has been shown to be very important in certain circumstances. The significance of the negative impact of simplified models must be quantified and weighed against the added cost and complexity of more elegant models.

It seems clear that underwater landslide tsunami generation models are very computationally expensive, whereas wave propagation models tend to be less demanding. Wave run-up appears to be well understood, and many well-established models exist to quantify this. It therefore makes sense to combine these three models in series such that the tsunami generation models are used to recreate the highly time and space dependent nature of the generation process, propagation models are used to replicate the wave evolution over open water, and wave run-up models reproduce the effects of coastal bathymetry, wave focussing, and shoaling, on wave run-up.

A variety of landslide and slope configurations have been modelled in the past. Therefore, the use of a benchmark configuration, as described in Section 3.2.6, by all models would make the process of comparison between models more consistent and significantly easier.

3.3 Summary

In this chapter, Section 3.1 presented details and some examples of results from previous laboratory underwater landslide experiments. These showed that the wave generation process is complex. Numerical models with a range of complexities have been developed to model these events, and

details of these were included in Section 3.2. Experimental results, such as those presented in this research, are a means by which these computational models can be validated.

The research to be described here follows on from the experimental work of Fleming et al (2005) and Watts et al (2001). The work of these earlier experimentalists with the benchmark landslide configuration is extended to look at a range of combinations of landslide density and initial submergence. Also, the entire water surface profile time histories will be measured using a newly developed LIF technique, instead of quantifying the water levels at discrete locations. Similar to the work of Fleming et al (2005), PTV will be used to measure the landslide and sub-surface water velocities.

Chapter 4: Methods

The motivation behind this experimental investigation of tsunami generation by underwater landslides was to generate a comprehensive dataset that would be suitable for numerical model comparisons. This dictated the use of the benchmark configuration as defined by the international tsunami research community (Grilli et al. 2003; Watts et al. 2001) and as discussed in Section 3.1. A variety of landslide densities and initial submergences were investigated in this current research, and it was envisioned that the data from this study would be of sufficient quality for comparisons with numerical models.

The use of electrical point wave gauges at specific locations can only give limited insights into the wave generation process, as the spatial changes in water profile between the gauge positions are not measured. There are also questions as to the influence of surface tension and meniscus effects on the gauge wires at the small laboratory scales, as well as the effect of having objects physically in the flow. To remedy this, a non-intrusive water level measurement technique was developed that minimised the disturbance to the water, and also captured the spatial as well as the temporal variations. This technique utilised Laser Induced Fluorescence (LIF) to measure the necessary wave parameters. A dye was added to the flume water that fluoresced under the influence of laser light. Digital video imaging recorded the position of the interface between the fluorescing water and the black backdrop of the surrounding darkened room.

To understand the physics behind the wave generation processes, the waves measured using LIF needed to be related back to the generation mechanism, the landslide motions. Particle Tracking Velocimetry (PTV) was used to track the location time history of the landslide's centre-of-mass. Single and double differentiation of the centre of mass position with respect to time yielded the velocity and acceleration time histories.

PTV was also used to observe the sub-surface water motions. Fine near-neutrally buoyant particles were dispersed throughout the fluid and illuminated using a white light sheet. The position time histories of the illuminated particles were recorded using a digital camera. Post-processing of these particle positions matched their locations from one frame to the next to generate particle tracks and fluid body velocity fields.

The use of these measurement techniques necessitated a high level of experimental repeatability. As will be discussed in later sections, the limited field of view from the camera set-ups required multiple camera locations be used for repeated runs of the same landslide configuration to be able to capture the entire wave and flow fields. The ability to consistently reproduce the same landslide motion meant

the three experimental measurements, water surface profiles with LIF, and landslide kinematics and sub-surface velocities with PTV, did not need to be performed simultaneously.

Section 4.1 describes the experimental flume set-up and gives details of the model landslide block. PTV was used extensively in this research and is referred to often throughout this thesis, and as such, details of the PTV methodology are initially presented in Section 4.2. This chapter continues in Section 4.3 with a description on how PTV was implemented to measure the landslide kinematics. The development of the LIF technique to measure water levels, and a discussion of its repeatability, is presented in Section 4.4. As this free surface measurement technique has been developed and used as a substitute for traditional wave gauges, its performance and capabilities compared with resistance wave gauges is also presented. Section 4.5 outlines the measurement of sub-surface velocities using PTV.

4.1 Experimental set-up

4.1.1 Flume

The wave tank used in these experiments was a 14.66 m long flume in the University of Canterbury's Fluid Mechanics Laboratory. The base and ends were made of 17 mm thick transparent acrylic sheeting and the sides were of 20mm thick sheets to form a 250 mm wide by 505 mm deep usable section. This flume was designed with minimal reinforcement between adjacent side panels to reduce the interference of the joints during optical data capture. Silicon-based sealant was used in these joints to prevent leakage. The flume was filled with tap water to a depth of 435 mm, leaving 70 mm of freeboard. 3 mm diameter threaded steel rod ties across the top of the flume were spaced at 0.8 m intervals to prevent the tops of the flume sidewalls from bowing due to the considerable hydrostatic water pressures.

This flume was housed in a 3.7 m wide, 18.9 m long, and 2.4 m high, room. All windows and other openings were blacked out to reduce outside light interference and to contain the laser light when it was operating in the darkened room. The base of the flume was 1.1 m above the floor on a steel square hollow section truss frame and was located 1.4 m out from one of the sidewalls. A workbench extended the full length of the opposite side, leaving a space of 1.3 m between it and the flume.

Gantry rails parallel with the flume supported an overhead trolley. The trolley could be moved to any position along the length of the flume room by a variable speed electric motor, and was used to support the various testing equipment.

4.1.2 Landslide Slope

An inclined ramp at an angle of 15° to the horizontal made of 12 mm thick acrylic was placed at one end of the flume. It was held in place by normal forces applied by the sidewalls, and supported by five pairs of vertical struts under the slope placed at regular spacing along the ramp's length. This planar slope extended out above the flume for a height of 0.135 m. This provided space well out of the water to place the equipment for holding and releasing the landslide. The ramp sloped continuously into the flume until it was 0.089 m from the flume floor.

A 2 mm deep step, 50 mm wide, was milled into the two edges of the top surface. This was to hold in place 50 mm wide strips of 0.8 mm thick stainless steel and 1.2 mm thick PVC plastic. The stainless steel strips were used to provide a means for the surface of the slope to transition from the 15 degree slope to the horizontal floor of the flume, and allow the landslide to slide smoothly down the slope and then along the floor where it would eventually stop due to friction. The PVC strips were used to provide a more slippery surface upon which the landslide would slide compared to the acrylic base material, and could be easily replaced when worn. The strips were held in place by small stainless steel screws mounted below the slope surface in counter-sunk holes, spaced 0.100 m apart. For the lower 0.089 m of height from the end of the planar slope to the floor of the flume, the mildly flexible stainless steel strips formed a catenary curve under their own weight. The equation of this curve was determined and profiles of this were cut from sheets of acrylic and fixed underneath the stainless steel strips to provide rigid support beneath. Equation 4.1 gives the water depth profile, in metres.

For: $0\text{ m} \le x < 1.297\text{ m}$

$$d(x) = x \cdot \tan(15^\circ) \tag{4.1a}$$

$1.297\text{ m} \le x < 1.807\text{ m}$

$$d(x) = -0.19(x-1.297)^3 - 0.1024(x-1.297)^2 + 0.2728(x-1.297) + 0.3475 \tag{4.1b}$$

$1.807 \le x$

$$d(x) = 0.435 \tag{4.1c}$$

The strips were used, instead of solid sheets extending across the entire width of the flume, so that the centre portion of the ramp was still transparent to allow light through for the PTV measurement of sub-surface water velocities. A photograph of the slope set-up and diagram of the flume are included in Figure 4.1 and Figure 4.2 respectively. Of note in the photograph is the opening at the base of the slope between the two strips. This opening between the main channel and the region behind the slope

allowed the movement of water between the two chambers, and was incorporated to prevent the landslide from aquaplaning as it moved off the slope. As the landslide passed through the transition curve, its rigidity meant the central section of the landslide moved away from the slope surface, leaving only the leading and trailing edges to move parallel to the slope surface. This increased the volume between the landslide and the slope, and water was sucked in to fill this void. As the landslide moved off the transition curve onto the tank floor, this volume decreased as the central section of the landslide returned to being parallel with the sliding surface. The reduced volume forced the water trapped between the landslide and the slope surface to escape. The opening at the transition curve allowed this water to escape behind the slope. Tests with this opening blocked resulted in the landslide aquaplaning excessively, due to the escaping water forcing up the leading edge of the landslide such that it lost contact with the slope. The approaching flow was directed under the moving landslide and the leading edge was lifted up further until the landslide was almost vertical. The disadvantage of the movement of water between the main channel and the space behind the slope is that mass continuity within the main channel is not preserved. It also had an effect on the wave amplitudes and potential energy. The significance of the exchange flows between the main channel and the region behind the slope is examined in Section 5.3.6.

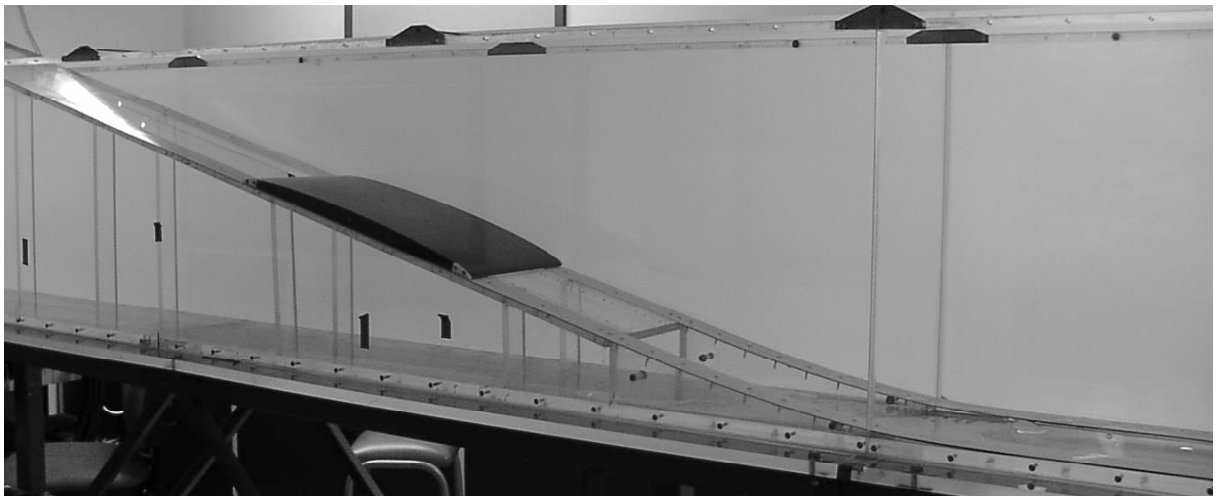

Figure 4.1. Photograph of the slope and landslide model within the wave tank.

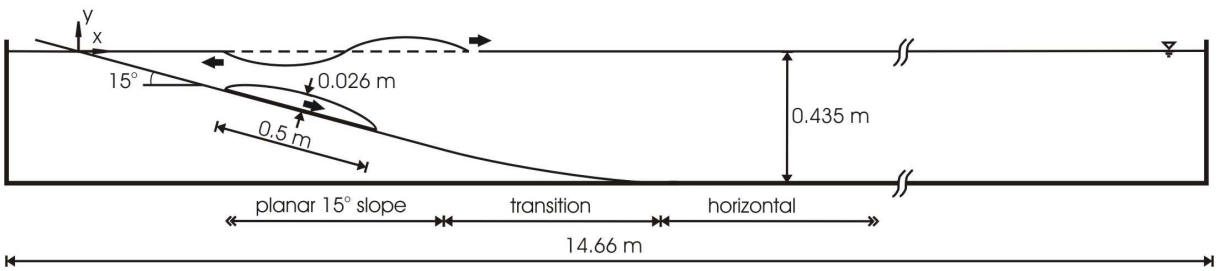

Figure 4.2. Schematic diagram of the flume, slope, and landslide.

Lubricant was applied on the slope surface to minimise any tendency for the model landslide to stick. After testing various lubricants, such as light oils and PTFE-based coatings, silicone grease was found to be most resistant to wearing, moisture, and time degradation, and had the advantage of being able to be applied under water.

Initial investigations showed that the wave field generated was highly dependent on the landslide stopping mechanism, and previous experimentalists have failed to note what technique they used to stop their sliding blocks when they reached the bottom of the slope. It is assumed that the blocks just topple over and stop when they reach the end of the slope, and their wave records end before this time. For heavier blocks with high accelerations and velocities, these times can be quite short. This does not allow sufficient time to observe the waves as they develop and propagate. As mentioned in Section 3.1, Fritz (2002) states that a large amount of kinetic energy of the landslide is removed from the system when solid block models are abruptly stopped at the bottom of the incline. This prevents energy conversion into wave energy, friction, drag, or turbulence, and results in small coefficients of conversion of landslide potential energy into wave energy. The abrupt stopping of laboratory block models from earlier research efforts is not able to recreate the long run-out lengths observed in nature.

To see the effect abruptly stopping the block at the toe of the slope had on the wave field, a tether was attached to the landslide that was just long enough for the block to slide normally from its initial position until the end of the slope. It was found that a block coming to a sudden stop created a wave with amplitude greater than the waves that were generated by the landslide if it were sliding and decelerating naturally. However, as the landslide slid for a shorter length of time, the total potential energy contained in the wave field would be lower. It was considered desirable that the landslide be allowed to progressively transition from sliding down the slope to run out on the flume floor of its own accord. This minimised the waves being generated by the sudden stopping of the block, and was considered to more closely represent the deposition of actual underwater landslide masses sliding along shallow slopes.

4.1.3 Model Underwater Landslide and Release Mechanism

The prismatic semi-elliptical model landslide was milled from a solid block of aluminium. The block was 0.5 m long (L_b = major axis length), 0.026 m thick ($2H_b$ = minor axis = 0.052 m), and 0.25 m wide (w). The total volume of the block was 2.419 litres. Hollow cavities were incorporated into the base of the block that could be filled with polystyrene or lead shot ballast to vary the total specific gravity of the landslide. A plastic sheet was screwed into place to cover the cavities and secure the ballast. To minimise the reflectivity, the landslide block was painted matt black. Photographs of the aluminium slider block are shown in Figure 4.3. AutoCAD drawings used to design the landslide models are included in Appendix A.

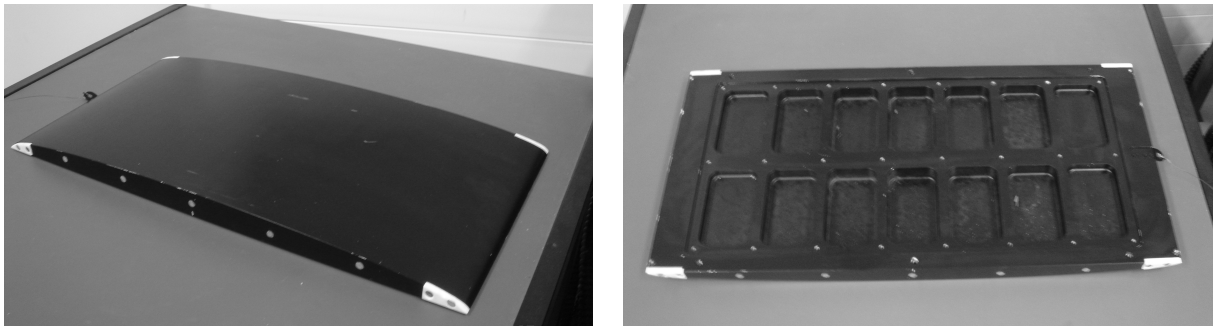

Figure 4.3. Photographs of the upper and lower surfaces of the aluminium sliding block.

Notches were milled into the four corners of the landslide, as shown by the white pieces in Figure 4.3. Screwed into these recesses were sections of polytetrafluoroethylene (PTFE), which had a very low friction coefficient. These were used to minimise the friction should the block touch the sidewalls, and also served to protect the soft acrylic sidewalls from the sharp leading edge of the block.

Small holes were drilled 1 mm into the surface of the base of the block, at the four corners along the leading and trailing edges. Into these were glued 3 mm diameter hardened steel balls. These spheres protruded 2 mm from the base of the slider block and formed the four small sliding surfaces upon which the block would slide along the PVC strips on the slope surface. To further reduce the sliding friction, silicon grease was applied to the slope surface to lubricate the steel balls.

A small metal loop was attached to the trailing edge of the block to allow a length of fishing line to be tied to the block. The trailing end of the fishing line had a loop tied into it. This fishing line was used to anchor the block to the release mechanism and hold it at the correct initial submergence prior to each experimental run. Different submergences were achieved by using different lengths of fishing line.

The release mechanism consisted of a block fixed to the upper section of the slope, well clear of the water. A hole was drilled horizontally through this block and a long metal pin was slid completely through this hole such that the tip of the pin stood proud of the block's surface. The loop on the end of the fishing line was passed over this extended part of the pin. The landslide was released by pulling the pin so the portion that was protruding withdrew into the release mechanism. With nothing to hold the fishing line, the landslide was free to move.

A light emitting diode (LED) was placed in the field of view of the camera as a means of timing the release. The tip of the release pin pressed on a switch when it was fully inserted into the release block and was holding the fishing line. This closed reed switch caused the LED to illuminate. When the pin

was pulled to release the block, the switch was opened and the LED turned off. The first frame in the recorded image sequences in which the LED was not illuminated was considered the start of the slide (time = zero).

The sliding characteristics and wave generation of this model landslide were thoroughly tested to ensure they were repeatable. However, to highlight the steps taken for the sake of test repeatability, the development of the landslide block will be briefly discussed. Model landslide prototypes, made from wood and aluminium sheeting, were initially constructed and preliminary tests with these prototypes were performed to assess the repeatability of the experimental set-up and measurement and analysis techniques. Analysis of the wave fields and landslide motions indicated that the wooden blocks were not sliding consistently. On a few occasions the block did not begin sliding immediately after it was released, staying stationary for a moment while it overcame the static friction. To address the issues of repeatability, modifications were made to the sliding blocks and slope surface.

As the slider blocks were constructed primarily of wood, they were susceptible to shrinkage, swelling, and warping when subjected to repeated wetting and drying cycles. The distorted shape of the blocks prevented them from sliding smoothly and reliably when released, and as such, caused obvious inconsistencies in the wave fields. It was decided to construct the landslide block, the one used in the experiments presented in this research, from a rigid piece of aluminium. Aluminium was chosen, as it was dimensionally stable and would not corrode in water. It also had a low density, compared to mild or stainless steel, to allow a range of lighter landslide densities to be tested. Heavier densities could be achieved by adding lead ballast.

Excessive wearing of the base of the prototype model landslides and the slope surface also contributed to the variations in the sliding characteristics between successive runs. As a consequence, the original PTFE hemispheres glued to the base of the wooden blocks were replaced with hardened steel for the aluminium version.

4.2 Particle Tracking Velocimetry

Particle Tracking Velocimetry is a technique that determines the motions of particles by tracking their positions from frame-to-frame in an image sequence. In this experimental program, PTV was used in two different settings. The first was to measure the motions of the landslide block as it slid down the slope. The second application was to measure the sub-surface water velocities.

4.2.1 General Description of the System

PTV and the related Particle Image Velocimetry (PIV) are two relatively recent visualisation methods, becoming more widely used with the introduction of digital video cameras and high performance

spersonal computers. Compared to earlier experimental methods for measuring fluid flow point velocities, such as Acoustic Doppler Velocimeters (ADV), Laser Doppler Anemometers (LDA), hot-wire anemometers, or pressure probes, PTV and PIV are able to resolve both the temporal and spatial variations of velocity. As they are optically based systems, PTV and PIV also allow the motions of non-fluids to be analysed.

In a PTV system, the movements of particles are recorded using digital photo/videography. Particles can take the form of anything from seed particles suspended in a fluid and illuminated by a light sheet, to dots on solid objects, provided there is sufficient contrast between the 'particle' and the background for particle identification algorithms to succeed. Separate algorithms track these particles from frame-to-frame, and particle velocities are calculated from their displacements during each time interval. Interpolating the particle velocities onto a uniform grid then generates a two-dimensional velocity field time history.

While both PTV and PIV can be used to generate velocity fields, PTV calculates the velocities of individual particles, whereas PIV calculates velocities of regions in the flow based on the cross correlation of image intensities. The advantages of PTV systems are that they are able to more accurately resolve velocities in regions of high shear when compared to PIV methods, and they can operate with low particle densities. The principal disadvantage of PTV methods is that the velocities are calculated for individual particles at the particle's location instead of on a regular grid. To generate a uniformly spaced velocity field, an interpolation scheme must be employed to estimate the velocities at the grid points based on the velocities of surrounding particles. This interpolation process works best when the particles are closely spaced (Plew 2005).

PTV requires specialised software to distinguish the particles within an image, to track them from one frame to the next, and interpolate the particle velocities onto a rectangular grid. The PTV software used in this experimental program was FluidStream, developed at the University of Canterbury for flow visualisation. A more in-depth introduction to PTV and the FluidStream software can be found in the program design manual (Nokes 2005a) and the user's guide (Nokes 2005b).

The key steps in PTV analyses are the particle identification process, the tracking of the particles through the image sequence, and the interpolation of the particle velocities to generate a two-dimensional velocity field time history. Each of these three steps, as implemented in FluidStream, is described in more detail below.

4.2.2 Particle Identification Process

The first step in determining the location and size of particles in an image is to convert it into a two-dimensional array of pixel colour values. Each pixel colour value has red, green, and blue intensities in the range between 0 and 255. Intensity fields may be based on any of the three colours, or an average of them. Greyscale images, such as those captured with monochromatic cameras, still record all three colours for each pixel, however, all three colours have the same intensity. FluidStream has a variety of particle identification algorithms. An average algorithm was used to identify the dots on the side of the landslide as it slid down the slope. A Gaussian algorithm was used to identify the particles suspended in the water for observations of sub-surface velocities.

The average algorithm traverses the pixel array identifying pixels with intensities above a user-defined threshold. When such a pixel is found the surrounding pixels are also analysed and those with intensities greater than the threshold are also considered to be part of the same particle. For each particle identified in this way, the size, intensity, and physical location are recorded. The position of the particle is calculated from the centre of mass, and the intensity is an average intensity of the pixels comprising the particle. The size of the particle, recorded as a radius, is determined from the number of pixels composing that particle, assuming it is circular. Maximum and minimum particle sizes can be stipulated to provide a more robust particle identification process. The main drawback of the average algorithm is its limited accuracy in locating a particle position. A particle's position can only be resolved to within half a pixel, and therefore the particle's location is accurate to within a quarter of a pixel (Nokes 2005a).

The Gaussian algorithm uses a slightly more sophisticated particle identification process, and as such, allows a more accurate estimate of the particle location. The pixel array is analysed to find local intensity maxima that exceed a user defined threshold value. Adjacent particles with intensity greater than a second user defined threshold are assumed to be part of the same particle unless another local maximum occurs, in which case a second particle is identified. To allow for non-uniformity in the intensity of the particles across the entire width and height of the image, the Gaussian algorithm intensities were measured relative to the local background intensity. The background intensity is calculated by averaging the intensity in a small region surrounding the pixel of interest. The size of this region could be varied, but was ten pixels square in these analyses.

A Gaussian curve is fit to the intensities of the pixels comprising each particle in both the x and y directions. The position of the particle is assumed to lie at the peak in the Gaussian distribution. Sub-pixel accuracy is achievable provided the particle extends to three pixels or more in each direction. The accuracy for particles smaller than this is the same as for the average algorithm. The particle radius is determined by the number of pixels, with intensities greater than the lower threshold, either

side of the pixel with maximum intensity. A minimum particle diameter may also be defined to aid the particle identification process.

The use of digital camera lenses with a wide viewing angle allows the greatest field of view to be recorded from a single camera location. However, it can also introduce noticeable distortion to the recorded images. This distortion is called 'barrel distortion' and has the effect of bowing vertical and horizontal lines away from the centre of the image. 'Pincushion' distortion is the opposite and causes lines to bow in towards the centre, as illustrated in Figure 4.4.

To correct barrel distortion, images of a rectangular calibration grid were recorded using identical camera settings as the test sequences. An uncorrected (or distorted) image was adjusted using the image processing software ImageStream (Nokes 2005c), that reduced the bowing of the grid lines. This correction is based on the work of Oranjen (1999). Equation 4.2 describes the correction used in ImageStream.

$$\mathbf{r}_s = (c_0 + c_1 r + c_2 r^2 + c_3 r^3)\mathbf{r}_d \tag{4.2}$$

where $\mathbf{r}_s$ is the pixel location in the source (distorted) image, $\mathbf{r}_d$ is the pixel location in the destination (undistorted) image, r is the magnitude of $\mathbf{r}_d$, and the c_i are user-defined coefficients. In the images captured for this experimental study the correction was relative to an origin located at the physical centre of the image. The four correction coefficients found in ImageStream were then applied in FluidStream at the particle identification stage, where the coordinates of the identified particles in the test sequence were adjusted to correct for barrel distortion.

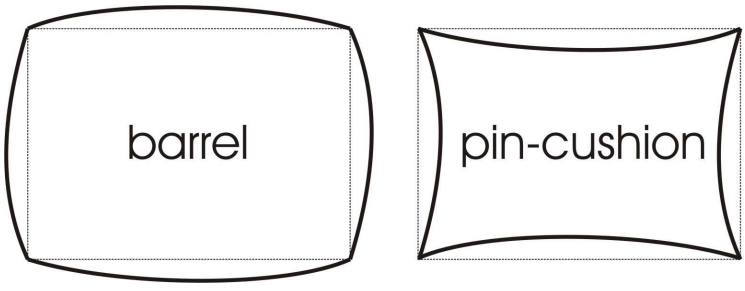

Figure 4.4. Camera lens-induced barrel and pin-cushion distortion.

4.2.3 Particle Tracking Process

With all the particles identified in each frame, the next step in the PTV analysis is the matching of the particles from one frame to the next. FluidStream uses an optimisation-based approach, in which the particles in a frame are matched to those in the subsequent frame based on the cost associated with each assignment. As a particle may have several possible candidate matches, the most desirable match is the one with the least cost. However, the optimal solution for all particles in the frame may not necessarily mean each individual particle is matched to the candidate with the lowest cost, and it may even mean that some particles are not matched at all. The optimisation algorithm uses a variety of costing strategies to determine the particle matches that produce the lowest overall cost considering all the particles in a frame. By minimising the total cost an optimal solution for all particles is obtained.

To calculate the cost associated with each possible match, FluidStream employs a variety of costing strategies. These strategies can be used individually, sequentially, or simultaneously with a weighting applied to each strategy, so that matches generated by previous costing strategies can be used to find more or improved matches (Plew 2005). The computational time required for the matching process can be greatly improved with the use of a search window. As each particle can only move a finite distance during one camera frame interval, a user-defined search window can be defined in the subsequent frame, limiting the number of possible matches to only those particles present in the search window.

Once the set of candidate matches has been determined for each particle, the analysis calculates the cost of each possible match based on the costing strategies selected. Further undesirable matches, having an unacceptably high cost, can be removed with the specification of a maximum matching costing (MMC). Matches with a cost exceeding the MMC are considered unreasonable and eliminated from the process. The selection of an appropriate value of the MMC is crucial to a successful analysis. If the MMC is set too low, then correct matches may be excluded. If the MMC is set too large then computational time will be increased as spurious candidate matches may be considered, but it also allows incorrect matches to be made for particles that have no correct match in the subsequent frame.

To further refine PTV analyses the user can define regions in each frame in which specific costing strategies can be applied. For instance, one particular costing strategy may work well for resolving the elliptical orbits of sub-surface fluid particles associated with wave motions, but may make a greater number of bad matches in other parts of the flow. This costing can then be applied to only the regions in each frame in which the orbital motions exist, leaving the remaining particles to be matched using other costing strategies.

FluidStream contains a variety of costing strategies, of which a combination of some or all of six different costings were used in this study. One of the strategies, the adjacency costing, is a state-based costing. A state based costing only requires information on the state of the particles in a frame, such as location, size, or intensity. The other five strategies used, local velocity, least-squares velocity, recent velocity, space-averaged acceleration, and path length, are matching-based costings. These require matches to have already been calculated to be able to determine costs. Therefore, the use of a matching-based costing requires a state-based costing to have been used previously to initiate the matching process.

The costs generated by these costing strategies are non-dimensional and typically lie between 0 and 1. A cost of 0 corresponds to a very desirable match, while a cost of 1 corresponds to the least desirable match. For clarity of explanation, consider two consecutive frames, frame 1 and frame 2, and costs are calculated for matching an arbitrary particle, P1, in frame 1 to an arbitrary particle, P2, in frame 2.

The adjacency costing is based on measuring the degree to which the pattern of particles surrounding particle P1 corresponds to the same pattern surrounding P2. The particles that lie within a user-defined rectangle surrounding P1 are found, as are those surrounding P2. All the particles in the rectangle centred on P1 are displaced by the vector $\mathbf{r}_{P2}$-$\mathbf{r}_{P1}$, where $\mathbf{r}_{P2}$ is the position of P2 and $\mathbf{r}_{P1}$ is the position of P1. The particle in the P2 rectangle that is closest (adjacent) to each of the particles in the rectangle of displaced frame 1 particles is found. The costing is the sum of the distances between the closest matches normalised by the distance between P1 and P2, as shown in Equation 4.3.

$$C_{12} = \frac{\sum_{i=1}^{n_1} \left| \mathbf{r}_i + \mathbf{r}_{P2} - \mathbf{r}_{P1} - \mathbf{r}_{\alpha_i} \right|}{n_1 \left| \mathbf{r}_{P2} - \mathbf{r}_{P1} \right|} \qquad \textbf{(4.3)}$$

where n_1 is the number of particles in the frame 1 rectangle that have closest neighbours in the frame 2 rectangle, $\mathbf{r}_i$ is the position of particle i in the frame 1 rectangle, and $\mathbf{r}_{\alpha i}$ is the position of the particle in the frame 2 rectangle that is closest to particle i in frame 1.

The local velocity costing uses estimates of particle velocities near P1 to predict its likely position in the next frame. The particles that lie within a user-defined rectangle around P1 and have a velocity estimate are used to calculate a representative velocity for P1. The contribution of each of the surrounding particles to the velocity estimate is weighted by the inverse of their distance from P1. This velocity is estimated as either a median, or an average velocity. The cost, shown in Equation 4.4, is normalised by the predicted displacement of P1 between frames 1 and 2.

$$C_{12} = \frac{\left|\mathbf{r}_{pred} - \mathbf{r}_{P2}\right|}{\left|\mathbf{r}_{pred} - \mathbf{r}_{P1}\right|} \tag{4.4}$$

where $\mathbf{r}_{\text{pred}}$ is the predicted location of P1 in frame 2 based on the velocity estimate, $\mathbf{r}_{\text{P2}}$ is the location of particle P2 in frame 2, and $\mathbf{r}_{\text{P1}}$ is the location of particle P1 in frame 1.

The least squares velocity costing is similar to the local velocity costing, and uses Equation 4.4 to calculate the cost. However the least squares velocity costing uses velocities of a predetermined number of nearest neighbour particles, surrounding P1, to estimate its velocity. A user defined two-dimensional polynomial is fitted to the velocities of the nearest neighbours in a least squares sense and this polynomial is interpolated/extrapolated to the location of P1 in order to estimate P1's velocity.

The recent velocity costing strategy also uses Equation 4.4 to calculate the matching costs. It assumes that accelerations in the particle motions are small and therefore if the velocity of the particle is known in the current frame, then the particle position in the following frame can be predicted using this velocity. This velocity estimate can be based on a match to P1 in the previous frame, a match to P2 in the subsequent frame, or both.

The space-averaged acceleration costing strategy is similar to the local velocity costing. However, instead of estimating velocities, this strategy estimates the acceleration of P1 based on the accelerations of particles that lie within a user-defined rectangle centred on P1. The contribution of each of the surrounding particles to the acceleration estimate is weighted by the inverse of their distance from P1. The cost is based on a comparison between the acceleration of the particle based on a match between P1 and P2 and the estimated acceleration. The cost is given by Equation 4.5.

$$C_{12} = \frac{\left|\mathbf{a}_{pred} - \mathbf{a}_{est}\right|}{\frac{1}{2}\left|\mathbf{a}_{pred} + \mathbf{a}_{est}\right|} \tag{4.5}$$

where $\mathbf{a}_{\text{pred}}$ is the predicted acceleration based on the match between P1 and P2, and $\mathbf{a}_{\text{est}}$ is the estimated acceleration.

The path length costing strategy is based on the undesirability of short particle paths, where a path is equivalent to the number of particles in a path or the number of frames in which a particle has been successfully matched. Short paths, or particles that have been tracked for very few frames, are seen as unreliable. The cost of this strategy is given by Equation 4.6

$$C_{12} = \frac{1}{particles\ in\ path} \tag{4.6}$$

where *particles in path* is the number of particles in the path created by matching P1 to P2.

FluidStream can perform three processes using the selected costing. The first is a full optimisation. This allows unlimited making and breaking of new and old matches based on the costs associated with the chosen strategy. The second, a residual optimisation, is used to make new matches using the particles currently unmatched. All matches made previously are left unaltered. The final process is a cleanup. This process works by evaluating the matches based on the selected costing strategy and removes those matches whose cost exceeds the MMC. No new matches are created during a cleanup process.

4.2.4 Velocity Field Generation Process

With the particle tracking process complete, the final step in the PTV analysis is the generation of a two-dimensional velocity field time history. Particles that have been matched in the previous and/or subsequent frame are able to have their velocities calculated, based on their displacement and the frame interval. The velocity calculation can be performed using a forward difference approximation if the particle is matched to a particle in the previous frame, a backward difference approximation if there is a match with the subsequent frame, or a central difference approximation if there are matches in the previous and subsequent frames. There is also the ability to use matches beyond the previous or subsequent frame. A polynomial least squares fit to the position of the particle tracked through multiple consecutive frames can be differentiated to obtain an estimate of the velocity. The use of the central difference and polynomial estimates may improve the estimate of the velocity, but may reduce the number of particles that can contribute to the interpolation. Generally, however, the reduction in the number of particles has a minor effect compared to the increase in confidence in the velocity through the use of central difference or polynomial estimates.

FluidStream has three interpolation schemes available. These are Delaunay or Thiessen triangulation, least squares polynomial fitting, and binning. The least squares approach was used in this study. See Nokes (2005a) for details of the other two interpolation schemes.

For the least squares interpolation scheme the user specifies a regular rectangular grid onto which the velocities will be interpolated. At each grid point, the velocities of a user-defined number of neighbouring particles are determined. A two-dimensional polynomial function, user-defined but 1st order in this study, is then fit to these velocities in a least squares sense. The velocity at the grid

pointiesis then interpolated from these fit curves. Velocities could not be calculated at grid points outside the region covered by particles.

There is also provision within the software to combine multiple velocity fields. This can be useful when the field of view of the camera arrangement is not capable of capturing the entire flow field with adequate resolution. The velocity fields from multiple camera positions observing different parts of the flow for repeated runs of the experiment can be juxtaposed spatially and/or temporally to create a complete velocity field time history. Velocities in the overlapping regions between fields can be averaged.

4.3 Measuring Landslide Kinematics with Particle Tracking Velocimetry

To measure the landslide kinematics using PTV, a series of red dots were applied to the side of the black coloured model landslide. A colour digital video camera recorded the block's motion against a white background and FluidStream was subsequently used to determine the dots' position time histories. Single and double differentiation of these functions produced velocity and acceleration time-histories.

Before and after each set of wave field measurements, the landslide motions were recorded using this technique. These tests were done to test for any changes to the slider motions that could have arisen during the four hours of water level measurements. Several repeats were performed to check the repeatability of the process.

The effect of residual sub-surface water velocities from previous tests could also affect the motion of the landslide down the slope. Therefore, the time between consecutive runs was also investigated. Tests were performed, in which the interval between runs was progressively increased, and slider motions were recorded and compared. A time between runs of greater than two minutes was found to be adequate to allow the sub-surface motions generated by the previous test to dissipate sufficiently so as to not affect the sliding of the block during the following run.

4.3.1 Equipment and Set-up

White plastic sheeting was placed behind the flume to provide a white background. Fluorescent tube ceiling lights in the room and a supplementary halogen spotlight were used to illuminate the landslide and provide adequate contrast between the red dots and the black landslide surface. The halogen spotlight was mounted on the overhead gantry trolley just below ceiling level and the direction of it was adjusted to prevent reflections off the flume sidewall from reaching the camera.

4.3.2 Image Capturing Equipment and Set-up

A Canon MV30i colour digital video camera was used to capture the image sequences. This camera had a resolution of 720 horizontal by 576 vertical pixels, and a frame rate of 25 Hz. The images were captured with an aspect ratio of 16:9 (H:V) to maximise the field of view. To reduce blurring of the images, the camera was set to record sequences in progressive scan mode at a shutter speed of $1/500^{th}$ second. The white balance and focus were manually adjusted.

The camera was connected to a PC via an IEEE 1394 'Firewire' cable and controlled directly from the computer using Adobe Premiere software. This software also captured the image sequences before saving them as an AVI video file. Premiere was also used to convert the AVI video clips into a sequence of TIFF images.

Due to the limited field of view of the camera and the restricted space beside the flume, the camera had to be moved to several downstream positions to record the entire track of the landslide motion. To aid the movement of the camera to the various locations, it was mounted on the trolley, at a distance of 1.0 m from the flume sidewall and 0.23 m above the floor of the flume. With the camera in this orientation, the resolution at the face of the landslide closest to the camera was 1.32 mm per pixel in the horizontal direction and 0.90 mm per pixel in the vertical. Between four and six adjacent camera positions were required to capture the entire motion of the landslide, depending on the length of run-out.

To signal the start of the landslide test, the release mechanism LED was placed in the field of view of the camera.

4.3.3 Image Analysis

To isolate the red dots from the black and white background of the white plastic sheeting and the black landslide image processing software, ImageStream (Nokes 2005c), was used. The TIFF images were passed through an excess red filter in which the average intensity of the blue and green components at each pixel was subtracted from the red intensity. The remaining red intensity became the red intensity at each pixel and blue and green intensities were set to zero. An example of this filtering process is shown in Figure 4.5 for a single frame in which the red dots on the side of the sliding block have been isolated from the background.

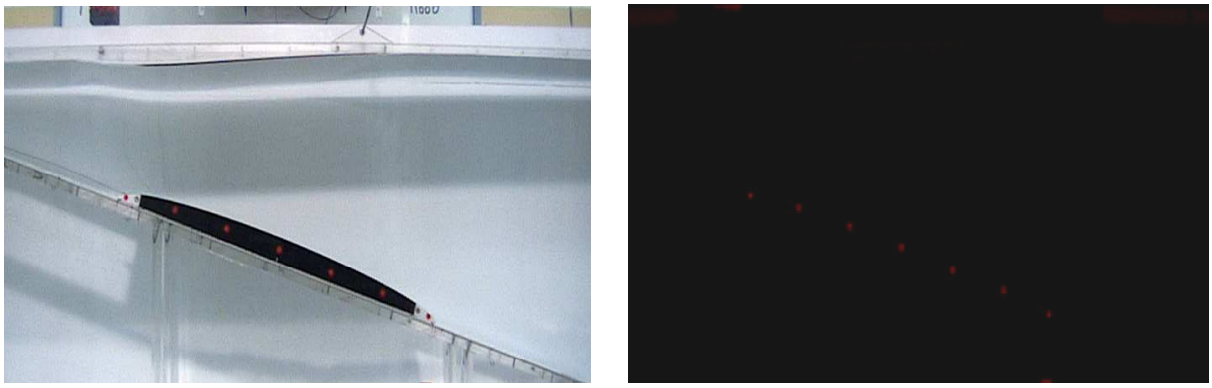

Figure 4.5. An original image (left) and its processed image (right) to remove all but the red dots on the side of the sliding block prior to the PTV analysis to find the landslide's kinematics.

Before inputting the filtered images into FluidStream, the barrel distortion correction constants for Equation 4.2 were determined. From analysing the images of the rectangular calibration grid taken before the landslide tracking tests, using identical camera settings, the calibration constants presented in Table 4.1 were determined. The filtered images were then input into FluidStream along with the barrel distortion correction.

Table 4.1. Barrel distortion correction coefficients for the tests to measure landslide kinematics.

Coefficient	value
c_0	1.040
c_1	-0.005
c_2	-0.030
c_3	-0.005

The PTV analysis, as outlined in section 4.2, identified the red dot at the landslide centre of mass and tracked it through the image sequences. The adjacency and space-averaged acceleration costings were used simultaneously, with weightings of 0.8 and 0.2 respectively. Adjacency was chosen as the arrangement of the dots on the landslide did not move relative to each other, other than the small rotation as it moved over the transition curve at the base of the slope. The adjacency costing could easily recognise and match the particles. The space-averaged acceleration was used to aid the matching process as the landslide rotated at the transition curve, as the dots on the landslide rotated collectively and the change in velocity and direction of each dot was comparable to the dots surrounding it. The costs for both strategies were calculated using rectangular regions 1000 mm x 1000 mm in size so that all the dots on the side of the landslide were included in the cost calculation. An MMC of 0.6 and search windows 200 mm x 200 mm centred on each particle were used in the analysis.

Applying the barrel distortion correction to the PTV technique to track the landslide provides more accurate results for the slide kinematics. To demonstrate the importance of the distortion correction the sliding block was moved horizontally and its motion recorded with a digital video camera. PTV analysis of this image sequence without compensating for the lens-induced distortion resulted in the dotted line in Figure 4.6. This shows how the block appears to drop in elevation by approximately 8mm and then rise back to its original height, even though its true motion was practically horizontal. Employing the distortion correction significantly reduced the apparent bowing, as shown by the solid line.

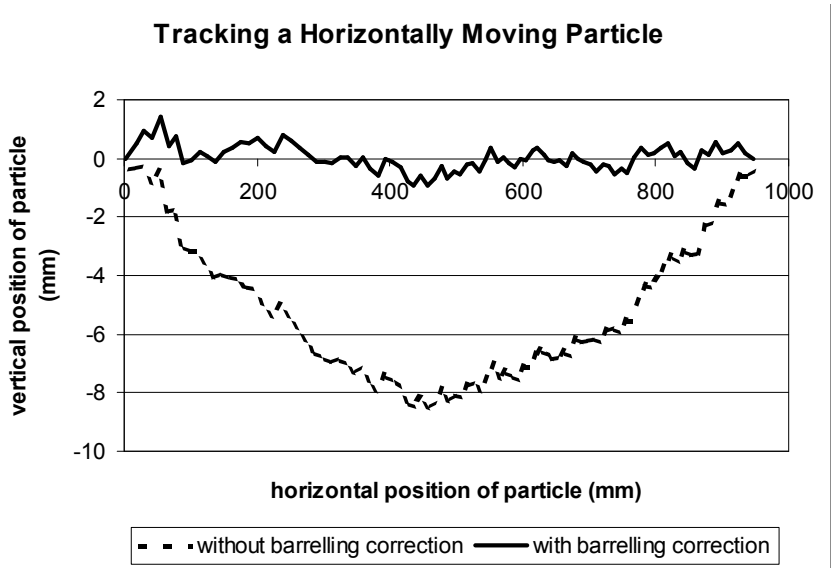

Figure 4.6. Plot showing how the track of a purely horizontally moving particle (tracked using the PTV technique described in section 4.2) has been corrected for camera lens-induced barrel distortion.

4.3.4 Repeatability of Slider Motion

After the construction of the new aluminium model landslide and modifications to the slope surface, the slide repeatability was assessed with the PTV technique. The results of this test are presented in Figure 4.7a where the landslide centre of mass location is plotted against time for ten of these runs. Although the repeatability was better then the original wooden block the data still showed significant differences between runs.

After the introduction of lubricant and observing the minimum two minute timing between successive runs, the slide repeatability was assessed again. Figure 4.7b plots 25 runs after the PTFE surface spray was used as a lubricant. Experimental runs were completed at 2-minute intervals. Of note in this graph is the variation of the horizontal position time-histories during the 3 days of testing. The gradual decrease in velocity over time was determined to be due to the thin layer of spray-on lubricant wearing off.

Figure 4.7c plots the horizontal position time histories of 25 runs with the silicone grease lubricant. The sliding characteristics of this experimental configuration was rigorously tested to determine if there were any ill effects on the test repeatability through changes over time or through wearing. These tests consisted of over 180 separate runs over three days. The minimal variations shown between 25 of these separate trials indicate that the modifications made increased the test repeatability, and that this regime is not significantly affected by time or wearing.

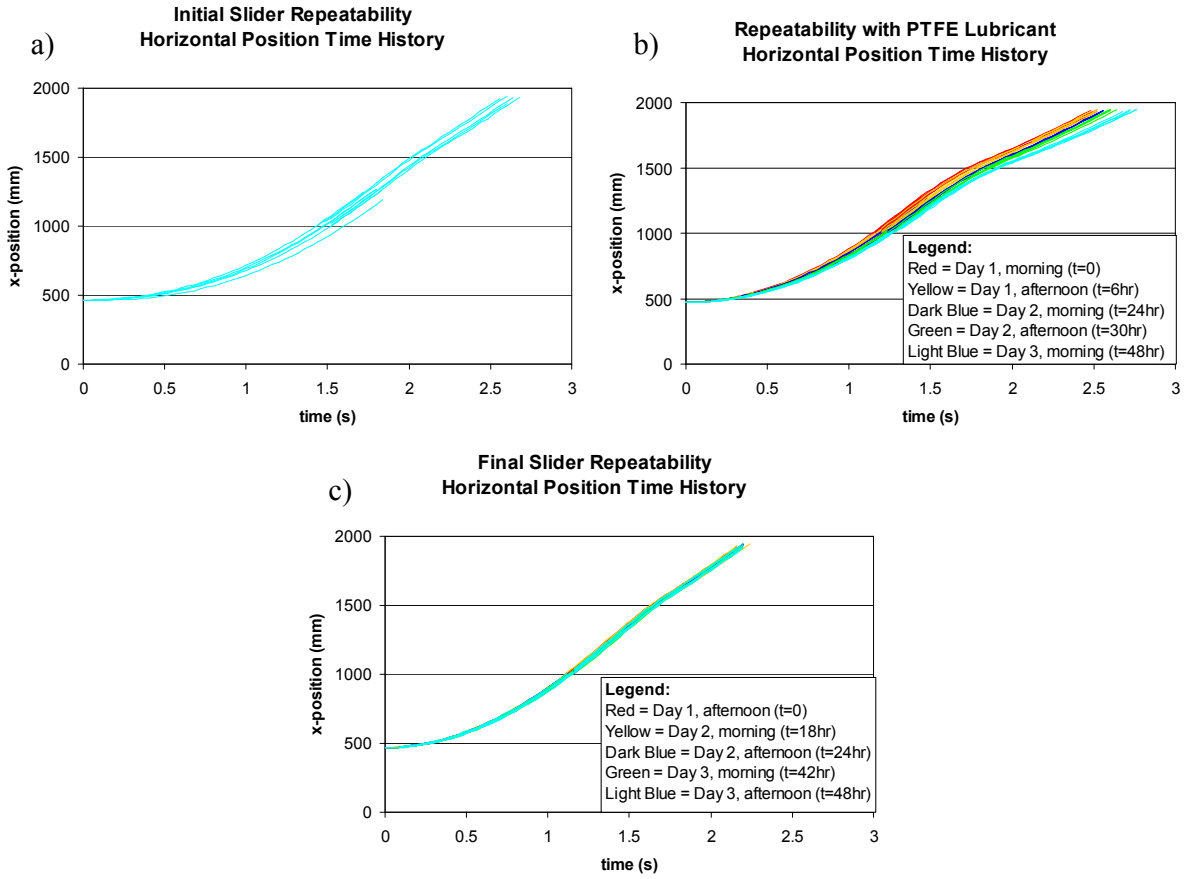

Figure 4.7. Repeatability of landslide centre-of-mass horizontal position time histories of: a) 10 runs immediately after the construction of the aluminium slider block, b) 25 runs using spray-on PTFE lubricant, and c) 25 runs after all modifications to the experimental configuration prior to the start of the main landslide tests. The light blue lines lie directly above the obscured red, yellow, dark blue, and green lines

Plots of the landslide centre of mass horizontal and vertical position and velocity time histories illustrate the final repeatability achieved after all the modifications to the landslide block, slope surface, and lubrication. Figure 4.8 shows the horizontal and vertical position time histories of the landslide centre of mass for one of the landslide configurations. The time histories from four repeated runs at the two upstream camera positions and two repeated runs at the three downstream camera positions are shown juxtaposed and overlaid. Figure 4.9 plots the corresponding horizontal and vertical velocity time histories. The increased noise in these plots is due to the noise present in the position time histories being amplified by the differentiation process. Even amplified, this noise is low compared to the magnitude of the velocities themselves.

To determine the position time history of the landslide centre of mass for the 15 landslide configurations (see Section 5.2 and Appendix B), measurements were taken before and after each set of wave field measurements. Tests were performed before and after in order to test for any changes to the slider motions that could have arisen during the time required for the water level measurements. Due to the limited field of view from the camera, the landslide motion was captured at a variety of downstream locations for repeated runs. Four repeated runs at the two upstream camera positions, observing the accelerating landslide, and two repeated runs at the remaining downstream camera positions were completed before and after the water level measurements.

The particle identification and matching processes, as outlined earlier, were performed for each of the image sequences and the particle locations recorded. The particle locations for each repeat and at each camera position were combined in MATLAB to form a complete landslide centre of mass position time history as it slid the entire length of the slope and ran out along the floor of the flume. Spline curves were fit to the combined position data. Each curve was then differentiated with respect to time to calculate the landslide velocity time history and acceleration time history.

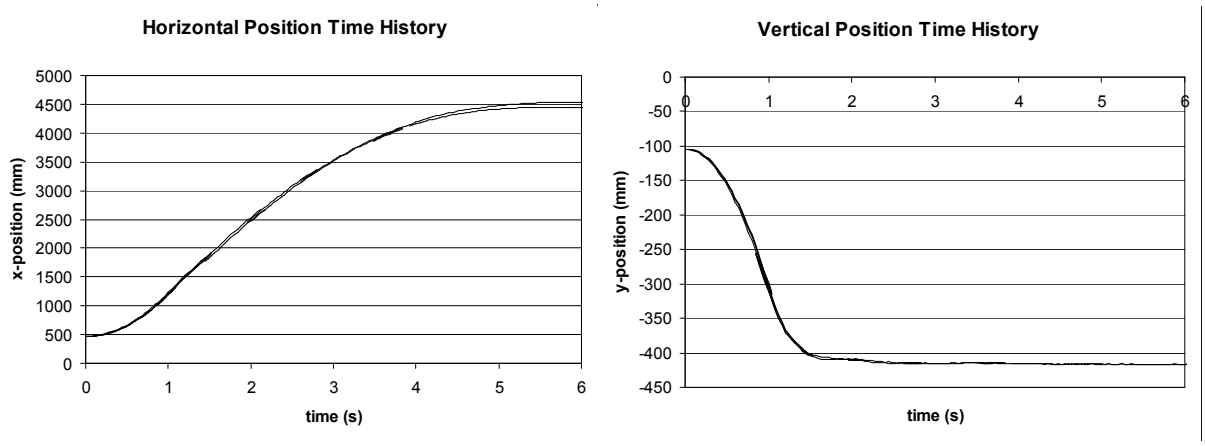

Figure 4.8. Example of repeatability of landslide centre-of-mass a) horizontal and b) vertical position time histories.

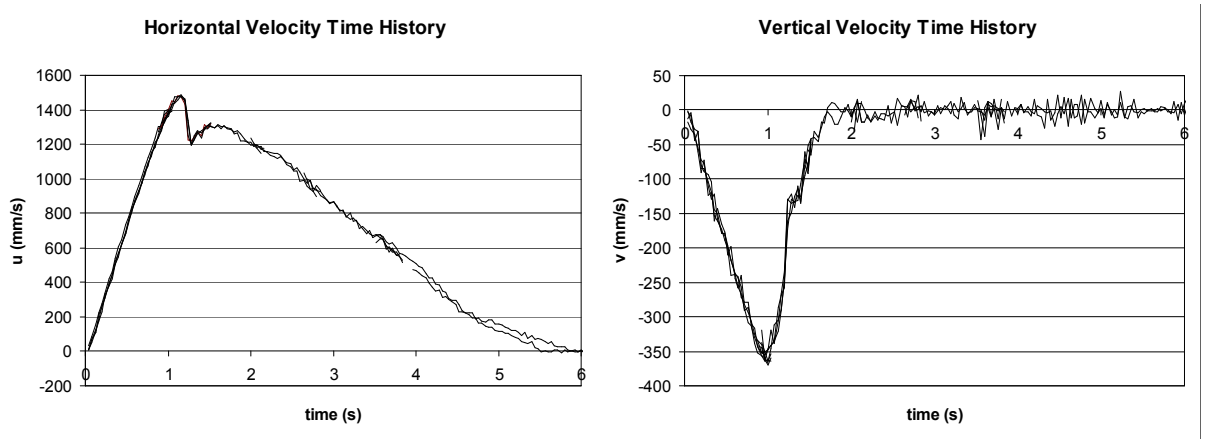

Figure 4.9. Example of repeatability of landslide centre-of-mass a) horizontal and b) vertical velocity time histories.

4.3.5 Experimental Procedure

The following list outlines the typical procedures for capturing movie clips of the landslide to determine its motions using PTV. Landslide motions were recorded directly before and after the water surface profile measurement experiments.

i) The flume was filled with fresh water and left for one day to degas. Any air bubbles that formed were removed before the tests.
ii) The Canon MV30i digital camera was attached to the gantry trolley and levelled using a spirit level. Its position relative to the front sidewall was determined.
iii) The halogen spotlight was securely attached to the gantry trolley and orientated so as to illuminate the red dots on the side of the landslide yet minimise reflections off the sidewall from reaching the digital camera.

iv) An image of a scaled calibration grid, placed in the plane of the inside face of the sidewall, was captured to determine scale and barrel distortion correction coefficients.
v) The gantry trolley was moved so that the camera observed the desired area. The position of the camera relative to the original shore was determined.
vi) The LED used to indicate the release of the landslide was placed in the field of view of the camera.
vii) The elliptical landslide block was placed on the submerged slope at the required initial submergence and attached to the release mechanism.
viii) The flume was left undisturbed until all waves had dissipated.
ix) The halogen spotlight and room lighting were activated.
x) Movie clips of the red dots on the side of the landslide were captured continuously from approximately 2 seconds before landslide release until approximately 13 seconds after release. Images were then stored to the PC hard drive.
xi) The baffles were lowered into the flume to aid dissipation of the waves, and left for 1 minute (see Section 4.4.4).
xii) For each repeat run, steps vii) to xi) were repeated, and for each change in camera position, steps v) and vi) were repeated.
xiii) The captured images were then analysed and manipulated as outlined in Section 4.3.3.

4.3.6 Errors

This section describes and quantifies the potential sources of errors in the PTV analysis and the determination of landslide position, velocity, and acceleration estimates.

Length scales, in mm/pixel, within the images were found by placing a regular rectangular grid in the same vertical plane as the red dots on the side of the landslide. The captured images were then rectified for barrel distortion. Length scales were calculated by dividing lengths within the grid by the corresponding number of pixels in the image. As the captured images were in a 16:9 aspect ratio, separate horizontal and vertical scales were needed. Nine grid and pixel lengths were measured at a variety of positions in the image and averaged to calculate the final scale in both the horizontal and vertical directions. Horizontal grid lengths were measured as 771 mm (± 1 mm), and the corresponding number of pixels was 583 pixels (± 2 pixels). Vertical grid lengths were measured as 462 mm (± 1 mm), and the corresponding number of pixels was 514 pixels (± 2 pixels). The horizontal and vertical length scales used in the PTV analysis, after correction for barrel distortion, were 1.32 mm/pixel (± 0.01 mm/pixel) and 0.90 mm/pixel (± 0.01 mm/pixel) respectively. Based on these error estimates, the error in length scale is better than 1%.

The errors associated with the time interval between frames was estimated by measuring the elapsed time for a large number of frames. The accuracy of the camera frame rate was found to be within ± 1.0 x 10^{-5} sec/frame. Based on the 25 Hz frame rate of the camera, the time step error is approximately 0.03%.

There are also possible errors with the particle identification processing of the red dots on the landslide. Illumination of the dots may not be uniform, preventing the intensities of sections of the dot in the image being above the threshold intensity. This may give the particle a non-uniform shape so its centre of mass may not coincide with the centre of the dot. Also, particle locations cannot be estimated better than ¼ pixel (Nokes 2005b). The absolute errors from non-uniformity of shape and ¼ pixel accuracy are considered similar at 0.33 mm.

Errors associated with particle tracking were eliminated. As there were only a maximum of seven particles in each frame it was clear by inspection that the particle matching process was correct.

The absolute error in particle location of ±0.33 mm produces an instantaneous velocity error of ±8.25 mm/s for the 25 Hz camera frame rate. Of all the experiments, the lowest maximum velocity magnitude was 950 mm/s. This error equates to an error in maximum velocity magnitude for the landslide motions of no more than 0.9%. For velocity magnitudes less than the maximum, the error is still less than 5% for velocities above 165 mm/s (or 6.58 mm displacement per frame interval). Therefore, for the portion of the experiments in which the landslide velocity is greater than 165 mm/s, which is approximately after the first 5 frames, velocity errors are less than 5%.

The maximum (initial) acceleration of the landslide occurs within the first few frames. Assuming the same 5% error in velocity applies when the initial acceleration occurs, the absolute error in acceleration is approximately 210 mm/s^2. The lowest initial acceleration for these tests was 835 mm/s^2 (for the SG5_IS1 combination), which translates to approximately 25% error in acceleration. For the highest initial acceleration of 1640 mm/s^2, this error reduces to less than 13%. However, as the time histories of landslide centre of mass position are smoothed with a spline curve, there will be some degree of averaging in particle locations. This will reduce the errors in the velocity and acceleration estimates.

The high level of sliding repeatability increases confidence in the reliability of the position, velocity, and acceleration time histories.

4.4 Measuring Water Levels With Laser Induced Fluorescence

For the past half-century experimentalists investigating laboratory water waves have relied predominantly on stationary point gauges to record water level time-histories. These gauges rely on sensing variations in electrical properties between two probes immersed in the water, and a calibration is performed to determine the relationship between the depth of immersion and either resistance or capacitance.

Point gauges are adequate for steady-state waves since wave amplitudes which don't change significantly as they propagate will result in the same water level time history as the wave profiles, as shown in Figure 4.10. However, if the waves are changing considerably as they propagate, then point wave gauges can only record the instantaneous water level as the wave passes the gauge, and information regarding spatial variation is lost.

These electrical point gauges, such as Resistance Wave Gauges (RWG) and Capacitance Wave Gauges (CWG), measure changes of water level over time at specific points in the flow. Many experimentalists have used these for recording both steady and unsteady wave phenomena. Lee et al (1993) used RWGs to measure water waves to compare with numerical results in a study into the interaction of transient non-linear waves with a submerged breakwater. The small-scale wave spectrum of ocean waves were recorded with RWGs by Gogineni et al (1990) to determine the radar backscattering from ocean surfaces.

Wiegel (1955), Rzadkiewics et al (1997), and Watts (2000) used RWGs to measure waves generated by the motions of submerged objects in studies of simulated underwater landslides. One gauge was located in the wave generation region to observe the non-steady wave characteristics, and additional gauges were placed downstream from the source mechanism to record the far-field wave amplitudes. Fritz et al (2003a) and (2003b) used CWGs to measure the wave heights of waves propagating from the impact of simulated sub-aerial landslides. Gauges were placed along their wave channel axis at 1m intervals, starting from the generation region. Raichlen and Synolakis (2003) used a two-dimensional array of gauges to measure the three-dimensional wave field generated by a submerged triangular wedge-shaped sliding block.

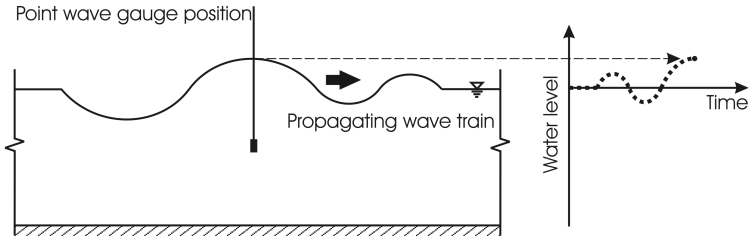

Figure 4.10. Typical wave tank with an electrical point wave gauge.

Numerical water wave models are able to predict entire wave fields, which include both spatial and temporal variations. Current practice is to compare the point gauge readings from experimental work with their equivalent time series in the model. If these agree relatively well, then they infer that the accuracy of their models extends past their point gauge locations to cover their entire wave domain (Enet et al. 2003). This may not be the case, and a technique needs to be developed to capture wave fields (spatial and temporal variation) experimentally, and to compare these results with wave fields generated computationally. In this way, the accuracy of these models can be more rigorously assessed.

The use of electrical wave gauges to measure wave amplitude time histories has many limitations. The first and most obvious is that they are point gauges, that is, they record water levels at discrete points in space. They are not able to discern the spatial variation of water level such as wave shape, or the evolution of water waves.

These resistance and capacitance wave gauges rely on sensing changes in the electrical properties of the water and the probes, and as such are influenced significantly by temperature and the chemical composition of the water. Therefore, these gauges require frequent and cumbersome calibration throughout the course of an experimental programme, and necessitate close monitoring of the surrounding environment to ensure variations in the aforementioned parameters do not greatly affect the readings. Also, a significant water depth is required as the gauges are immersed a specific distance, and as such are not suitable for measuring wave run-up due to the reduced water depth up a sloping beach. As the probes are physically in the water, they may affect the passage of waves, as water must flow around the wires. Surface tension on the gauges cause menisci to form and these are observed to reverse direction as the water depth increases and decreases, leading to possible errors in water level readings, especially at smaller laboratory scales.

Recording water levels optically has many advantages over wave gauges, the main one being its ability to capture the spatial variation of the waves as well as the temporal variations. However, recording the wave profiles through the sidewalls under ambient light conditions has the problem of interference of the reversing menisci, as only the intersection of the free surface with the near and far

sidewalls is distinguishable. In order to capture the wave profiles and run-up heights away from any sidewalls a means of distinguishing the water surface in a vertical plane between the sidewalls was developed. This was achieved by the use of Laser Induced Fluorescence (LIF). By projecting a thin vertical laser light sheet through the wave tank containing a low concentration of fluorescing dye, the surface wave profile in the illuminated plane was captured by a digital camera and stored on a PC. Analysis of the resulting image sequence and a transformation from image coordinates to physical coordinates allowed wave profile time histories to be plotted.

What follows is a description of the technique and the experimental set-up required to capture water levels at points in the flow, wave profiles over a length of water surface, and wave run-up heights. The laser and fluorescent dye combination used here in the development of this technique are described, as are the image capturing and data processing methods. To evaluate the performance of the LIF technique, the water level time histories from the LIF method are compared with results from simultaneous measurements with traditional RWGs.

There have been many applications of LIF in experimental fluid dynamical experiments in the past, but the use of it in quantitative water level measurements is apparently new. Previous uses have included visualisation of turbulent structures (Hsu, Kuang and Sun 2001; Lommer and Levinsen 2002; Shiono and Feng 2003), the determination of the presence and concentration of chemical and biological substances (Arnold, Bombach, Kappeli and Schlegel 1997; Houcine, Vivier, Plasari, David and Villermaux 1996; Kozlova, Lobacheva, Pravdin, Romakina, Sinichlin and Tuchin 1991; Zhou, Lu, Li, Sheng and Duan 1994), and in the visualisation of the spread and dilution of jets and plumes (Shy, Yeh and Chu 1997; Tian and Roberts 2003; VanLerberghe, Santiago, Dutton and Lucht 2000). Studies by Wang and Davidson (2001) into a profile tracking system for discharges into a co-flowing environment used the fluorescence of the dyed jet fluid as a means of measuring its extent of spread. The light intensity provided a measure of the variation of concentration of the dye in the jet and thus the extent of mixing with the ambient fluid was determined.

The optical technique used in this current experimental study relies on a similar principle in that the fluorescing dye highlights the interface between the water and air. In this case, however, variations in concentration, and hence light intensities, are not important. Only the interface between the two contrasting fluids is of interest.

Similar experiments looking at free surface profiles have been done in the past. The experiments of Mori and Chang (2003), looking into turbulent jet discharges into a wavy environment, used LIF to observe the jet centreline movement and free surface elevations simultaneously. Yeh and Ghazali (1987) used LIF in their study on the transition of a bore as it ran up a beach. Unlike the LIF

experiments performed in this current experimental study, their LIF observations were qualitative only.

In this application of LIF a small concentration of fluorescent dye is stirred into the flume water, and illuminated with a vertical laser light sheet orientated parallel with the longitudinal axis of the wave tank. The dye in the water column fluoresces due to excitation by the laser light, and this contrasts with the surrounding darkness of a blacked-out room. A high-resolution digital video camera is used to record a series of images of the illuminated water. In each frame the interface between the regions of high and low light intensity marks the location of the free surface.

This LIF technique is well suited to water wave experiments as it has few of the drawbacks of electrical wave gauges, and is able to capture the spatial variations of waves as well as their temporal development. Temperature dependence of recording wave time histories is eliminated with LIF, and the system only needs one calibration for each camera location and set-up. The LIF technique does not require any minimum water depth or probe submergence to work, and so can be used to measure wave run-up where wave gauges will not fit due to their size. Another advantage of non-intrusive measurement is the elimination of flow disturbance and surface tension and menisci reversal effects. Other advantages over electrical wave gauge methods include the ease of adaptability to the experimental set-up with regards to location and resolution. Resolution of the LIF wave records is dependent on the resolution of the digital video camera and can be increased or decreased as necessary by adjusting the proximity of the camera to the subject. Higher resolutions come at the expense of spatial coverage.

4.4.1 Equipment and Set-up

To provide luminescence, Lambda Physik's Lambdachrome Rhodamine 6G laser fluorescent dye was added to the wave tank water, to an overall concentration of approximately 0.1 mg/L. Rhodamine 6G has a typical excitation wavelength of approximately 525 nm and a higher emission wavelength of 555 nm.

A 1 mm thick neodymium yttrium vanadate ($Nd:YVO_4$) laser light sheet, with a wavelength of 532 nm, excited the dye solution. In this case, a Spectra-Physics Millennia IIs continuous-wave visible laser was used at a power output of 2.0 W. The light from the laser head was passed through a fibre-optic cable to a divergent laser sheet generator, so that the power level of the final light sheet was reduced to approximately 1.0 W due to losses in the fibre-optic connections. This combination of laser power output and dye concentration provided a distinct contrast at the water-to-air interface. The effects of minor variations in laser and dye properties were not significant, as the camera aperture was used to adjust the light levels reaching the camera CCD.

The laser was mounted directly above the water to project a vertical light sheet parallel to the long axis of the tank and the direction of wave propagation. The light sheet generator projected a divergent sheet with an approximate 45° spread. The height of the sheet generator above the water surface was 0.500 m. The equipment set-up used to capture wave profiles is shown in Figure 4.11. To maintain the 0.140 m distance of the light sheet relative to the outside face of the flume sidewall and the 1.155 m from the camera, the laser was mounted on the gantry trolley.

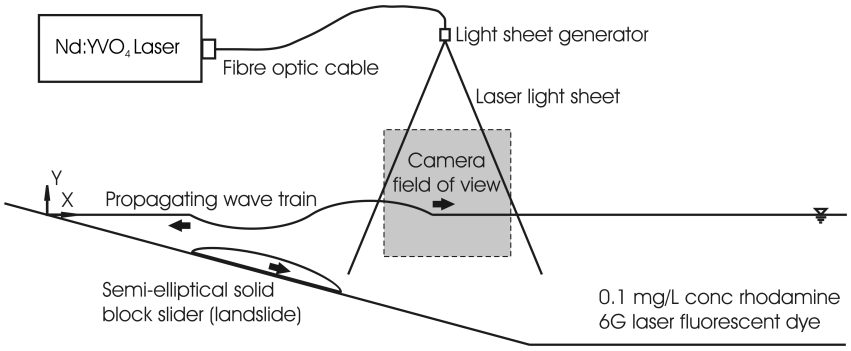

Figure 4.11. Experimental set-up for LIF water level measurement of underwater landslide-induced tsunami.

4.4.2 Image Capturing Equipment and Set-up

A 25 mm Pentax lens mounted on a Pulnix TM1010 10-bit monochromatic progressive scan camera with a 1008 x 1008 pixel resolution and a 25.4 mm square CCD was used to capture images of the free surface response to the release of the model landslide. The frame rate was set to 15 Hz and shutter speeds were set high, at $1/500^{th}$ second, to reduce image blur. A Heliopan orange-22 colour filter was attached to the lens to filter out the 532 nm wavelength light from the laser but allow the 555 nm wavelength light of the fluorescing water to pass.

LabVIEW was used to capture frames from the camera and store them in a 2 GB RAM buffer on a PC via a Bitflow frame-grabber card. The stored images were archived to hard disc as a sequence of JPEG images, where only the highest 8 bits of the intensity signal were stored in the JPEG files.
To eliminate the interference of the water line at the sidewall nearest the camera and to capture the water surface in the illuminated plane, the camera was mounted slightly higher than the water level. As a result, this technique would be equally applicable for wave tanks with transparent sidewalls as for opaque-sided wave tanks or flumes provided there is adequate distance between the illuminated plane and the wall, as shown in Figure 4.12, or if the sidewall is low enough.

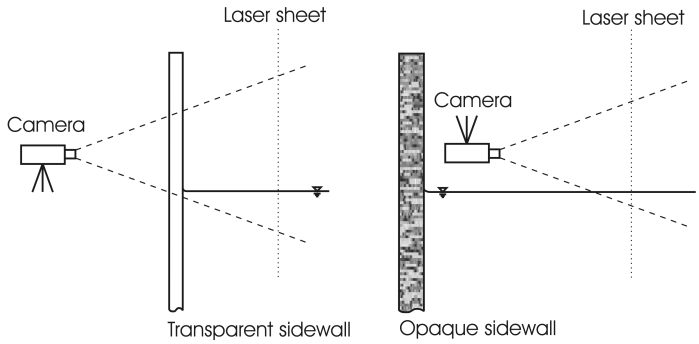

Figure 4.12. Camera mounting options for transparent and concrete sided wave tanks.

To allow different sections of water level to be observed without changing the camera location relative to the laser sheet, both were mounted on the gantry trolley. The camera was mounted 1.155 m from the light sheet, giving a field of view of approximately 400 mm x 400 mm. This provided a resolution of approximately 3 pixels per millimetre in the illuminated plane. The camera was mounted 0.146 m above the still water level. The video capture was manually started a few seconds before landslide release and recording stopped automatically after a pre-determined number of frames were captured. This length of time was greater than the time required for the waves to propagate to the end of the tank and return to the generation region. The LED connected to the release mechanism, used to indicate landslide release, was placed in the camera frame.

4.4.3 Image Analysis

ImageStream (Nokes 2005c), an image processing software package developed by the University of Canterbury's Civil Engineering Fluids group, was used to determine the light intensity of each pixel in each of the saved JPEG images, on a scale between 0 and 255. The arrays of pixel intensities were then imported into MATLAB for further processing and plotting. The position of the interface between dark and light pixels was examined and the transition from the high intensity light of the fluorescing water to the low light intensity of the air signalled the location of the water surface. A simple scaling procedure then transformed the water level from pixel space to physical space.

Before the image sequences from the tests were analysed, they were rectified to remove the barrel distortion caused by the camera lens. ImageStream was again used to determine the barrel distortion correction constants for Equation 4.2. Before the water level tests a rectangular calibration grid was placed in the same vertical plane as the laser light sheet. From analysing the images of the grid, taken using identical camera settings as the water level tests, the calibration constants presented in Table 4.2 were found. The calibration constants for the wave run-up tests are presented in Table 4.3. The corrected images were then used in ImageStream for subsequent analysis.

Table 4.2. Barrel distortion correction coefficients for water level measurement tests.

Coefficient	value
c_0	1.015
c_1	0.0
c_2	-0.005
c_3	-0.010

Table 4.3. Barrel distortion correction coefficients for wave run-up measurement tests.

Coefficient	value
c_0	1.030
c_1	-0.025
c_2	0.0
c_3	-0.007

An illustration of the image processing used is illustrated in Figure 4.13. The top image is from a raw JPEG image of a 58 mm (crest-to-trough) wave passing from left-to-right. The middle image shows the intensity field of the same image where a range of shades indicates the relative intensities of each pixel. The lower image is a contour plot of the pixel intensity field. Due to the steep intensity gradient at the water surface, the contours appear as a single curve.

It was important to adjust the camera properties such as focus, intensity thresholds, and gains such that the interface between water and air (dark and light) was as sharp and smooth across the water surface as possible. If these were adjusted correctly, as can be seen in Figure 4.14, then the transition from high to low intensity occurred very rapidly, typically across one pixel. The fluctuations in intensity between 20 and 60, between 0 mm and 10 mm above the free surface, are due to flaring of the light fluorescing from the water.

Figure 4.13. Illustration of image analysis process; a) raw JPEG image, b) pixel intensity field, and c) pixel intensity contours.

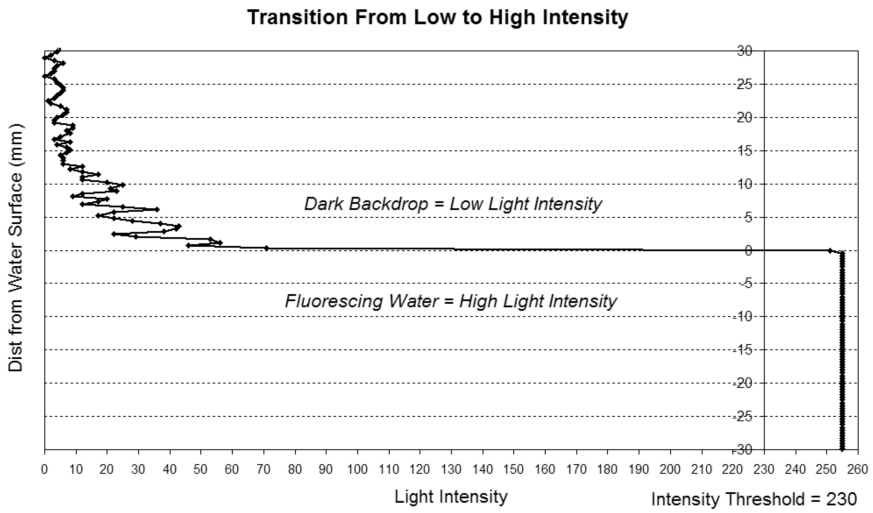

Figure 4.14. A typical transition from low to high intensity at the interface between air and water for a column of pixels.

Instead of determining the position of the high-to-low intensity interface to the nearest pixel, linear interpolation of pixel intensities between adjacent pixels allowed sub-pixel resolution to be possible. The threshold pixel intensity, the intensity above which a pixel was deemed to represent the fluorescent water and below which was air, was chosen such that it was above the noise level of the low light intensity of the dark background, yet below the maximum intensity threshold of 255, to allow for linear interpolation to locate the interface. This threshold was held constant for all image sequences from a particular camera set-up and lighting condition, and was typically chosen to have a value of 230.

Crossing the interface from water to air resulted in a rapid drop in light intensity. Selecting a higher intensity threshold defined the water surface as a point closer to the water's side of the interface, creating a downward bias. Lower intensity thresholds defined the water surface to be nearer the air's side of the interface, creating an upwards bias. However, the wave heights were not significantly affected by the value of the threshold intensity chosen. Several seconds of still water were recorded before each test to set the location of the still water surface for the chosen intensity threshold and the wave heights were measured relative to this. Any biasing of the wave heights due to the chosen value of the intensity threshold would have the same effect on the location of the measured still water level.

On its path to the camera the fluorescent light had to pass through the transparent acrylic sidewall. The acrylic sheeting had a refractive index of 1.51, compared to 1.0003 for air, and as such, the water level position was corrected for refraction errors. Also, as the camera was mounted slightly above the water level, to reduce interference of the water level at the sidewall, the data also required correcting for scaling errors due to parallax, as shown in Figure 4.15.

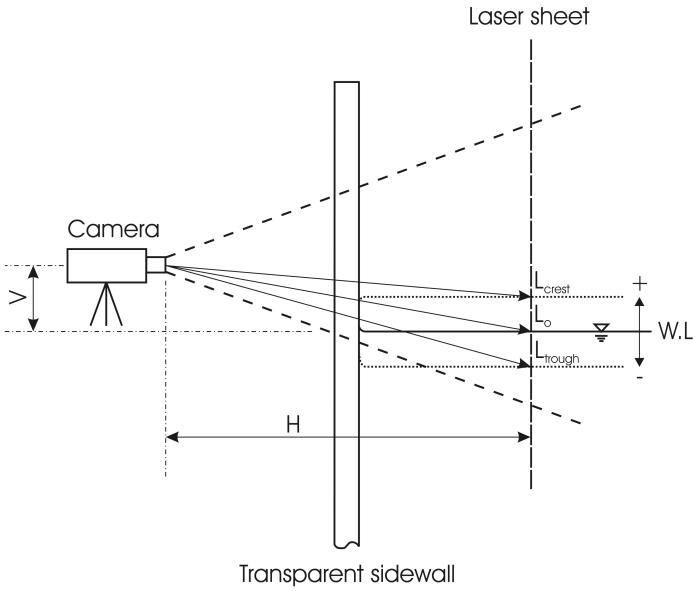

Figure 4.15. Water level errors due to camera angle (parallax).

The expression used to correct the water level for parallax errors is given in Equation 4.7.

$$WL_{corrected} = \left[1 - \left(\frac{\frac{V}{H} * WL}{L_o}\right)\right] * WL \qquad \textbf{(4.7)}$$

where: WL = refraction-corrected water level (positive and negative)

V = vertical distance of camera above still water level

H = horizontal distance of camera from laser light sheet

$WL_{corrected}$ = water level corrected for camera angle-induced scaling errors

L_{crest} = distance from camera to positive water level

L_o = distance from camera to still water level

L_{trough} = distance from camera to negative water level

One of the disadvantages of this LIF method is its inefficiency in covering large areas. Many wave tanks have dimensions in the order of tens-of-metres, and electrical point gauges can be placed at any location and spacing as each gauge is relatively independent of the others. Using the LIF method over long lengths in these tanks could require significantly reduced resolution, as each unit length would be resolved by fewer pixels. To overcome this, the water level time histories can be measured using this LIF technique at multiple locations. Although it would be desirable to record these images simultaneously, the use of multiple cameras was not necessary as the experiments were shown to be sufficiently repeatable. In this study, a single camera was used to observe the flow in different locations for repeated runs of the same experiment. The camera and laser sheet were placed at the

shoreline to record the propagation of the landslide-generated waves up the slope. The trolley-mounted camera and light sheet were then moved further downstream to observe the downstream propagation and continued evolution of the waves. The water profiles were then combined to create a wide field of view of the surface response.

The main water surface profile experiments used 31 consecutive camera positions to record water levels from approximately 0.3 m upstream of the original shoreline to 10.1 m downstream. This allowed a large length of the water surface to be observed, over which the waves propagated and evolved. Each image sequence was analysed separately to identify the water surface profile time history. The individual sections of water surface were then juxtaposed to create a water surface profile over 10 m long. The combined surface was then filtered in MATLAB using a 'symmlet-6' wavelet decomposition, which removed the frequency components significantly higher than those associated with the wave field (Daubechies 1992; Mallat 1999; Mix and Olejniczak 2003; Strang and Nguyen 1997). These high frequencies came about from the water levels at the joins between adjacent camera positions not exactly matching, and from the shadows cast by the stainless steel cross ties above the water surface. The wavelet decomposition broke down the water surface profile, at each time step, into different levels of detail, or frequency components. Only the highest levels of detail were able to resolve the high frequency anomalies in the water surface profiles. These levels were discarded and the remaining levels were recombined to form the filtered water surface profile. Wavelet-based methods have historically been shown to be more useful for the analysis of non-stationary signals than more conventional Fourier transforms. Low-pass filters were found to produce a phase shift in the wave peaks, and moving average-type filters were not effective in removing the noise without reducing the peaks.

Due to surface tension and friction effects, the meniscus was convex as the wave ran up the beach, forming a rounded nose, but the water profile inverted to become concave as the water ran down the ramp, as seen in two examples of raw images of wave run-up in Figure 4.16. Note that the camera used to record these images was rotated 75° from the horizontal so as to make the 15° slope appear vertical. The left image illustrates the concave nature of the drawn-down water surface, and the right image shows the convex nose structure of the wave running up the beach. The surface tension effects at the small laboratory scale meant some consideration was required to define the location of the shore.

Figure 4.16. Raw images of a) wave run-down, and b) wave run-up, illustrating the issue of meniscus reversal. Image a) shows the draw-down of the shoreline as the landslide initially accelerates down the slope. Image b) shows the wave run-up that occurs moments later. Note that the 15° sloping beach is shown as vertical in these images.

There were several options available in defining the wave run-up/down, including the wetted length and linear and polynomial interpolation/extrapolation of the intersection of the water level and beach, but it was decided to use the water level at a specified distance from the ramp surface. This was used to try to negate some of the viscous effects present in the laboratory-scale experiments. This distance from the ramp was normally of the order of a few pixels, which scaled to between 1.0 to 1.5 mm, still significantly closer to the beach slope than is possible with electrical gauges. Evaluating water levels nearer to the slope surface would produce run-up time series severely affected by menisci changes, and further away from the slope surface could produce less accurate run-up height estimates. The wave run-up height was determined by inspecting the interface between low and high light intensity from this single pixel column offset from the slope surface.

For the recording of wave run-up, the camera was positioned 0.100 m above the still water level and 0.462 m from the outer face of the sidewall. The laser sheet was 0.120 m from the sidewall. The closer proximity of the camera to the laser sheet allowed a higher resolution of 0.233 mm per pixel to be recorded compared to the 0.399 mm per pixel resolution of the water level measurements.

4.4.4 Repeatability and Performance of the Laser Induced Fluorescence Technique

Through checking the repeatability of the wave field generation process, anomalous free surface oscillations were detected when two experimental runs were performed within 15 minutes of each other. Although two minutes was sufficient time to allow the residual sub-surface water velocities, generated from preceding runs, to dissipate sufficiently so as to have negligible effects on the slider

motions, it was insufficient time for the surface waves to completely dissipate. It was found that a small amplitude seiche was set up in the tank after each run, which was barely detectable by the naked eye due to its long period and wavelength. To be able to perform the multiple repeated runs for each landslide configuration and measurement technique in a timely manner, a method to dissipate the seiche was devised.

Seiching is a phenomenon in which external forcing creates a free standing wave within an enclosed body of water that then oscillates at its natural frequency. The dotted line in Figure 4.17 is a time-history plot of water level for an underwater landslide experiment at a point approximately 800 millimetres from the shoreline. Inspecting the water level after 1.7 minutes, the typical time required to record a run and retrieve the slider block, a 1-2 millimetre amplitude oscillation was seen to slowly dissipate over the remaining thirteen minutes. Even ten minutes after the block was released, the seiche had an amplitude of ±0.25 millimetres, a magnitude still able to be resolved with the LIF method. Woven paper mats were placed at the far end of the tank to try to dissipate the seiche, but were found to be effective at absorbing the higher frequency wave components, but ineffective with the low frequency seiche. The period of the seiche was of the order of 15 seconds.

As it was desirable to dissipate this seiche as quickly as possible to minimise the time required between successive runs, a number of wave absorption methods were investigated. Due to the cost and complexity of active methods, only passive wave absorption was considered. A technique used often and with success has been to put a very gentle (less than 1:10) slope at the far end of the tank (Ouellet and Datta 1986). The principle behind this technique is to promote the breaking of the waves and dissipation of the wave energy through turbulence and viscous effects. One of the advantages of this is its simple construction and implementation, and its effectiveness over a wide range of wavelengths and amplitudes. The main disadvantage of this method is the significant sizes of these slopes, which are often prohibitive in laboratory environments where space is at a premium.

A more compact wave dissipation structure with potentially similar effectiveness is based on the caisson. These have different arrangements of chambers and apertures that promote energy dissipation through viscous effects and resonance. The advantage of this form of wave absorption is its reduced size compared to sloped beaches, but they have the disadvantage of only being effective for specific ranges of wave properties and the requirement for tuning of the system to minimise the reflected waves (Lebey and Rivoalen 2002).

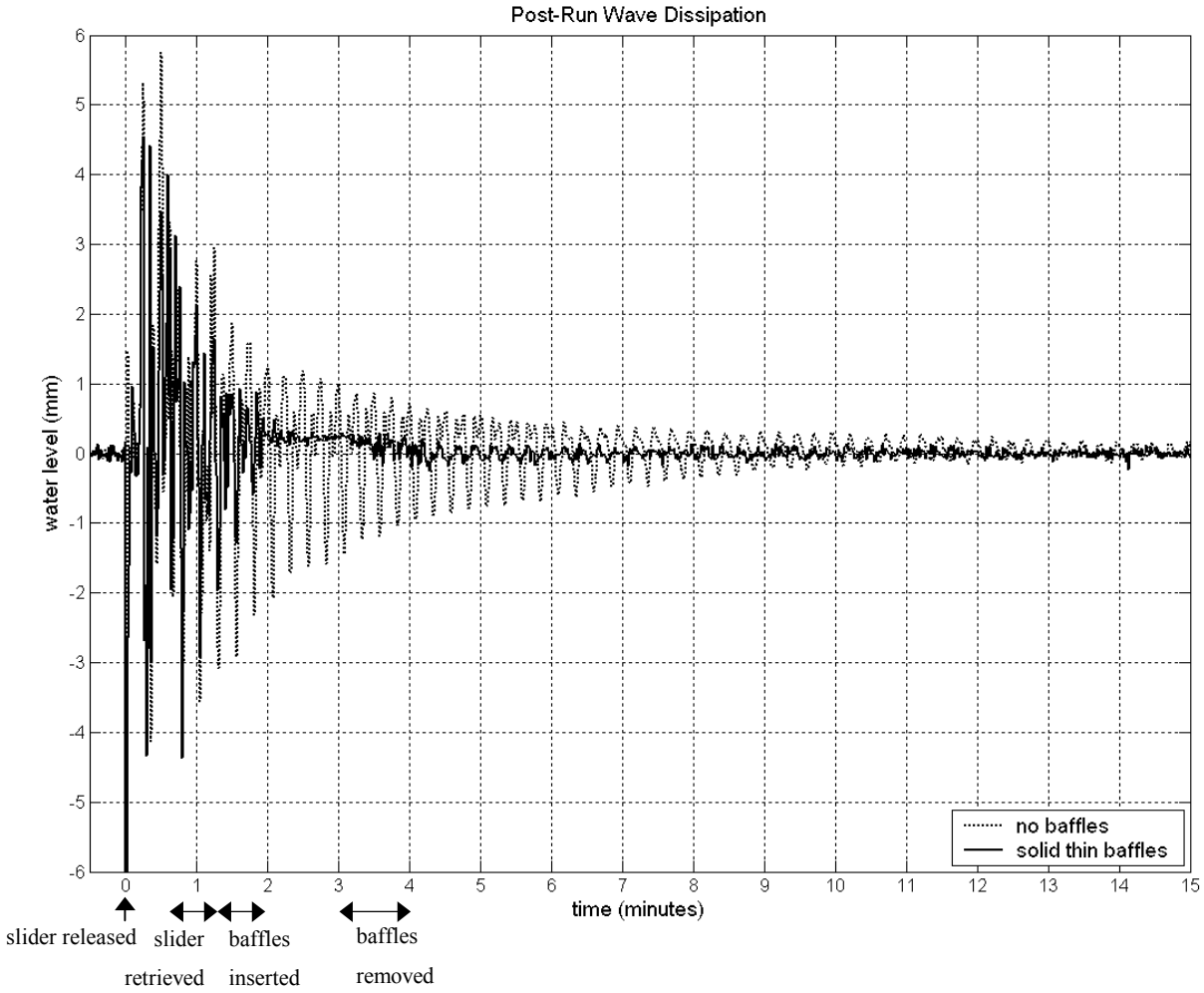

Figure 4.17. Comparison of water level time-histories, with and without the baffle-type seiche dissipation, after a typical test at a point approximately 800 millimetres from the shoreline.

To dissipate the seiche observed in this tank, it was decided to implement the use of temporary baffle walls to compartmentalise the length of the flume. After a run, four gates were lowered into the tank at regular intervals along its length and left for approximately one minute, essentially dividing the 15-metre tank into five 3-metre long compartments. These walls limited the permissible wavelengths to less than 6-metres, and made it impossible to sustain a length-of-the-tank seiche. The gates were gently removed and the water allowed to settle for a further three minutes. These gates covered the full height and width of the tank cross-section, and were made of 2 millimetre thick acrylic sheeting. 17 millimetre thick plywood gates were initially tested but were found to regenerate a substantial seiche when the gates were removed, due to the large volume of water that they displaced.

The solid line in Figure 4.17 illustrates the effectiveness of the wave dissipation method utilising removable baffle walls. The baffles were lowered into the tank 80 seconds after the sliding block was released, left for 1 minute, and then removed. The seiche amplitude after a further 2 minutes, 6 minutes after the block was released, is approximately ±0.13 millimetres. Without the baffles, it

would take over 15 minutes for the seiche to dissipate naturally to this magnitude. After examining the results from the seiche tests, an interval of 6 minutes after slider release was settled upon as sufficient time for the seiche to dissipate and the next run to commence.

Figure 4.18 illustrates the final repeatability of the water level measurements. In this figure, three repeats were performed with the same experimental configuration (block specific gravity of 4.02, and initial submergence of 0.2 times the slider length). The water surface profiles 4.667 seconds after the block was released are plotted. These three repeats are actually made up of 93 individual runs, and the small misalignments of some of the peaks are due to the 15Hz camera frame rate only being able to resolve the timing to within 0.0667 seconds. With typical wave speeds of approximately 1.5 m/s, this corresponds to peak positioning of ±0.05 m.

To compare the performance of the LIF technique with traditional wave gauge methods, several tests were performed with both the LIF and RWG wave recorders operating simultaneously. Three electrical gauges were placed parallel to the laser sheet in the region above the base of the slope, approximately 0.145 m apart. The gauges were placed behind the light sheet so that they did not obscure the fluorescing water from the camera.

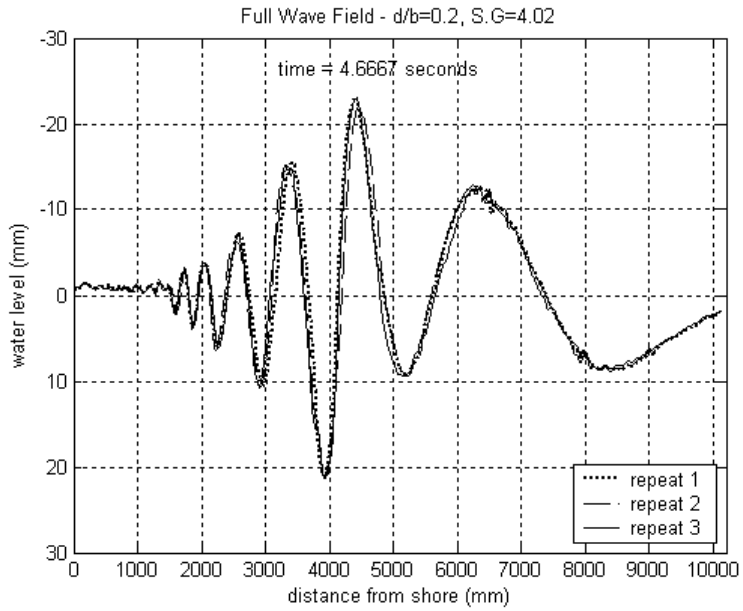

Figure 4.18. Example of repeatability of water level profiles. A wave field test repeated 3 times at each camera position, measured 4.667 seconds after the slider was released.

Point LIF water level readings were determined at the same positions as the resistance wave gauges, and the two records compared. As the slider block was prismatic, the tank was a uniform width, and the light sheet and RWGs were in the central portion of the channel away from the boundary effects of the sidewalls, the waves generated were considered 2-dimensional.

Churchill Controls Limited manufactured the resistance wave gauges used in this comparison. They consisted of a pair of 275mm long 1.5mm diameter stainless steel wires spaced 12.5mm apart. The wires were immersed in the water and the electrical current that flowed between them was linearly proportional to the depth of immersion. A Wave Monitor Module carried the energising and sensing circuits and means for compensating for the resistance of the probe connecting cables. The current was sensed by the wave monitor, which provided an analogue output voltage proportional to the instantaneous depth of immersion. An A/D converter provided this data as a digital output at 16 Hz for storage on a Campbell Scientific CR10X datalogger before being uploaded to a PC, separate to that used for the LIF data. Output files were in a comma separated value (CSV) text format with each probe reading stored as raw millivolts tagged with date and time data. The RWGs were not affected by lighting conditions or the dye necessary for the LIF technique (Churchill Controls Ltd 1977).

Calibration was needed to convert the raw probe data from millivolts to a length scale. Each probe was firstly set up with a standardised immersion depth of 70.0mm. The wave monitor was then adjusted to compensate for the resistance of each probe connecting cable to ensure the 70.0mm immersion equated to a zero voltage output. The raw voltage output can be correlated to wave height by varying the depth of immersion of each probe in still water by a known amount and noting the corresponding change in output voltage. Raising and lowering the probes in 5 mm increments and noting the corresponding change in the output voltage, the immersion depth of the probes were plotted against output voltage to find the relating constant, as shown in Equation 4.8.

$$dv = CV \tag{4.8}$$

where dv = vertical displacement relative to initial 70 mm depth (mm)

C = constant

V = output voltage (V)

Tests in which large, moderate and very small waves were created were used to compare the two techniques. Comparisons for the largest and smallest waves are presented in Figure 4.19. Note that each horizontal gridline represents two pixels in the plot of the largest waves, and one pixel in the small wave height plot.

The RWGs were calibrated to an accuracy of 0.2 mm. The LIF method was calibrated completely independently by converting pixel lengths into actual lengths, as described previously. The 1008 by 1008 pixel resolution of the camera captured a field of view of approximately 450 mm by 450 mm, resulting in a resolution of 0.466 mm/pixel. With the LIF technique able to resolve wave heights down to sub-pixel level, the water levels were captured at an absolute resolution and accuracy of better than 0.1mm. As illustrated in Figure 4.19, the LIF method produced point measurements of water level comparable to those of the RWGs.

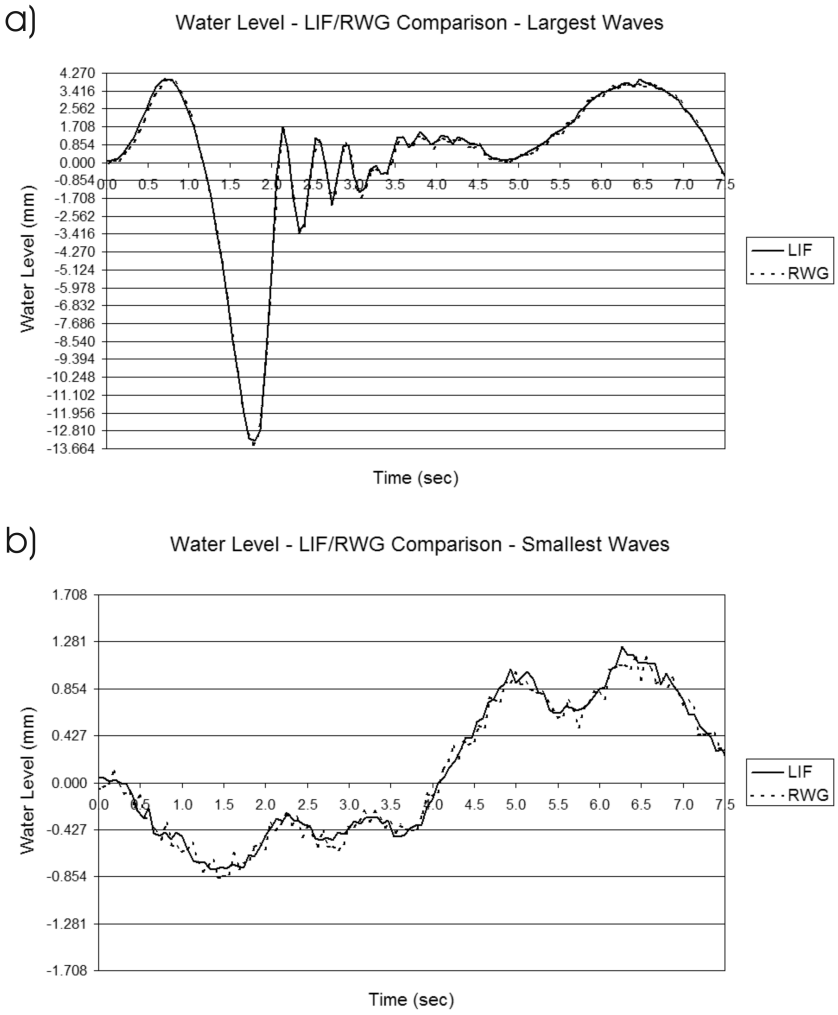

Figure 4.19. Plots of water levels measured using LIF and RWG for comparison of performance for large and small wave heights. Note the different gridline intervals, as one pixel = 0.427 mm.

4.4.5 Experimental Procedure

The following list outlines the typical procedures for capturing digital images of the fluorescing water to determine the water surface profile and wave run-up time histories using LIF. Experiments to measure the landslide motions were completed directly before and after the water surface measurement tests.

i) The flume was filled with fresh water and left for one day to degas. Any air bubbles that formed were removed before the tests.
ii) The Pulnix TM1010 digital camera was attached to the gantry trolley and orientated to the required angle using an inclinometer. Its position relative to the water level at the laser light sheet was determined.
iii) The laser sheet generator was securely attached to the gantry trolley and orientated so that the light sheet was vertical, parallel with the long axis of the flume, and covered the area captured by the digital camera.
iv) An image of a plastic ruler, placed in the plane of the light sheet, was captured to determine scale. An image of a calibration grid was captured to determine the barrel distortion correction coefficients.
v) The gantry trolley was moved so that the camera viewing area and laser sheet were in the desired position. The position of the camera relative to the original shore was determined.
vi) The LED used to indicate the release of the landslide was placed in the field of view of the camera.
vii) The elliptical landslide block was placed on the submerged slope at the required initial submergence and attached to the release mechanism.
viii) The flume was left undisturbed until all waves had dissipated.
ix) The laser light sheet was activated and the room lights were turned off.
x) Images were captured continuously from approximately 2 seconds before landslide release until approximately 13 seconds after release. Images were then stored to the PC hard drive.
xi) The baffles were lowered into the flume to aid dissipation of the waves, and left for 1 minute (see Section 4.4.4).
xii) For each repeat run, steps vii) to xi) were repeated, and for each change in camera position, steps v) and vi) were repeated.
xiii) The captured images were then analysed and manipulated as outlined in Section 4.4.3.

4.4.6 Errors

This section describes and quantifies the potential sources of errors in the LIF analysis and the determination of water and run-up levels.

The captured images were rectified for barrel distortion using the images of the calibration grid taken just prior to the tests. Length scales, in mm/pixel, within the corrected images were found by placing a ruler in the same vertical plane as the laser light sheet. Length scales were calculated by dividing lengths on the ruler by the corresponding number of pixels in the image. For the water level tests five ruler and pixel lengths were measured and averaged to calculate the final scale. A typical ruler length was measured as 300 mm (± 0.5 mm), and the corresponding number of pixels was 752 pixels (± 1 pixel). The length scale used in the LIF water level analysis, after correcting for barrel distortion, was 0.399 mm/pixel (with an error of ± 0.001 mm/pixel). For the wave run-up tests five ruler and pixel lengths were measured and averaged to calculate the final scale. A typical ruler length was measured as 230 mm (± 0.5 mm), and the corresponding number of pixels was 989 pixels (± 1 pixel). The length scale used in the wave run-up water level analysis, after correcting for barrel distortion, was 0.233 mm/pixel (± 0.0007 mm/pixel). Based on these error estimates, the error in length scale is approximately 0.3% for both water level and wave run-up analyses.

The errors associated with the time interval between frames was estimated by measuring the elapsed time for a large number of frames. The accuracy of the camera frame rate was found to be less than ± 9.8×10^{-6} sec/frame. Based on the 15 Hz frame rate of the camera, the time step error is less than 0.02%.

As mentioned in section 4.4.3, the LIF analysis process allows the interface between water and air to be determined to sub-pixel level. This sub-pixel resolution is typically better than ¼ of a pixel. For water levels ¼ of a pixel length equates to approximately 0.0998 mm, and compared to the smallest maximum wave amplitude of 8.0045 mm, the error in measuring maximum water levels no more than approximately 1%. For wave run-up levels ¼ of a pixel length equates to 0.0583 mm, and compared to the smallest run-up height of 6.8463 mm, the error in measuring the maximum wave run-up is less than 0.9%.

The corrections applied to the images and the analysis process to remove the effects of barrel distortion, refraction, and parallax, effectively eliminated the errors associated with these phenomena.

The greatest error in the wave fields is related to the frame rate of the camera. The 15 Hz frame rate of the Pulnix TM1010 camera allows initiation of the landslide, indicated by the release mechanism's LED, to be resolved to within 0.0667 s. With a typical wave propagation speed of 1.5 m/s, the generated waves could potentially travel 0.1 m in the time required to capture a frame. Therefore, the accuracy in determining the downstream position of the waveforms is ± 0.05 m. This does not affect the accuracy of the measured wave heights.

4.5 Measuring Sub-surface Velocities with Particle Tracking Velocimetry

Following on from the description of PTV in section 4.2, the application of this technique for sub-surface flow visualisation is presented.

PTV was used to measure the sub-surface water velocities in several areas. The first was in the vicinity of the slope, the region in which the landslide was moving with appreciable acceleration and deceleration. The flow structure over the landslide and in the wake region was observed. The other positions were downstream, beyond the final resting place of the slider. In these regions, the water velocities were gradually less affected by the landslide motions and so the sub-surface velocities under the propagating wave train could be distinguished more easily.

To view the water velocities, the water was seeded with fine near-neutrally buoyant particles. These suspended particles were illuminated with a white light sheet. The contrast between these illuminated particles and the black background was recorded with a digital video camera. PTV software identified and matched these particles from frame-to-frame to determine the velocities present in the water.

4.5.1 Equipment and Set-up

The flume, landslide, and slope configuration were identical to those used for the LIF and landslide tracking measurements. All the lights in the room were turned off and a black sheet was placed behind the flume to provide a dark background.

The water was seeded with fine Pliolite VTAC (vinyl toluene-acrylate) resin particles with diameters in the range of 180-250 μm. Pliolite resin has a specific gravity of 1.03, slightly greater than that of water, so the particles settle out over time. However, the fall velocities of these particles are negligible compared to the fluid velocities in the landslide experiments. Therefore, for these experiments, the particles were considered to be neurally buoyant.

Before being added to the flume, the Pliolite particles were mixed with approximately 150 ml of water. The water contained a small quantity of surfactant to allow the hydrophobic particles to fall into suspension. The Pliolite particle slurry was drawn into a 50 mL syringe and enough of the slurry was added to the flume to have approximately 2000 particles illuminated in the camera frame. The particles were injected below the surface of the water at various locations along the length of the flume to obtain an even distribution of particles. The particles were then mixed throughout the flume fluid and allowed to rest for a period of time such that the residual stirring motions had decayed but not so long as to allow the particles to settle out. Between tests, the water was stirred to re-suspend the

particles that had settled to the bottom. The flume was left for a sufficiently long rest period before the next test was started.

To illuminate the particles, a light box was placed above the flume to project a white light sheet into the Pliolite-seeded water. The light box consisted of an encased 2 kW halogen tube, from which light was allowed to escape only from a 400 mm by 5 mm slit. A further description of the light box can be found in Plew (2005). The horizontal coverage of the light was sufficient to ensure particles at the edges of the filming area were also illuminated. The divergence of the light meant the sheet thickness increased to approximately 10 mm at the bottom of the water column. A light sheet thicker than a laser sheet was desirable as fewer particles moved in and out of the light sheet between frames, enhancing the PTV matching process. The light sheet was placed 0.150 m from the outer surface of the sidewall. The light box was mounted on the overhead gantry trolley to allow it to be moved to the different places of interest in the flume. A photograph of the light box arrangement is shown in Figure 4.20.

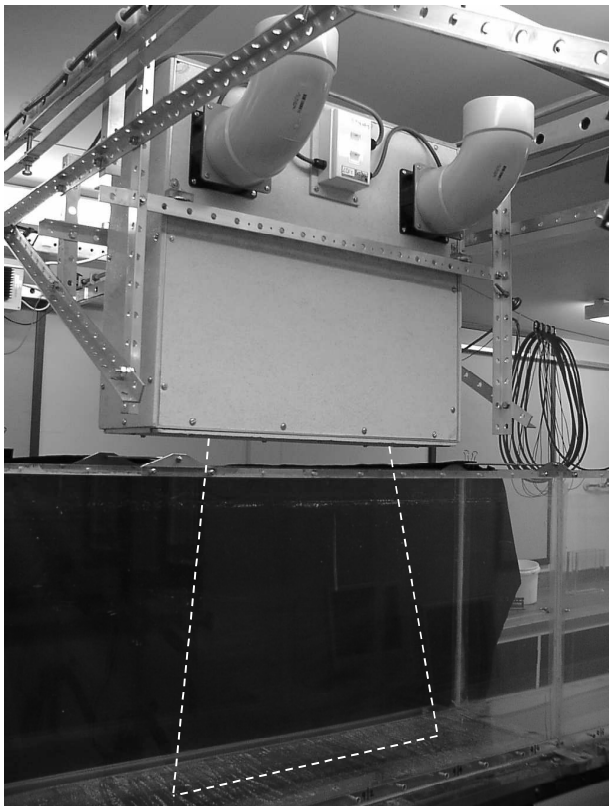

Figure 4.20. Light box set-up. The dotted line indicates the extent of the white light sheet. The two ducts in the upper portion of the picture are cooling ducts for the halogen light bulb.

4.5.2 Image Capturing Equipment and Set-up

A 25 mm Pentax lens mounted on a JAI CV-M4+CL 8-bit monochromatic progressive scan camera with 1268 x 1024 pixel resolution and a 16.9 mm square CCD was used to capture images of the Pliolite seeded water for the PTV analysis. The frame rate was 24 Hz and shutter speeds were set to $1/200^{th}$ second to reduce image blur. Bitflow software was used to capture frames from the camera and store them in a 2 GB RAM buffer on a PC-based computer via a frame-grabber card. The stored images were archived to hard disc as a sequence of bitmap images.

The JAI CV-M4+CL camera was chosen as its frame rate was higher than the Pulnix TM1010 camera, used in the water level and wave run-up measurements, and its resolution was higher than the Canon MV30i used in recording the landslide motions. The higher frame rate allowed the circular orbits of the water below the water surface to be accurately resolved and increased the success of the PTV analysis by reducing the inter-frame particle displacements. The higher resolution provided increased accuracy in locating the particle positions. Through better position estimates, more accurate estimates of velocity were obtained.

The camera was mounted on the gantry trolley at a distance of 1.010 m from the flume sidewall. The field of view was approximately 360 mm wide and 290 mm high when mounted in this configuration, 1.170 m from the light sheet. This provided a resolution of approximately 3.5 pixels per millimetre in the illuminated plane. The field of view of the camera was not large enough to capture the entire water depth. Thus, image sequences were recorded of the upper half and lower half of the water column separately, for repeated runs of the same experiment. The camera was 0.105 m below the water surface when observing the upper section and 0.305 m below the surface when recording the lower section. The limited lateral extent of the camera's field of view also necessitated pairs of upper and lower image sequences at ten different downstream camera positions to observe the entire generation region, from x=0 m to approximately x=3 m. The observations of the water column at x=4 m, 5 m, 6 m, 7 m, and 8 m, each only required one upper and one lower region to be captured.

To signal the start of the landslide test, the release mechanism LED was placed in the field of view of the camera.

4.5.3 Image Analysis

Before inputting the bitmap images to FluidStream, the barrel distortion correction constants for Equation 4.2 were determined. From analysing the images of a rectangular calibration grid taken before the sub-surface velocity tests, using identical camera settings as the test sequences, the calibration constants presented in Table 4.4 were found. The images were then input into FluidStream along with the barrel distortion correction.

Table 4.4. Barrel distortion correction coefficients for sub-surface velocity measurement tests.

Coefficient	value
c_0	1.015
c_1	-0.005
c_2	-0.004
c_3	-0.005

The PTV analysis, as outlined in section 4.2, identified the Pliolite particles using a Gaussian identification algorithm and tracked them through the image sequences. The nature of the flow in the upper and lower portions of the water column was quite different. The upper region contained the orbital motions associated with the surface wave motions, whereas the lower regions contained the highly turbulent wake behind the landslide as it passed by. This required different PTV costing strategies to effectively match the particles in the images captured in the upper and lower regions. Image sequences of the upper portion of the water column required six sequential costings to be used, as did sequences of the lower portion. At some camera positions, a combination of the upper and lower costings was used, as the two flow types were present in the same image sequence. This occurred in the upstream sections of the slope where both the wake behind the landslide and the orbital wave motions were present.

The costing strategies used in the upper regions, to effectively match the particles tracing the orbital wave motions, were an adjacency optimisation, followed by a local velocity optimisation, recent velocity cleanup, path length clean up, recent velocity optimisation, and a local velocity cleanup. A summary of the costing strategy details is given in Table 4.5.

Table 4.5. Details of costing strategies used in PTV analyses in the upper portion of the water column.

	Costing type	Weighting	Costing window size (W x H)	MMC	Search window size (W x H)	Optimisation type
1	Adjacency	1.0	30 mm x 30 mm	0.5	20 mm x 20 mm	Full
2	Local velocity	1.0	20 mm x 20 mm	0.3	15 mm x 10 mm	Full
3	Recent velocity	1.0	N/A	0.2	20 mm x 20 mm	Cleanup
4	Path length	1.0	N/A	0.2	20 mm x 20 mm	Cleanup
5	Recent velocity	1.0	N/A	0.9	20 mm x 20 mm	Full
6	Local velocity	1.0	20 mm x 20 mm	0.3	15 mm x 10 mm	Cleanup

To match the particles moving in the turbulent wake behind the landslide a different set of costing strategies was used in the lower region of the image sequences. This set consisted of an adjacency optimisation, followed by a least squares velocity optimisation on the residual particles, local velocity

optimisation, least squares velocity residual optimisation, recent velocity optimisation, and a path length cleanup. A summary of the costing strategies used in the lower portion of the water column is presented in Table 4.6. Note that the two least squares velocity residual optimisations are based on the number of surrounding particles, not on the particles in a window of specific size centred on each particle. Therefore, no costing window size is defined for these two costings.

Table 4.6. Details of costing strategies used in PTV analyses in the lower portion of the water column.

	Costing type	Weighting	Costing window size (W x H)	MMC	Search window size (W x H)	Optimisation type
1	Adjacency	1.0	30 mm x 30 mm	0.5	20 mm x 20 mm	Full
2	Least squares velocity	1.0	6 neighbours	0.5	6 mm x 6 mm	Residual
3	Local velocity	1.0	20 mm x 20 mm	0.3	10 mm x 10 mm	Full
4	Least squares velocity	1.0	6 neighbours	0.5	6 mm x 6 mm	Residual
5	Recent velocity	1.0	N/A	0.9	20 mm x 20 mm	Full
6	Path length	1.0	N/A	0.25	20 mm x 20 mm	Cleanup

Figure 4.21 shows the particle tracks for one of the tests. These tracks span the time from 3.533-6.133 s after landslide release. This observation region, spanning the entire water depth from 6.828-7.228 m downstream, was beyond the final resting place of the block. Clearly visible are the elliptical fluid particle motions in the upper regions of the water column, and the motions parallel with the flume floor at the bottom of the image. Particle orbits are in a clockwise direction. The discontinuity in the particle tracks at approximately y = -202 mm is the join between the two camera positions used to capture the entire water depth.

After the particle tracking process, the particle velocities were interpolated onto a uniform grid, as described in Section 4.2.4. The velocity field results are presented in Chapter 5.

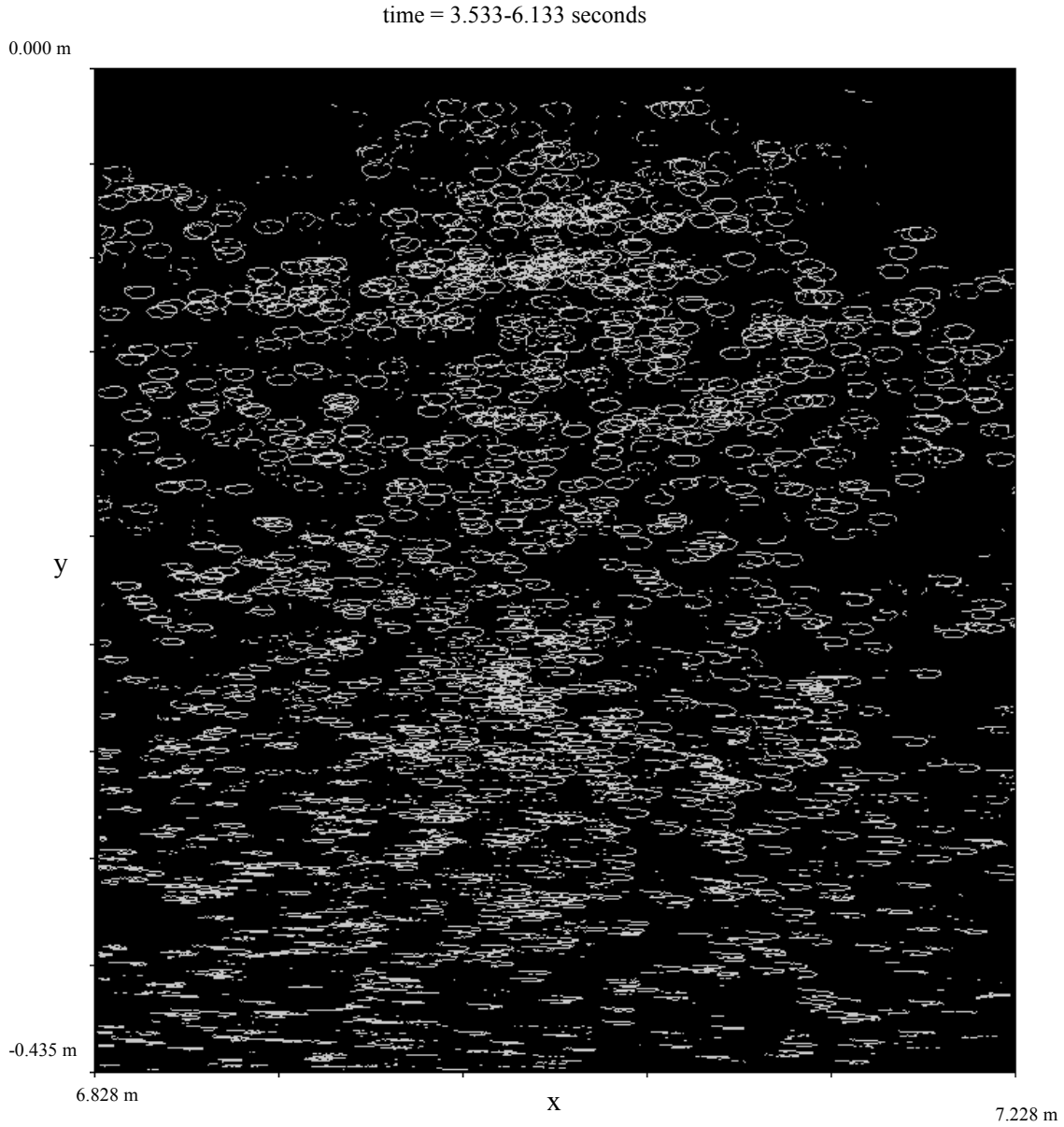

Figure 4.21. Particle tracks from the PTV experiments for times between 3.533 and 6.133 seconds. The entire water depth is shown for a region between 6.828 and 7.228 m downstream. Particle orbits are in a clockwise direction.

4.5.4 Repeatability and Performance of the Particle Tracking Velocimetry Technique

The integrity of the PTV velocity data was checked by comparing the horizontal and vertical velocity time histories, measured just below the surface, with the surface elevation time history at the same downstream position. For the trailing wave packet, the horizontal velocities were found to be in phase with the free surface movements, and the phase of the vertical velocities were trailing by 90°. An example of this is shown in Figure 4.22, in which the time histories of water level and subsurface velocities, measured at x/L_b = 4.8, are compared for the SG5_IS1 combination, where x is the

horizontal spatial dimension and L_b is the length of the landslide. Sub-surface velocities were measured at y/D =-0.172, where y is the vertical spatial dimension and D is the constant channel depth. Note that the leading crest and trough were still influenced by the interaction between the landslide motions and the water motions, rather than being freely propagating waves, and hence the phase difference is not as apparent.

To check the repeatability of the PTV tests, the horizontal and vertical velocity time histories, measured at identical positions, were compared for repeated runs of the same test configuration. Figure 4.23, shows the horizontal velocity time history for four repeated runs of test combination SG5_IS1, measured at $x/L_b = 4.8$ and y/D =-0.172. This figure shows the repeatability of sub-surface velocity measurements using PTV is very good. Both the timing and magnitude of the local maxima and minima are shown to be highly repeatable.

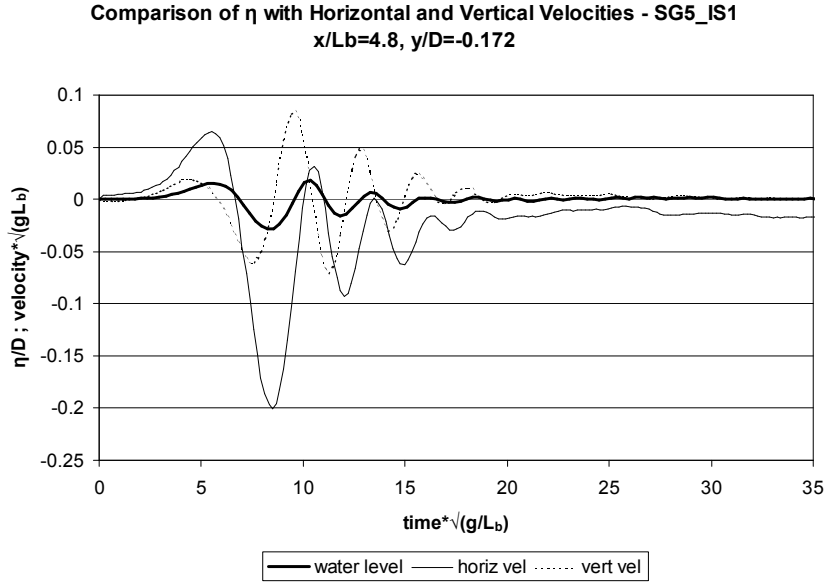

Figure 4.22. Comparison of the time histories of water level and horizontal and vertical velocities, measured at $x/L_b = 4.8$, for test combination SG5_IS1. The sub-surface velocities were measured at y/D =-0.172.

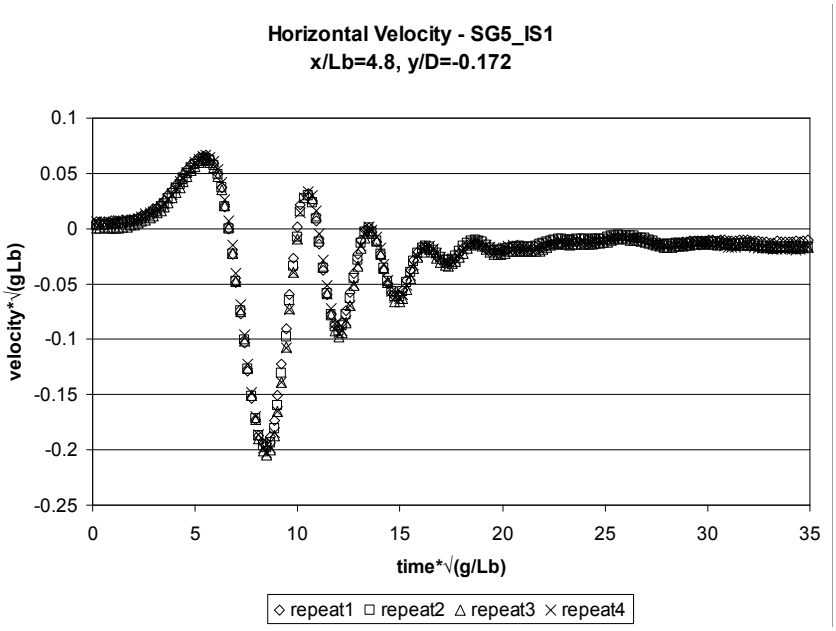

Figure 4.23. Horizontal velocity time history for four repeated runs of test combination SG5_IS1, measured at x/L_b = 4.8 and y/D =-0.172,

4.5.5 Experimental Procedure

The following list outlines the typical procedures for capturing digital images of the illuminated and seeded water column to determine the sub-surface water velocities using PTV. These PTV tests were performed independently of the water surface and landslide motion measurement experiments.

i) The flume was filled with fresh water and left for one day to degas. Any air bubbles that formed were removed before the tests.
ii) The JAI CV-M4+CL digital camera was attached to the gantry trolley and levelled using a spirit level. Its position relative to the water level at the white light sheet was determined.
iii) The light box was securely attached to the gantry trolley and orientated so that the light sheet was vertical, parallel with the long axis of the flume, and covered the area captured by the digital camera.
iv) An image of a plastic ruler, placed in the plane of the light sheet, was captured to determine scale. An image of a calibration grid was captured to determine the barrel distortion correction coefficients.
v) The Pliolite particle slurry was injected and stirred throughout the flume.
vi) The gantry trolley was moved so that the camera viewing area and white light sheet were in the desired position. The position of the camera relative to the original shore was determined.
vii) The LED used to indicate the release of the landslide was placed in the field of view of the camera.

viii) The elliptical landslide block was placed on the submerged slope at the required initial submergence and attached to the release mechanism.

ix) The flume was left undisturbed until sub-surface motions had dissipated sufficiently.

x) The white light sheet was activated and the room lights were turned off.

xi) Images were captured continuously from approximately 2 seconds before landslide release until approximately 13 seconds after release. Images were then stored to the PC hard drive.

xii) The baffles were lowered into the flume to aid dissipation of the sub-surface motions, and left for 1 minute (see Section 4.4.4).

xiii) For each repeat run, steps viii) to xii) were repeated, and for each change in camera position, steps vi) and vii) were repeated.

xiv) The captured images were then analysed and manipulated as outlined in Section 4.5.3.

4.5.6 Errors

This section describes and quantifies the potential sources of errors in the PTV analysis to calculate the sub-surface velocities.

The captured images were rectified for barrel distortion using the images of the calibration grid taken just prior to the tests. Length scales, in mm/pixel, within the corrected images were found by placing a ruler in the same vertical plane as the laser light sheet. Length scales were calculated by dividing lengths on the ruler by the corresponding number of pixels in the image. Five ruler and pixel lengths were measured and averaged to calculate the final scale. A typical ruler length was measured as 350 mm (± 0.5 mm), and the corresponding number of pixels was 1235 pixels (± 1 pixel). The length scale used in the sub-surface velocity analysis, after correcting for barrel distortion, was 0.283 mm/pixel (± 0.001 mm/pixel). Based on this error estimate, the error in length scale is approximately 0.2%.

The errors associated with the time interval between frames was estimated by measuring the elapsed time for a large number (1000) of frames. The accuracy of the camera frame rate was found to be within ± 6.9 x 10^{-6} sec/frame. Based on the 24 Hz frame rate of the camera, the time step error is approximately 0.02%.

There are also possible errors with the particle identification processing if the particle image is not Gaussian, if the particles appear to overlap, or if the illumination of the particles is not sufficient to distinguish it from the background. If the particles are smaller than 3 particles in diameter and not suitably illuminated to fit a Gaussian curve to the intensities, then particle location estimates are accurate to no better than ¼ pixel. It is also possible for a single particle to have multiple intensity peaks due to shape, shadowing, orientation, and multiple light sources (Plew 2005). A particle

location accuracy of ±¼ pixel corresponds to an instantaneous velocity of approximately ±1.8 mm/s at a camera speed of 24 Hz. A wide range of velocities was present in the observed flows, but typically these were between 20 mm/s and 100 mm/s. Pixel identification errors for this range of velocities are between 9% and 2%. With maximum velocities measured at over 200 mm/s, the error associated with pixel identification on maximum sub-surface velocity estimates is better than 1%.

The scale of the errors associated with the particle matching process is difficult to quantify. These errors arise from incorrect particle matches and can only be detected through visual inspection. Inspection includes comparing them with surrounding matches and by ensuring that particle paths are consistent. The matching process is controlled by the selection of costing strategies and their parameters. A variety of strategies and parameters were investigated and those that provided the highest quality matches were chosen. The final proportion of successful matches was between 70% and 80% of the total particles, and these matches are assumed to be correct based on visual inspection. The remaining 20% to 30% of the particles left unmatched either had no correct particles to match to in the next frame or the costing strategies deemed all potential matches as unreliable. Missed particle matches introduced little error, but slightly reduced the density of particles with velocity estimates.

The interpolation of the velocities of randomly spaced matched particles onto a regular grid can also generate errors. These errors can be minimised if the particle spacing is small. Where particles are widely spaced, they may be in separate regions of the flow, and therefore the interpolation from these particle velocities may not accurately portray the velocity at the grid point. The particle identification and tracking algorithms were refined to ensure the greatest density and coverage of particle velocities to maximise the accuracy of the interpolation process.

4.6 Summary

This chapter has detailed the experimental apparatus and techniques used to measure the motions of model underwater landslides, and the sub-surface velocities and wave field that they generated. The properties of the flume, slope, and landslide model were outlined in Section 4.1. The processes involved in the particle tracking system for measuring the landslide kinematics and sub-surface water velocities were presented in Section 4.2. Section 4.3 contained details of the equipment and image capturing and analysis systems for quantifying the position, velocity, and acceleration time histories of the landslide. The apparatus and methods to measure the water surface profile and wave run-up time histories, using laser induced fluorescence, were described in detail in Section 4.4. This technique was found to produce results comparable to those from resistance wave gauges. Section 4.5 described the equipment, image capturing methods, and image processing to generate velocity fields of the sub-surface flows. An analysis of the possible errors involved in each process was also given.

Through developing the experimental set up, it was apparent that the current specification of the benchmark configuration did not uniquely define the sliding characteristics. The specification of the landslide specific gravity did not take into account the sliding friction, which depended on the choice of landslide and slope materials and the level of lubrication. The landslide deceleration was also not specified. Sections 5.3.4 and 6.5.5 describe how the landslide deceleration has a significant effect on the wave generation. The acceleration profile of the landslide would be a more appropriate specification for a benchmark experiment. Considering that a range of slope angles occur in nature (see Chapter 2), the specification of a 15° slope angle in the benchmark was not necessarily realistic of all landslides. However, due to friction effects at laboratory scale, slopes were limited to greater than about 10°.

Chapter 5: Experimental Results and Discussion

Using the techniques presented in Chapter 4, an experimental programme was completed to measure the wave fields generated by laboratory underwater landslides for fifteen combinations of specific gravity and initial submergence. Landslide motions and sub-surface water velocities were also measured. This chapter begins in Section 5.1 with an overview of the experiments performed, including the combinations of specific gravity and initial submergence. Following this, in Section 5.2, are details of the landslide kinematics, such as landslide velocity, acceleration, and deceleration. Results from the water level measurements of wave amplitudes and wave run-up and run-down are then discussed in Section 5.3. This includes an estimate of the effects of the movement of water between the main channel and behind the slope. The presentation of sub-surface velocities, in Section 5.4, concludes the chapter. Representative results are presented and discussed in the text and complete datasets are included in the appendices.

5.1 Experimental Programme

Specific gravity is defined as the ratio of the total unsubmerged mass of the block, m_b, and the mass of water displaced by the landslide, m_o, as shown in Equation 5.1. A combination of polystyrene blocks, water, and lead shot was placed into the cavities within the block to increase the total block mass to achieve the desired specific gravity. The mass of displaced water was measured as 2.417 kg. Given a density of water, ρ_o, of 999 kg/m^3 at 16°C, the volume of the landslide, v_b, was calculated as 2.419 litres. In air, the empty block mass was 3.930 kg.

$$\text{specific gravity} = \frac{m_b}{m_o} \tag{5.1}$$

Equation 5.2 defines the non-dimensional initial submergence as the ratio of the depth of water directly above the landslide centre of mass at its initial starting position, d_{bo}, and the length of the landslide block along the slope, L_b.

$$\text{initial submergence} = \frac{d_{bo}}{L_b} \tag{5.2}$$

The parameters used to describe underwater landslide-generated waves in the laboratory environment are shown in Figure 5.1. The water surface, η, varies spatially and temporally. Individual waveforms, with amplitude, a, propagate over varying water depth, d, at the phase speed, c_p. Run-up height, r_y, is the vertical elevation reached by the wave relative to the intersection of the still water level with the original beach location. Run-up length, r_x, is the horizontal distance the tsunami propagated inland, also measured relative to the beach-to-still water level intersection. The coordinate system originates

from the intersection point between the still water level and the slope. The landslide parameters are landslide thickness, h_b, and landslide length, L_b, sliding along an incline at an angle of θ to the horizontal in a constant water depth, D.

Five different values of Specific Gravity (SG), as defined in Table 5.1, and five values of Initial Submergence (IS), as defined in Table 5.2, were used. Test SG5_IS5 combined the highest specific gravity with the shallowest initial submergence, and produced the largest water level response. SG5_IS1 combined the heaviest specific gravity with the deepest submergence, while SG1_IS5 combined the lightest specific gravity with the shallowest submergence, and both of these produced some of the smallest responses. A range of combinations were not tested as they were expected to create small waves and suffer from resolution issues. The fifteen combinations of specific gravity and initial submergence tested are presented in Table 5.3.

For each combination of specific gravity and initial submergence, PTV was used to measure landslide position time histories and LIF was used to record water surface profile time histories. The landslide motions were recorded before and after the water level measurements to check the sliding characteristics had not changed during that time. The sliding characteristics were found to be consistent throughout the testing process.

To check the repeatability of the LIF processes, the SG5_IS4 combination had water levels recorded three times. As this test was found to be repeatable, as shown in Figure 4.18, it was decided that only one set of measurements was necessary for subsequent combinations, providing significant time savings.

Sub-surface water velocities were measured for two combinations, SG1_IS5 and SG5_IS1. The SG1_IS5 combination was chosen because the lightest density produced water motions that the PTV software could satisfactorily resolve, and the longest runout length allowed the block to slide for a considerable length and produced a well-defined turbulent wake. SG5_IS1 was chosen to observe the flows around landslides with heavier densities and deeper submergences, and to compare with the flows from the SG1_IS5 test.

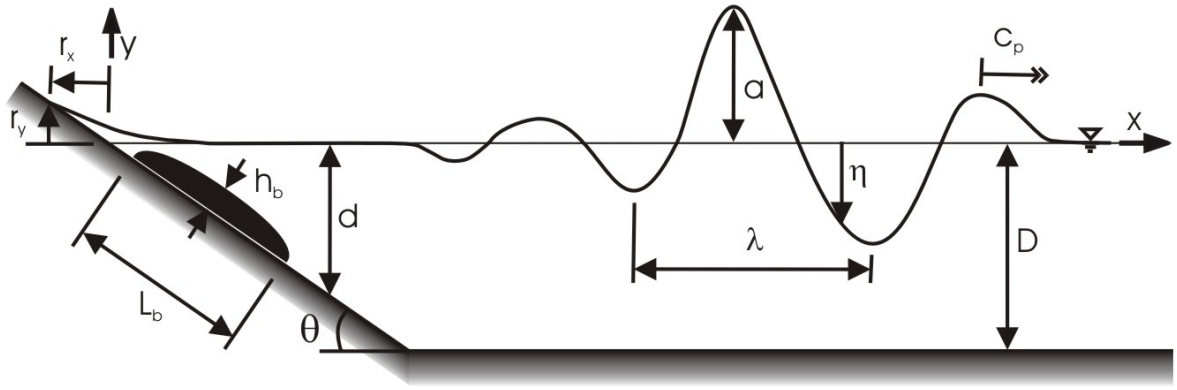

Figure 5.1. Definition of underwater landslide generated water wave parameters.

Table 5.1. Values of Specific Gravity (SG) used.

Specific Gravity ($SG=m_b/m_o$)		
Lightest	SG1	1.63
	SG2	2.23
	SG3	2.83
	SG4	3.42
Heaviest	SG5	4.02

Table 5.2. Values of non-dimensional Initial Submergence (IS) used.

Initial Submergence ($IS=d_{bo}/L_b$)		
Deepest	IS1	0.5
	IS2	0.4
	IS3	0.3
	IS4	0.2
Shallowest	IS5	0.1

Table 5.3. Combinations of Specific Gravity (SG) and Initial Submergence (IS) experimentally tested. Some combinations were not tested due to possible measurement resolution issues arising from small amplitude waves.

Combinations	IS5	IS4	IS3	IS2	IS1
SG5	tested	tested	tested	tested	tested
SG4	tested	tested	tested	tested	
SG3	tested	tested	tested		
SG2	tested	tested			
SG1	tested				

Much of the data presented in this chapter is non-dimensional. Horizontal lengths such as run-up heights and downstream positions have been non-dimensionalised by the landslide length, L_b.

$$\text{non-dimensional horizontal length} = \text{horizontal length} / L_b \quad \textbf{(5.3)}$$

Vertical position and water level have been non-dimensionalised by the constant water depth, D.

$$\text{non-dimensional vertical length} = \text{vertical length} / D \quad \textbf{(5.4)}$$

Accelerations have been non-dimensionalised by the gravitational acceleration, g.

$$\text{non-dimensional acceleration} = \text{acceleration} / g \quad \textbf{(5.5)}$$

Velocities have been non-dimensionalised in the following way.

$$\text{non-dimensional velocity} = \text{velocity} \Big/ \sqrt{gL_b} \quad \textbf{(5.6)}$$

Times have been non-dimensionalised in the following way.

$$\text{non-dimensional time} = \text{time} \sqrt{g / L_b} \quad \textbf{(5.7)}$$

5.2 Landslide Centre of Mass Kinematics

Landslide kinematics were determined by measuring the position time history of the landslide's centre of mass using PTV. The instantaneous motion of the landslide was important because it could be related to the characteristics of the wave field. Velocity and acceleration magnitudes were calculated by differentiating and double-differentiating the position data with respect to time respectively. Section 5.2.1 presents maximum velocity data. Initial and constant accelerations are detailed in Sections 5.2.2 and 5.2.3 respectively. Maximum landslide deceleration data is presented in Section 5.2.4.

5.2.1 Maximum Velocity

An example of the landslide centre of mass velocity time history is shown in Figure 5.2 for the SG3_IS5 combination. The velocity time histories for the other test configurations are shown in

Appendix B. Each configuration exhibits similar general behaviour. The landslide velocity initially increased almost linearly from rest and reached a maximum at the bottom of the slope, at which point the block slowed and came to rest along the flume floor. As indicated by the increasing velocity of the landslide at the toe of the slope, terminal velocity was not reached. This can be contrasted with the slider motions of Watts (1997), in which his landslides rapidly reached terminal velocity. His formalism for describing the landslide motions, described in Section 3.1.1, relied heavily on the initial acceleration and terminal velocity. For situations in which the landslide does not reach terminal velocity, this formalism cannot uniquely define its motions.

Inspecting Figure 5.3, the non-dimensional maximum landslide velocity increased non-linearly with increasing specific gravity and decreasing initial submergence. Higher specific gravities induced higher accelerations, enabling the landslide to reach higher velocities for the same slide distance. Decreasing initial submergences increased the slide length available, hence the longer duration of acceleration and the higher velocities attained.

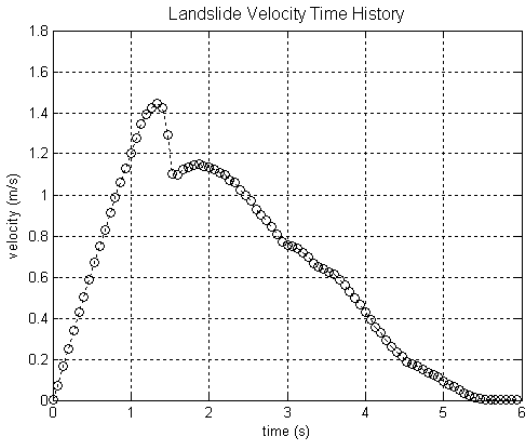

Figure 5.2. Landslide centre of mass velocity time history for SG3_IS5 test.

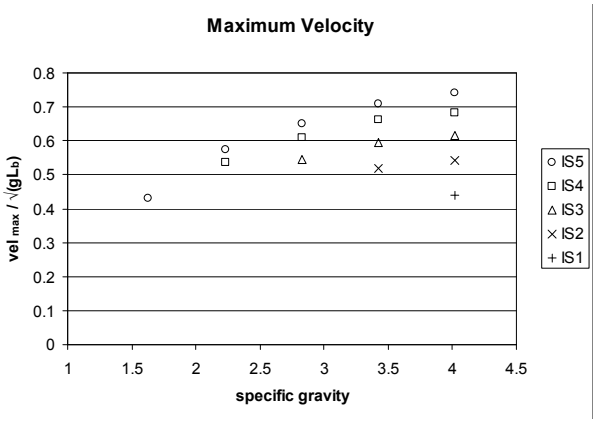

Figure 5.3. Maximum landslide centre of mass velocity for various specific gravities and initial submergences.

5.2.2 Initial Acceleration

Landslide acceleration is a key parameter in characterising the generated wave field. Landslide specific gravity indicates the difference in density between the landslide and the surrounding water. The measured acceleration is related to the specific gravity, but it also takes into account factors such as friction.

Figure 5.4 is a time history plot of the landslide centre of mass acceleration for the SG3_IS5 test. Appendix B contains acceleration time history plots for the remaining test combinations. The general form of the acceleration plots are similar for all the specific gravity and initial submergence combinations, with only the magnitude and timing of the accelerations differing. The rapid increase to the peak acceleration typically occurred within two camera frames, or 0.133 seconds. Initial acceleration was taken as this peak value. The acceleration decreased slightly as the landslide progressed down the slope, before rapidly decelerating as the block reached the base of the slope and transitioned to sliding along the flume floor. A phase of roughly constant deceleration occurred as the landslide slowed and finally stopped. During the landslide experiments of Watts (1997), the accelerations peaked almost instantaneously before rapidly decreasing as the block approached terminal velocity. His acceleration time histories were typically measured for durations of 0.6 seconds.

Figure 5.5 illustrates the independence of non-dimensional initial acceleration on initial submergence, and its dependence on specific gravity. The proximity of the landslide to the free surface did not have a significant effect on the acceleration. As a landslide with a specific gravity of 1.0 should theoretically produce zero acceleration, it is clear from Figure 5.5, that the landslide initial acceleration was non-linearly dependent on specific gravity.

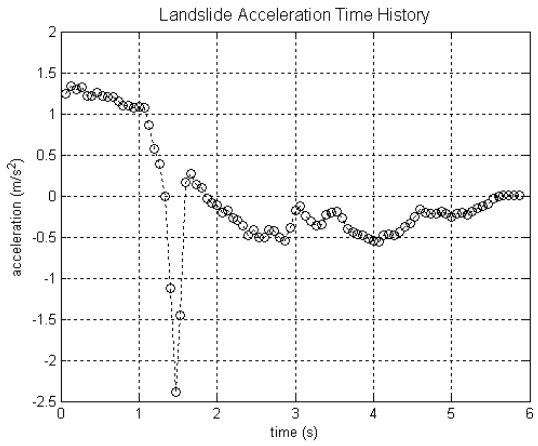

Figure 5.4. Landslide centre of mass acceleration time history for SG3_IS5 test.

5.2.3 Constant Acceleration

Many researchers have used initial acceleration and terminal velocity in their parameterisation, consistent with that developed by Watts (1997). Assuming the acceleration decays from the initial acceleration to zero uniformly, then the initial acceleration and terminal velocity can be used with simple equations of motion to uniquely define the general landslide motion time history for the time before the landslide begins decelerating. However, for experimental studies on shallow slopes or for short slide durations, the landslide may not reach terminal velocity. In this case, the initial acceleration alone is not enough to describe the landslide motions.

This present research considers the average constant acceleration, combined with the slide duration, to be more appropriate for characterising the motions of landslides that do not reach terminal velocity, for the period of time before the landslide begins to decelerate. The constant acceleration was calculated by linear curve fitting of the initial positive acceleration portion of the velocity time history. As the constant velocities were used in the numerical models, a further description of the constant acceleration calculation is given in Chapter 7. Constant accelerations will have advantages for numerical modelling, as a single constant acceleration value and slide duration can be stipulated instead of defining the entire acceleration time history. The constant acceleration values for the fifteen landslide configurations are plotted in Figure 5.5. The equation of a power law curve fit to the data is given in Equation 5.8.

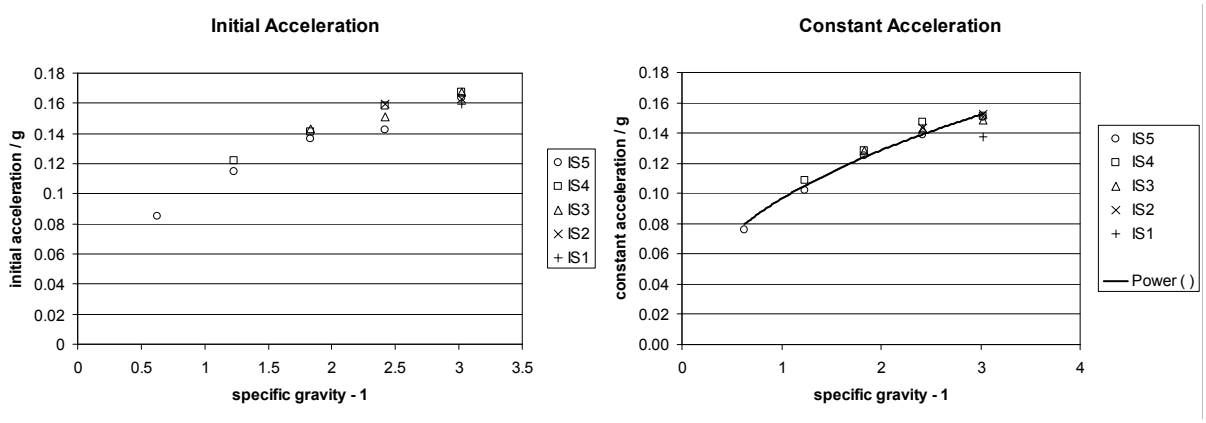

Figure 5.5. Landslide centre of mass initial and constant acceleration for various specific gravities and initial submergences.

$$a_{const} / g = 0.0965\left(\frac{m_b}{m_o} - 1\right)^{0.415} \qquad r^2 = 0.954 \qquad \textbf{(5.8)}$$

5.2.4 Maximum Deceleration

The non-dimensional maximum centre of mass deceleration magnitudes plotted in Figure 5.6 characterise the sudden deceleration experienced by the landslide as it reached the toe of the slope. It should be noted that these deceleration values are less reliable due to the short duration of rapid deceleration and the possibility that the 15 Hz camera frame rate was not able to fully resolve the peak deceleration. The magnitude of the maximum deceleration increased with higher specific gravities and shallower initial submergences. The higher specific gravities induced larger accelerations and the shallow submergences increased the duration of acceleration, allowing higher landslide velocities to be reached at the base of the slope.

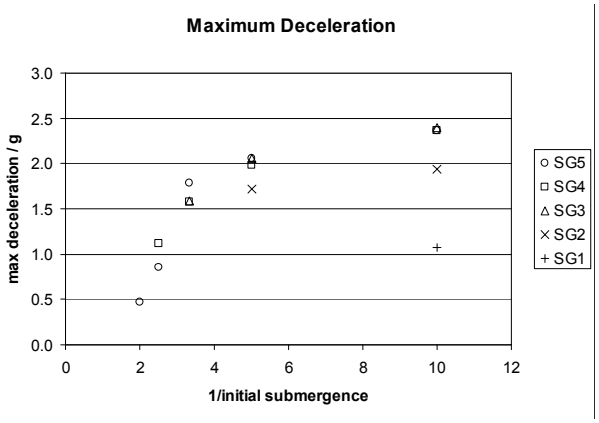

Figure 5.6. Maximum landslide centre of mass deceleration magnitude, measured at the toe of the slope, for various specific gravities and initial submergences.

5.3 Wave Fields

The evolution of the waves through space and time are described in Section 5.3.1 through the observation of the water surface time histories and profiles respectively. The changes in the periods, lengths and total number of waves are also inspected. Section 5.3.2 presents the maximum and minimum water levels. This is followed by Section 5.3.3 with details of the wavelengths and wave phase speeds. This provides insights into the dependence of the generated wave field on the initial landslide characteristics. Section 5.3.4 describes the extent of wave run-up and run-down at the shore. This is an important parameter as it is the wave magnitudes at the shore that are of immediate concern in practical situations. Indications of the likely draw-down and wave inundation, as well as the times at which these occur, are useful for communities with assets situated in the coastal area. Section 5.3.5 presents landslide and fluid energy results. Seismologists use the energy released during an earthquake to quantify the magnitude of an event. Similarly, water potential and kinetic energy and landslide potential and kinetic energy are possible measures as to an underwater landslide's potential for destruction. The time histories of the various energy forms also provide insights into the mechanisms in which the energy is transferred from the landslide potential energy into other forms of energy, such as the wave field potential energy. This research appears to be the first experimental

tsunami study in which full water surface profile time histories are generated. The wave potential energy can be determined from this spatial and temporal water level information. The internal kinetic energy of the water motions can be estimated from the sub-surface velocity distribution. Section 5.3.6 estimates the significance of the movement of water between the main channel and behind the slope.

5.3.1 General Wave Field Properties

Figure 5.7 shows the water surface profiles of the SG3_IS5 test at successive times between 0.600 s and 5.600 s. The solid black bars indicate the approximate position of the landslide. Present in the first frame at time = 0.600 s is the 1st crest, 1st trough, and the beginnings of the 2nd crest propagating downstream. The wave trough causing the run-down observed at the beach is also present as a trough propagating upstream. In fact, by t = 0.6 seconds this trough had already reached the beach. The following frames illustrate the evolution of these waves as they propagated. The 1st crest amplitude continued to increase initially, peaked, and then gradually decreased as the wave entered deeper water and its wavelength increased. The 1st trough and 2nd crest also exhibited this behaviour, although at later times. The continual generation of small amplitude waves with short wavelengths at the upstream end created a propagating wave packet. Similar plots of water surface profiles are included in Appendix C for all fifteen specific gravity and initial submergence combinations.

Figure 5.8 shows the water surface time histories of the SG3_IS5 test at successive positions down the flume between 0.500 m and 5.500 m. Presenting water level time histories in this way simulates the information available from point gauges, such as electrical resistance and capacitance gauges. Present in the first frame at a position of 0.500 m downstream of the original shoreline are the first four wave crests and troughs. The water surface was essentially flat after time = 2.500 s because the waves at the trailing end of the wave train were being generated downstream of this location and hence did not propagate past this position. This implies that the waves generated beyond this location did not have a significant upstream propagating component. The time history at 1.500 m clearly illustrates the decrease in amplitude of successive waves. The waves at successive downstream positions had increasing periods, as the waves had a greater distance and time to disperse.

The water level profiles in Figure 5.7 and time histories in Figure 5.8 are presented in a continuous manner in a two-dimensional wave field plot in Figure 5.9. In this form the wave propagation speeds are more clearly seen. The wave speeds relative to the landslide are also illustrated. From this plot it can be seen that the 1st crest formed ahead of the landslide centre of mass and the 1st trough formed behind it. The point at which these two waveforms met initially followed the landslide centre of mass as it slid down the slope. This phenomenon was observed for all fifteen tests, as shown by the plots in Appendix C.

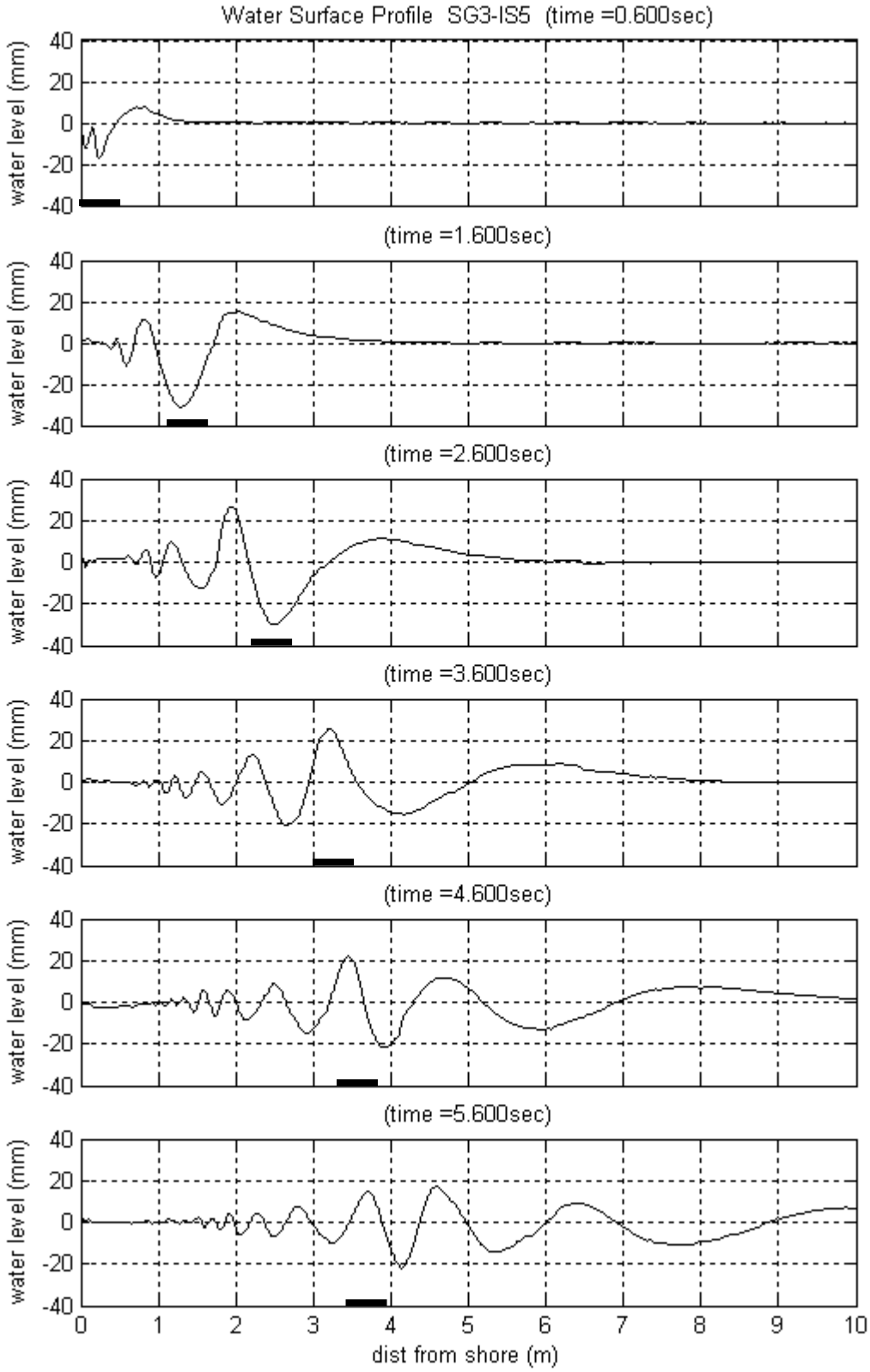

Figure 5.7. Water surface profiles at time = 0.600, 1.600, 2.600, 3.600, 4.600, and 5.600 seconds for SG3_IS5 test. The solid black bars indicate the approximate position of the landslide.

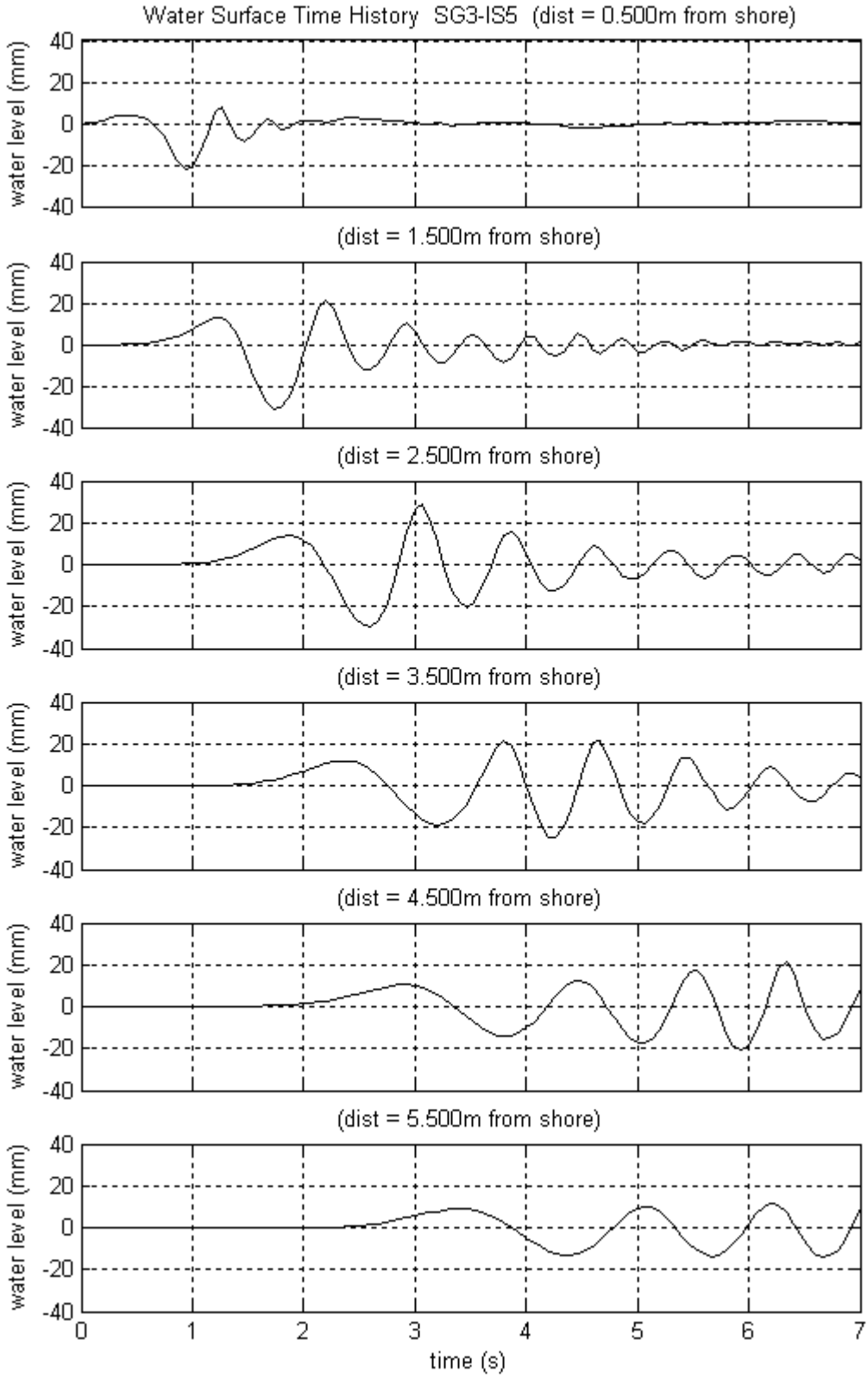

Figure 5.8. Water level time histories at positions 0.500, 1.500, 2.500, 3.500, 4.500, and 5.500 metres from the original shoreline for SG3_IS5 test.

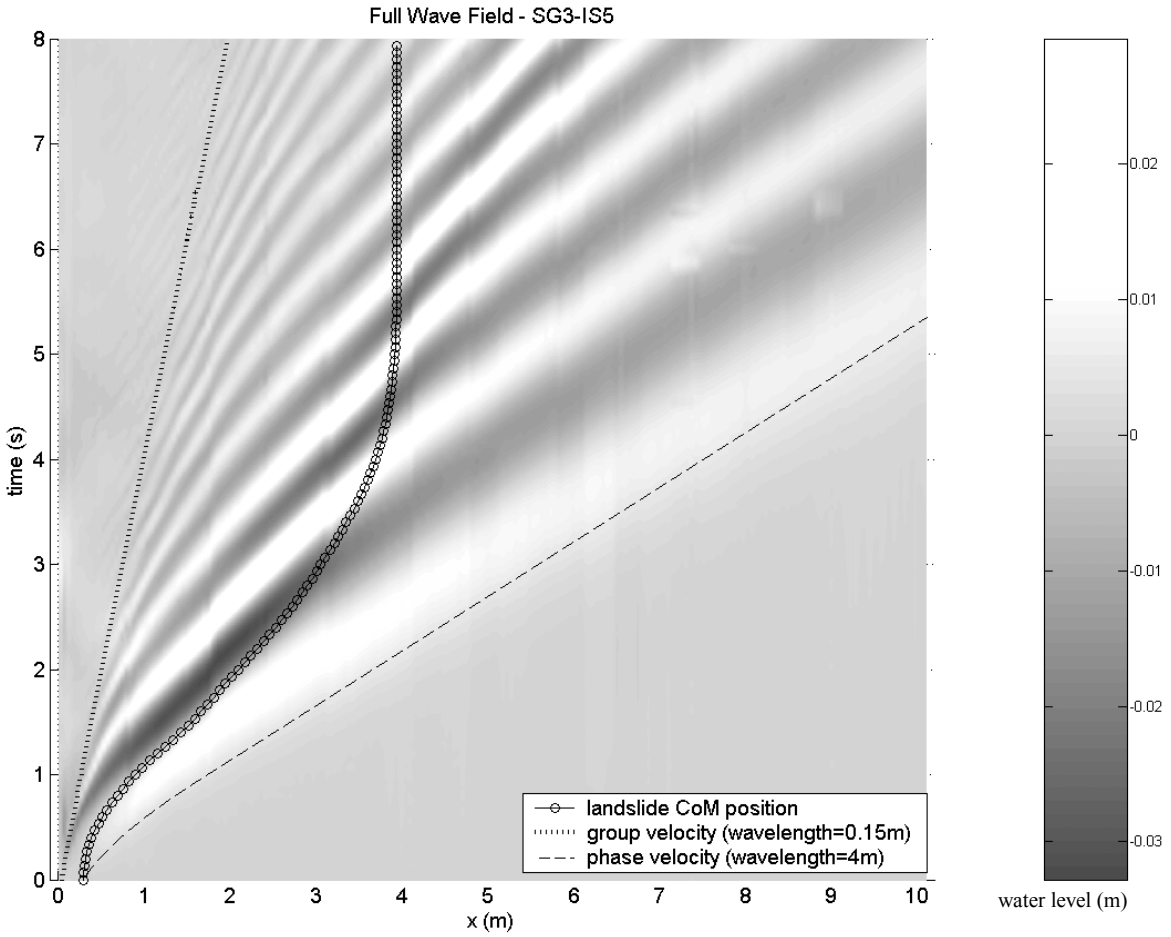

Figure 5.9. 2-dimensional wave field plot of water surface profile time history for the SG3-IS5 test. White indicates wave crests and black indicates wave troughs. Note the various wave speeds present within the wave train. Landslide position time history and 0.15 m and 4.0 m wavelength characteristic curves are also shown.

At this point, a qualitative description of the wave generation processes illustrated in the two-dimensional wave field plots is given. As the landslide began to slide a packet of waves, made up of a spectrum of wavelengths, was generated. This packet is clearly defined in Figure 5.9, bounded almost entirely by the two characteristic curves in the x-t plane. Wave dispersion spread the packet as it propagated. The energy within the packet propagated at the group velocity of the corresponding wavelengths within the spectrum. The expression relating wave phase speed, C_p, to wavelength, λ, and water depth, d(x), is given by Equation 5.9 (United States Army Corps of Engineers 2002). This equation is based on linear theory and the assumption that the wave amplitudes are small compared to the water depth. The maximum wave amplitudes presented in Section 5.3.2 show that the large amplitudes are weakly non-linear. However, linear theory holds for waves with amplitudes well beyond the linear limits, and is often used for weakly and moderately non-linear waves.

$$C_p(x) = \sqrt{\frac{g\lambda}{2\pi}\tanh\left(\frac{2\pi d(x)}{\lambda}\right)} \quad \textbf{(5.9)}$$

The phase speed is related to the group speed, C_g, through Equation 5.10 (United States Army Corps of Engineers 2002).

$$C_g(x) = nC_p(x) \quad \textbf{(5.10)}$$

The parameter, n, is defined in Equation 5.11.

$$n = \frac{1}{2}\left[1 + \frac{\frac{4\pi d(x)}{\lambda}}{\sinh\left(\frac{4\pi d(x)}{\lambda}\right)}\right] \quad \textbf{(5.11)}$$

The period of the wave, T, can be calculated from the wavelength and phase speed using the expression given in Equation 5.12 (United States Army Corps of Engineers 2002).

$$T = \frac{\lambda}{C_p} \quad \textbf{(5.12)}$$

The leading wave in the packet had the longest wavelength, initially comparable in length to that of the landslide. This wave had phase and group velocities that were very similar, so dispersion was not significant. As such, the leading wave propagated essentially unchanged. The leading wave crest was generated by the horizontal motion of the landslide pushing up the water in front of it. The acceleration of the surrounding fluid created a water pressure distribution over the moving landslide. The impulse of high pressure ahead of the landslide forced the water surface directly above it up to form the 1st wave crest. This wave had a phase velocity that exceeded the slider velocity throughout its motion, and therefore the initial crest propagated freely ahead of the landslide once it was generated. The ratio of landslide velocity to the wave phase speed can be defined as a slider Froude number, Fr, as given in Equation 5.13. Throughout all the experiments the Froude number, based on the instantaneous landslide velocity and the local water depth, for all waves never exceeded 1.

$$Fr = \frac{landslide\ velocity\ (t)}{C_p} \quad \textbf{(5.13)}$$

The accelerating fluid above and the turbulent wake behind the sliding block created a region of low pressure. This low pressure pulled the water surface down to form a depression. The continued motion of the landslide transferred energy into the part of wave field localised around the landslide. The first crest amplitude rapidly stopped increasing in amplitude, whereas the trough amplitude continued to increase because the landslide was reinforcing this depression in the free surface. This wave trough was forced to propagate at the same speed as the accelerating landslide due to the low pressure region being directly connected to the sliding block. A forced wave is one that is forced to propagate at anything other than its natural free propagation speed. The 1st trough was free to propagate once the landslide reached the bottom of the slope and began to slow. The decrease in velocity of the block disrupted the low pressure region, and the landslide's connection with the trough could not be maintained. Although not obvious during these experiments, the increasing depth of water above the landslide would have also played a role in severing the connection between the slider and the trough above it. If the depth were to have continued increasing the pressure field at the surface would have been less affected by the landslide motions until the depth was so great that the trough could have propagated independently of the landslide regardless of its velocity. As a forced wave the first trough had an increasing amplitude, considerably larger than the leading crest. After the landslide started to slow and the trough was released to propagate as a free wave, its amplitude decayed due to wave dispersion.

The subsequent waves in the packet contained shorter and shorter wavelengths, so waves further back in the wave train had progressively slower phase speeds. The group velocity of these waves, the speed at which energy was propagated, was slower than their phase speed. As such, waves near the front of the wave packet were destroyed and new waves were generated at the trailing edge of the packet. The slider left behind these waves, as their phase speed was less than that of the accelerating landslide. This corresponded to a case where $Fr < 1$. As these waves were formed through energy left behind by preceding waves, there was no direct exchange of energy between the fast moving landslide and the waves in the tail of the wave packet. The wave generation was clearly visible in the two dimensional wave field plots, corresponding to approximately the 0.15 m characteristic curve. The downstream position at which these new waves were created was moving downstream over time, though at a substantially slower speed than the wave propagation and landslide speeds. This contributed to the spreading of the wave packet. As individual waves were generated along the slope, their speeds increased as they moved off the slope into deeper water. Also, waves further back in the wave train had smaller amplitudes than those in front.

The speed of the rear edge of the wave packet should have depended on initial submergence, with the energy of the shorter wavelengths propagating faster for deeper submergences. However, the shorter wavelength waves would have reached a water depth at which their speed would have been

independent of depth, after which their speed would have been governed by wavelength alone. Assuming an identical range of wavelengths was generated for all submergences, though not necessarily with the same energy distribution, the deeper water depths associated with deeper submergences would have allowed the waves to travel faster. Looking at the orientation of the trailing edge of the wave packet in the two dimensional wave field plots in relation to the 0.15 m characteristic curve, there is an indication that this was so. Due to the subtlety of this effect, it proved difficult to quantify this trend, though there was clear qualitative evidence. The same applied to the leading waves with long wavelengths. Once the waves propagated off the slope into water with constant depth, the waves seemed to propagate at similar speeds irrespective of initial submergence.

The water surface behind the wave packet was essentially flat, apart from the small well-defined waves that propagated up the slope. These waves ultimately formed the run-up and run-down observed at the shore. Tracing these waves back along the x-t plane, their generation source could be estimated. The trough that formed over the rear end of the landslide propagated upslope as well as downstream. This was clearly the source of the maximum run-down observed at the shore. The source of the wave responsible for the wave run-up was not so clear, but this wave appeared to be generated near the location of the base of the slope. Wave run-up and run-down are further investigated in Section 5.3.4 and in the numerical modelling in Chapter 6.

These qualitative results alone provide valuable insight into the physics of real underwater landslide induced tsunami events. A landslide will generate waves with maximum initial length of the order of that of the landslide. The implication is that landslides of small lateral dimensions will generate waves with small wavelengths, and as waves lose energy more rapidly for higher frequencies, the waves that are generated will attenuate more rapidly than longer wavelengths. Small vertical dimensions of landslides will also induce smaller amplitudes. Dispersion will act to spread the wave packet, further reducing the energy density.

In a real event with similar characteristics as this experimental configuration, such as a long and thin slider moving for a moderate distance along a near-constant incline with a moderate angle, the leading waves can be expected to maintain their size and shape more than the trailing waves. The trailing waves will be highly dispersive, so waves will be forming continuously on the trailing edge. The initial submergence of the landslide and the profile of the slope will have a significant effect on the speed of the waves, with deeper water having higher velocities, particularly for longer wavelengths. The interaction of the landslide pressure field with the surface wave pressure field will also be important, as the location of the low pressure region above the landslide relative to the wave field can act to reinforce or suppress the waves above. This is explored again from an energy standpoint in Section 5.3.5, and a theoretical model is used to look at this interaction in more detail in Chapter 6.

5.3.2 Maximum Wave Amplitudes

Figure 5.10 plots the maximum crest and trough amplitudes for each of the fifteen test combinations. These tended to increase for heavier specific gravities and shallower initial submergences. Note that these are the maximum amplitudes of waves propagating downstream. The maximum wave run-up amplitudes observed on the shore above the landslide, of immediate concern to coastal population and infrastructure, are given in Section 5.3.4. Wave amplitude values are included as they are quantities used by several previous researchers following the formalism of Watts (1997). The wave height, H, to still water depth, D, ratio was greater than 0.03 for the leading waves of some of the test combinations, especially during the time of generation and initial propagation. Wave height is defined as the sum of the wave crest and trough amplitude. Using the recommended range of applicability of linear wave theory of Le Méhauté (1976), the largest amplitude waves in the train were weakly non-linear oscillatory waves. However, linear theory remains applicable for waves with amplitudes well beyond the linear limits, and is often used for weakly and moderately non-linear waves with acceptable accuracy.

Appendix C contains further plots, including the maximum non-dimensional amplitudes of the first crest, first trough, and second crest, for each specific gravity and initial submergence combination. Also presented is the non-dimensional time and downstream position at which the maximum crest and trough amplitude occur. Appendix C also contains plots of the maximum and minimum water level time history and envelope for each of the fifteen test combinations.

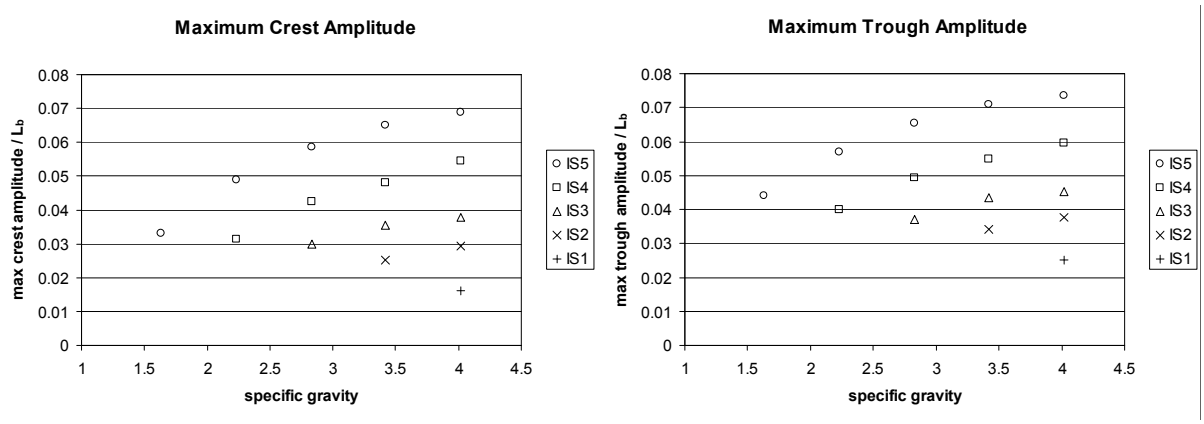

Figure 5.10. Maximum crest and trough amplitude for various specific gravities and initial submergences.

5.3.3 Wavelengths and Speeds

Wavelength is an important wave quantity, not only because it is a useful descriptor of a wave, but also because it governs the propagation speeds of deep and intermediate depth water waves. Wave period is also an important quantity in physical situations, as it provides an indication as to the time between subsequent waves. Should these waves impact a shoreline, then the period would be necessary to determine if preceding waves have enough time to fully recede before the subsequent wave run-up. During the Papua New Guinea event, in 1998, witnesses stated that later waves arrived before previous waves had fully receded (Davies et al. 2003). This allowed the waves to ride in on top of the earlier waves, allowing them to reach further inland.

Illustrated in the water surface profiles in Figure 5.7, the water surface time histories in Figure 5.8, and the two-dimensional wave field plot in Figure 5.9, the wavelength of each wave increased with time. Figure 5.11 plots the time history of the length of the first trough and second crest for the SG3_IS5 case. Plots for the other cases are presented in Appendix C. The first trough, generated by the initial movement of the landslide, started with an initial length of 0.25 m, or half the length of the landslide. The first trough length then continued to increase, practically linearly, over time. The following wave crest formed due to dispersion of the leading trough. The second crest length also increased almost linearly with time. It should be noted that the lengths of the first trough and second crest were calculated as the distance between the locations at which the water surface intersected with the original still water level.

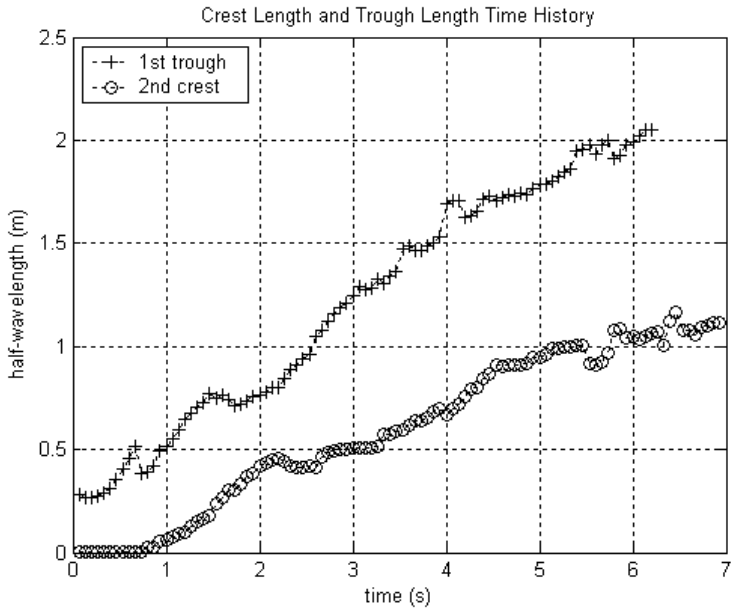

Figure 5.11. Time history of the length of the first trough and second crest for the SG3_IS5 case.

As previously mentioned, wavelengths govern the speeds of deep and intermediate water depth waves. It would therefore be sensible to plot the theoretical speeds of some waves with an assumed wavelength. These characteristic curves, plotted in the x-t plane, indicate the x-position of a wave at any time, taking into account the varying water depth along the slope. The same two characteristic curves have been superimposed onto the two-dimensional wave field plots in Figure 5.9 and Appendix C. The characteristic curve that corresponded closely with the leading crest assumed a wavelength of 4.0m and originated at the initial landslide centre of mass position. This characteristic was based on the phase speed of a 4.0 m long wave. The other characteristic assumed a wavelength of 0.15 m, and was based on the group velocity of the wave, and originated at the initial landslide trailing edge position. This characteristic corresponded well with the rear of the wave packet. Group velocity, which is the speed at which energy in a wave is propagated, is the correct speed when dealing with the generation of waves through dispersion. The individual waves themselves should be compared to phase speed-based characteristic curves.

The range of characteristic curve wavelengths, from 4.0 m to 0.15 m, agrees with the observed wavelengths. From the water surface profiles in Figure 5.7 and Appendix C, the leading crest had an initial half-wavelength of approximately 0.5 m to 1.0 m, and gradually increased to several metres as the wave dispersed. The phase speed of waves with long wavelengths are independent of wavelength, so the characteristic curves for 2.0 m, 4.0 m, and 6.0 m or greater wavelengths were similar. The waves at the end of the packet had lengths of a fraction of a metre, so the correspondence of the 0.15 m characteristic was not unreasonable.

A variety of spectral analysis techniques were investigated to quantify the dominant wavelengths in the wave field, including windowed (short-time) Fourier transforms, wavelet transforms, Hilbert transforms, and empirical mode decompositions. However the interpretation of the results of these techniques was not straightforward and did not seem to provide any further insights than fast Fourier transforms (FFT) and plots of the power spectral density (PSD). The FFT is a more commonly used spectral analysis tool, so was used here to quantify the dominant wavelengths, even though it was clear that the water surface profiles were not stationary signals. The disadvantage of the FFT was that any information contained within the free surface profiles about the spatial distribution of the wavelength components was lost.

Performing a fast Fourier transformation on a water surface profile provided an indication of the dominant wavelengths in the water surface record. The FFT was used over the entire water surface profile extending from the shore to the end of the measured domain. As the wavelengths of similar dimension as the measured domain were required to be resolved, windowing of the FFT domain was not used. Figure 5.12 plots the power spectral density, derived from the FFT, of the water surface

profile at seven consecutive times, ranging from 0.667 to 4.0 seconds, for the SG3_IS5 combination. The 1st wave crest began propagating out of the observed domain after approximately 4 seconds. Wavelengths in this figure have been normalised by the landslide length. The features of the PSD from this test were also present in the other specific gravity and initial submergence combinations. Inspecting Figure 5.12, it can be seen that as time progressed energy was gradually transferred from the shorter wavelengths into the longer wavelengths. Only a small amount of energy remained invested in the waves with length shorter than the landslide length. The increase in total energy as time progressed was also evident, especially between t = 0.667 and t = 1.333 seconds. The results of this analysis also provided quantitative evidence of the continually increasing wavelengths present in the wave train.

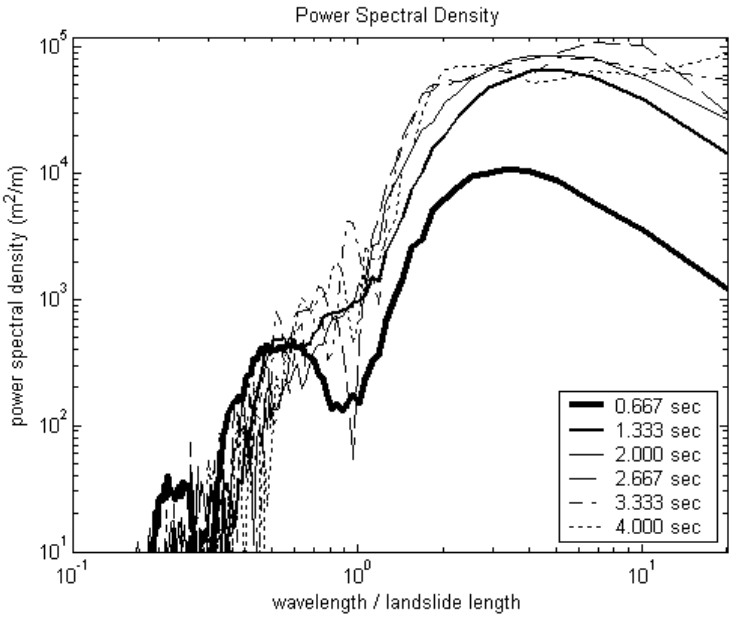

Figure 5.12. Power spectral density of the water surface profiles at 0.667, 1.333, 2.000, 2.667, 3.333, and 4.000 seconds to find the dominant wavelengths for the SG3_IS5 test. Wavelengths have been non-dimensionalised by the landslide length. Note the increasing dominance of the longer non-dimensional wavelengths at later times.

5.3.4 Maximum Wave Run-up and Run-down

The level of maximum wave run-up and run-down is physically important, as this is of immediate concern for population and structures upslope of an underwater landslide. An indication of the maximum height and time of inundation would highlight those who might be in danger from a possible tsunami. Also, public understanding that a tsunami inundation may be preceded by a large draw-down of the water level at the shore may allow them to recognise the signs of an approaching tsunami wave crest and move to higher ground.

Wave run-up and run-down heights along the slope were measured vertically from the original still water level. The run-up and run-down lengths, the horizontal distance from the original intersection of the water and the slope surfaces, can be calculated from the geometry. Note that the scale of the laboratory experiments dictated that the wave run-up measurements were affected by surface tension.

A typical wave run-up height time history is presented in Figure 5.13 for test SG3_IS5, and Appendix D contains run-up time history plots for the remaining combinations. The key features of wave run-up height time histories, for the various specific gravity and initial submergence combinations, was a large initial draw-down followed by a rebound to a level close to the original water level. This was followed by a positive run-up and relaxation back to something close to the original mean water level.

The non-dimensional wave run-down observed at the shore decreased with deeper initial submergences, as shown in Figure 5.14. The dependence on specific gravities was relatively weak. The wave run-down and the 1st wave trough were formed by the same mechanism, namely the initial draw-down of the water surface above the landslide. The depression that formed over the rear end of the block propagated in both the upstream direction, to cause the large initial draw-down at the shoreline, and downstream as the 1st wave trough. The magnitudes of these two parameters were governed by the strength of this initial water surface depression. The correlation between the maximum run-down height and the maximum 1st wave trough amplitude, as shown in Figure 5.15, confirms the common origin of these two phenomena.

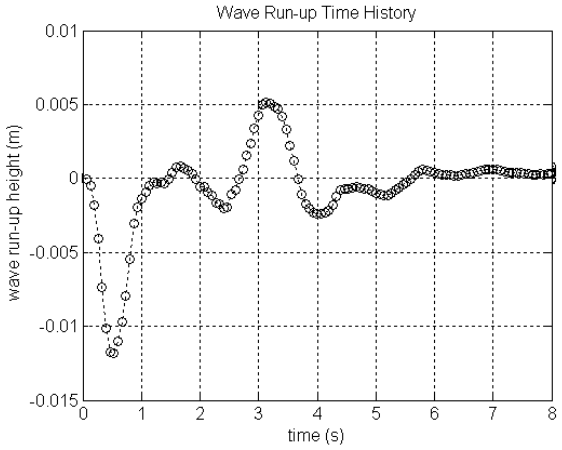

Figure 5.13. Wave run-up height time history for the SG3_IS5 test.

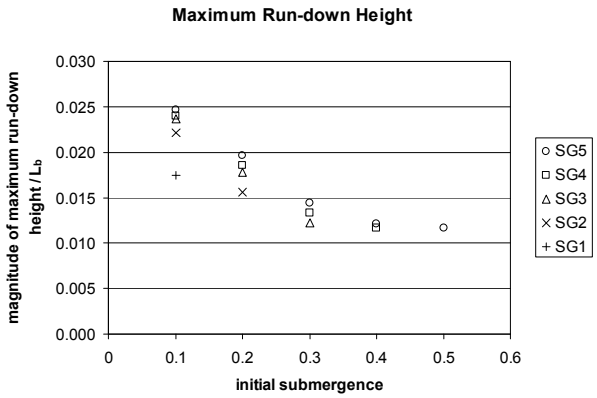

Figure 5.14. Maximum wave run-down height as functions of specific gravity and initial submergence.

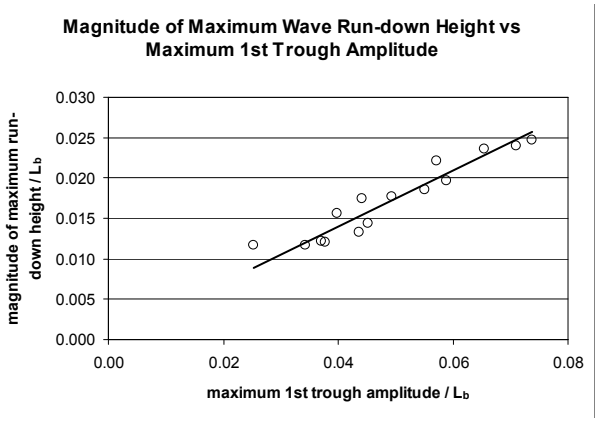

$$\frac{|r_{y,\min}|}{L_b} = 0.3489 \frac{1st\ trough\ amplitude}{L_b}$$

$$r^2 = 0.900$$

Figure 5.15. Maximum 1st trough wave amplitude versus magnitude of maximum wave run-down height.

As shown in Figure 5.16, the non-dimensional time at which the maximum wave run-down occurred was independent of specific gravity, dependent solely on the initial submergence of the landslide. The maximum run-down occurred later for deeper submergences because the landslide was initially further downstream, and the initial water surface depression that formed over the landslide had further to travel upstream. A power law curve fit to this data results in the expression given in Equation 5.14.

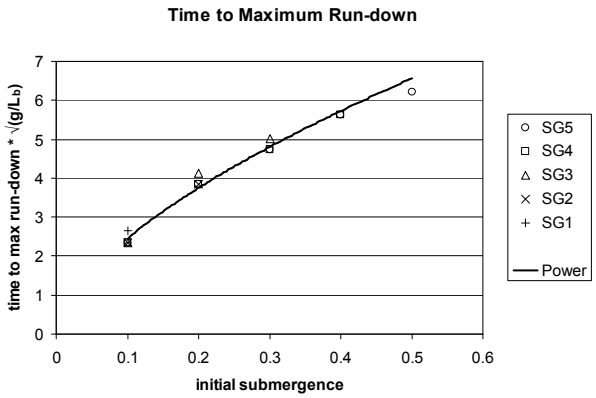

Figure 5.16. Time of occurrence of maximum wave run-down height as functions of specific gravity and initial submergence.

$$\frac{time\ to\ r_{y,\min}}{\sqrt{g/L_b}} = 10.017\left(IS\right)^{0.611} \qquad \textbf{(5.14)}$$

$$r^2 = 0.982$$

An approximate time of occurrence of maximum wave run-down was calculated, based on the wave phase speed given in Equation 5.9, and compared with the measured values, as shown in Figure 5.17. Wave troughs with a length of 0.5m, approximately the length of the landslide, were hypothetically generated at various downstream positions, corresponding to the initial location of the landslide, and propagated upstream towards the shore. The ratio of the measured and calculated propagation times are plotted in Figure 5.17 as a function of initial submergence. This resulted in ratios within 18% of unity.

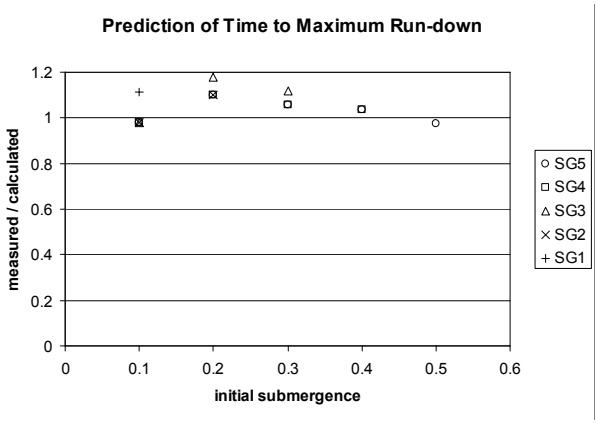

Figure 5.17. Comparison of measured time of occurrence of maximum wave run-down with calculated values assuming a specific wavelength trough was generated above the initial landslide position and propagated upstream.

The trends observed in the maximum non-dimensional wave run-up data, presented in Figure 5.18, indicate that the maximum wave run-up heights increased for heavier specific gravities and shallower initial submergences. It was theorised that the positive run-up peak occurred as a result of a wave generated by the short duration, but high magnitude, deceleration of the landslide upon reaching the base of the slope. The wave generated at this point and time propagated upstream and ran up the slope. Preliminary tests with the landslide block tethered so that it abruptly stopped at the base of the slope, resulted in the generation of waves with amplitudes larger than those initially generated by the accelerating landslide. The removal of the tether and allowing the landslide to slow naturally along the flume floor resulted in a significant reduction in the magnitude of the wave generated by the slowing block. However, the maximum positive run-up height was still dominated by the run-up of this landslide deceleration-induced wave. This indicated that landslide deceleration could have a significant affect on the magnitudes of the observed wave run-up

As illustrated in Figure 5.6, the magnitude of the maximum deceleration increased with increasing specific gravity and shallower initial submergences. To provide further evidence of the landslide deceleration origins of the run-up height observed, Figure 5.19 plots maximum non-dimensional wave run-up heights against maximum non-dimensional landslide velocities and decelerations at the base of the slope. The data from all fifteen combinations collapsed onto one curve when the maximum velocity was used as the independent variable. It appeared that this was also the case when the maximum deceleration was used as the independent variable, but now the reduced accuracy of the deceleration values led to greater spread in the data.

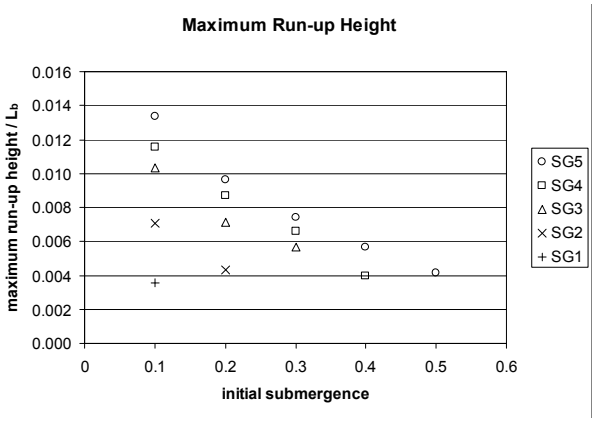

Figure 5.18. Maximum wave run-up height for various specific gravities and initial submergences.

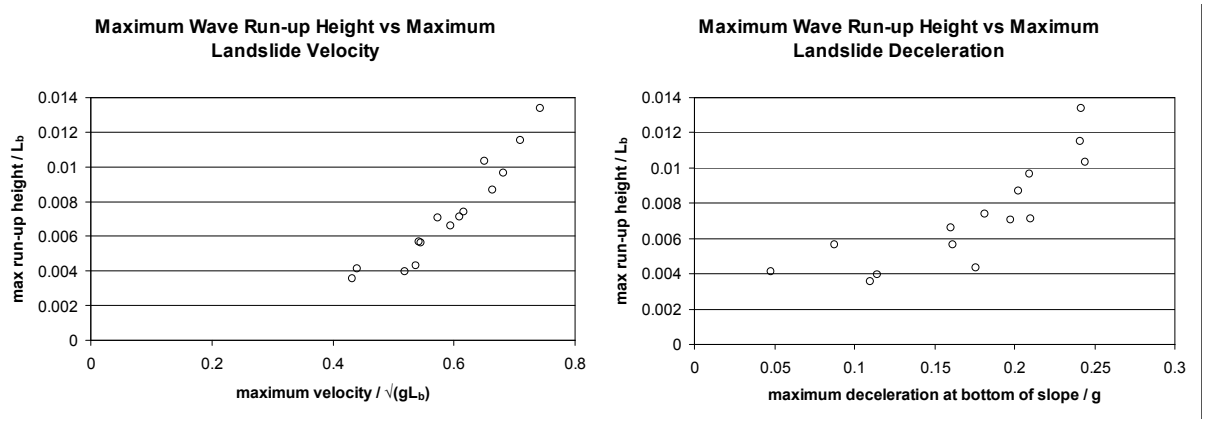

Figure 5.19. Maximum wave run-up height versus maximum landslide velocity and maximum landslide deceleration at the base of the slope.

Figure 5.20 indicates that the non-dimensional time of maximum run-up occurred earlier for deeper initial submergences. The dependence on specific gravities was relatively weaker. The added mass and shorter slope distances caused the landslide to reach the base of the slope earlier. As the run-up peak was likely to have been created by the deceleration of the block at toe of the slope, the maximum run-up occurred earlier. A power law curve fit to this data resulted in the expression given in Equation 5.15.

$$\frac{time\ to\ r_{y,\max}}{\sqrt{g/L_b}} = -7.644\left(IS\right) + 14.989 \qquad r^2 = 0.721 \qquad \textbf{(5.15)}$$

Based on the theory that the large wave run-up was caused by the landslide deceleration at the base of the slope, the travel time for a wave generated above the toe of the slope to travel back to the beach was calculated. A wavelength of 0.5 m, equal to the length of the landslide, was assumed and the time for this wave to propagate upstream to the shore was added to the time for the landslide to reach the base of the slope. These times were calculated, based on the wave phase speed given in Equation 5.9, for all fifteen test combinations and the ratio of measured and calculated times are plotted in Figure 5.21. All ratios were within 7% of unity and this strongly supported the hypothesis that the run-up was caused by the deceleration of the slider at the bottom of the slope.

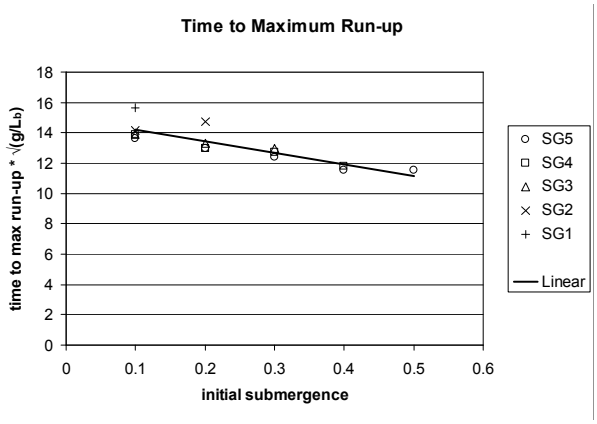

Figure 5.20. Time of occurrence of maximum wave run-up height for various specific gravities and initial submergences.

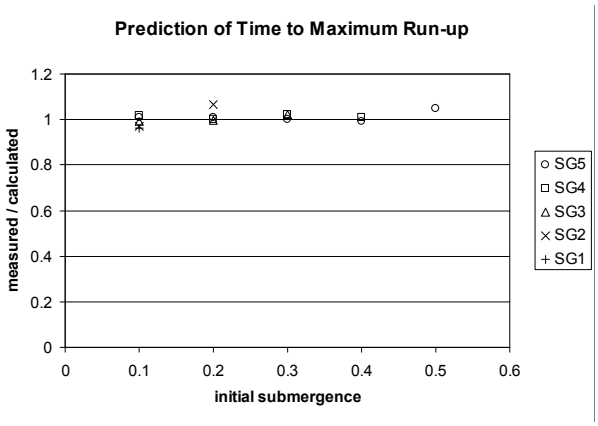

Figure 5.21. Ratio of measured to calculated time of occurrence of maximum wave run-up assuming a 0.5m wavelength crest was generated above the toe of the slope and propagated upstream.

Based on these results, it was possible to speculate on the physical generation of waves that impacted the shore following the underwater landslide. The accelerated flow over, and the turbulent wake behind, the moving landslide created a region of low pressure. The water surface was then drawn down over this region of low pressure. This trough propagated both upstream and downstream, with most of the wave energy propagating offshore. The onshore component of the trough propagated up the slope to cause the water level at the shore to drop.

The sudden decrease in acceleration as the landslide reached the base of the slope generated a wave crest. This crest then propagated back upstream to cause the run-up observed at the shore. It was unclear if a downstream component of the wave crest was generated as well, as the amplitude of this wave would have been small in comparison to the amplitude of the waves in the trailing wave packet of the downstream propagating waves. A possible mechanism for the generation of the onshore propagating wave crest was a region of high pressure forming behind the decelerating landslide. As the landslide moved down the slope, fluid in behind the landslide was drawn offshore as well. The

landslide then reached the base of the slope and decelerated. The momentum of the fluid moving offshore caused it to squash against the rear of the slowing landslide, leading to a rise in the local fluid pressure. The higher pressure caused a wave crest to form on the surface, which then propagated onshore.

The idea that the maximum wave run-up was generated by the deceleration of the landslide has important implications to the hazard assessment of underwater landslide generated tsunami. The idea that the run-up mechanism is dependent on the magnitude of the decrease in landslide acceleration implies that a landslide that runs out and decelerates gradually would produce little or no significant wave run-up onshore. However, these hypotheses are based on two-dimensional test configurations. The test results presented by Liu et al (2005) indicated that significant wave run-up could occur behind the landslide due to the horizontal fluid flow around a three-dimensional slider. The convergence of the lateral flows behind the landslide ran up the shore to generate a noticeable run-up. Further details of these tests are presented in Section 3.1.2.

The present research results confirmed that the deceleration of the landslide at the base of the slope was dependent on its velocity. There was no mechanism within the experimental set-up with which to systematically vary the deceleration without changing the initial landslide conditions (such as specific gravity or initial submergence). Instead, the idea that upstream propagating wave crests are generated by the abrupt decrease in acceleration of the landslide is investigated using a numerical model. In a numerical framework, the landslide deceleration is controlled independently from the landslide configuration, and hence the effect of decreases in acceleration can be investigated. Details of this are presented in Chapter 6.

5.3.5 Energy

The instantaneous potential energy contained in the waves was calculated as

$$\text{wave } E_p(t) = \frac{1}{2}\rho_o g w \int_0^{\infty} \eta(t)^2 dx \tag{5.16}$$

where ρ_o = water density

g = acceleration of gravity

w = flume/landslide width

η = water level

x = downstream position

t = time

The wave potential energy integration limits were actually between 0.0 m and 10.1 m downstream. However, provided waves had not propagated out of our observed domain and the water surface beyond 10.1 m was still, the integration was still valid.

The instantaneous landslide kinetic energy was calculated as

$$\text{block } E_k(t) = \frac{1}{2} m_b vel(t)^2 \tag{5.17}$$

where m_b = unsubmerged landslide mass

vel = landslide velocity

The instantaneous landslide potential energy was calculated by multiplying the submerged mass of the landslide by the vertical fall distance relative to its initial position, and was calculated as

$$\text{block } E_p(t) = g(m_b - m_0)(y(t_0) - y(t)) \tag{5.18}$$

where m_0 = mass of water displaced by landslide

$y(t_0)$ = initial landslide vertical position

$y(t)$ = instantaneous landslide vertical position

Figure 5.22 plots the time histories of wave potential energy, landslide kinetic energy, and the change in landslide potential energy, for the SG3_IS5 test. Appendix E plots the energy time histories for the remaining test combinations of specific gravity and initial submergence. The key features of these plots are similar for each of the combinations. Some of the block potential energy was converted into landslide kinetic energy as it slid down the slope. The remaining potential energy was dissipated as friction on the sliding surface. The motion of the landslide set in motion some of the surrounding fluid, converting some of the block kinetic energy into kinetic energy of the water. Some of the energy in the water motions was then passed into the wave potential energy, the remainder being dissipated through friction. The initial amount of energy imparted by the landslide was small, but as it accelerated down the slope, it continually pumped energy into the wave field. As the landslide moved, it experienced several drag forces. Along with surface friction and form drag, wave energy propagated away from the slider.

It was clear that the maximum wave potential energy occurred after the maximum landslide kinetic energy occurred. Note that wave potential energy decreased when waves propagated out of the observed region, typically after approximately 4 seconds. The wave energy continued to increase after the landslide had reached the base of the slope and started slowing. The rate of transfer probably decreased but did not stop completely until the landslide came to a halt. The key point is that acceleration was not necessary for energy to be transferred from the landslide to the wave field. Provided the landslide was in motion energy could be transferred, as it was the interaction of the pressure field around the landslide and the free surface that determined the effectiveness of this transfer. This is explored further in Chapter 6.

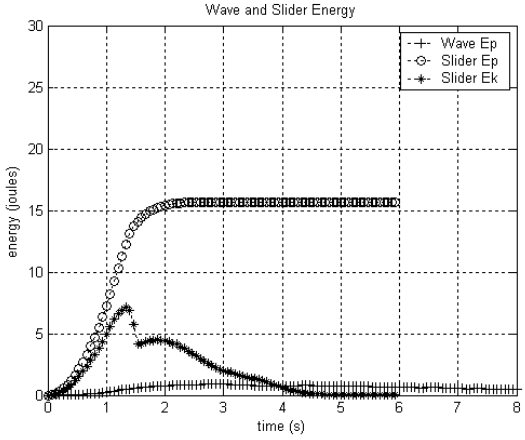

Figure 5.22. Time histories of wave potential energy (wave Ep), landslide kinetic energy (block Ek), and landslide potential energy converted (block Ep), for the SG3_IS5 test.

The wave potential energy time histories in Appendix E show that the wave potential energy increased, peaked, and decreased slightly. This decrease occurred before the waves began propagating out of the observed domain at approximately 4 seconds. The reason for this drop in energy was likely due to the interaction between the pressure field around the landslide and the surface wave field. Inspecting the sequence of water surface profiles in Figure 5.7 for the SG3_IS5 combination, for t = 0.6, 1.6, and 2.6 seconds, the first trough was directly above the rear end of the landslide. This location had a lower pressure due to the accelerating flow over the landslide combining with the turbulent wake. The low pressure above the rear end of the landslide acted to reinforce the wave trough, increasing the wave potential energy during this time. By t = 3.6 seconds, the first trough had propagated ahead of the landslide so the first trough amplitude no longer increased. The landslide also slowed so the low pressure region was not as strong, but the low pressure region was now acting to suppress the second crest. This led to an overall decrease in the wave potential energy. This concept is explored further in Chapter 6 using a numerical model.

Figure 5.23 shows the conversion ratio of maximum landslide kinetic energy to maximum wave potential energy was between 2.8% and 13.8%. This quantity indicated the maximum efficiency with which the landslide motions could pass energy into the wave field. Shallow initial submergences and lighter specific gravities increased the efficiency. Watts (1997) found conversion rates of solid block kinetic energy into wave potential energy of between 3% and 7%. However, his expression for energy conversion was calculated as a function of the landslide terminal velocity and the square of the maximum wave amplitude.

Figure 5.24 plots the time histories of the ratio of wave potential energy to landslide kinetic energy, grouped by initial submergence. The times on the horizontal axes have been normalised by the time of maximum landslide velocity (also the time of maximum landslide kinetic energy). The landslide kinetic energy was modified by dividing by the landslide specific gravity. This modification was implemented because the energy in the wave field depended on the kinetic energy of the fluid flow field, not intrinsically on the energy (or mass) of the landslide. For example if two different sliders were travelling with the same velocity, then their impact on the wave field would be the same regardless of how heavy the sliders were. In doing this, the time histories for the various specific gravities at each of the five initial submergences showed very similar trends. Interestingly, the time histories show a period of increase in energy ratio before a plateau and then a continued increase. The plateau region indicated that the growths in wave potential energy and modified landslide kinetic energy were similar.

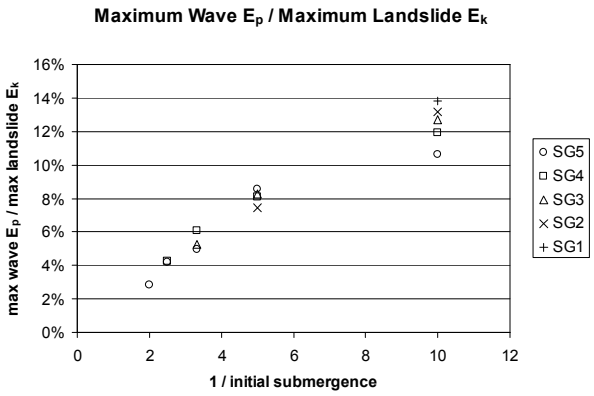

Figure 5.23. Percentage conversion ratio of maximum landslide kinetic energy to maximum wave potential energy.

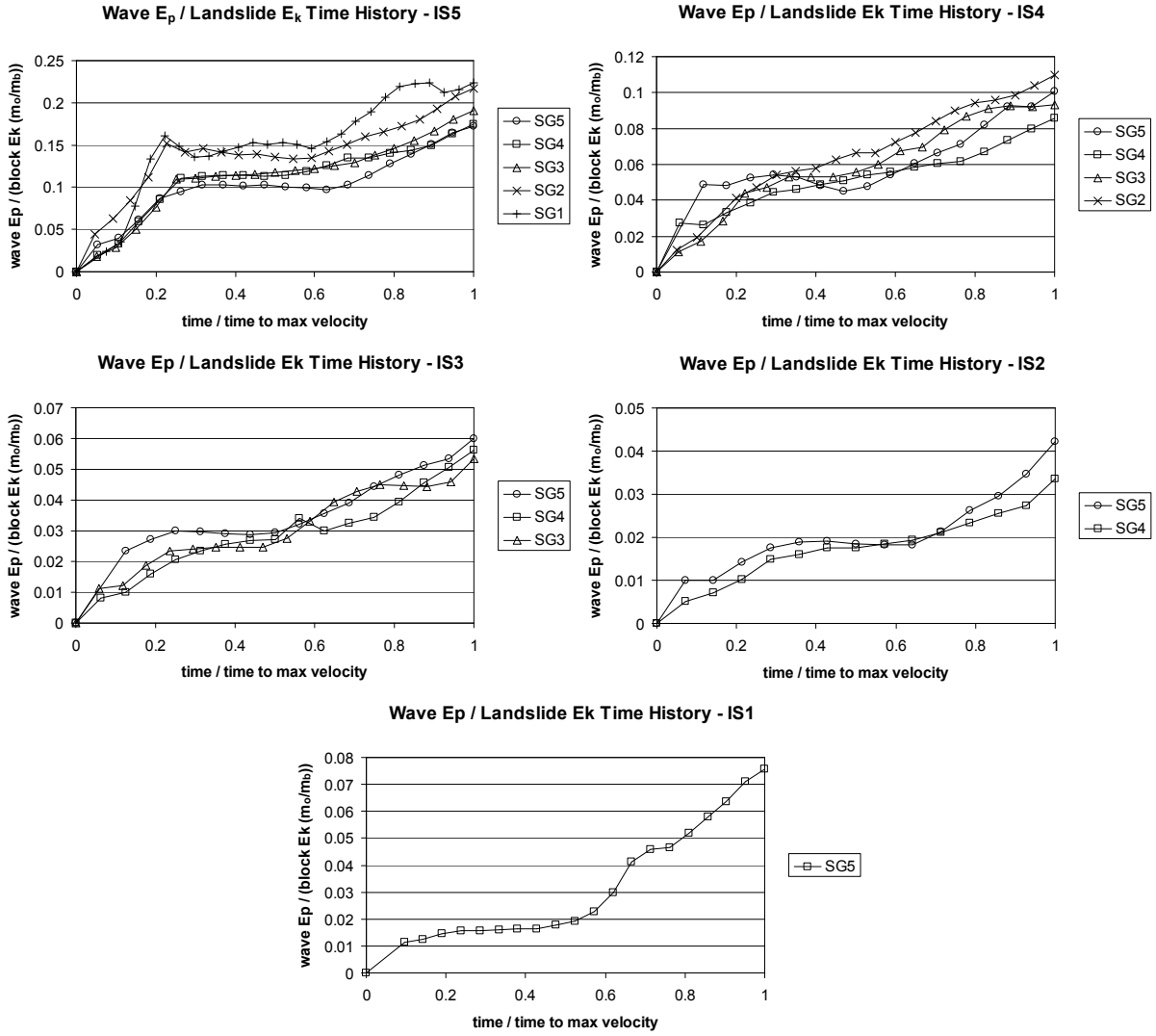

Figure 5.24. Time history of the ratio of wave potential energy to landslide kinetic energy. Times are normalised by the time of maximum landslide velocity. Landslide kinetic energy is modified by dividing by specific gravity.

The conversion ratio of maximum landslide potential energy to maximum wave potential energy is presented in Figure 5.25. This quantity indicated the possible maximum wave field energy for a given landslide geometry. Conversion rates ranged between 1.1% and 5.9%, and were greater for shallower initial submergences. The effect of increasing specific gravity was relatively weak. Weigel (1955) found typical rates of 1-2% for conversion of landslide potential energy into wave potential energy. His wave potential energies were calculated as a function of the sum of the 1st wave trough and 2nd wave crest amplitudes, squared.

The conversion ratio of maximum potential energy to maximum kinetic energy of the landslide ranged between 32.9% and 50.4%, as shown in Figure 5.26. This quantity indicated the proportion of the gravitational potential energy of the landslide transferred into its motion, and indicated the amount of energy dissipated through friction and other such effects. The efficiency of conversion was influenced by changes in specific gravity, with efficiency increasing for heavier landslides. The increase in energy conversion with shallower initial submergences was relatively minor.

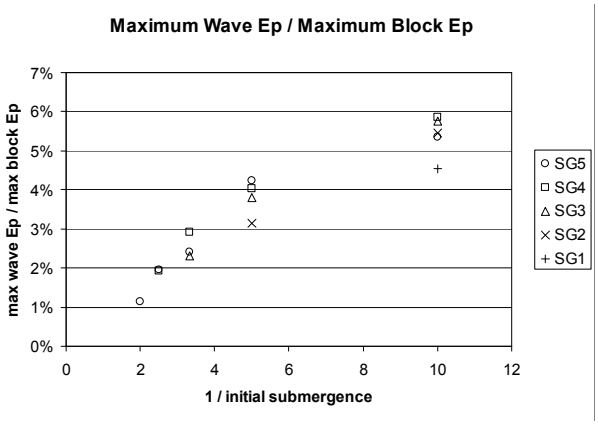

Figure 5.25. Percentage conversion ratio of maximum landslide potential energy to maximum wave potential energy

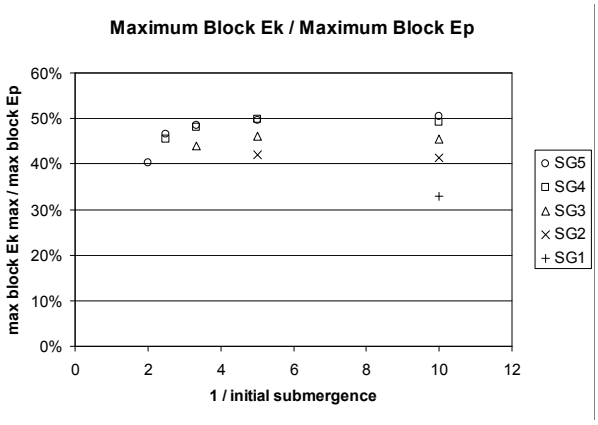

Figure 5.26. Percentage conversion ratio of maximum landslide kinetic energy to maximum landslide potential energy

From the energy time history plots in Figure 5.22 and Appendix E, it was clear that the maximum wave potential energy occurred at a time later than that of the maximum landslide kinetic energy. Figure 5.27 plots the ratio of time to maximum wave potential energy to time to maximum landslide kinetic energy, for various specific gravities and initial submergences. It was clear that the period of positive acceleration was not the only time over which energy was passed into the wave field. There was substantial energy transfer into the wave field after the time of maximum velocity and as the landslide decelerated.

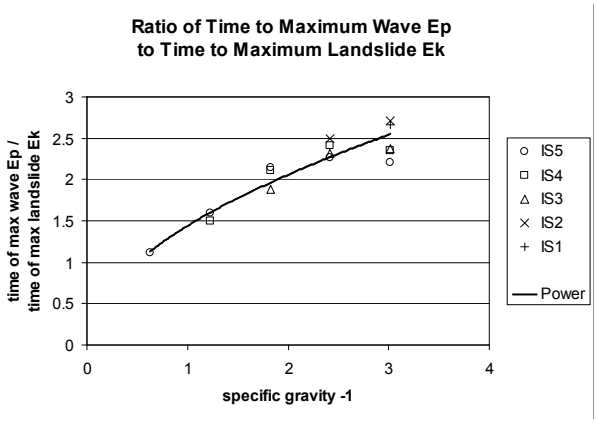

$$\frac{\text{time to max wave } E_p}{\text{time to max landslide } E_k} = 1.439\left(\text{S.G-1}\right)^{0.518}$$

$$r^2 = 0.915$$

Figure 5.27. Ratio of time to maximum wave potential energy to time to maximum landslide kinetic energy, for various specific gravities and initial submergences.

5.3.6 Significance of Exchange Flow

As detailed in Section 4.1.2, an opening was left at the base of the slope to allow water to pass between the main channel and the space behind the slope. This opening was necessary to reduce the severe aquaplaning of the landslide as it passed through the transition curve. With the passage of the landslide over the transition curve, the low pressure on the underside of the landslide drew water into the main channel from behind the slope. As the landslide moved off the transition curve onto the tank floor, the water trapped under the landslide was able to escape back through the opening into the region behind the slope.

To assess the effect of this exchange flow, the continuity of mass of water in the main channel was checked. This was done by spatially integrating η along the length of the observed water surface, as a function of time. It was found that this integral was at times non-zero even before waves had propagated out of the observed domain. Some of the excess or deficit in mass could be explained by noise in the water surface profiles. This noise arose when the individual sections of water surface,

from the different camera positions, were joined to create the entire 10 m long water surface. With the 15 Hz frame rate of the Pulnix TM1010 camera and typical wave propagation speeds of 1.5 m/s, the generated waves could potentially travel 0.1 m in the time required to capture a frame. Therefore, the accuracy in determining the downstream position of a waveform was ± 0.05 m. Mismatches in wave positioning at the join between adjacent sections of water surface may have led to a slight momentary over or underestimation of the fluid mass.

Two examples of the time history of $\int \eta \, dx$ are given in Figure 5.28 for the SG5_IS5 and SG5_IS1 combinations. Between approximately $0.7 < t < 2.8$ for the SG5_IS1 case, and between approximately $1.3 < t < 3.7$ for the SG5_IS5 case, the positive value of $\int \eta \, dx$ for the original data (dotted line) indicated there was an excess of fluid within the main channel. This excess fluid was beyond what random wave positioning errors could account for. Waves began leaving the measured domain after approximately $t = 4$ seconds leading to the large loss of mass after this time. The solid lines in Figure 5.28 show $\int \eta \, dx$ after a correction was applied that removed the excess water. This correction is described below.

To confirm that the excess water in the main tank came from behind the slope, a set of tests were performed to measure the water level time history of the water behind the slope. The same LIF technique used to measure the water surface profiles in the main tank was employed. The landslide with the heaviest specific gravity was used with all five initial submergences. Three repeat runs were recorded for each of the five combinations and the results showed similar repeatability as the LIF measurements in the main channel.

The water surface captured in the camera frame was space-averaged across the frame to determine a water level time history for the water behind the slope for each combination. The area of water exchanged between the two sides of the slope was determined by multiplying the space-averaged water level by the length of water surface behind the slope. A comparison between the time-history of the area of water moved from behind the slope with the spatial integral of water surface profile, confirmed that the gain in water in the main channel predominantly came from behind the slope. Figure 5.29 plots the time histories of the exchanged water areas for the SG5_IS5, SG5_IS4, SG5_IS3, SG5_IS2, and SG5_IS1 combinations. The black circles in these plots indicate the approximate time at which the centre of the landslide reached the transition curve at the base of the slope. The solid lines are $\int \eta \, dx$, as a function of time, and show that there was a net gain in water after the landslide reached the base of the slope. The excess water remained in the main channel for approximately the next two seconds. The dotted lines plot the area of water lost from behind the slope. There was a clear correlation between these two quantities, and this tended to confirm that the movement of water

beneath the slope was the primary cause of the larger manifestations of mass excess and deficit within the main channel.

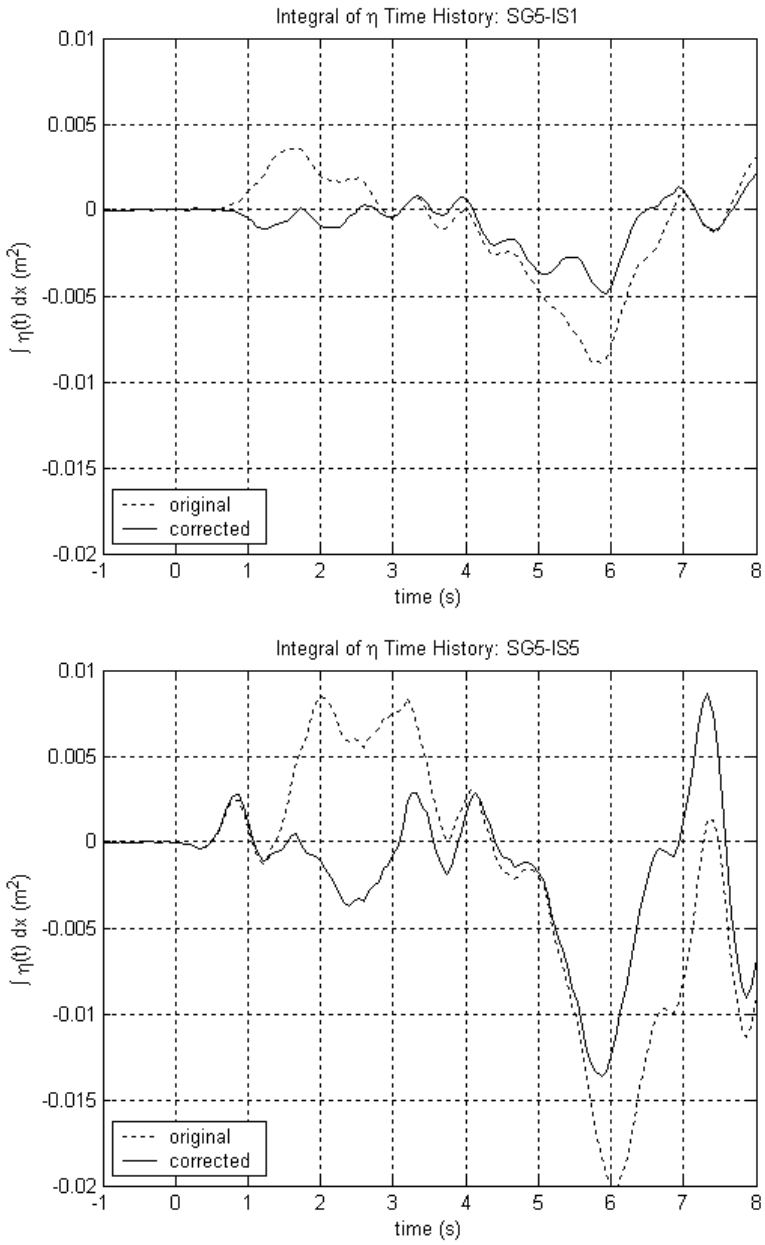

Figure 5.28. Time history of the spatial integral of η for the SG5_IS5 combination with and without allowing for movement of water between the main channel and behind the slope. Waves begin leaving the measured domain after approximately t = 4 seconds.

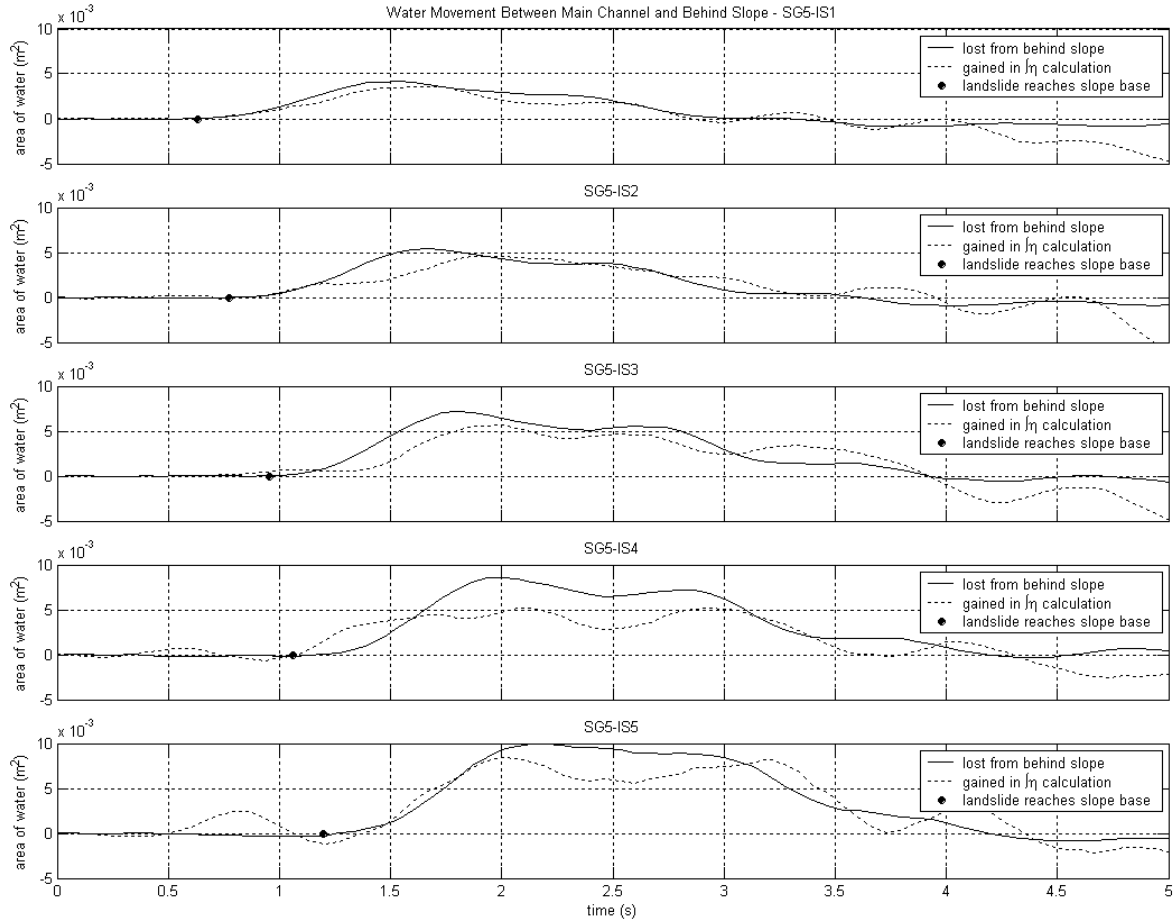

Figure 5.29. Comparison of the area of water gained in the main channel with the area of water lost from behind the slope for the SG5_IS5, SG5_IS4, SG5_IS3, SG5_IS2, and SG5_IS1 cases.

To determine the effect of the movement of water between the main channel and behind the slope, a correction method was devised. A possible correction for the flow of water between the main channel and the region behind the slope involved incrementally removing the water that was drawn into the main channel. Likewise, water that was removed from the main channel was reintroduced. The area of water lost from behind the slope during each time step, measured during the experiments, was determined. As each increment of water was allowed to move into the main channel during the experiments, the correction involved removing this area of water from the main channel at each time step. This ensured that no significant excess or deficit of fluid was introduced in the main channel.

This correction method required several assumptions to be made regarding the speed of the water movement, at what downstream position the water from behind the slope entered the main channel, and in what direction the water moved once in the main channel. Assuming the water moving out of, or into, the main channel from behind the slope travelled as a shallow water wave the wave phase speed given by Equation 5.9 simplified to Equation 5.19. Substituting the constant water depth of 0.435 m, an estimate of the propagation speed of the water moving between the main channel and

behind the slope was found to be 2.066 m/s. Therefore, in 1/15th of a second, or one camera frame at 15Hz, the water was expected to move 0.1377m.

$$C_p(x) = \sqrt{gd(x)} \tag{5.19}$$

It was unclear exactly where the water from behind the slope appeared on the water surface as it re-entered the main channel. However, as the exchange flow occurred through the opening in the slope surface at the transition curve, it was assumed that the excess or deficit appeared in the proximity of the transition curve.

The noise in the spatial integral of η, from random wave positioning errors, precluded the use of the instantaneous change in $\int \eta \, dx$ to calculate the area of water moving between the two sides of the slope. Instead the time history of the water level behind the slope provided the best estimate of the exchange flow. Time histories of the water behind the slope were only available for the five cases with the heaviest specific gravity (SG5). The fluid increments removed from the main channel were then assumed to propagate downstream at the shallow water wave phase speed. During 1/15th of a second, this increment of water propagated 0.1377 m downstream, after which another increment of water was injected or removed, dependent on whether there was an increase or decrease in the water level behind the slope. This injection and removal process is illustrated in Figure 5.30. The water surface time history of the injected or removed water was calculated and applied to the original water surface profile.

The spatial integral of η was re-calculated for the corrected water surface profile time history, and is shown as the solid lines in Figure 5.28 for the SG5_IS5 and SG5_IS1 combinations. Assuming the correction was valid, the remaining non-zero values of the integral of η were predominantly due to the noise in the water surface profiles generated by the mismatches in wave positions.

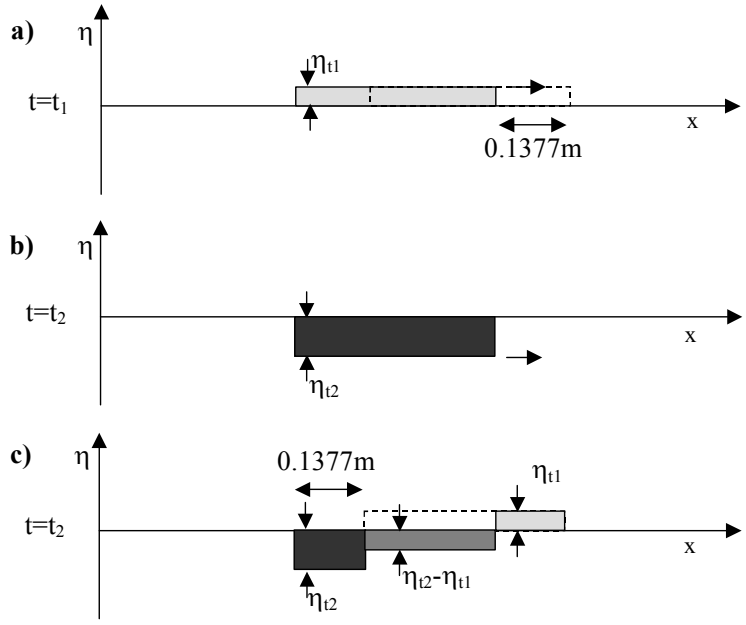

Figure 5.30. Diagram to illustrate how each increment of water area is added to the water surface and propagated. In this example, the increments of water are rectangular in shape. a) At $t=t_1$, an increment of fluid appears on the free surface. This increment propagates 0.1377m each time step. b) At $t=t_2$, another increment of fluid appears on the free surface. This second increment combines with the first increment of fluid, as shown in c).

As the momentum of the fluid escaping through the opening at the base of the slope would most likely push the majority of the fluid increments downstream, the assumption was made that the increments of water only propagated downstream. Also, the lack of waves between the shore and the main wave packet in the original data suggested that very little of the exchange flow propagated upstream. This assumption provided conservative estimates as to the effects of the correction on the original wave field. By not splitting the increment of fluid into backward and forward propagating portions, the corrections had the largest amplitude. This allowed the greatest reinforcement or suppression of the original wave amplitudes and led to the largest changes in wave potential energy.

The sensitivity of the proposed correction to the wave field to the length and shape of the increments of water was investigated. Two increment shapes were investigated. The first assumed that the increments of fluid were rectangular in shape, as shown in Figure 5.30. Although simple to implement, the rectangular shape had the disadvantage of making the corrected water surface profiles very jagged, as the correction was made up of a series of step shapes. To provide a smoother corrected surface profile, sinusoidal shaped increments of water were also tried. Examples of the profiles of the corrections using rectangular and sinusoidal shaped increments of water, at t = 4.00 s for the SG5_IS5 case, are given in Figure 5.31. Both the rectangular and sinusoidal shaped increments of water were introduced or removed from the main channel between $1.297 < x < 1.807$ m. This

region corresponded to the portion of slope occupied by the transition curve. The maximum height of the rectangular increments of water were determined by dividing the area of water moving between the main channel and behind the slope by the 0.51 m length of the increment. The sinusoidal increments had maximum heights twice that of the rectangular increments to ensure they had the same area. The sinusoidal profiles were considered to be a more realistic shape, as the injection or removal of fluid would deflect the water surface in a smooth manner. The dominant signals apparent in the profiles of the correction, shown in Figure 5.31, had half-wavelengths of approximately 1.6 m. Substituting this wavelength and the 0.435 m constant water depth into Equation 5.9 resulted in 1.9 m/s as an estimate of the propagation speed of the combined increments of water. This propagation speed was similar to the initial assumption of the increments propagating at the shallow water wave speed of 2.06 m/s.

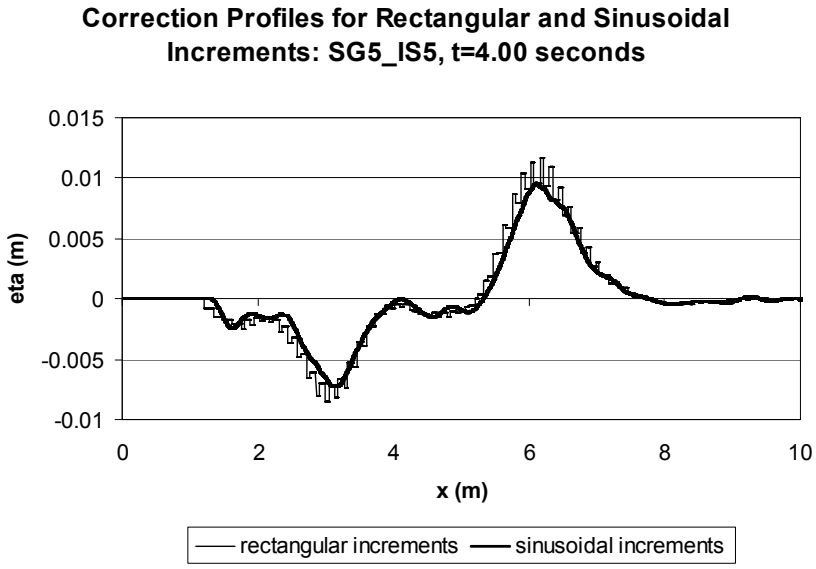

Figure 5.31. Example of the water surface profiles of the exchange flow, using 0.51m long rectangular and sinusoidal shaped increments of water, for the SG5_IS5 combination. Note the jaggedness of the correction profiles when rectangular increments are used.

To examine the sensitivity of the correction process to the length of the increment, 0.51 m long and 1.02 m long sinusoidal increments, centred on the middle of the transition curve, were applied to the wave field. The height of each 1.02 m long increment was half the height of the corresponding 0.51 m long increments.

Figure 5.32 plots the magnitude and ratio of maximum crest amplitude, trough amplitude, and wave potential energy, between the original and corrected data. Corrections were based on 0.51m long rectangular, 0.51m long sinusoidal, and 1.02m long sinusoidal shaped increments of water. Generally, applying the correction had a noticeable effect on the maximum trough amplitude and wave potential energy. Based on the use of 0.51 m long sinusoidal correction increments, the maximum trough amplitude increased by between 22% and 28%, with the percentage increase seemingly insensitive to the initial submergence. The change to the maximum wave potential energy ranged between a 5% decrease to an 18% increase, with the percentage increase tending to rise with shallower submergences. The slight increases in maximum crest amplitude ranged between 2% and 12%, with the larger increases tending to occur for deeper submergences. The trends exhibited by the original data, namely the increasing maximum wave amplitudes and potential energy for shallower submergences, remained the same for the corrected data.

Shallower submergences appeared to be more sensitive than the deeper submergence configurations to the correction applied here. Logic dictated that the shallow submergence and heavy landslide density cases would be the most sensitive to the correction for the exchange of water between the main channel and behind the slope. These configurations, with the heaviest landslide masses and the longest slide distances, had the landslide travelling the fastest when it reached the transition curve. The speed at which the landslide traversed the transition curve determined the magnitude of the exchange flows. For instance, for a very slow landslide passing over the transition curve, the decrease in pressure on the underside of the landslide would be very small and the exchange flow would be minimal.

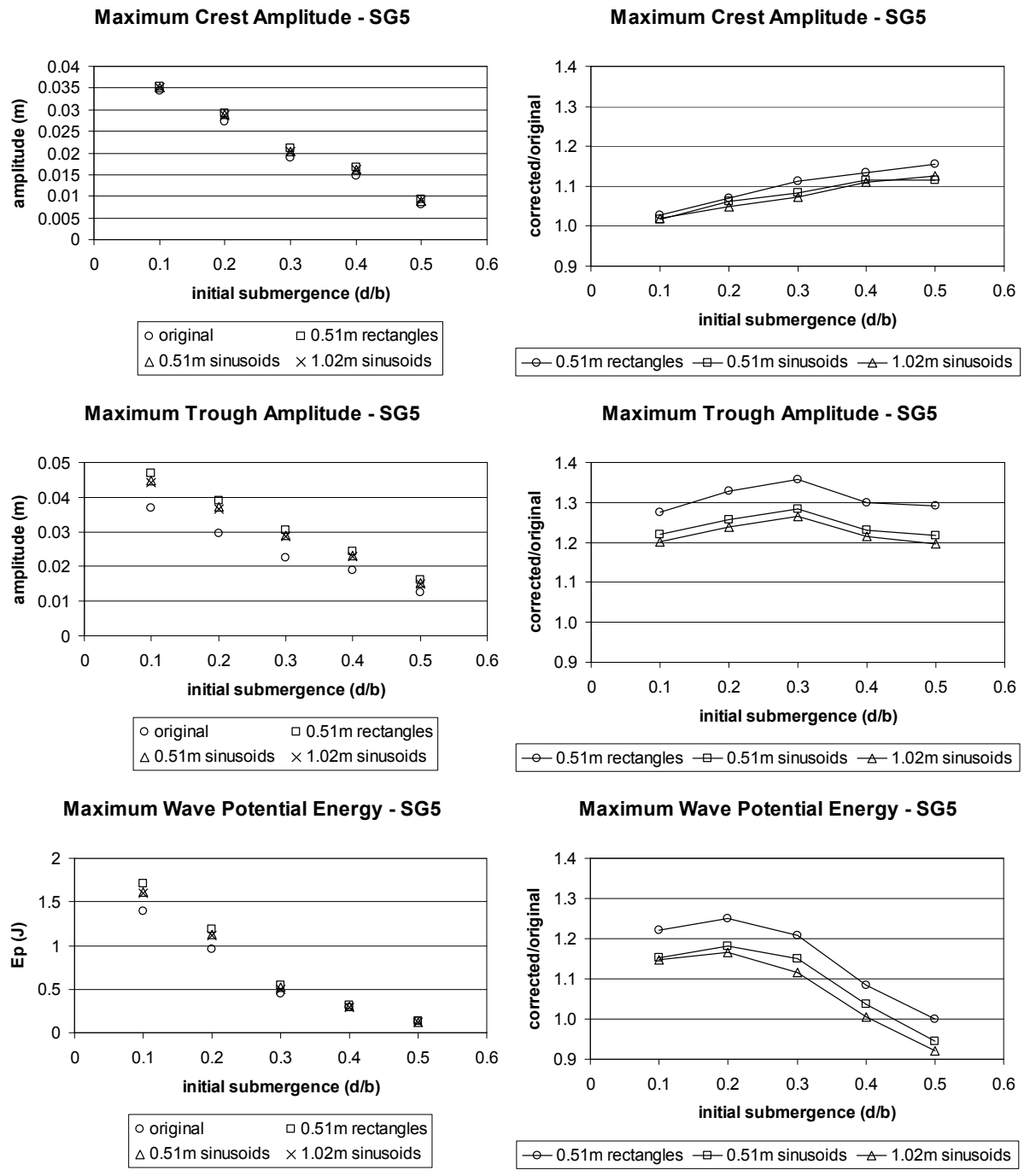

Figure 5.32. Magnitude and ratio of maximum crest amplitude, trough amplitude, and wave potential energy, between the original and corrected data. Corrections are based on 0.51m long rectangular, 0.51m long sinusoidal, and 1.02m long sinusoidal shaped increments of water.

Figure 5.32 illustrates how the corrected wave fields were slightly sensitive to the shape of the increments of fluid exchanged between the main channel and behind the slope. Compared to 0.51 m long sinusoidal increments, the use of 0.51 m long rectangular increments increased the difference between original and corrected maximum crest amplitudes by an average of 2%. The average increase in the difference between the original and corrected maximum trough amplitudes and potential energies were 7% and 6% respectively. The differences in the corrections using 0.51m and 1.02 m

long sinusoidal increments of water were very small, so this method of correction appeared to be less sensitive to increment length. However, as the increment tended to an infinite length the height of the increment would tend to zero and there would be zero correction.

As shallower submergences appeared to be more sensitive than the deeper submergence configurations to the correction process, comparisons between the SG5_IS5 and SG5_IS1 combinations are presented here to illustrate where, when, and how the correction affects the original wave fields. Figure 5.33 plots the original and corrected water surface profiles at t=0.80, 1.60, and 4.00 seconds for the SG5_IS1 combination. The position of the landslide centre of mass at these times is also shown. The correction was based on 0.51m long sinusoidal shaped increments of water. At t = 0.80 s, the slider had just reached the transition curve and the correction was not significant. By t = 1.60 s, the landslide had just passed through the transition curve, drawing a quantity of fluid into the main channel from behind the slope. To correct for this some fluid was removed from the main channel. This initial correction was apparent as the smaller leading crest amplitude and the increase in the amplitude of the leading trough. By t = 4.00 seconds, the slider was clear of the transition curve and the addition and removal of increments of water was complete. The exchange flow propagated slightly faster than the original waves, so the reinforcement of the leading trough was no longer apparent at t = 4.00 s. However, the leading crest amplitude was now more suppressed. In the corrected profile, the amplitude of the second crest was slightly amplified and the second trough was slightly suppressed. The correction tended to shift the location of the leading crest slightly downstream of the original crest position. The correction process did not affect the positioning of the other waves.

Figure 5.34 plots similar surface profiles at t=1.00, 2.00, and 4.00 seconds for the SG5_IS5 combination. At t = 1.00 s, the slider had not reached the transition curve so no correction was required. By t = 2.00 s, the landslide had just passed through the transition curve. The corresponding removal of fluid from the main channel was apparent as the slightly smaller leading crest amplitude and the significant increase in the amplitude of the leading trough. By t = 4.00 seconds, the slider was clear of the transition curve and the subsequent propagation and interaction of the exchange flows with the original wave field was similar to that for the SG5_IS1 case. In the corrected profile, the amplitude of the second trough was slightly suppressed and the third crest was increased slightly. Similarly to the SG5_IS1 case, the correction tended to shift the location of the leading crest slightly downstream of the original crest position, while the position of the other waves were not affected.

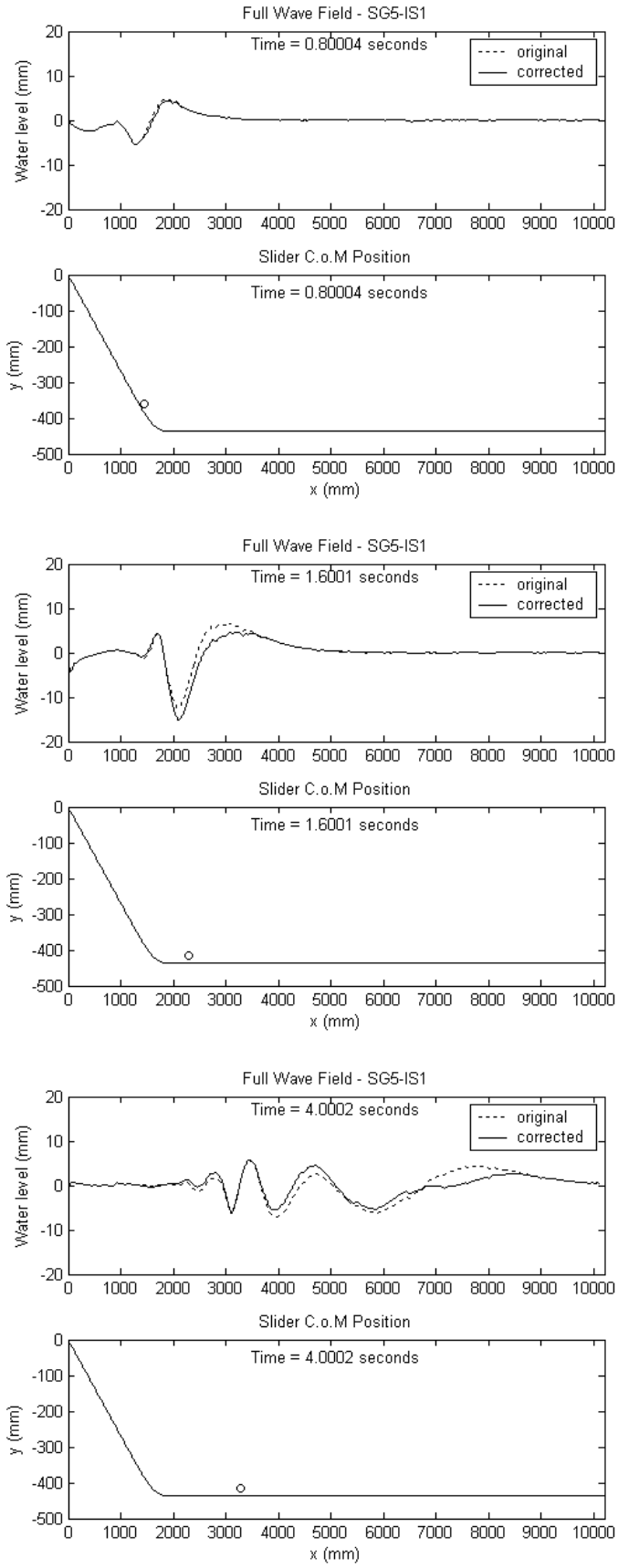

Figure 5.33. Original and corrected water surface profiles at t=0.80, 1.60, and 4.00 seconds for the SG5_IS1 combination. The correction is based on 0.51m long sinusoidal shaped increments of water.

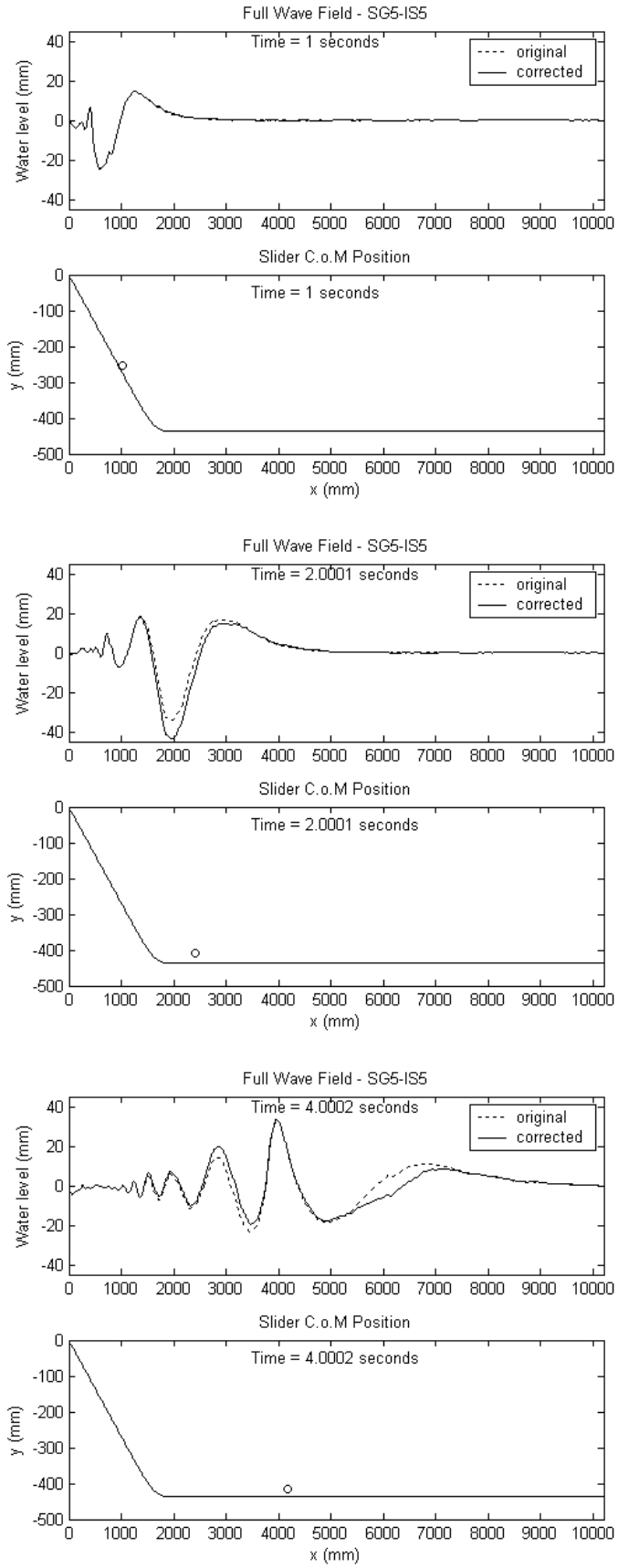

Figure 5.34. Original and corrected water surface profiles at t=1.00, 2.00, and 4.00 seconds for the SG5_IS5 combination. The correction is based on 0.51m long sinusoidal shaped increments of water.

Figure 5.35 shows the wave potential energy time history for the SG5_IS1 and SG5_IS5 combinations, both before and after the exchange flow correction. As shown by the water surface profile at t = 2.00 seconds for the SG5_IS1 case, in Figure 5.33, the increase in the leading trough amplitude was somewhat balanced by the decrease in the leading crest amplitude. The result was that the correction reduced the peak energy by approximately 5%. The time of maximum energy occurred slightly earlier. The water surface profile at t = 4.00 seconds, presented in Figure 5.33, shows how the increase in the second crest amplitude was offset by the decrease in the second trough amplitude upon the application of the correction. The first trough amplitude decreased slightly and the first crest amplitude decreased by 38%. This resulted in a substantial decrease in the corrected wave potential energy between $2.5 < t < 5.0$ compared to the uncorrected energy time history.

For the SG5_IS5 case, shown in Figure 5.34, the increase in the leading trough amplitude at t = 2.00 seconds was more substantial than the decrease in the leading crest amplitude, which resulted in an increase in the peak potential energy. The correction increased the peak energy by approximately 18%. The time of maximum energy remained unaffected. The water surface profile at t = 4.00 seconds, presented in Figure 5.34, shows how the correction increased the third crest amplitude and decreased the second trough amplitude by similar amounts. Compared to the SG5_IS1 case, the leading trough amplitude was not suppressed and there was only a 26% decrease in the first crest amplitude. Therefore, the decrease in the wave potential energy for the corrected case compared to the uncorrected case was not as significant as for the SG5_IS1 case between $3.8 < t < 5.4$ seconds.

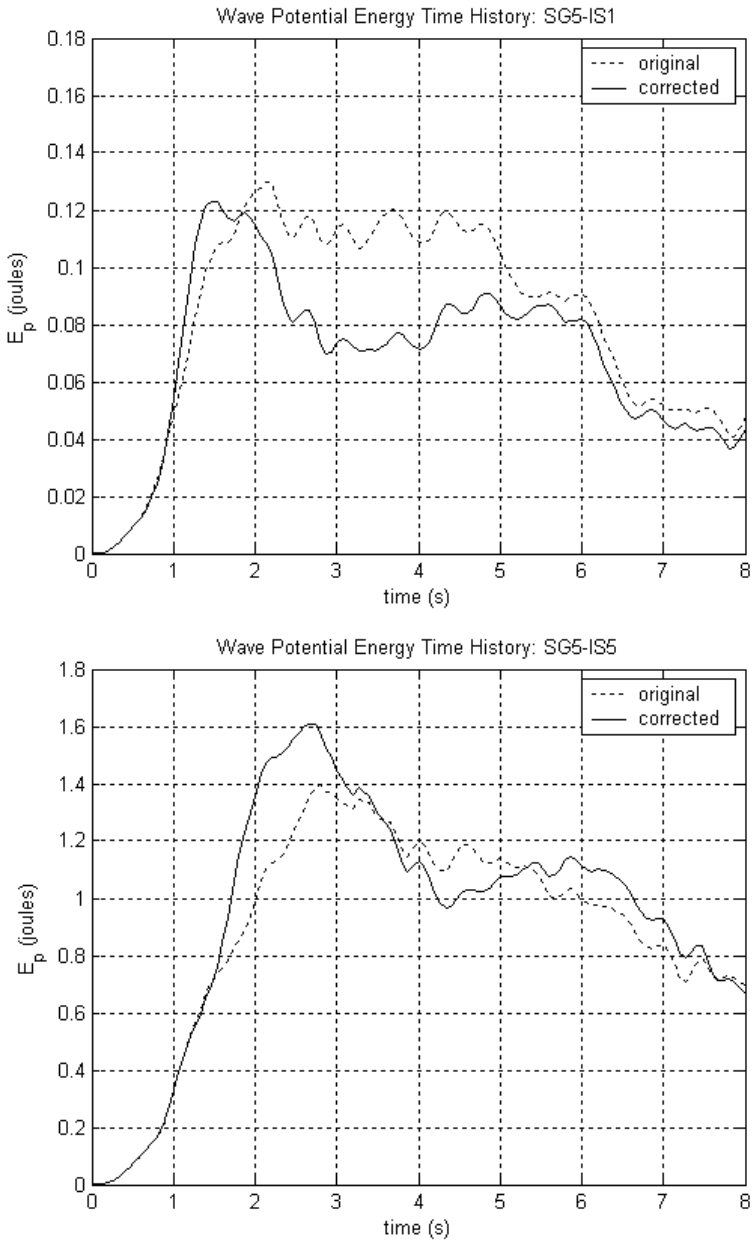

Figure 5.35. Original and corrected wave potential energy time history for the SG5_IS5 and SG5_IS1 combinations.

The smooth water surface profiles and clear trends in maximum crest amplitude, trough amplitude, and wave potential energy, for various initial submergences indicated that this method of correcting the wave field for the exchange of fluid between the main channel and behind the slope was plausible. However there was still uncertainty as to the proper form of the correction, as this proposed correction method was based on several assumptions. These assumptions included the propagation speed of the exchange flows being equivalent to the shallow water wave speed, the exchange flow being introduced between 1.297m < x < 1.807m, that all the increments of fluid propagated downstream only, and that the increments of fluid were 0.51 m long sinusoidal shapes. It was also assumed that the exchange flow could be corrected for by adding and removing discrete increments of fluid from the main

channel, and that the changes in water level behind the slope was a direct measure of the area of water that should be added or removed from the main channel.

Due to the ambiguity as to the actual form of the correction that should be applied, the data presented in this research were not corrected for the movement of fluid between the main channel and behind the slope. Instead this investigation into a possible correction provided an estimate of the possible errors in the data, and where these errors were most significant.

The correction appeared to only have a significant effect on the leading crest and trough. The correction tended to suppress the leading crest amplitude slightly and move the crest position further downstream. The largest crest amplitude increased slightly by between 2% and 12%, with the larger increases tending to occur for deeper submergences. The correction also tended to temporarily reinforce the leading trough amplitude. The maximum trough amplitude increased by between 22% and 28%, with the percentage increase relatively insensitive to the initial submergence. The changing wave amplitudes resulted in changes to the maximum wave potential energy that ranged between a 5% decrease and an 18% increase. The percentage increase tended to become larger for shallower submergences. The correction for the SG5_IS5 configuration resulted in a 28% increase in the maximum corrected trough amplitude and an 18% increase in maximum corrected wave potential energy. This configuration was considered to provide upper-bound correction values for the fifteen test configurations. The heavier mass and longer slide distance of the SG5_IS5 configuration produced the greatest movement between the main channel and behind the slope, and therefore required the largest corrections. Although the other 10 configurations, with lower specific gravities, were not investigated, their corrections were expected to be smaller than those for the equivalent SG5 cases.

5.4 Sub-surface Velocities

PTV was used to observe the flow structures and quantify the velocities in the fluid for underwater landslides. The velocity fields presented in Section 5.4.1 highlight the flow structures present in the SG5_IS1 and SG1_IS5 configurations. Fluid particle trajectories are presented and discussed in Section 5.4.2. The vertical velocity profiles below the waves are plotted in Section 5.4.3. Qualitative comparisons with linear theory are also made. Section 5.4.4 details the calculation of the fluid kinetic energy. The process of estimating the quantity of kinetic energy in the region downstream of the slope from the wave potential energy is presented.

5.4.1 Velocity Fields

Figure 5.36 is an image sequence of the sub-surface water particle velocity vector field for the SG5_IS1 test combination. The spatial coverage of this image sequence extended over the entire

water depth and from the shore to 3.0 m downstream, to encompass the slope, transition curve, and the majority of the run-out region. The direction of the vectors point in the flow direction, and the colour and the length of the vectors indicate the magnitude of the velocity. The lines in these figures are instantaneous streamlines and the dotted lines indicate the position of the slope surface. The first eight frames of the velocity field illustrate the motion of the water outward and upward ahead of the landslide. The high water pressure in front of the landslide pushed the water up towards the surface to form the 1st crest. The fluid was then forced up and over the landslide, where the increasing velocities created low pressures that drew down the water surface to form the 1st trough. The formation and increasing amplitude of the first trough further constricted the flow of water over the landslide.

As the landslide moved past, the remaining wake velocities adjacent to the slope surface and tank floor were in the direction of landslide motion downstream. For continuity of mass, the water in the upper region of the water column gently flowed upstream. As the landslide moved past the transition curve at t = 1.25 seconds, a large rotating eddy was left behind. This eddy remained stationary at the base of the slope. The velocities in the eddy were significantly larger than the velocities of the water motions below the waves that were trailing the leading crest and trough. Compared to the maximum landslide velocity of 0.974 m/s the maximum absolute water particle velocity measured over the top surface of the accelerating landslide as it passed through the transition curve was only 21% of this.

The image sequence of the sub-surface water particle velocity vector field for the SG1_IS5 combination is shown in Figure 5.37. The outward and upward flow ahead of the landslide and the accelerating flow up and over the landslide is clearly visible throughout the image sequence. The shallow initial submergence further constricted the flow over the top of the landslide compared to the SG5_IS1 combination. Residual downstream motions were also left in the wake of the landslide. The gentle upstream mass continuity flow and the rotating eddy at the base of the slope, after the passing of the landslide and first trough, observed in the SG5_IS1 experiment was not as obvious in this image sequence. This was due to the wave fields being dominated by the motions associated with the trailing wave train and not by the wake motions. Compared to the maximum landslide velocity of 0.956 m/s, the maximum fluid velocity measured in the very constricted flow between the landslide and the depressed water surface at the top of the slope was 30% of this. The maximum landslide velocity occurred at approximately t = 1.8 seconds when the landslide reached the base of the slope, whereas the maximum water particle velocity occurred earlier at approximately 1.0 seconds.

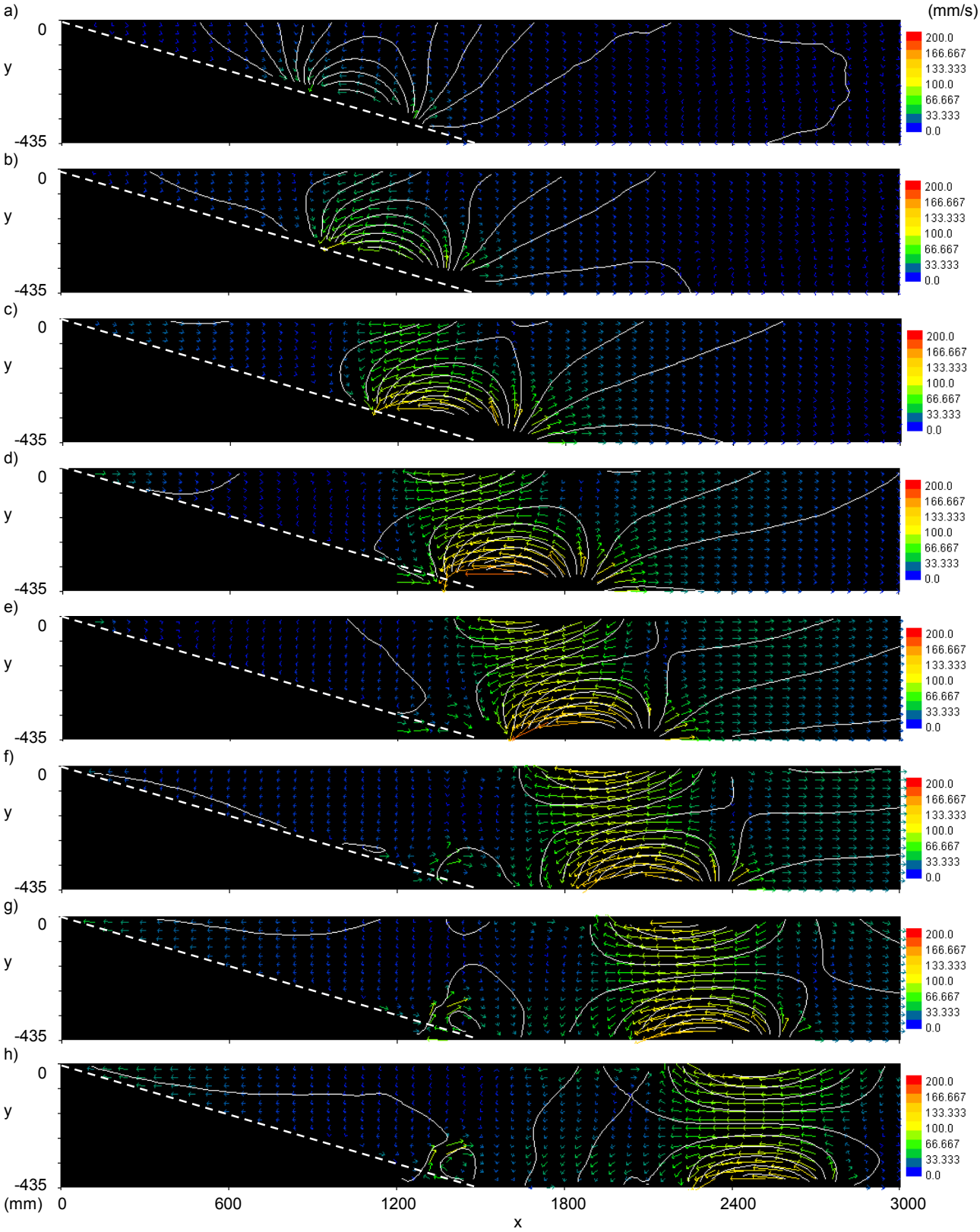

Figure 5.36. Velocity vector field for the SG5_IS1 combination at a) t=0.25 s, b) t=0.50 s, c) t=0.75 s, d) t=1.00 s, e) t=1.25 s, f) t=1.50 s, g) t=1.75 s, h) t=2.00 s. Streamlines have been superimposed onto the images. The position of the slope is indicated by the dotted line.

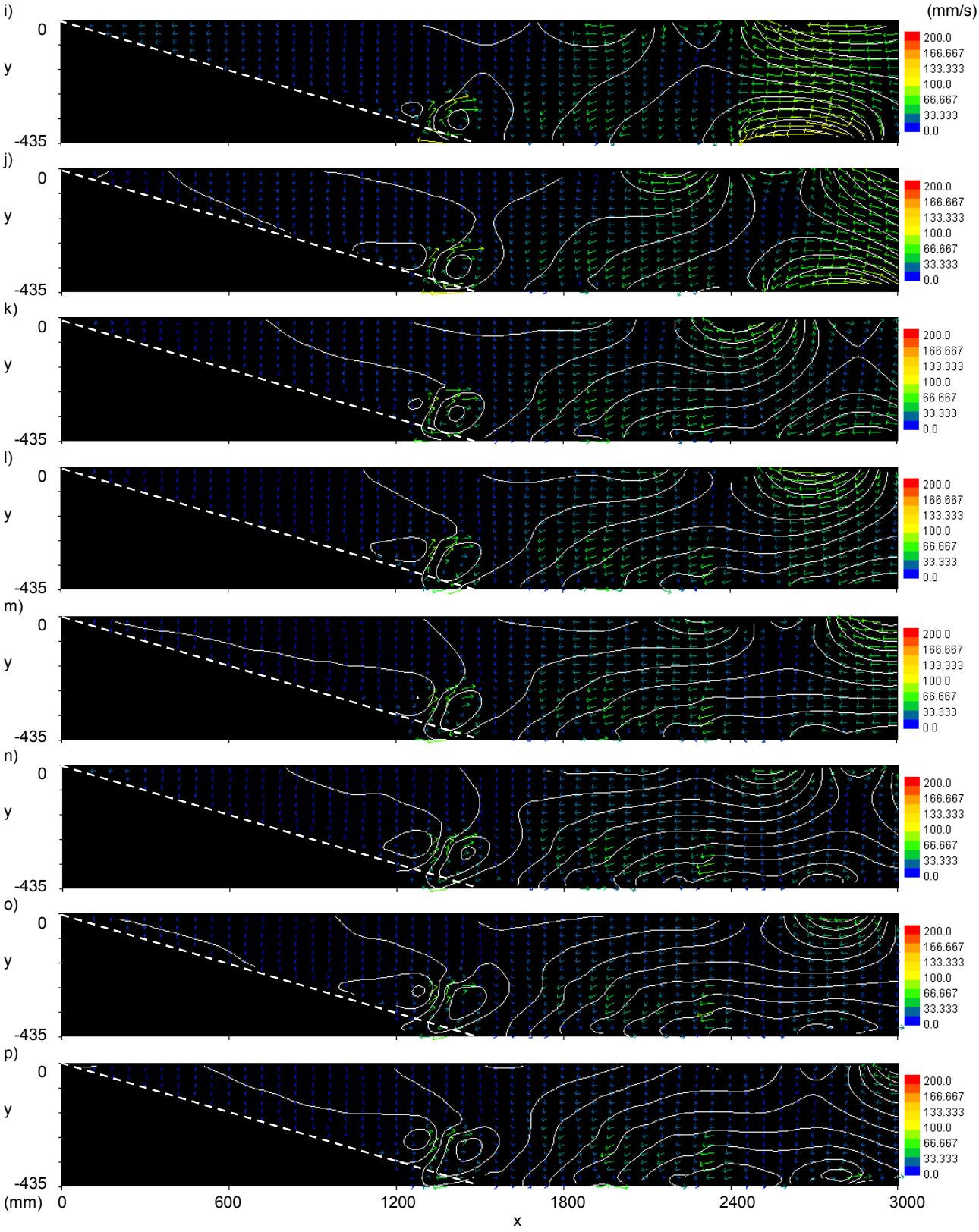

Figure 5.36 continued. Velocity vector field for the SG5_IS1 combination at i) t=2.25 s, j) t=2.50 s, k) t=2.75 s, l) t=3.00 s, m) t=3.25 s, n) t=3.50 s, o) t=3.75 s, p) t=4.00 s. Streamlines have been superimposed onto the images. The position of the slope is indicated by the dotted line.

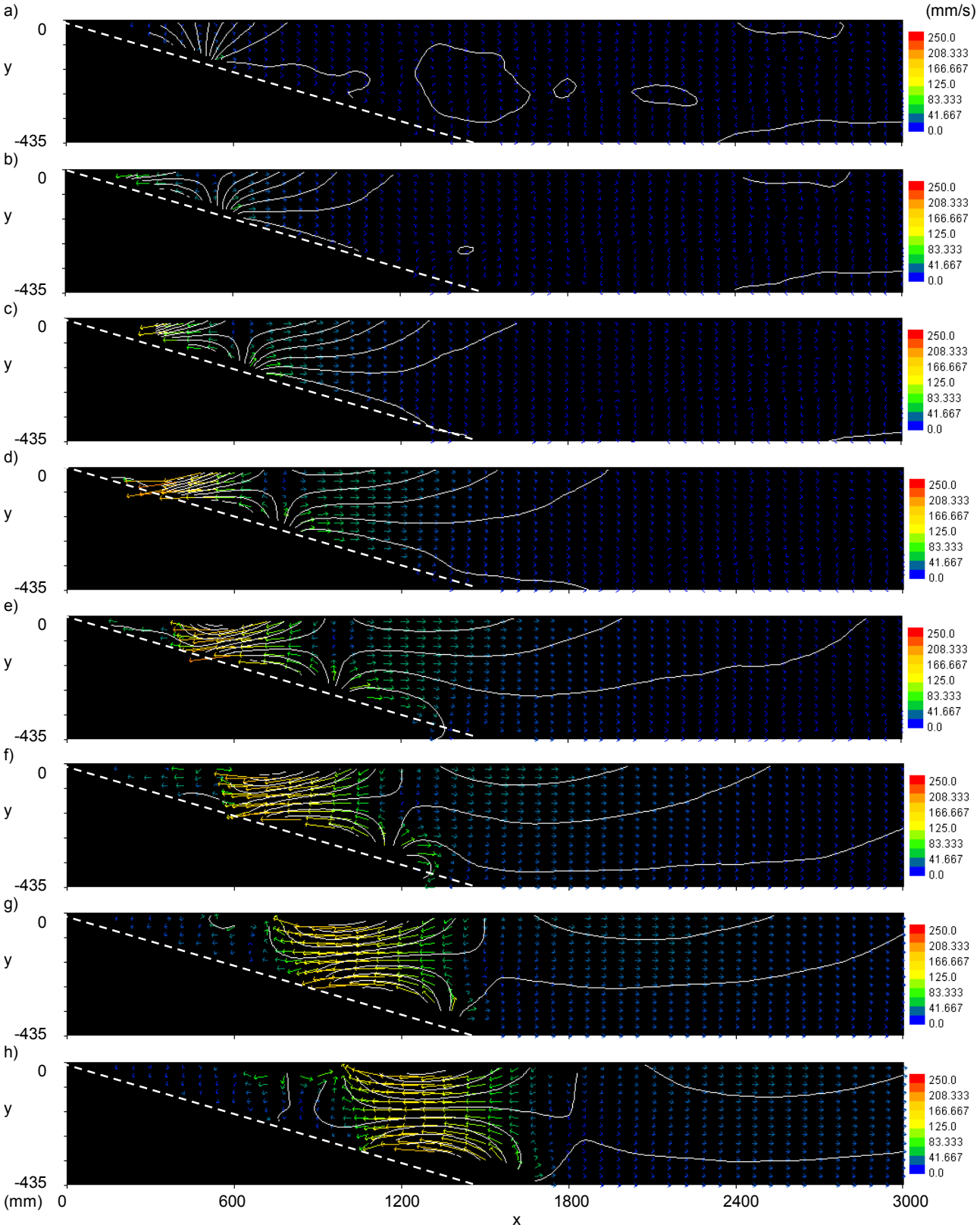

Figure 5.37. Velocity vector field for the SG1_IS5 combination at a) t=0.25 s, b) t=0.50 s, c) t=0.75 s, d) t=1.00 s, e) t=1.25 s, f) t=1.50 s, g) t=1.75 s, h) t=2.00 s. Streamlines have been superimposed onto the images. The position of the slope is indicated by the dotted line.

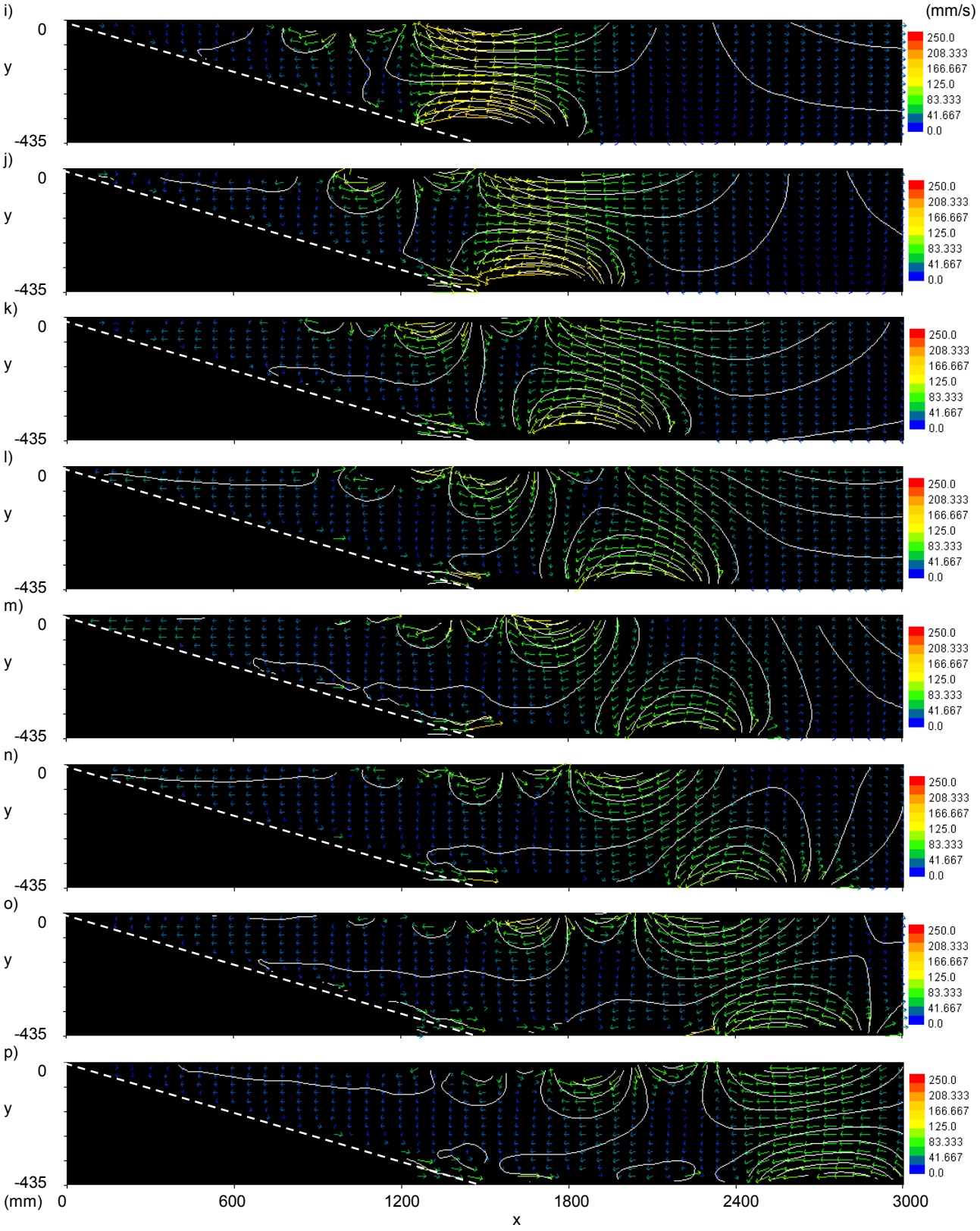

Figure 5.37 continued. Velocity vector field for the SG1_IS5 combination at i) t=2.25 s, j) t=2.50 s, k) t=2.75 s, l) t=3.00 s, m) t=3.25 s, n) t=3.50 s, o) t=3.75 s, p) t=4.00 s. Streamlines have been superimposed onto the images. The position of the slope is indicated by the dotted line.

Of interest in both of the velocity field image sequences were the significant velocities at the base of the slope, at approximately x = 1300 mm, after the passage of the landslide. The low pressure under the landslide generated these velocities as it passed through the transition curve, drawing water from behind the slope. As explained in Section 4.1.2, this opening was used to reduce the aquaplaning of the landslide as it passed through the transition curve. As the landslide moved off the transition curve onto the tank floor, the water trapped under the landslide was able to escape back through the opening into the region behind the slope. The significance of the exchange of water between the main channel and behind the slope is discussed in Section 5.3.6.

5.4.2 Particle Trajectories

Figure 4.22 plots time histories of water level and horizontal and vertical velocities, measured at $x/L_b = 4.8$, for test combination SG5_IS1. It shows that the horizontal velocities of the wave train, apart from the leading crest, were in phase with the free surface movements, and the phase of the vertical velocities was trailing by 90°. Figure 5.38 plots the trajectory of a particle in the SG5_IS1 test, with an initial starting position far downstream of the slope, at $x/L_b = 11.863$ and $y/D = -0.345$. The trajectory covered the time span from $0 \leq t/\sqrt{(g/L_b)} \leq 35.43$. The first wave to arrive at this location was a crest, which caused the particle to move up and downstream. As shown in Figure 5.39, the following trough had a similar amplitude so the particle continued clockwise until it returned to near its starting position. The following crest and trough pair had different amplitudes, so the particle orbit was not circular. The pig tail-shaped trajectory was due to the second trough amplitude being significantly larger than the second crest. The subsequent crests and troughs had similar amplitudes, leading to essentially closed elliptical particle paths.

The general shape of the water particle trajectories at other downstream locations, away from the region directly influenced by the landslide motions, was expected to be similar. However, wave evolution through dispersion would slowly change the wavelength and amplitude of the waves within the train, thereby subtly affecting the size and shape of the orbital motions. Larger amplitudes would increase the diameter of the circular orbits. The wavelength to water depth ratio of the leading waves was greater than the trailing waves. As such the particle orbits of the leading waves would become flatter for particles at greater depth. This is illustrated in Figure 4.21, in which the particle orbits were elliptical near the free surface, and tended to horizontal to-and-fro motions near the bed. For the trailing waves, with smaller wavelength to depth ratios, the particle trajectories were expected to remain circular. However, the diameter of the circular motions would decrease with depth.

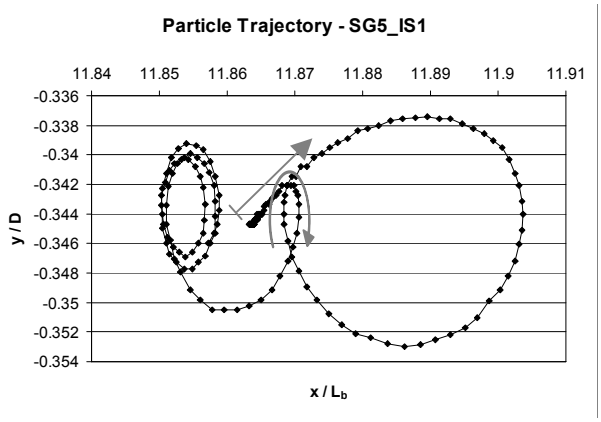

Figure 5.38. Trajectory of a particle in the SG5_IS1 test, with an initial starting position of x/Lb = 11.863 and y/D = -0.345. The trajectory covers the time span from $0 \leq t/\sqrt{(g/L_b)} \leq 35.43$.

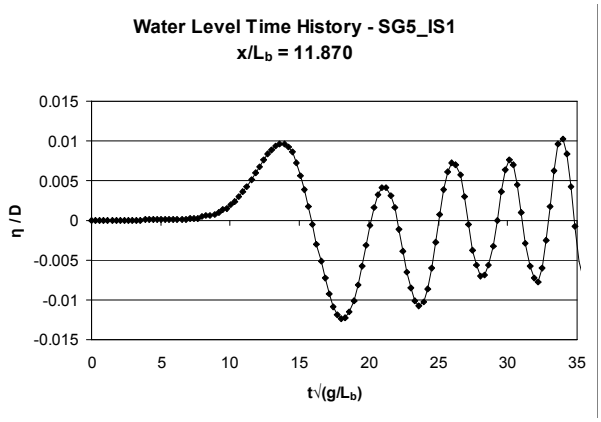

Figure 5.39. Water level time history at $x/L_b = 11.87$ showing the variation in wave amplitudes.

5.4.3 Vertical Velocity Profile

The water level time histories at $x/L_b = 6.0$, downstream of the region covered by the slope, from the SG5_IS1 and SG1-IS5 tests were extracted and the times at which wave crests and troughs passed these points were recorded. The sub-surface horizontal water velocity distributions below the crests and troughs were extracted from the PTV velocity data at $x/L_b = 6.0$ at these times. The water velocities below crests and troughs were used for the sake of convenience, as below these waveforms the theoretical vertical velocities tended to zero for a sinusoidal wave. The formulation for calculating the horizontal velocity distribution below a crest or trough as a function of depth, y, is shown in Equation 5.20 (United States Army Corps of Engineers 2002). The theoretical velocity distributions were calculated using classical linear wave theory for a sinusoidal wave train. The waves generated in the present research were weakly non-linear and not purely sinusoidal, so the calculated velocity profiles should be seen as an approximation and not a theoretical prediction of the experimental sub-surface velocities.

$$u_i(y) = \frac{\eta_i g T_i}{\lambda_i} \frac{\cosh[2\pi(y+D)/\lambda_i]}{\cosh(2\pi D/\lambda_i)} \cos\theta \quad \textbf{(5.20)}$$

The subscript *i* refers to the *i*th wave, g is the acceleration of gravity, T_i and λ_i are the period and wavelength if the *i*th wave respectively, y is the vertical spatial coordinate, D is the constant water depth, and θ is the wave phase angle. The parameter η is the water level measured positive above the still water level. The vertical coordinate, y, is a variable from 0 mm at the free surface to –435mm at the bottom of the tank.

For each wave crest or trough, estimates of its period, T_i, and wavelength, λ_i, were made. As the wave train was far from periodic, values for each individual wave was estimated separately. To calculate wavelength, the distance between adjacent maxima (or minima) in the water level profiles were determined at the time at which the crest (or trough) passed by. For example, for a crest passing $x/L_b = 6.0$, the wavelength was the distance between the trough downstream and the trough upstream of the crest. For instances in which there was no waveform upstream and downstream, then the wavelength was estimated by multiplying the distance between the waveform and the one adjacent by a factor of two. For example, this occurred for the leading crest for which there is no trough upstream, so its wavelength was calculated as twice the distance between the crest and the following trough.

The periods of the waves were also determined in a similar way. For example, the wave period of a crest passing $x/L_b = 6.0$ was the time between the preceding and the following trough to pass $x/L_b = 6.0$. For crests or troughs at the beginning or end of the water level time history, periods were estimated by multiplying the half-periods by two.

As a means of ensuring the wavelengths and periods were of appropriate magnitude the wave phase speeds, C_p, were calculated using Equations 5.21 and 5.22 and compared. Velocity estimates from the two formulations were typically within 10% of each other.

$$C_p = \frac{\lambda_i}{T_i} \quad \textbf{(5.21)}$$

$$C_p = \sqrt{\frac{g\lambda_i}{2\pi} \tanh\left(\frac{2\pi D}{\lambda_i}\right)} \quad \textbf{(5.22)}$$

The vertical profile of the horizontal velocity, below wave crests and troughs passing $x/L_b = 6.0$, is show in Figure 5.40 for the SG5_IS1 combination, and Figure 5.41 for the SG1_IS5 combination. Velocity profiles measured during the experiments and derived from linear theory are plotted. It should be noted that the times at which the measured and theoretical velocity distributions are plotted may not be exactly the same due to differing frame rates, the theoretical distributions are within $1/15^{th}$ of a second (15Hz Pulnix camera was used to measure the wave heights, lengths, and periods) and the PTV-derived velocities are within $1/24^{th}$ of a second (24Hz Jai camera). The maximum difference in time between when the measured and calculated distributions occur was 0.017 s ($1/60^{th}$ of a second). A comparison between experimental results and numerical model predictions is presented in Chapter 7.

Generally, linear theory provided a reasonable approximation to the measured horizontal velocity distributions. However there were times and regions in the flows that the linear sinusoidal wave train assumption was inadequate. For the SG5_IS1 case, the distribution below the leading crest was measured to be close to uniform. Theory overestimated the velocities in the upper half of the water column. The first trough and second crest and trough profiles were also dissimilar. These mismatches were due to the inability of the linear theory to incorporate the complex flows surrounding the landslide as it passed $x/L_b = 6.0$. The strong velocities in the x-direction just above the tank floor, highlighted in Section 5.4.1, were clearly visible in the measured velocity profiles. These were due to the wake motions following the passage of the landslide. This volume flux was balanced by the gentle velocities, in the onshore direction, in the remainder of the water column. This was particularly clear in the velocity distributions below the third, fourth, and fifth crests and troughs.

For the SG1_IS5 case, the leading crest and trough were well predicted by linear theory. The second and third crests and troughs were influenced by the flow over the landslide, so theory did not predict the horizontal velocity distributions well. The velocity distributions away from the tank floor for subsequent wave crests and troughs were predicted well by linear theory. However, the slow upstream drift that was also present in this test configuration degraded the match between velocity magnitudes. The high velocities in the positive x-direction following the landslide were also visible in the measured velocity profiles at bed level.

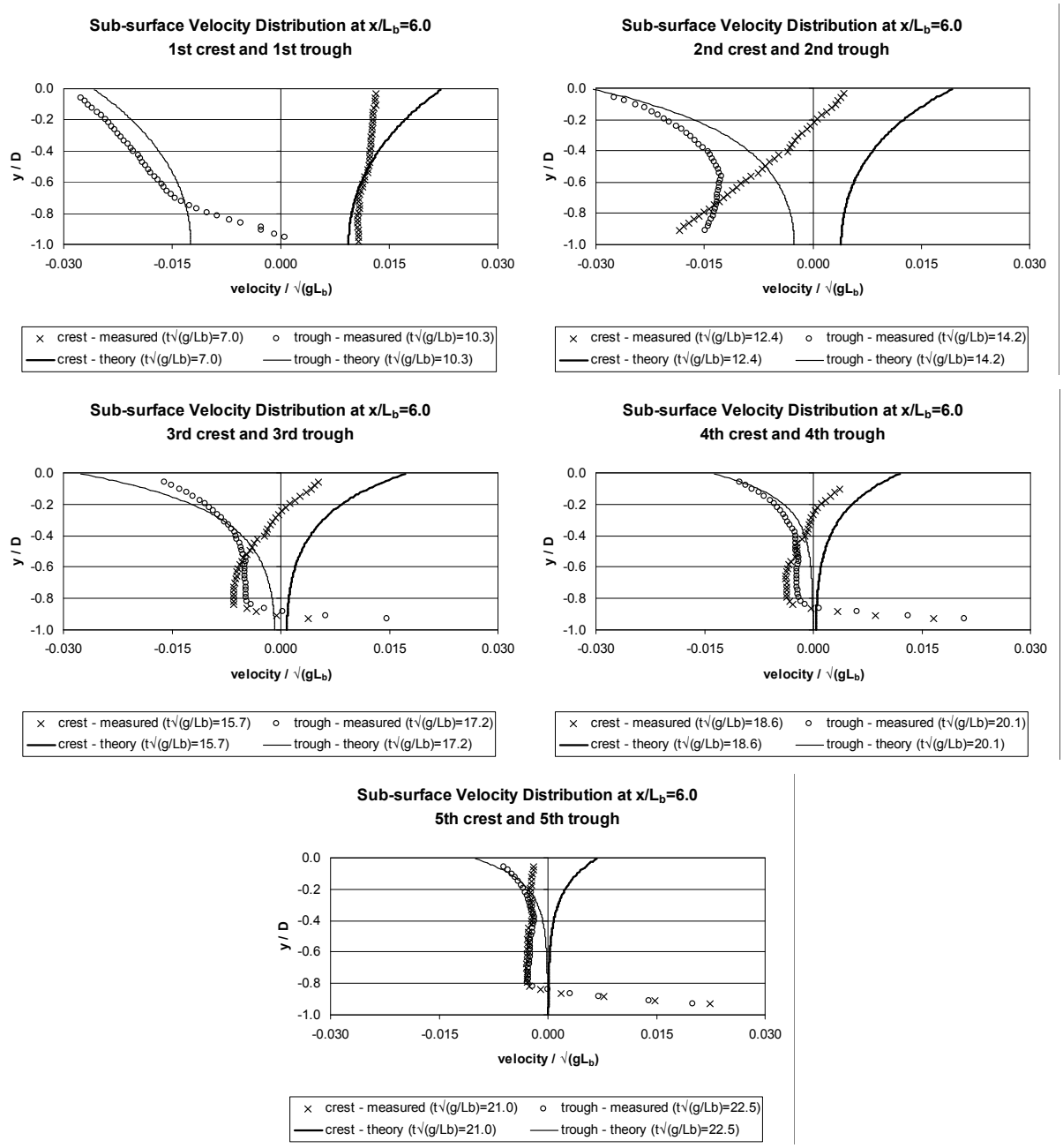

Figure 5.40. Sub-surface horizontal velocity profiles below wave crests and troughs for the SG5_IS1 test combination at x/L_b=6.0.

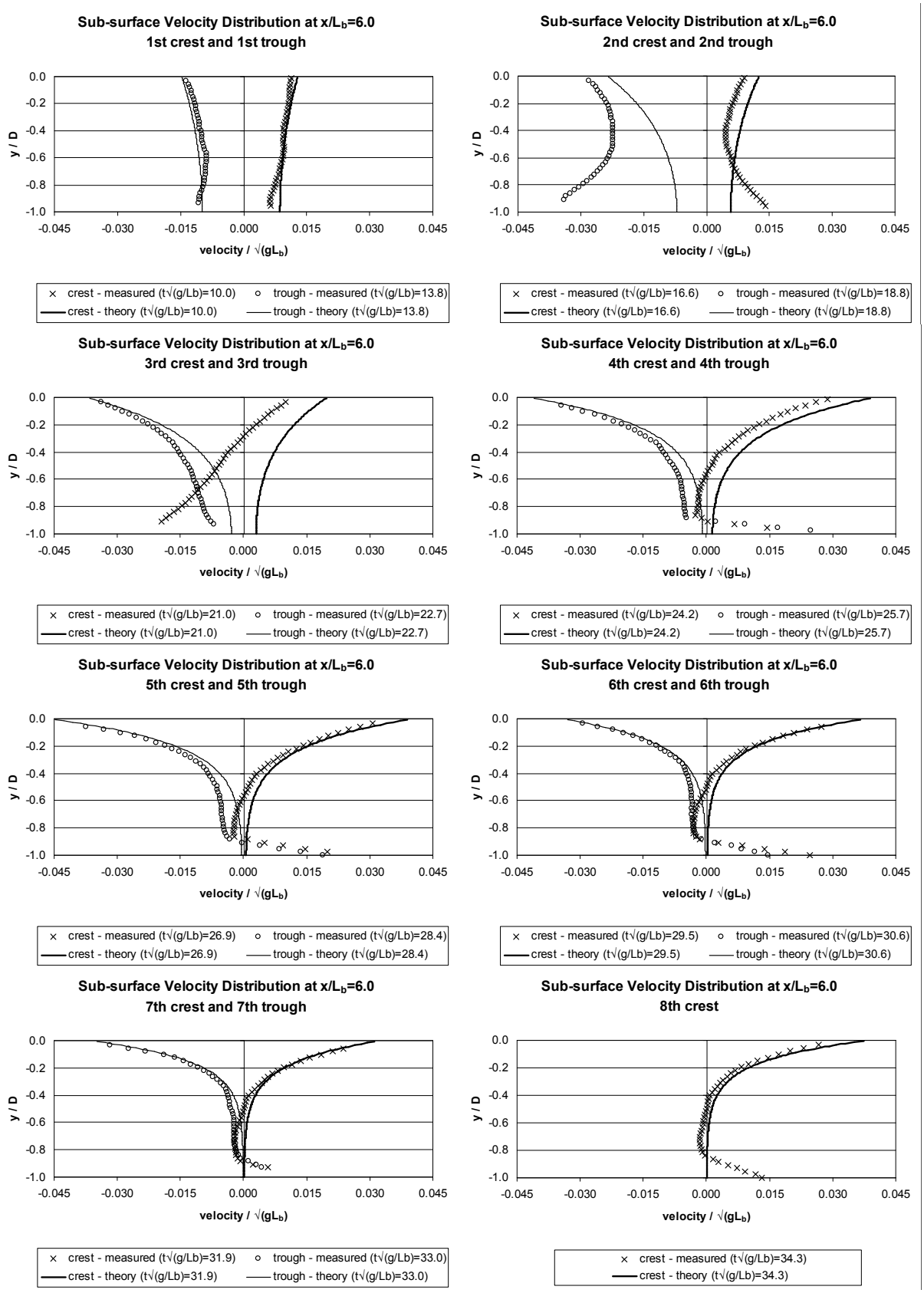

Figure 5.41. Sub-surface horizontal velocity profiles below wave crests and troughs for the SG1_IS5 test combination at x/L_b=6.0.

5.4.4 Energy

As well as the ability to observe the sub-surface fluid flow, the measured velocity field provided a means to calculate the kinetic energy of the fluid motions. The fluid kinetic energy time history could then by compared to the time histories of the wave potential energy and the landslide kinetic and potential energies, to confirm the energy transfer mechanisms between the landslide and the wave field. The instantaneous depth-averaged kinetic energy of the water at any x-location was calculated as

$$\text{depth-averaged water } E_k(x,t) = \rho_o w \cdot d(x) \cdot \overline{\frac{1}{2}\left[u^2(x,t) + v^2(x,t)\right]} \qquad \textbf{(5.23)}$$

where ρ_o = water density

w = flume/landslide width

$d(x)$ = local water depth

$u(x,t), v(x,t)$ = instantaneous horizontal and vertical fluid velocity

$\overline{\frac{1}{2}\left[u^2(x,t) + v^2(x,t)\right]}$ = depth-averaged fluid velocity term

Figure 5.42 plots the depth-averaged water kinetic energy, normalised by the maximum kinetic energy, versus non-dimensional downstream position (x/L_b) and time ($t(g/L_b)^{0.5}$) for the SG5_IS1 combination. The position of high fluid kinetic energy corresponded to the position time history of the rear end of the landslide as it accelerated down the slope. The motion of the fluid as it was accelerated over the landslide and flow separation was the primary source of its kinetic energy. Also obvious in this plot is the presence of significant fluid kinetic energy at the shore at $4 < t(g/L_b)^{0.5} < 10$, caused by the large wave run-up. The steady rotating eddy present near the base of the slope, and shown in the PTV velocity field images in Figure 5.36, shows up clearly as a near-vertical light-coloured stipe at $x/L_b = 2.7$ in Figure 5.42. The additional near-vertical stripes correspond to other stationary eddies, left behind by the slider. The light-coloured diagonal stripes above and below the region of highest kinetic energy indicate the motions associated with the particle motions below the waves.

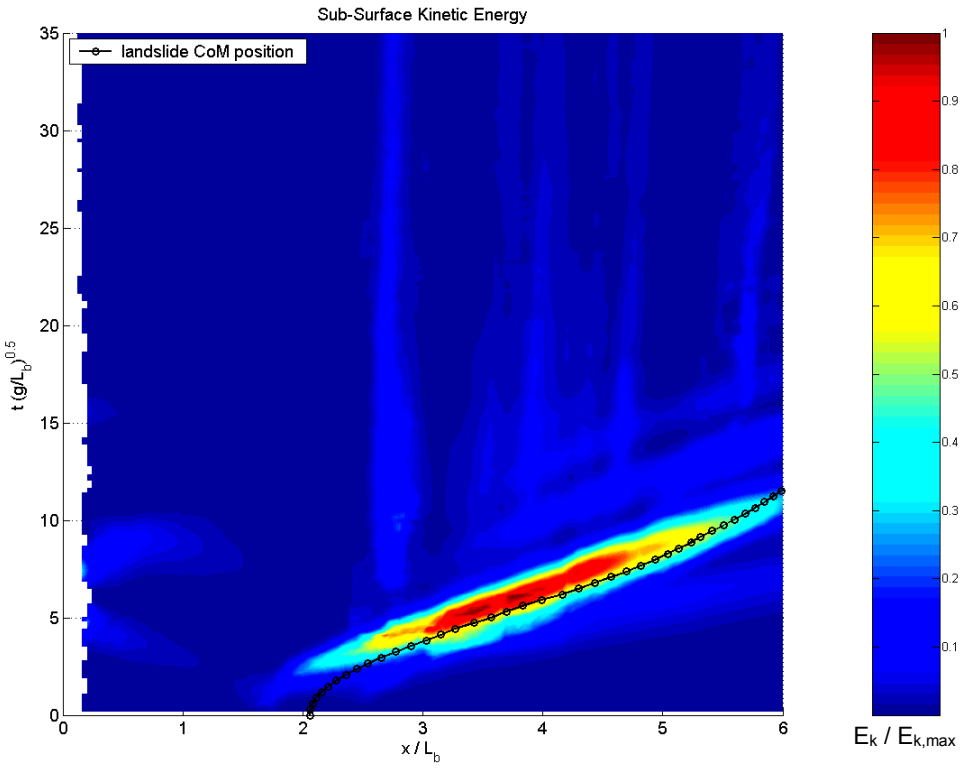

Figure 5.42. Depth-averaged water kinetic energy, normalised by the maximum kinetic energy, versus non-dimensional downstream position (x/L_b) and time ($t(g/L_b)^{0.5}$) for the SG5_IS1 combination. The position of the landslide centre of mass is also plotted.

For the SG5_IS1 case, shown in Figure 5.43, the region of high kinetic energy also followed the rear end of the landslide. When the landslide reached the bottom of the slope and slowed, near $x/L_b = 3.0$, the region of high kinetic energy slowly overtook the rear of the landslide to coincide with the landslide centre off mass, and the energy began to reduce. The kinetic energy associated with downstream propagating wave motions was also present. However, the relative magnitude of the motions surrounding the landslide and the wave motions was significantly larger than the motions of the upstream propagating waves, so the energy associated with the wave run-up was not as apparent. The stationary eddies present in Figure 5.42 are not as apparent in the SG1_IS5 results.

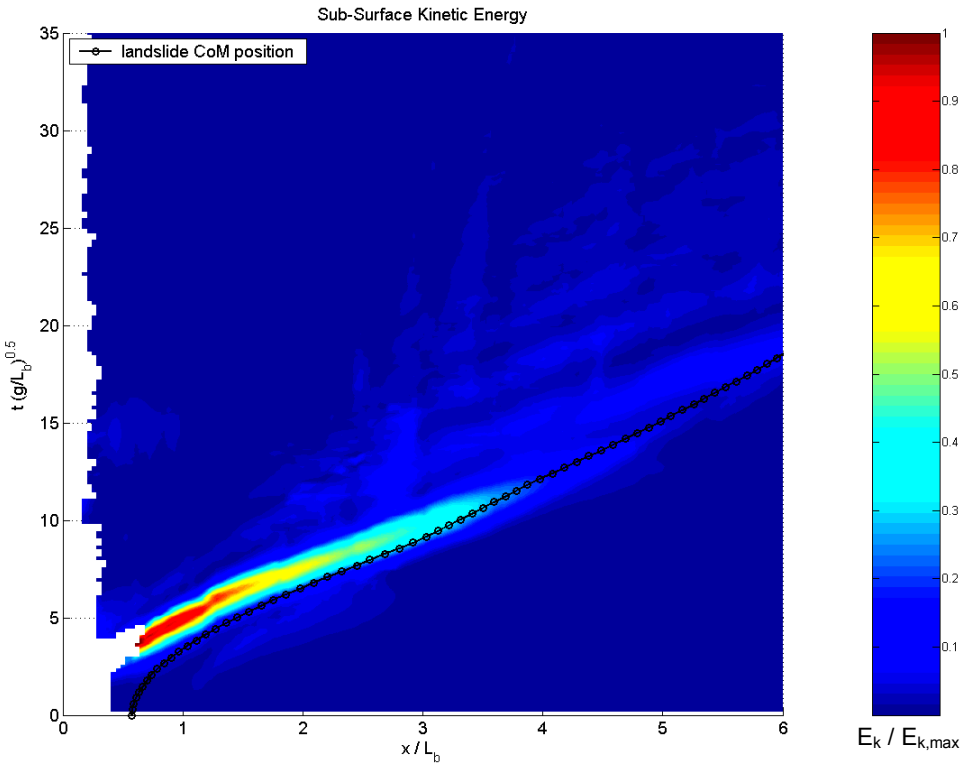

Figure 5.43. Depth-averaged water kinetic energy, normalised by the maximum kinetic energy, versus non-dimensional downstream position (x/L_b) and time ($t(g/L_b)^{0.5}$) for the SG1_IS5 combination. The position of the landslide centre of mass is also plotted.

The sub-surface velocity field for the SG5_IS1 and SG1_IS5 cases were measured continuously from x/L_b = 0.0 to 6.0. This region covered the area affected by the flows over and around the landslide, and allowed the wave potential and kinetic energy to be calculated directly in the inshore region. However, this short spatial extent meant wave energy propagated past x/L_b = 6.0 very quickly. However, measuring the sub-surface velocities out to x/L_b = 20.0, the distance to which the water surface profiles were measured, would have taken a prohibitive amount of time. To calculate the total fluid energy (potential and kinetic) offshore, the kinetic energy of the fluid was estimated from the wave potential energy using standard equipartitioning theory.

Equipartitioning is the concept that the energy content of the fluid is equally divided between potential energy and kinetic energy. This applies for linear sinusoidal waves, and can be demonstrated to also apply for solitary waves. It was found that most of the waves generated in the present research were linear, with the exception of some weakly non-linear leading waves. According to Fritz (2002), for non-linear waves, the kinetic energy tends to dominate the potential energy as the wave steepness increases, to reach a maximum kinetic to potential energy ratio of 1.22 at the wave breaking limit. The weakly non-linear waves were far from the breaking limit.

The fluid kinetic energy was measured at specific downstream positions, offshore from the slope region. The wave potential energy was calculated at the same downstream positions. The partitioning between the kinetic energy and the potential energy of the waves at these positions was then assumed to apply along the length of the channel downstream of $x/L_b = 6.0$. The level of fluid kinetic energy downstream of $x/L_b = 6.0$ was calculated directly from the wave potential energy propagating between $x/L_b = 6.0$ and 20.0.

The level of partitioning of fluid energy between potential and kinetic energy in the waves passing $x/L_b = 6.0$, 8.0, 10.0, 12.0, 14.0, and 16.0 was calculated from the water level and PTV data. Far from the landslide region, the sub-surface motions were assumed to be entirely associated with the wave field, and not with the flow of water over and around the landslide. Close to the generation region, the kinetic energy was expected to be higher than the potential energy due to the accelerated flow over the landslide and the turbulent wake motions. Measuring the kinetic energy in the entire inshore region captured all this energy.

The potential energy passing a particular location was calculated using Equation 5.24. This equation is similar to Equation 5.16 apart from the removal of the spatial integration. This can be thought of as the energy passing a particular point, and is similar to the methods of Weigel (1955) and Watts (1997) to estimate the wave potential energy from point wave gauge records. The kinetic energy was calculated in a similar way, with the horizontal and vertical velocities passing the point of interest used in Equation 5.23 to estimate the kinetic energy.

$$\text{wave } E_p(x,t) = \frac{1}{2}\rho_o g w \eta(x,t)^2 \qquad \textbf{(5.24)}$$

The velocity fields did not always cover the entire water depth at the various downstream positions of interest. This was due to missing PTV matches, most likely due to poor lighting or the absence of particles. To overcome this the velocity fields were carefully extrapolated to provide coverage over the entire water depth to fill in the missing regions. Re-calculating the kinetic energy with full velocity field coverage, it was found that the missing velocities had no significant impact on the kinetic energy estimates.

To confirm the repeatability of the energy calculations, four repeated runs for the SG1_IS5 combination were completed and the energy passing $x/L_b = 14.0$ was calculated for each. Table 5.4 details the ratio of water kinetic energy to potential energy for the SG1_IS5 combination at $x/L_b = 14$. In all four repeats, the velocity fields were extrapolated to cover the entire flow depth. The water potential and kinetic energy time histories passing $x/L_b = 14.0$ were time integrated over a wave

period. The ratio of kinetic energy to potential energy of the first trough, calculated through a time integration between when the first crest and second crest passed x/L_b = 14.0, was found to be approximately 0.70 for all four repeats. This ratio increased to an average of 0.81 for the third wave crest. The repeatability shown by this provided confidence in the energy calculations.

Table 5.4. Ratio of water kinetic energy to potential energy for the SG1_IS5 combination at x/L_b = 14. Both energies have been time integrated over a wave period.

	Repeat 1	Repeat 2	Repeat 3	Repeat 4	Mean
1st trough	0.70	0.69	0.72	0.71	0.70
2nd crest	0.70	0.69	0.66	0.69	0.68
2nd trough	0.81	0.76	0.74	0.78	0.77
3rd crest	0.90	0.78	0.78	0.78	0.81

Figure 5.44 summarises the ratio of kinetic energy to potential energy for the SG5_IS1 and SG1_IS5 combinations. The two energies were calculated for each wave as a time integral over its wave period passing x/L_b = 6.0, 8.0, 10.0, 12.0, 14.0, and 16.0. The mean energy ratios at each downstream position illustrated the trends in the energy ratios as a function of downstream position. Close to the generation and landslide run-out region, at x/L_b = 6.0, the kinetic energies were considerably higher than the potential energies. This was due to the additional kinetic energy associated with the flow of water around the landslide and the residual wake motions as it ran out past x/L_b = 6.0. For the SG5_IS1 case, the energy ratio dropped to below 1.0 to reach a minimum at x/L_b = 12.0 before increasing to 1.12 at x/L_b = 16.0. The mean energy for the SG1_IS5 case tended to drop and oscillate weakly downstream of x/L_b = 6.0. This suggested that there was not a steady equal partitioning between kinetic and potential energy. Instead there seemed to be some energy transfer between the two energies as time progresses and as the waves propagated.

For the SG5_IS1 case, the mean kinetic to potential energy ratio of all waves downstream of x/L_b = 6.0 was approximately 0.97 and approximately 0.82 for the SG1_IS5 combination. Linear and weakly non-linear waves, of which the generated waves were, should theoretically exhibit equipartitioning of wave potential and kinetic energy. These results suggested this might not be the case, especially early on in the wave generation and propagation process. Therefore both full equipartitioning and 80% partitioning were used to provide an upper and lower estimate of the ratio of fluid kinetic energy to fluid potential energy.

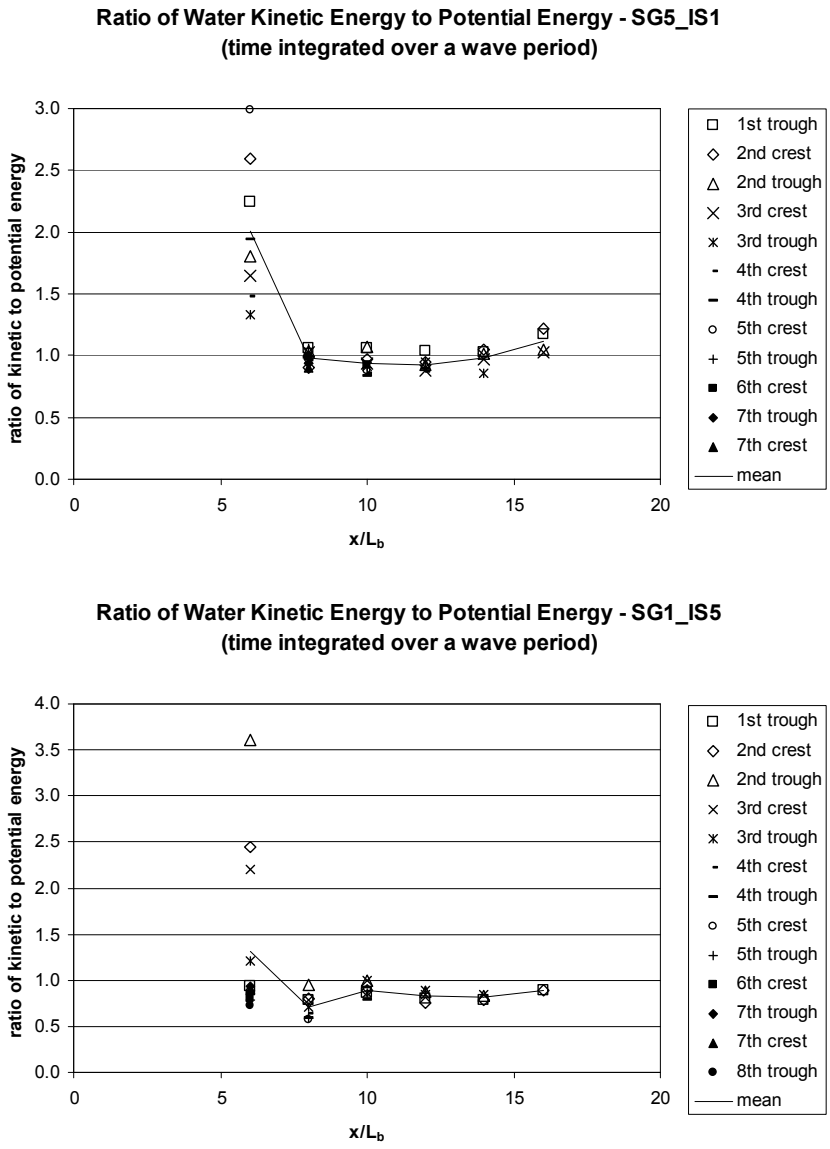

Figure 5.44. Plots of the ratio of water kinetic energy to potential energy for the SG5_IS1 and SG1_IS5 combinations at various downstream positions for different waves. Both energies have been time integrated over a wave period.

With the entire sub-surface velocity field time-history measured in the inshore region, between x/L_b = 0.0 and 6.0, the kinetic energy contained within this region was calculated as an area-averaged energy time history using Equation 5.25. Outside of this region the PTV record was discontinuous, and the kinetic energy required estimation using the wave potential energy. Based on either of two assumptions, the first being that there was equipartioning between water kinetic and potential energy, and the second being that the kinetic energy was 80% of the potential energy, an upper and lower estimate of the fluid kinetic energy was determined.

$$\text{area-averaged wave } E_k(t) = \rho_o w \cdot area \cdot \overline{\overline{\frac{1}{2}\left[u^2(t) + v^2(t)\right]}} \quad \textbf{(5.25)}$$

where $area$ = area of water viewed in the PTV experiments

$\overline{\overline{\frac{1}{2}\left[u^2(t) + v^2(t)\right]}}$ = area-averaged fluid velocity term

The upper kinetic energy estimate was determined by summing together the kinetic energy time history for $0 < x/L_b < 6.0$ and the potential energy time history for $6.0 < x/L_b < 20.0$. The lower kinetic energy estimate was determined by combining the kinetic energy time history for $0 < x/L_b < 6.0$ and 80% of the potential energy time history for $6.0 < x/L_b < 20.0$. Time histories of the water potential and kinetic energy for $0 < x/L_b < 6.0$, $6.0 < x/L_b < 20.0$, and $0.0 < x/L_b < 20.0$ are shown in Figure 5.45 for the SG5_IS1 and SG1_IS5 combinations.

The difference in maximum water kinetic energy between the upper estimate, using full equipartitioning, and the lower estimate, using only 80% of the potential energy, was only 2.2% and 0.8% for the SH5_IS1 and SG1_IS5 tests respectively. The difference in the overall shape of the time histories was small as well. For full equipartitioning the peak fluid kinetic energy occurred at $t/\sqrt{(g/L_b)} = 7.38$, compared to $t/\sqrt{(g/L_b)} = 6.64$ for 80% partitioning, for the SG5_IS1 case. The significance of this difference was further reduced by the fact that the kinetic energy peak occurred at an energy plateau between $t/\sqrt{(g/L_b)} = 5.5$ and 8.0. For the SG1_IS5 case, there was no change to the time of maximum kinetic energy, occurring at $t/\sqrt{(g/L_b)} = 9.60$.

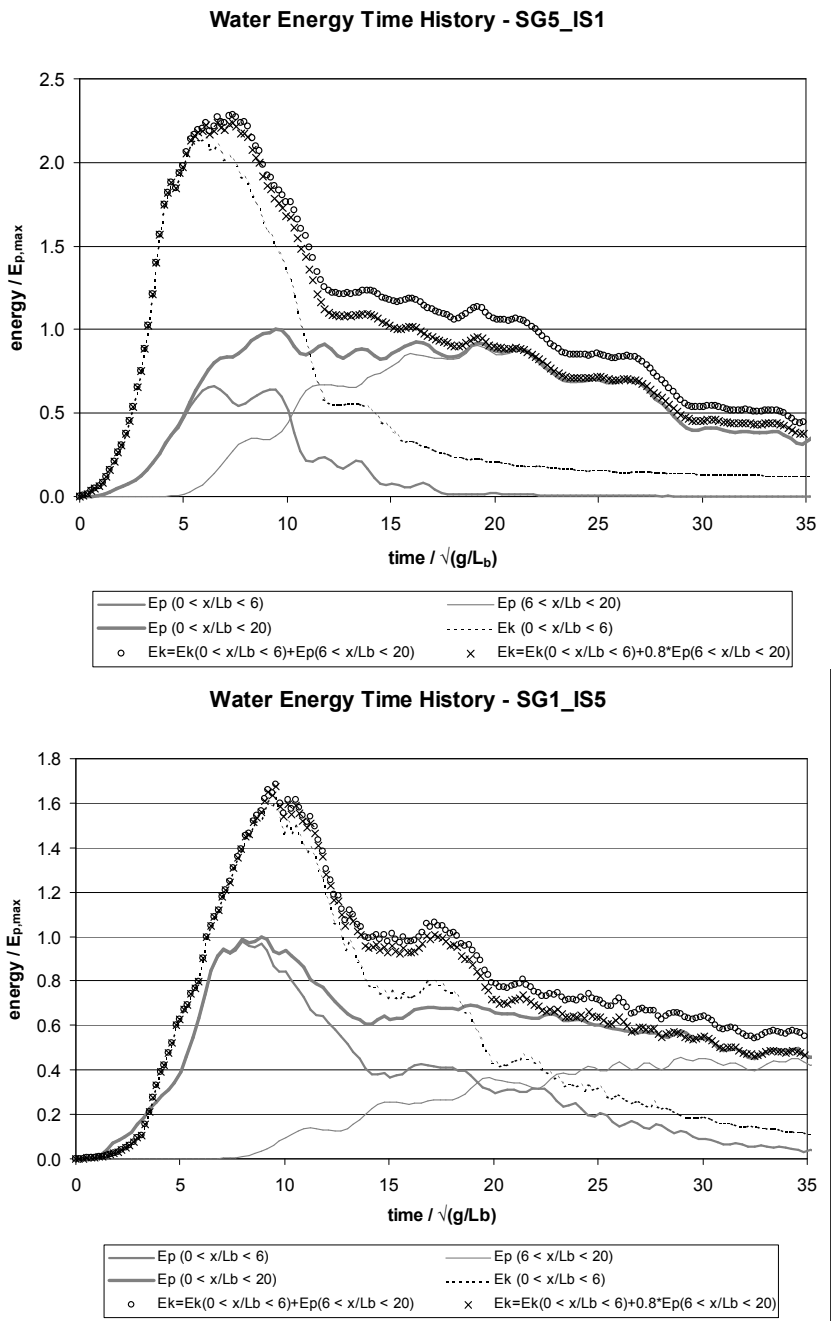

Figure 5.45. Time histories of the water potential and kinetic energy contained in the inshore and offshore regions, for the SG5_IS1 and SG1_IS5 combinations.

Figure 5.46 plots the landslide kinetic, landslide potential, fluid kinetic, and fluid potential energy time histories for the SG5_IS1 and SG1_IS5 configurations. Full equipartitioning between kinetic and potential energy of the fluid was used to estimate the fluid kinetic energy for the SG5_IS1 case. The SG1_IS5 case assumed 80% partitioning of energy.

The maximum landslide kinetic energy occurred when the landslide was travelling fastest, which occurred when the landslide reached the transition curve. The time of maximum potential energy of the landslide occurred when it moved off the slope onto the horizontal channel bed. For the SG5_IS1

and SG1_IS5 cases, the time of maximum fluid kinetic energy also coincided with the time at which the landslide reached the horizontal channel bed.

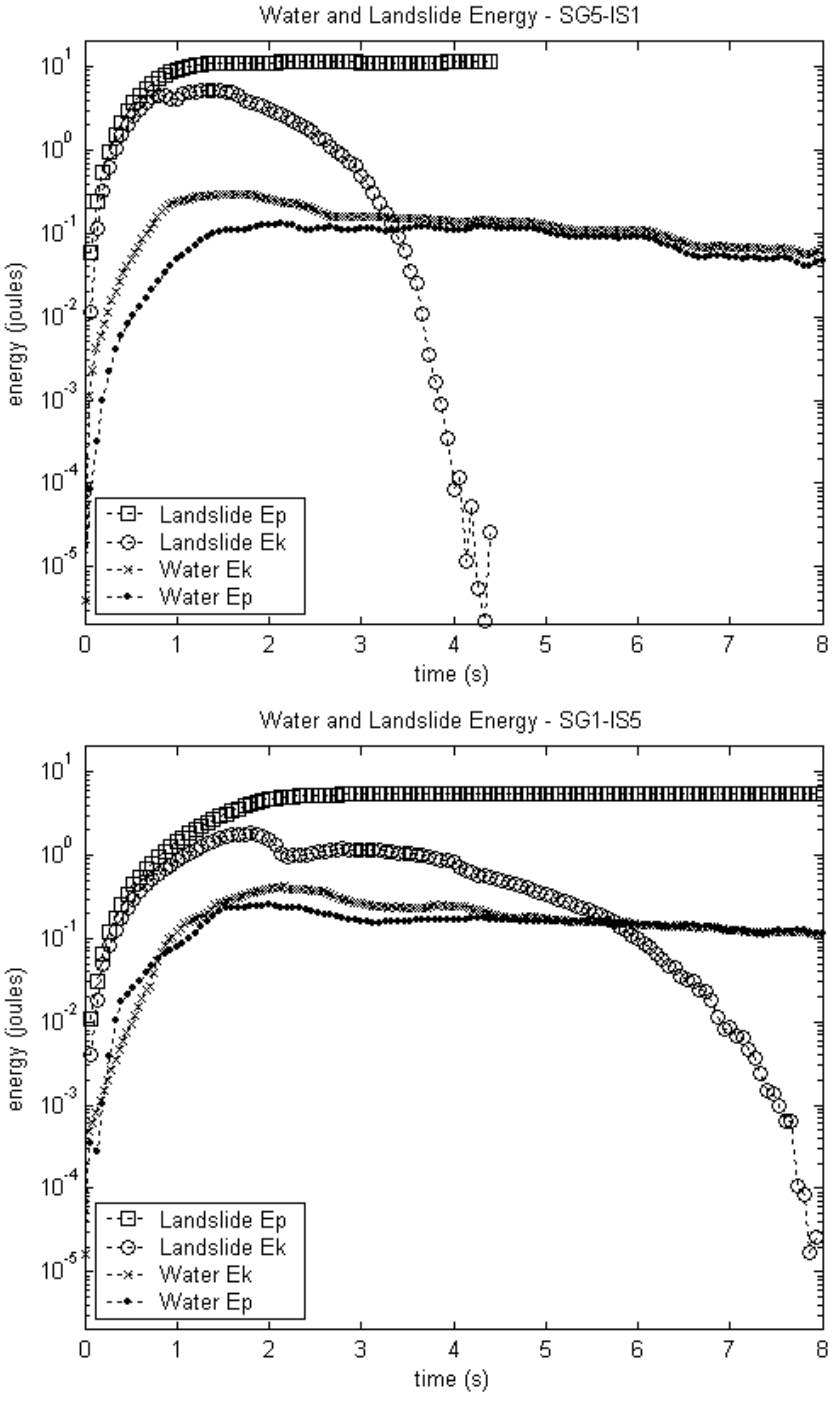

Figure 5.46. Time history of landslide and water kinetic and potential energy for the SG5_IS1 and SG1_IS5 cases. SG5_IS1 water kinetic energy assumes full equipartitioning, SG1_IS5 water kinetic energy assumes 80% partitioning.

For the SG5_IS1 case, the maximum wave potential energy occurred later than the other three forms of energy. For the SG1_IS5 case, the maximum wave potential energy occurred after the maximum landslide kinetic and potential energy occurred, but before the fluid kinetic energy reached a maximum. The difference in relative timing of maximum wave potential energy and maximum fluid kinetic energy between the SG5_IS1 and SG1_IS5 cases was due to the different durations of interaction between the landslide's pressure field and the wave field, as described in Section 5.3.1. Wave potential and kinetic energy began to decrease after approximately 4 seconds as wave energy propagated out of the measured domain. Table 5.5 summarises the ratios of the magnitude and time of maximum fluid kinetic energy to the maximum time and magnitude of the wave and landslide energy, for the SG5_IS1 and SG1_IS5 cases.

Table 5.5. Ratio of magnitude and time of maximum fluid kinetic energy to the maximum time and magnitude of the wave and landslide energy, for the SG5_IS1 and SG1_IS5 cases.

	SG5_IS1	SG1_IS5
water $E_{k,max}$/water $E_{p,max}$	2.3	1.7
water $E_{k,max}$/landslide $E_{k,max}$	0.057	0.23
water $E_{k,max}$/landslide $E_{p,max}$	0.026	0.076
time of water $E_{k,max}$/time of water $E_{p,max}$	0.78	1.1
time of water $E_{k,max}$/time of landslide $E_{k,max}$	1.2	1.2

Conceptually, the movement of energy can be speculated. The landslide was released and began to slide down the slope. The landslide kinetic energy was derived from the landslide potential energy, with greater conversions occurring for heavier landslides. The remaining landslide potential energy was dissipated as friction on the sliding surface. The moving slider set in motion the surrounding fluid, converting some of the landslide kinetic energy into kinetic energy of the fluid. The velocity distribution resulted in a pressure distribution in the fluid, which in turn disturbed the free surface. The potential energy in the waves came from the fluid kinetic energy. The quantity of wave potential energy was dependent on the position and duration of interaction between the landslide and the wave field. The fluid kinetic energy not converted into wave potential energy was eventually dissipated as friction. The fluid kinetic energy was measured for the SG5_IS1 and SG1_IS5 configurations only. 100% and 80% partitioning of fluid kinetic energy and wave potential energy was found in the offshore region for each case respectively. The differences in the magnitude and time of maximum fluid kinetic energy between full equipartitioning and 80% partitioning was small. This suggested that the use of between 100% and 80% energy partitioning for the remaining configurations would produce acceptable estimates of the fluid kinetic energies in the offshore region.

5.5 Summary

The landslides on shallow 15° slopes used in this present research were found to not reach terminal velocity, unlike several earlier researchers using 45° slopes. As the landslide began to slide a packet of waves, made up of a spectrum of wavelengths, was generated. Wave dispersion spread the packet as it propagated. New waves were continually forming on the rear of the wave packet.

The moving landslide created a water pressure distribution in the surrounding fluid. The impulse of high pressure ahead of the landslide forced the water surface directly above it up to form the first wave crest. This wave had a phase velocity that exceeded the slider velocity throughout its motion, and therefore the initial crest propagated freely out ahead of the landslide once it was generated. As the first crest quickly moved away from the landslide the crest amplitude rapidly stopped increasing in amplitude. The first crest had the longest wavelength, initially comparable in length to that of the landslide.

The accelerating fluid above and the turbulent wake behind the moving landslide created a region of low pressure. This low pressure drew down the water surface to form the first trough. The trough amplitude continued to increase because the sustained motion of the landslide transferred energy into the part of wave field localised around the landslide. This wave trough was forced to propagate at the same speed as the accelerating landslide. The interaction of the landslide pressure field with the surface wave pressure field was important, as the location of the low pressure region above the landslide relative to the wave field acted to reinforce or suppress the waves above. This had a substantial effect on the increase or decrease in wave potential energy. When the low pressure acted to draw down a wave trough, the wave potential energy increased. When the low pressure was below a wave crest, it acted to suppress the crest amplitude, leading to an overall decrease in wave potential energy. The ratio of maximum wave potential energy to maximum landslide kinetic energy was between 2.8% and 13.8%. The ratio of maximum wave potential energy to maximum landslide potential energy ranged between 1.1% and 5.9%. The ratio of maximum wave potential energy to maximum fluid kinetic energy was estimated to be 43.5% and 58.8% for the SG5_IS1 and SG1_IS5 cases respectively.

The first trough that formed over the rear end of the landslide propagated upslope to cause the large run-down observed at the shore. It was theorised that the maximum wave run-up occurred as a result of a wave generated by the short duration, but high magnitude, deceleration of the landslide upon reaching the base of the slope. A wave crest generated at that point and time propagated upstream and ran up the slope.

A possible correction for the SG5_IS5 configuration provided an estimate of the maximum effect of the movement of water between the main channel and behind the slope. The greatest corrections resulted in a 28% increase in the maximum corrected trough amplitude and an 18% increase in maximum corrected wave potential energy. The correction also tended to suppress the leading crest amplitude slightly and move the crest position further downstream.

Chapter 6: Semi-Analytical Model

The wave generation process of a moving submerged object in a constant depth channel was investigated using a semi-analytical model. The simplified geometry allowed a variety of phenomena, observed during the experimental tests, to be investigated further in a more controlled setting. Section 6.1 introduces the model approach. The governing equations of the model are outlined in Section 6.2, along with the non-dimensionalisation and solution method. The acceleration profile and landslide height decay are also detailed. Section 6.3 and 6.4 investigate the solution sensitivity to slider shape and wave number resolution respectively. This is followed by a comprehensive study into the effects of the model's controlling parameters in Section 6.5. The source mechanism of the run-up wave is also confirmed using the simplified model. Model results are compared against data from the experiments in Section 6.6.

6.1 Introduction

The intention of this portion of the research was to develop a semi-analytical model that used a simple geometry in which to investigate several features observed in the experiments. These included the interaction between the wave field and the slider motions, and the dependence of maximum wave potential energy on the slider acceleration and channel and landslide geometry. Although not a primary aim of this investigation, some comparisons were be made with the experimental results. The primary mathematical derivation of the governing equations and solution method of the semi-analytical model were due to Dr Roger Nokes at the University of Canterbury. This mathematical framework was implemented in Matlab (version 6.5) and modified with various slider shapes, acceleration profiles, and decay models.

The two-dimensional semi-analytical model generated the free surface elevation as a function of offshore position and time as the slider moved. It assumed the fluid was inviscid and the flow was irrotational, and therefore ignored friction effects and the wake generation. However it was considered that the effects of these were secondary to the main features of the flow field. The key to the model approach was the assumption of linearity. The advantages of the linear assumption were substantial. The linear assumption meant both the wave height and slider thickness was small when compared to the water depth. This allowed the boundary conditions to be evaluated at the undisturbed free surface location instead of at the displaced surface, and at the bed level instead of at the level of the top of the slider. It also allowed non-linear terms in the boundary conditions to be neglected. The advantage of linearised equations was that the principle of superposition enabled complex solutions to be generated from the summation of simple solutions. The solutions in this case were constructed from a spectrum of free wave modes. Due to the unbounded nature of the domain this spectrum was continuous.

To avoid the complexity of varying water depth, the submerged object was moved horizontally along the bed of an infinitely long constant depth channel. The absence of the slope had several effects on the wave solution. The main effect was the lack of dispersion due to changing water depth, leading to incorrect prediction of the spatial distribution of waves. The absence of a slope in the semi-analytical model also lacked the energy dissipation of wave run-up and breaking.

A decaying slider height was introduced to model a decaying slide. This would represent cases in which deposition of landslide material on the slope would cause the slide to decrease in height. It could also be used to crudely model the effect of the increasing water depth to slide length ratio for a domain with varying depth.

6.2 Model Description

6.2.1 Model Domain

The landslide configuration consisted of an arbitrarily shaped object, with a shape defined by the function f(x,t) and maximum thickness of $h_b(t)$, submerged in a channel of constant depth, D, and unlimited horizontal extent. The landslide had a length of $L_b=2L$, which did not vary with time or location. The coordinate origin was located at the undisturbed free surface directly above the initial centre of mass position of the submerged object. The movement of the submerged obstacle was stipulated by an initial acceleration, a_0, and subsequent acceleration time history. The model domain is illustrated in Figure 6.1. Of interest was the position of the free surface as a function of time and space.

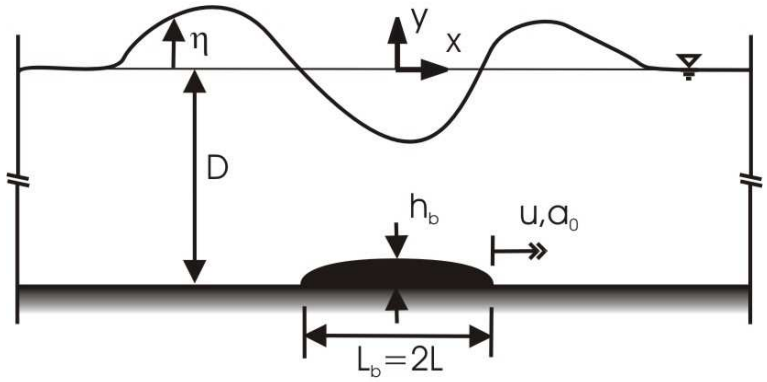

Figure 6.1. Schematic diagram of semi-analytical model domain, and definition of parameters.

6.2.2 Governing Equations

The bottom boundary, as a function of space and time, $y_b(x,t)$, can be expressed as

$$y_b(x,t) = -D + h_b(t) f\left(\theta(t)\right) \tag{6.1}$$

where $f(\theta(t))$ is the bottom boundary height distribution. $\theta(t)$ is defined as

$$\theta = x - x_0(t) \tag{6.2}$$

where $x_0(t)$ is the slider's position as a function of time.

The governing partial differential equation is

$$\nabla^2 \phi = 0 \tag{6.3}$$

where ϕ is the velocity potential. The PDE is subject to the boundary conditions

$$\frac{\partial \phi}{\partial y} = \frac{dy_b}{dt} \quad on \;\; y = -D \tag{6.4}$$

$$\frac{\partial \eta}{\partial t} = \frac{d\phi}{dy} \quad on \;\; y = 0 \tag{6.5}$$

and

$$\frac{\partial \phi}{\partial t} + g\eta = 0 \quad on \;\; y = 0 \tag{6.6}$$

with initial conditions

$$\phi(x, y, 0) = 0 \tag{6.7}$$

$$\eta(x, 0) = 0 \tag{6.8}$$

This formulation has invoked the linear assumption at both the free surface and the bottom boundary. Therefore the boundary conditions can be applied at $y=0$ and $y=-D$ instead of at $y=\eta$ and $y=y_b$. The first boundary condition states that the vertical velocities at $y=-D$ are due to the vertical motions of the bottom boundary as a function of time. The second boundary condition is the kinematic free surface condition and the third boundary condition is the dynamic free surface condition.

6.2.3 Non-dimensionalisation

The linearisation of the equations allows a solution to be generated by the superposition of simple free modes of the form

$$e^{i(kx-\omega t)} \tag{6.9}$$

where ω is the angular frequency of free waves and k is the corresponding wave number. The governing equations and variables are non-dimensionalised using the following scheme.

$$x' = \frac{x}{L} \tag{6.10a}$$

$$y' = \frac{y}{D} \tag{6.10b}$$

$$\eta' = \frac{\eta}{D} \tag{6.10c}$$

$$f' = \frac{f}{D} \tag{6.10d}$$

$$t' = t\sqrt{\frac{a_0}{2L}} \tag{6.10e}$$

$$\omega' = \omega\sqrt{\frac{2L}{g}} \tag{6.10f}$$

$$k' = kL \tag{6.10g}$$

$$\Lambda = \frac{2\pi}{kL} \tag{6.10h}$$

$$\phi' = \phi\sqrt{\frac{2}{a_0 L^3}} \tag{6.10i}$$

$$E_p' = \frac{1}{2}\int_{-\infty}^{\infty}\left(\frac{\eta}{D}\right)^2 d\left(\frac{x}{L}\right) \tag{6.10j}$$

$$E_k' = \frac{1}{2}\left(\frac{dx}{dt}\right)^2 \frac{2}{a_0 L} \tag{6.10k}$$

$$\zeta = \frac{E_p}{E_k} = \frac{E_p'}{E_k'}\frac{1}{\lambda^2} \tag{6.10l}$$

Variables associated with the x and y coordinates have been non-dimensionalised by different length scales. Therefore k and x are scaled with L, while y, η, and f are scaled with D. Time has been scaled using a_0, as this typical acceleration scale will primarily determine the temporal response of the system. Similarly, free waves are controlled by g and therefore g has been used in the scaling of ω. The parameter Λ is defined as a non-dimensional wavelength. E_p' is a non-dimensional wave potential energy and will be used throughout this investigation as a measure of the energy present in the wave field as a result of the slider motions. E_k' is a non-dimensional slider kinetic energy. The dimensional ratio of wave potential energy to slider kinetic energy, ζ, is related to the non-dimensional ratio of wave potential energy to slider kinetic energy by λ^{-2}.

The non-dimensional form of the governing equation becomes

$$\tau^2 \frac{\partial^2 \phi}{\partial x^2} + \frac{\partial^2 \phi}{\partial y^2} = 0 \tag{6.11}$$

where all parameters are non-dimensional and the primes have been dropped for clarity.

The non-dimensional forms of the boundary conditions become

$$\frac{\partial \phi}{\partial y} = \tau^2 \frac{dy_b}{dt} \quad on \;\; y = -1 \tag{6.12}$$

$$\tau^2 \frac{\partial \eta}{\partial t} = \frac{\partial \phi}{\partial y} \quad on \;\; y = 0 \tag{6.13}$$

$$\frac{1}{2}\frac{\partial \phi}{\partial t} + \frac{\tau \eta}{\lambda^2} = 0 \quad on \;\; y = 0 \tag{6.14}$$

The non-dimensional form of the initial conditions is the same as the dimensional forms, with the superscript primes dropped.

Three non-dimensional parameters have arisen from the non-dimensionalisation of the governing equations. The first represents the ratio of the water depth to the slider's half-length.

$$\tau = \frac{D}{L} \tag{6.15}$$

The second parameter represents the relative importance of the slider's acceleration to the acceleration due to gravity.

$$\lambda^2 = \frac{a_0}{g} \tag{6.16}$$

The third parameter is the ratio of the slider's initial thickness, h_{b0}, to the water depth.

$$\rho = \frac{h_{b0}}{D} \tag{6.17}$$

6.2.4 Solution Method

The solution method is based on the analysis of wave patterns made by obstacles in a steady stream given by Lighthill (1978).

The solutions are assumed to take the forms

$$\phi(x,y,t) = \int_{-\infty}^{\infty} e^{i(kx-\omega t/\lambda)} \left[a(k,t) e^{k\tau y} + b(k,t) e^{-k\tau y} \right] dk \tag{6.18}$$

and

$$\eta(x,t) = \int_{-\infty}^{\infty} e^{i(kx-\omega t/\lambda)} c(k,t) dk \tag{6.19}$$

The non-dimensional form of Equation 6.9 is

$$e^{i(kx-\omega t/\lambda)} \tag{6.20}$$

The angular frequency and wave number of free waves are related through the non-dimensional dispersion relation

$$d(\omega,k) = -\omega^2 + 2k \tanh(k\tau) = 0 \tag{6.21}$$

The coefficients *a*, *b*, and *c* are complex and depend on *k* and *t*. The solution is the real part of these two equations. The assumed solution automatically satisfies the governing equation, so the evaluation of the spectral components, *a*, *b*, and *c* is the essence of the problem.

The velocity potential, ϕ, is related to the slider motions through the bottom boundary condition. Therefore the form of the slider shape, *f*, is also written in the form of a Fourier integral. For convenience the derivative of *f* is defined as

$$\frac{df}{d\theta} = \int_{-\infty}^{\infty} e^{ik(x-x_0)} p(k) dk \tag{6.22}$$

The unsteady motion is incorporated into the x_0 term that now appears in the complex exponential. As the slider's shape does not change with time, except for the temporal dependence of thickness captured in the $h_b(t)$ term, the Fourier coefficients, *p(k)*, are independent of *t*. Details of the slider shape are presented in Section 6.3.

The dimensionless form of the bottom boundary, y_b, is expressed as

$$y_b(x,t) = -1 + \rho h_b(t) f(\theta) \tag{6.23}$$

where h_b is now the non-dimensional form, with an initial value 1. By definition, $f(\theta)$ is already dimensionless.

The slider shape, $f(\theta)$, position time history, $x_0(t)$, and thickness, $h_b(t)$, remain in general form. These are defined later for specific slider configurations. The solution process continues by utilising the three boundary conditions, Equations 6.12-6.14, to obtain the spectral coefficients, a, b, and c. In reality only $c(k,t)$ is required to determine the water surface profile. Using Equations 6.18, 6.22, and 6.23, Equation 6.12 becomes

$$\begin{aligned} &\int_{-\infty}^{\infty} e^{i(kx-\omega t/\lambda)} \left[k\tau a(k,t) e^{-k\tau} - k\tau b(k,t) e^{k\tau} \right] dk \\ &= \rho\tau^2 \left[\frac{dh_b}{dt} \int_{-\infty}^{\infty} e^{ik(x-x_0)} \frac{p(k)}{ik} dk - h_b(t) \frac{dx_0}{dt} \int_{-\infty}^{\infty} e^{ik(x-x_0)} p(k) dk \right] \end{aligned} \tag{6.24}$$

As each Fourier mode is linearly independent of all the others, equating coefficients and solving Equation 6.24 for $b(k,t)$ in terms of $a(k,t)$ and $p(k)$ gives

$$b(k,t) = a(k,t) e^{-2k\tau} - \frac{\rho\tau}{k} p(k) e^{-k\tau} \left[\frac{dh_b}{dt} \frac{1}{ik} - h_b(t) \frac{dx_0}{dt} \right] e^{i(\omega t/\lambda - kx_0)} \tag{6.25}$$

If we redefine $a^*(k,t)=a(k,t)e^{-k\tau}$, drop the superscript *, and substitute Equation 6.25 into Equation 6.18, we obtain

$$\begin{aligned} &\phi(x,y,t) = \\ &\int_{-\infty}^{\infty} e^{i(kx-\omega t/\lambda)} \left[a(k,t) \cosh k\tau(y+1) - \frac{\rho\tau}{k} p(k) e^{-k\tau(y+1)} e^{i(\omega t/\lambda - kx_0)} \left[\frac{dh_b}{dt} \frac{1}{ik} - h_b(t) \frac{dx_0}{dt} \right] \right] dk \end{aligned} \tag{6.26}$$

Performing a similar operation of differentiating and comparing coefficients for the second boundary condition, Equation 6.13, results in the following expression for $a(k,t)$ in terms of $c(k,t)$

$$a(k,t) = \frac{1}{k\tau \sinh(k\tau)} \left[\tau^2 \left(\frac{\partial c}{\partial t} - i\omega c/\lambda \right) - \rho\tau^2 e^{-k\tau} e^{i(\omega t/\lambda - kx_0)} p(k) \left(\frac{dh_b}{dt} \frac{1}{ik} - h_b(t) \frac{dx_0}{dt} \right) \right] \tag{6.27}$$

Substituting the necessary derivatives and equating coefficients in the last boundary condition, Equation 6.14, results in a second expression relating $a(k,t)$ and $c(k,t)$.

$$\frac{1}{2}\cosh(k\tau)\left(\frac{\partial a}{\partial t}-i\,\omega a/\lambda\right)-\frac{1}{2}\frac{\rho\tau}{k}p(k)e^{-k\tau}e^{i(\omega t/\lambda-kx_0)}$$
$$\left[\frac{d^2h_b}{dt^2}\frac{1}{ik}+ikh_b\left(\frac{dx_0}{dt}\right)^2-h_b\frac{d^2x_0}{dt^2}-2\frac{dx_0}{dt}\frac{dh_b}{dt}\right]+\frac{\tau}{\lambda^2}c(k,t)=0 \quad \textbf{(6.28)}$$

Equations 6.27 and 6.28 provide two equations for *a(k,t)* and *c(k,t)* which are solved for *c(k,t)*. Substituting Equation 6.27 and its time derivative into Equation 6.28 results in a differential equation for *c(k,t)*.

$$\frac{d^2c}{dt^2}-\frac{2i\omega}{\lambda}\frac{dc}{dt}+\left(2k\tanh(k\tau)-\omega^2\right)\frac{c}{\lambda^2}$$
$$=\rho p(k)e^{-k\tau}e^{i(\omega t/\lambda-kx_0)}\left[\left(\frac{d^2h_b}{dt^2}\frac{1}{ik}+ikh_b\left(\frac{dx_0}{dt}\right)^2-h_b\frac{d^2x_0}{dt^2}-2\frac{dx_0}{dt}\frac{dh_b}{dt}\right)(1+\tanh k\tau)\right] \quad \textbf{(6.29)}$$

Note that the wave number, *k*, is simply a parameter and therefore the partial time derivatives of *c(k,t)* can be written as ordinary time derivatives. This can be simplified to

$$\frac{d^2c}{dt^2}-\frac{2i\omega}{\lambda}\frac{dc}{dt}+d(\omega,k)\frac{c}{\lambda^2}=\rho p(k)e^{i(\omega t/\lambda-kx_0)}G(k,t) \quad \textbf{(6.30)}$$

where *d(ω,k)* is the dispersion relation given in Equation 6.21. Noting that

$$e^{-k\tau}(1+\tanh k\tau)=\frac{1}{\cosh(k\tau)} \quad \textbf{(6.31)}$$

we have

$$G(k,t)=\frac{\left(\frac{d^2h_b}{dt^2}\frac{1}{ik}+ikh_b\left(\frac{dx_0}{dt}\right)^2-h_b\frac{d^2x_0}{dt^2}-2\frac{dx_0}{dt}\frac{dh_b}{dt}\right)}{\cosh(k\tau)} \quad \textbf{(6.32)}$$

As *d(ω,k)=0* we have finally

$$\frac{d^2c}{dt^2}-\frac{2i\omega}{\lambda}\frac{dc}{dt}=\rho p(k)e^{i(\omega t/\lambda-kx_0)}G(k,t) \quad \textbf{(6.33)}$$

The solution for the wave field, *η(x,t)*, involves two steps. The first is the numerical integration of Equation 6.33 to determine the spectral coefficients *c(k,t)*. Numerical integration for a range of *k* values is required as analytical solutions are not readily available for this equation. The result of using a numerical integration approach is that *c(k,t)* is not a continuous function of k. Instead it is only evaluated for specific values of wave number. Therefore in solving the equations a range of wave numbers must be defined, as discussed in Section 6.4. This has important implications for the

resolution of the model. The range of wave number values governs the smallest wavelengths, and the interval between k values limits the largest wavelengths, able to be resolved by the model.

Equation 6.33 can be written as two first order ordinary differential equations (ODEs). Therefore we let

$$c_1(k,t) = c(k,t) \tag{6.34}$$

and

$$c_2(k,t) = \frac{dc(k,t)}{dt} \tag{6.35}$$

Equation 6.33 can be rewritten as

$$\frac{dc_1}{dt} = c_2 \tag{6.36}$$

and

$$\frac{dc_2}{dt} = \frac{2i\omega}{\lambda} c_2 + K(k,t) \tag{6.37}$$

where *K(k,t)* is the forcing function given by

$$K(k,t) = \rho p(k) e^{i(\omega t/\lambda - kx_0)} G(k,t) \tag{6.38}$$

Noting that c_1 and c_2 are complex, we have

$$\frac{dc_1^{\,r}}{dt} = c_2^{\,r} \tag{6.39a}$$

$$\frac{dc_1^{\,i}}{dt} = c_2^{\,i} \tag{6.39b}$$

$$\frac{dc_2^{\,r}}{dt} = \frac{2i\omega}{\lambda} c_2^{\,i} + K^r(k,t) \tag{6.39c}$$

$$\frac{dc_2^{\,i}}{dt} = \frac{2i\omega}{\lambda} c_2^{\,r} + K^i(k,t) \tag{6.39d}$$

where the superscripts ^{r} and ^{i} refer to real and imaginary parts respectively. Equations 6.39a-d require initial conditions

$$c_1^{\,r}(k,0) = c_1^{\,i}(k,0) = 0 \tag{6.40}$$

$$c_2^{\,r}(k,0) = c_2^{\,i}(k,0) = 0 \tag{6.41}$$

As detailed in Appendix F, these initial conditions require

$$\frac{dx_0}{dt}(0) = 0 \tag{6.42}$$

and

$$\frac{dh_b}{dt}(0) = 0 \tag{6.43}$$

Equations 6.42 and 6.43 essentially state that at $t = 0$, the slider must be stationary and its size cannot be decaying. The generation of the initial conditions and their specific requirements for slider initial motion and thickness decay functions are presented in more detail in Appendix F. Equations 6.39a-d are solved using a 4th order Runge-Kutta ODE solver.

The second step in obtaining the solution for the wave field, η(x,t), is the inversion of the Fourier transform in Equation 6.19. So

$$\eta(x,t) = \int_{k_{\min}}^{k_{\max}} \cos(kx - \omega t/\lambda)\, c^r(k,t) - \sin(kx - \omega t/\lambda)\, c^i(k,t)\, dk \tag{6.44}$$

This integral is evaluated numerically using Simpson's rule. Only the real part is required for the solution of $\eta(x,t)$.

6.2.5 Acceleration Model

The displacement function, $x_0(t)$, was defined in a piecewise manner, as an approximation to the displacement of the landslide during the experiments. The flexibility in the definition of the landslide kinematics allowed a variety of wave field and slider motion interaction characteristics to be investigated, as presented in Section 6.5. The slider kinematics are defined by three parameters, one associated with the initial acceleration, λ, and two time parameters.

The first model, which is called 'A1', consists of an indefinite constant acceleration of magnitude a_0. In dimensional coordinates the distance travelled by the slider, $x_0(t)$, is given by

$$x_0(t) = \frac{1}{2} a_0 t^2 \tag{6.45}$$

In non-dimensional terms, the displacement, $x_0(t)$, velocity, $dx_0(t)/dt$, and acceleration functions, $d^2x_0(t)/dt^2$, for $0 \le t \le \infty$, become

$$x_0 = t^2 \tag{6.46}$$

$$\frac{dx_0}{dt} = 2t \tag{6.47}$$

$$\frac{d^2x_0}{dt^2} = 2 \tag{6.48}$$

These functions are required in Equation 6.32 and the forcing function given by Equation 6.38.

The second slider model, which is called 'AD1', is an idealised form of the experimental landslide kinematics. The slider acceleration, a_0, is assumed constant until $t = t_{max}$, representative of the time at which the landslide reaches the base of the slope. After the initial acceleration a constant deceleration occurs until $t = t_{zero}$, at which point the slider comes to a rest. The fluctuations in the landslide deceleration time history, as shown by the example in Figure 5.4 for the SG3_IS5 combination, are ignored in this simplified model. In non-dimensional terms, the displacement function for a constant acceleration followed by a constant deceleration is

$$\begin{aligned} x_0'(t') &= t'^2 && for\ 0 \le t' \le t'_{\max} \\ &= t'_{\max}{}^2 + 2t'_{max}\left(t'-t'_{max}\right) - \frac{t'_{max}\left(t'-t'_{max}\right)^2}{\left(t'_{zero}-t'_{\max}\right)} && for\ t'_{\max} \le t' \le t'_{zero} \\ &= t'_{\max}{}^2 + t'_{max}\left(t'_{zero}-t'_{\max}\right) && for\ t'_{zero} \le t' \end{aligned} \quad \textbf{(6.49)}$$

where t_{max} and t_{zero} define the deceleration rate. The superscript primes have been shown to clarify that these parameters are in non-dimensional form. The derivative and double derivative of Equation 6.49 provide the respective slider velocity and acceleration functions.

The third model, which is called 'ACV1', consists of a constant slider acceleration, a_0, for the duration between $0 \le t \le t_{max}$. An indefinite constant velocity follows the initial acceleration. In non-dimensional terms, the slider acceleration function for a constant acceleration followed by a constant velocity is

$$\begin{aligned} \frac{d^2x_0}{dt^2}(t) &= 2 \quad for\ 0 \le t \le t_{\max} \\ &= 0 \quad for\ t_{\max} \le t \le \infty \end{aligned} \quad \textbf{(6.50)}$$

6.2.6 Decay Model

Two slider height decay models were used. The first, which is called 'decay1', is a case of no decay in slider height. In dimensionless form, this is

$$h_b(t) = 1 \quad \textbf{(6.51)}$$

The second model, which is called 'decay2', implements a decay model to reduce the thickness of the slider with time in an exponential way. This represents cases in which deposition of landslide material on the slope causes the slide to decrease in height. In some respects it mimics the changing depth of the experimental configuration in the constant depth semi-analytical model. A reduction in the ratio of

slider thickness to the constant water depth in the model corresponds to an increase in the local water depth relative to the constant slider thickness as the landslide moves down the slope during the experiments. As such, the decay model is only used in the context of model comparisons with experimental results, and is discussed in Section 6.6.

This model satisfies Equation 6.43 and the initial conditions in Equations 6.40 and 6.41, provided the exponential parameter $\varepsilon>1$. This initial condition requirement is discussed further in Appendix F. A further property of this decay model is that it is valid for all time and results in a slider thickness that reduces to a constant value. However, the reducing thickness of the slider results in a decrease in average water level due to the loss of mass. The dimensionless slider height function, $h_b(t)$, for the decaying slider thickness is

$$h_b(t) = (1-h_1)e^{-\gamma t^{\varepsilon}} \tag{6.52}$$

where h_1 is the final slider thickness, and γ and ε are parameters that control the thickness decay. Equation 6.52, its time derivative, and its double time derivative are then introduced into Equation 6.32.

6.3 Slider Shape

The solution sensitivity to slider shape was investigated by examining the water surface response for a variety of slider profiles. This included a sawtooth, cosine, cosine^2, and quartic shaped slider, as shown by the shape functions in Figure 6.2. In the experiments the landslide had a semi-elliptical cross-sectional area. In non-dimensional coordinates this became a half-circle. However, the infinite slopes at the leading and trailing edge were problematic so the semi-circular shape was replaced with an equivalent shape in the semi-analytical model that had finite slopes at its extremities. Each slider shape had a non-dimensional length of 2, spanning $-1 \le x \le 1$, and a maximum non-dimensional height of 1.

Figure 6.3 plots water surface profiles, measured at $t(a_0/2L)^{0.5} = 5$, for simulations using sawtooth, cosine, cosine^2, and quartic shaped sliders. Each of these simulations used identical non-dimensional parameters, as presented in Table 6.1. There were significant differences in the wave amplitudes of the water surface profiles between the different slider shapes. However, it was noted that the wave response for the sawtooth and cosine^2 shapes was almost identical. The areas of these two shapes were the same. Figure 6.4 plots water surface profiles, measured at $t(a_0/2L)^{0.5} = 5$, for simulations using the same slider shapes and non-dimensional parameters as Figure 6.3 except the non-dimensional heights of the sliders had been scaled so that the slider areas were identical to the area of

a sawtooth shape with a maximum non-dimensional height of 1. The wave response for all five slider shapes was now almost identical. This meant that provided the sliders had similar length and area, the specific shape of the slider had only a minor influence on the wave response. This implied that for real events, predicting the length and area (volume) of a landslide was significantly more important than accurately predicting its shape.

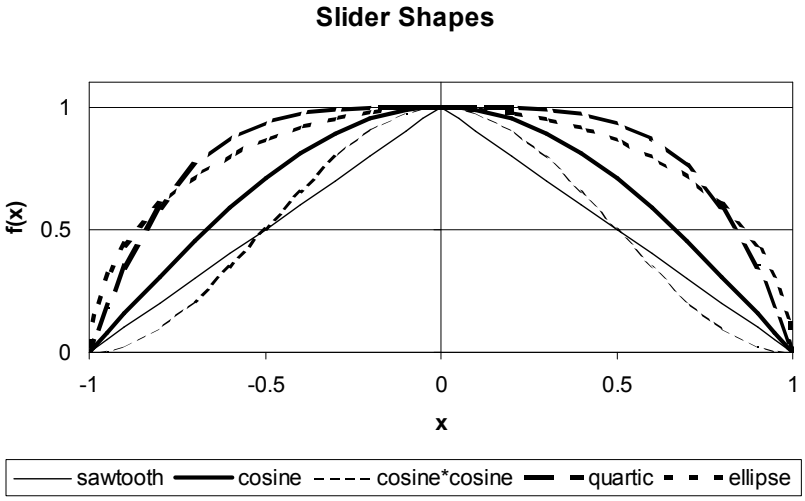

Figure 6.2. Slider shape functions, f(x), for sawtooth, cosine, cosine^2, quartic, and elliptical shaped sliders.

Table 6.1. Non-dimensional parameters for simulations investigating the effect of slider shape.

τ	λ	ρ	acceleration model	$t_{max}\sqrt{(a_0/2L)}$	$t_{zero}\sqrt{(a_0/2L)}$	decay model	h_1	γ	ε
2.0	0.39	0.1	A1	-	-	decay1	-	-	-

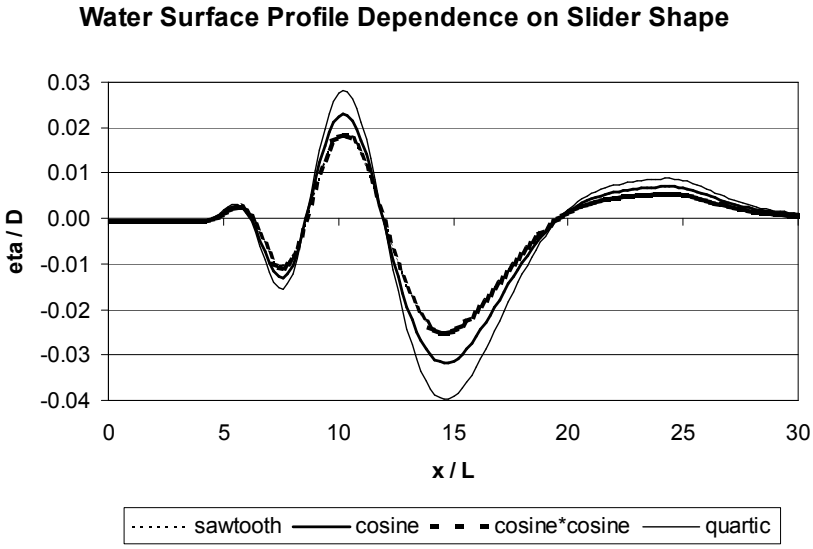

Figure 6.3. Water surface profiles at $t(a_0/2L)^{0.5} = 5$ for simulations using sawtooth, cosine, cosine^2, and quartic shaped sliders. Each simulation uses identical non-dimensional parameters, including a non-dimensional length of 2 and a non-dimensional height of 1.

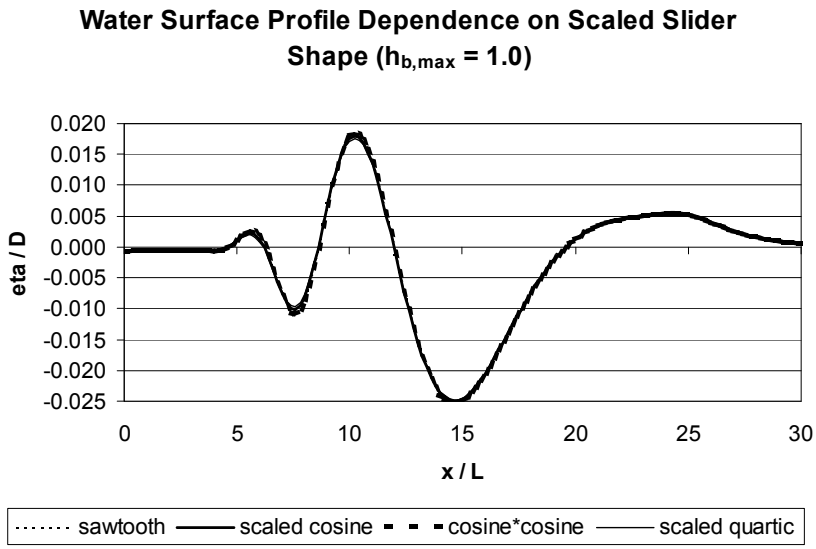

Figure 6.4. Water surface profile at $t(a_0/2L)^{0.5}$ = 5 for simulations using sawtooth, cosine, cosine^2, and quartic shaped sliders. Each simulation uses identical non-dimensional parameters, including a non-dimensional length of 2. The non-dimensional height of each slider is scaled so that the sliders have identical areas.

Although the solution was relatively insensitive to slider shape, the quartic shape was chosen for subsequent simulations because it had the closest physical resemblance to the elliptical slider used in the experiments. It had a steep, but not infinite, slope at the ends and zero slope at its centre. Its height was scaled to ensure its area matched that of the elliptical slider used in the experiments. Therefore the quartic had a maximum non-dimensional height of 0.982, or $f(x=0) = 0.982$. The relative dimensions of the slider were varied within the model via the parameters τ and ρ, defined in Equations 6.15 and 6.17 respectively. The shape function for the quartic shape is

$$f(x) = 0.982(1-x^4) \quad for \quad -1 \le x \le 1 \tag{6.53}$$

and

$$\frac{df}{dx} = -3.928x^3 \quad for \quad -1 \le x \le 1 \tag{6.54}$$

The Fourier coefficients for the quartic are

$$p(k) = -\frac{1.964}{\pi}\left[\frac{1}{k^4}\left(ik^3e^{-ik} + 3k^2e^{-ik} - 6ike^{-ik} - 6e^{-ik} + ik^3e^{ik} - 3k^2e^{ik} - 6ike^{ik} + 6e^{ik}\right)\right] \tag{6.55}$$

$$for\ k \neq 0$$

and using L'hopital's rule

$$p(0) = 0 \tag{6.56}$$

Therefore, for k=0, the forcing function, *K(k,t)*, given by Equation 6.38, becomes

$$K(0,t) = 0.982\rho\frac{4}{5\pi}\frac{d^2h_b}{dt^2} \tag{6.57}$$

6.4 Resolution of Wave Number Spectrum

The dependence of the generated wave fields on the resolution of the wave number spectrum was assessed by varying the increment in non-dimensional wave number, *kL*, from 1/10 to 1/160. The corresponding water surface profiles at $t(a_0/2L)^{0.5} = 5$, using the non-dimensional parameters presented in Table 6.2, were plotted and compared. As shown in Figure 6.5, wave number increments of 1/20 or finer produced wave fields that were independent of the increment of *kL*. The real and imaginary spectral coefficients, at $t(a_0/2L)^{0.5} = 5$, were plotted as a function of wave number for the same range of wave number increments. From the representative plot of real coefficients shown in Figure 6.6, a wave number increment of 1/80 or finer produced spectral coefficients that were independent of the increment of *kL*. Given these observations, a wave number increment of 1/80 was used in all subsequent analyses. The coefficients were limited to a wave number range, from –1 < kL < 0, for clarity.

Table 6.2. Non-dimensional parameters for simulations assessing the grid resolution.

τ	λ	ρ	acceleration model	$t_{max}\sqrt{(a_0/2L)}$	$t_{zero}\sqrt{(a_0/2L)}$	decay model	h_1	γ	ε
2.0	0.39	0.1	A1	-	-	decay1	-	-	-

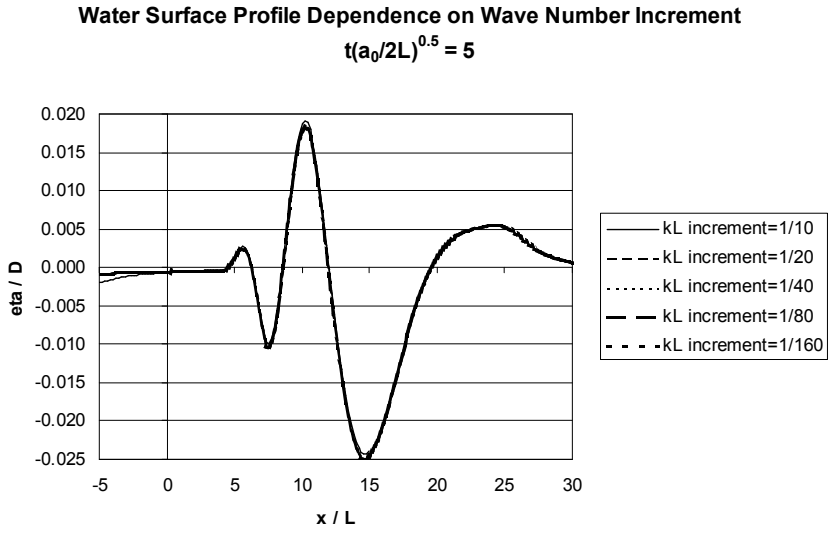

Figure 6.5. Water surface profile at $t(a_0/2L)^{0.5} = 5$, for a range of wave number intervals.

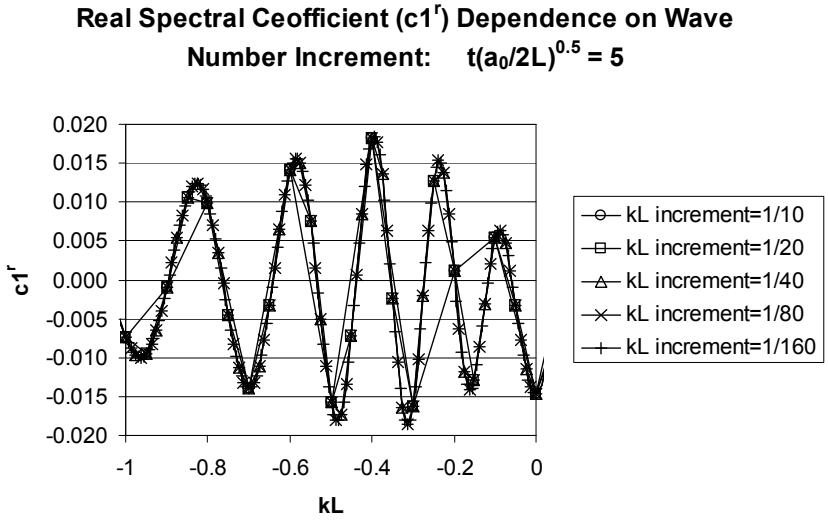

Figure 6.6. Representative real spectral coefficients, at $t(a_0/2L)^{0.5} = 5$, as a function of wave number, for a range of wave number increments.

Aside from solution accuracy, the increment of wave number also had another important property. As mentioned in Section 6.2.4, wavelength is related to wave number by the expression given in Equation 6.10h. Therefore the smallest *kL* value limited the largest wavelengths resolved by the model. Therefore, a *kL* interval of 1/80 allowed wavelengths of up to 160π to be resolved. Also, the limitation of the smallest wave number caused the solution to repeat itself, and hence the simulation times were necessarily limited. In contrast, the range of kL values governed the smallest wavelengths able to be resolved by the model. The power spectral density, defined as the sum of the squares of the real and imaginary coefficients (c1r and c1i), was plotted as a function of wave number, at four different times, in Figure 6.7. This figure shows that essentially all the energy was contained by wave numbers typically within the range of $-5 \leq kL \leq 5$. To ensure all of the energy was captured during the semi-analytical model simulations, a more conservative range of wave numbers was used. A *kL* range of $-10 \leq kL \leq 10$ was used for subsequent simulations, with the added benefit of allowing the small wavelengths to be resolved. The maximum *kL* value, when substituted into Equation 6.10h, allowed wavelengths as small as π/5 to be resolved. For a slider with a non-dimensional length of 2, the smallest waves that could have been modelled were approximately one-third of the length of the slider. The very short wavelength waves, observed at the trailing end of the wave packets during the experiments, would not be resolved. However, the dominant long wavelength leading waves and the longer waves in the wave train would be resolved.

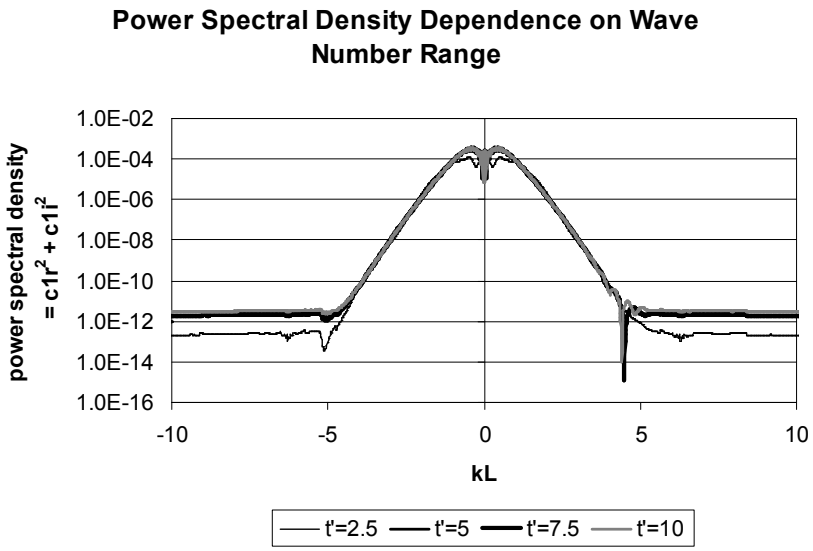

Figure 6.7. Power spectral density versus wave number for $t(a_0/2L)^{0.5}$ = 2.5, 5.0, 7.5, and 10.0.

6.5 Model Parametric Study and Results

The number of dimensionless parameters in the constant depth semi-analytical model made a full exploration of the parameter space a complex and time consuming task. Therefore only several key parameters were investigated in any detail, and the results were predominantly qualitative. This section explores the effect of the acceleration profile, the ratio of the slider speed to the wave phase speeds, and the non-dimensional parameters λ and τ. The slider deceleration was also investigated in terms of its ability to generate upstream propagating waves. It was clear from the spectral solution, developed in Section 6.2, that there was a linear dependence of wave amplitude on the non-dimensional parameter ρ. Naturally, the wave potential energy increased like ρ^2, while wave speeds, periods, and lengths were not affected by variations in ρ.

The ratio of the slider's speed relative to the wave propagation speed is an important parameter, as it is one of the factors that indicate the duration over which the slider interacts with the wave field. As it has been previously shown, the level of interaction between the slider and the wave field has a significant effect on the wave amplitudes and energies. Therefore, the Froude number was used here to control the duration of this interaction. A slide Froude number can be defined as the ratio of the slider's speed and the shallow water wave propagation speed, as shown with dimensional parameters, by

$$Fr = \frac{dx/dt}{\sqrt{gD}} \tag{6.58}$$

where the denominator is the shallow water wave speed given in Equation 5.19. In reality, the leading waves will be propagating at a speed slightly less than the shallow water wave speed. Using non-dimensional parameters, the expression for Froude number becomes

$$Fr = \frac{dx}{dt}\sqrt{\frac{a_0 L}{2gD}} \tag{6.59}$$

Substituting in Equations 6.15 and 6.16, gives

$$Fr = \frac{dx}{dt}\frac{\lambda}{\sqrt{2\tau}} \tag{6.60}$$

The wave potential energy was of interest in this investigation, as it provided an indication of the effectiveness of the transfer of energy from the slider into the wave field. The directionality of the energy propagation offered insights into the possible threat posed by the waves to those upstream and downstream of the slide. The backward propagating energy within the wave field was calculated as a spatial integral from $-\infty < x/L < 0$, and the forward propagating energy from $0 < x/L < \infty$. This simple method only provided an indication as to the energy content in the backward and forward propagating energies, as it assumed that all the backward propagating energy formed, or was ultimately located, on the negative-x half of the domain, and the forward propagating energy was only present on the positive-x side of the domain. Should backward propagating waves form on the positive-x side of the domain, such as from a sudden slider deceleration, the forward propagating energy would be contaminated by the additional energy, until the backward propagating energy left the positive-x side of the domain. Also, the spatial integral from $-\infty < x/L < 0$ would not detect the backward propagating energy until it reached the negative-x side of the domain.

6.5.1 Dependence on Acceleration Profile

To investigate the effect of the acceleration profile three different acceleration models, as described in Section 6.2.5, were used. Acceleration model A1 consisted of an indefinite constant acceleration, AD1 consisted of a constant acceleration followed by a constant deceleration, and ACV1 consisted of a constant acceleration followed by an indefinite constant velocity. The ACV1 and AD1 models were two approximations to landslides in the field. ACV1 represented a landslide that accelerated up to terminal velocity, such as a landslide that ran out on a long and constant slope. The AD1 case modelled a case where the landslide did not reach terminal velocity before decelerating, possibly due to encountering the base of the slope. Acceleration model A1 was not realistic for real events, as this model allowed infinite slider kinetic energies. However, it did allow the effects of prolonged acceleration to be investigated. The simulation parameters are presented in Table 6.3. These values would represent a situation in which a quartic shaped landslide, with a length of 500 metres and a thickness of 25 metres, sliding in water 500 metres deep. Its initial acceleration would be equivalent

to 4% of the acceleration of gravity. For the AD1 and ACV1 models, this slider would accelerate for 53.5 seconds, and for the AD1 model, the slider would decelerate at a constant rate for a further 53.5 seconds. For the values of λ, τ, and $t = t_{max}$ given in Table 6.3, Fr = 0.3. An investigation into the effect of Froude number is given in Section 6.5.2.

Table 6.3. Non-dimensional parameters of simulations investigating the solution dependence on acceleration profile.

acceleration model	τ	λ	ρ	$t_{max}\sqrt{(a_0/2L)}$	$t_{zero}\sqrt{(a_0/2L)}$	decay model
A1	2.0	0.2	0.05	-	-	decay1
AD1	2.0	0.2	0.05	1.5	3.0	decay1
ACV1	2.0	0.2	0.05	1.5	-	decay1

Figure 6.8 plots the time history of backward and forward propagating wave potential energy for the three acceleration profiles. The initial shapes of the backward propagating wave potential energy time histories, until $t = t_{max}$, were the same for all three acceleration profiles. This was not unexpected as until $t = t_{max}$, all three acceleration profiles had the same acceleration time history. The initial energy growth was due to the increase in the amplitude of the trough that formed over the slider. This trough propagated both backwards and forwards. After $t = t_{max}$, the potential energy for the A1 acceleration model continued increasing, and appeared to approach a constant value. For the simulation with the ACV1 model, the wave potential energy remained constant after $t = t_{max}$. For the slider using the AD1 acceleration model, the potential energy increased rapidly after $t(a_0/L)^{0.5} \approx 2$. This large increase in energy was due to a crest propagating into the negative-x domain. The crest was generated by the slider deceleration and is investigated in more detail in Section 6.5.5. Backward propagating waves began moving out of the modelled domain, at $x/L = -60$, at $t(a_0/L)^{0.5} = 6$.

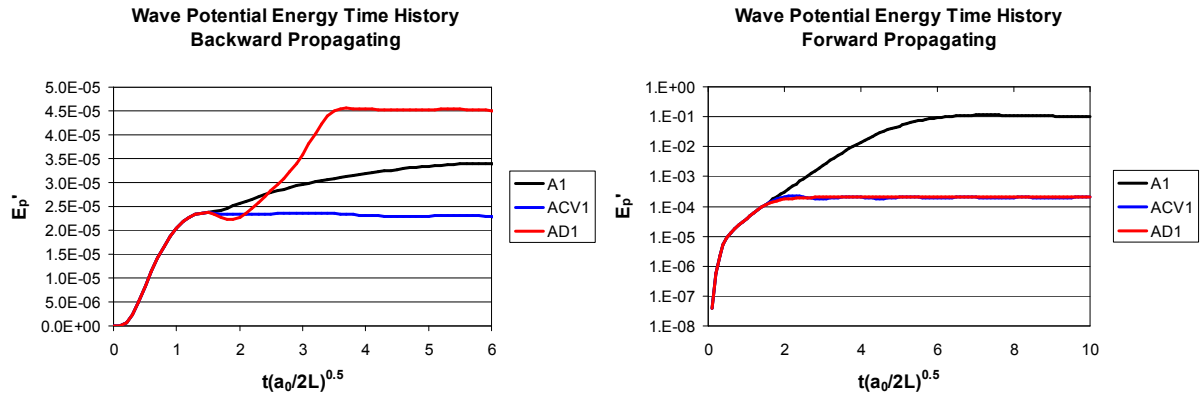

Figure 6.8. Time history of backward and forward propagating wave potential energy for A1, ACV1, and AD1 acceleration profiles.

When plotted on a semi-logarithmic scale, the forward propagating wave potential energy time histories for the different acceleration profiles tended to increase initially towards a peak value and then plateau. However there was a significant range in the energy magnitude of these plateaus. The maximum energy for the A1 model was over two orders of magnitude greater than the maximum energies for the ACV1 and AD1 models. The initial increase in energy before $t(a_0/L)^{0.5} = 1.5$, was the same for all three acceleration profiles, and was due to the low pressure surrounding the slider drawing down the water surface to form the first trough. At $t(a_0/L)^{0.5} = 1.5$, the forward propagating wave potential energy was an order of magnitude larger than the backward propagating wave potential energy at the same time. For $t(a_0/L)^{0.5} > 1.5$, the differences in energy magnitude and time history for each case could be explained by the interaction between the wave field and the slider. Note that the forward propagating waves did not begin moving out of the modelled domain, at x/L = 120, until well after $t(a_0/L)^{0.5} = 10$.

The forward propagating wave potential energy for the A1 acceleration model case is reproduced in Figure 6.9. With the energy plotted on linear scales, instead of logarithmic scales, the energy increased, peaked, and then decreased slightly to approach what appeared to be a constant value. Figure 6.10 plots the two-dimensional wave field for the A1 case. The increase and decrease in energy around the peak energy was due to the interaction of the slider's pressure field and the surface wave field. The low pressure surrounding the slider drew down the water surface to form the first trough. As the slider was controlled by an indefinite constant acceleration, the slider velocity continued to increase, and its instantaneous Froude number also increased. As the Froude number approached Fr = 1, the slider and the wave trough phase speeds become similar and the continued presence of the low pressure source below the trough led to energy being injected into the leading trough. The slider began to move faster than the wave phase speeds, at approximately $t(a_0/L)^{0.5} = 5$. The gradual removal of the low pressure region from below the first trough meant that the energy input into that part of the wave field decreased and eventually stopped. The low pressure surrounding the slider began to move to a position below the first crest, acting to suppress the crest's amplitude. This led to the decrease in wave potential energy. As the slider and its low pressure region moved ahead of the wave packet altogether, the work done on the wave energy field reduced and the energy within the packet stabilised to a constant value. An interesting feature of the two-dimensional wave field plot for the A1 case, shown in Figure 6.10, was the wave crest that tracked along with the constantly accelerating slider ahead of the main wave packet. This crest was simply a result of energy conservation as the slider moved through the stationary fluid, similar to the flow over a bottom disturbance in a supercritical open channel flow. Due to the constantly changing velocity of the slider, the amplitude, and potential energy, of the single crest was not constant. However, the changes in its amplitude would have been small. Irrespective of this, the potential energy within the main packet of

waves would approach a constant value, as the slider and the single crest were far ahead of, and could no longer do work on, the wave packet.

For the ACV1 and AD1 acceleration models, the maximum forward propagating wave potential energy was over two orders of magnitude smaller than the energy in the A1 model. This was because after $t = t_{max}$ the sliders stopped accelerating, and with the waves propagating significantly faster than the slider (Fr = 0.3), the slider's low pressure region did not have a substantial time with which to interact with the leading wave trough. Figure 6.9 plots the forward propagating wave potential energy time history for the ACV1 case. With the energy plotted on linear scales, instead of logarithmic scales, it was seen that after the initial increase in energy, caused by the low pressure surrounding the slider drawing down and increasing the amplitude of the leading trough, the energy peaked and then oscillated around a constant value. This was due to the interaction of the slider's low pressure region and the wave field. With Fr = 0.3, the constant slider speed was less than the propagation speed of the first trough. The leading trough very quickly moved ahead of the slider and the initial increase in energy ceased. Following the leading trough was the second crest. The low pressure region now acted to suppress the amplitude of the crest, leading to a decrease in energy. The second crest soon moved ahead of the slider and the second trough came under the influence of the low pressure. The amplitude of the second trough increased and the energy increased again. This continued as the subsequent crests and troughs moved over the low pressure region and their amplitudes decreased and increased accordingly. As the slider did not decelerate, the low pressure region surrounding the slider did not diminish. This meant the slider's pressure field would affect all waves that propagated past the slider. The two-dimensional wave field for the ACV1 case, presented in Figure 6.10, shows the position of the slider relative to the waves. The waves propagated over the slider's low pressure field resulting in the oscillations in the wave potential energy, as described above. The effect of Froude number on the wave field energy is investigated further in Section 6.5.2.

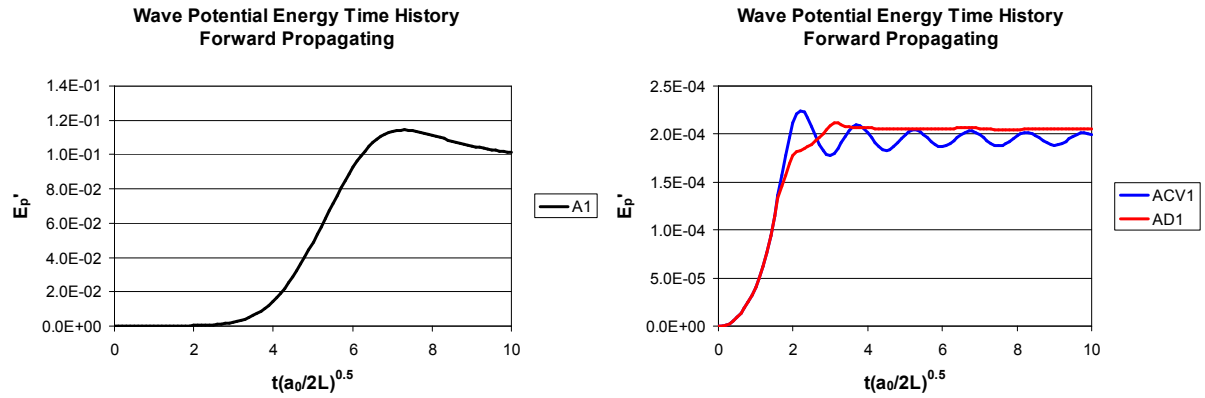

Figure 6.9. Forward propagating wave potential energy time history for A1, ACV1, and AD1 acceleration profiles.

For the AD1 case the wave potential energy increased and tended to a constant value, as plotted in Figure 6.9 with linear scales. As with the A1 and ACV1 cases the initial increase in wave potential energy was due to the slider's pressure field generating the leading trough. At $t = t_{max}$ the slider began to decelerate until its velocity was zero and the low pressure region dissipated. The diminishing velocity prevented any significant suppression or reinforcement of the trailing waves, as observed in the ACV1 case. Therefore, the energy in the forward propagating wave packet tended not to oscillate.

The interaction of the slider's pressure field and the surface waves had a strong influence on the potential energy of the wave field. The speed and position of the slider relative to the waves were the key factors that controlled the growth rate, magnitude, and oscillations in the wave potential energy.

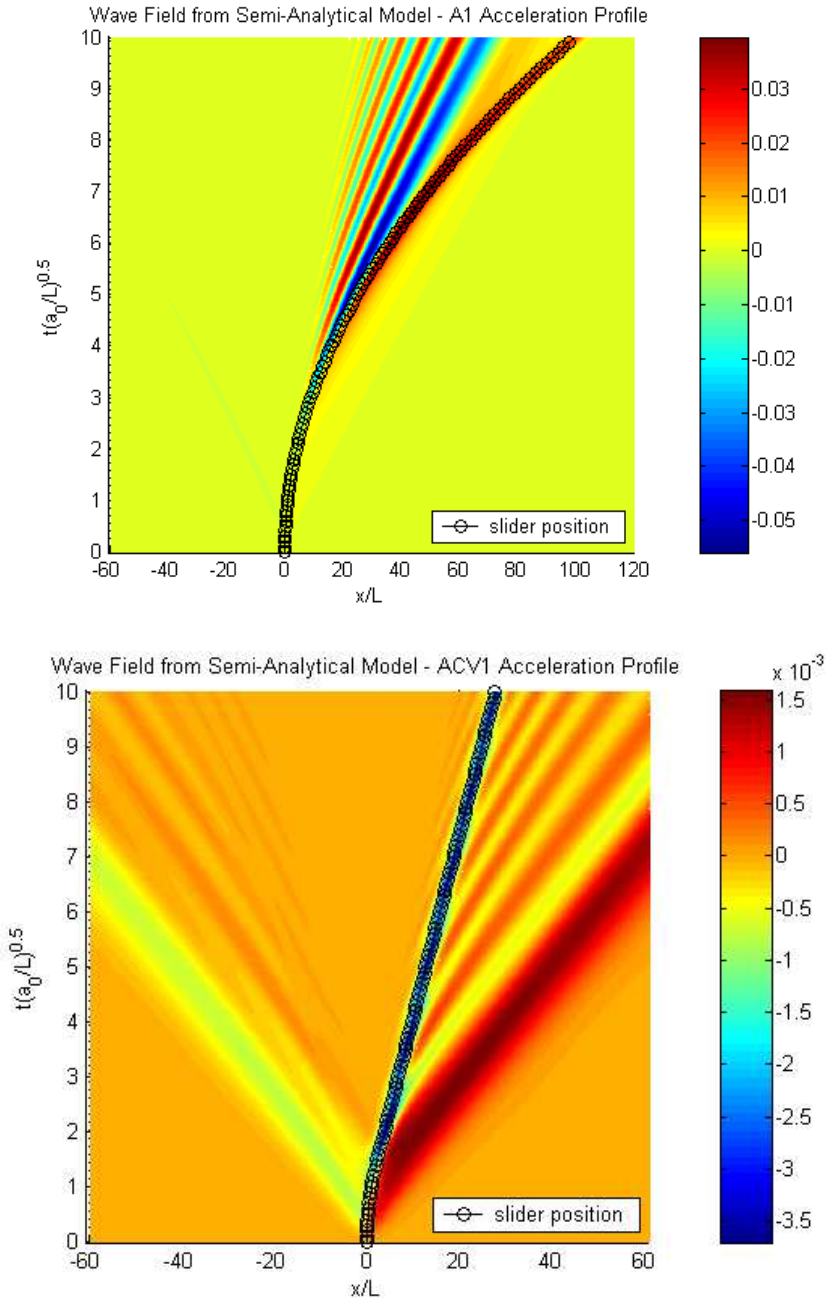

Figure 6.10. 2-dimensional wave field plot of water surface profile time history for the A1 and ACV1 acceleration profile. Red indicates wave crests and blue indicates wave troughs. The position of the slider relative to the wave field is indicated.

6.5.2 Dependence on Froude Number

To explore the effect of Froude number on the wave field energies, five simulations using the ACV1 acceleration model were simulated with varying Froude number. Each case involved the slider undergoing the same initial acceleration, but with each slider accelerating for increasing durations, after which the acceleration instantly became zero and the slider moved at a constant velocity. Therefore, each slider has a different constant velocity. The values of Froude number used in this investigation were Fr = 0.3, 0.5, 0.7, 1.0, and 1.5. The non-dimensional simulation parameters are presented in Table 6.4. For typical underwater landslide events in nature, Froude numbers are nearly always less than 1. Not only did this investigation look at the dependence of wave potential energy for a variety of sub-critical configurations (Fr<1), but it also explored the wave response for resonant (critical, Fr=1) and super-critical configurations (Fr>1).

Table 6.4. Non-dimensional parameters of simulations investigating slide Froude numbers.

acceleration model	τ	λ	ρ	$t_{max}\sqrt{(a_0/2L)}$	$t_{zero}\sqrt{(a_0/2L)}$	Fr	decay model
ACV1	2.0	0.2	0.05	1.5	-	0.3	decay1
ACV1	2.0	0.2	0.05	2.5	-	0.5	decay1
ACV1	2.0	0.2	0.05	3.5	-	0.7	decay1
ACV1	2.0	0.2	0.05	5.0	-	1.0	decay1
ACV1	2.0	0.2	0.05	7.5	-	1.5	decay1

Figure 6.11 plots the time histories of backward and forward propagating wave potential energy for the five different Froude numbers. The initial growth rate of backward propagating wave potential energy was independent of the slider's constant velocity. As explained in Section 6.5.1, the initial energy growth was due to the increase in the amplitude of the trough that formed over the slider. The energy tended to increase and approach what appeared to be a constant value. The magnitude of the maximum backward propagating energy increased as Froude number increased from Fr = 0.3 to Fr = 0.7. The longer periods of acceleration were responsible for the higher energies. However, the maximum energies appeared less sensitive to Froude numbers beyond Fr = 0.7. The acceleration phases of these cases were long enough that the backward propagating trough was fully formed, and further increases in the duration of acceleration would not influence the trough or the backward propagating wave potential energy. Backward propagating waves began moving out of the modelled domain, at x/L = -60, at approximately $t(a_0/L)^{0.5} = 6$.

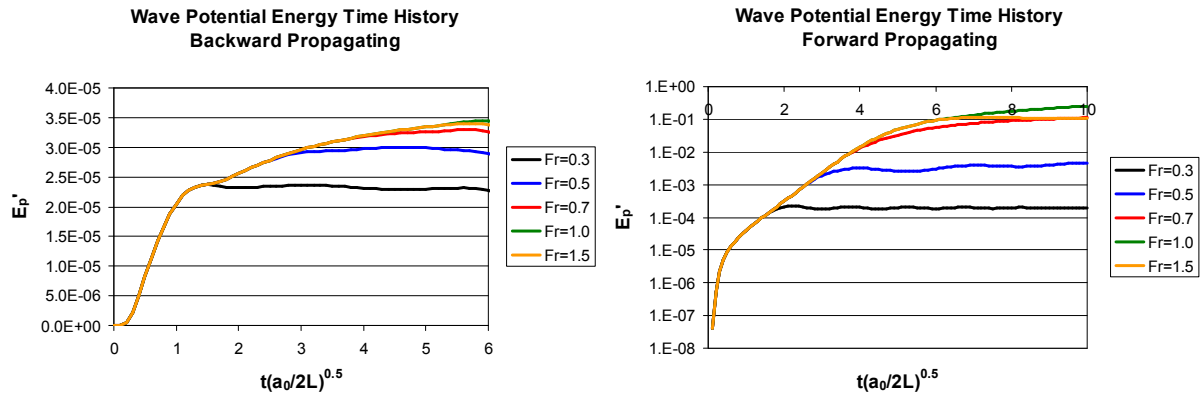

Figure 6.11. Time history of backward and forward propagating wave potential energy for various slide Froude numbers, plotted in semi-logarithmic coordinates.

The potential energy contained in the forward propagating waves was highly dependent on the final velocity of the sliders, as shown in Figure 6.11. When plotted on a semi-logarithmic scale, the forward propagating wave potential energy time histories for the different Froude numbers tended to increase initially. For $Fr \neq 1.0$, the energy increased towards a peak value and then reached a plateau. However there was a significant range in the magnitude of energy in these plateau regions. The magnitude of the maximum energy increased as the Froude number increased from Fr = 0.3 towards Fr = 1.0. This was because higher final velocities, for larger Froude numbers, allowed the slider to keep up with the wave trough for a longer duration. The slider's low pressure region had more time to interact with the leading trough and would therefore resulted in larger leading trough amplitudes and wave potential energies. For Fr = 1.0, the wave potential energy continued increasing with time, and so did not reach a maximum value during the time span of the simulations. When Fr = 1.5, the wave potential energy reached a maximum that was slightly greater than the maximum energy for the Fr = 0.7 case.

Figure 6.12 plots the ratio of maximum wave potential energy to maximum slider kinetic energy, for various slider Froude numbers. It is clear from this figure that the higher energy ratios occurred for Froude numbers close to unity. There was a clear resonant peak for $Fr \approx 1$. Note that the forward propagating waves did not begin moving out of the modelled domain, at x/L = 120, until well after $t(a_0/L)^{0.5} = 10$. The maximum energies were for the duration between $0 \leq t(a_0/L)^{0.5} \leq 10.0$. As the slider wave potential energy was still increasing beyond $t(a_0/L)^{0.5} = 10.0$ for Fr = 1, the potential to kinetic energy ratio was expected to be greater than the value given in Figure 6.12. Although the maximum wave potential energies for the Fr = 0.7 and 1.5 cases were similar, as shown in Figure 6.11, the higher maximum slider kinetic energy for the Fr = 1.5 case meant the efficiency with which slider kinetic energy was converted to wave potential energy was lower. The relationship between dimensional and non-dimensional ratios of wave potential energy to slider kinetic energy is given by Equation 6.10l.

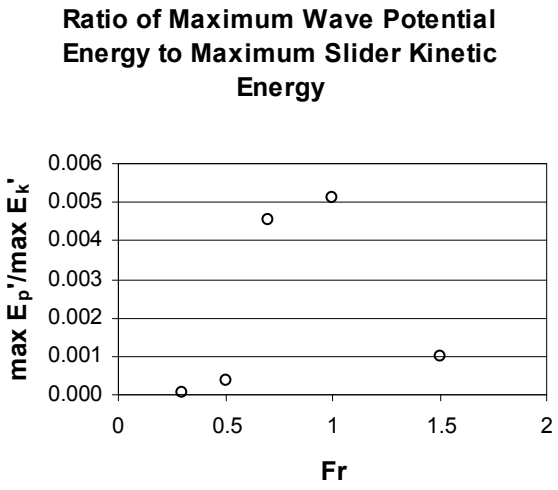

Figure 6.12. Ratio of maximum wave potential energy to maximum slider kinetic energy, for various slide Froude numbers.

The forward propagating wave potential energy for the Fr = 0.3 case is plotted in Figure 6.9 (ACV1 case). Section 6.5.1 describes how the oscillations in energy were caused by the suppression of wave crests and the reinforcement of wave troughs, as the wave field propagated past the slider's low pressure region, for this situation. The interaction of the slider's pressure field and the wave field generated a similarly oscillating forward propagating wave potential energy time history for the Fr = 0.5 case.

The case with Fr = 0.7 and 1.0 illustrated resonance-like behaviour, where the forward propagating wave potential energy continually increased with time. The low pressure around the slider caused the formation of the first trough, leading to an initial increase in the wave potential energy. The slider stopped accelerating and continued at a constant speed just as the region of lowest pressure surrounding the slider coincided with the leading wave trough. For the Fr = 1.0 case, the slider speed was similar to the propagation speed of the first trough. Therefore the low pressure continued to increase the amplitude of the leading trough, and increased the wave potential energy. However, for the Fr = 0.7 case, the slider slowly got left behind the leading trough, so the energy growth slowly diminished. The wave potential energy time histories for the Fr = 0.7 and 1.0 cases are shown in Figure 6.13. Provided the phase speed of the first trough and the slider speed remained similar for a substantial length of time, the energy would continue to increase. However, there is a limit to this, as the trough amplitude can only increase as much as the finite water depth will allow. The two-dimensional wave field in Figure 6.14 shows the position of the slider relative to the waves for the case of Fr = 1.0. The tracking of the slider with the leading trough is clearly seen.

For the case with Fr > 1, the initial increase in energy was also due to the low pressure surrounding the slider drawing down the water surface to form the first trough. The continued presence of the low pressure source below the trough caused its amplitude to increase. Similarly to the indefinite constant acceleration profile investigated in Section 6.5.1, the longer duration of positive acceleration when Fr > 1 caused the slider to reach a speed faster than the trough and energy could no longer be input into the first trough. The wave potential energy decreased slightly as the low pressure region moved below the leading crest, acting to suppress its amplitude. This is illustrated in the wave potential energy time history shown in Figure 6.13. The slider's speed was significantly greater than the phase speed of the wave packet, so as soon as the slider moved ahead of the wave packet entirely the wave potential energy stabilised at a constant value. The two-dimensional wave field in Figure 6.14 shows the position of the slider relative to the waves. This figure shows how the slider first encountered the leading trough and crest before moving ahead of the wave packet, giving rise to the increase and slight decrease in wave potential energy. A single crest was observed to track with the slider as it moved ahead of the main wave packet. Similarly to the A1 acceleration case investigated in Section 6.5.1, the crest was analogous to the flow over a bottom disturbance in a supercritical open channel flow. This crest was simply a result of energy conservation as the slider moved through the stationary fluid. The constant velocity of the slider meant the amplitude, and potential energy, of the single crest was constant. Irrespective of this, the potential energy within the main packet of waves approached a constant value, as explained in Section 6.5.1.

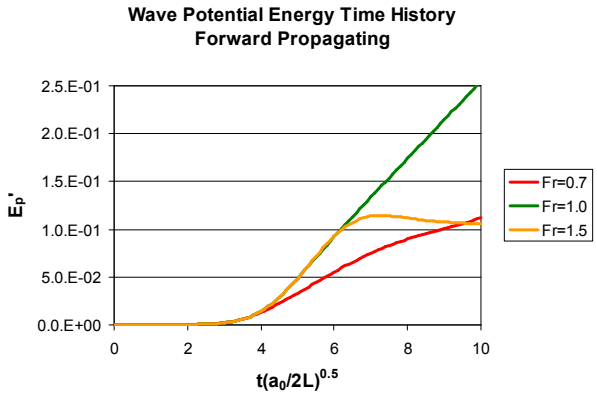

Figure 6.13. Time history of forward propagating wave potential energy for Fr=0.7, 1.0, and 1.5, plotted in linear coordinates.

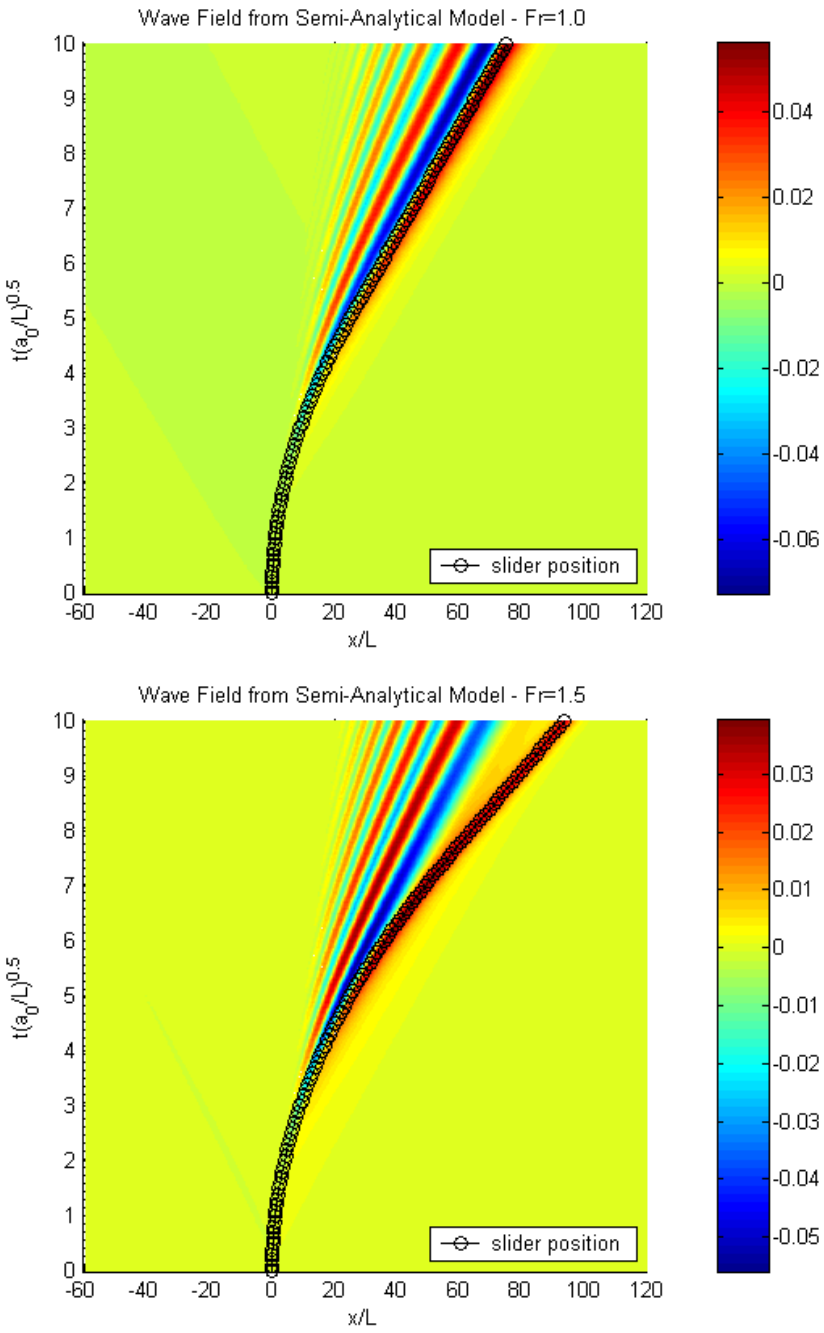

Figure 6.14. 2-dimensional wave field plots of water surface profile time history for Fr=1.0 and Fr=1.5. Red indicates wave crests and blue indicates wave troughs. The position of the slider relative to the wave field is indicated.

6.5.3 Dependence on Parameter λ

The dependence of the wave solution on the non-dimensional parameter, λ, was investigated by running five simulations for different values of λ. As an indefinite constant acceleration was unrealistic of real events, a constant acceleration followed by a constant velocity was used as the slider's acceleration profile. The effect of slider decelerations is given in Section 6.5.1. The

investigation in Section 6.5.2 shows that the energy in the wave field is highly sensitive to Froude number. Therefore, the time of maximum velocity, t_{max}, was modified for each value of λ to maintain a constant Froude number. As the initial acceleration increased, and hence λ increased, a shorter duration of acceleration was required to maintain the same Froude number. A value of Fr = 0.5 was chosen for this investigation as it avoided the complexity of resonance. The values of λ used were λ = 0.05, 0.10, 0.20, 0.30, and 0.50. The non-dimensional parameters used in the simulations are presented in Table 6.5. Note that λ^2 is the ratio of initial slider acceleration to gravitational acceleration, so, assuming gravity to be a constant, an increase in λ corresponds to an increase in slider acceleration. Time was non-dimensionalised by a_0, so changing values of λ changed the time scale also.

Table 6.5. Non-dimensional parameters of simulations investigating the solution dependence on λ.

acceleration model	τ	λ	ρ	$t_{max}\sqrt{(a_0/2L)}$	$t_{zero}\sqrt{(a_0/2L)}$	decay model
ACV1	2.0	0.05	0.05	10.000	-	decay1
ACV1	2.0	0.10	0.05	5.000	-	decay1
ACV1	2.0	0.20	0.05	2.500	-	decay1
ACV1	2.0	0.30	0.05	1.667	-	decay1
ACV1	2.0	0.50	0.05	1.000	-	decay1

The slider velocities, and hence the slider kinetic energies, were governed by t_{max}, as given by Equation 6.47. Since a different value of t_{max} was required to maintain the same Froude number for each value of λ, each simulation resulted in different non-dimensional slider kinetic energy. As such, Figure 6.15 plots the ratio of maximum backward and forward propagating wave potential energy to maximum slider kinetic energy for various values of λ. A power law curve fit to the data produced the expression given in Equation 6.61 for the backward propagating energy ratio, and Equation 6.62 for the forward propagating energy ratio. These curve fits showed that the backward propagating and forward propagating energy ratios tended to increase as $\lambda^{4.4}$ and $\lambda^{2.4}$ respectively. The magnitude of the exponents indicated a very strong dependence on initial slider acceleration. Therefore, without appropriate specification of the initial acceleration in numerical models the wave energy cannot be simulated accurately. The backward propagating energy had a stronger dependence on slider acceleration than the forward propagating energy. The relationship between dimensional and non-dimensional ratios of wave potential energy to slider kinetic energy was given by Equation 6.10l.

At the limit as $\lambda \rightarrow 0$, and a_0 correspondingly tended to zero, it was expected that no waves would form and therefore there would be no energy propagated backward or forward. The wave potential energy time history for a slider with an ACV1 acceleration profile and Fr < 1 is described further in Section 6.5.1 and 6.5.2.

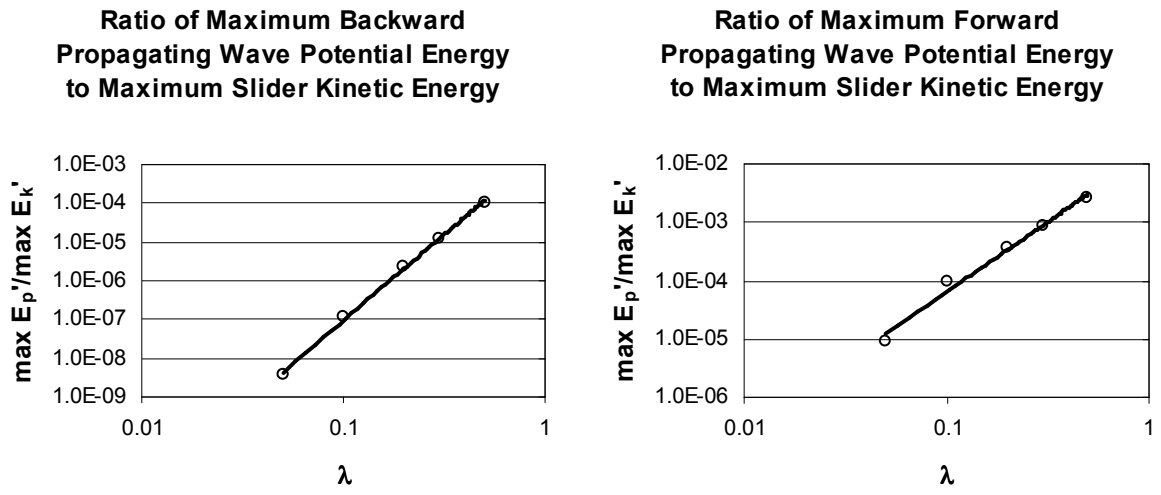

Figure 6.15. Ratio of maximum backward and forward propagating wave potential energy to maximum slider kinetic energy, for various values of λ.

For the backward propagating energy, the power law curve fit results in

$$\frac{\max E_p'}{\max E_k'} = 0.00257\lambda^{4.433} \qquad r^2 = 0.998 \tag{6.61}$$

and for the forward propagating energy, the power law curve fit results in

$$\frac{\max E_p'}{\max E_k'} = 0.0162\lambda^{2.404} \qquad r^2 = 0.987 \tag{6.62}$$

6.5.4 Dependence on Parameter τ

The dependence of the wave solution on the non-dimensional parameter, τ, was investigated by running simulations for five different values of τ, whilst keeping all other parameters constant. The values of τ used were τ = 0.50, 1.0, 2.0, 5.0, and 10.0. The maximum wave potential energy as a function of τ was determined for three values of λ. The non-dimensional parameters used in the simulation are presented in Table 6.6. Similarly to the investigation into the dependence of λ in Section 6.5.3, a constant acceleration followed by a constant velocity was used as the slider's acceleration profile. The time of maximum velocity, t_{max}, was modified for each value of τ and λ to maintain a constant Froude number of Fr = 0.5, as is done in Section 6.5.3.

Table 6.6. Non-dimensional parameters for simulations investigating the solution dependence on τ.

acceleration model	τ	λ	ρ	$t_{max}\sqrt{(a_0/2L)}$	$t_{zero}\sqrt{(a_0/2L)}$	decay model
ACV1	0.50	0.1	0.05	2.500	-	decay1
ACV1	1.0	0.1	0.05	5.536	-	decay1
ACV1	2.0	0.1	0.05	5.000	-	decay1
ACV1	5.0	0.1	0.05	7.906	-	decay1
ACV1	10.0	0.1	0.05	11.180	-	decay1
ACV1	0.50	0.2	0.05	1.250	-	decay1
ACV1	1.0	0.2	0.05	1.768	-	decay1
ACV1	2.0	0.2	0.05	2.500	-	decay1
ACV1	5.0	0.2	0.05	3.953	-	decay1
ACV1	10.0	0.2	0.05	5.590	-	decay1
ACV1	0.50	0.3	0.05	0.833	-	decay1
ACV1	1.0	0.3	0.05	1.179	-	decay1
ACV1	2.0	0.3	0.05	1.667	-	decay1
ACV1	5.0	0.3	0.05	2.635	-	decay1
ACV1	10.0	0.3	0.05	3.727	-	decay1

Figure 6.16 plots the ratio of maximum backward and forward propagating wave potential energy to maximum slider kinetic energy as a function of τ. The backward propagating energy ratio was divided by $\lambda^{4.433}$, and the forward propagating energy ratio was divided by $\lambda^{2.404}$, as shown to be appropriate in the investigation into the dependence of wave potential energy on λ in Section 6.5.3. The maximum backward and forward propagating potential energy had a strong trend towards increasing for smaller values of τ. The parameter τ is the ratio of the water depth to the slider half-length. Therefore, as τ increased, and all other non-dimensional parameters were kept constant, the water depth increased relative to the length of the slider. Figure 6.16 illustrates how the ratio of wave potential energy to slider kinetic energy decreased as τ increased. At the limit as $\tau \to \infty$ the generation of waves was not expected. As the water depth increased, for a fixed slider length, the pressure field surrounding the slider would become less able to influence the free surface and generate waves.

Least squares power law curve fits to the maximum backward and forward propagating energy ratios led to the relationships given in Equations 6.63 and 6.64 respectively. The curve fit in Equation 6.63 indicated that the ratio of maximum backward propagating wave potential energy to maximum slider kinetic energy was related by a $\lambda^{4.433}\tau^{-2.194}$ power law. The curve fit in Equations 6.64 indicated the relationship for the maximum forward propagating energy was $\lambda^{2.404}\tau^{-1.612}$. However, the least squares power law curve fit of the forward propagating energy data was not as close as the fit for the backward propagating energy. This suggested that the dependence of wave energy on the initial slider acceleration was similar to the dependence on water depth. Note that the maximum forward propagating energy was at least one order of magnitude larger than the maximum backward propagating energy.

The collapse of the data in Figure 6.16 suggested that the effects of τ and λ were decoupled. However, this investigation was based on a single Froude number (Fr = 0.5) and an ACV1 acceleration profile. The investigation in Section 6.5.2 shows that there is some Froude number dependence of the λ term in Equations 6.63 and 6.64.

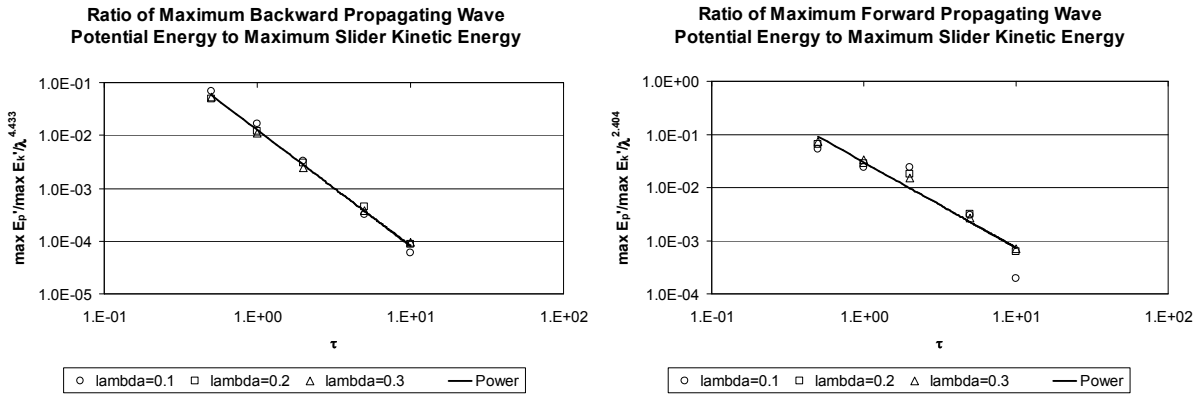

Figure 6.16. Ratio of maximum wave potential energy to maximum slider kinetic energy as a function of τ and λ. Power law fits to the data are also shown.

For backward propagating wave potential energy

$$\frac{max\ E'_{p,backward}}{max\ E'_k} = 0.0126\lambda^{4.433}\tau^{-2.194} \qquad r^2 = 0.995 \tag{6.63}$$

and for forward propagating wave potential energy

$$\frac{max\ E'_{p,forward}}{max\ E'_k} = 0.0297\lambda^{2.404}\tau^{-1.612} \qquad r^2 = 0.920 \tag{6.64}$$

6.5.5 Slider Deceleration as a Run-up Generation Mechanism

To confirm that the maximum wave run-up observed in the experiments was due to the deceleration of the landslide as it passed over the base of the slope, the model was used to generate upstream propagating waves by varying the magnitude of the deceleration. Eight simulations were performed, with varying levels of deceleration. The change in acceleration occurred at the same time in each case. Decreasing the time the slider took to return to zero velocity, t_{zero}, generated larger magnitude decelerations. The simulation parameters are presented in Table 6.7. The chosen values of t_{zero} produce values for the expression $d^2x_0/dt^2(t_{max}<t<t_{zero})/a_0$ of 1.0, 0, -0.25, -0.5, -1.0, -2.0, -4.0, and –8.0, respectively. The two cases in which $d^2x_0/dt^2(t_{max}<t<t_{zero})/a_0$ = 1.0 and 0 were special cases in which there was no deceleration.

Table 6.7. Non-dimensional parameters of simulations investigating slider deceleration as a run-up generation mechanism.

acceleration model	τ	λ	ρ	$t_{max}\sqrt{(a_0/2L)}$	$t_{zero}\sqrt{(a_0/2L)}$	$d^2x_0/dt^2(t_{max}<t<t_{zero})/a_0$	decay model
A1	2.0	0.4	0.05	2.50	-	1.00	decay1
ACV1	2.0	0.4	0.05	2.50	-	0	decay1
AD1	2.0	0.4	0.05	2.50	12.5000	-0.25	decay1
AD1	2.0	0.4	0.05	2.50	7.5000	-0.50	decay1
AD1	2.0	0.4	0.05	2.50	5.0000	-1.00	decay1
AD1	2.0	0.4	0.05	2.50	3.7500	-2.00	decay1
AD1	2.0	0.4	0.05	2.50	3.1250	-4.00	decay1
AD1	2.0	0.4	0.05	2.50	2.8125	-8.00	decay1

Figure 6.17 plots the maximum amplitude of the leading backward propagating crest and trough for various slider deceleration magnitudes. The maximum amplitude of the wave crests that propagated behind the slider, in the negative-x direction, was directly related to the magnitude of the slider deceleration. The larger the deceleration, the larger the maximum amplitude of the backward propagating crests. The maximum amplitude of the leading upstream-propagating troughs, however, was independent of the deceleration magnitude. If there were a nearby shore to the left of the origin, it would first observe a draw down, whose magnitude depended on the initial movement of the slider. The magnitude of any subsequent run-up would be directly related to the magnitude of the slider deceleration. In the simulations the upstream propagating wave crest was observed to disperse into a train of waves. This was not observed in the experiments, as there was not enough time for the wave to disperse before it encountered the shore.

Due to the simplicity of the acceleration model, the effect of the abruptness of the change in acceleration was not investigated. However, it is speculated that the amplitude of the backward propagating crest is dependent on both the change in acceleration and the rate at which the change occurs. It is expected that abrupt changes in acceleration will produce larger crests than if the acceleration changes by the same amount but over a longer duration.

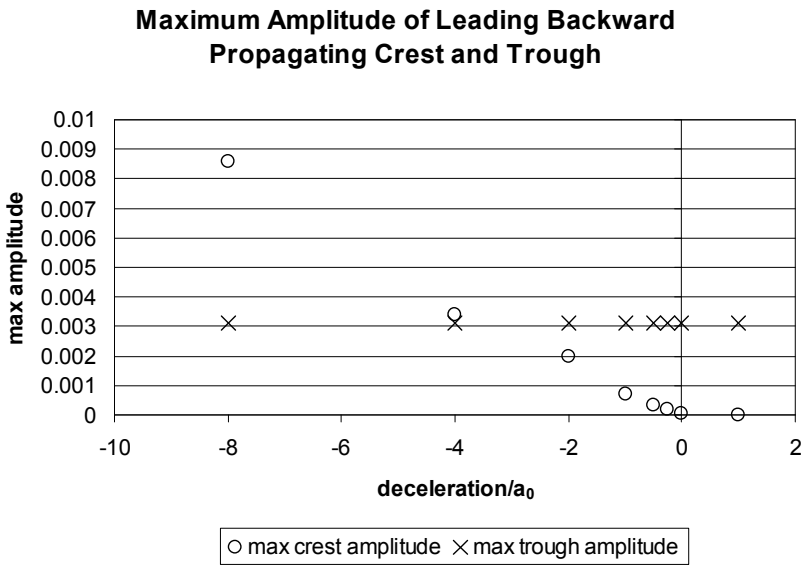

Figure 6.17. Maximum amplitude of the leading backward propagating crest and trough for various slider deceleration magnitudes.

6.6 Comparison with Experimental Data

The semi-analytical model was used to simulate one of the experimental configurations and the results were compared with experimental data. The aim of this brief investigation was to see if a constant depth model could be used to simulate a changing depth system. Described here is one approach to modelling a variable depth in a constant depth model. The SG5_IS5 configuration was simulated here. The shallow initial submergence of this case subjected the slider to the greatest change in local water depth as it slid down the slope. The performance of the semi-analytical model in predicting the wave response for other configurations was similar. The non-dimensional parameters were determined for the SG5_IS5 experimental test configuration, and these are presented in Table 6.8. A thorough description of the calculation of the AD1 acceleration profile parameters, a_0, t_{max},, and t_{zero}, is presented in Section 7.6.1. The experimental data was non-dimensionalised using the scheme outlined in Section 6.2.3. Note that the x coordinate in the experimental data was offset so the origin was centred above the initial landslide centre of mass position instead of at the original shoreline. This was to ensure consistency with the spatial domain definition of the model.

The τ parameter is the ratio of the water depth to the slider's half-length. The value for τ is not defined in a changing depth system. As a first try, a value of τ based on the constant water depth downstream of the slope was used. For the SG5_IS5 configuration, this corresponded to $\tau = 1.74$. The results below show that the wave heights generated by this approach were under-predicted. A τ value based on the initial water depth above the slider produced wave amplitudes significantly larger than the measured amplitudes. A τ value based on the average of the constant and initial water depths

also over-predicted the wave amplitudes. Another simulation was performed with τ based on the average of the constant and initial water depths, but a decaying slider thickness model was used. For this situation, $\tau = 1.02$.

Section 6.2.6 describes the decay2 model, which reduces the thickness of the slider with time. This represents cases in which the deposition of landslide material on the slope causes the slide to decrease in height. In this comparison with experimental data, this decay model mimicked the changing depth of the experimental configuration in the constant depth model. A reduction in the ratio of slider thickness to the constant water depth in the model corresponded to an increase in the local water depth relative to the constant slider thickness as the landslide moved down the slope during the experiments. The decay model parameters are presented in Table 6.8. An increasing rate of thickness reduction occurred between $0 \leq t \leq t_{max}$ and a decreasing rate of thickness reduction occurred between $t_{max} \leq t \leq t_{zero}$. The ratio of the initial to final slider thickness, h_b/h_1, was the same as the ratio of the local water depth of the initial landslide position to the constant water depth in the experimental configuration. The slider tended to a constant thickness to represent the landslide running out along the horizontal floor of the tank, during which there was no change in the ratio of landslide thickness to water depth.

Table 6.8. Non-dimensional parameters of simulations of the SG5_IS5 experimental configuration.

τ	λ	ρ	acceleration model	$t_{max}\sqrt{(a_0/L)}$	$t_{zero}\sqrt{(a_0/L)}$	decay model	h_1	γ	ε
1.74	0.3882	0.0598	AD1	1.9119	9.8428	decay1	0	0	2
1.02	0.3882	0.0598	AD1	1.9119	9.8428	decay2	0.1733	0.01	4

Figure 6.18 plots simulated and experimental free surface profiles at $t(a_0/L)^{0.5} = 3$, 6 and 9 for the SG5_IS5 combination. For this configuration, a slider with $\tau = 1.74$ without decaying thickness and a slider with $\tau = 1.02$ with decaying thickness was used. The semi-analytical model under predicted the wave crest and trough amplitudes for the $\tau = 1.74$ case. The location of the leading crest was modelled well at all three times, but the phase speeds of the trailing waves was slightly too fast, leading to a small offset of the waves relative to the measured waves. The shape of the leading waves was modelled well, and the wavelengths were similar. For the $\tau = 1.02$ case, the amplitudes of the leading crest and trough at $t(a_0/L)^{0.5} = 3$ were modelled well. However, as time progressed the wave amplitudes of the model became dissimilar to the measured amplitudes. At $t(a_0/L)^{0.5} = 6$ the predicted leading crest had not travelled as far as the measured crest, and by $t(a_0/L)^{0.5} = 9$ the leading two crests and troughs were well behind the respective measured waves. For both simulations, the number of waves generated in the wave train was significantly less in the model. It was likely the lack of slope was preventing the dispersion of the waves from being accurately modelled. The absence of the slope

in the model meant the wave field near the shore was not well predicted, as wave run-up and run-down was not possible in a constant depth model.

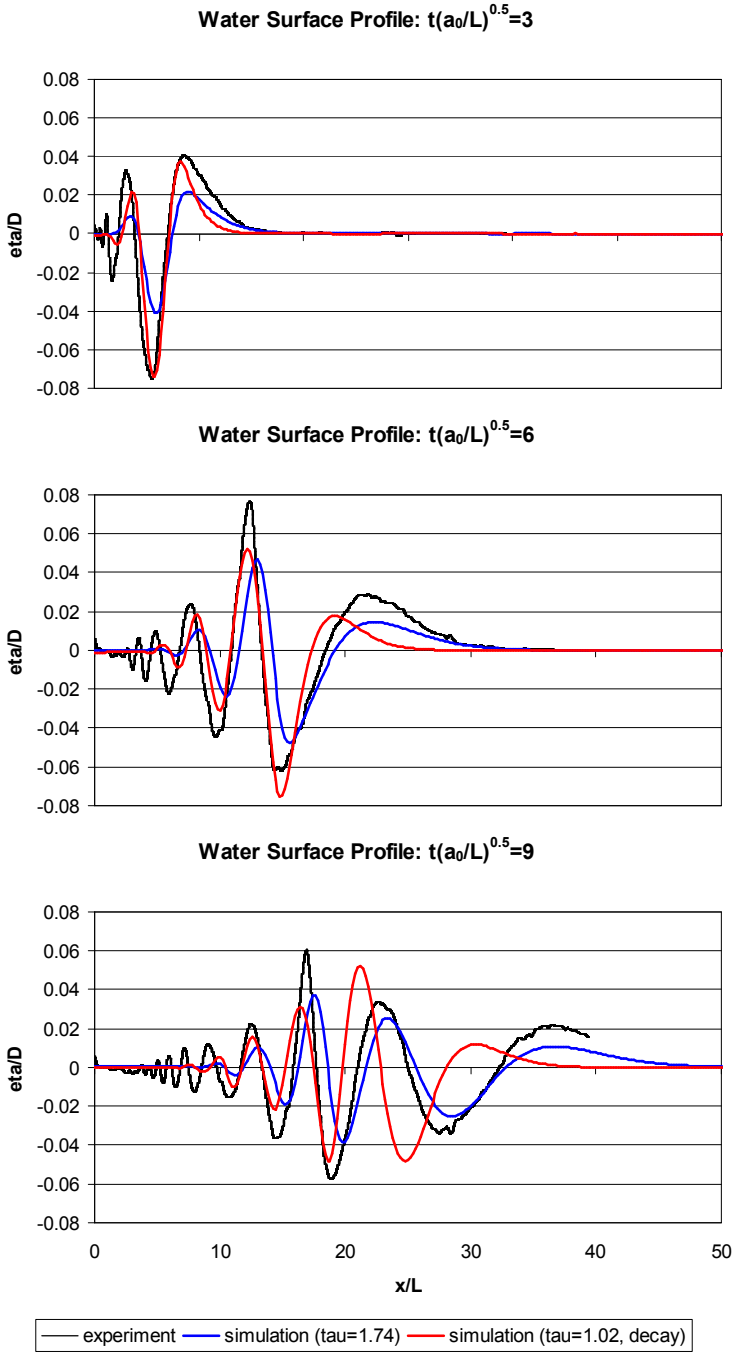

Figure 6.18. Simulated and measured water surface profiles at $t(a_0/L)^{0.5}$ = 3, 6 and 9 for the SG5_IS5 combination.

Figure 6.19 plots simulated and experimental time histories at x/L = 10 and 20 for the SG5_IS5 combination. The arrival times of the wave train and the first crest were modelled well for the τ = 1.74 case. For the τ = 1.02 case, the arrival of the wave packet and the leading crest were not well modelled at x/L = 10. However, the subsequent wave arrival times were predicted well. By x/L = 20, the arrival times of the wave packet and most of the waves were under-predicted. Apart from the leading crest, the predicted wave periods were similar to the measured periods.

The spatial variation of maximum crest and trough amplitudes is plotted in Figure 6.20. The maximum wave amplitude was under-predicted everywhere for the τ = 1.74 case. For the τ = 1.02 case, the maximum trough amplitudes were modelled well, but the crest amplitudes were under-predicted. The growth of the crest and trough amplitudes near x/L = 0 were not modelled well for both cases. The lack of slope was likely to be the cause of the poor predictions of the measured wave amplitudes near the shore, and prevented any wave run-up of run-down from being modelled.

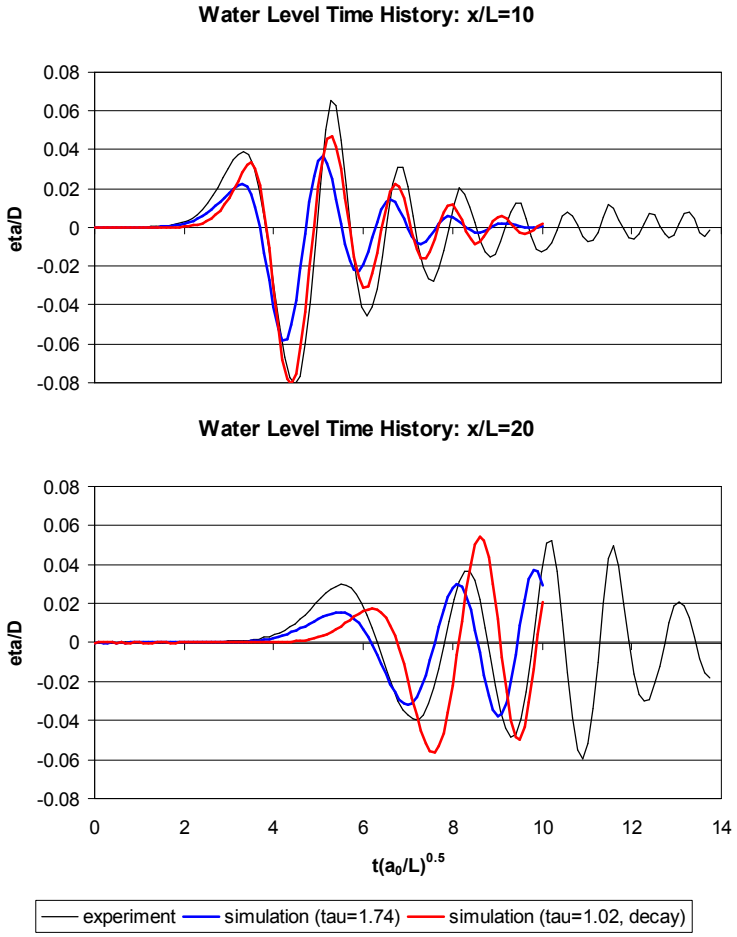

Figure 6.19. Simulated and measured water level time histories at x/L = 10 and 20 for the SG5_IS5 combination.

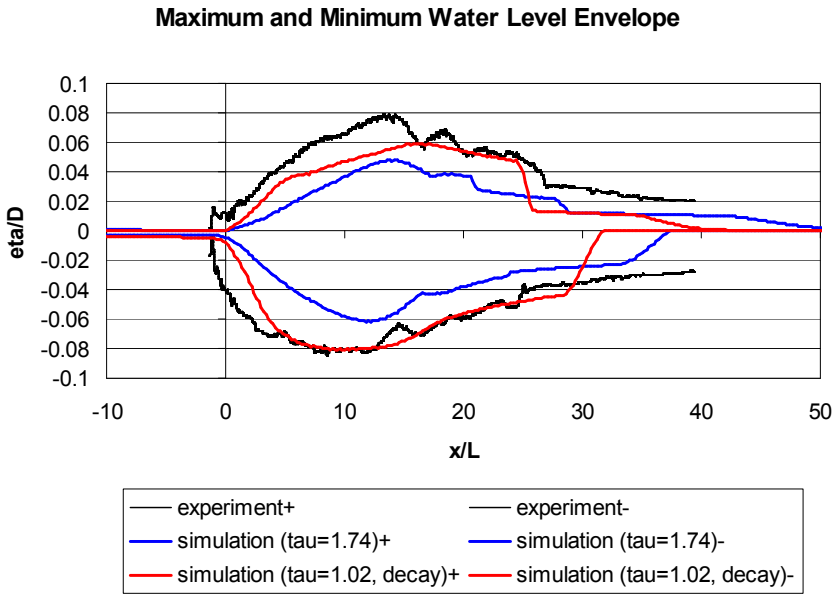

Figure 6.20. Spatial distribution of maximum crest and trough amplitudes for the SG5_IS5 configuration.

Figure 6.21 plots simulated and measured wave potential energy time histories for the SG5_IS5 combination. The under-prediction of the water levels meant the estimated wave potential energies were also underestimated. The model predicted only 40% of the maximum energy for the $\tau = 1.74$ case, and 63% for the $\tau = 1.02$ case. The initial energy growth was also not well modelled, particularly for the simulation with $\tau = 1.74$. For the $\tau = 1.02$ case, the energy growth rate between $1.5 < t(a_0/L)^{0.5} < 3$ was similar to the measured energy growth. Time of maximum wave potential energy was over-predicted by 14% and 29% for the $\tau = 1.74$ and $\tau = 1.02$ cases respectively.

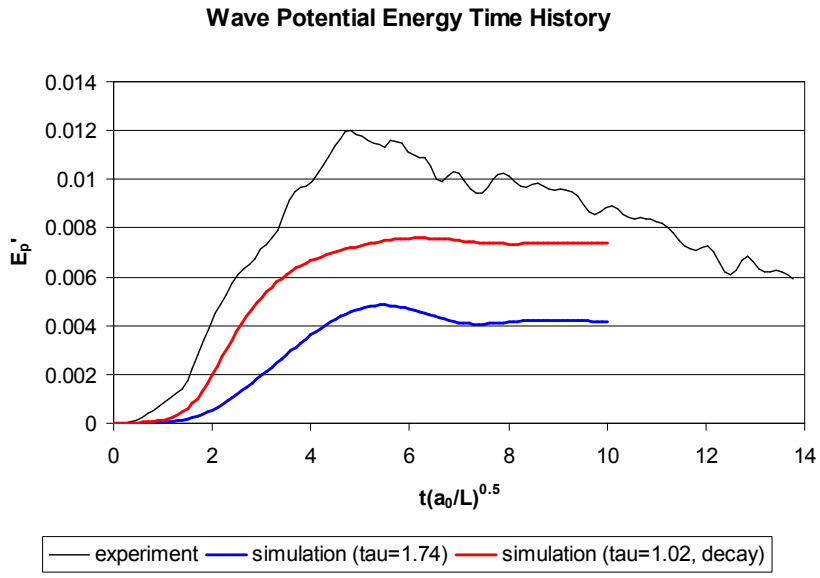

Figure 6.21. Simulated and measured wave potential energy time history for the SG5_IS5 combination.

Generally, the semi-analytical model, simulating a constant depth domain, struggled to model the changing depth configuration of the experiments. Only some of the bulk qualities of the wave field, measured during the experiments, could be predicted. The spatial distribution of the maximum trough amplitude was modelled well with $\tau = 1.02$ and a decaying slider thickness. However, the wave phase speeds, periods, and wavelengths were not predicted accurately for this case, with the $\tau = 1.74$ case performing better in this regard. The $\tau = 1.74$ case also predicted the arrival time of the wave packet well, but substantially under-predicted the wave amplitudes. Generally, the model predicted significantly fewer waves in the wave train. It is likely the lack of slope was preventing the dispersion of the waves from being accurately modelled. Also, the absence of the slope in the model meant the waves near the shore were not well predicted, as wave shoaling, run-up, and run-down were not possible in a constant depth model.

6.7 Model Discussion and Summary

The analysis of a moving submerged object in a simplified and idealised arrangement of the semi-analytical model allowed a variety of phenomena observed in the experiments to be explored. The variations in the growth, magnitude, and decay of energy as a function of time was explained by the interaction of the pressure distribution surrounding the moving slider with the wave field, in particular, the first crest and trough. This phenomenon, easily observed in the model and detailed in Section 6.5.1 for a variety of acceleration profiles, helped explain the variety of energy time histories measured during the experiments. If the low pressure region surrounding the slider coincided with a wave trough, then the trough deepened and the wave potential energy increased. If the low pressure was below a wave crest, then it tended to suppress the crest and cause the energy to decrease.

For a landslide with indefinite constant acceleration, the implication was that the slider would eventually overtake the wave train. Once this happened, the pressure distribution around the landslide would no longer do work on the wave field and the energy would stabilise to a constant amount (assuming no energy losses). However, this situation was considered not realistic for real events, as it allowed infinite slider kinetic energies. A landslide that underwent a constant acceleration followed by a constant deceleration was considered a more realistic situation. This acceleration profile could occur for a landslide that did not reach terminal velocity before decelerating, possibly due to encountering a change in slope topography. The reduced extent of movement of the landslide would limit the availability of landslide kinetic energy to be input into the wave field. The deceleration of the landslide would also generate backward propagating wave crests, which could pose a possible risk to development upslope from the slide.

A slider that accelerated up to a constant velocity was also investigated. This could possibly occur for a landslide that ran out on a long and constant slope. This scenario, with a constantly moving slider interacting with the wave field was investigated for various magnitudes of constant velocity. The case in which the constant slider speed and the wave propagation speeds were similar, or when the Froude number was close to unity, was investigated numerically in Section 6.5.2. Slides with Froude numbers closest to unity converted substantially more energy into forward propagating wave potential energy than slides with a Froude number dissimilar to unity. When $Fr \approx 1$, a resonance effect existed and the wave potential energy continued to grow with time. However, for typical underwater landslide events in nature, Froude numbers are nearly always less than 1. The backward propagating wave potential energy was not as sensitive to Froude number. For $Fr < 1$, the wave packet propagated forward at a speed greater than that of the slider. The leading trough very quickly moved ahead of the slider and the increase in the amplitude of the trough, and the growth in the wave potential energy, ceased. The energy oscillated as the low pressure distribution surrounding the slider encountered the trailing waves and suppressed the wave crests and reinforced the wave troughs.

The investigation of the dependence of the solution on the non-dimensional parameters λ and τ was described in Section 6.5.3 and 6.5.4 respectively. Smaller values of λ tended to reduce the magnitude of the backward and forward propagating wave potential energies. For a slider with an infinitesimally small value of λ, and hence an infinitesimally small initial acceleration, it was expected that no waves would form. Therefore, the wave potential energy for this case would tend to zero. For the parameter range used in Section 6.5.3, the ratio of maximum backward and forward propagating wave potential energy to maximum slider kinetic energy tended to increase as $\lambda^{4.4}$ and $\lambda^{2.4}$ respectively. The backward propagating energy had a stronger dependence on slider acceleration than the forward propagating energy. The magnitude of the exponents indicated a very strong dependence of wave energy on the initial slider acceleration, and highlighted the importance of the appropriate specification of the initial acceleration in numerical simulations.

Increasing τ has the effect of decreasing the wave potential energy. This was because an increase in τ corresponded to an increase in water depth relative to the slider length, assuming all other parameters remained constant. The greater water depth reduced the ability of the slider's pressure field to penetrate to the free surface to generate waves. For the parameter range used in Section 6.5.4, the ratio of maximum backward propagating wave potential energy to maximum slider kinetic energy was related by a $\lambda^{4.433}\tau^{-2.194}$ power law. The relationship for the maximum forward propagating energy was $\lambda^{2.404}\tau^{-1.612}$. This suggested that the dependence of wave energy on the initial slider acceleration was similar to the dependence on water depth. This investigation, based on a single Froude number ($Fr = 0.5$) and an ACV1 acceleration profile, suggested that the effects of τ and λ were decoupled.

The semi-analytical model was used in Section 6.5.5 with a variety of slider decelerations. It showed that the abrupt deceleration, as experienced by the landslide in the experiments as it reached the base of the slope, was capable of generating the necessary upstream propagating wave crest to generate the run-up observed at the shore. The magnitude of the upstream propagating waves was dependent on the magnitude of the change in acceleration. Although not investigated, it was speculated that the greater the abruptness of the change in acceleration, the larger the size of the backward propagating wave crest. This has important implications to the hazard assessment of actual events. Theoretically a landslide that decelerated gradually would not produce any significant onshore wave run-up. However, this is based on two-dimensional configurations. Three-dimensional slides, described in Chapter 3, are capable of generating significant wave run-up when the lateral flows around landslides converge behind the landslide.

As shown by the comparison of the semi-analytical model results with experimental data for the SG5_IS5 configuration in Section 6.6, the constant depth model struggled to model the changing depth configuration of the experiments. Only some of the bulk qualities of the wave field could be predicted with adequate accuracy. The $\tau = 1.02$ case with decaying slider thickness modelled the spatial distribution of the maximum trough amplitude well, and the $\tau = 1.74$ case with constant slider thickness predicted the wave phase speeds, periods, and wavelengths. The lack of slope prevented the dispersion of the waves from being accurately modelled. Also, the absence of the slope in the model meant the waves near the shore were not well predicted.

Chapter 7: Boundary Element Method Model

One of the main objectives of the experimental modelling of underwater landslide induced tsunami is to generate a comprehensive dataset suitable for comparisons with, and validation of, numerical models. With increasingly easy access to computational power, numerical modelling of wave generation processes is becoming a common practice, although adequate validation of these models is requisite. Presented here are details of a Boundary Element Method (BEM) numerical model used to simulate the underwater landslide induced wave generation process. Results from the model are compared to the data from the experiments.

7.1 Introduction

Similar to the semi-analytical model presented in Chapter 6 the BEM model described herein, developed by Dr Roger Nokes at the University of Canterbury, was based on inviscid and irrotational flow theory. Wake generation was not modelled. The linear approximation was also invoked and applied to the free surface and the bottom boundary conditions. Considering that this model is currently unpublished, details of the model formulation and solution technique are provided, based on the notes of the model's author.

7.2 BEM Model Description

7.2.1 Model Domain

The spatial domain within the BEM model closely matched that of the experimental configuration, with the actual smooth transition curve used in the experiments bridging between the uniform slope and horizontal floor. Other configurations were possible, including an abrupt transition from slope to floor, a semi-infinite slope, and a constant depth domain. Only the experimental configuration was used during this comparative study with the experimental results, although the constant depth domain was used to compare the BEM model's behaviour to that of the semi-analytical model described in Chapter 6.

A schematic diagram of the BEM model domain is shown in Figure 7.1. The origin is at the top left of the diagram, on the axis of symmetry, and extends as far as x_r to the right. As the flow domain is finite, waves that reach the boundary at x_r will reflect. A value of x_r is chosen such that waves do not reach x_r for the duration of the simulation. The small gap between the top of the slope and the still water surface prevents solution singularities as waves propagate into the wedge at the top of the slope. Essentially the coordinate origin has been inset slightly to the right of the true shoreline. The solution dependence on the size of this inset, x_{inset}, is investigated in Section 7.4. Typically $x_{inset}/L = 0.1$ is adequate. As there is no means of determining the level of energy dissipation from wave breaking on

the shore, an energy preserving solution is obtained by having an identical slider move in the mirrored domain to the left of the y-axis. Waves propagating upslope and moving out through the gap into the next half of the domain will be balanced by an identical wave moving into the domain. The slider is defined to be 2L in length, h_b in maximum thickness, and initially centred at $x = x_0$.

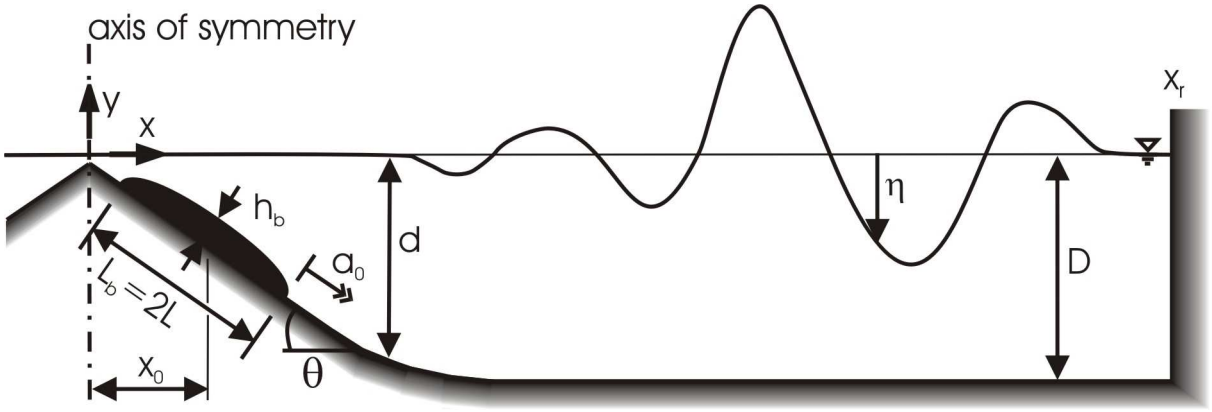

Figure 7.1. Schematic diagram of BEM model domain, and definition of parameters.

7.2.2 Key equations

The governing partial differential equation is

$$\nabla^2 \phi = 0 \tag{7.1}$$

where ϕ is the velocity potential. The PDE is subject to the linearised boundary conditions

$$\frac{\partial \phi}{\partial x} = 0 \quad on \quad x = 0 \tag{7.2}$$

$$\frac{\partial \phi}{\partial x} = 0 \quad on \quad x = x_r \tag{7.3}$$

$$\frac{\partial \eta}{\partial t} = \frac{\partial \phi}{\partial y} \quad on \quad y = 0 \tag{7.4}$$

$$\frac{\partial \phi}{\partial t} + g\eta = 0 \quad on \quad y = 0 \tag{7.5}$$

and

$$-\frac{\partial \phi}{\partial n} = v_{nb} \quad on \quad y = -y_b(x,t) \tag{7.6}$$

where n is an outward normal, v_{nb} is the normal velocity of the boundary (taken as positive when into the domain), and $y_b(x,t)$ is the position of the bottom boundary as a function of x and t.

The initial conditions are

$$\phi(x, y, t) = 0 \tag{7.7}$$

$$\eta(x, 0) = 0 \tag{7.8}$$

The first and second boundary conditions state that there is no flow through the ends of the domain at $x = 0$ and $x = x_r$. The third boundary condition is the kinematic free surface condition and the fourth boundary condition is the dynamic free surface condition. These are the same boundary conditions used in the semi-analytical model in Chapter 6, but are repeated here for completeness. The fifth boundary condition states that the motion of the slider only imparts a motion to the surrounding fluid that is normal to its own motion.

The specification of the bottom boundary condition is important, as this is the driving force for the wave motions. The motion of the slider generates motion and pressure changes in the surrounding fluid, which in turn, pass energy to the wave field on the free surface. The nature of the boundary condition is a normal velocity specification, as shown by Equation 7.6. As the slider moves the fluid ahead of it is forced in the direction of the domain, normal to the boundary without the slider. As the slider passes, the fluid moves back towards the boundary. The first assumption is that the slider is long and thin. Therefore

$$\frac{h_b}{L} \ll 1 \tag{7.9}$$

Based on this condition it is assumed that the motion of the slider only imparts a motion to the surrounding fluid that is normal to the bottom boundary without the slider. Also, because the slider is assumed to be thin, the boundary condition in Equation 7.6 can be applied at the boundary itself. The boundary is independent of time so Equation 7.6 applies on $y = -y_b(x)$.

7.2.3 Non-dimensionalisation

As mentioned in Chapter 6, implementing a numerical model within a non-dimensional framework is highly desirable. All length scales have been non-dimensionalised by L. Time has been scaled using the initial constant acceleration, a_0, as this typical acceleration scale will primarily determine the temporal response of the system. The governing equations and variables are non-dimensionalised using the following scheme.

$$x' = \frac{x}{L} \tag{7.10a}$$

$$y' = \frac{y}{L} \tag{7.10b}$$

$$\eta' = \frac{\eta}{L} \tag{7.10c}$$

$$n' = \frac{n}{L} \tag{7.10d}$$

$$y_b' = \frac{y_b}{L} \tag{7.10e}$$

$$t' = t\sqrt{\frac{a_0}{L}} \tag{7.10f}$$

$$\phi' = \phi \frac{1}{\sqrt{a_0 L^3}} \tag{7.10g}$$

$$v_{nb}' = \frac{v_{nb}}{\sqrt{a_0 L}} \tag{7.10h}$$

Three non-dimensional parameters appear in the dimensionless equations. The first two are identical to those given in Chapter 6, namely

$$\tau = \frac{D}{L} \tag{7.11}$$

and

$$\lambda^2 = \frac{a_0}{g} \tag{7.12}$$

The third parameter is the ratio of the slider's initial thickness, h_b, to its half-length.

$$\rho = \frac{h_b}{L} \tag{7.13}$$

The non-dimensional form of the governing PDE becomes

$$\nabla^2 \phi = 0 \tag{7.14}$$

where all variables are non-dimensional and the primes have been dropped for clarity.

The non-dimensional forms of the boundary conditions become

$$\frac{\partial \phi}{\partial x} = 0 \quad on \quad x = 0 \tag{7.15}$$

$$\frac{\partial \phi}{\partial x} = 0 \quad on \quad x = x_r \tag{7.16}$$

$$\frac{\partial \eta}{\partial t} = \frac{\partial \phi}{\partial y} \quad on \quad y = 0 \tag{7.17}$$

$$\lambda^2 \frac{\partial \phi}{\partial t} + \eta = 0 \quad on \quad y = 0 \tag{7.18}$$

and

$$-\frac{\partial \phi}{\partial n} = v_{nb} \quad on \quad y = -d(x) \tag{7.19}$$

where d(x) is the variable water depth. The non-dimensional form of the initial conditions is the same as the dimensional forms, with the superscript primes dropped. The dimensionless parameter λ appears explicitly in Equation 7.18, but τ and ρ are contained within the v_{nb} term.

7.2.4 Slider Rigidity

The rigidity of the slider dictates the formulation of the bottom boundary condition of Equation 7.19. The solution dependence on slider rigidity is investigated in Section 7.8. Firstly, we will consider a flexible slider that can follow the shape of the boundary along which it travels. This would be a reasonable assumption for naturally occurring landslides and turbidity currents. Therefore, the motion of the slider can be envisaged as shown by the representative diagram in Figure 7.2. As the slider passes through the transition from the slope to the horizontal bed the slider deforms to fit the shape of the bottom topography. In this case the slider motion is always parallel to itself. Therefore v_{nb} in Equation 7.19 can be found from the slider shape and speed.

The bottom boundary is given by

$$y_b(t) = -d(x) + H(t) f(s - s_0(t)) \tag{7.20}$$

where H(t) is some amplitude function, $f(s-s_0(t))$is a shape function for the slider, s is an arclength measure along the boundary from x=0, and $s_0(t)$ is the position of the slider's centre of mass in arclength coordinates. If we define

$$u(t) = s - s_0(t) \tag{7.21}$$

to be the local coordinates relative to the centre of mass then

$$y_b(t) = -d(x) + H(t) f(u) \tag{7.22}$$

and f(u) is zero outside the domain $-1 \le u \le 1$ (u is dimensionless). The normal velocity, v_{nb}, for the flexible slider case is calculated by

$$\begin{aligned} v_{nb} &= \frac{dy_b}{dt} \\ &= \frac{d}{dt}\left(-\rho f(u)\right) \\ &= -\rho \frac{df}{du}\frac{du}{dt} \\ &= -\rho \frac{df}{du}\frac{ds_0}{dt} \end{aligned} \tag{7.23}$$

Therefore any combination of slider geometry and acceleration regime can be used in Equation 7.23 to generate the velocity of the fluid normal to the boundary, over the slider.

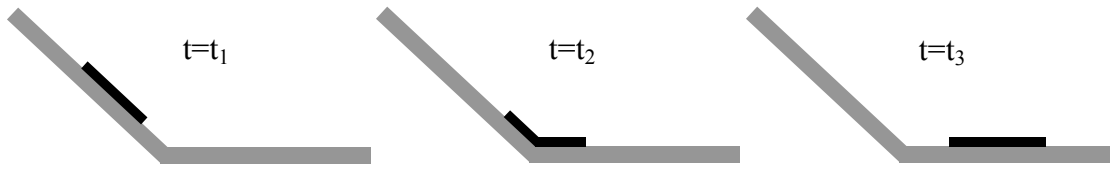

Figure 7.2. Flexible slider motion over representative topography.

Although a flexible slider may be more representative of real events, the experimental configuration had a rigid slider. As it moved from the slope to the horizontal bed the base of the slider moved away from the bottom boundary, as illustrated in Figure 7.3. As the slider traversed the transition it had a velocity component normal to itself. Therefore, this normal velocity must contribute to v_{nb} used in the boundary condition in Equation 7.19. This normal velocity is calculated as

$$v_{nb} = \frac{dx_i}{dt} \cdot \underline{n}_i \tag{7.24}$$

where x_i is the position of a point on the slider and $\underline{n}_i$ is a unit inward normal at the same point. This normal velocity is in addition to the velocities of the fluid over the slider, as presented in Equation 7.23. When the motion is parallel to the slider dx_i/dt has no normal component and v_{nb} is dependent purely on the slider shape and speed.

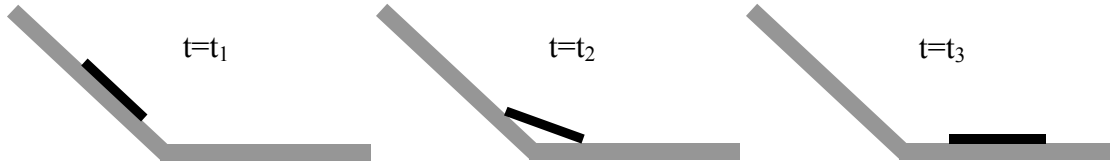

Figure 7.3. Rigid slider motion over representative topography.

7.2.5 Solution method

The Boundary Element Method (BEM) is a numerical method highly suited to solving Laplace's equation when the solution on the boundary is of primary importance. Here we were mainly interested in calculating the free surface elevation, $\eta(x,t)$. This quantity is related to ϕ on the free surface boundary. The boundary element method is a well established technique so no details of this are provided here, but Beer and Watson (1992), Brebbia and Walker (1979), and Raamachandran (2000) are three examples of texts that provide background into the subject. Provided here are the BEM details specific to this application.

The boundary of the flow domain was broken up into a number of linear elements and linear basis functions were used to describe the variation of ϕ along an element. As will be explained further in Section 7.3, the free surface was resolved by $N_{fs} = 400$ equally spaced elements, the right boundary by $N_r = 5$ elements, the bottom boundary by $N_b = 200$ elements, and the slider was resolved by $N_s = 49$ elements.

The boundary conditions required by Laplace's equation must have the form

$$\alpha\phi + \beta\frac{\partial\phi}{\partial n} = \gamma \tag{7.25}$$

where one or both of α and β are non-zero. All of the boundary conditions for this problem are of this form, except for Equations 7.17 and 7.18 on the free surface. These equations involve both η and ϕ. Eliminating η from these equations gives

$$\lambda^2\frac{\partial^2\phi}{\partial t^2} + \frac{\partial\phi}{\partial y} = 0 \quad on\ y=0 \tag{7.26}$$

To convert Equation 7.26 into the form of Equation 7.25, $\partial^2\phi/\partial t^2$ is approximated using backward finite differences. Using a third order scheme

$$\frac{\partial^2\phi}{\partial t^2} = -\frac{1}{12\Delta t^2}\left[35\phi(t) - 104\phi\left(t-\Delta t\right) + 114\phi\left(t-2\Delta t\right) - 56\phi\left(t-3\Delta t\right) + 11\phi\left(t-4\Delta t\right) + \mathrm{O}(\Delta t^3)\right] \quad \textbf{(7.27)}$$

For the finite difference approximation to the boundary condition on the free surface, Equation 7.26 becomes

$$\frac{35\lambda^2}{12\Delta t^2}\phi + \frac{\partial\phi}{\partial y} = \frac{\lambda^2}{12\Delta t}\left[104\phi\left(t-\Delta t\right) - 114\phi\left(t-2\Delta t\right) + 56\phi\left(t-3\Delta t\right) - 11\phi\left(t-4\Delta t\right)\right] \quad \textbf{(7.28)}$$

on y=0

The free surface elevation can be obtained from Equation 7.18.

$$\eta = -\lambda^2\frac{\partial\phi}{\partial t} \quad \textbf{(7.29)}$$

Using a third order approximation to the first derivative, η becomes

$$\eta = -\frac{\lambda^2}{12\Delta t}\left[-\phi\left(t+2\Delta t\right) + 8\phi\left(t+\Delta t\right) - \phi\left(t-\Delta t\right) + \phi\left(t-2\Delta t\right)\right] \quad \textbf{(7.30)}$$

In order to evaluate η at time = t, the solution for ϕ is calculated for two additional time steps, Δt, before and after time = t. The time step is appropriately small to ensure stability and to limit noise.

Also of interest are the full domain solutions for pressure, p, and velocity $\underline{u}$. These are obtained from the ϕ field, which are generated on a rectangular grid within the domain.

$$\underline{u} = \nabla\phi \quad \textbf{(7.31)}$$

so using non-dimensional parameters, the velocities are calculated as

$$u = \frac{\partial\phi}{\partial x} \quad \textbf{(7.32)}$$

and

$$v = \frac{\partial\phi}{\partial y} \quad \textbf{(7.33)}$$

From Bernoulli's pressure equation an expression for pressure, in dimensional terms, is

$$\frac{p}{\rho} = -\frac{\partial \phi}{\partial t} - \frac{1}{2}\left(u^2 + v^2\right) \tag{7.34}$$

Non-dimensionalising u and v with $(a_0 L)^{0.5}$ and p with $\rho g L$, dimensionless pressure becomes

$$p = \lambda^2 \left[-\frac{\partial \phi}{\partial t} - \frac{1}{2}\left(\left(\frac{\partial \phi}{\partial x}\right)^2 + \left(\frac{\partial \phi}{\partial y}\right)^2 \right) \right] \tag{7.35}$$

7.2.6 Slider Shape

A quartic shape, an approximation to the semi-elliptical slider used in the experiments, was used in the BEM model. The quartic shape had the same non-dimensional length and area as the semi-ellipse. Therefore, the height of the quartic slider was slightly less than that of the experiment. This quartic shape was the same as that used in the constant depth semi-analytical model, detailed in Chapter 6. It had a non-dimensional length ranging between $-1 \le u \le 1$ and a non-dimensional height of 0.982. Results from the BEM model were compared with data from simulations using the semi-analytical model in Section 7.5. The shape function, $f(u)$ for the quartic is

$$f(u) = 0.982\left(1 - u^4\right) \quad for \quad -1 \le u \le 1 \tag{7.36}$$

and

$$f'(u) = -3.928u^3 \quad for \quad -1 \le u \le 1 \tag{7.37}$$

7.2.7 Acceleration Model

Two displacement functions, $s_0(t)$, similar to the two models used in Chapter 6, were considered. The first acceleration model, which is called 'A2', consisted of an indefinite constant acceleration. It was used to generate results to compare with similar simulations using the semi-analytical model, detailed in Chapter 6. In dimensional coordinates the distance travelled by the slider is given by

$$s_0(t) = \frac{1}{2} a_0 t^2 \tag{7.38}$$

In dimensionless coordinates this becomes

$$s_0 = \frac{1}{2} t^2 \quad for \; 0 \le t \tag{7.39}$$

The second slider model, which is called 'AD2', was an idealised form of the experimental landslide displacement. The slider acceleration, a_0, was assumed constant until a time at which the landslide reached the base of the slope, t_{max}. After this a constant deceleration occurred until $t = t_{zero}$, at which

point the slider came to a rest. In non-dimensional terms, the displacement function for a constant acceleration followed by a constant deceleration is

$$
\begin{aligned}
s_0'(t') &= \frac{1}{2}t'^2 && for\ 0 \le t' \le t'_{\max} \\
&= \frac{1}{2}t'^2_{\max} + t'_{max}\left(t'-t'_{max}\right) - \frac{t'_{max}}{2}\frac{\left(t'-t'_{max}\right)^2}{\left(t'_{zero}-t'_{\max}\right)} && for\ t'_{\max} \le t' \le t'_{zero} \\
&= \frac{1}{2}t'^2_{\max} + \frac{1}{2}t'_{max}\left(t'_{zero}-t'_{\max}\right) && for\ t'_{zero} \le t'
\end{aligned}
\qquad \textbf{(7.40)}
$$

where t_{max} and t_{zero} define the acceleration and deceleration rate, and hence are two additional non-dimensional parameters. The superscript primes have been shown to clarify that these parameters are in non-dimensional form.

7.3 Grid Resolution

The dependence of the generated wave fields on time step and boundary element grid resolution was assessed. A model domain ranging from $0 \le x/L \le 120$ was used. For this domain size it was found that a time step of 0.025, 200 bottom elements, 400 free surface elements, 49 slider elements, and 5 right-hand end boundary elements, produced water surface profiles independent of grid resolution. This time step and these numbers of elements were used for all subsequent simulations. Water level profiles at $t(a_0/L)^{0.5} = 9.5$ for the non-dimensional slider parameters presented in Table 7.1, for various time step and boundary element grid resolutions, are plotted in Figure 7.4. Note that the wave solution was only output at every fourth BEM model time step.

Table 7.1. Non-dimensional parameters for simulations assessing the grid resolution.

τ	λ	ρ	x_0/L	acceleration model	$t_{max}\sqrt{(a_0/L)}$	$t_{zero}\sqrt{(a_0/L)}$	topography
1.74	0.404	0.104	2.0	A2	-	-	with slope

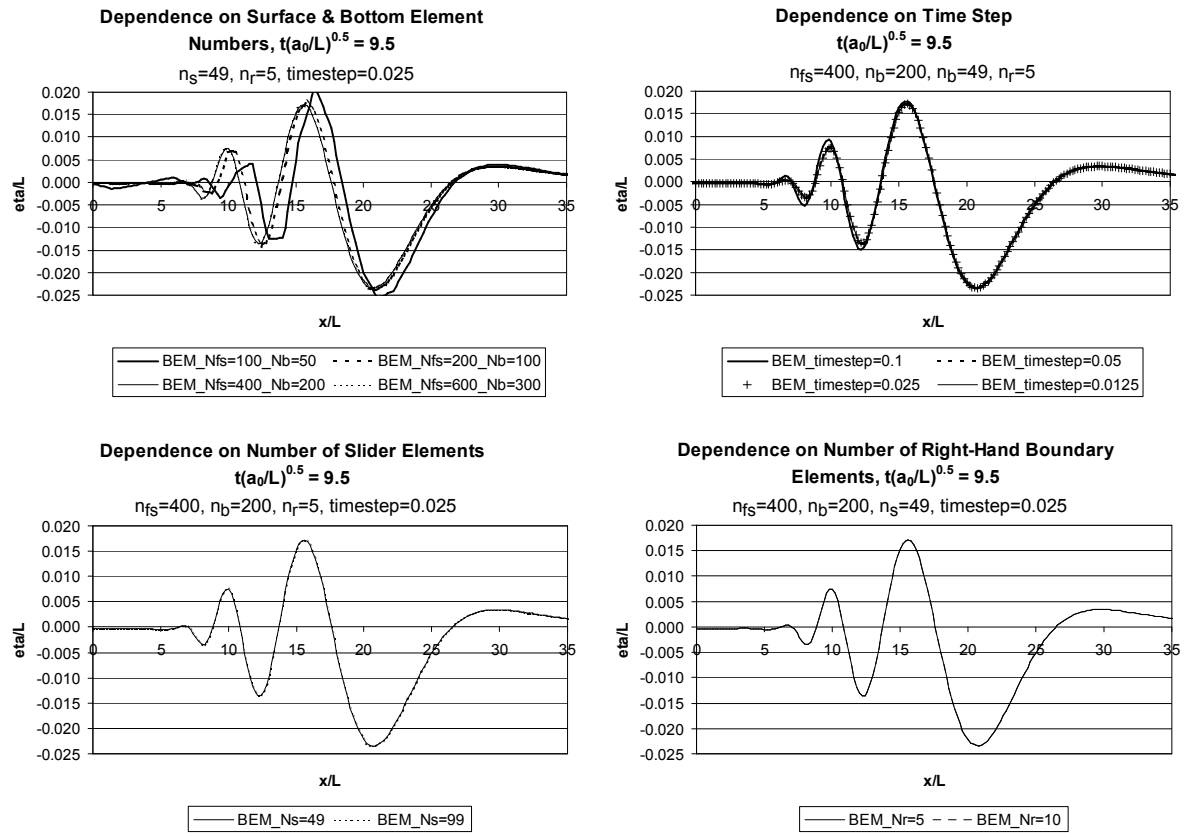

Figure 7.4. Water surface profiles at $t(a_0/L)^{0.5}$ = 9.5 for the same non-dimensional slider parameters for various time step and boundary element grid resolutions.

7.4 Shoreline Inset

As stated in Section 7.2.1, a small gap between the top of the slope and the still water surface was necessary in the BEM model domain to prevent solution singularities and noise generation as waves propagated into the wedge at the top of the slope. It also provided a means with which waves and energy could pass between the left and right halves of the domain, allowing an energy preserving solution to be possible. Essentially the coordinate origin was inset slightly to the right of the true shoreline. The solution dependence on the size of this inset, x_{inset}, is investigated here. Water level profiles at $t(a_0/L)^{0.5}$ = 25.0, using the non-dimensional slider parameters presented in Table 7.2, are plotted in Figure 7.5a for x_{inset}/L = 0.1 and 0.025. The water surface profiles appeared essentially independent of x_{inset} for values of x_{inset}/L = 0.1 and 0.025. Also, the level of noise near the shoreline was not significantly greater when the inset was small (x_{inset}/L = 0.025), as shown by the close-up view of the water surface near the shore in Figure 7.5b. To ensure the noise levels remained low, the conservative value of x_{inset}/L = 0.1 was used for subsequent simulations.

Table 7.2. Non-dimensional parameters for simulations assessing the dependence on x_{inset}.

τ	λ	ρ	x_0/L	acceleration model	$t_{max}\sqrt{(a_0/L)}$	$t_{zero}\sqrt{(a_0/L)}$	topography
1.74	0.390	0.104	1.040	AD2	3.095	15.881	with slope

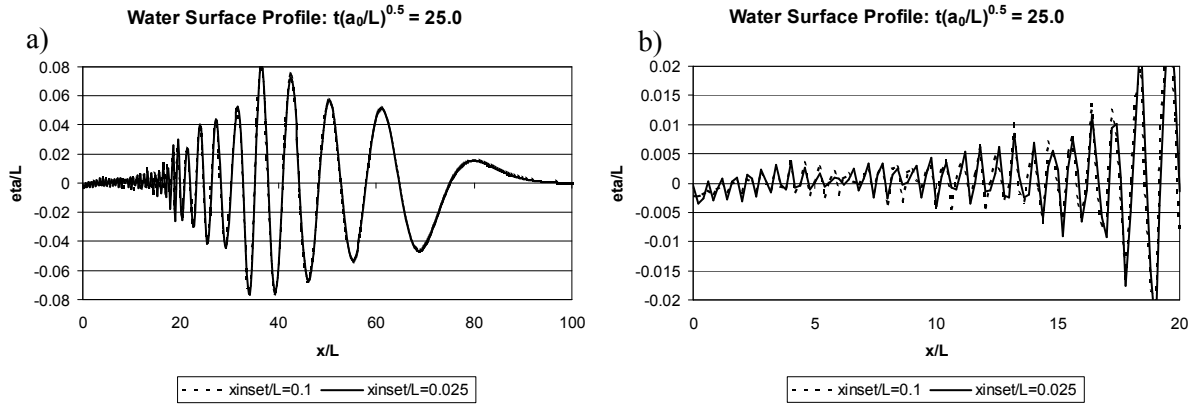

Figure 7.5. Water surface profiles at $t(a_0/L)^{0.5}$=25.0 for the same non-dimensional slider parameters for various values of x_{inset}. a). The water surface profile between 0<x/L<100, and b). a close-up view of the surface profile near the shore.

7.5 Comparison with Semi-Analytical Model

As a check on the accuracy of the BEM model, water surface profiles were compared with those from a semi-analytical model simulation using the same parameters. This also provided a check on the robustness of the BEM model and to ensure the BEM grid resolution was sufficient to obtain similar accuracy to the semi-analytical model. A quartic-shaped slider moving in a constant depth channel was simulated in both models, using the parameters presented in Table 7.3. As the semi-analytical model was comprised of a continuous spectrum of free wave modes, the BEM model results were expected to approach a solution similar to that produced by the semi-analytical model as the element and time resolution increased. Figure 7.6 plots water surface profiles at $t(a_0/L)^{0.5}$ = 9.5 for the semi-analytical and BEM models, and shows that the profiles were very similar. The BEM model used a time step of 0.025, 200 bottom elements, 400 surface elements, 49 slider elements, and 5 right-hand boundary elements. Using the stated grid resolution, the accuracy of the BEM model was deemed adequate for the purpose of comparison with the semi-analytical model and experimental results.

Table 7.3. Non-dimensional parameters for the BEM and semi-analytical model comparison simulation.

BEM Model						
τ	**λ**	**$\rho=h_b/L$**	**acceleration model**	**$t_{max}\sqrt{(a_0/L)}$**	**$t_{zero}\sqrt{(a_0/L)}$**	**topography**
1.74	0.404	0.104	A2	-	-	constant depth
Semi-analytical Model						
τ	**λ**	**$\rho=h_b/D$**	**acceleration model**	**$t_{max}\sqrt{(a_0/2L)}$**	**$t_{zero}\sqrt{(a_0/2L)}$**	**decay model**
1.74	0.404	0.06	A1	-	-	decay1

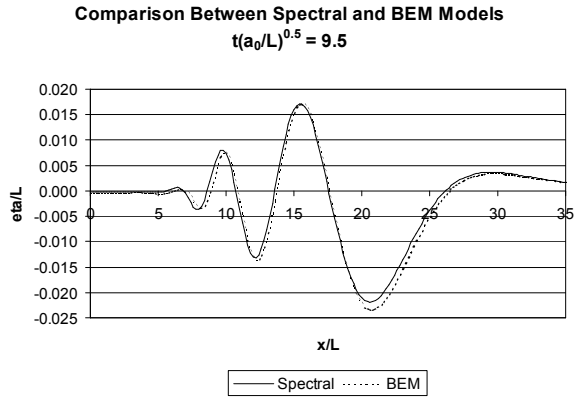

Figure 7.6. Water surface profiles at $t(a_0/L)^{0.5}$=9.5 for the semi-analytical and BEM models using the same non-dimensional slider parameters.

7.6 Comparison With Experimental Data

The BEM model was used to simulate each of the fifteen configurations of specific gravity and initial submergence used in the experiments. The BEM model results were then compared with the experimental data. The non-dimensional parameters were determined for each of the fifteen experimental test configurations, and these are presented in Table 7.4. The experimental data was non-dimensionalised using the BEM non-dimensionalisation outlined in Section 7.2.3.

As an example of the calculation of the non-dimensional parameters from the experimental configurations, the landslide velocity time history for the SG5_IS5 case is shown in Figure 7.7. The landslide's constant initial acceleration, a_0, was calculated through linear regression fitting of the positive acceleration portion of the landslide velocity time history. The rate of increase in velocity decreased as the landslide approached its maximum velocity, vel_{max}, at time $t = t_{peak}$. Therefore, the linear fit was performed for velocities between $0 \leq t \leq 0.8t_{peak}$. The linear approximation to the increasing velocity was extrapolated until velocity = vel_{max}, the maximum velocity measured in the experiment. The approximation to the time of maximum velocity, t_{max}, was the time at which the linear approximation reached vel_{max}. The approximation to the time at which the landslide returned to zero velocity, t_{zero}, was determined by forcing the area below the approximated velocity profile to be the same as the area below the measured velocity profile. This meant that the slider in the BEM simulations travelled the same distance as the landslide in the experiments. The trapezoidal rule was used to calculate the area below the measured velocity profile, vel_{area}. Hence t_{zero} was calculated using the formulation given in Equation 7.41. The parameters t_{max} and t_{zero} were non-dimensionalised by $(L/a_0)^{0.5}$.

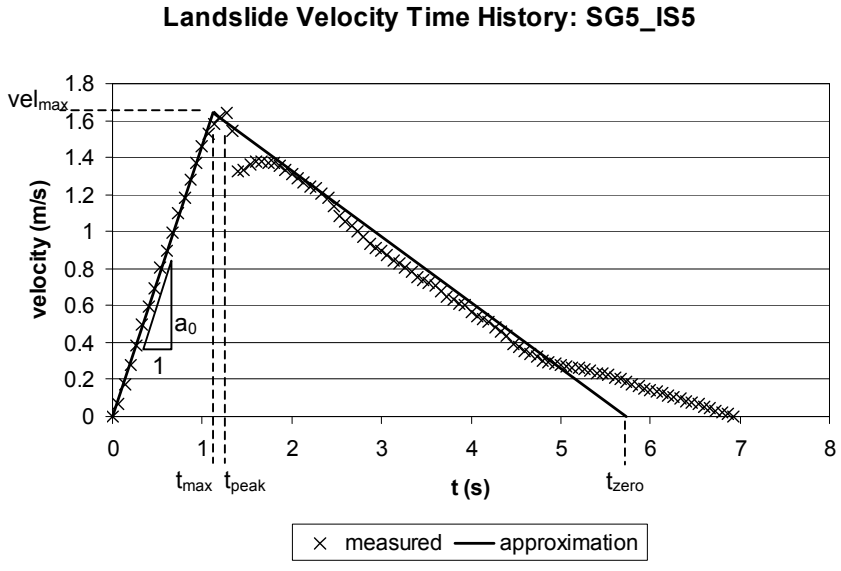

Figure 7.7. Approximation to the landslide velocity time history to calculate a_0, t_{max}, and t_{zero}, for the SG5_IS5 case.

$$t_{zero} = \frac{vel_{area} - \frac{1}{2} t_{\max} vel_{\max}}{\frac{1}{2} vel_{\max}} + t_{\max} \tag{7.41}$$

Table 7.4. Non-dimensional parameters for simulations comparing the BEM results with experimental data.

N_{fs}	N_r	N_b	N_s	acceleration model	topography	slider shape
400	5	200	49	AD2	with slope	quartic

	τ	λ	ρ	x_0/L	$t_{max}\sqrt{(a_0/L)}$	$t_{zero}\sqrt{(a_0/L)}$
SG5_IS5	1.74	0.388	0.104	1.040	2.704	13.920
SG5_IS4	1.74	0.389	0.104	1.784	2.479	13.254
SG5_IS3	1.74	0.385	0.104	2.532	2.264	12.851
SG5_IS2	1.74	0.390	0.104	3.280	1.966	12.958
SG5_IS1	1.74	0.371	0.104	4.024	1.677	10.779
SG4_IS5	1.74	0.373	0.104	1.040	2.690	11.827
SG4_IS4	1.74	0.384	0.104	1.784	2.443	12.191
SG4_IS3	1.74	0.378	0.104	2.532	2.222	12.676
SG4_IS2	1.74	0.379	0.104	3.280	1.940	13.024
SG3_IS5	1.74	0.353	0.104	1.040	2.607	11.353
SG3_IS4	1.74	0.358	0.104	1.784	2.405	11.911
SG3_IS3	1.74	0.358	0.104	2.532	2.154	12.242
SG2_IS5	1.74	0.320	0.104	1.040	2.534	12.112
SG2_IS4	1.74	0.330	0.104	1.784	2.306	12.201
SG1_IS5	174	0.257	0.104	1.040	2.375	12.377

7.6.1 Maximum Wave Amplitude and Energy

Figure 7.8 compares the simulated maximum crest amplitude, trough amplitude, and wave potential energy with corresponding experimental results for all fifteen specific gravity and initial submergence combinations. Generally, the simulations slightly under-predicted the maximum crest amplitude, with ratios of simulated amplitudes to measured amplitudes ranging between 0.77 and 1.01. Simulations with shallow submergences tended to produce values closer to the measured maximum crest amplitudes. The numerical model generally produced maximum trough amplitudes larger than those measured in the experiments. Predicted trough amplitudes tended to be closer to the measured values for heavier specific gravities. The ratio between the simulated and the measured maximum wave potential energy were generally between 0.73 and 1.29.

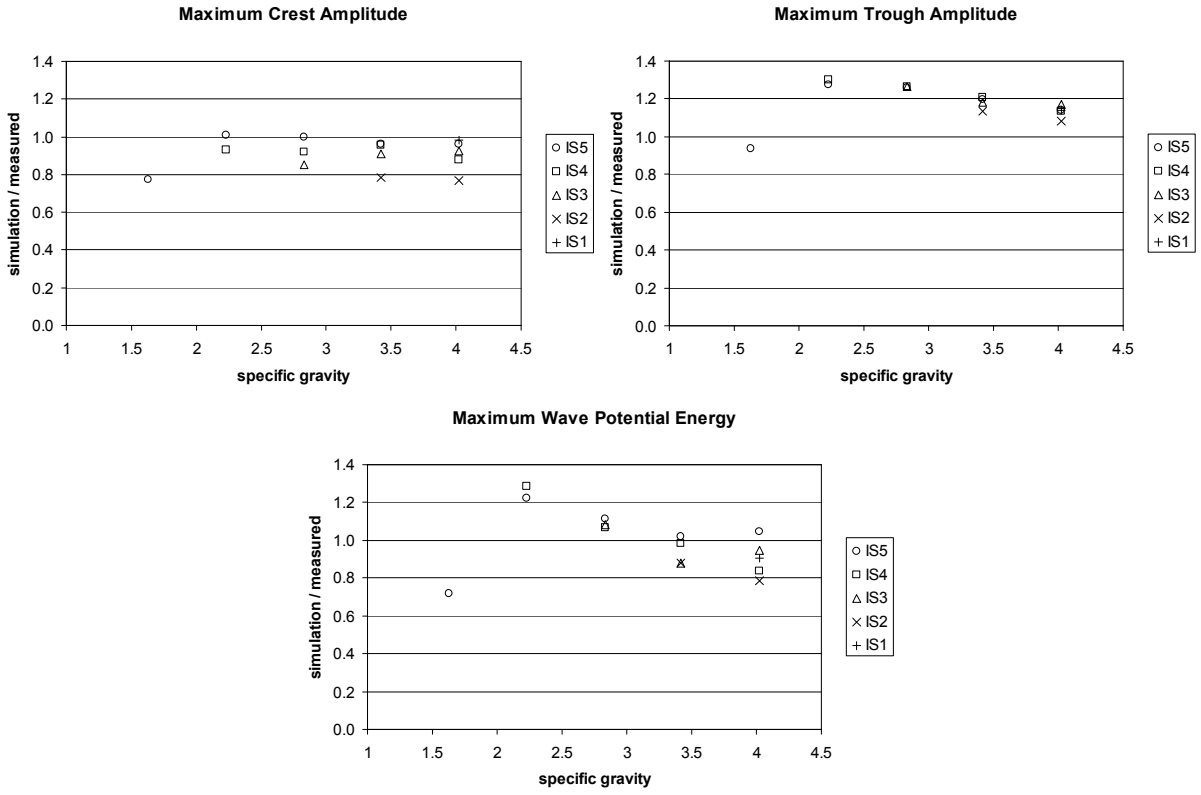

Figure 7.8. Comparison of simulated maximum crest amplitude, trough amplitude, and wave potential energy with corresponding experimental results.

It is clear from the plots in Figure 7.8 that the SG1_IS5 configuration was contrary to the general trends. The reason this configuration was not well modelled was due to the simple definition of the slider acceleration profile in the BEM model. As illustrated in Figure 7.7, the acceleration profile was assumed to consist of a constant acceleration and a constant deceleration. However, the measured landslide velocity time history for the SG1_IS5 case, shown in Figure 7.9, did not increase linearly to a maximum velocity. For an initial acceleration that matched well with the experimental acceleration, the time of maximum velocity could not be matched simultaneously. If the time of maximum velocity was closely matched, then the initial acceleration was under predicted. From the analysis of the sensitivity of the model to changes in a_0 and t_{max}, in Section 7.7, the mismatch in either the acceleration or the time of maximum velocity had a significant effect on the ability of the model to accurately model the experiments. Only the velocity time history for the SG1_IS5 case exhibited a significantly non-linear initial increase in velocity.

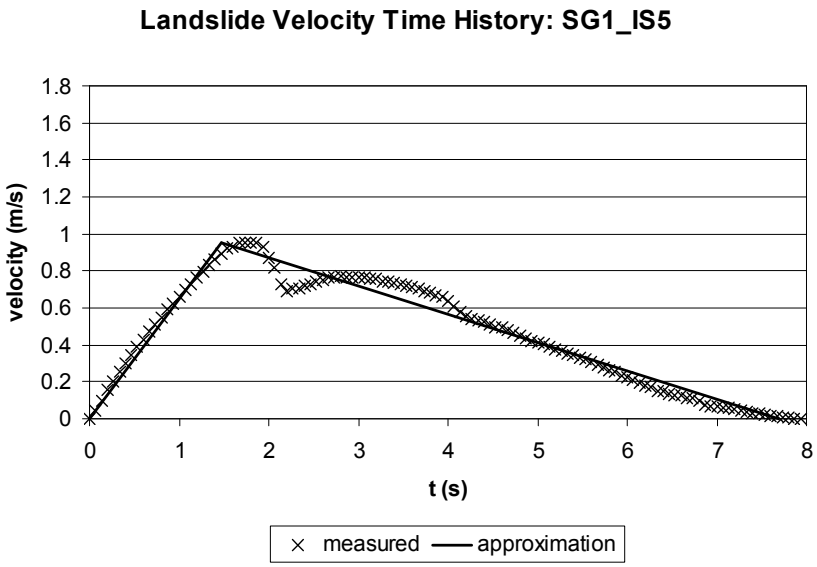

Figure 7.9. Approximation to the landslide velocity time history for the SG1_IS5 case.

7.6.2 Water Surface Profile and Time History

As the agreement between the BEM model results and the experimental data was similar for all cases, except for the SG1_IS5 configuration, representative free surface profiles and time histories for the SG5_IS5 case are presented here to illustrate the similarities and differences. The larger wave amplitudes of the SG5_IS5 case allow the subtle similarities and differences between the model and experimental data to be observed most easily. The differences exhibited by the SG1_IS5 case are also highlighted. Plots for the remaining cases are included in Appendix G.

Figure 7.10 plots simulated and experimental free surface profiles at five discrete times for the SG5_IS5 combination. The BEM model was able to predict the wave amplitudes quite well, as well as the range of amplitudes within the wave train. The phase speed of the waves was slightly over predicted, leading to the offsets in the location of the waves. The profiles at $t(a_0/L)^{0.5} = 3.5$ were very similar, but by $t(a_0/L)^{0.5} = 6.5$ the leading crest amplitude was not as large as the measured crest amplitude. The BEM model also over predicted the leading trough amplitude, and a possible reason for this is discussed in Section 7.9.

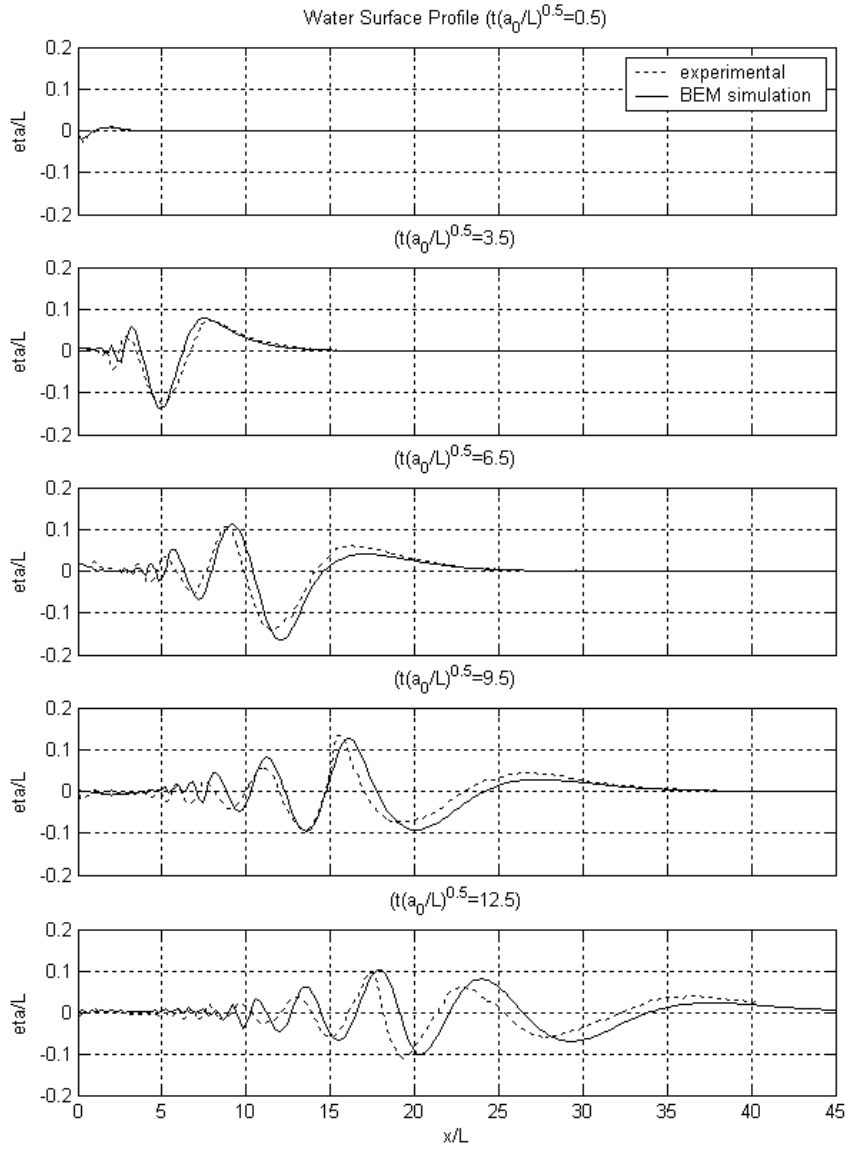

Figure 7.10. Simulated and measured water surface profiles at $t(a_0/L)^{0.5}$ = 0.5, 3.5, 6.5, 9.5, and 12.5 for the SG5_IS5 combination.

Figure 7.11 plots the measured and simulated water level time histories for the SG5_IS5 combination at five downstream positions ranging from close to the top of the slope to the end of the measured domain. The water level time history at x/L = 0.2 measured the waves that ran up and down the shore. The maximum run-down, caused by the initial downward movement of the landslide, was simulated well with regards to timing and amplitude. The maximum run-up amplitude, caused by the deceleration of the landslide at the base of the slope, was also simulated well. However, the time of occurrence was earlier than that measured in the experiments, and the reason for this is discussed in Section 7.9. At greater distances downstream the first crest period was slightly shorter in the model, and the slight over prediction of the phase speed led to a temporal advancement of the wave train compared to the measured waves. Table 7.5 presents the ratios of the simulated and measured times at which the first four wave crests pass x/L=20 for the SG5_IS5 and SG5_IS1 combinations. These

ratios show that the BEM model predictions of the crest arrival times were between 1.8% and 3.1% earlier than the measured times for the SG5_IS5 case, and between 2.0% and 3.6% for the SG5_IS1 case. The sensitivity of the temporal differences between simulated and measured times to a_0, t_{max}, and t_{zero}, is investigated in Section 7.7. The time at which the initial disturbance reaches each downstream position was simulated accurately.

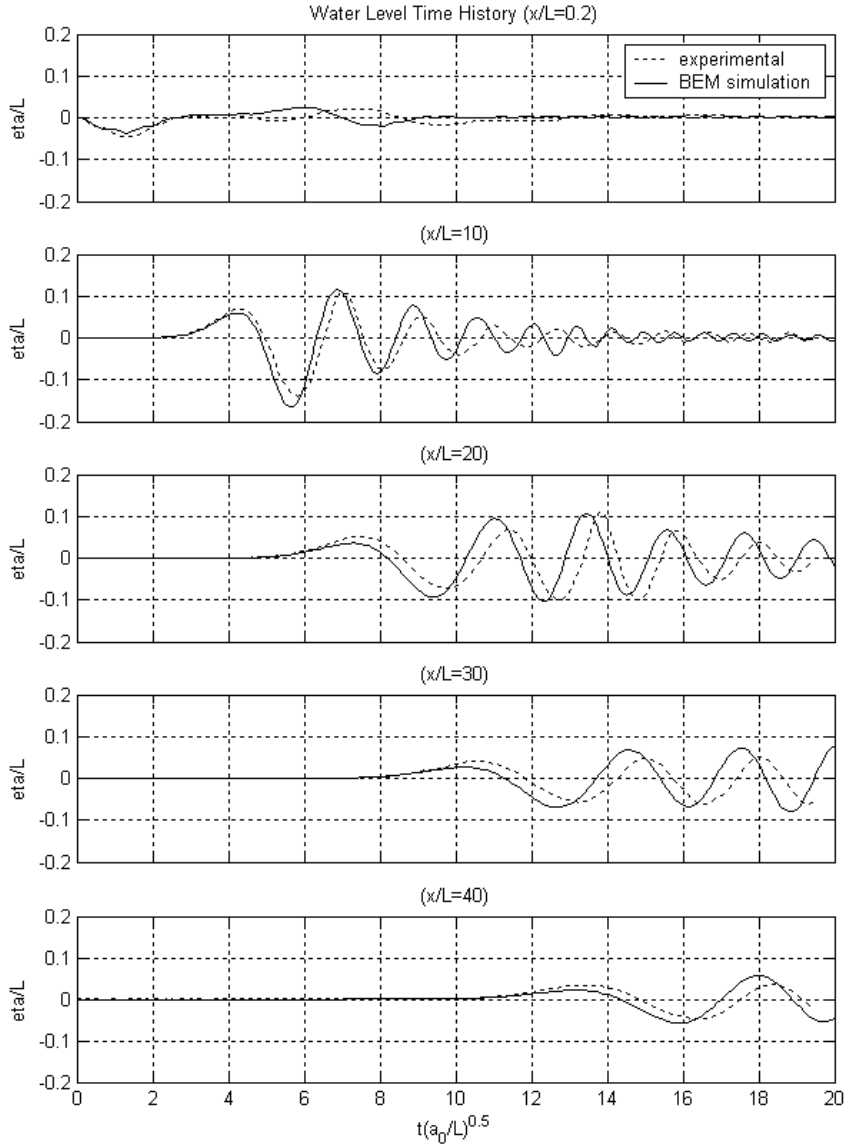

Figure 7.11. Simulated and measured water level time histories at x/L = 0.2, 10, 20, 30, and 40 for the SG5_IS5 combination.

Table 7.5. Ratios of the simulated and measured times at which the first four wave crests pass x/L=20 for the SG5_IS5 and SG5_IS1 combinations.

Ratios of the simulated to the measured times at which crests pass x/L=20				
	1st crest	2nd crest	3rd crest	4th crest
SG5_IS5	0.979	0.969	0.980	0.982
SG5_IS1	0.977	0.964	0.977	0.980

The plots in Figure 7.12 show the spatial and temporal distribution of the maximum crest and trough amplitudes for the SG5_IS5 combination. These show that the simulated maximum amplitude envelopes very closely matched the measured maximum amplitude distribution. The growth rates of the maximum amplitudes were also modelled accurately. The over prediction of the maximum trough amplitude is clear in these plots, and is discussed further in Section 7.9. The maximum crest and trough amplitude envelopes and time histories for the other configurations, except for the SG1_IS5 case, were similar. Although Figure 7.8 tends to show that the maximum crest amplitudes were under-predicted and the maximum trough amplitudes were over-predicted, the maximum amplitude envelope and time history in Figure 7.12 show that across the entire spatial and temporal range of the simulated domain, the wave field was generally modelled accurately.

As mentioned earlier, the poor approximation of the experimental velocity time history with a constant acceleration and constant deceleration model for the SG1_IS5 case led to a wave response less than that of the experiments. This is illustrated in Figure 7.13 by the general under prediction of the maximum wave amplitudes.

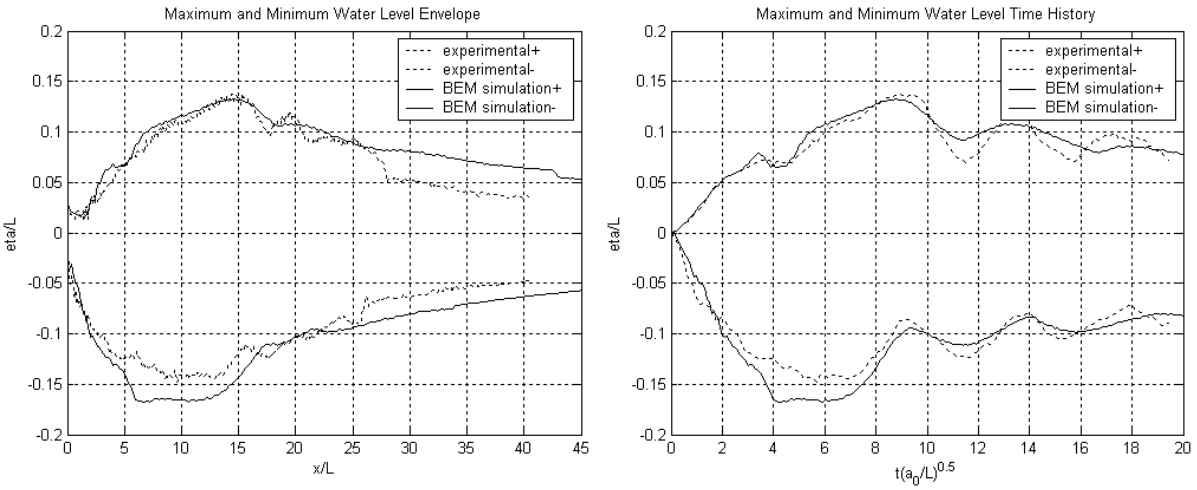

Figure 7.12. Spatial and temporal distribution of the maximum crest and trough amplitudes for the SG5_IS5 combination.

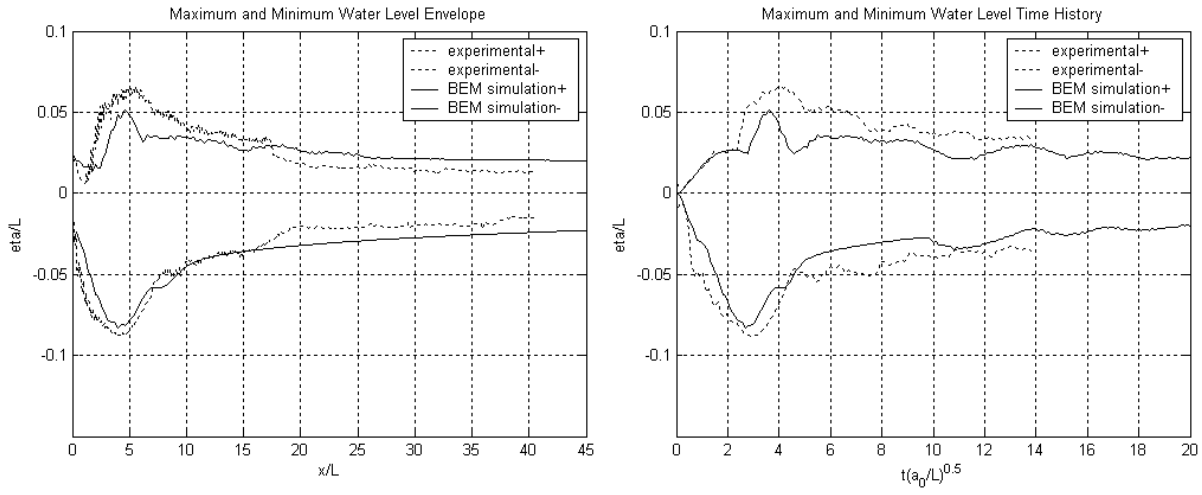

Figure 7.13. Spatial and temporal distribution of the maximum crest and trough amplitudes for the SG1_IS5 combination.

7.6.3 Energy

A representative wave potential energy time history for the SG5_IS5 case is presented here to illustrate the similarities and differences between the BEM model results and the experimental data. Figure 7.14 plots the wave potential energy time history for the SG5_IS5 combination. The model predicted the energy growth and time of peak energy well. The slightly over predicted amplitudes of the first trough led to a slight over prediction of maximum wave potential energy for the SG5_IS5 case. The differences in maximum wave potential energy for the other configurations are shown in Figure 7.8.

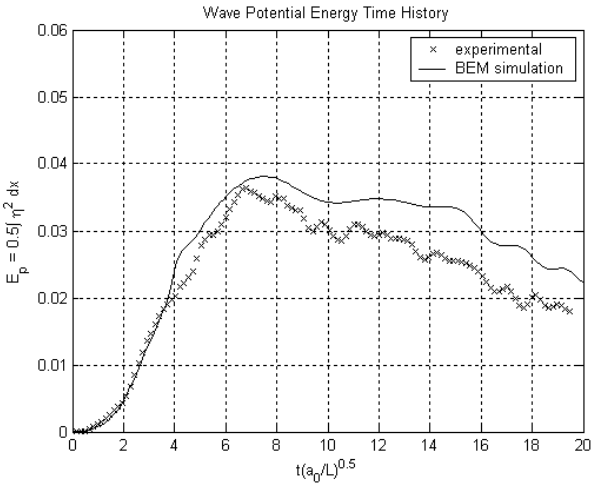

Figure 7.14. Wave potential energy time history for the SG5_IS5 combination.

Sub-surface velocity fields were measured for the SG5_IS1 and SG1_IS5 cases only. However, due to the poor predictions of the wave field for the SG1_IS5 case, the sub-surface velocities were also poorly modelled. Therefore, sub-surface velocity and kinetic energy data are not presented for this case. Figure 7.15 plots the time history of the kinetic energy of the fluid contained between $0 \leq x/L \leq 12$ for the SG5_IS1 combination. The initial growth rate of water kinetic energy in the BEM model was very similar to the measured growth. However, the predicted energy growth soon decayed so that the prediction of maximum kinetic energy was 45% less than the measured energy maximum. The form of the increase, peak, and decay in simulated kinetic energy was similar to the measured form. The additional kinetic energy present in the experimental data was due to the wake motions, which the inviscid and irrotational BEM model could not predict.

The wave potential energy time history for the SG1_IS5 combination is plotted in Figure 7.16. The potential energy was measured between $0 \leq x/L \leq 12$. The substantial under prediction of the wave amplitudes led to a 28% under prediction in the maximum wave potential energy. The growth rate of the wave potential energy in the model was similar to the measured growth rate because the initial acceleration of the model was similar to the experimental acceleration. However, the reduced time of acceleration, due to having a t_{max} value less than the measured value, resulted in the energy growth in the model being truncated.

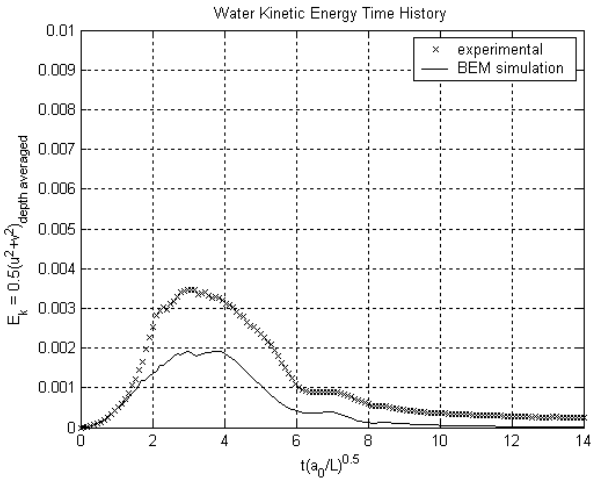

Figure 7.15. Wave kinetic energy time history for the SG5_IS1 combination.

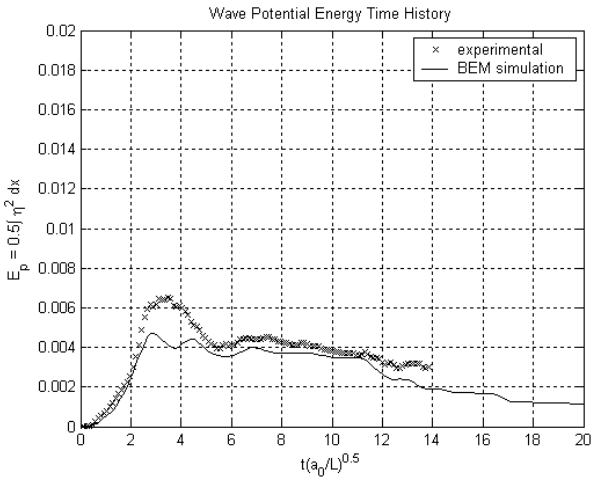

Figure 7.16. Wave potential energy time history for the SG1_IS5 combination.

7.6.4 Sub-surface Velocity Profiles

Figure 7.17 plots sub-surface horizontal velocity profiles measured during the experiments and simulated by the BEM model for the SG5_IS1 combination. These water velocity distributions occurred below the crests and troughs as they pass $x/L_b = 6.0$. The water velocities below crests and troughs were used for the sake of convenience, as below these waveforms the vertical velocities associated with the wave motions were at a minimum. The velocity profiles presented here are at times as close to the actual times the crests and troughs pass $x/L_b = 6.0$ that the camera frame rate and the model solution time step allow. However, it should be noted that a slight difference in timing (phase) might lead to significant deviations of the velocities from those expected to occur below the actual crests and troughs.

Generally, the velocities within, and the shape of, the simulated profiles were reasonable predictions of the measured velocities. For example, the velocities below the first crest were simulated well, as were the velocities in the upper half of the water column below the first trough. However, the inability of the inviscid and irrotational model to predict the wake motions behind the landslide meant the magnitudes in some other locations were not well modelled. In particular, the model did not predict the downstream flow above the bed after the passage of the landslide, as observed in the experiments. In the experiments, the offshore flows above the bed were countered by a gentle onshore flow in the upper portions of the water column. The model could not predict this so it tended to over-predict the magnitudes of the velocities below the crests and under-predict the velocity magnitudes below the troughs. This was best illustrated in the velocity profiles for the third and fourth crests and troughs. Note that the times that the crests and troughs passed $x/L_b = 6.0$ were slightly earlier than the equivalent measured times. This was consistent with the slightly higher phase speed predicted by the model, as shown by the water level time histories in Figure 7.11. The BEM model predictions of

velocity profile matched more closely the experimental velocities compared to those calculated from linear theory, as described in Section 5.4.3.

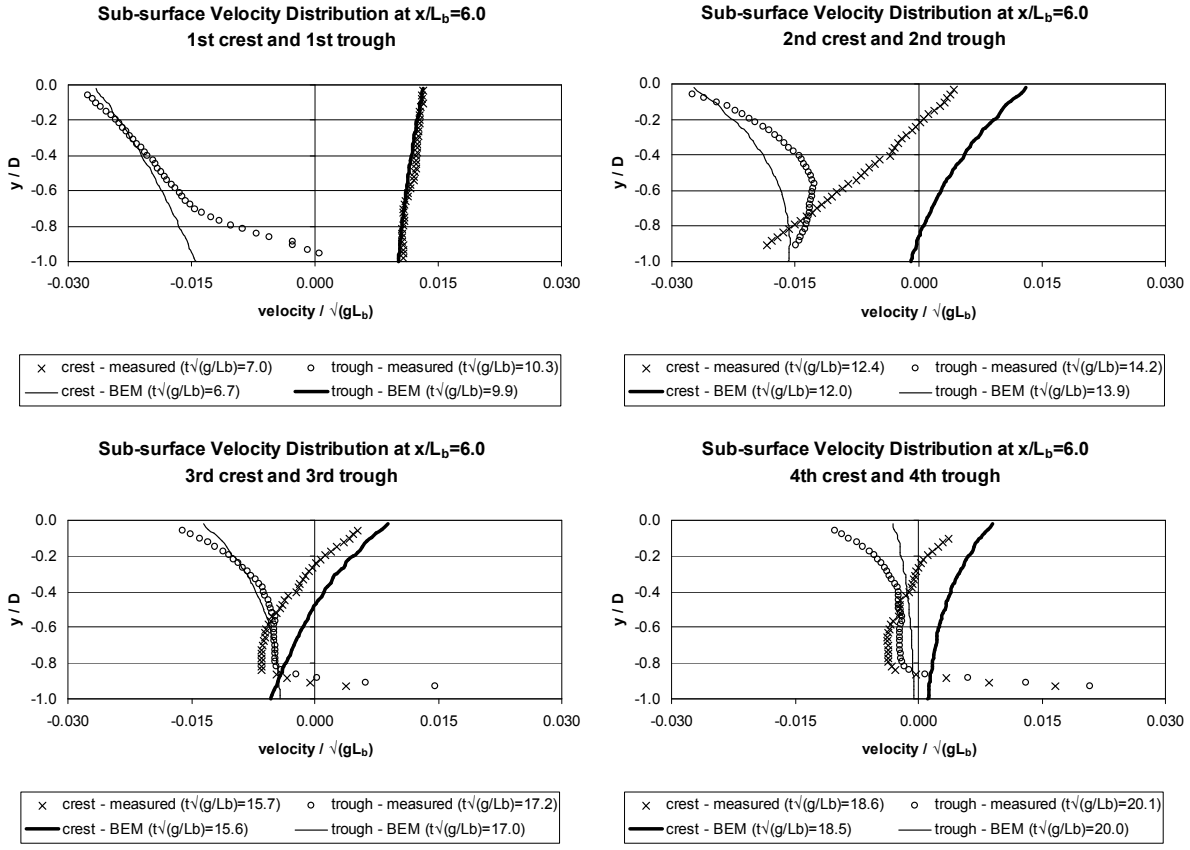

Figure 7.17. Sub-surface horizontal velocity profiles below wave crests and troughs for the SG5_IS1 test combination at x/L_b=6.0.

7.7 Sensitivity to Magnitude and Duration of Acceleration

The use of a constant acceleration and a constant deceleration to approximate the motions of the experimental landslide in the BEM model required the parameters a_0, t_{max}, and t_{zero}, to be calculated, as described in Section 7.6. As these values formed part of an approximation to the actual landslide motion, the solution sensitivity to the three parameters was investigated. The BEM model was re-run for the SG5_IS5 and SG5_IS1 cases, with ±10% variations independently applied to each of a_o, t_{max}, and t_{zero}. The sensitivity of the maximum crest amplitude, maximum trough amplitude, and maximum wave potential energy, to the variations in the three parameters are presented in Table 7.6. The sensitivity of the temporal differences between the simulated and measured times at which the first four wave crests pass x/L=20 to a_0, t_{max}, and t_{zero}, are presented in Table 7.7.

The percentage changes presented in Table 7.6 for two representative configurations, the SG5_IS5 and SG5_IS1 cases, clearly show that the initial acceleration and the time to maximum velocity had a significant effect on the maximum wave potential energy. A ±10% variation in a_0 or t_{max} resulted in changes to the maximum energy of between 16% and 25% for the two configurations. This was consistent with the semi-analytical model investigation of the dependence of the wave energy on initial slider acceleration, in Section 6.5.3, in which the wave potential energy was found to be highly sensitive to the initial landslide acceleration. The sensitivity of the maximum crest amplitude was moderate, with changes in amplitude of between 7% and 13% for the same variation in a_0 and t_{max}. For the SG5_IS5 configuration the ±10% variation in a_0 or t_{max} had a very slight effect on the maximum trough amplitudes, with changes of between 0% and 5%. For the SG5_IS1 configuration, the sensitivity was greater with changes of between 8% and 17%. The maximum crest amplitude, trough amplitude, and potential energy appeared relatively insensitive to the changes in the deceleration parameter, t_{zero}. Changes to the maximum amplitude and energy values for the SG5_IS5 and SG5_IS1 cases ranged between 0% and 6% for a ±10 variation in t_{zero}. Therefore, the maximum wave amplitudes and potential energy was highly dependent on the initial landslide acceleration but relatively insensitive to landslide deceleration. From a modelling point of view, any approximation to the landslide acceleration must ensure that the initial acceleration magnitude and duration are accurately modelled. Ideally the exact slider acceleration time history would be defined continuously.

Table 7.6. Differences in maximum crest amplitude, trough amplitude, and wave potential energy, for +10% and –10% variations in a_o, t_{max}, and t_{zero}. This is for the SG5_IS5 and SG5_IS1 configurations.

SG5_IS5 Configuration			
	Change in maximum crest amplitude	**Change in maximum trough amplitude**	**Change in maximum wave potential energy**
a_0 +10%	+7.3%	+4.4%	+22.3%
a_0 -10%	-7.5%	+0.5%	-22.8%
t_{max} +10%	+8.7%	+4.5%	+25.2%
t_{max} -10%	-7.2%	+1.5%	-21.0%
t_{zero} +10%	+3.0%	0.0%	+5.2%
t_{zero} -10%	-2.2%	+0.1%	-5.4%
SG5_IS1 Configuration			
	Change in maximum crest amplitude	**Change in maximum trough amplitude**	**Change in maximum wave potential energy**
a_0 +10%	+11.5%	+10.8%	+20.1%
a_0 -10%	-12.8%	-16.9%	-22.2%
t_{max} +10%	+8.4%	+8.6%	+16.3%
t_{max} -10%	-10.8%	-15.9%	-20.6%
t_{zero} +10%	+0.3%	+1.1%	+1.8%
t_{zero} -10%	-0.4%	-1.1%	-1.8%

Table 7.7 presents the changes in the ratio of the simulated and measured times at which the first four wave crests passed x/L=20, for ±10% variations in a_o, t_{max}, and t_{zero}. These changes were for the two representative configurations, SG5_IS5 and SG5_IS1. A ±10% variation in a_0 resulted in changes to the ratios of between –0.0248 and +0.0202 for the SG5_IS5 case. The changes were between –0.0139 and +0.0092 for the SG5_IS1 case. The sensitivity of the temporal differences to variations in t_{max} was relatively small. For the SG5_IS5 case, the changes in the time differences generally lay between –0.0145 and +0.0073. For the SG5_IS1 case, there was no change to the time differences for ±10% variations in t_{max}. There was negligible effect on the time differences for changes in t_{zero} for both SG5_IS5 and SG5_IS1 configurations.

As mentioned in Section 7.6.2, the BEM model predictions of the crest arrival times at x/L = 20 were between 1.8% and 3.1% earlier than the measured times for the SG5_IS5 case, and between 2.0% and 3.6% for the SG5_IS1 case. A 10% decrease in a_0 reduced these differences to between zero and 1.53%. For the SG5_IS1 case, a 10% decrease in a_0 reduced these differences from between 2.0% and 3.6% to between 1.23% and 2.73%. This shows that uncertainty in the magnitude of the initial

acceleration may account for some of the phase speed differences observed in the comparison of the BEM results with experimental data.

Table 7.7. Change in the ratio of the simulated and measured times at which the first four wave crests pass x/L=20, for ±10% variations in a_o, t_{max}, and t_{zero}. This is for the SG5_IS5 and SG5_IS1 configurations.

SG5_IS5 Configuration				
	Change in 1st crest ratio	**Change in 2nd crest ratio**	**Change in 3rd crest ratio**	**Change in 4th crest ratio**
a_0 +10%	-0.0073	-0.0199	-0.0248	-0.0097
a_0 -10%	+0.0105	+0.0153	+0.0202	+0.0133
t_{max} +10%	0	-0.0088	-0.0145	0
t_{max} -10%	0	0	+0.0073	+0.0063
t_{zero} +10%	0	0	-0.0073	0
t_{zero} -10%	0	0	0	0
SG5_IS1 Configuration				
	Change in 1st crest ratio	**Change in 2nd crest ratio**	**Change in 3rd crest ratio**	**Change in 4th crest ratio**
a_0 +10%	-0.0139	-0.0057	-0.0060	-0.0050
a_0 -10%	+0.0003	+0.0089	+0.0092	+0.0081
t_{max} +10%	0	0	0	0
t_{max} -10%	0	0	0	0
t_{zero} +10%	0	0	0	0
t_{zero} -10%	0	0	0	0

7.8 Dependence on Slider Rigidity

The experimental configuration required the use of a longitudinally rigid slide. The motion of the landslide as it passed over the transition curve was not entirely realistic, as landslides tend to be flexible, allowing them to bend and deform over deviations in the slope. To examine the effect of a flexible slider, to more accurately model real events, the model was re-run for the SG5_IS5 to SG5_IS1, and SG5_IS5 to SG2_IS5 cases. These repeats allowed the landslide to flex as it passed over the transition curve, preventing the central section from moving away from the slope surface. Slider rigidity could have a significant impact on the wave field. As the landslide moved away from the slope, as it passed over the transition curve, it was essentially acting as a piston pushing fluid away from and then drawing it back towards the slope.

Generally the maximum crest amplitude, trough amplitude, and wave potential energy, decreased when a flexible slider was used in place of a rigid slider in the BEM model. This was due to the reduced landslide motions normal to the slope surface. This decrease was more significant for deeper initial submergences, as shown in Figure 7.18. For the SG5_IS1 case the reduction in maximum wave potential energy was almost 70%. The reduction in the wave response to a flexible slider appeared relatively insensitive to landslide specific gravity.

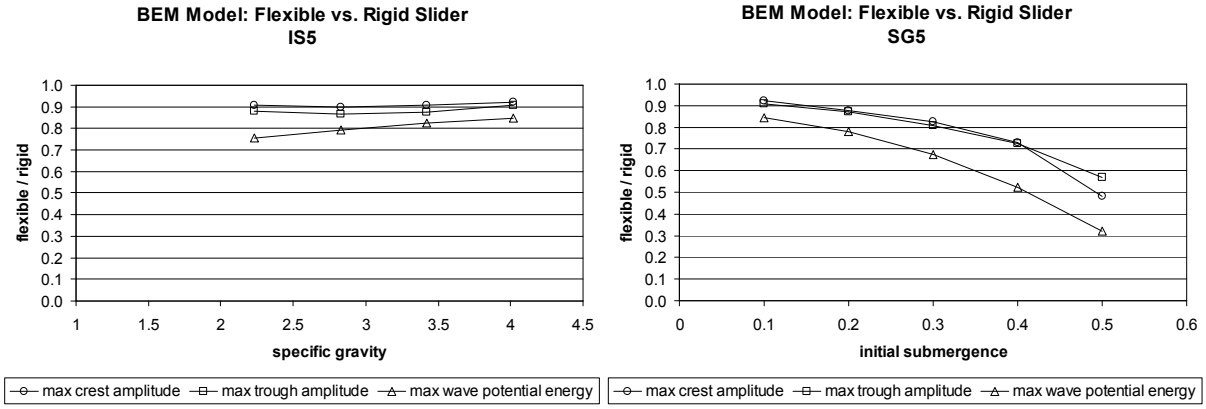

Figure 7.18. Ratio of maximum crest amplitude, trough amplitude, and wave potential energy, for a flexible slider compared to the equivalent rigid slider.

7.9 BEM Model Discussion and Summary

The BEM model was based on inviscid and irrotational flow theory, and the linear approximation was invoked and applied to the free surface and the bottom boundary conditions. The numerical model generally produced maximum crest amplitudes lower, and maximum trough amplitudes larger, than those measured in the experiments. Simulations with shallow submergences and heavier specific gravities tended to produce results closer to the measured results. The SG1_IS5 configuration was not well modelled because the assumption of a constant initial acceleration was not a good approximation to the initial non-linear growth in velocity.

The characteristics of the wave generation that the BEM model simulated well were the magnitude and range of wave amplitudes within the wave packet, the arrival time of the wave group, the amplitude of the run-up and run-down at the shore, the time the maximum run-down occurred, and the form and magnitude of the wave potential energy time history. The aspects that this model did not consistently simulate well were the magnitude of the fluid kinetic energy, time of maximum wave run-up, and the wave phase speeds.

The key to model calibration is to determine how the differences between simulation and experimental results arise, and to remove or mitigate their effect. However, modification of existing BEM code is a substantial undertaking, and one too large to incorporate into this current research. Therefore, some possible explanations for the inconsistencies in the model predictions are offered but not implemented in the model. The most significant effect almost certainly arose from the fact that an inviscid and irrotational model, such as this, could not reproduce flow separation and therefore generated a different pressure distribution over the landslide surface. The lack of the wake motions in the model velocities led to lower fluid kinetic energy estimates. The wake motions were not significant at early times, and probably accounted for the good initial agreement between the model prediction and the experimental measurements of kinetic energy for the SG5_IS1 case. However, the inability of the model to simulate the wake did not appear to have a significant effect on the wave amplitudes and potential energy. For the SG5_IS1 configuration, the maximum fluid kinetic energy was under predicted by 45%, whereas the wave potential energy was only under predicted by 9%. This suggested the wake did not make a substantial contribution to the wave generation process.

A second possible cause for the differences between model predictions and experimental results was the use of a piecewise constant acceleration model. The acceleration time histories were assumed to consist of a constant acceleration and constant deceleration phase. The differences between this and the actual acceleration profile may account for some of the timing issues. Certainly for the SG1_IS5 case, the approximation to the experimental kinematics was not suitable.

The model tended to predict an earlier arrival time of maximum wave run-up compared to the measured time. The poor matches between the times of maximum wave run-up occurred because the slider's acceleration profile was approximated. The model's initial acceleration was stipulated to be similar to the measured acceleration. This generally caused the time of maximum velocity to be under predicted, as described in Section 7.6. The slider in the BEM model began decelerating earlier, and the crest that propagated upslope was generated earlier. This was compounded by the fact that the model accuracy diminished as the water depth approached zero depth at the shore.

The BEM model assumed a perfect seal around the slope, so water could not move through the slope. However, as shown in Section 5.3.6, there was movement of water between the main channel and the area behind the slope during the experiments. Also, the model assumed a perfect seal existed between the slider and the slope surface and the sidewalls. In reality, the slider was resting just above the slope on spherical steel feet, and a gap was required between the slider and the sidewall to minimise friction. The investigation in Section 5.3.6 into a possible correction provided an estimate of the possible errors in the data due to the movement of water between the main channel and the space behind the slope. The analysis showed that the correction tended to suppress the leading crest amplitude slightly and

move the crest position further downstream. The suppression and downstream offset of the leading crest with the application of the correction was mirrored in the BEM model results.

The model tended to enlarge the leading trough amplitude by between approximately 10% and 30% over the measured values. The correction for the movement of water between the main channel and behind the slope also tended to temporarily reinforce the leading trough amplitude. The correction increased the maximum trough amplitude by between 22% and 28% over the measured amplitudes. The correction resulted in changes to the maximum wave potential energy that ranged between a 5% decrease to an 18% increase. The model energies were between approximately 30% lower and 30% greater than the experimental values. Therefore, some of the differences between the numerical results and the experimental data, particularly the leading crest and trough amplitudes and the maximum wave potential energy, may be attributed to the movement of water between the main channel and behind the slope during the experiments.

The sensitivity of the wave phase speed to the initial acceleration magnitude and duration was illustrated in Section 7.7. It showed that uncertainty in the magnitude of the initial acceleration may account for at least some of the phase speed differences observed in the comparison of the BEM results with experimental data. Also, the BEM model did not include any friction effects. Although a minor effect, friction arising from the boundary layers on the sidewalls and the floor of the channel in the experiments would have acted to slow the waves. This may have, at least partially, contributed to the measured wave speeds being slightly slower than the simulated wave speeds.

One of the stated goals of this research was to generate a significant experimental data set of sufficient quality, parameter range, and accuracy, to be used as a tool for verification and calibration of numerical models. This chapter showed that the data captured during the experimental study was suitable for a comprehensive comparison with numerical model results. The wide parameter range allowed the determination of the conditions for which the model was most suited. In the case of the BEM model shallow submergences and heavier specific gravities were modelled most accurately. The use of a constant acceleration and constant deceleration to approximate the landslide velocity time history was not suitable for all situations. With most models capable of generating detailed profiles of the free surface, the spatial and temporal range and resolution of this experimental data allowed a more detailed comparison with simulated wave fields than could be provided by point wave gauge data. The sub-surface velocity fields, measured using PTV, provided another tool for verifying the predicted velocities of models capable of generating full domain results.

Chapter 8: Conclusions

8.1 Conclusions

The importance of the study of underwater landslide generated tsunami has steadily increased since people's awareness of this phenomenon has been heightened due to recent events in the world's oceans. The focus of this research was to generate underwater landslide-induced tsunami water level data of sufficient quality for comprehensive verification of numerical models. This work also aimed to enhance our understanding of the fluid dynamics involved in underwater landslide-induced tsunami. This included an understanding of how the motion of the slide material manifested itself as a water wave, and the fluid dynamical mechanisms involved in the generation and propagation processes.

The review of the literature in Chapter 2 illustrated the characteristics, and chronological and global extent of underwater landslide-induced tsunami events. Compared to earthquake-induced tsunami, underwater landslide tsunami are essentially considered as a point source mechanism. As such the extent of damage of underwater landslide tsunami is generally more constrained than those with earthquake origins. The danger of landslide tsunami is the short travel times and the localised damage potential. Typically triggered by seismic events, movement of underwater sediments often occur in liquefiable sands. The tendency for saturated sands to compress when shaken increases the pore water pressures, reducing the shear strength of the soil. The variety of forms and the morphology of underwater landslides were also highlighted.

Chapter 3 reviewed the literature pertaining to previous laboratory and numerical research into underwater landslide generated tsunami. The use of electrical point gauges in earlier research could only provide limited data about the generation and evolution of waves due to their very limited spatial coverage. This chapter also highlighted the need for quality benchmark data suitable for comprehensive comparisons with, and validation of, numerical models. Depending on the complexity of the numerical model used, many parameters pertaining to underwater landslides could be calculated. These included such things as water surface position, wave and run-up heights, and sub-surface velocity and pressure fields. The ideal experimental dataset would contain all of this information. The landslide characteristics required as inputs into these models included position time history, volume, density, mass, shape, deformability, and slope geometry.

The experimental methods for measuring the landslide kinematics, wave field, and sub-surface velocities were described in Chapter 4. The two-dimensional configuration used in this experimental study was consistent with the benchmark experiments described in the scientific literature. This consisted of a prismatic semi-elliptical landslide moving down a 15° slope. The channel was 0.435 m deep and the landslide had a length of 0.500 m and a maximum thickness of 0.026 m. The bottom of

the slope was modified in this case to allow the landslide to run-out along the bottom of the channel, with the aim that a more realistic landslide motion was modelled. It should be noted that slides in these experiments did not reach terminal velocity. It was found that the specification of the benchmark configuration did not uniquely define the landslide motions, and therefore did not uniquely define the free surface response. The landslide and slope system was developed to ensure a high level of slide repeatability. This repeatability was critical to this experimental work, as different measurement positions and techniques were used for repeated experimental runs.

A non-intrusive technique utilising laser induced fluorescence was developed to resolve the spatial and temporal variations of the water surface. A small concentration of fluorescent dye was stirred into the tank fluid, and illuminated with a vertical laser light sheet orientated parallel with the longitudinal axis of the wave tank. The dye in the water column fluoresced due to excitation by the laser light, and this contrasted with a dark background. The interface between the regions of high and low light intensity marked the location of the free surface, and was captured with a high-resolution digital video camera. Detailed information of wave heights, lengths, propagation speeds, and shore run-up were measured, and water surface profile time histories were typically measured between $0 \leq x \leq 10.1$ metres, and $-1 \leq t \leq 8.0$ seconds after the release of the landslide. The LIF technique provided a more detailed perspective of the wave field and generation process, and was found to produce results with resolution and accuracy comparable to those of traditional electrical point wave gauges.

Particle tracking velocimetry was used to measure the landslide kinematics and sub-surface velocity profiles. This allowed the landslide and fluid kinetic energies, and the sub-surface velocity fields, to be quantified and compared to the free surface response.

The results from the experimental tests, in which the landslide specific gravity and initial submergence were varied, were presented in Chapter 5. The experiments highlighted the complex interaction between the slider and the wave field. The measurement of full water surface profile time histories proved advantageous for closely observing and quantifying the initial generation and propagation of laboratory tsunami waves. As the landslide began to slide a packet of waves, made up of a spectrum of wavelengths, was generated. The moving landslide created a water pressure distribution in the surrounding fluid. The impulse of high pressure ahead of the landslide forced the water surface directly above it up to form the first wave crest. This wave had a phase velocity that exceeded the slider velocity throughout its motion, and therefore, the initial crest propagated freely ahead of the landslide once it was generated. This prevented the pressure field surrounding the slider from interacting further with the leading crest. As the first crest quickly moved away from the landslide the crest rapidly stopped increasing in amplitude. The first crest had the longest wavelength, initially comparable in length to that of the landslide. As this wave had phase and group velocities that were

very similar, dispersion was not as significant as for the subsequent waves. This allowed the leading crest to propagate without significant change in form.

The accelerating fluid above, and the turbulent wake behind, the moving landslide created a region of low pressure. This low pressure drew down the water surface to form the first trough. The trough amplitude continued to increase because the sustained motion of the landslide transferred energy into the part of the wave field localised around the landslide. The decrease in velocity of the landslide as it reached the bottom of the slope in the experiments disrupted the low pressure region and the landslide's connection with the trough could not be maintained. This released the trough, and as it propagated as a free wave, its amplitude decayed due to wave dispersion. The subsequent waves in the train formed through dispersion of the leading waves. By comparing the instantaneous position and speed of the landslide relative to the wave field, it was found that the point at which the leading crest and trough met was centred above the landslide centre of mass and remained there as the block slid down the slope.

Although the depth of the tank was not great enough it was expected that increasing water depth would reduce the effect of the landslide motions on the pressure field at the surface, thereby also acting to sever the connection between the landslide and the first trough.

By observing the water surface profile time histories and the spectral analysis results, the wavelength components of the wave field were assessed at various times. The frequency dispersion of the waves was evident, as waves further behind in the wave train propagated more slowly than those in front, acting to spread the packet as it propagated, and the wavelengths of the individual waves increased with time. The increasing water depth in the wave generation region caused further wave dispersion. The energy within the wave packet propagated at the group velocity of the corresponding wavelengths within the spectrum. The group velocities of the waves trailing the leading crest were slower than their phase speed. Therefore, the amplitude of waves near the front of the wave packet slowly decreased and new waves were continually generated at the trailing edge of the packet. The downstream position at which the new waves were created was moving downstream over time, though at a substantially slower speed than the wave propagation and landslide speeds. The trailing waves had smaller amplitudes to those in front. Therefore, the greatest danger is posed by the leading waves, which have the largest amplitudes. The maximum crest and trough amplitudes tended to increase for heavier specific gravities and shallower initial submergences.

The energy cascade consisted of some of the landslide potential energy being converted into landslide kinetic energy as it slid down the slope. The remaining potential energy was dissipated as friction on the sliding surface. The motion of the landslide set in motion some of the surrounding fluid,

converting some of the landslide's kinetic energy into kinetic energy of the water. Some of the energy in the water motions was then passed into the wave potential energy, the remainder being dissipated through friction. The interaction of the landslide pressure field with the surface wave pressure field is important, as the location of the low pressure around the landslide relative to the wave field acts to reinforce or suppress the waves above. This has a substantial effect on the increase or decrease in wave potential energy. When the low pressure acts to draw down a wave trough, the wave potential energy increases. When the low pressure is below a wave crest, it acts to suppress the crest amplitude, leading to an overall decrease in wave potential energy. The close matching of slider and leading trough speeds allow the longest duration over which a positive interaction can occur. Should the slider's low pressure region coincide with the leading trough for a long duration, then the wave potential energy can increase significantly.

The maximum wave potential energy occurred at a time later than that of the maximum landslide kinetic energy. Therefore, the period of positive landslide acceleration is not the only time over which energy is passed into the wave field. It is possible for substantial energy transfer into the wave field to occur after the time of maximum velocity and as the landslide decelerates. Provided the landslide is in motion, energy can be transferred, as it is the interaction of the landslide's pressure field and the free surface that determines the effectiveness of the transfer. The ratio of maximum wave potential energy to maximum landslide kinetic energy was between 0.028 and 0.138. Shallow initial submergences and lighter specific gravities increased this efficiency. The ratio of maximum wave potential energy to maximum landslide potential energy ranged between 0.011 and 0.059 and tended to be greater for shallower initial submergences. The effect of increasing specific gravity was relatively weak. The conversion ratio of maximum potential energy to maximum kinetic energy of the landslide ranged between 0.329 and 0.504. This level of energy transfer was for the laboratory configuration with the steel spheres on the base of the landslide moving over smooth plastic sheeting coated in silicone grease. The sliding friction is expected to be significantly greater for soil-to-soil slide interfaces, leading to reduced transfer of landslide potential energy into landslide kinetic energy. However, should the landslide aquaplane, then a layer of fluid above the slope-to-landslide interface will reduce the sliding friction and allow greater energy transfer.

The wave trough initially generated above the rear end of the landslide propagated in both the onshore and offshore directions. The onshore-propagating trough was found to cause the large initial draw-down at the shore. The magnitude of the maximum wave run-down was directly related to the maximum amplitude of the leading downstream-propagating wave trough, and tended to decrease for lighter specific gravities and deeper initial submergences. The time at which the maximum wave run-down occurred was independent of specific gravity, dependent solely on the initial submergence of the landslide. The maximum wave run-up height observed at the shore occurred as a result of a wave

generated by the short duration, but high magnitude, deceleration of the landslide upon reaching the base of the slope. A wave crest generated at that point and time propagated onshore. The maximum wave run-up heights increased for heavier specific gravities and shallower initial submergences. This was confirmed through numerical modelling. Simulations with the semi-analytical model showed that the magnitude of the upstream propagating wave was dependent on the magnitude of the deceleration of the slider. While wave run-up may appear to pose a greater hazard than the draw down of water at the shore, significant wave run-down can cause substantial increases in the pore water pressures in the soils at the shore. This may lead to further landslides or the collapse of coastal land and structures into the water. Numerical modelling indicated that the onshore propagating waves were dispersive. Should a landslide occur far from shore, the onshore propagating waves may break into a train of waves and decrease in amplitude.

The visualisation of sub-surface velocities, using PTV, allowed the generation mechanism of the wave field to be confirmed. The upward flow over the front of the sliding block highlighted a region of high pressure that forced the water directly above into a wave crest. The accelerating flow over the top, and flow separation on the rear, of the landslide created a region of low pressure that drew down the water surface into a wave trough. After the passing of the landslide, a significant flow of water, in the direction of landslide motion, was established adjacent to the slope surface and tank floor. For continuity of mass, a gentle upstream flow was observed in the remainder of the water column. Near the base of the slope, several large, near stationary, rotating eddies were left behind in the wake as the landslide moved past.

Flow separation and the motion of the fluid as it was accelerated over the landslide created high fluid kinetic energies above the rear of the landslide. Downstream of the final run-out distance of the landslide and the wave generation region, the partitioning of the total wave energy between kinetic and potential energy was found to be between 80% and 100%. The ratio of maximum wave potential energy to maximum fluid kinetic energy was estimated to be 0.435 and 0.588 for the SG5_IS1 and SG1_IS5 cases respectively. For both cases the time of maximum fluid kinetic energy coincided with the time at which the landslide reached the horizontal bed at the base of the transition curve.

A semi-analytical model, based on inviscid and irrotational theory, was used to investigate the wave generation process of a moving submerged object in a constant depth channel in Chapter 6. The simplified geometry allowed a variety of phenomena, observed during the experimental tests, to be investigated further in a more controlled setting. In particular, the wave response to different acceleration profiles and magnitudes, water depths, and slider Froude numbers was examined. The model showed that slides with Froude numbers closest to unity converted substantially more energy into offshore propagating wave potential energy than slides with a Froude number dissimilar to unity.

When Fr≈1, a resonance-type effect existed and the wave potential energy continued to grow with time. However, underwater landslides in nature tend to have Fr < 1. The onshore propagating wave potential energy was not as sensitive to Froude number.

The effect of the slider acceleration parameter, λ, and the geometric parameter, τ, were quantified. An investigation with the semi-analytical model suggested that the dependence of wave energy on the initial slider acceleration was stronger than the dependence on water depth, and highlighted the need for the accurate specification of the initial slider acceleration in numerical simulations. The effects of λ and τ appeared to be decoupled, for a single Froude number and acceleration profile. A further result from the semi-analytical model simulations was that the specific shape of the slider had only a minor influence on the wave response, provided the slider's length and area were known. The constant depth model was not able to simulate the changing water depth of the experimental configuration accurately.

The boundary element model described in Chapter 7, also based on inviscid and irrotational theory, was used to simulate the laboratory experiments. It was found that even though the model was based on linear equations, the wave field properties were generally predicted accurately. In particular the magnitude and range of wave amplitudes within the wave packet, the arrival time of the wave group, the amplitude of the run-up and run-down at the shore, the time the maximum run-down occurred, and the form and magnitude of the wave potential energy time history were simulated accurately. The ratios of maximum wave potential energy to maximum slider kinetic energy were predicted to within ± 29%. The model predictions of the crest arrival times were within 3.6% of the measured times. Even though the inviscid and irrotational flow theory of the BEM model was not capable of predicting the wake motions, leading to a 45% underestimation of the maximum fluid kinetic energy for the SG5_IS1 case, the wave amplitudes and potential energies were accurately predicted. This suggested that the flow separation and the wake motions only had a secondary influence on the wave generation process. However, the inability to model the down-slope fluid motions adjacent to the channel bed and the gentle onshore drift in the upper portion of the water column, after the slider passed, led to velocity profiles dissimilar to the measured profiles.

A sensitivity analysis with the BEM model highlighted the need for appropriate approximations to the magnitude and duration of the initial acceleration to ensure correct modelling of the wave generation process and wave energies and phase speeds. The wave field properties were not as sensitive to the slider deceleration. The suitability of the experimental data, as a tool for verification and calibration of numerical models, was confirmed.

8.2 Novel Contributions

Previous tsunami experimentalists relied on fifty-year-old technology that interfered with the flow field, provided only limited data, required frequent and cumbersome calibration, and could only be used in specific situations. This project used newly developed techniques to allow the entire wave and water velocity field to be visualised and measured. Optically based techniques, Laser Induced Fluorescence (LIF) and Particle Tracking Velocimetry (PTV), allowed for continuous spatial and temporal variations of surface and sub-surface motions to be captured. This research developed these techniques and applied them to produce an extensive data set for use in the calibration of numerical models.

The experimental configuration used in this study was based on a benchmark configuration developed by the tsunami research community and described in the literature. These experiments covered a wide range of parameters not previously investigated in such a rigorous and controlled manner, and ultimately provide a dataset for this benchmark problem of sufficient quality, parameter range, and accuracy suitable for numerical model validation.

A semi-analytical spectral model, based on inviscid and irrotational flow theory, was used to explore some of the key phenomena associated with the wave generation process in a simplified flow domain. Finally a boundary element method model was used to generate numerical data to compare with the experimental results.

8.3 Future Research Considerations

This research has provided broad and detailed measurements of the wave field and sub-surface velocity distributions, suitable for validation of numerical models. However, several important parameters were not investigated, in particular the slope angle, water depth, and landslide porosity. The slope angle and water depth were both limited to 15° and 0.435 m respectively. Variations in one or both of these would provide different slide distances. As the literature states that the landslide runout lengths tend to be longer on shallower slopes, the longer slide distances and durations would allow greater interaction between the landslide and the wave field. The effect of this prolonged interaction could be investigated in future research, particularly with a landslide that reaches terminal velocity. It is also expected that the influence of the pressure field surrounding the landslide would have less effect on the wave field as the water depth above the landslide increases. The effect of the reduced wave response to increasing water depth could also be quantified.

Surface tension issues generate significant difficulties in scaling up laboratory results. Also, allowing for the complexities in nature, such as varying bathymetry, bottom roughness, and landslide geometry,

makes numerical modelling the only effective way to simulate real life events. Therefore, the creation and development of numerical models is required. Laboratory experimental results and field measurements of actual events still provide the only means with which to calibrate and verify these numerical models. To some extent validated models possess some predictive qualities. The available scope in the continual development of numerical models leaves plenty of future research opportunities. For instance, the BEM model developed during this research can be improved by specifying the actual landslide acceleration time history instead of approximating it by defined periods of constant acceleration.

This experimental work was completed using a rigid landslide model in a two-dimensional configuration. The generation of a comprehensive dataset using granular slide material is still required to verify numerical models of landslides comprised of deformable material. The porosity of the granular material is expected to significantly reduce the wave response compared to rigid block landslides. However, issues surrounding the scaling of grain size and distribution in the experiments compared to field scale need careful consideration. Also, the effects of soil cohesion need some thought. Perhaps a perforated rigid landslide would provide the porosity without the added complexity of grain size effects. Detailed measurements from three-dimensional underwater landslide experiments are required for comparison with three-dimensional numerical wave models.

References

Abe, K. (1981). "A New Scale of Tsunami Magnitude, Mt." Tsunamis: Their Science and Engineering. Proceedings of the International Tsunami Symposium, May 1981, Sendai-Ofunato-Kamaishi, Japan, l. Iida and T. Iwasaki, eds., Terra Scientific Publishing Company, 91-101.

Andrew, N., and Francis, M. (2003). *The living reef : the ecology of New Zealand's rocky reefs*, Craig Potton Publishing, Nelson, N.Z.

Arnold, A., Bombach, R., Kappeli, B., and Schlegel, A. (1997). "Quantitative measurements of OH concentration fields by two-dimensional laser-induced fluorescence." *Applied Physics B: Lasers and Optics*, 64(5), 579-583.

Bardet, J. P., Synolakis, C. E., Davies, H. L., Imamura, F., and Okal, E. A. (2003). "Landslide tsunamis: Recent findings and research directions." *Pure and Applied Geophysics*, 160(10-11), 1793-1809.

Barnes, G. E. (2000). *Soil mechanics : principles and practice*, Macmillan, Basingstoke [England].

Barnes, P., M., Cheung, K. C., Smits, A., P., Almagor, G., Read, S., A.L., Barker, P., R., and Froggatt, P. (1991). "Geotechnical analysis of the Kidnappers Slide, upper continental slope, New Zealand." *Marine Geotechnology*, 10(1-2), 159-188.

Beer, G., and Watson, J. O. (1992). *Introduction to finite and boundary element methods for engineers*, Wiley, Chichester, England.

Brebbia, C. A., and Walker, S. (1979). *Boundary element techniques in engineering*, Newnes-Butterworths, London.

Bryant, E. (2001). *Tsunami : the underrated hazard*, Cambridge University Press, Cambridge ; New York.

Churchill Controls Ltd. (1977). *Wave Monitor: Technical Manual*.

Daubechies, I. (1992). *Ten lectures on wavelets*, Society for Industrial and Applied Mathematics, Philadelphia, Pa.

Davies, H. L., Davies, J. M., Perembo, R. C. B., and Lus, W. Y. (2003). "The Aitape 1998 tsunami: Reconstructing the event from interviews and field mapping." *Pure and Applied Geophysics*, 160(10-11), 1895-1922.

Day, S. J., Watts, P., Grilli, S. T., and Kirby, J. T. (2005). "Mechanical models of the 1975 Kalapana, Hawaii earthquake and tsunami." *Marine Geology*, 215(1-2 SPEC ISS), 59-92.

De Lange, W. P., and Moon, V. G. (2004). "Estimating earthquake and landslide tsunami hazard for the New Zealand coast." *Bulletin of the New Zealand Society for Earthquake Engineering*, 37(2), 62-69.

Enet, F., Grilli, S. T., and Watts, P. (2003). "Laboratory Experiments for Tsunamis Generated by Underwater Landslides: Comparison with Numerical Modeling." *Proceedings of the Thirteenth (2003) International Offshore and Polar Engineering Conference, May 25 2003-May 30 2003*, Honolulu, HI, United States, 1717-1724.

Fine, I. V., Rabinovich, A. B., Bornhold, B. D., Thomson, R. E., and Kulikov, E. A. (2005). "The Grand Banks landslide-generated tsunami of November 18, 1929: Preliminary analysis and numerical modeling." *Marine Geology*, 215(1-2 SPEC ISS), 45-57.

Finn, W. D. L. (2003). "Landslide-generated tsunamis: Geotechnical considerations." *Pure and Applied Geophysics*, 160(10-11), 1879-1894.

Fleming, J. G., Walters, R. A., Sue, L. P., and Nokes, R. I. (2005). "Experimental Design For Solid Block and Granular Submarine Landslides: A Unified Approach." Tsunamis: Case Studies and Recent Developments, K. Satake, ed., Springer, 259-277.

Fritz, H. M. (2002). "Initial Phase of Landslide Generated Impulse Waves," PhD, Swiss Federal Institute of Technology, Zurich, Switzerland.

Fritz, H. M., Hager, W. H., and Minor, H. E. (2003a). "Landslide generated impulse waves. 1. Instantaneous flow fields." *Experiments in Fluids*, 35(6), 505-519.

Fritz, H. M., Hager, W. H., and Minor, H. E. (2003b). "Landslide generated impulse waves. 2. Hydrodynamic impact craters." *Experiments in Fluids*, 35(6), 520-532.

Gogineni, S., Bush, D., and Katsaros, K. (1990). "Quasi-laboratory measurements on Lake Washington for investigating radar backscattering from ocean surfaces." *10th Annual International Geoscience and Remote Sensing Symposium - IGARSS '90, May 20 1990*, College Park, MD, USA, 1067-1069.

Grilli, S. T., Kirby, J. T., Liu, P. L. F., Brandes, H., and Fryer, G. J. (2003). "Workshop on Model Validation and Benchmarking For Tsunami Generation by Submarine Mass Failure - Proposal Submitted to NSF." Honolulu, Hawaii.

Grilli, S. T., and Subramanya, R. (1996). "Numerical modeling of wave breaking induced by fixed or moving boundaries." *Computational Mechanics*, 17(6), 374-391.

Grilli, S. T., Vogelmann, S., and Watts, P. (2002). "Development of a 3D numerical wave tank for modeling tsunami generation by underwater landslides." *Engineering Analysis with Boundary Elements*, 26(4), 301-313.

Grilli, S. T., and Watts, P. (1999). "Modeling of waves generated by a moving submerged body. Applications to underwater landslides." *Engineering Analysis with Boundary Elements*, 23(8), 645-656.

Grilli, S. T., and Watts, P. (2005). "Tsunami generation by submarine mass failure. I: Modeling, experimental validation and sensitivity analyses." *Journal of Waterway, Port, Coastal and Ocean Engineering*, 131(6), 283-297.

Hampton, M. A., Lee, H. J., and Locat, J. (1996). "Submarine landslides." *Reviews of Geophysics*, 34(1), 33-59.

Heinrich, P. (1992). "Nonlinear Water-Waves Generated by Submarine and Aerial Landslides." *Journal of Waterway Port Coastal and Ocean Engineering-Asce*, 118(3), 249-266.

Horikawa, K., and Shuto, N. (1981). "Tsunami Disasters and Protection Measures in Japan." Tsunamis: Their Science and Engineering. Proceedings of the International Tsunami Symposium, May 1981, Sendai-Ofunato-Kamaishi, Japan, l. Iida and T. Iwasaki, eds., Terra Scientific Publishing Company, 9-22.

Horrillo, J., Kowalik, Z., and Shigihara, Y. (2006). "Wave Dispersion Study in the Indian Ocean Tsunami of December 26, 2004." *Science of Tsunami Hazards*, 25(1), 42-63.

Houcine, I., Vivier, H., Plasari, E., David, R., and Villermaux, J. (1996). "Planar laser induced fluorescence technique for measurements of concentration fields in continuous stirred tank reactors." *Experiments in Fluids*, 22(2), 95-102.

Hsu, C. T., Kuang, J., and Sun, J. H. (2001). "Flapping instability of vertically impinging turbulent plane jets in shallow water." *Journal of Engineering Mechanics*, 127(5), 411-420.

Imamura, F., and Hashi, K. (2003). "Re-examination of the source mechanism of the 1998 Papua New Guinea earthquake and tsunami." *Pure and Applied Geophysics*, 160(10-11), 2071-2086.

Imamura, F., and Imteaz, M. M. A. (1995). "Long Waves in Two Layers: Governing Equations and Numerical Model." *Science of Tsunami Hazards*, 13(1), 3-24.

Ishihara, K. (2002). "Failure of Slopes and Soil Property Characterization - 2nd Lumb Lecture in Hong Kong." Hong Kong, 1-38.

Jiang, L., and Leblond, P. H. (1992). "The Coupling of a Submarine Slide and the Surface-Waves Which It Generates." *Journal of Geophysical Research-Oceans*, 97(C8), 12731-12744.

Kanoglu, U. (2003). "Nonlinear Evolution and Runup of a Solitary Wave Over a Sloping Beach." *Long Waves Symposium*, AUTh, Thessaloniki, Greece, 281-288.

Kennedy, A. B., Chen, Q., Kirby, J. T., and Dalrymple, R. A. (2000). "Boussinesq modeling of wave transformation, breaking, end runup. I: 1D." *Journal of Waterway Port Coastal and Ocean Engineering-Asce*, 126(1), 39-47.

Kozlova, T. G., Lobacheva, M. I., Pravdin, A. B., Romakina, M. Y., Sinichlin, Y. P., and Tuchin, V. V. (1991). "Laser spectroscopy of carotenoids in plant bioobjects." *International Conference on Laser Applications in Life Sciences Part 1 (of 2), Aug 27-31 1990*, Moscow, USSR, 159-160.

Le Méhauté, A. (1976). *An introduction to hydrodynamics and water waves*, Springer-Verlag, N.Y.

Lebey, M., and Rivoalen, E. (2002). "Experimental study of the working principal and efficiency of a superposed inclined planes wave absorber." *Ocean Engineering*, 29(11), 1427-1440.

Lee, H. J., Kayen, R. E., Gardner, J. V., and Locat, J. (2003). "Characteristics of Several Tsunamigenic Submarine Landslides." Submarine mass movements and their consequences : 1st international symposium, J. Locat and J. Mienert, eds., Kluwer Academic Publishers, Boston, 357-366.

Lee, J. J., Chang, C., and Zhuang, F. (1993). "Interaction of nonlinear waves with coastal structures." *Proceedings of the 23rd International Conference on Coastal Engineering, Oct 4-9 1992*, Venice, Italy, 1327-1340.

Lighthill, M. J. (1978). *Waves in fluids*, Cambridge University Press, Cambridge [Eng.] ; New York.

Liu, P. L. F., Wu, T. R., Raichlen, F., Synolakis, C. E., and Borrero, J. C. (2005). "Runup and rundown generated by three-dimensional sliding masses." *Journal of Fluid Mechanics*, 536, 107-144.

Locat, J., and Lee, H. J. (2002). "Submarine landslides: Advances and challenges." *Canadian Geotechnical Journal*, 39(1), 193-212.

Lommer, M., and Levinsen, M. T. (2002). "Using Laser-Induced Fluorescence in the Study of Surface Wave Turbulence." *Journal of Fluorescence*, 12(1), 45-50.

Lynett, P. J., Borrero, J. C., Liu, P. L. F., and Synolakis, C. E. (2003). "Field survey and numerical simulations: A review of the 1998 Papua New Guinea tsunami." *Pure and Applied Geophysics*, 160(10-11), 2119-2146.

Mallat, S. G. (1999). *A wavelet tour of signal processing*, Academic, San Diego, Calif. ; London.

Mariotti, C., and Heinrich, P. (1999). "Modelling of submarine landslides of rock and soil." *International Journal for Numerical and Analytical Methods in Geomechanics*, 23(4), 335-354.

Martel, S. J. (2004). "Mechanics of landslide initiation as a shear fracture phenomenon." *Marine Geology*, 203(3-4), 319-339.

McAdoo, B. G., Pratson, L. F., and Orange, D. L. (2000). "Submarine landslide geomorphology, US continental slope." *Marine Geology*, 169(1-2), 103-136.

Mix, D. F., and Olejniczak, K. J. (2003). *Elements of wavelets for engineers and scientists*, Wiley-Interscience, Hoboken, NJ.

Mori, N., and Chang, K.-A. (2003). "Experimental study of a horizontal jet in a wavy environment." *Journal of Engineering Mechanics*, 129(10), 1149-1155.

Murty, T. S. (2003). "Tsunami wave height dependence on landslide volume." *Pure and Applied Geophysics*, 160(10-11), 2147-2153.
New Scientist. (2004). "Hawaiian Tsunami Left a Gift at the Foot of Kohala Volcano." *New Scientist*, 2464(2464), 14.
Nokes, R. I. (2005a). "FluidStream v6.01: System Theory and Design." Christchurch, New Zealand, Particle Tracking Velocimetry (PTV).
Nokes, R. I. (2005b). "FluidStream v6.01: User's Guide." Christchurch, New Zealand, Particle Tracking Velocimetry (PTV).
Nokes, R. I. (2005c). "ImageStream v5.01: System Theory and Design." Christchurch, New Zealand, Image Processing.
Ojanen, H. (1999). "Automatic Correction of Lens Distortion by Using Digital Image Processing." http://www.math.rutgers.edu/~ojanen/undistort/undistort.pdf.
Okal, E. A. (2003). "T waves from the 1998 Papua New Guinea earthquake and its aftershocks: Timing the tsunamigenic slump." *Pure and Applied Geophysics*, 160(10-11), 1843-1863.
Ouellet, Y., and Datta, I. (1986). "A Survey of Wave Absorbers." *Journal of Hydraulic Research*, 24(4), 265-280.
Papadopoulos, G. A., and Kortekaas, S. (2003). "Characteristics of Landslide Generated Tsunamis From Observational Data." Submarine mass movements and their consequences : 1st international symposium, J. Locat and J. Mienert, eds., Kluwer Academic Publishers, Boston, 367-374.
Peacock, K. (2002). "Stations Should Have a Tsunami Tactical Plan." Star, 14.
Plew, D. R. (2005). "The Hydrodynamic Effects of Long-line Mussel Farms," PhD, University of Canterbury, Christchurch, New Zealand.
Raamachandran, J. (2000). *Boundary and finite elements : theory and problems*, CRC Press; Narosa Pub. House, Boca Raton, New Delhi.
Raichlen, F., and Synolakis, C. E. (2003). "Run-up From Three-Dimensional Sliding Masses." *Long Waves Symposium*, AUTh, Thessaloniki, Greece, 247-256.
Ruff, L. J. (2003). "Some aspects of energy balance and tsunami generation by earthquakes and landslides." *Pure and Applied Geophysics*, 160(10-11), 2155-2176.
Rzadkiewicz, S. A., Mariotti, C., and Heinrich, P. (1997). "Numerical simulation of submarine landslides and their hydraulic effects." *Journal of Waterway Port Coastal and Ocean Engineering-Asce*, 123(4), 149-157.
Sauer, F. M., and Wiegel, R. L. (1946). "Memorandum on Laboratory Experiments on Waves Generated by an Underwater Landslide." *HE-116-218*, University of California, Berkeley, California.
Shiono, K., and Feng, T. (2003). "Turbulence measurements of dye concentration and effects of secondary flow on distribution in open channel flows." *Journal of Hydraulic Engineering*, 129(5), 373-384.
Shuto, N. (1991). "Tsunami Intensity and Disasters. Proceedings of the Fifteenth Interbational Tsunami Symposium, 1991, Vienna, Austria." Tsunamis in the World, S. Tinti, ed., Kluwer Academic Publishers, 197-216.
Shy, S., Yeh, W. J., and Chu, C. C. (1997). "Velocity measurements and flow visualizations of jet interaction with a sharp density interface." *Proceedings of the 1997 ASME Fluids Engineering Division Summer Meeting, FEDSM'97. Part 13 (of 24), Jun 22-26 1997*, Vancouver, Can, 3.
Strang, G., and Nguyen, T. (1997). *Wavelets and filter banks*, Wellesley-Cambridge Press, Wellesley, MA.
Synolakis, C. E. (1987). "The Runup of Solitary Waves." *Journal of Fluid Mechanics*, 185, 523-545.

Tappin, D. R., Watts, P., McMurtry, G. M., Lafoy, Y., and Matsumoto, T. (2001). "The Sissano, Papua New Guinea tsunami of July 1998 - offshore evidence on the source mechanism." *Marine Geology*, 175(1-4), 1-23.

Tarman, H. I., and Kanoglu, U. (2003). "Numerical Simulation of Long Wave Runup on a Sloping Beach." *Long Waves Symposium*, AUTh, Thessaloniki, Greece, 273-279.

Tian, X., and Roberts, P. J. W. (2003). "A 3D LIF system for turbulent buoyant jet flows." *Experiments in Fluids*, 35(6), 636-647.

Tinti, S., Armigliato, A., Manucci, A., Pagnoni, G., Zaniboni, F., Yalciner, A. C., and Altinok, Y. (2006). "The generating mechanisms of the August 17, 1999 Izmit bay (Turkey) tsunami: Regional (tectonic) and local (mass instabilities) causes." *Marine Geology*, 225(1-4), 311-330.

Tinti, S., and Bortolucci, E. (2000a). "Analytical investigation on tsunamis generated by submarine slides." *Annali Di Geofisica*, 43(3), 519-536.

Tinti, S., and Bortolucci, E. (2000b). "Energy of water waves induced by submarine landslides." *Pure and Applied Geophysics*, 157(3), 281-318.

Tinti, S., Bortolucci, E., and Romagnoli, C. (2000). "Computer simulations of tsunamis due to sector collapse at Stromboli, Italy." *Journal of Volcanology and Geothermal Research*, 96(1-2), 103-128.

United States Army Corps of Engineers. (2002). "Water Wave Mechanics: Chapter 1, Section 1." Coastal Engineering Manual: Part II, Washington, D.C. : Dept. of the Army, U.S. Army Corps of Engineers.

VanLerberghe, W. M., Santiago, J. G., Dutton, J. C., and Lucht, R. P. (2000). "Mixing of a sonic transverse jet injected into a supersonic flow." *AIAA Journal*, 38(3), 470-479.

Walters, R. (2003). "Tsunami Runup: Model Development and Testing." *Long Waves Symposium*, AUTh, Thessaloniki, Greece, 289-296.

Walters, R. A., National Institute of Water and Atmospheric Research (Canterbury, N. Z., and Canterbury, E. (2003). "Kaikoura District engineering lifelines project." Environment Canterbury, Christchurch [N.Z.].

Wang, H. J., and Davidson, M. J. (2001). "A profile tracking system for investigating the behaviour of discharges in moving environments." *Experiments in Fluids*, 31(5), 533-541.

Ward, S. N. (2001). "Landslide tsunami." *Journal of Geophysical Research-Solid Earth*, 106(B6), 11201-11215.

Watts, P. (1997). "Water Waves Generated by Underwater Landslides," PhD, California Institute of Technology, Pasadena, California.

Watts, P. (1998). "Wavemaker curves for tsunamis generated by underwater landslides." *Journal of Waterway Port Coastal and Ocean Engineering-Asce*, 124(3), 127-137.

Watts, P. (2000). "Tsunami features of solid block underwater landslides." *Journal of Waterway Port Coastal and Ocean Engineering-Asce*, 126(3), 144-152.

Watts, P., and Grilli, S. T. (2003). "Underwater Landslide Shape, Motion, Deformation, and Tsunami Generation." *Proceedings of the Thirteenth (2003) International Offshore and Polar Engineering Conference, May 25 2002-May 30 2003*, Honolulu, HI, United States, 1709-1716.

Watts, P., Grilli, S. T., Tappin, D. R., and Fryer, G. J. (2005). "Tsunami generation by submarine mass failure. II: Predictive equations and case studies." *Journal of Waterway, Port, Coastal and Ocean Engineering*, 131(6), 298-310.

Watts, P., Imamura, F., Bengston, A., and Grilli, S. T. (2001). "Benchmark cases for tsunamis generated by underwater landslides." *Proceedings of the Fourth International Symposium Waves 2001, Sep 2-6 2001*, San Francisco, CA, 1505-1514.

Watts, P., Imamura, F., and Grilli, S. T. (2000). "Comparing Model Simulations of Three Benchmark Tsunami Generation Cases." *Science of Tsunami Hazards*, 18(2), 107-123.

Wiegel, R. L. (1955). "Laboratory studies of gravity waves generated by movement of submerged body." *American Geophysical Union -- Transactions*, 36(5), 759-774.

Wright, S. G., and Rathje, E. M. (2003). "Triggering mechanisms of slope instability and their relationship to earthquakes and tsunamis." *Pure and Applied Geophysics*, 160(10-11), 1865-1877.

Yeh, H. H., and Ghazali, A. (1987). "Nearshore Behaviour Of Bore On A Uniformly Sloping Beach." *Twentieth Coastal Engineering Conference, Proceedings of the International Conference.*, Taipei, Taiwan, 877-888.

Zhou, J., Lu, D., Li, Z., Sheng, K., and Duan, Y. (1994). "C2 concentration measurement in the exhaust gas of a gasoline engine by laser-induced fluorescence." *Zhongguo Jiguang/Chinese Journal of Lasers*, 21(3), 230-232.

Appendix A: Landslide Model Drawings

Construction drawings for the semi-elliptically shaped landslide, generated using AutoCAD 2002, are presented in Figures A.1 to A.3.

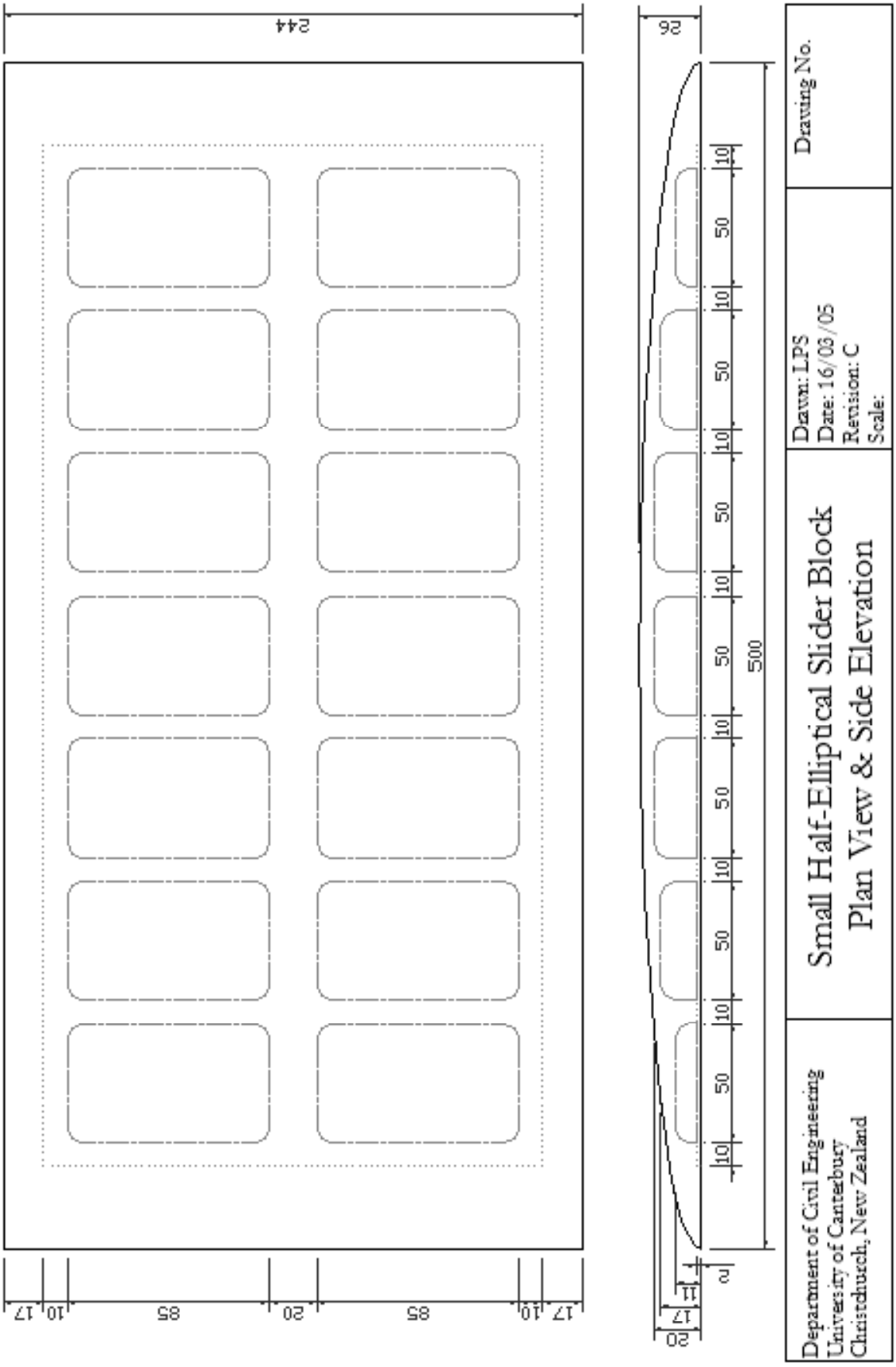

Figure A.1. Landslide plan view and side elevation construction drawings.

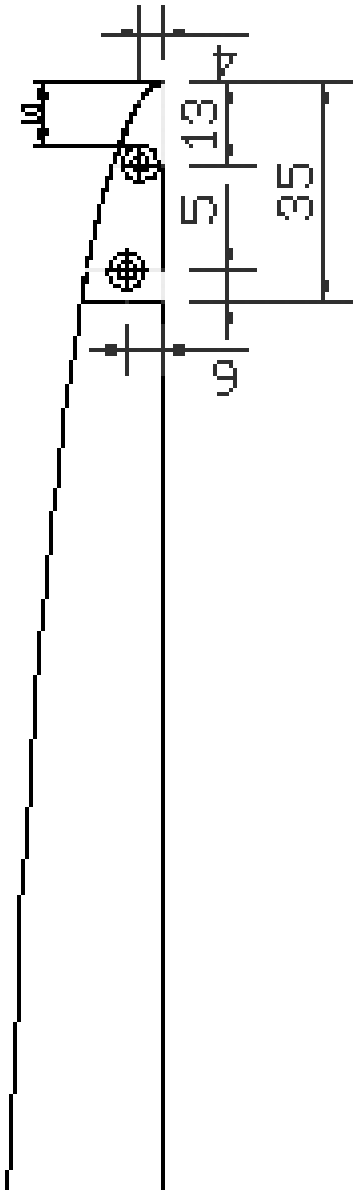

Small Half-Elliptical Slider Block
Plastic Block Corner Detail

Figure A.2. Landslide plastic corner detail construction drawings.

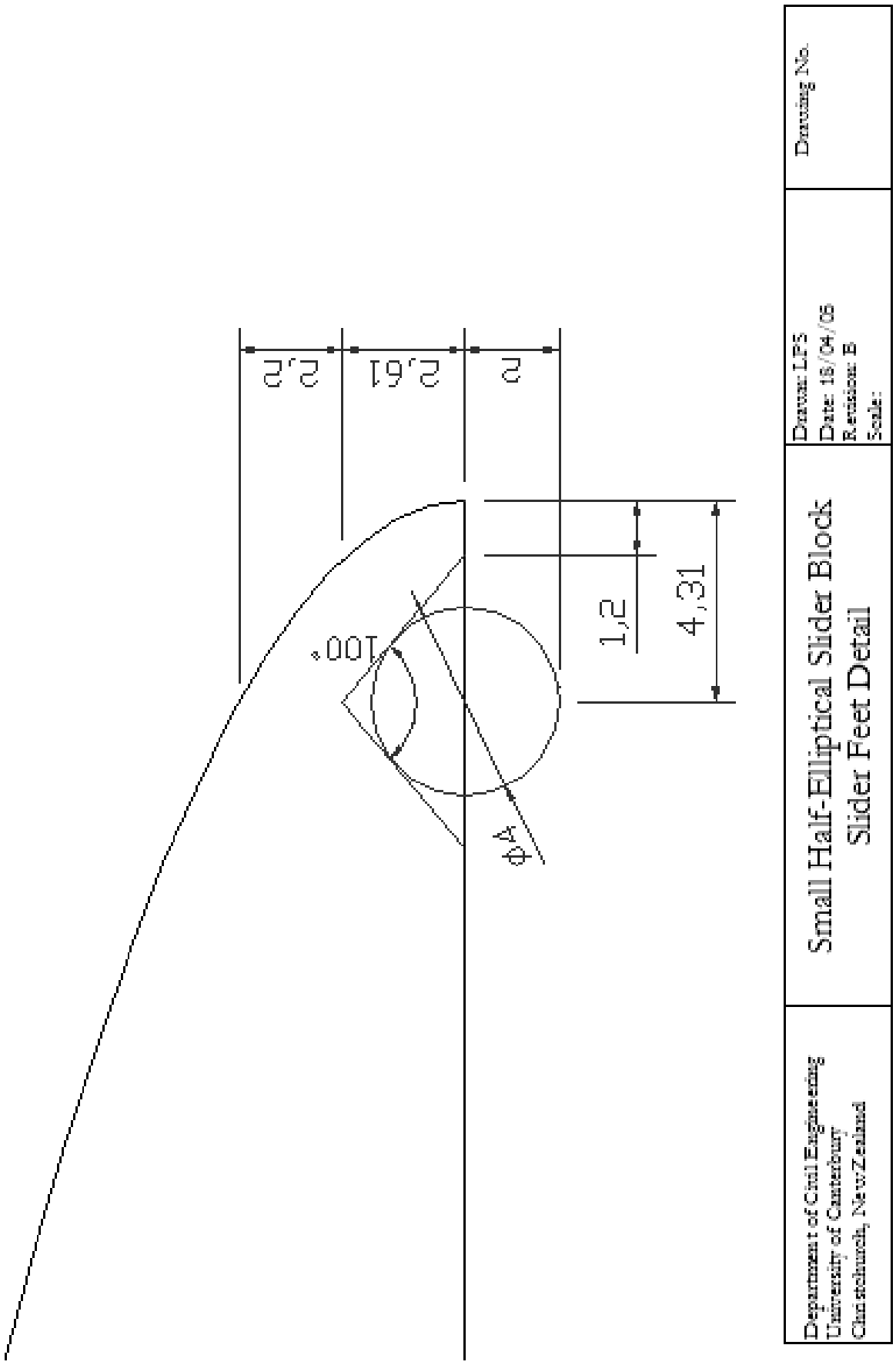

Figure A.3. Landslide feet detail construction drawings.

Appendix B: Landslide Kinematics

Plots of the landslide velocity and acceleration time histories for each of the fifteen specific gravity and initial submergence combinations are presented in Figures B.1 to B.15.

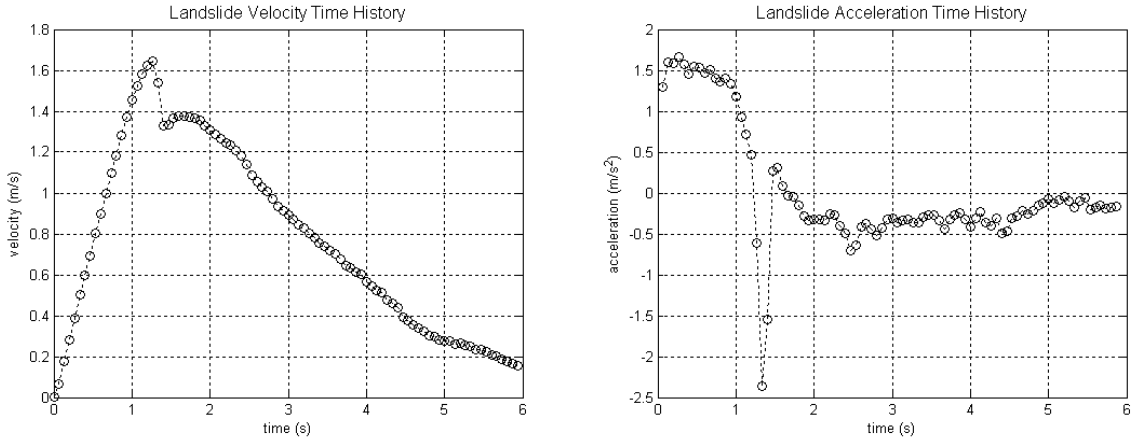

Figure B.1. Landslide centre of mass velocity and acceleration time history for the SG5_IS5 configuration.

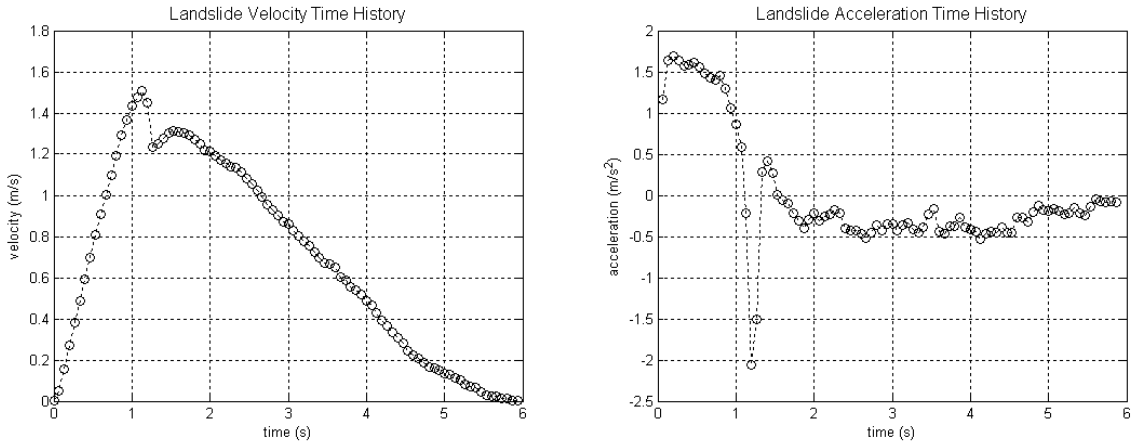

Figure B.2. Landslide centre of mass velocity and acceleration time history for the SG5_IS4 configuration.

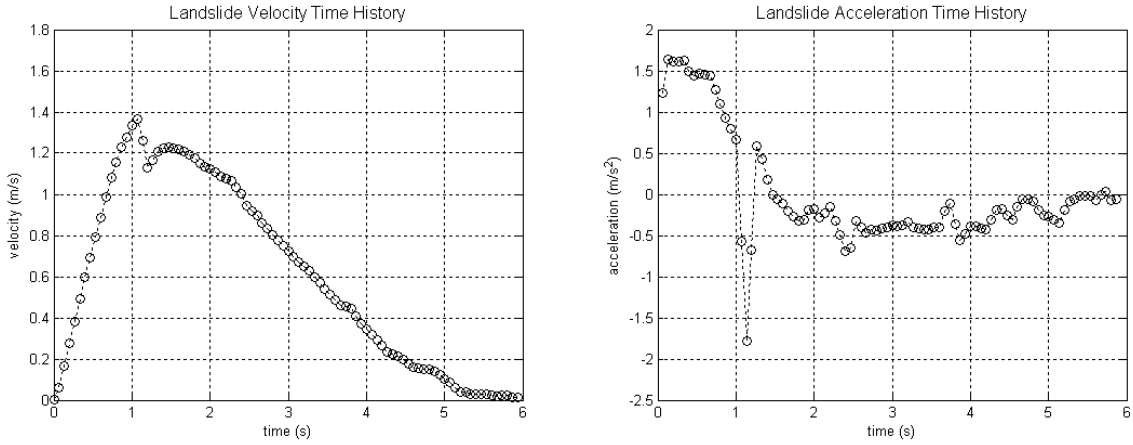

Figure B.3. Landslide centre of mass velocity and acceleration time history for the SG5_IS3 configuration.

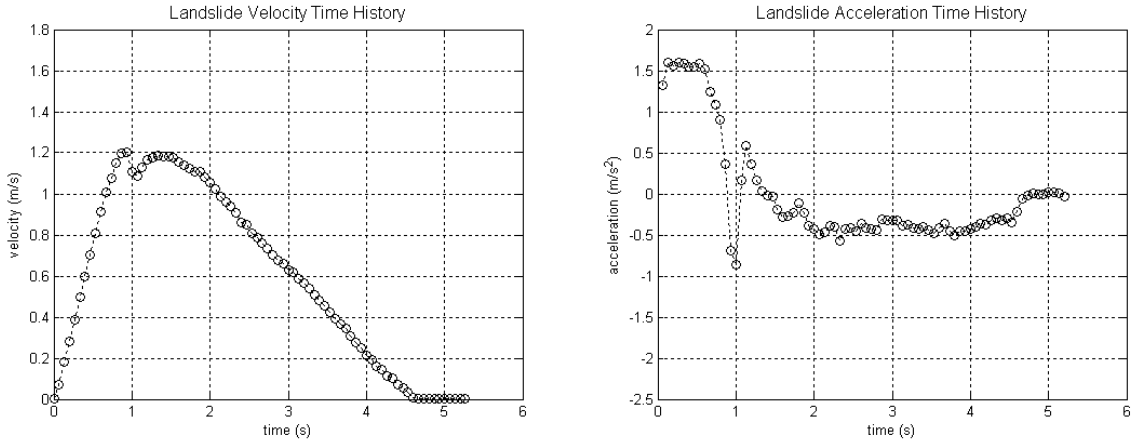

Figure B.4. Landslide centre of mass velocity and acceleration time history for the SG5_IS2 configuration.

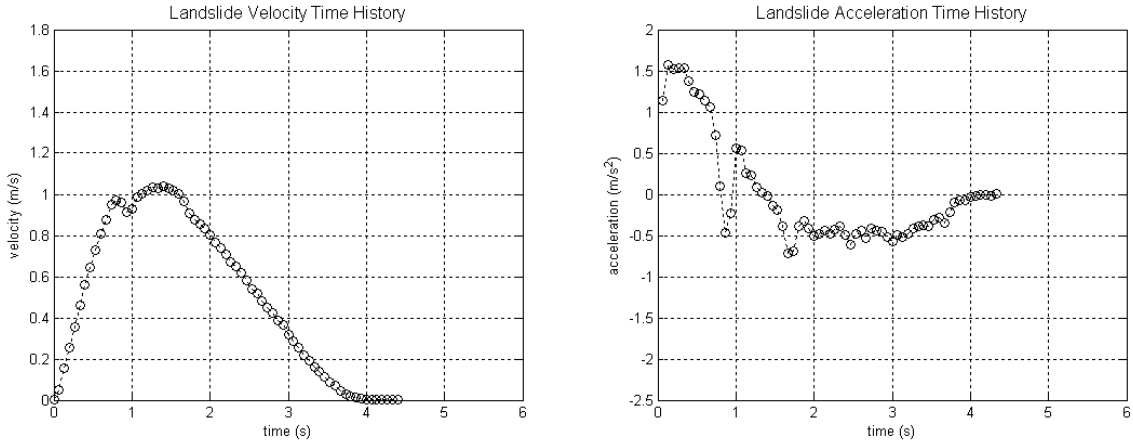

Figure B.5. Landslide centre of mass velocity and acceleration time history for the SG5_IS1 configuration.

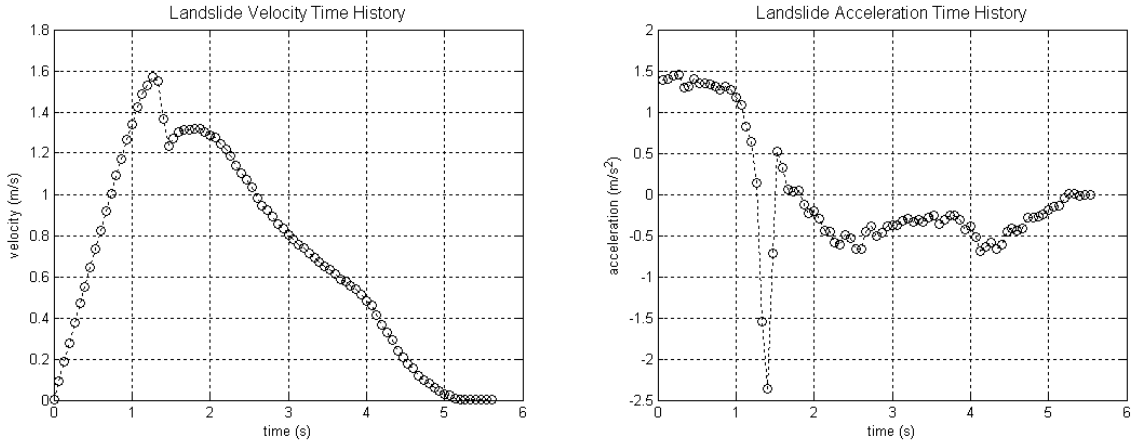

Figure B.6. Landslide centre of mass velocity and acceleration time history for the SG4_IS5 configuration.

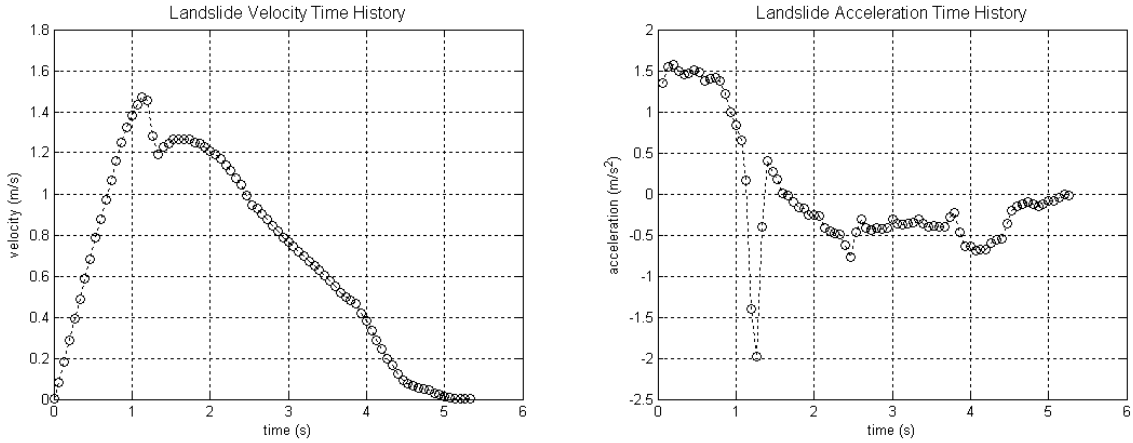

Figure B.7. Landslide centre of mass velocity and acceleration time history for the SG4_IS4 configuration.

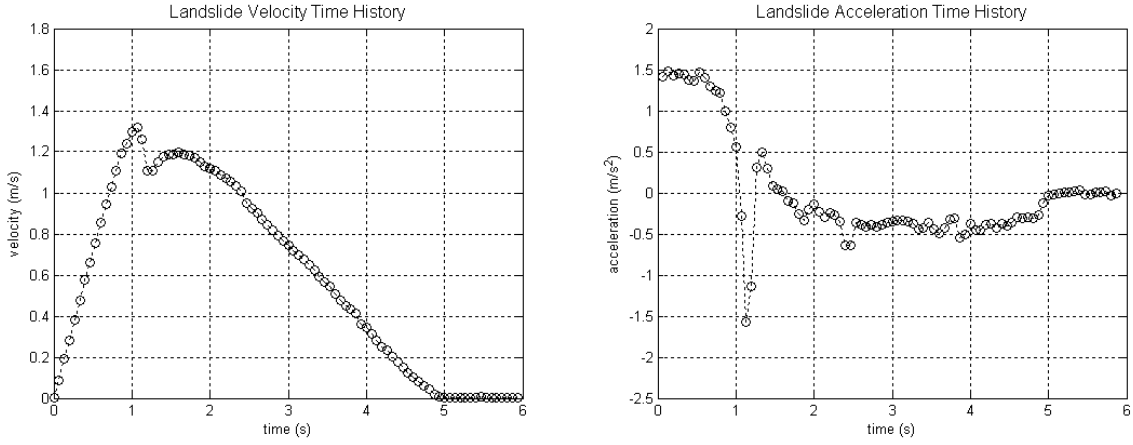

Figure B.8. Landslide centre of mass velocity and acceleration time history for the SG4_IS3 configuration.

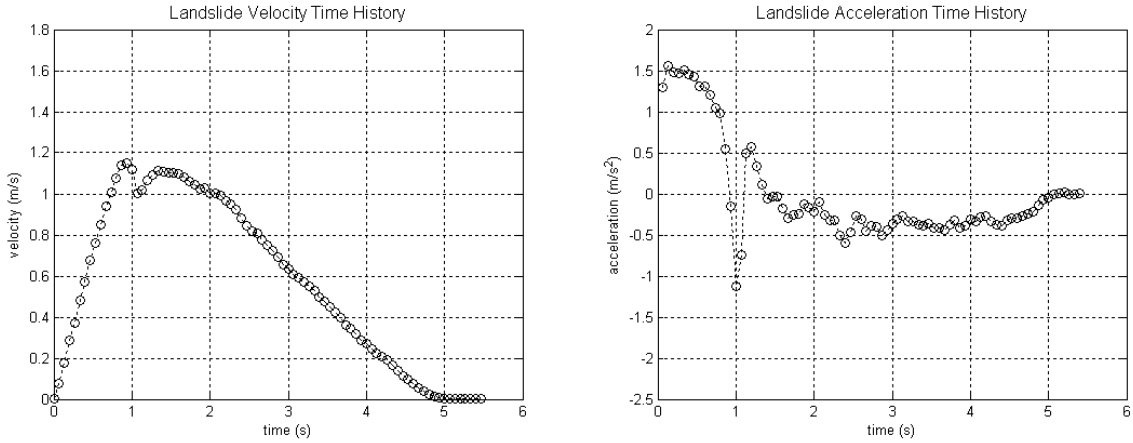

Figure B.9. Landslide centre of mass velocity and acceleration time history for the SG4_IS2 configuration.

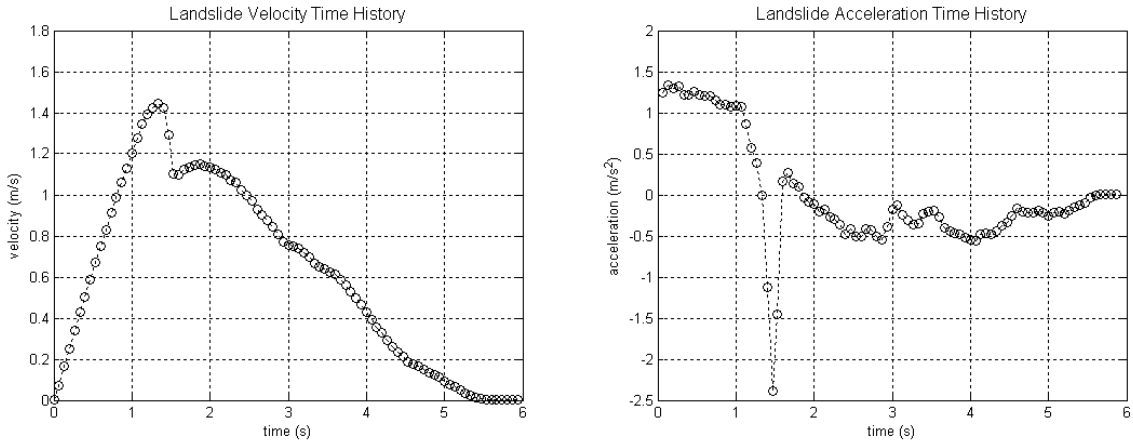

Figure B.10. Landslide centre of mass velocity and acceleration time history for the SG3_IS5 configuration.

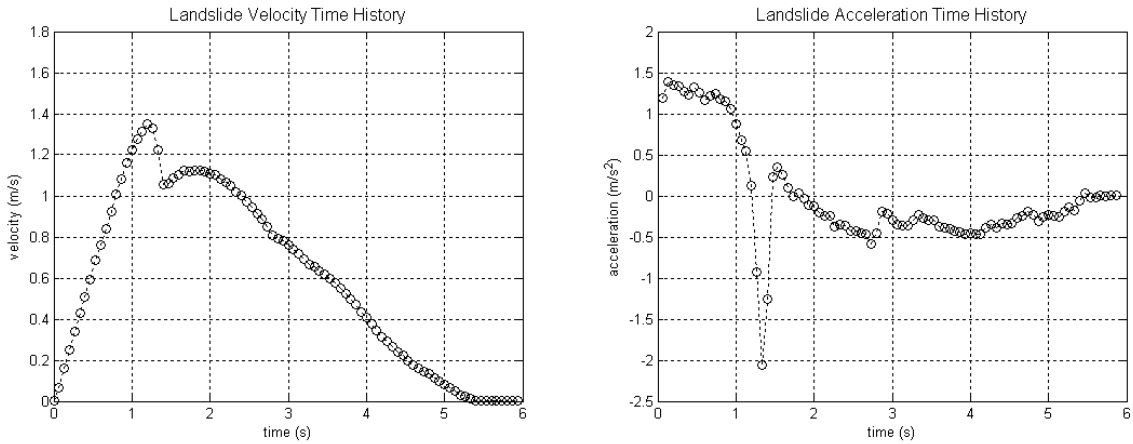

Figure B.11. Landslide centre of mass velocity and acceleration time history for the SG3_IS4 configuration.

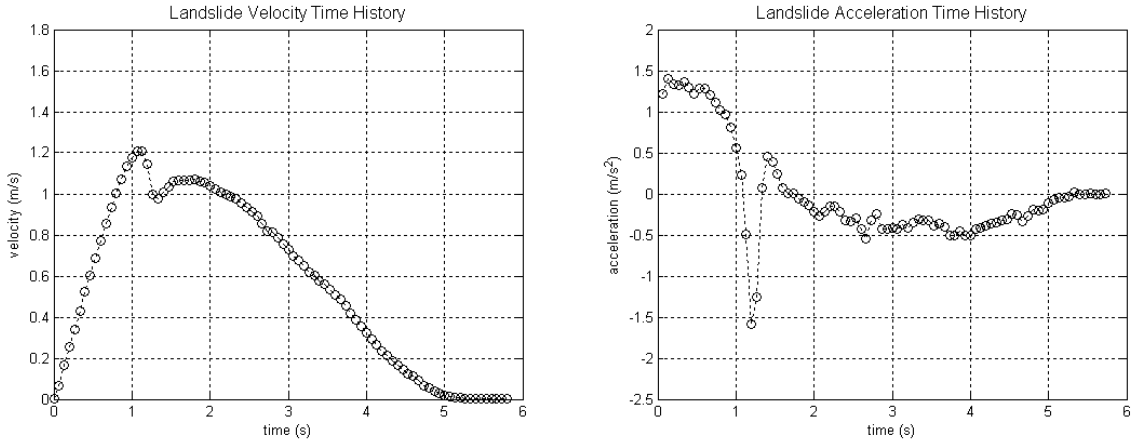

Figure B.12. Landslide centre of mass velocity and acceleration time history for the SG3_IS3 configuration.

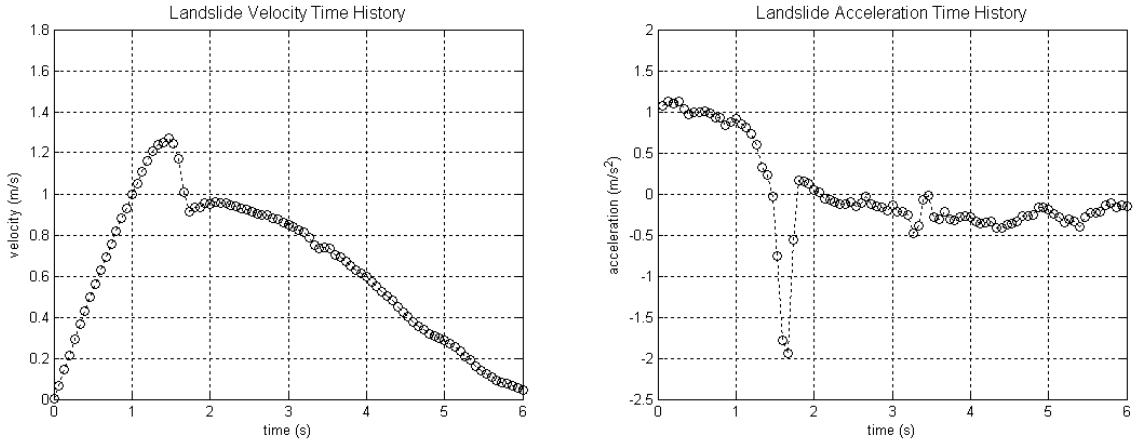

Figure B.13. Landslide centre of mass velocity and acceleration time history for the SG2_IS5 configuration.

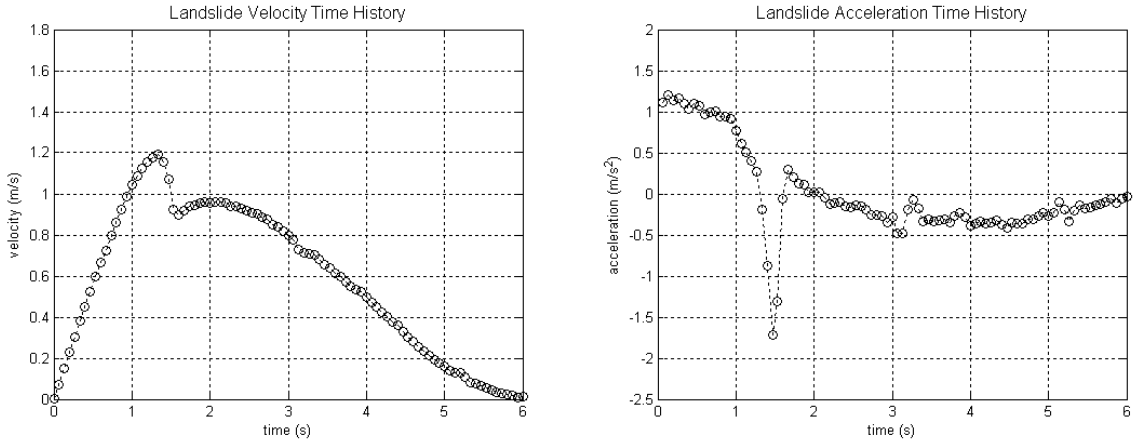

Figure B.14. Landslide centre of mass velocity and acceleration time history for the SG2_IS4 configuration.

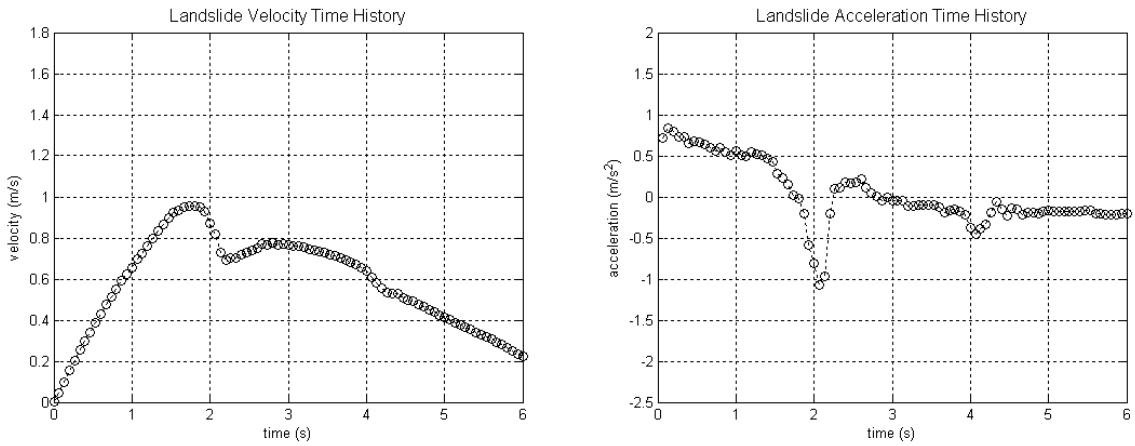

Figure B.15. Landslide centre of mass velocity and acceleration time history for the SG1_IS5 configuration.

Appendix C: Wave Fields

C.1 Two-Dimensional Wave Field Plot

Two-dimensional wave field plots of the water surface profile time history for each of the fifteen specific gravity and initial submergence combinations are presented in Figures C.1 to C.15.

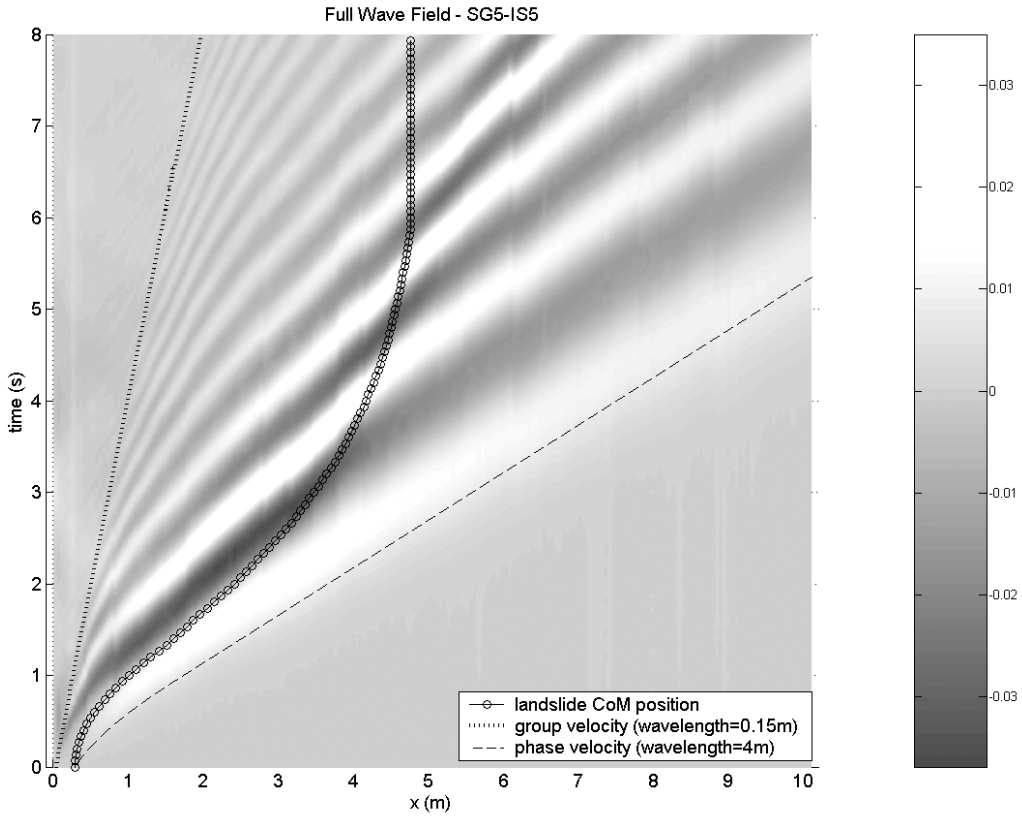

Figure C.1. 2-dimensional wave field plot of the water surface profile time history for the SG5-IS5 test.

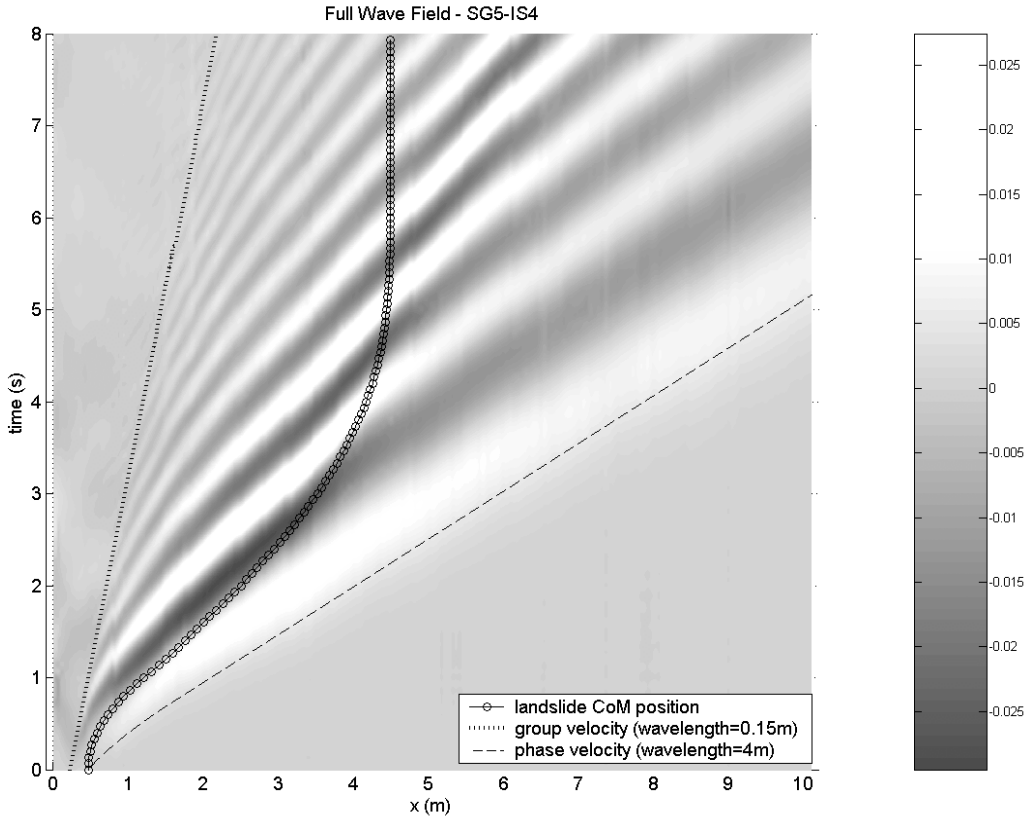

Figure C.2. 2-dimensional wave field plot of the water surface profile time history for the SG5-IS4 test.

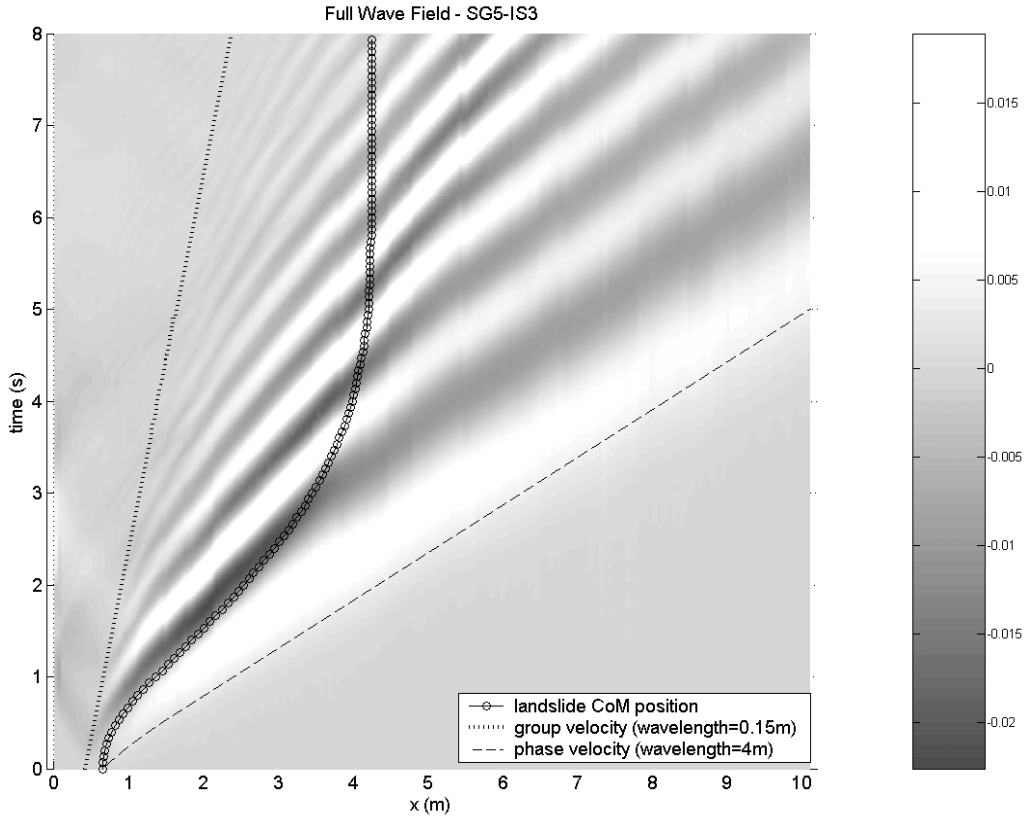

Figure C.3. 2-dimensional wave field plot of the water surface profile time history for the SG5-IS3 test.

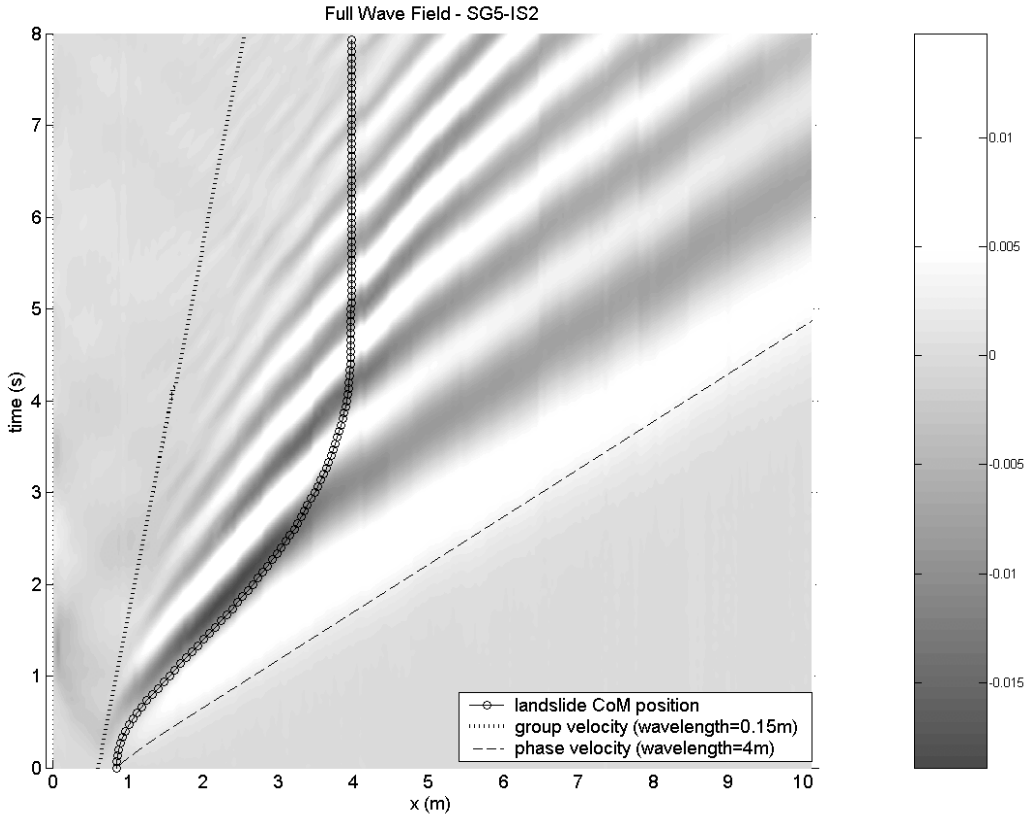

Figure C.4. 2-dimensional wave field plot of the water surface profile time history for the SG5-IS2 test.

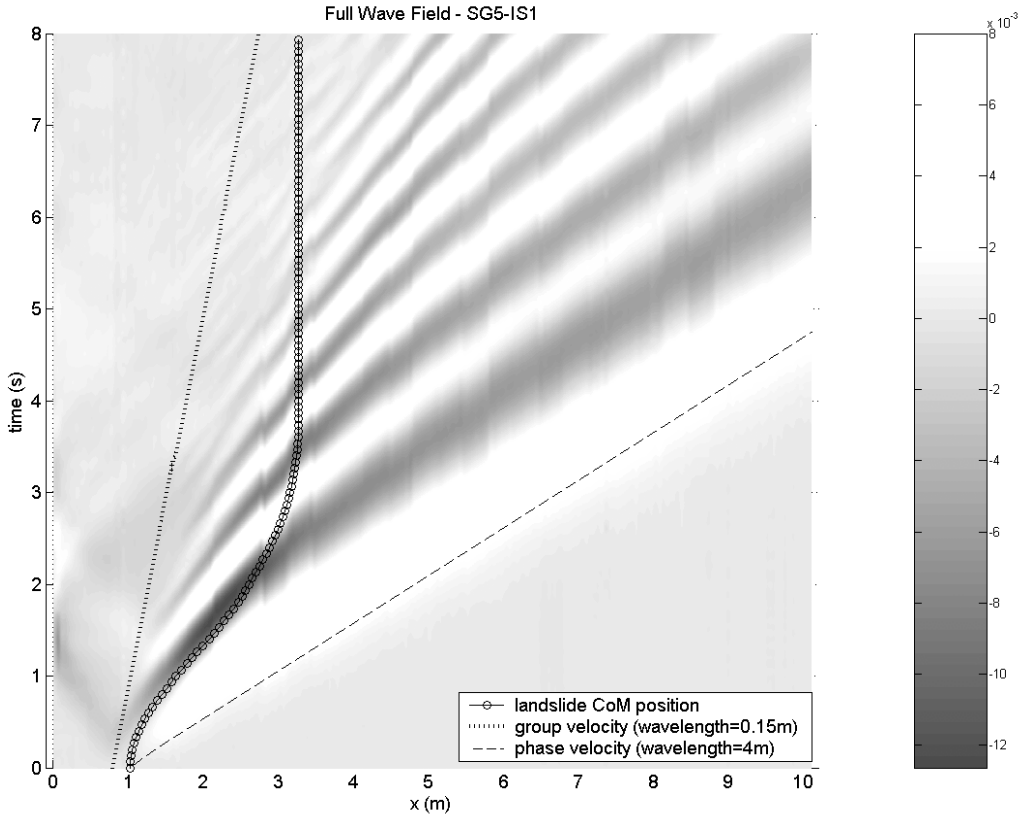

Figure C.5. 2-dimensional wave field plot of the water surface profile time history for the SG5-IS1 test.

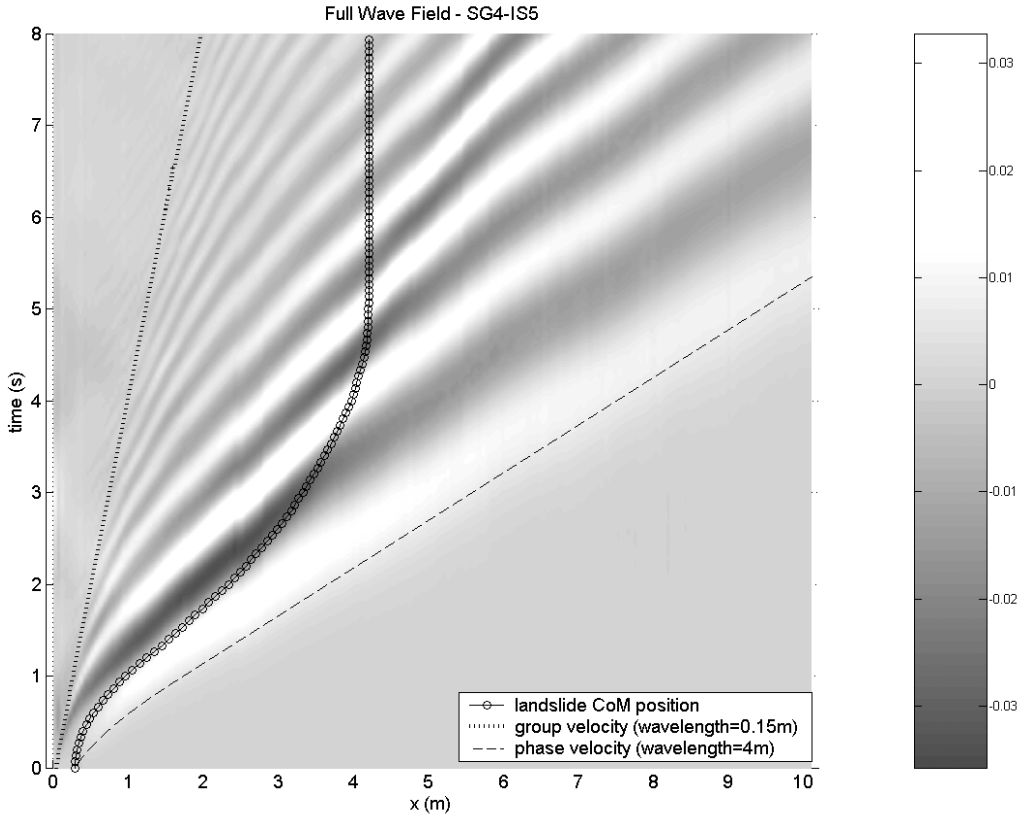

Figure C.6. 2-dimensional wave field plot of the water surface profile time history for the SG4-IS5 test.

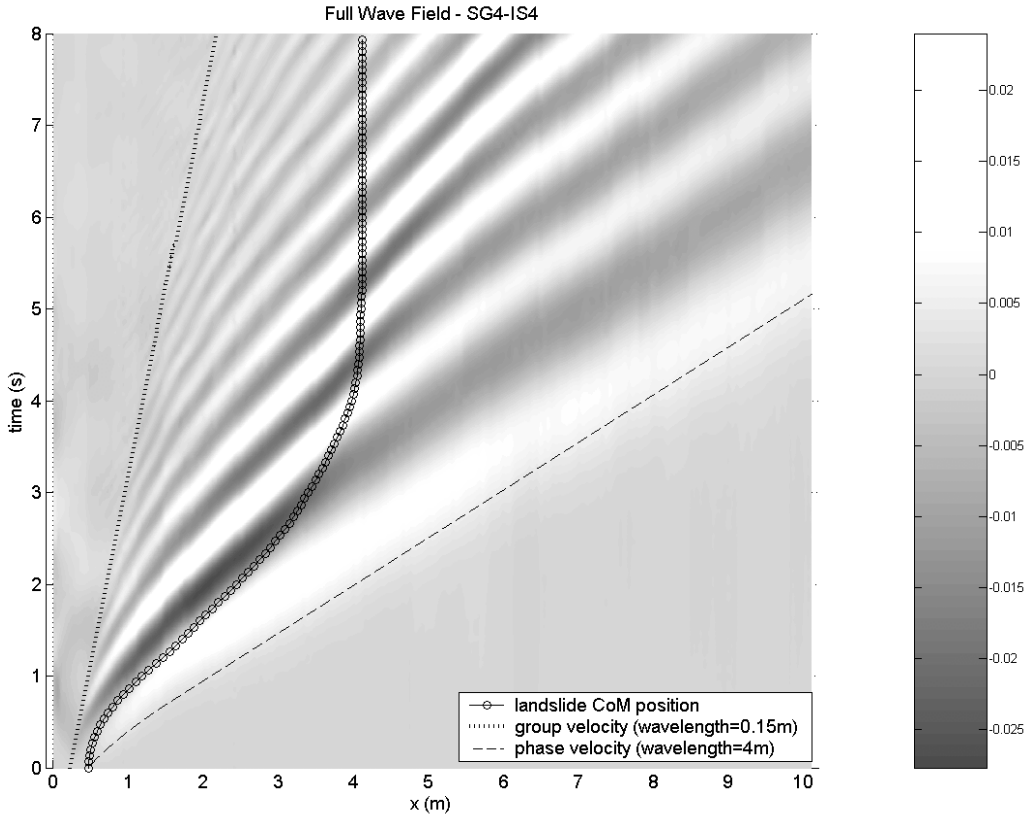

Figure C.7. 2-dimensional wave field plot of the water surface profile time history for the SG4-IS4 test.

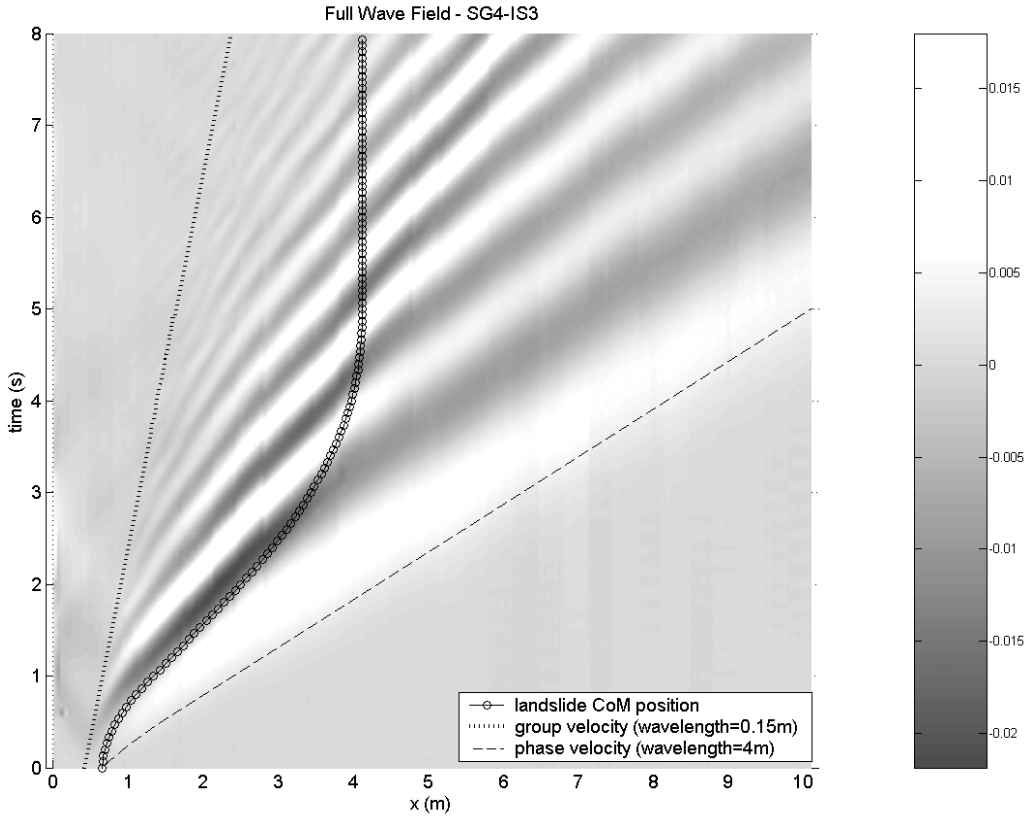

Figure C.8. 2-dimensional wave field plot of the water surface profile time history for the SG4-IS3 test.

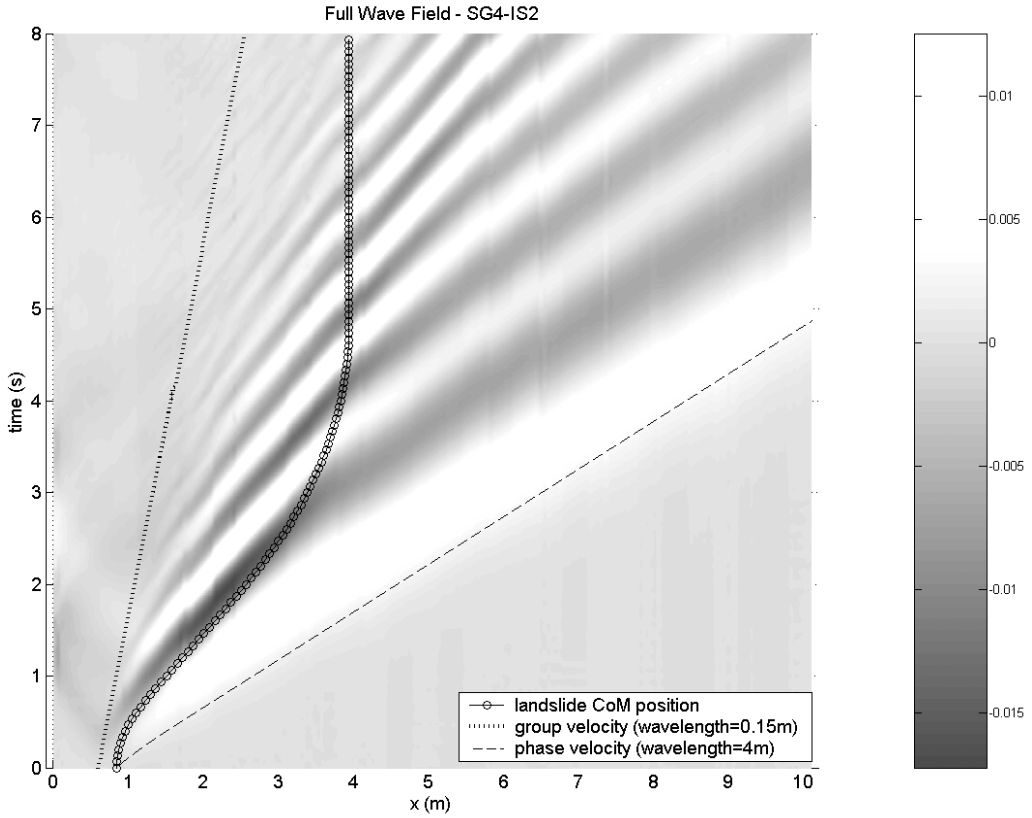

Figure C.9. 2-dimensional wave field plot of the water surface profile time history for the SG4-IS2 test.

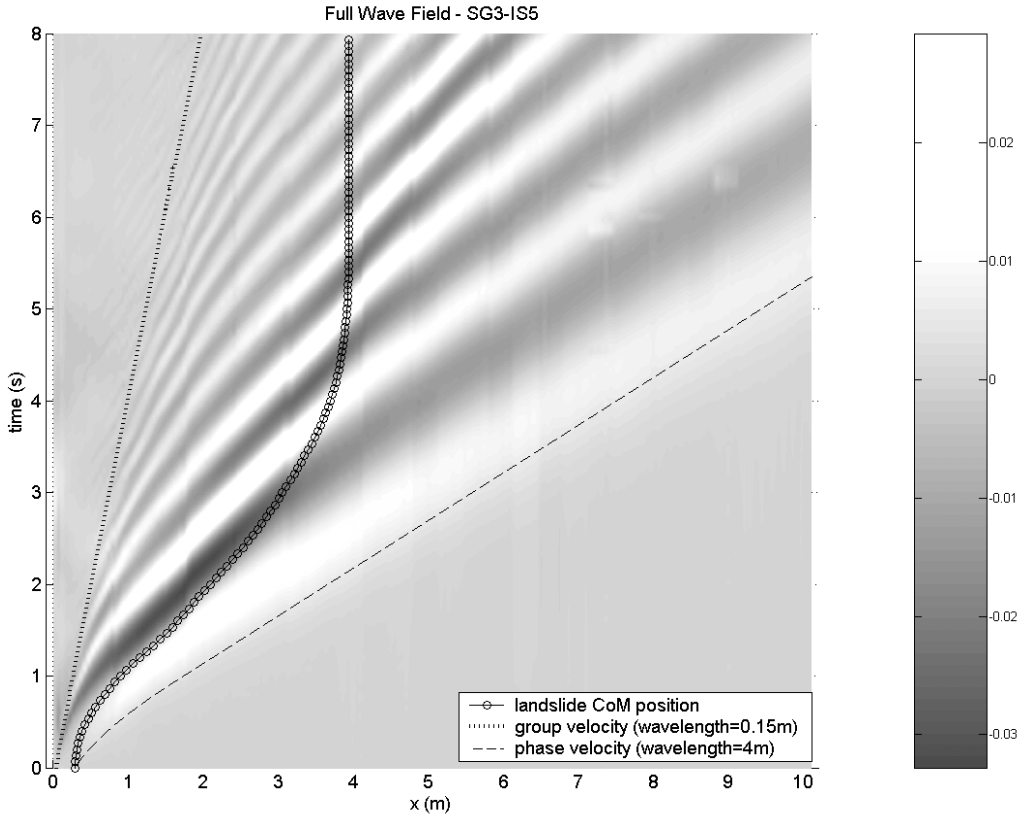

Figure C.10. 2-dimensional wave field plot of the water surface profile time history for the SG3-IS5 test.

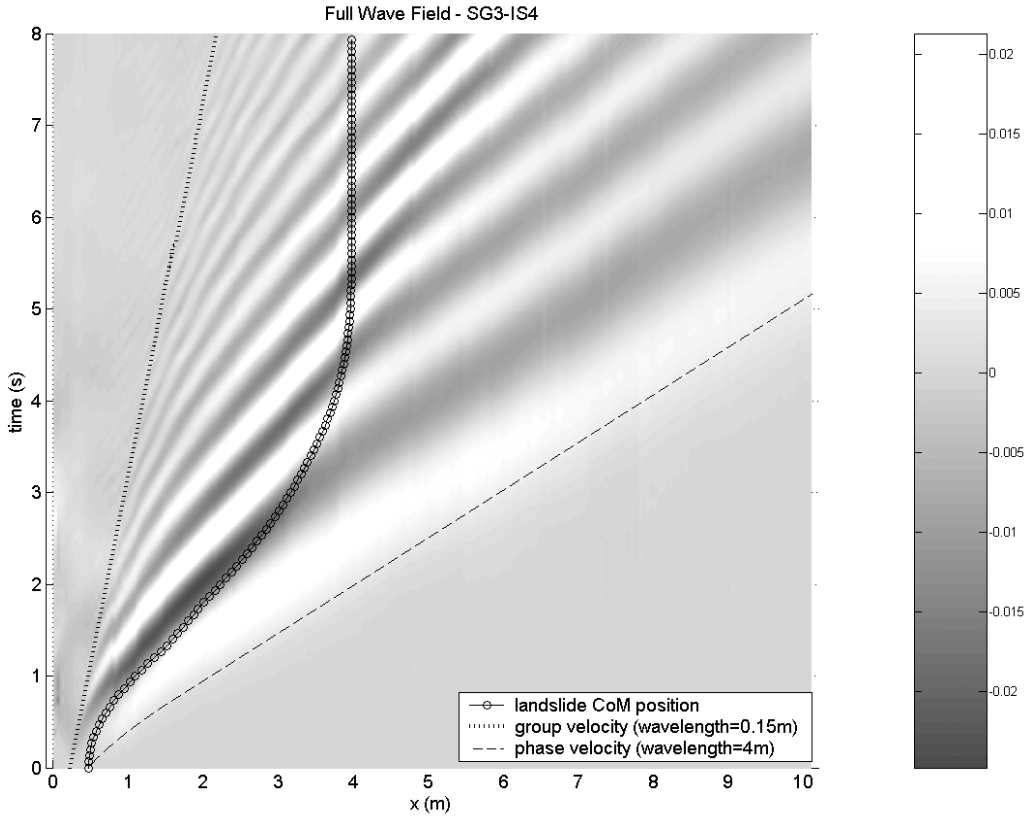

Figure C.11. 2-dimensional wave field plot of the water surface profile time history for the SG3-IS4 test.

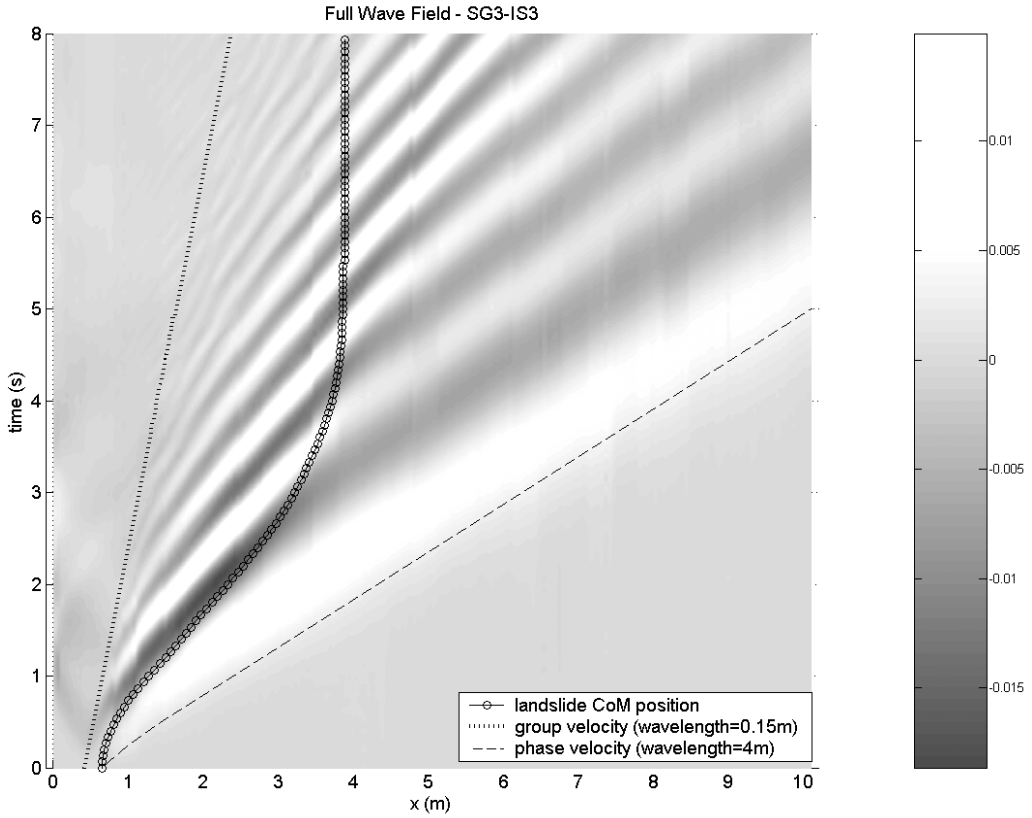

Figure C.12. 2-dimensional wave field plot of the water surface profile time history for the SG3-IS3 test.

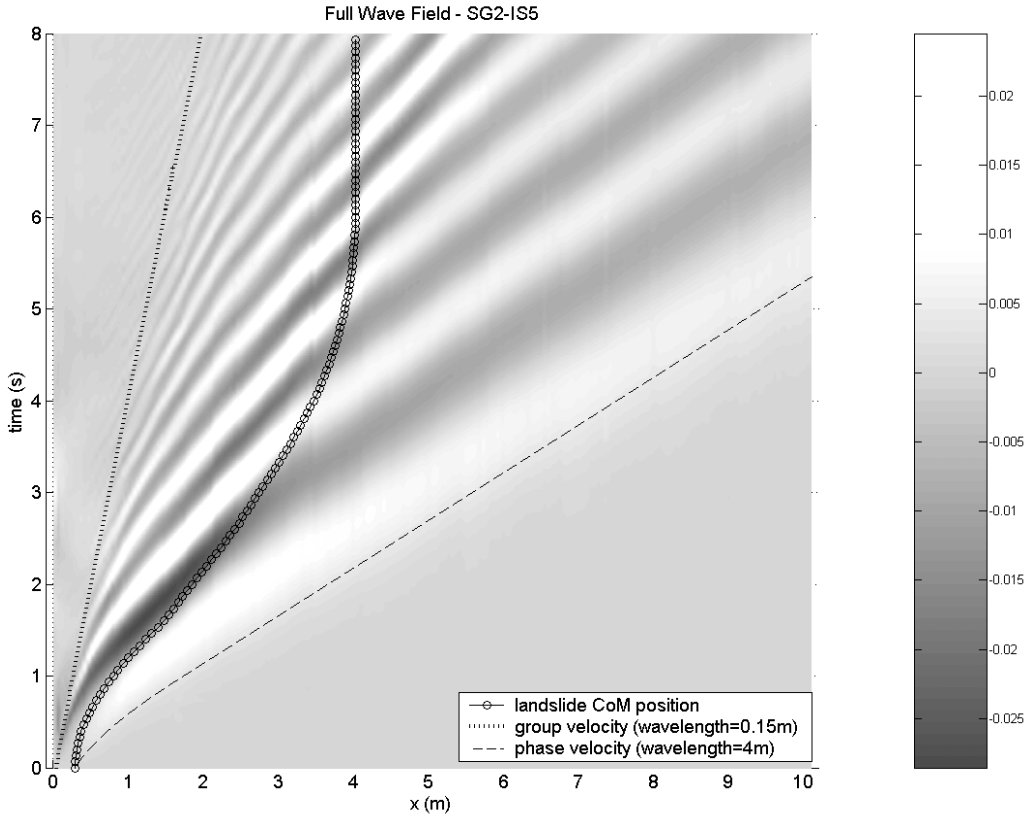

Figure C.13. 2-dimensional wave field plot of the water surface profile time history for the SG2-IS5 test.

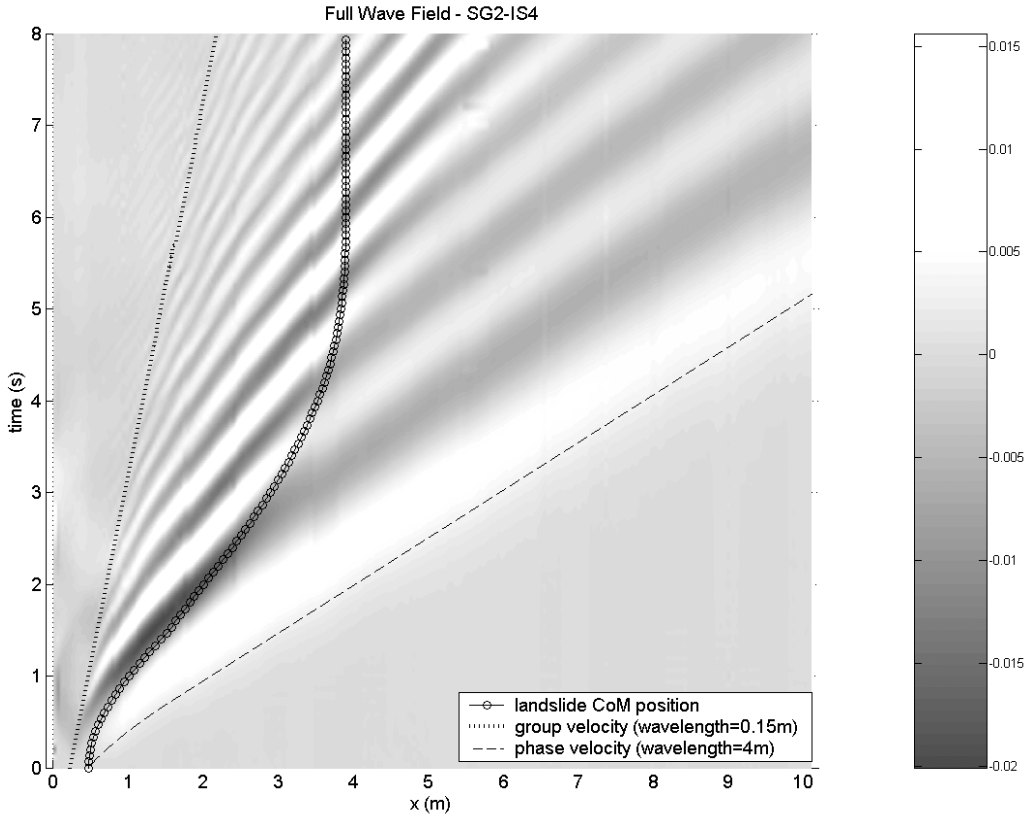

Figure C.14. 2-dimensional wave field plot of the water surface profile time history for the SG2-IS4 test.

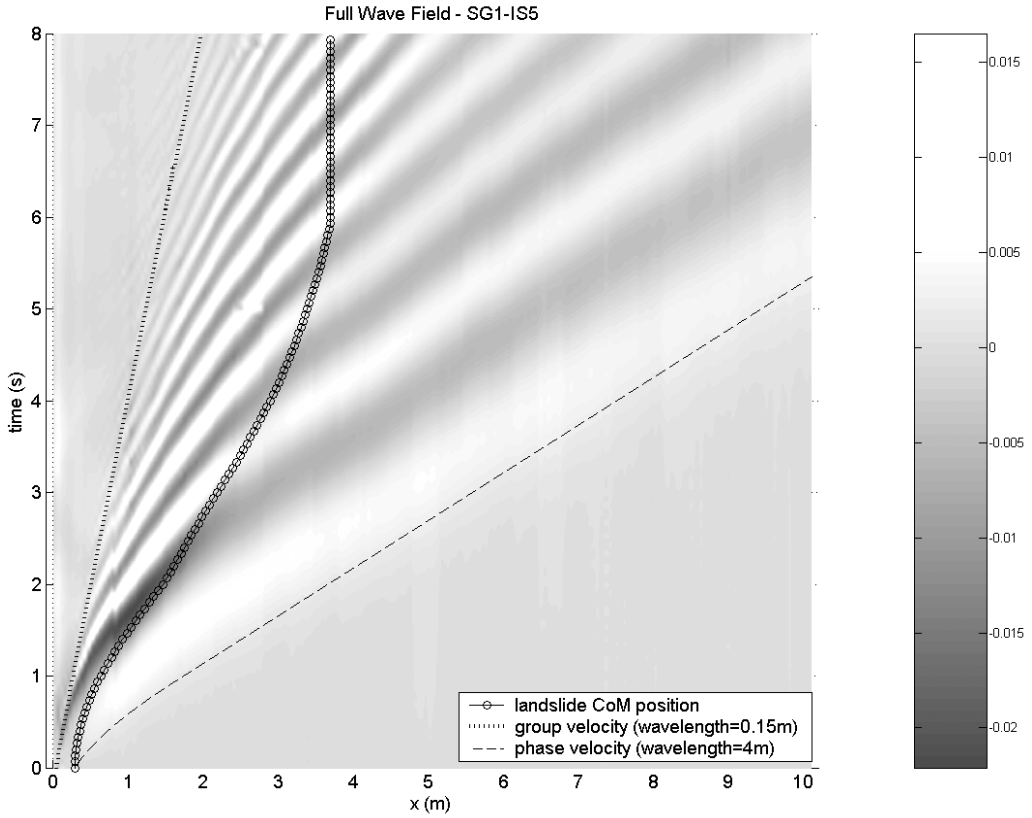

Figure C.15. 2-dimensional wave field plot of the water surface profile time history for the SG1-IS5 test.

C.2 Water Surface Profile

Plots of the water surface profiles at t=0.60, 1.60, 2.60, 3.60, 4.60, and 5.60 seconds, for each of the fifteen specific gravity and initial submergence combinations, are presented in Figures C.16 to C.30.

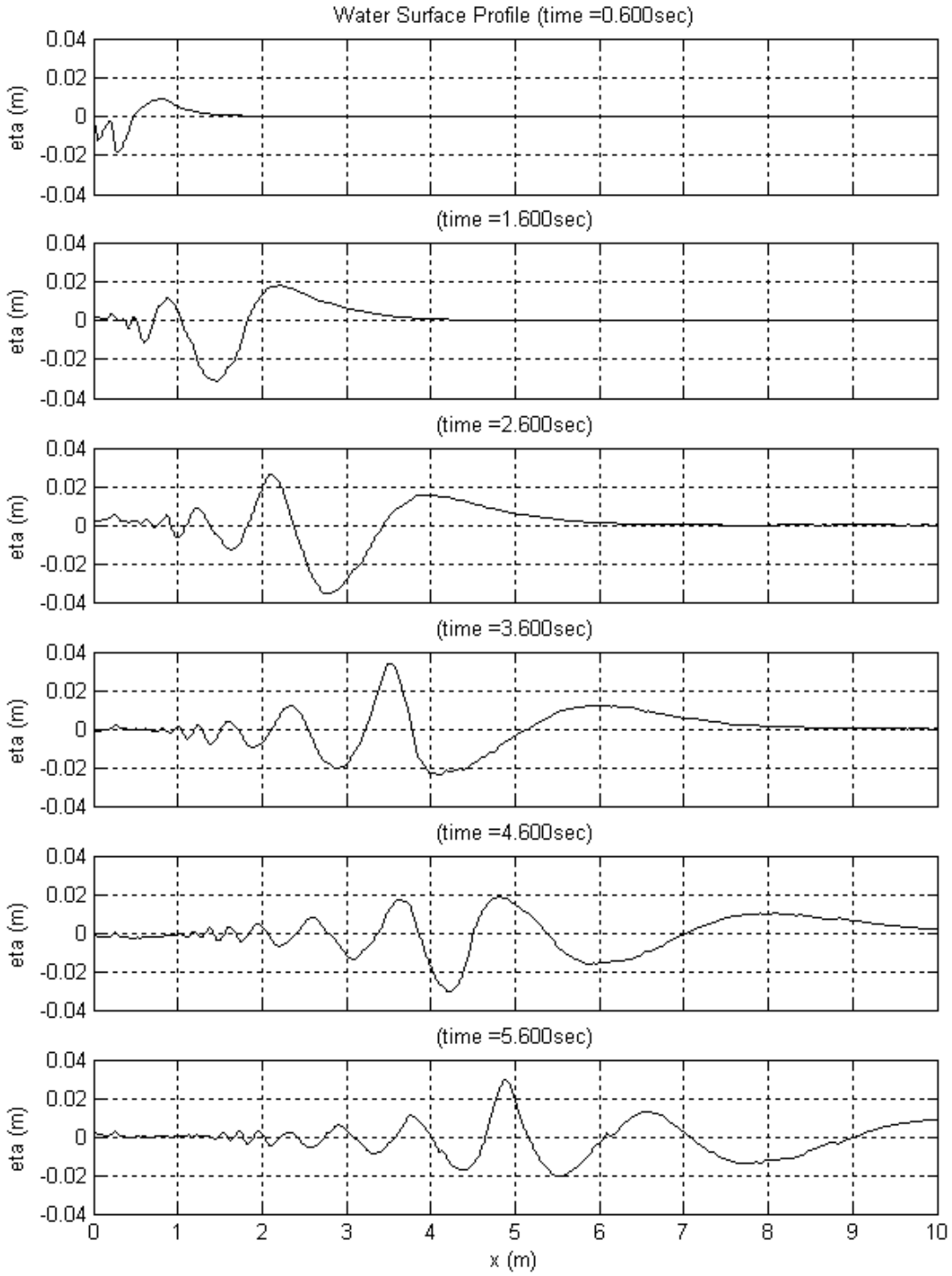

Figure C.16. Water surface profiles at t=0.60, 1.60, 2.60, 3.60, 4.60, and 5.60 seconds for the SG5_IS5 configuration.

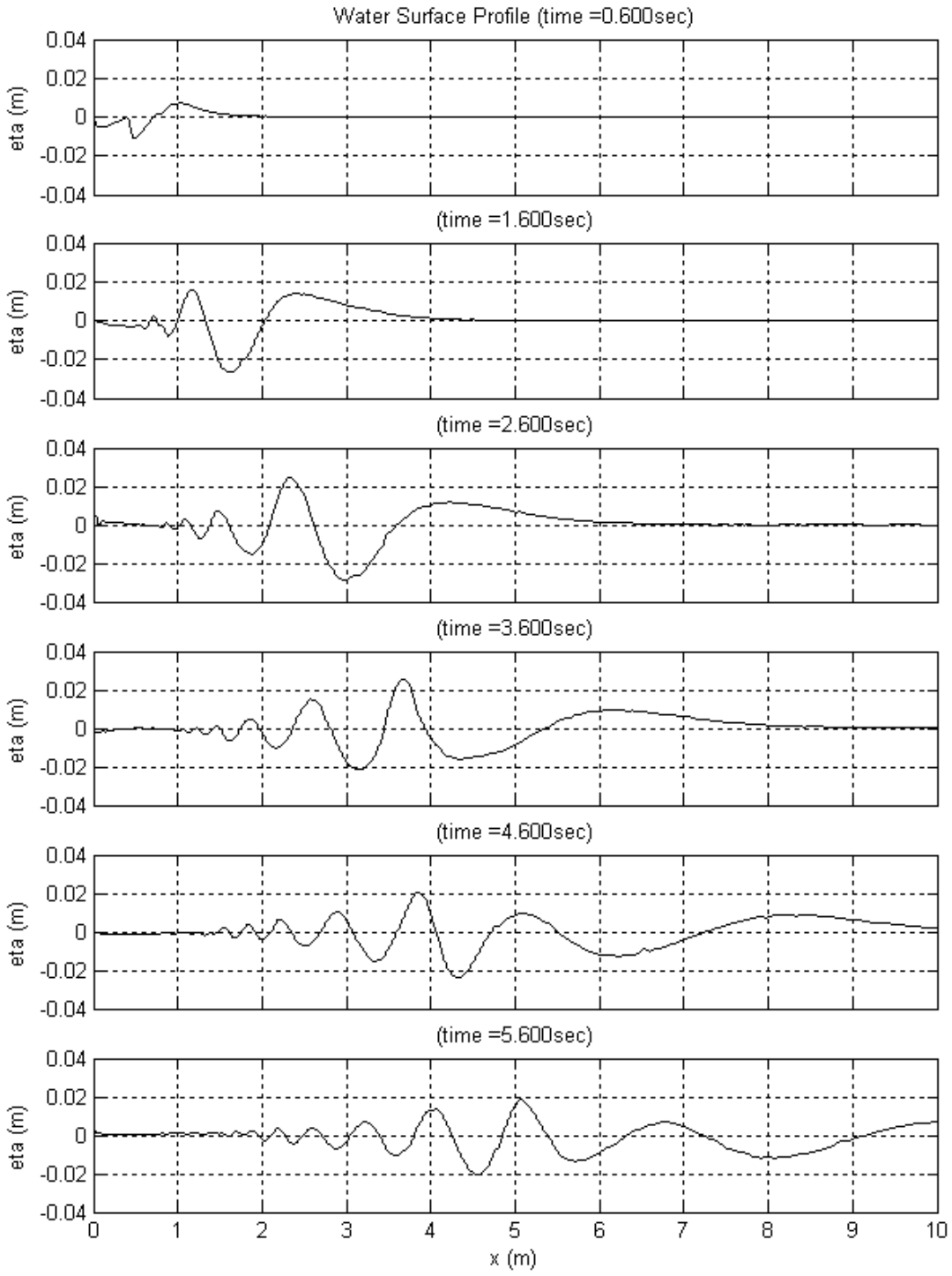

Figure C.17. Water surface profiles at t=0.60, 1.60, 2.60, 3.60, 4.60, and 5.60 seconds for the SG5_IS4 configuration.

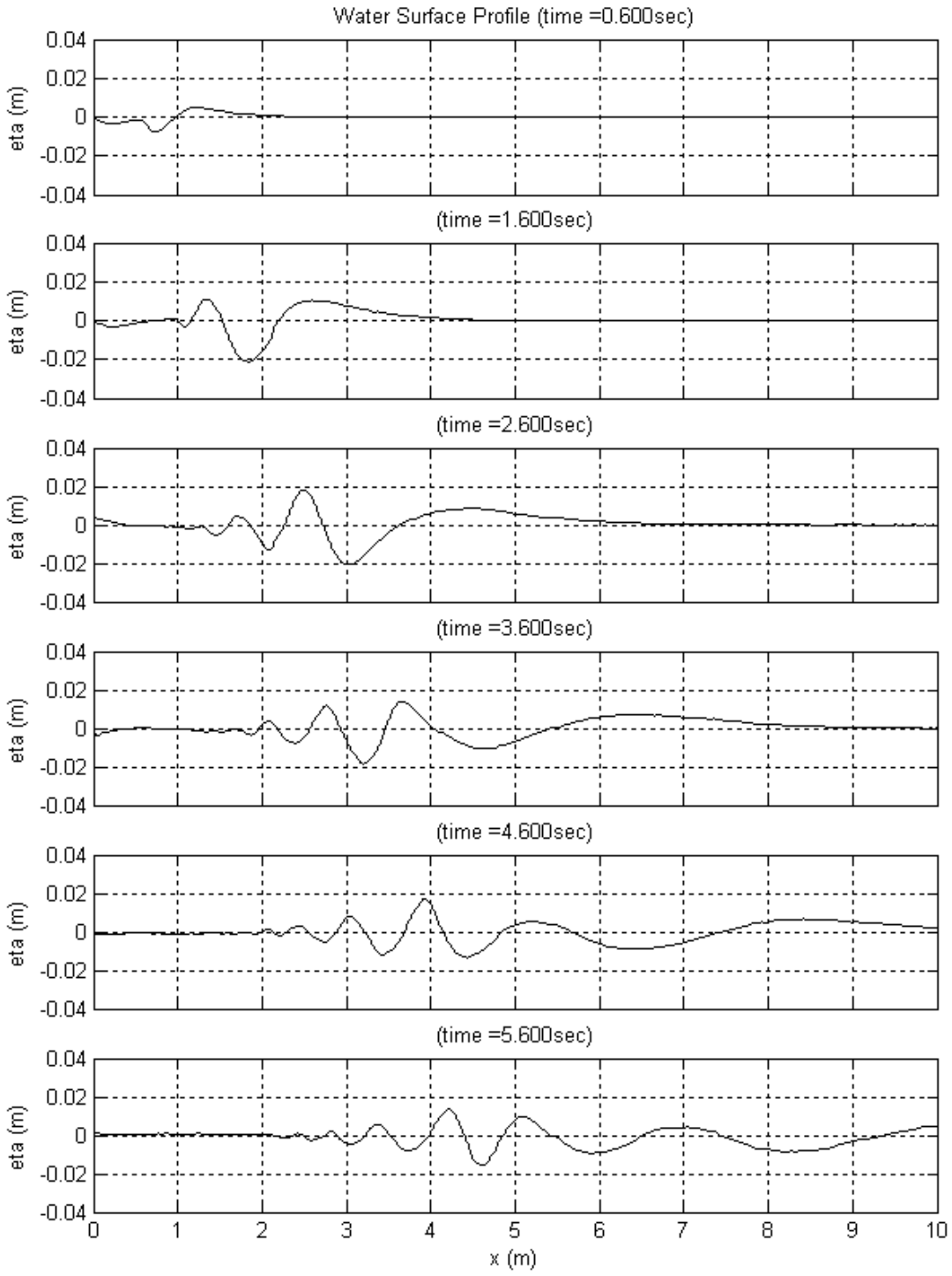

Figure C.18. Water surface profiles at t=0.60, 1.60, 2.60, 3.60, 4.60, and 5.60 seconds for the SG5_IS3 configuration.

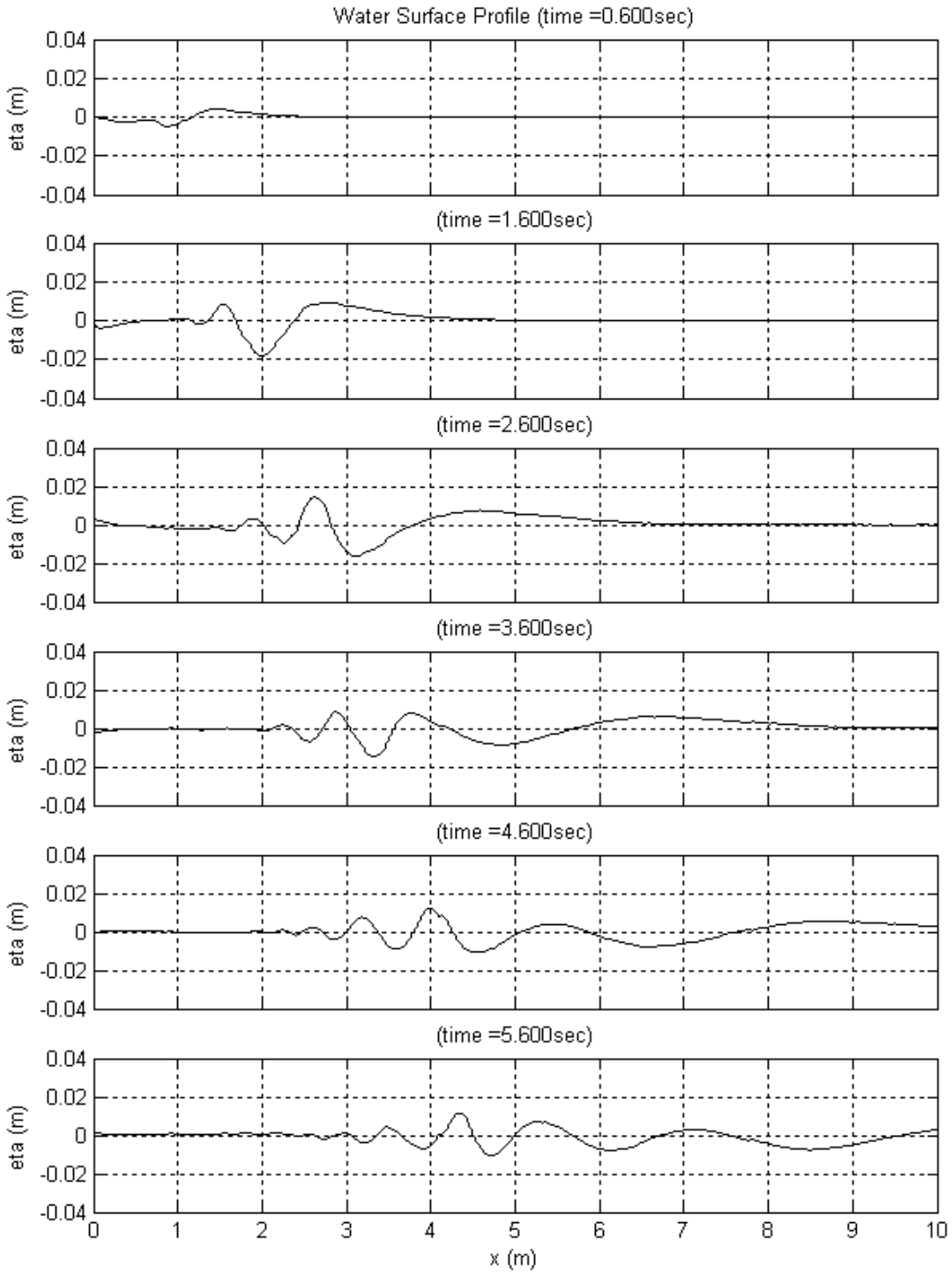

Figure C.19. Water surface profiles at t=0.60, 1.60, 2.60, 3.60, 4.60, and 5.60 seconds for the SG5_IS2 configuration.

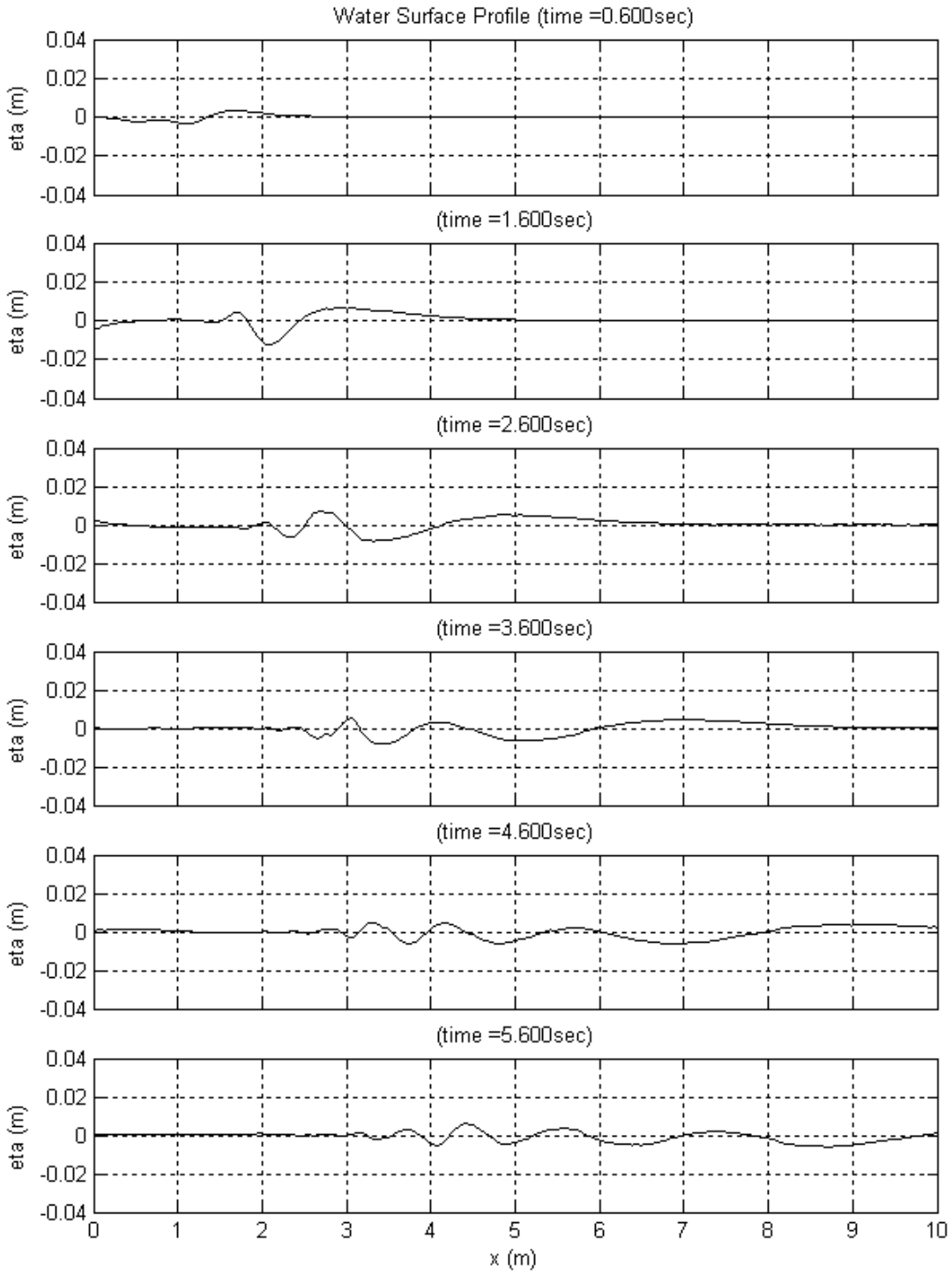

Figure C.20. Water surface profiles at t=0.60, 1.60, 2.60, 3.60, 4.60, and 5.60 seconds for the SG5_IS1 configuration.

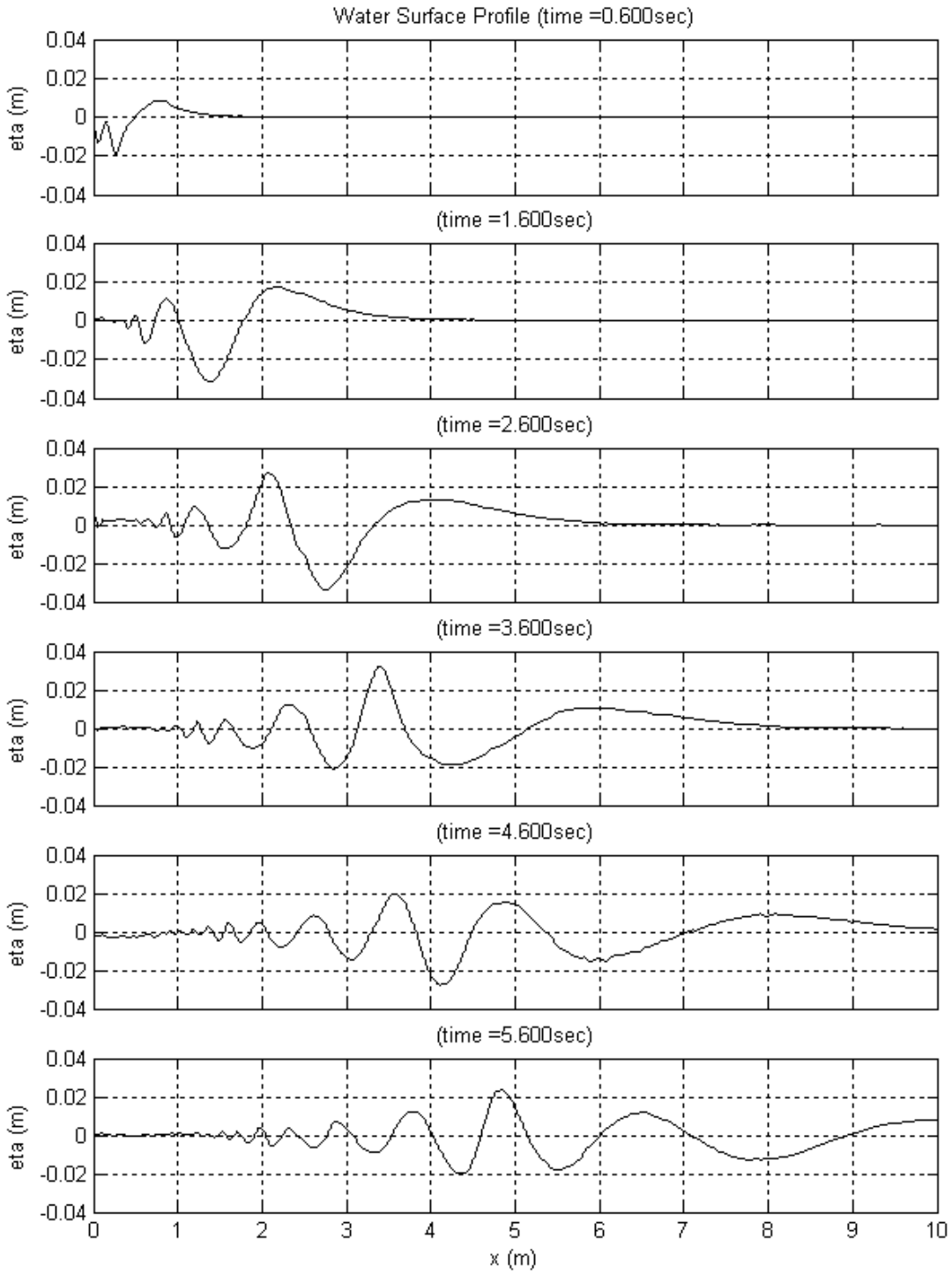

Figure C.21. Water surface profiles at t=0.60, 1.60, 2.60, 3.60, 4.60, and 5.60 seconds for the SG4_IS5 configuration.

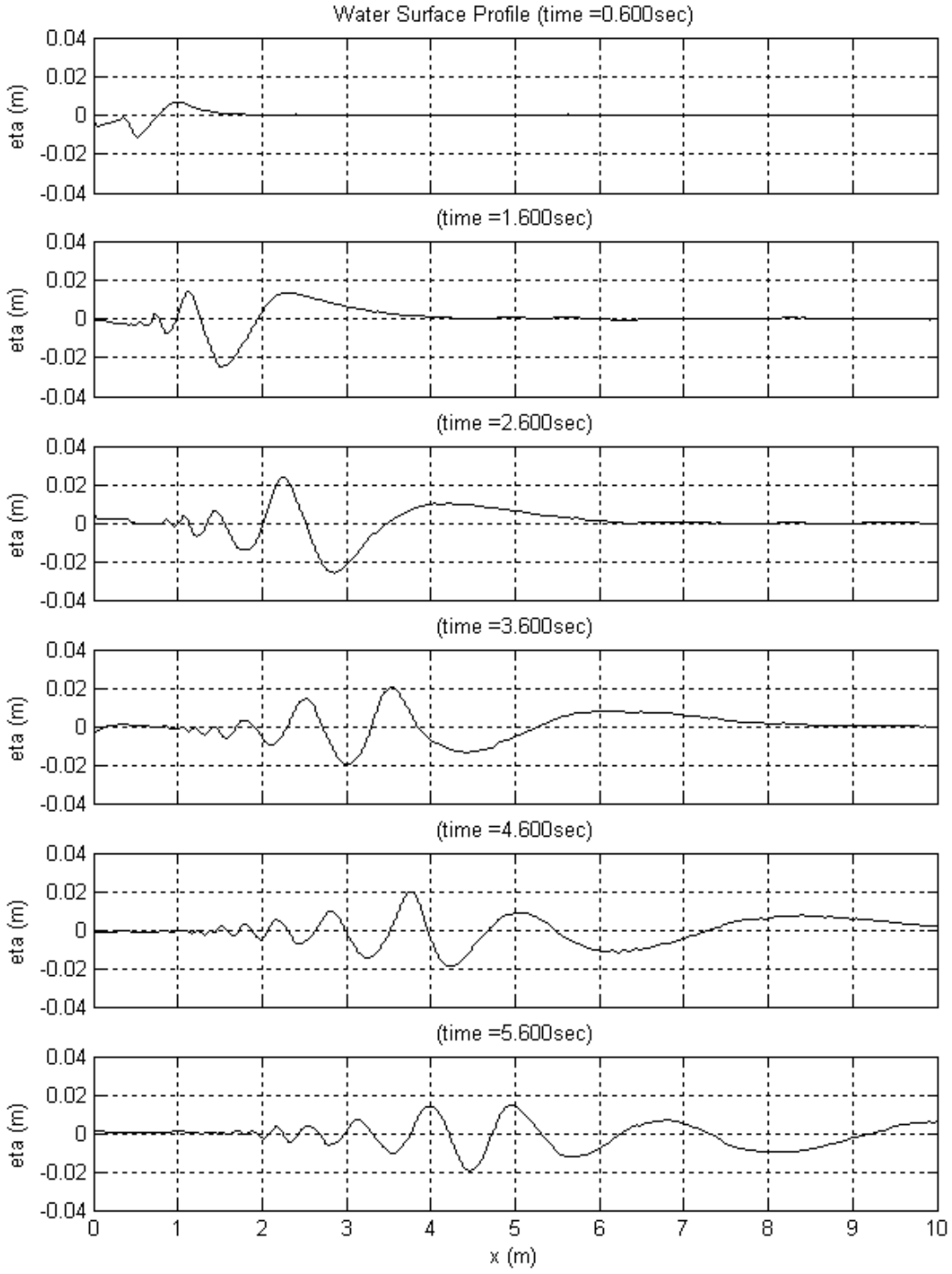

Figure C.22. Water surface profiles at t=0.60, 1.60, 2.60, 3.60, 4.60, and 5.60 seconds for the SG4_IS4 configuration.

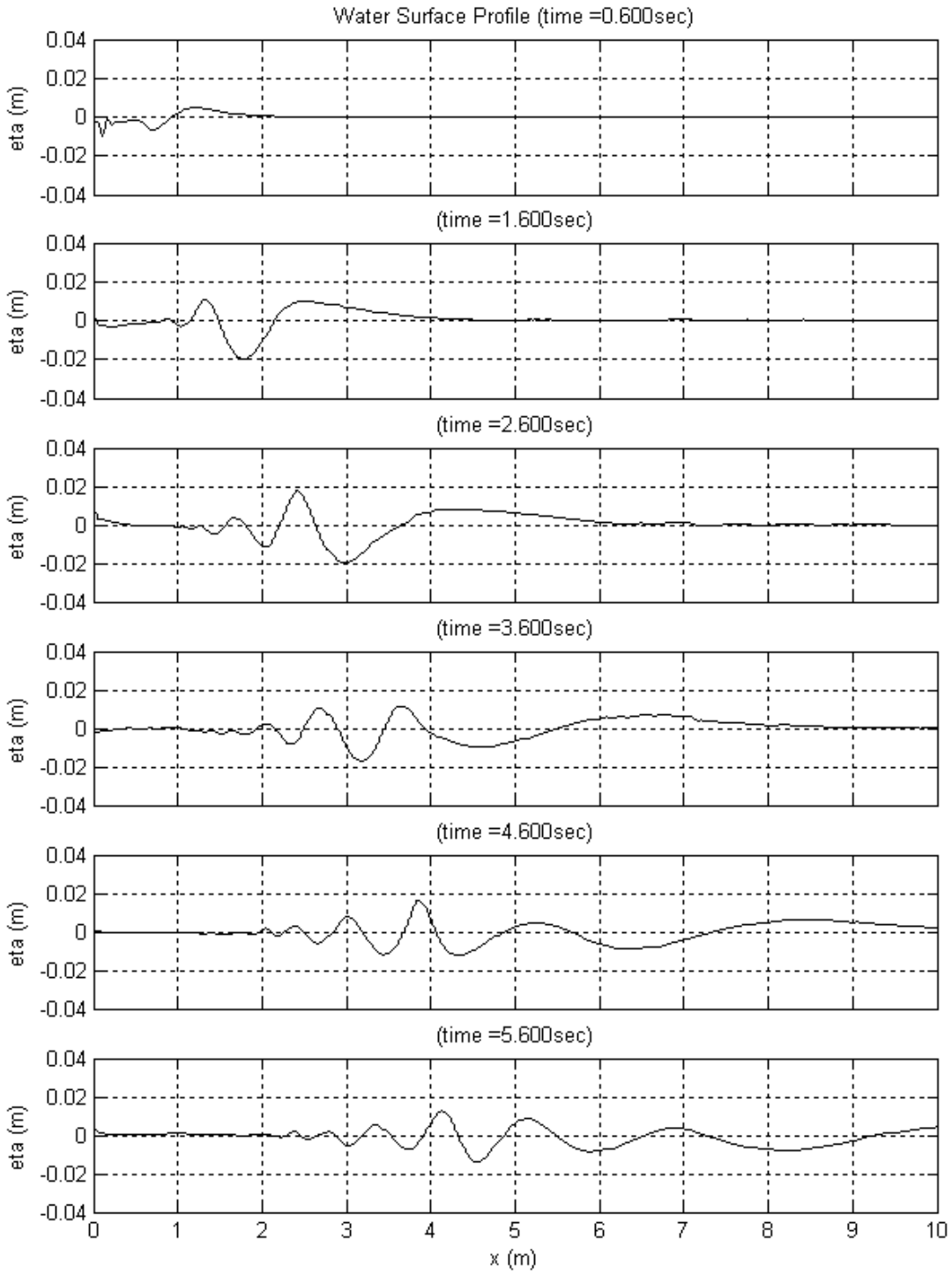

Figure C.23. Water surface profiles at t=0.60, 1.60, 2.60, 3.60, 4.60, and 5.60 seconds for the SG4_IS3 configuration.

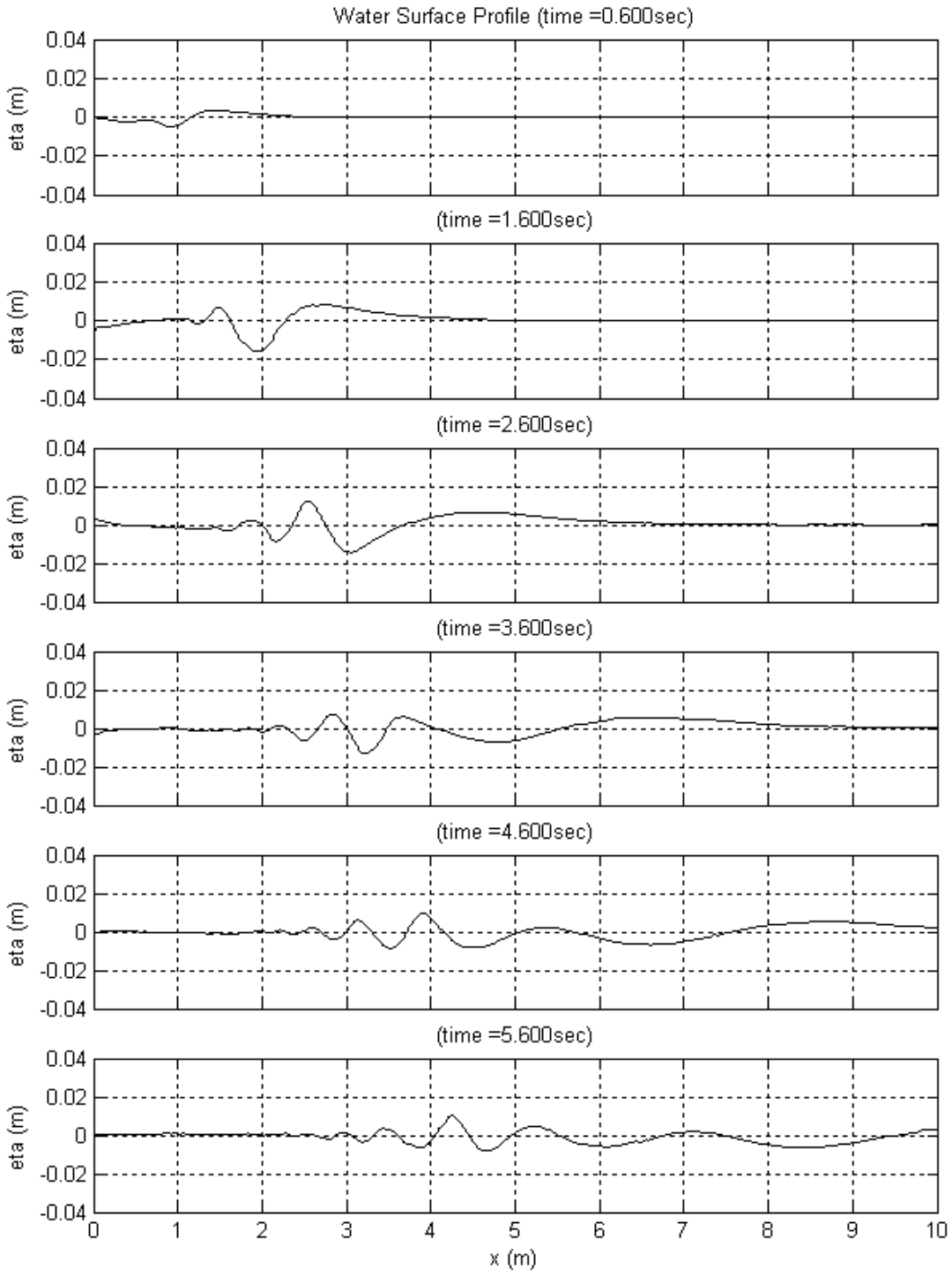

Figure C.24. Water surface profiles at t=0.60, 1.60, 2.60, 3.60, 4.60, and 5.60 seconds for the SG4_IS2 configuration.

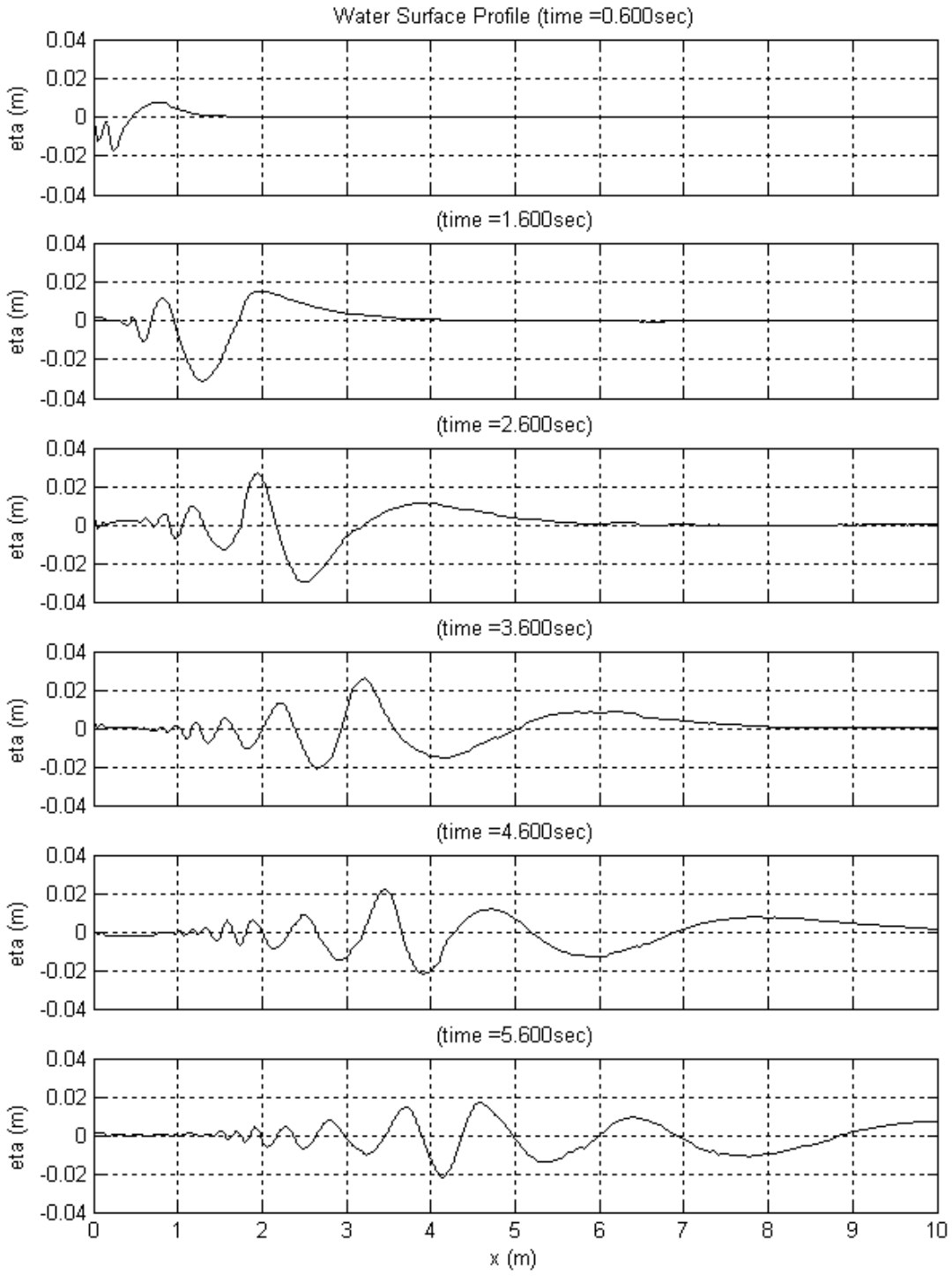

Figure C.25. Water surface profiles at t=0.60, 1.60, 2.60, 3.60, 4.60, and 5.60 seconds for the SG3_IS5 configuration.

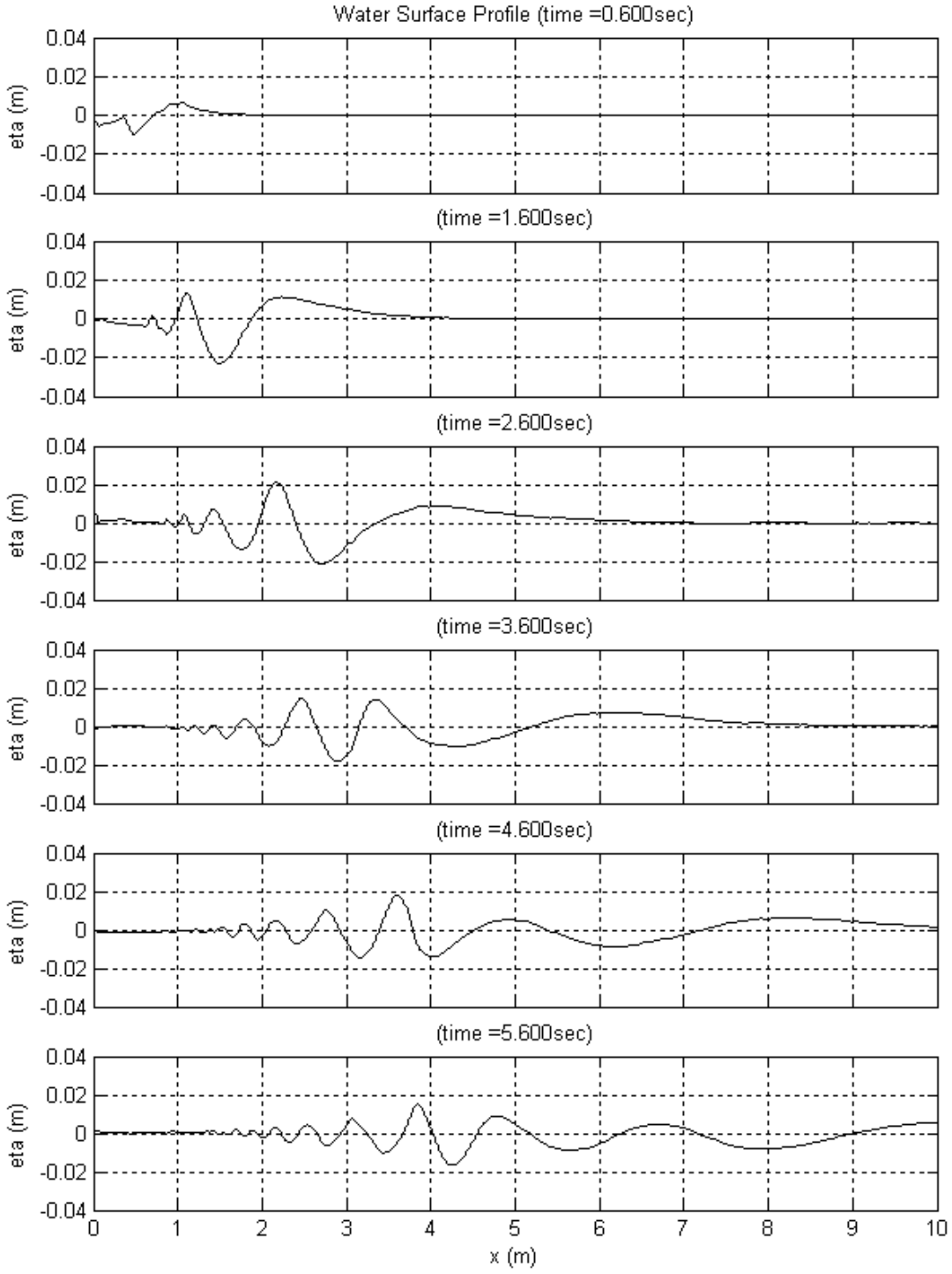

Figure C.26. Water surface profiles at t=0.60, 1.60, 2.60, 3.60, 4.60, and 5.60 seconds for the SG3_IS4 configuration.

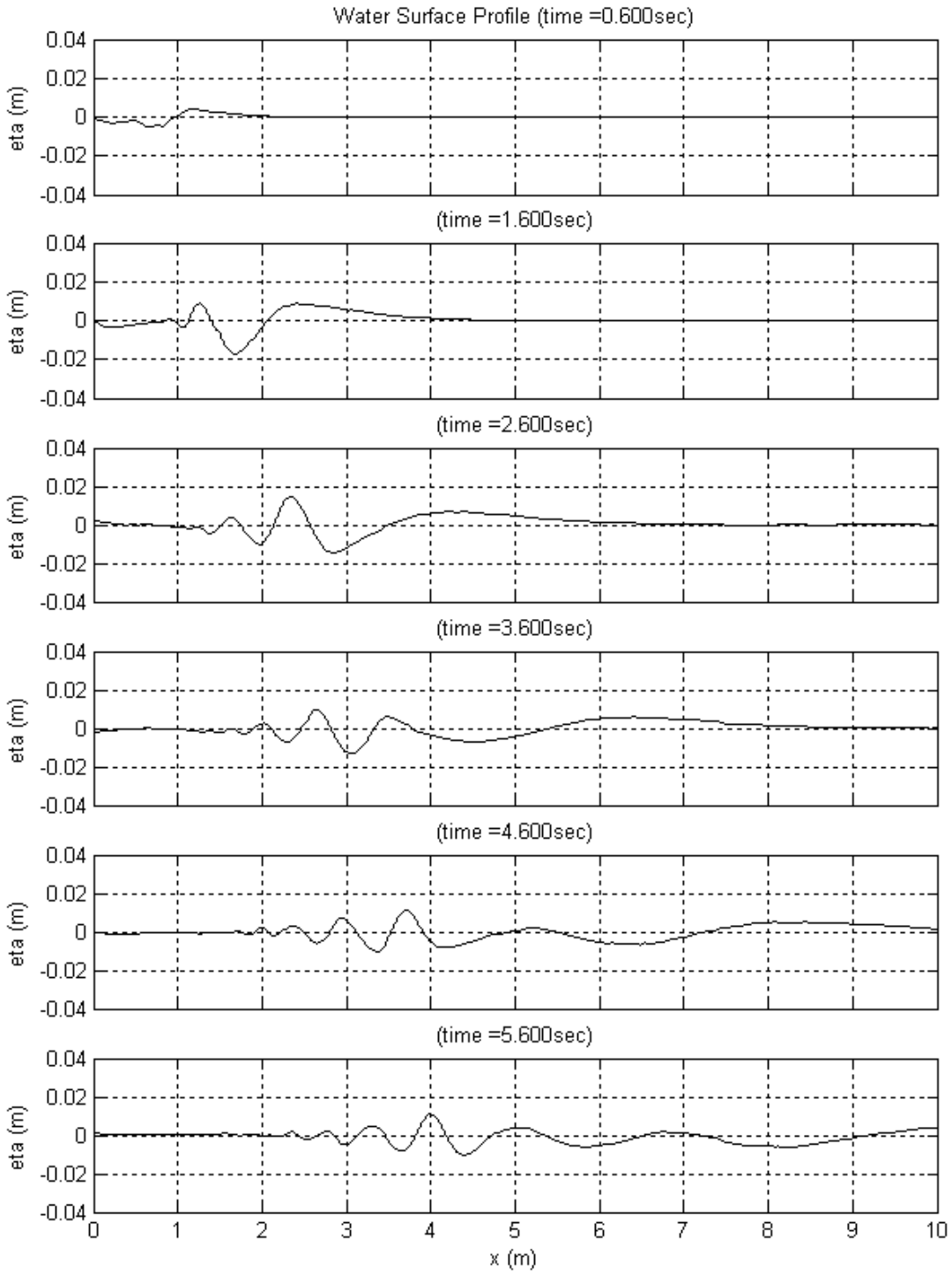

Figure C.27. Water surface profiles at t=0.60, 1.60, 2.60, 3.60, 4.60, and 5.60 seconds for the SG3_IS3 configuration.

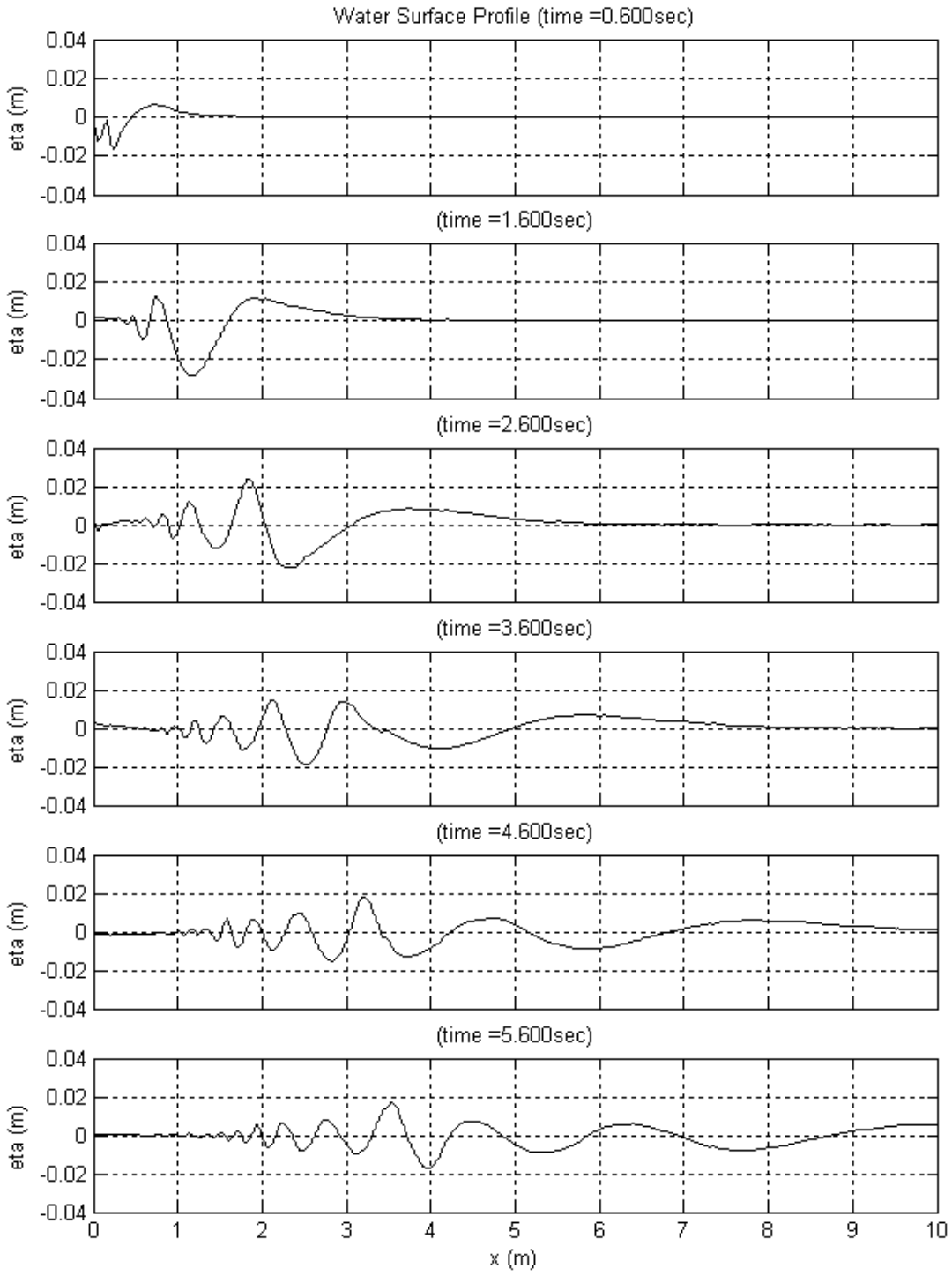

Figure C.28. Water surface profiles at t=0.60, 1.60, 2.60, 3.60, 4.60, and 5.60 seconds for the SG2_IS5 configuration.

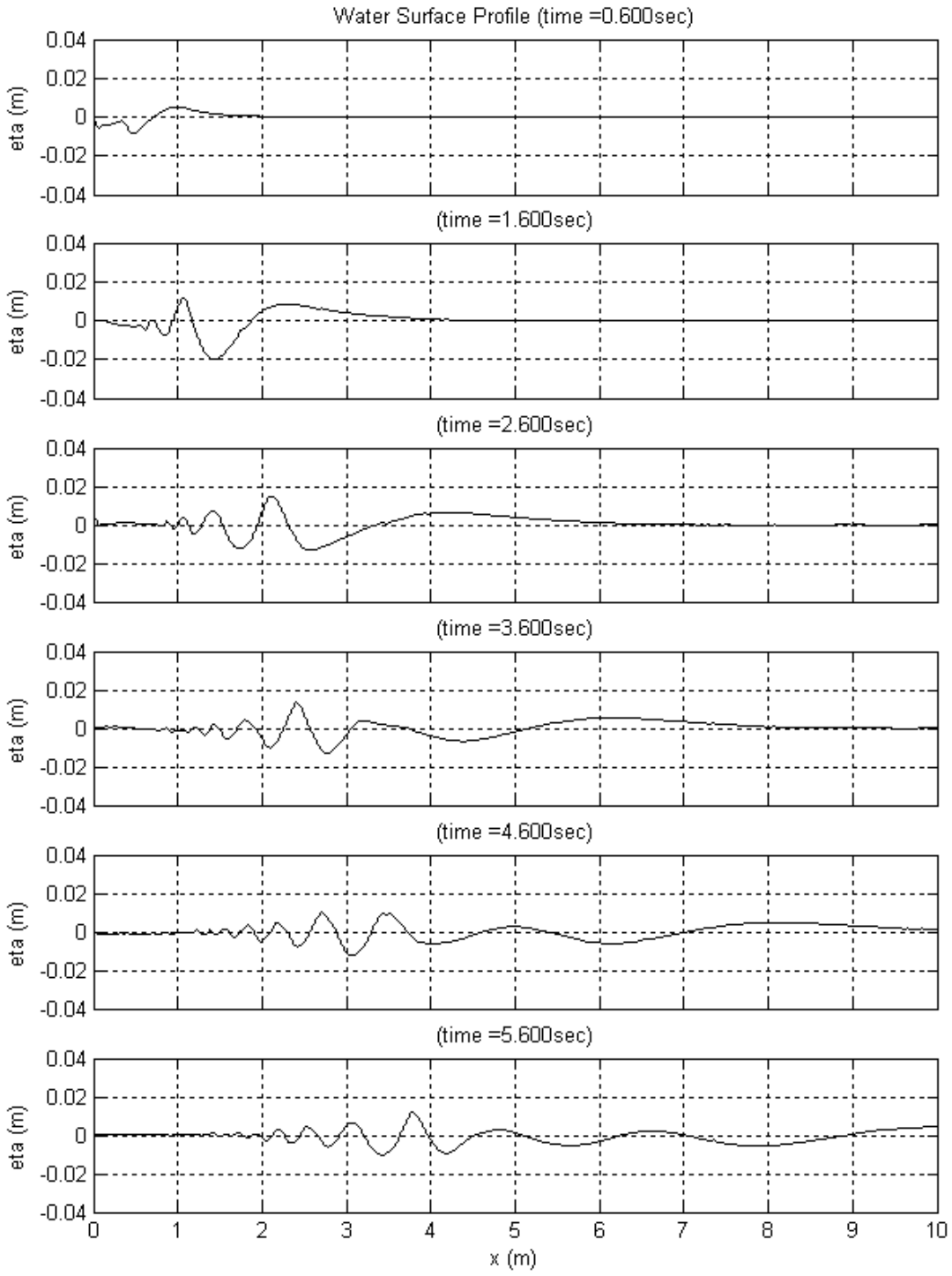

Figure C.29. Water surface profiles at t=0.60, 1.60, 2.60, 3.60, 4.60, and 5.60 seconds for the SG2_IS4 configuration.

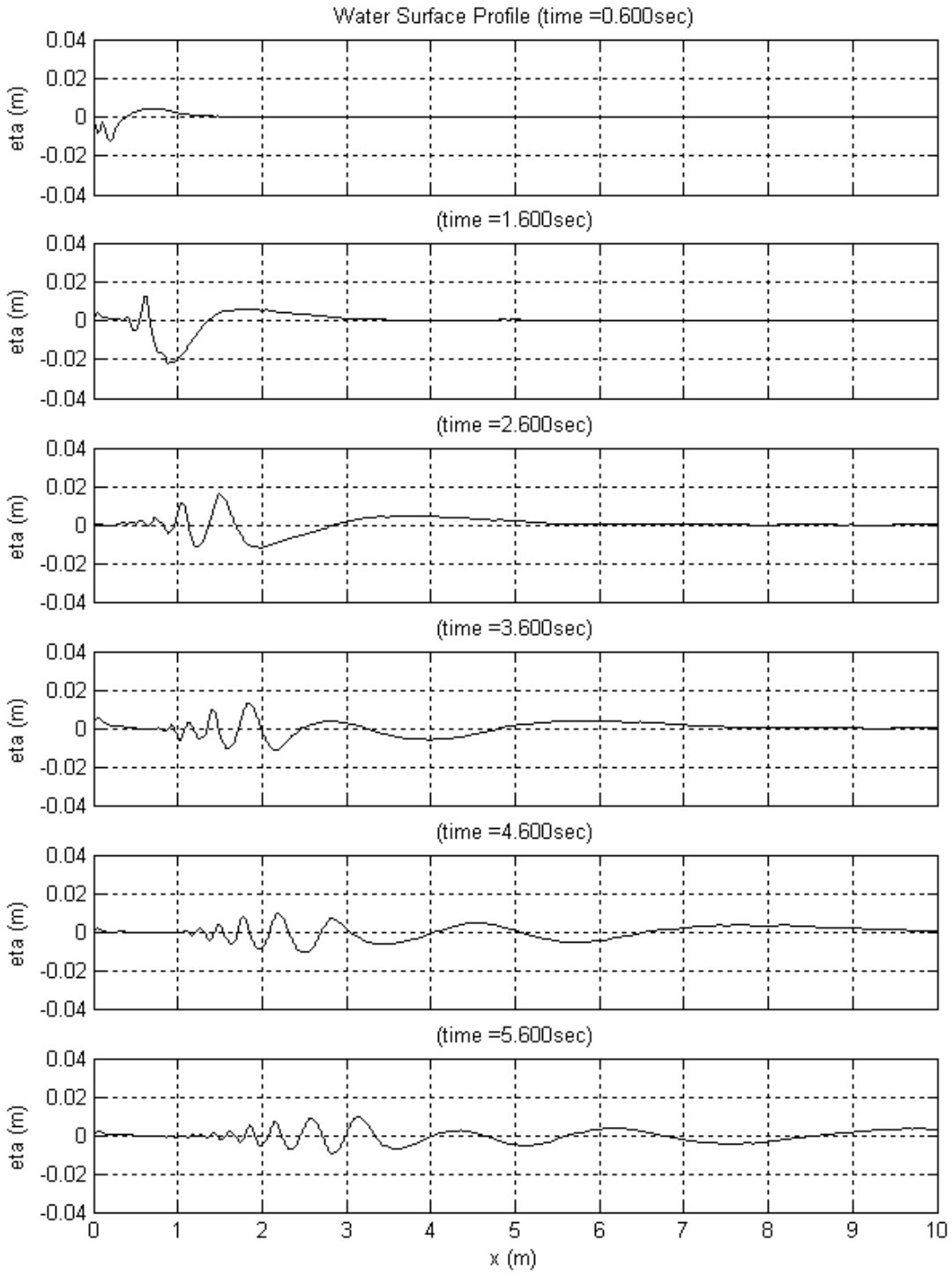

Figure C.30. Water surface profiles at t=0.60, 1.60, 2.60, 3.60, 4.60, and 5.60 seconds for the SG1_IS5 configuration.

C.3 Water Surface Time History

Plots of the water surface time histories at x=0.50, 1.50, 2.50, 3.50, 4.50, and 5.50, for each of the fifteen specific gravity and initial submergence combinations, are presented in Figures C.31 to C.45.

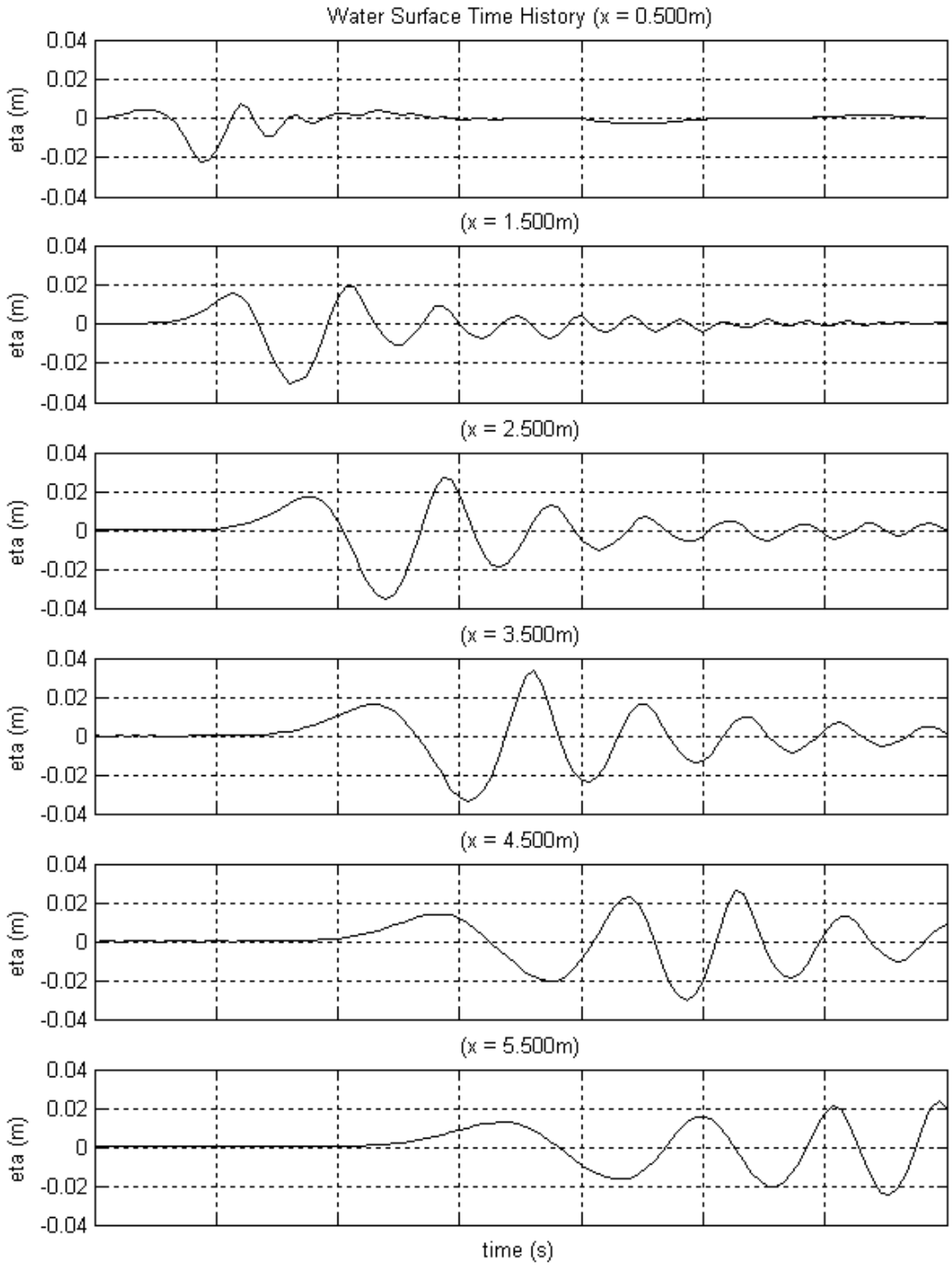

Figure C.31. Water surface time histories at x=0.50, 1.50, 2.50, 3.50, 4.50, and 5.50 for the SG5_IS5 configuration.

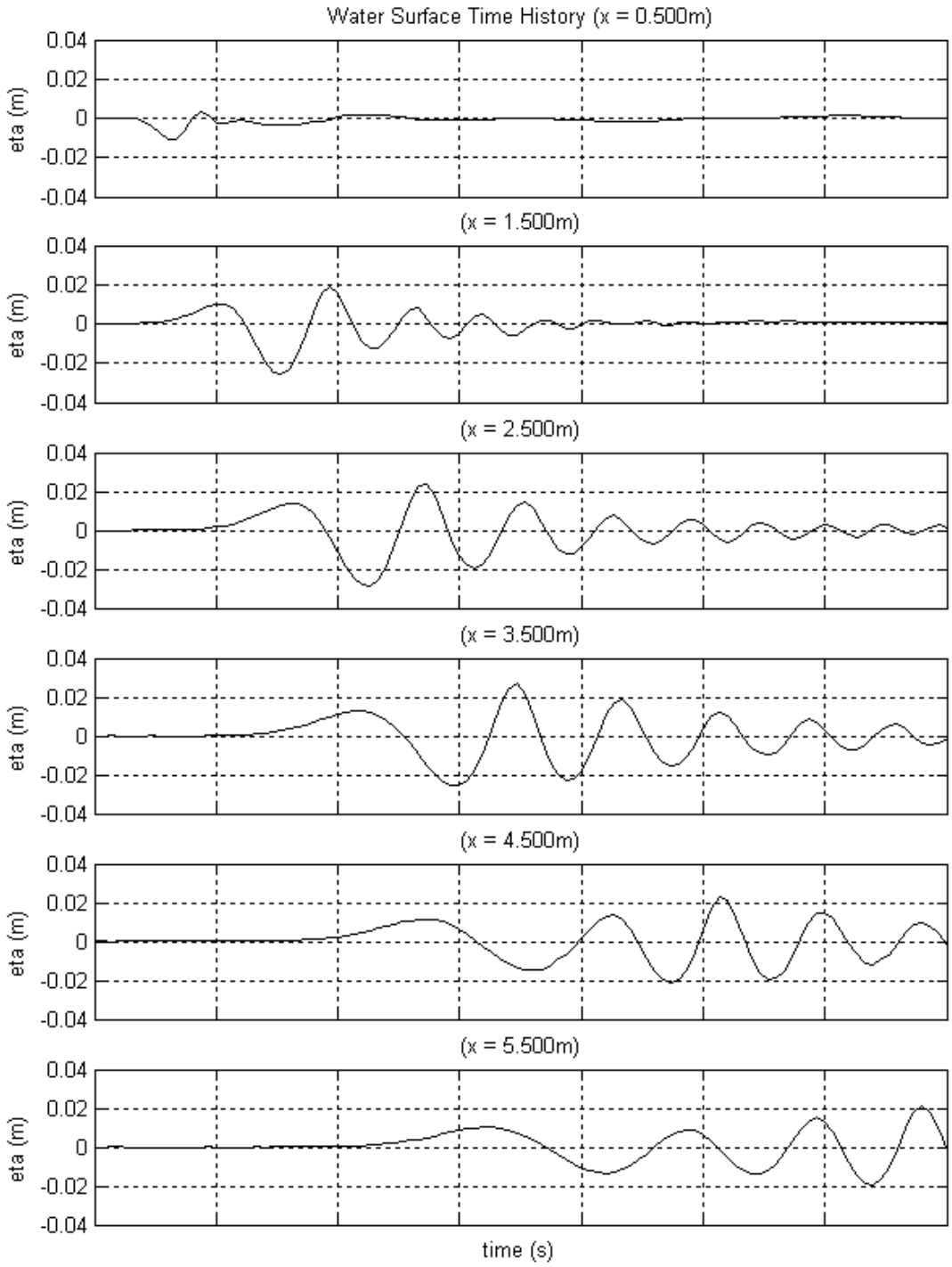

Figure C.32. Water surface time histories at x=0.50, 1.50, 2.50, 3.50, 4.50, and 5.50 for the SG5_IS4 configuration.

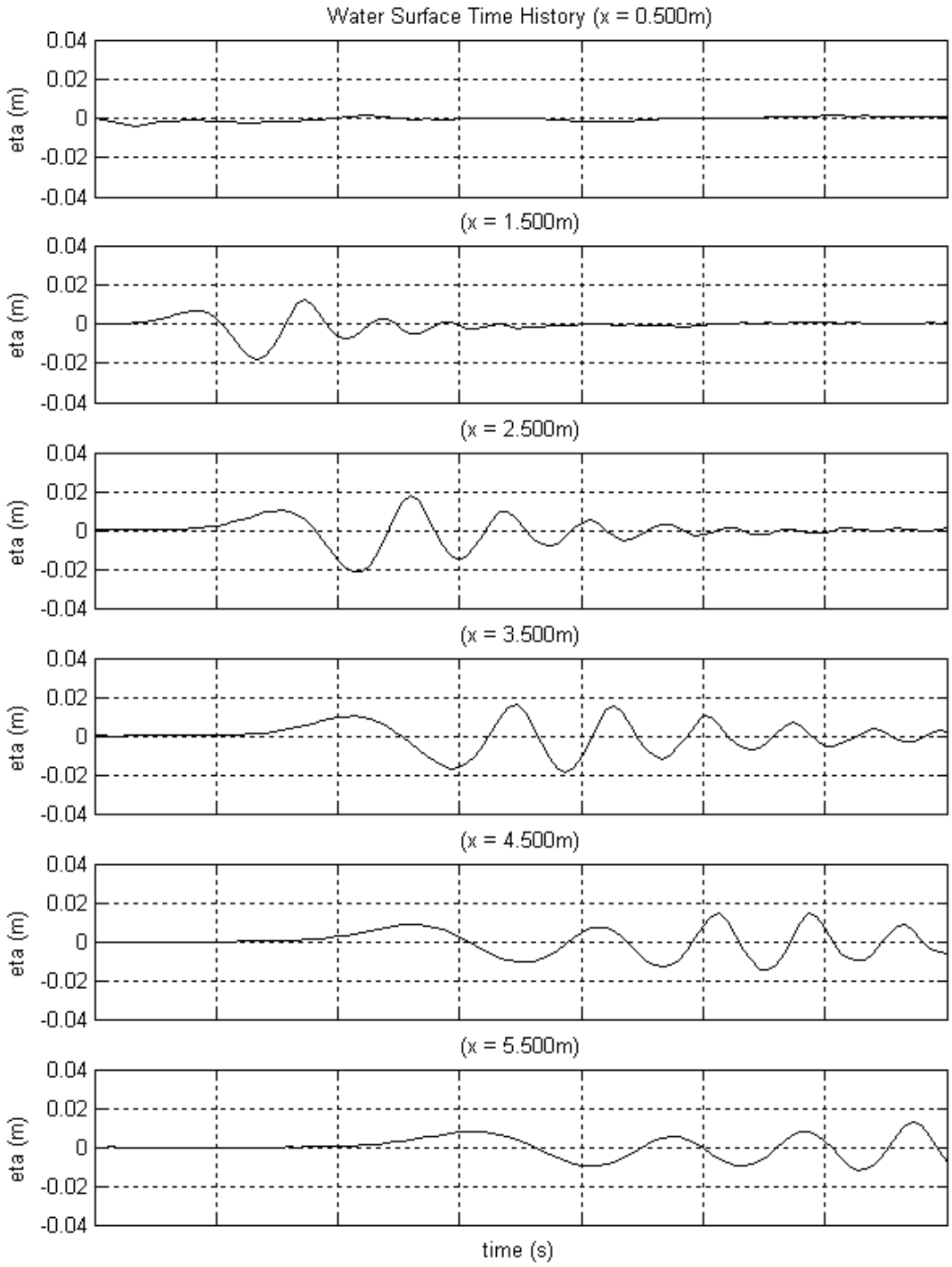

Figure C.33. Water surface time histories at x=0.50, 1.50, 2.50, 3.50, 4.50, and 5.50 for the SG5_IS3 configuration.

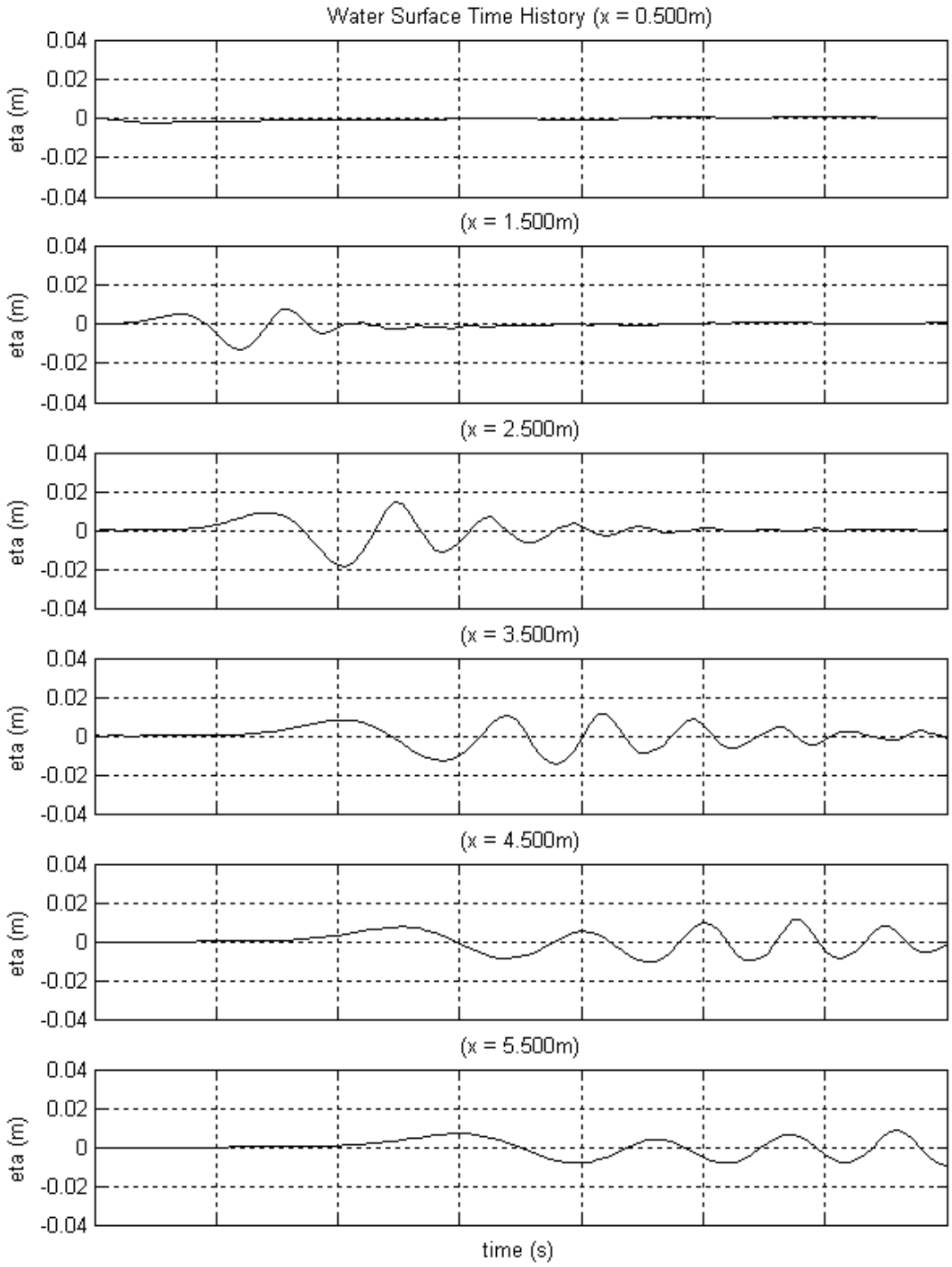

Figure C.34. Water surface time histories at x=0.50, 1.50, 2.50, 3.50, 4.50, and 5.50 for the SG5_IS2 configuration.

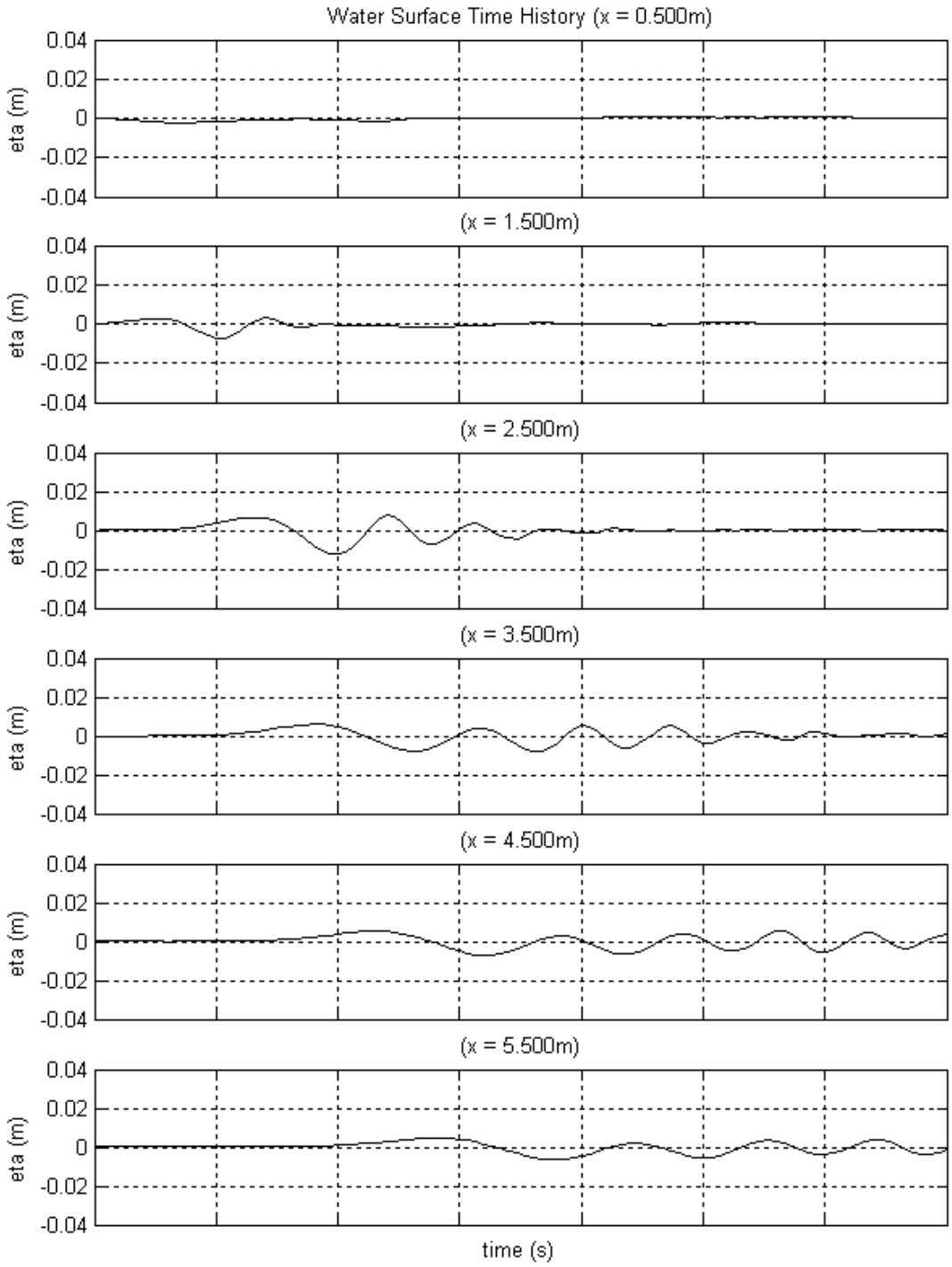

Figure C.35. Water surface time histories at x=0.50, 1.50, 2.50, 3.50, 4.50, and 5.50 for the SG5_IS1 configuration.

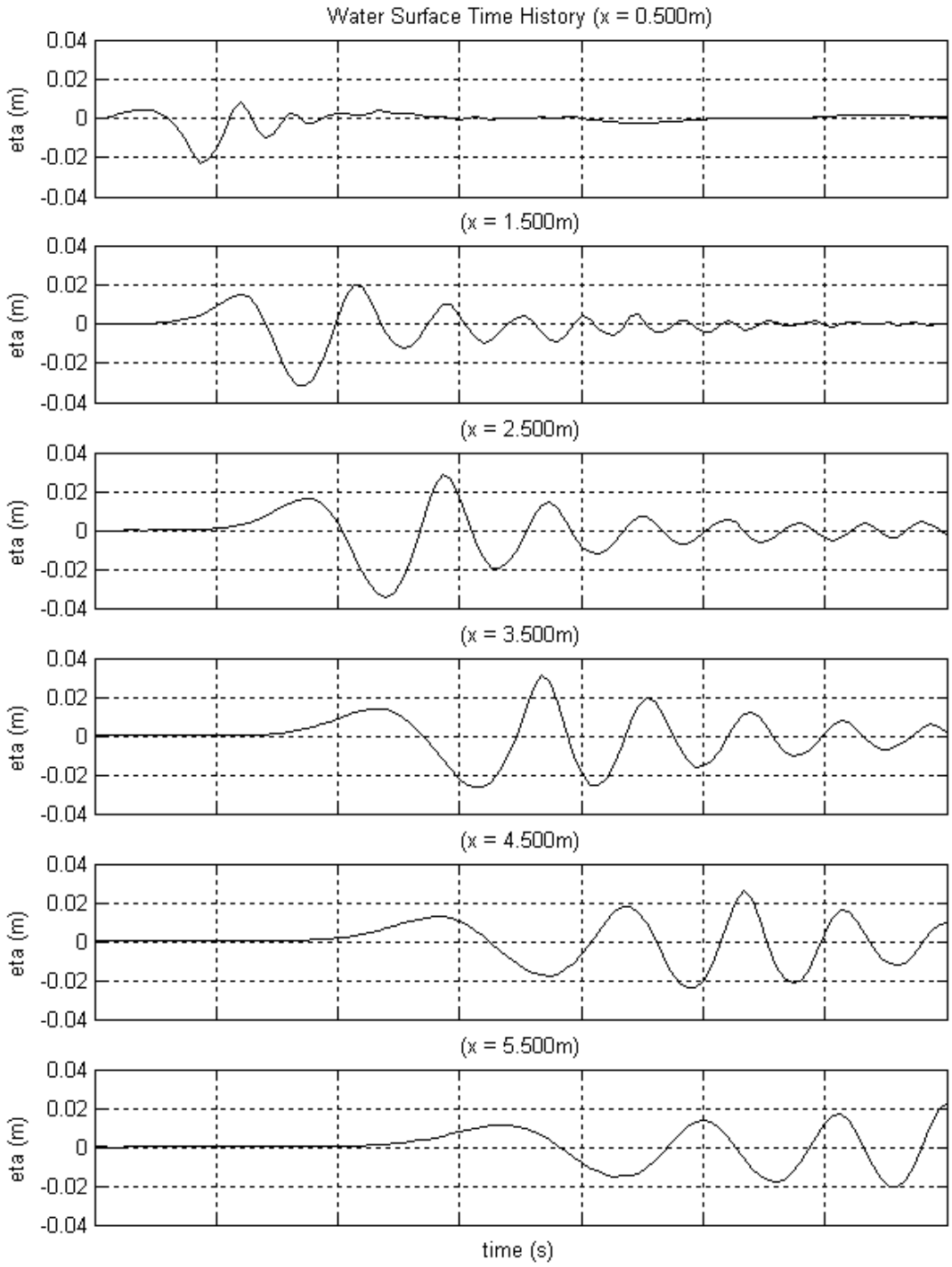

Figure C.36. Water surface time histories at x=0.50, 1.50, 2.50, 3.50, 4.50, and 5.50 for the SG4_IS5 configuration.

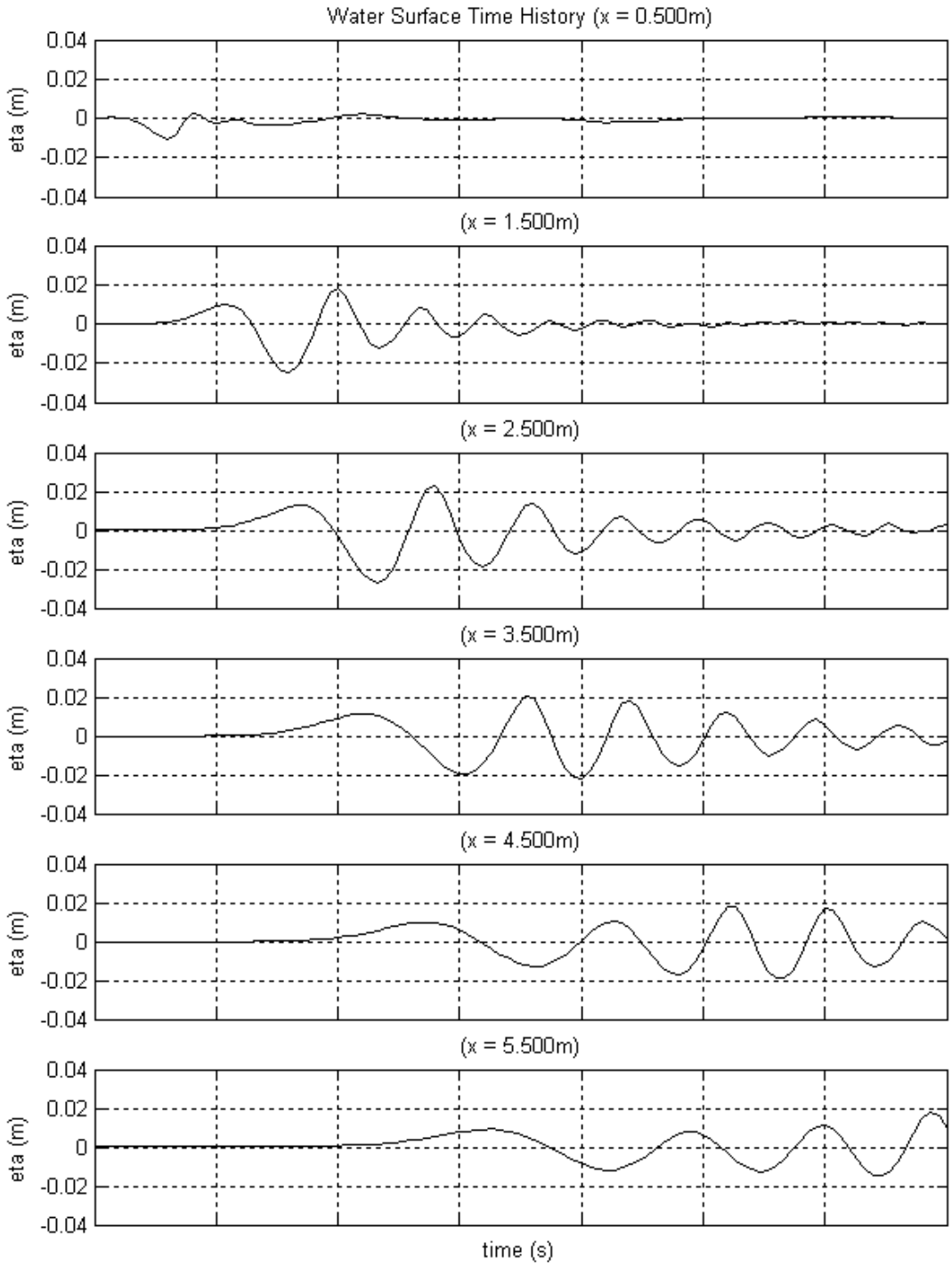

Figure C.37. Water surface time histories at x=0.50, 1.50, 2.50, 3.50, 4.50, and 5.50 for the SG4_IS4 configuration.

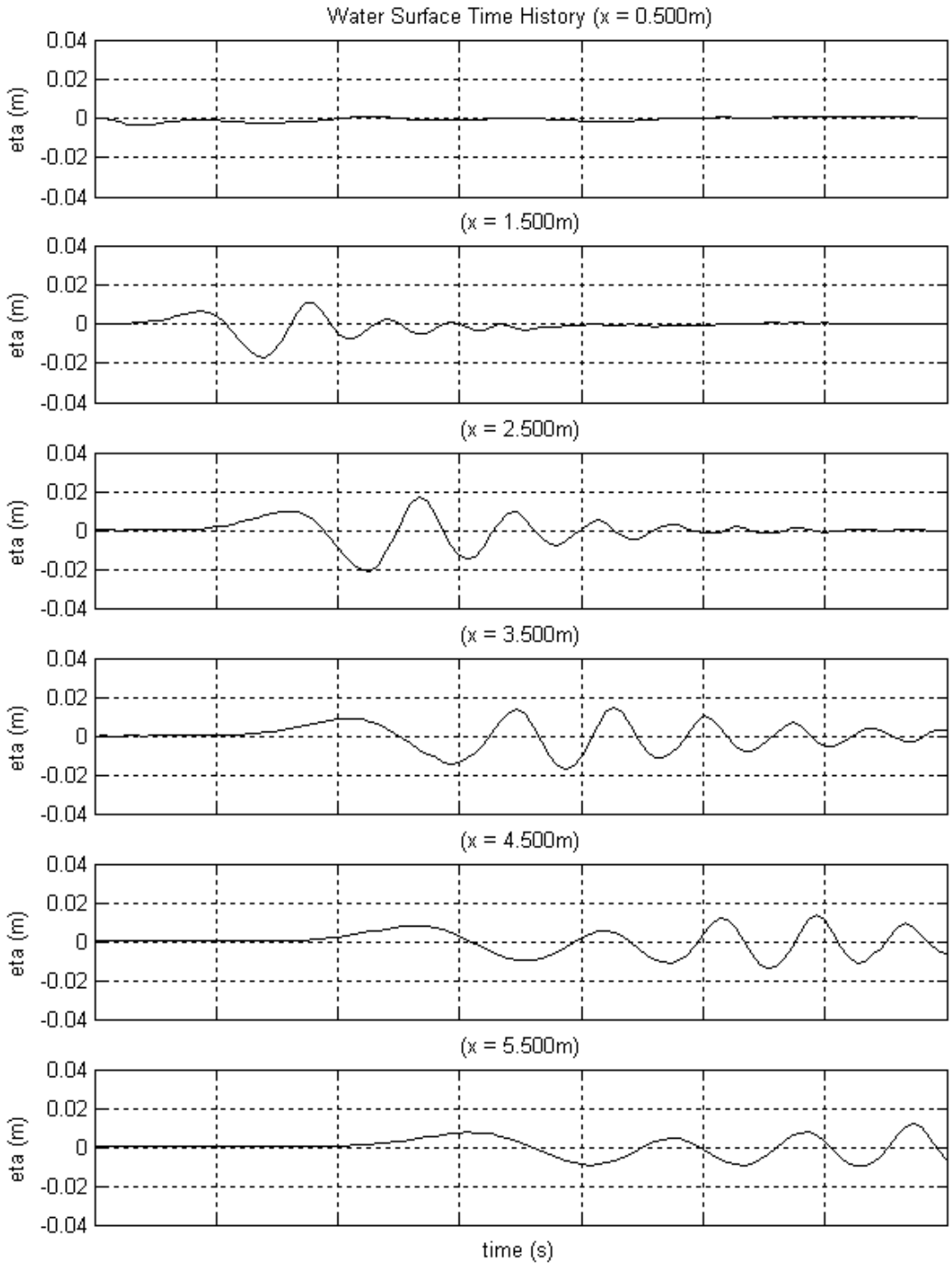

Figure C.38. Water surface time histories at x=0.50, 1.50, 2.50, 3.50, 4.50, and 5.50 for the SG4_IS3 configuration.

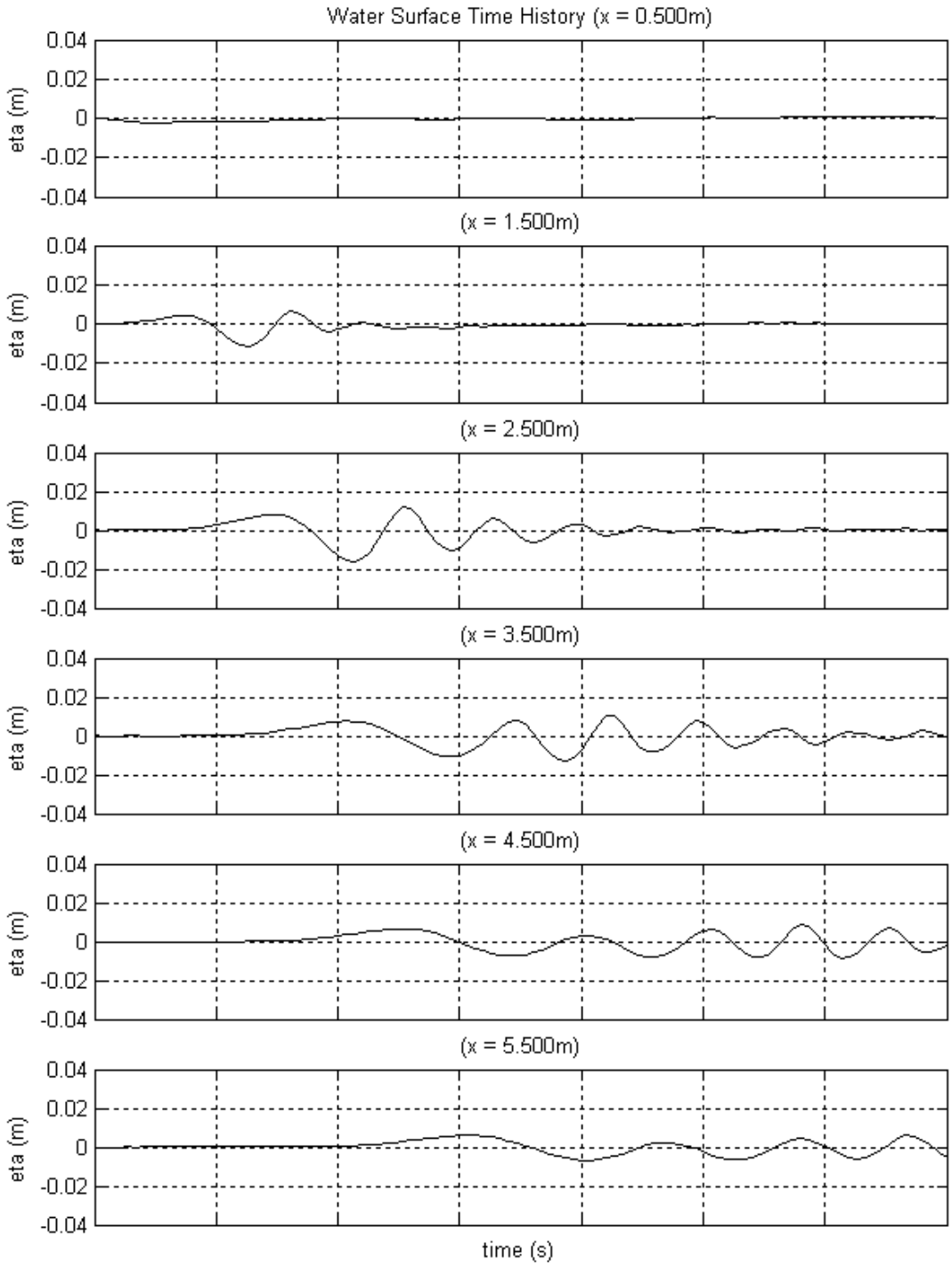

Figure C.39. Water surface time histories at x=0.50, 1.50, 2.50, 3.50, 4.50, and 5.50 for the SG4_IS2 configuration.

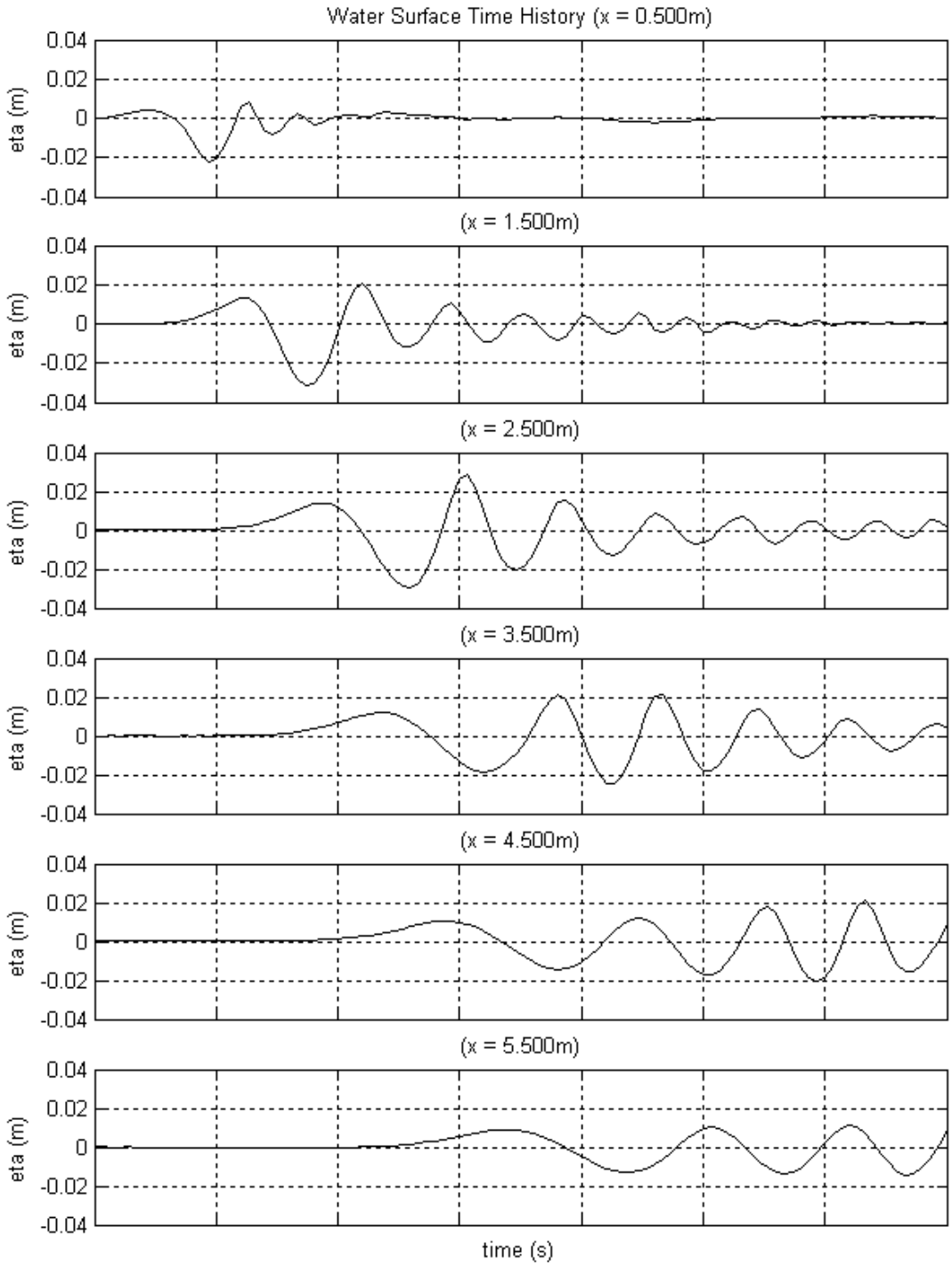

Figure C.40. Water surface time histories at x=0.50, 1.50, 2.50, 3.50, 4.50, and 5.50 for the SG3_IS5 configuration.

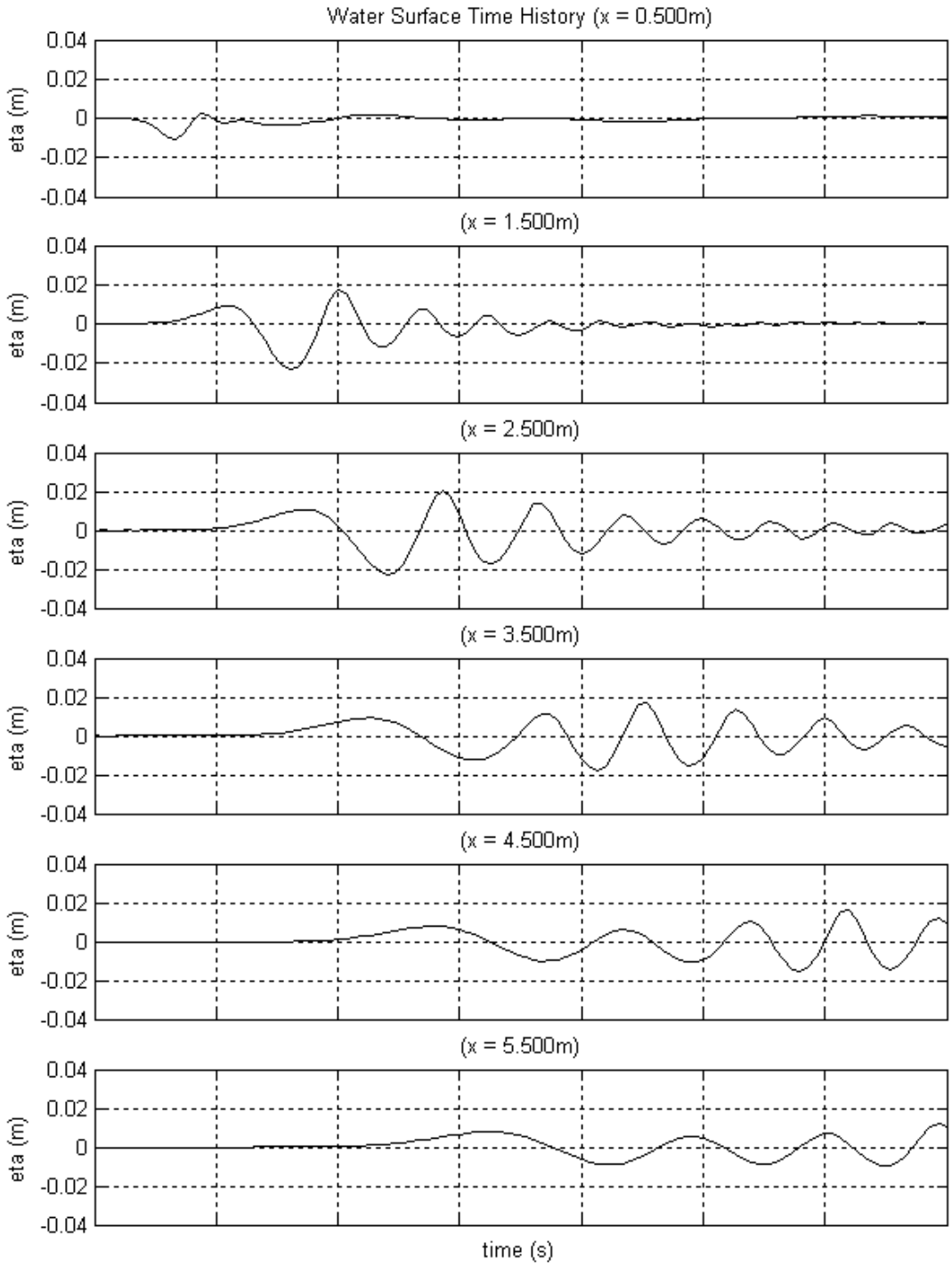

Figure C.41. Water surface time histories at x=0.50, 1.50, 2.50, 3.50, 4.50, and 5.50 for the SG3_IS4 configuration.

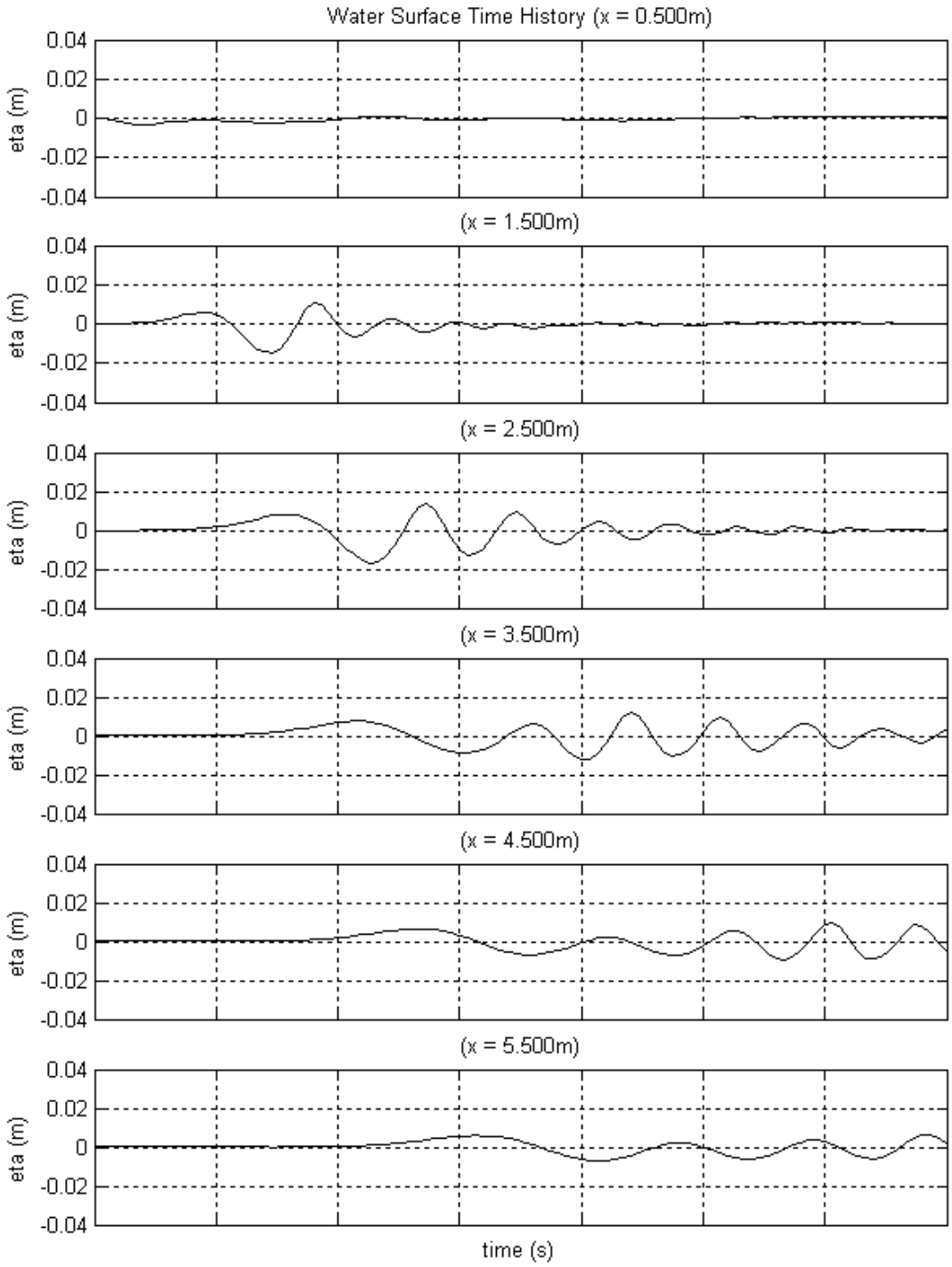

Figure C.42. Water surface time histories at x=0.50, 1.50, 2.50, 3.50, 4.50, and 5.50 for the SG3_IS3 configuration.

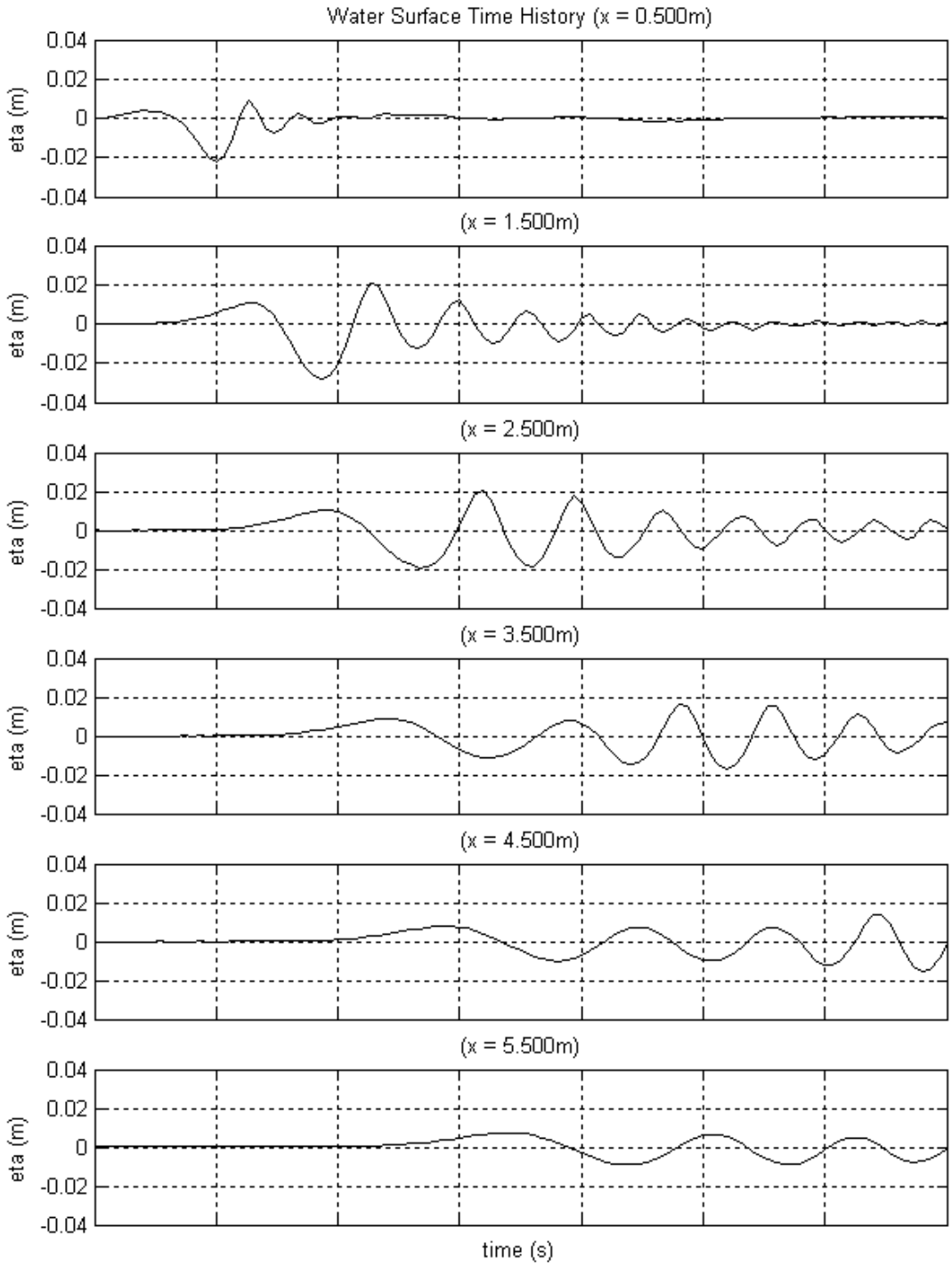

Figure C.43. Water surface time histories at x=0.50, 1.50, 2.50, 3.50, 4.50, and 5.50 for the SG2_IS5 configuration.

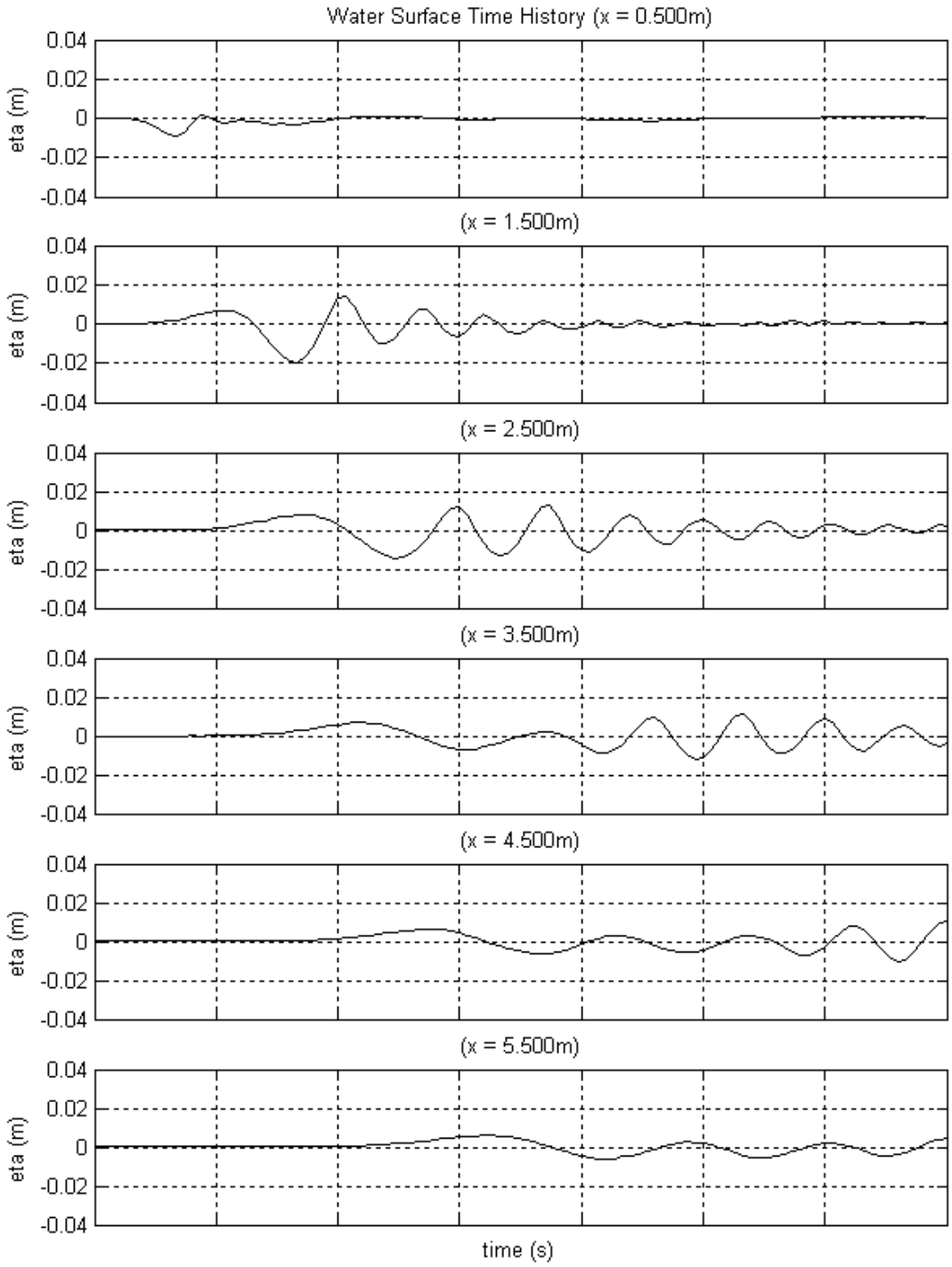

Figure C.44. Water surface time histories at x=0.50, 1.50, 2.50, 3.50, 4.50, and 5.50 for the SG2_IS4 configuration.

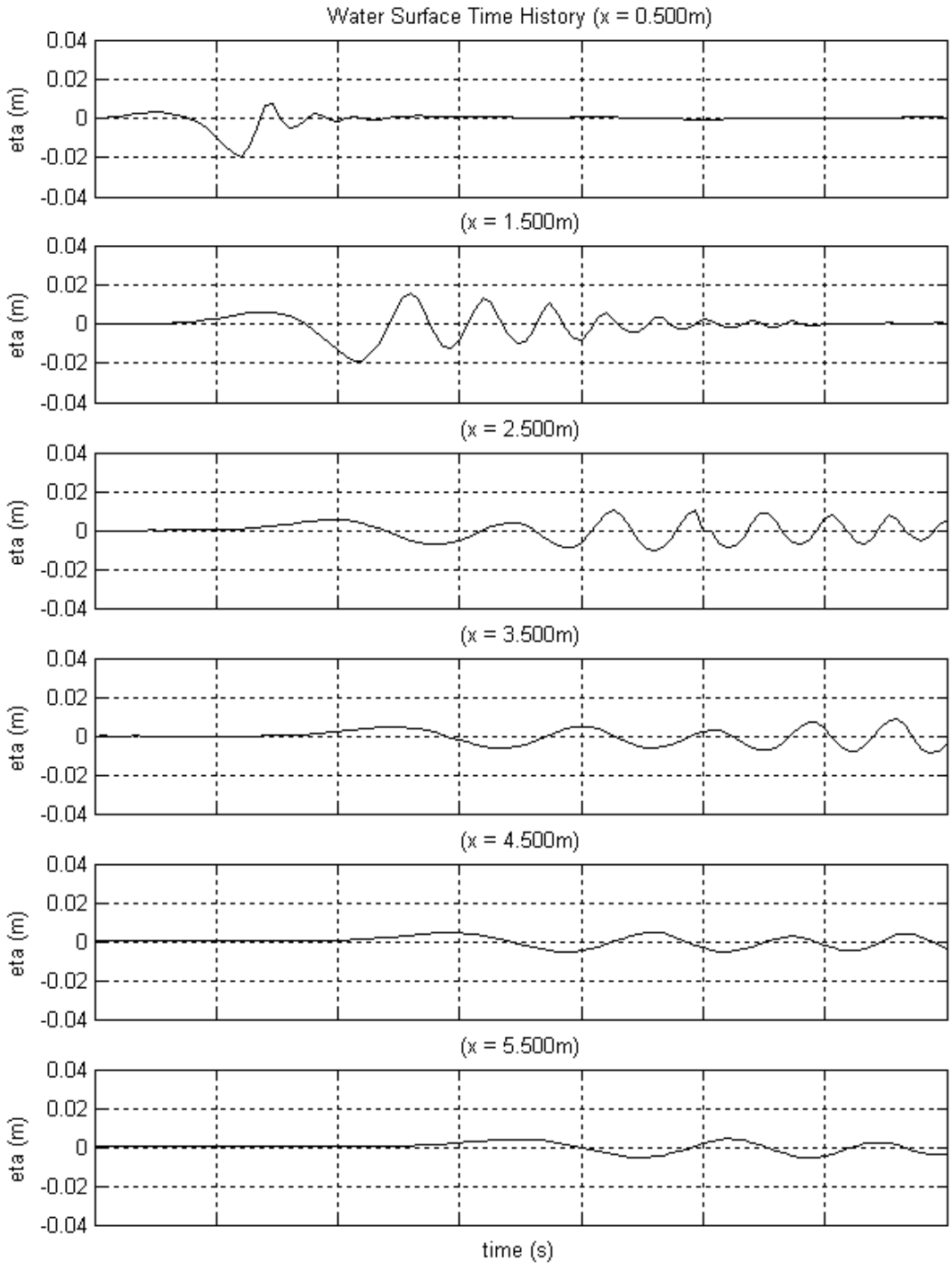

Figure C.45. Water surface time histories at x=0.50, 1.50, 2.50, 3.50, 4.50, and 5.50 for the SG1_IS5 configuration.

C.4 Maximum Water Level Envelope and Time History

Although maximum expected wave heights are important from a hazard point of view, which wave is largest is often irrelevant. Therefore, plots of the maximum and minimum water level envelope and time history for each of the fifteen specific gravity and initial submergence combinations are presented in Figures C.46 to C.60.

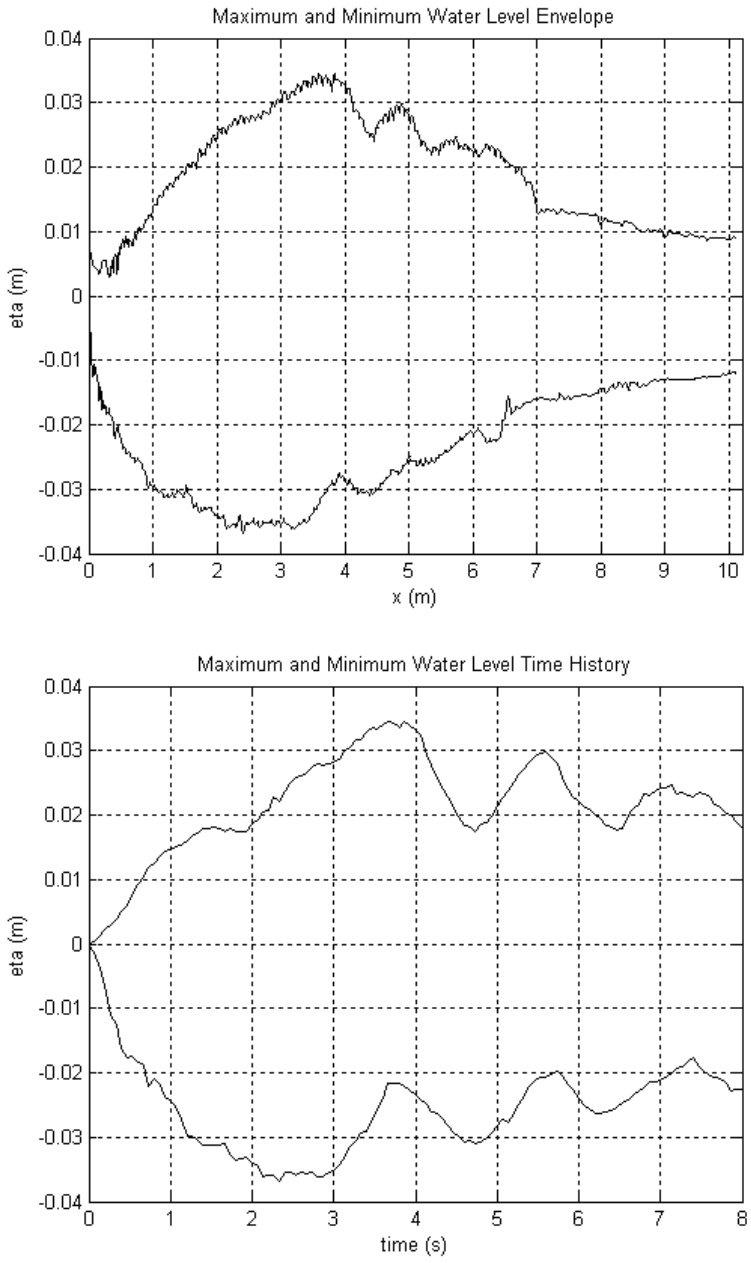

Figure C.46. Maximum and minimum water level envelope and time history for the SG5_IS5 configuration.

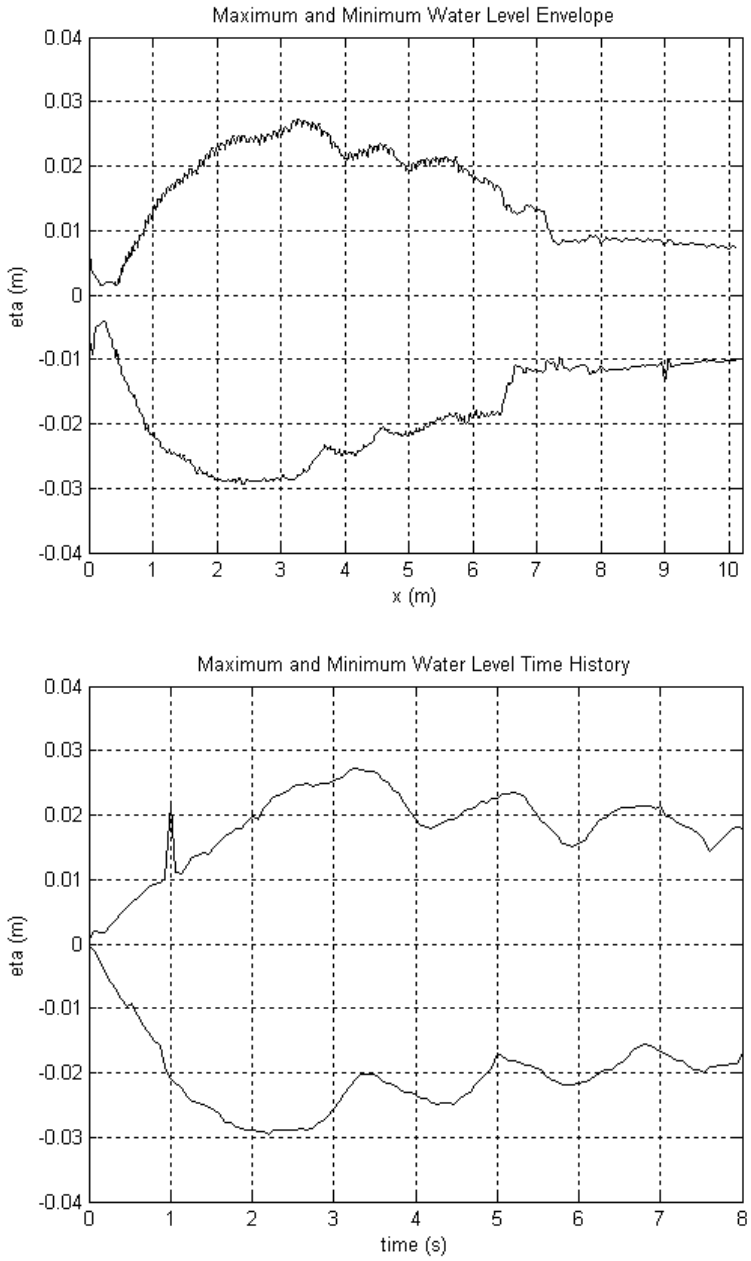

Figure C.47. Maximum and minimum water level envelope and time history for the SG5_IS4 configuration.

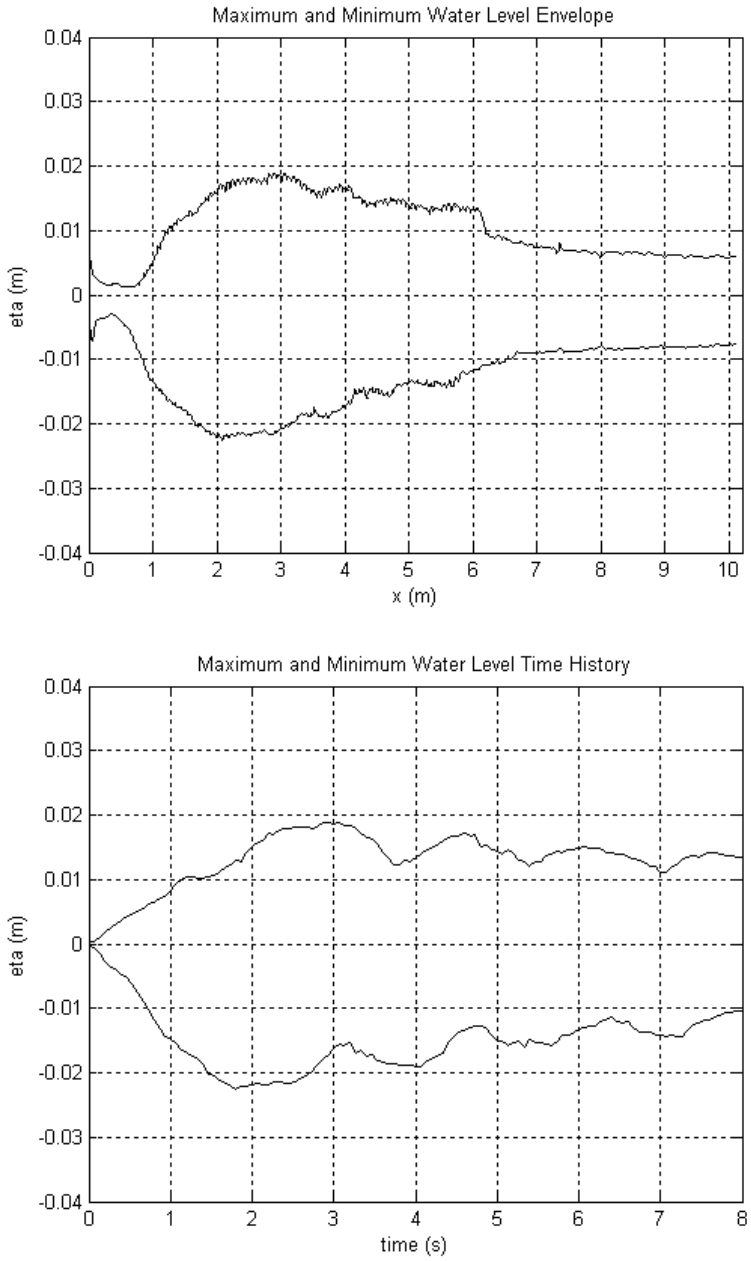

Figure C.48. Maximum and minimum water level envelope and time history for the SG5_IS3 configuration.

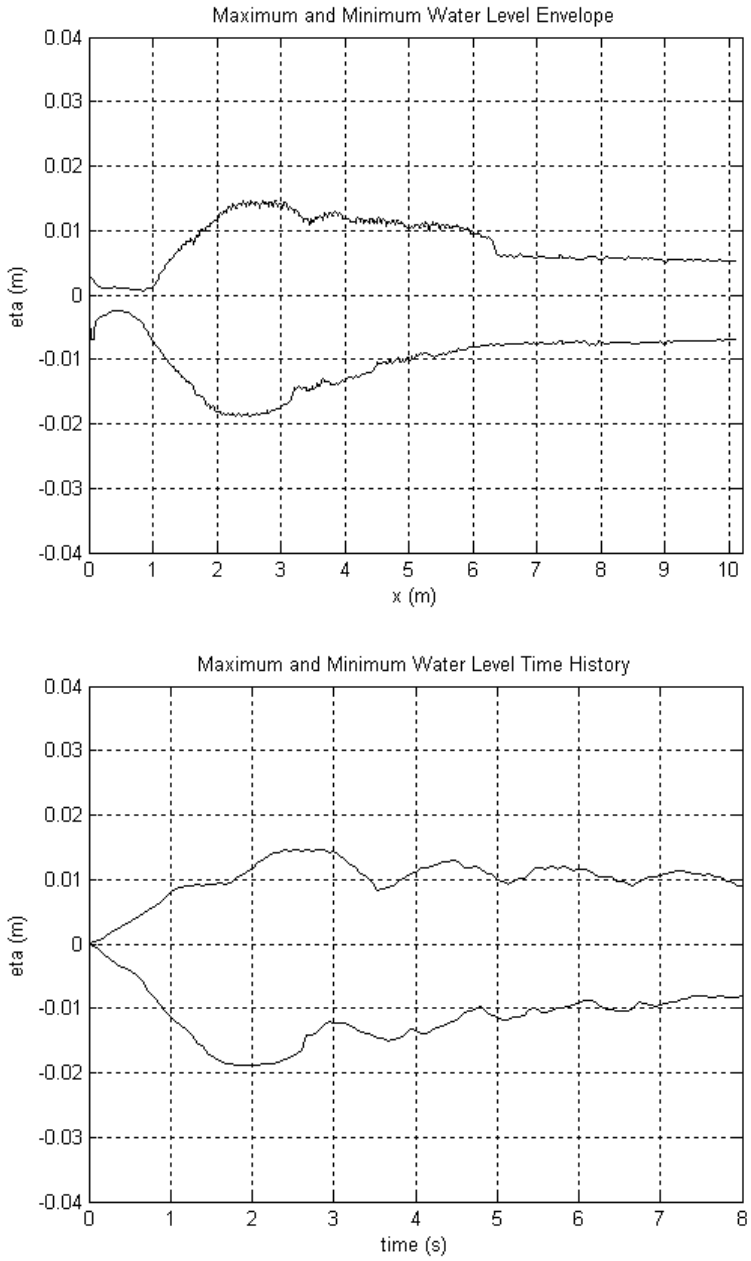

Figure C.49. Maximum and minimum water level envelope and time history for the SG5_IS2 configuration.

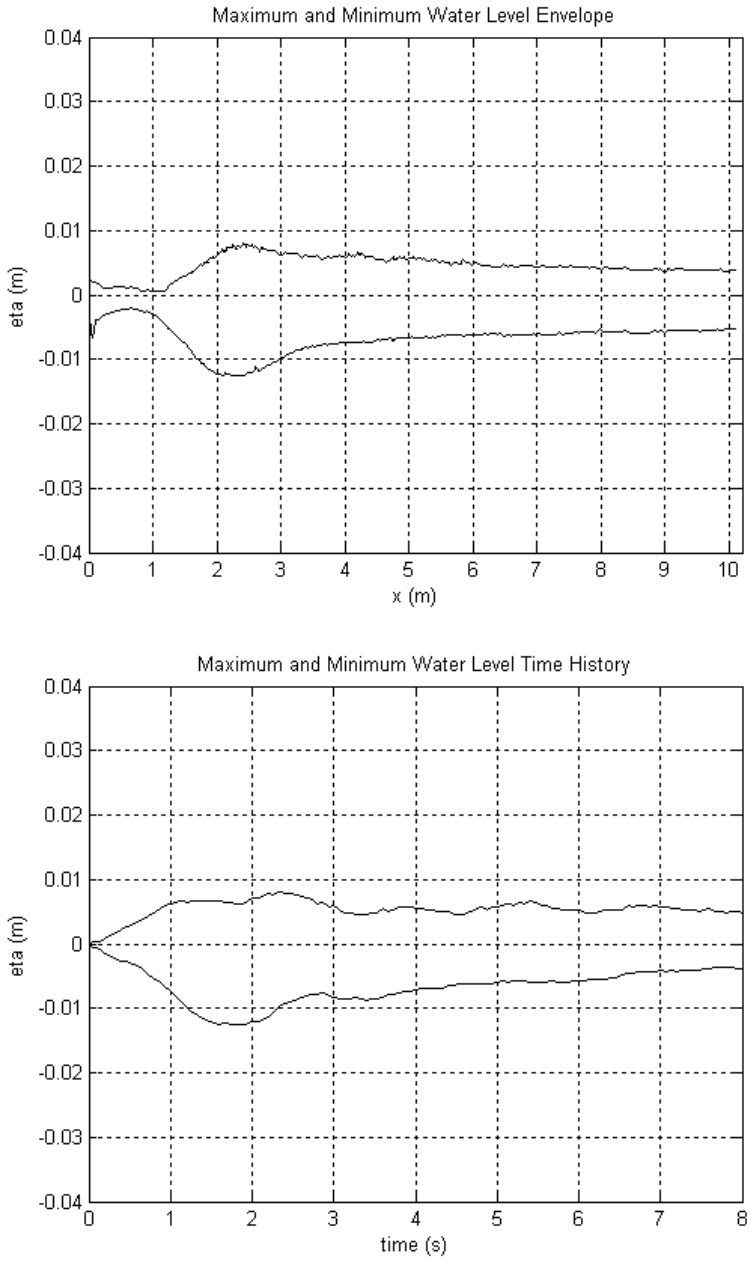

Figure C.50. Maximum and minimum water level envelope and time history for the SG5_IS1 configuration.

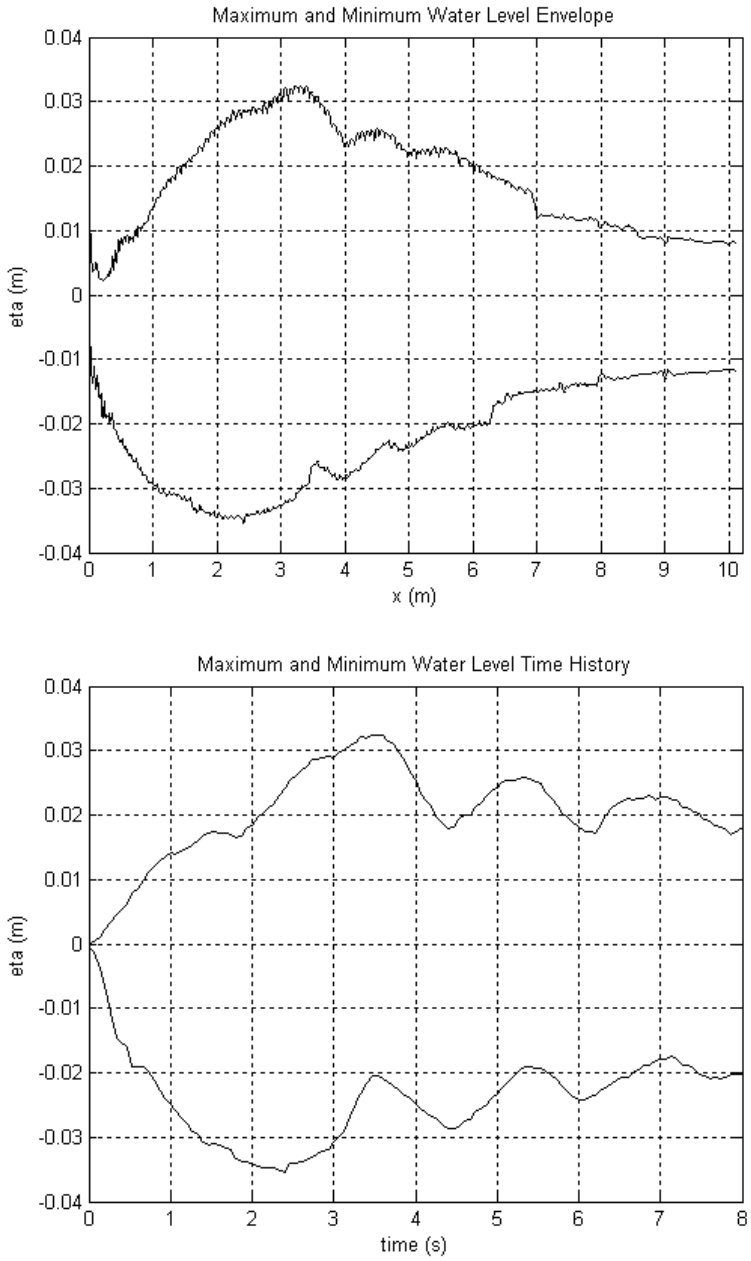

Figure C.51. Maximum and minimum water level envelope and time history for the SG4_IS5 configuration.

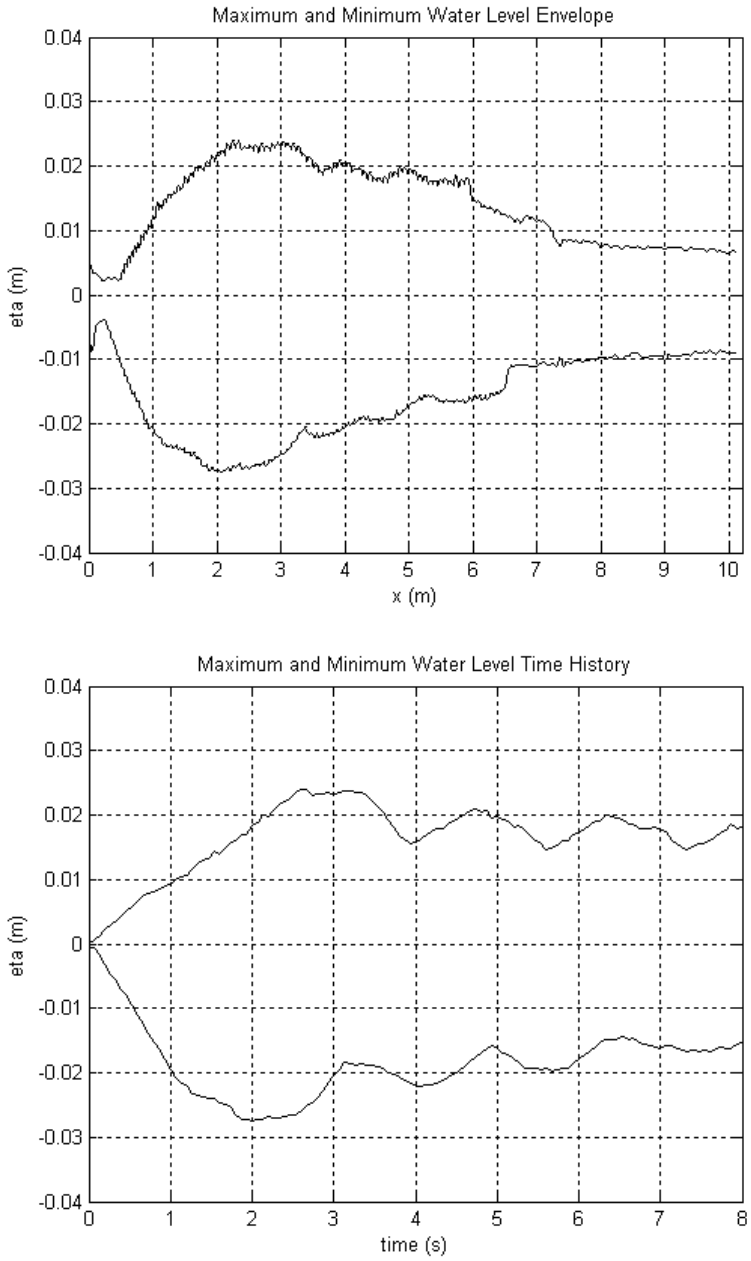

Figure C.52. Maximum and minimum water level envelope and time history for the SG4_IS4 configuration.

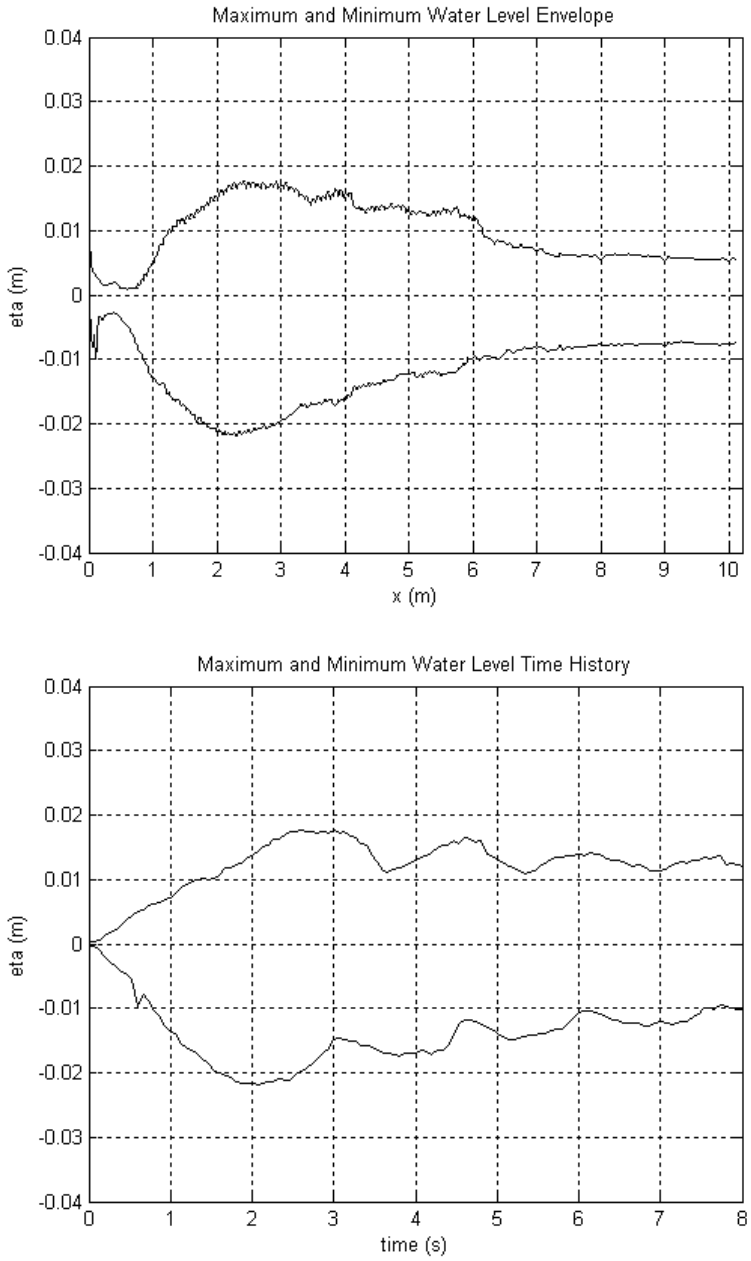

Figure C.53. Maximum and minimum water level envelope and time history for the SG4_IS3 configuration.

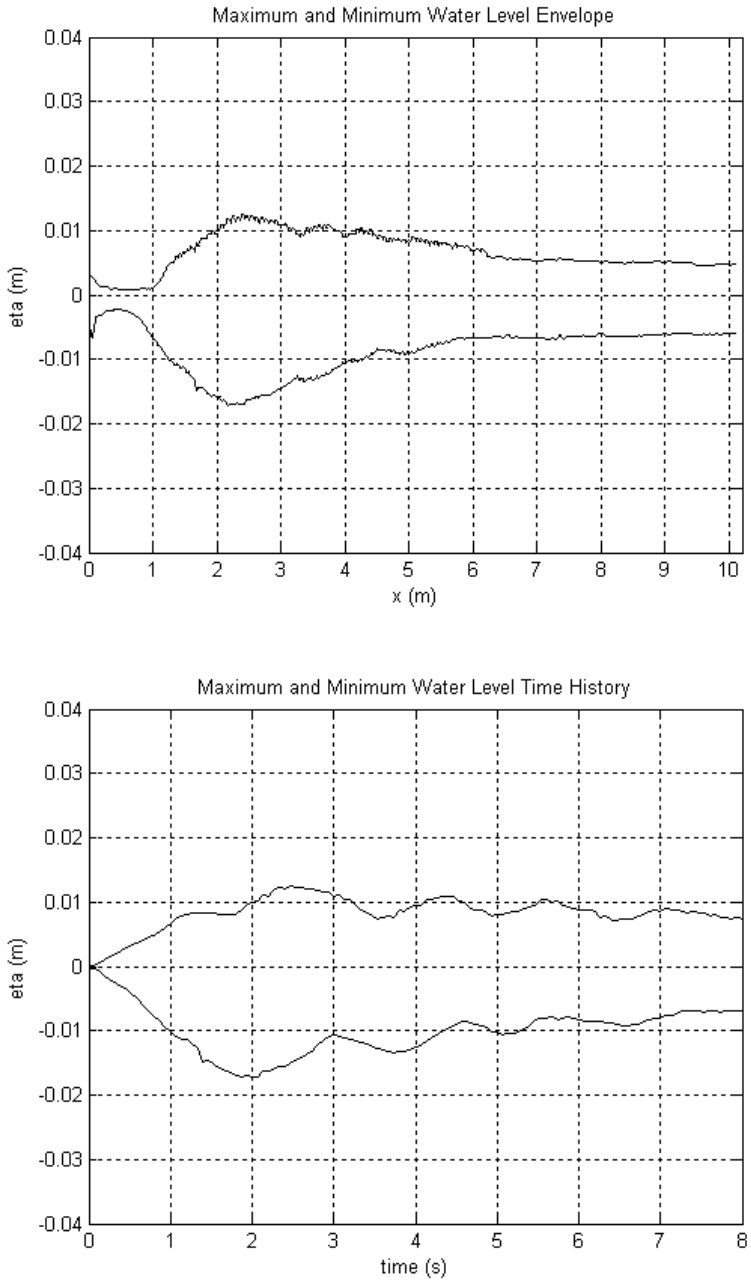

Figure C.54. Maximum and minimum water level envelope and time history for the SG4_IS2 configuration.

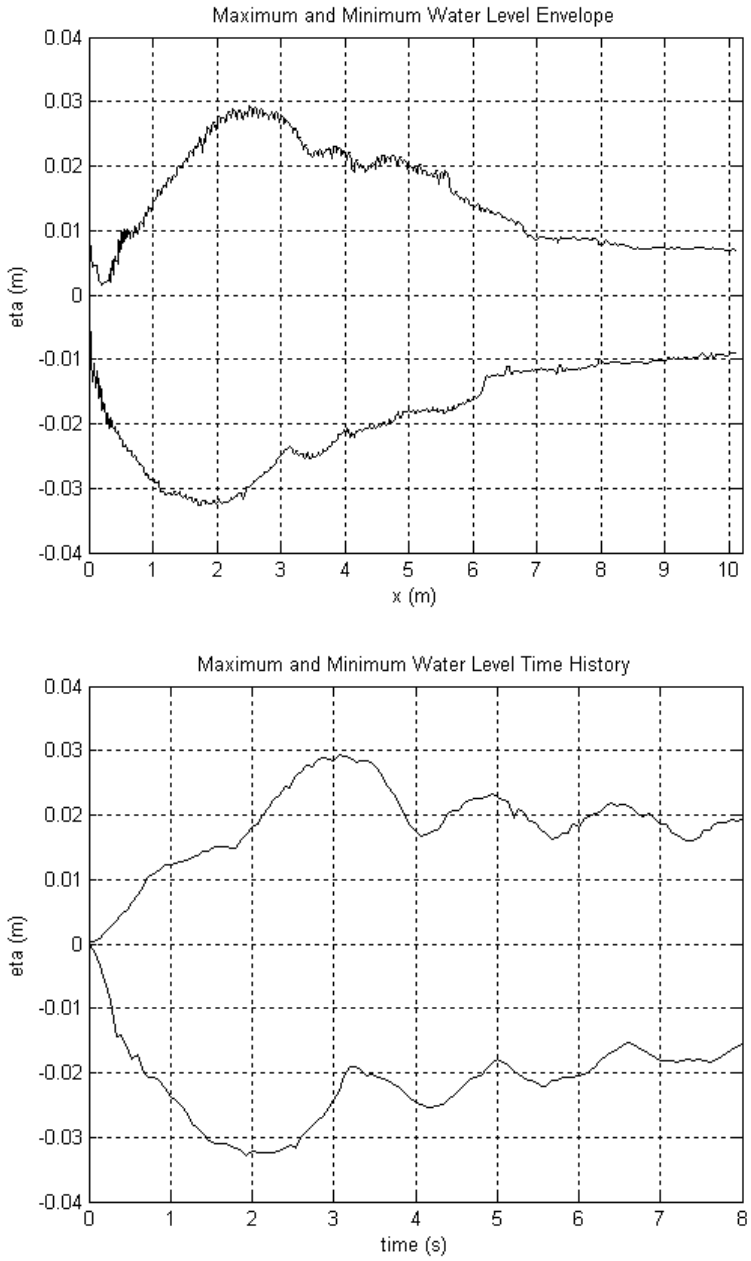

Figure C.55. Maximum and minimum water level envelope and time history for the SG3_IS5 configuration.

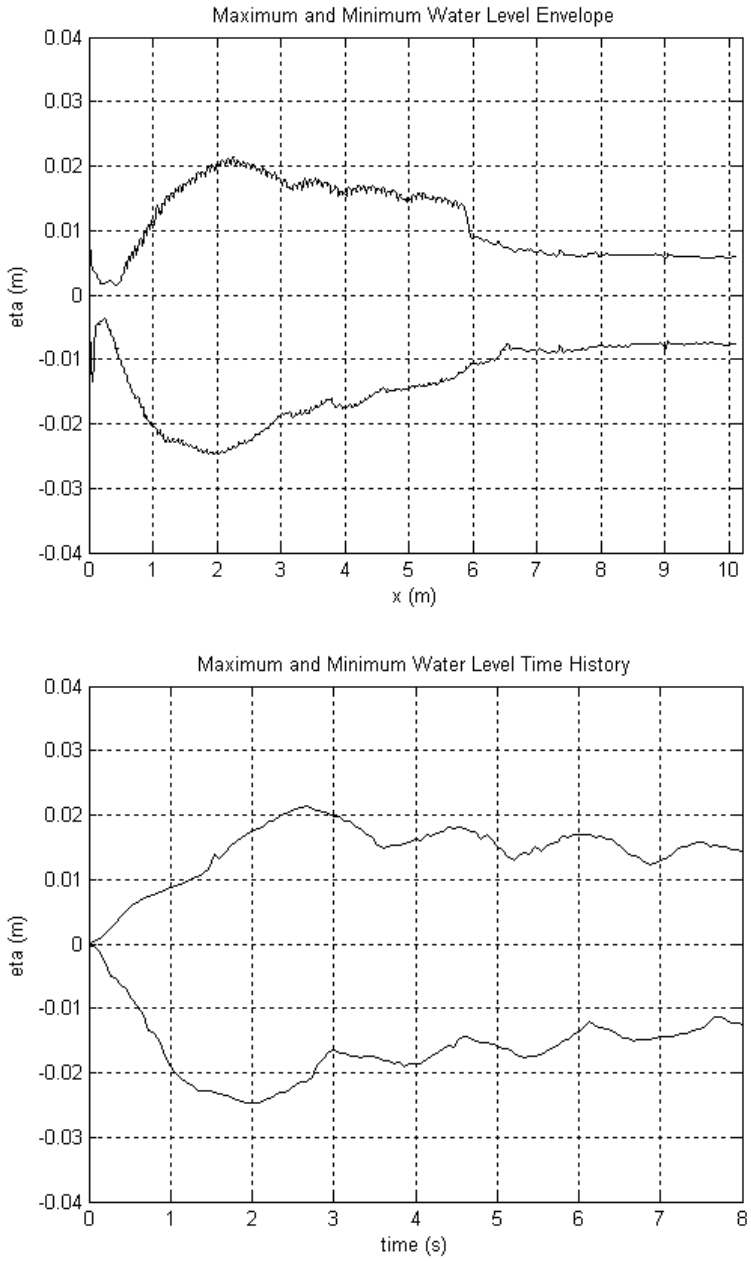

Figure C.56. Maximum and minimum water level envelope and time history for the SG3_IS4 configuration.

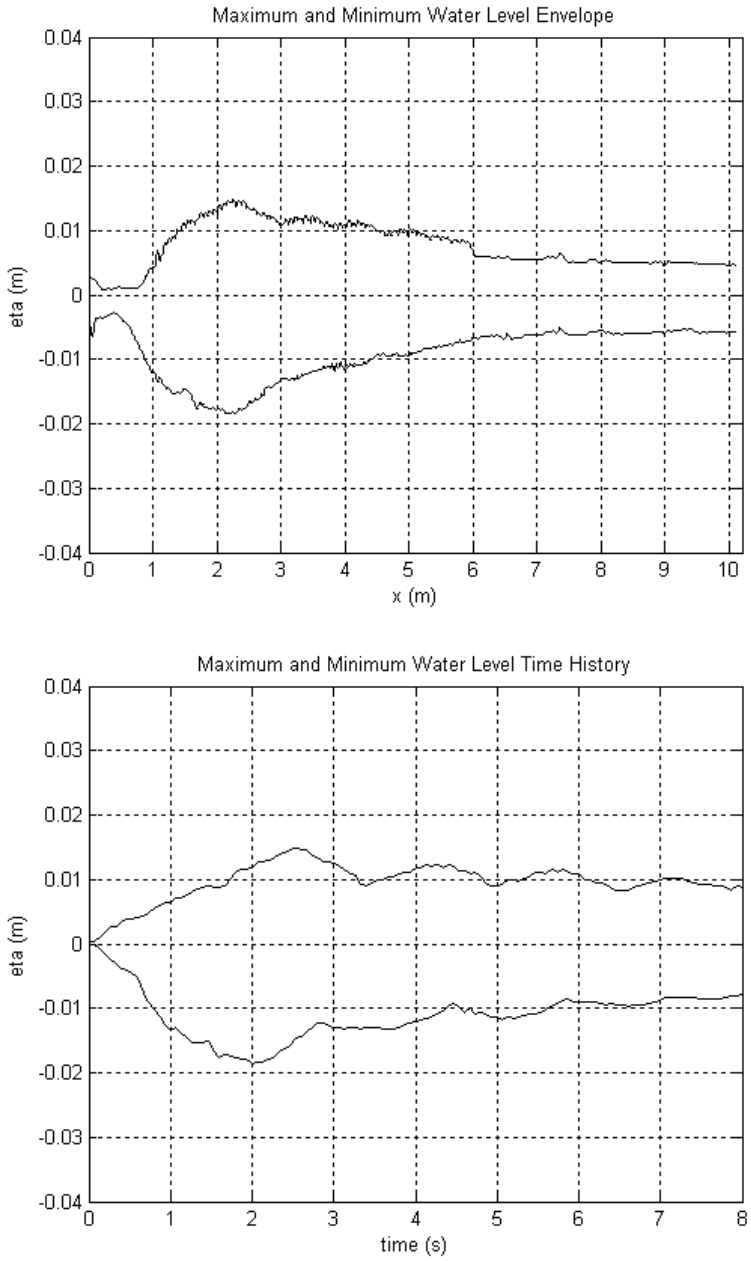

Figure C.57. Maximum and minimum water level envelope and time history for the SG3_IS3 configuration.

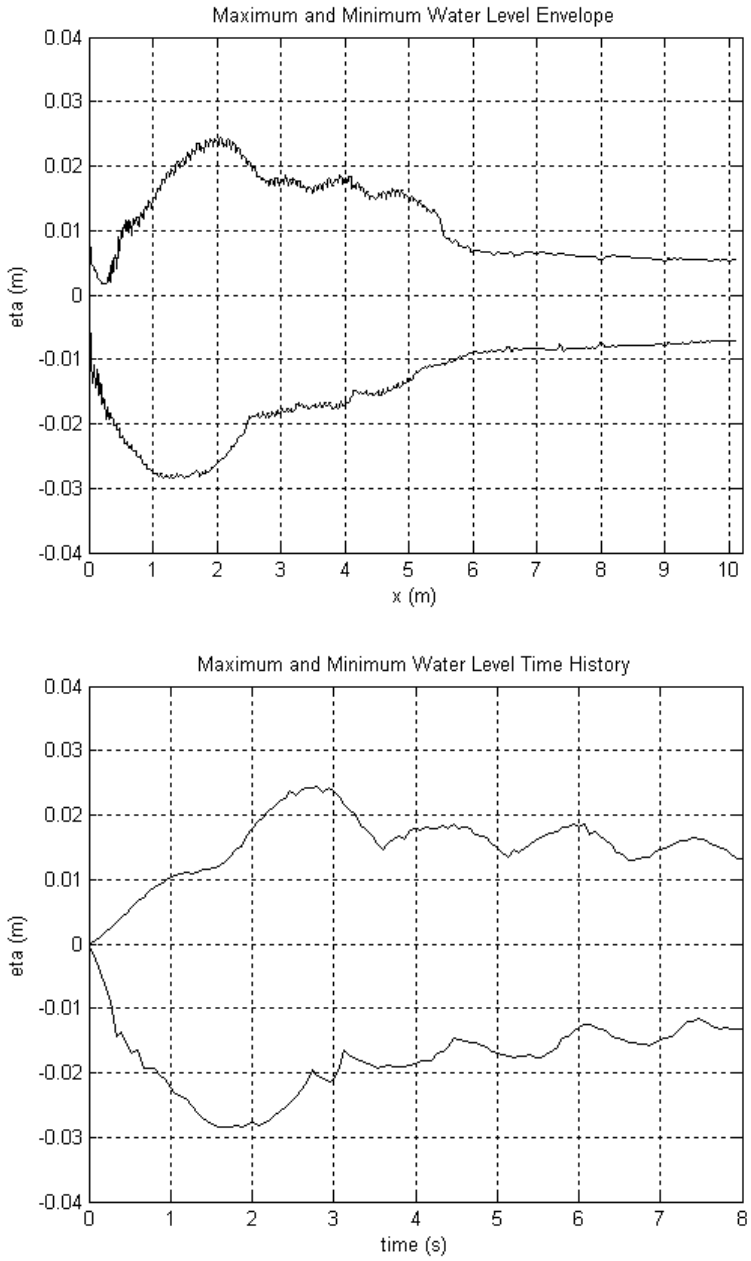

Figure C.58. Maximum and minimum water level envelope and time history for the SG2_IS5 configuration.

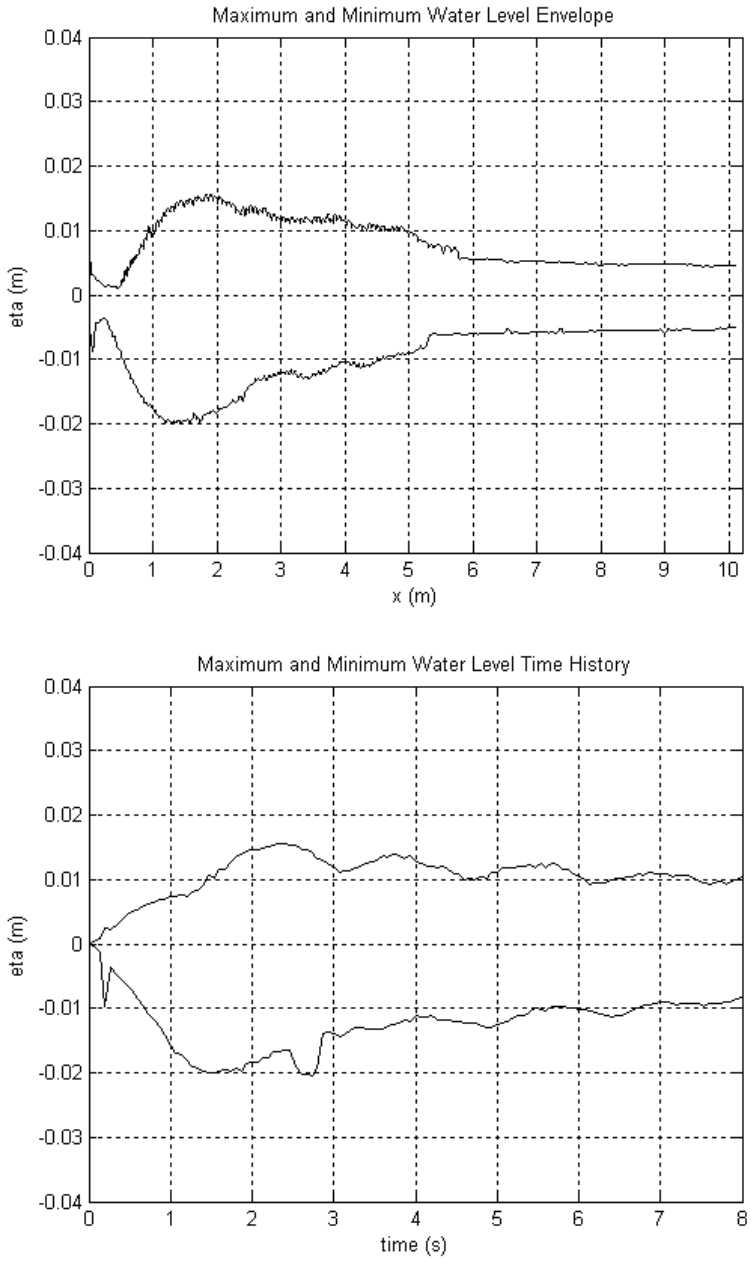

Figure C.59. Maximum and minimum water level envelope and time history for the SG2_IS4 configuration.

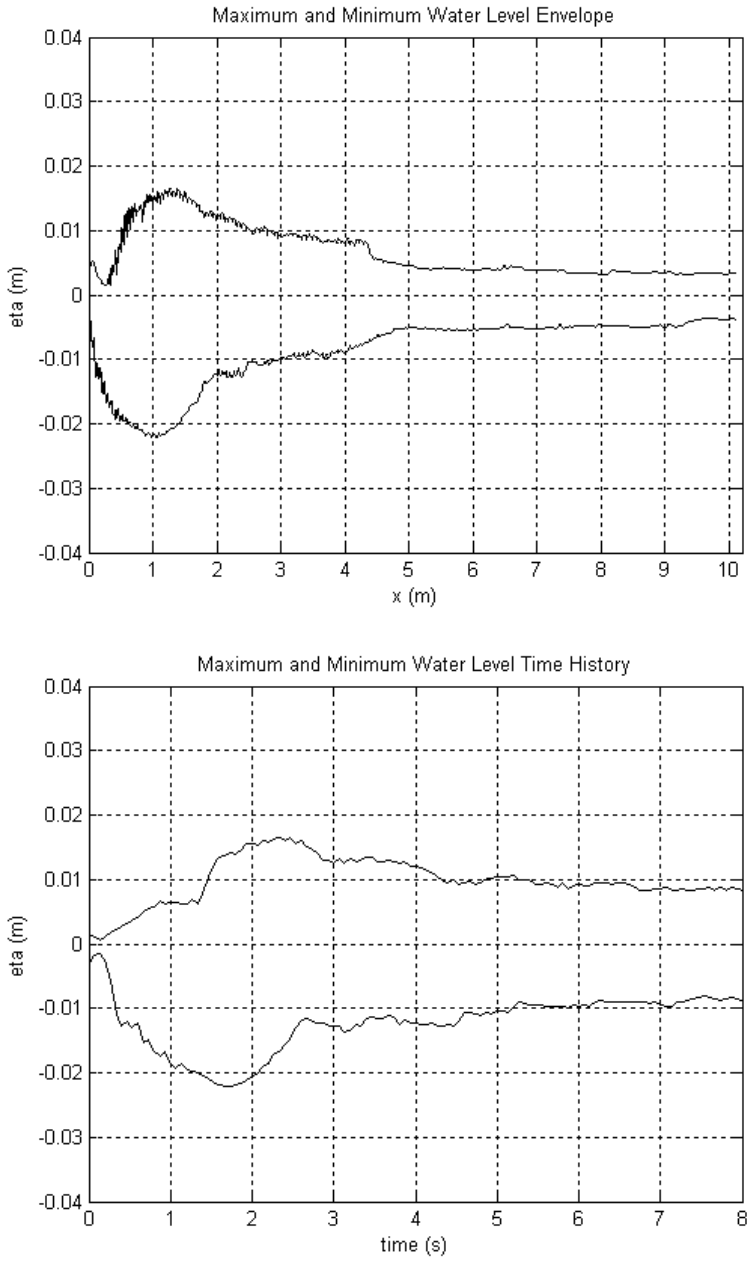

Figure C.60. Maximum and minimum water level envelope and time history for the SG1_IS5 configuration.

C.5 Crest and Trough Amplitude Time History

Plots of the first crest, first trough, and second crest amplitude time histories, for each of the fifteen specific gravity and initial submergence combinations, are presented in Figures C.61 to C.75.

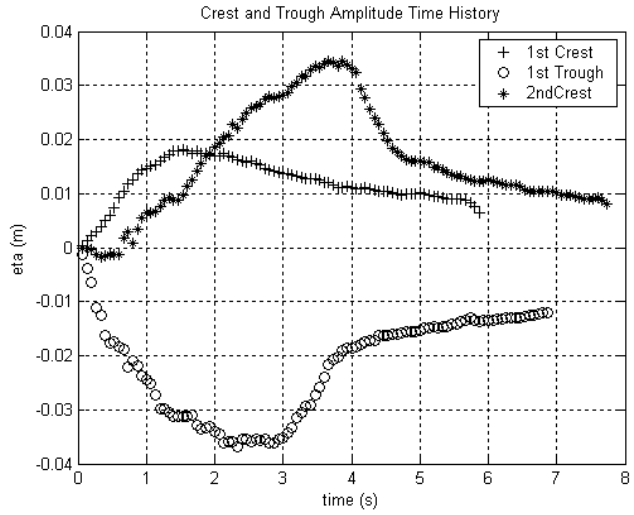

Figure C.61. First crest, first trough, and second crest amplitude time history for the SG5-IS5 test.

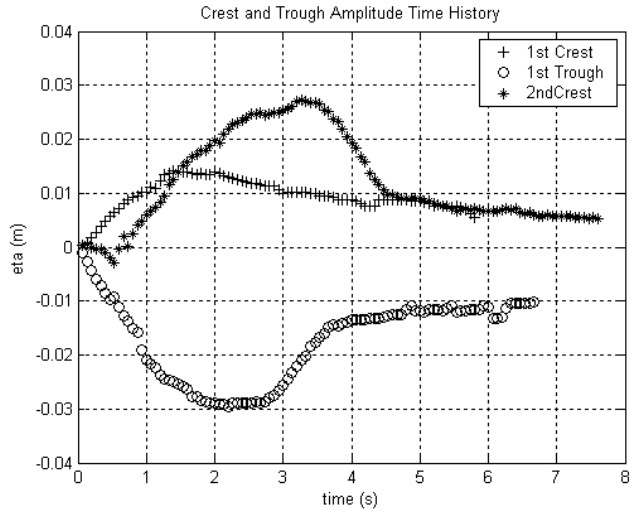

Figure C.62. First crest, first trough, and second crest amplitude time history for the SG5-IS4 test.

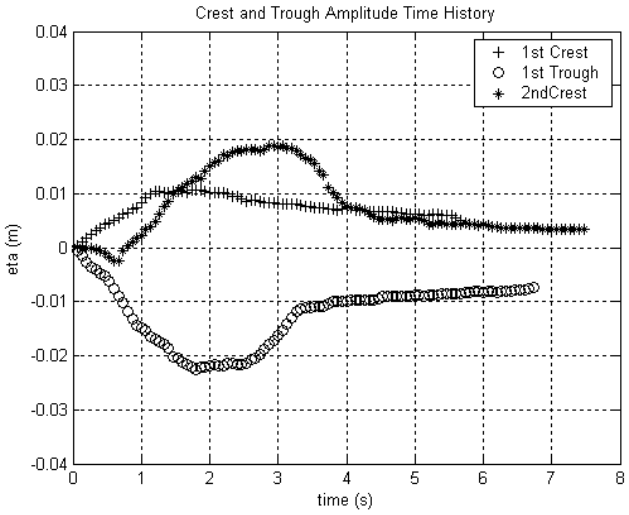

Figure C.63. First crest, first trough, and second crest amplitude time history for the SG5-IS3 test.

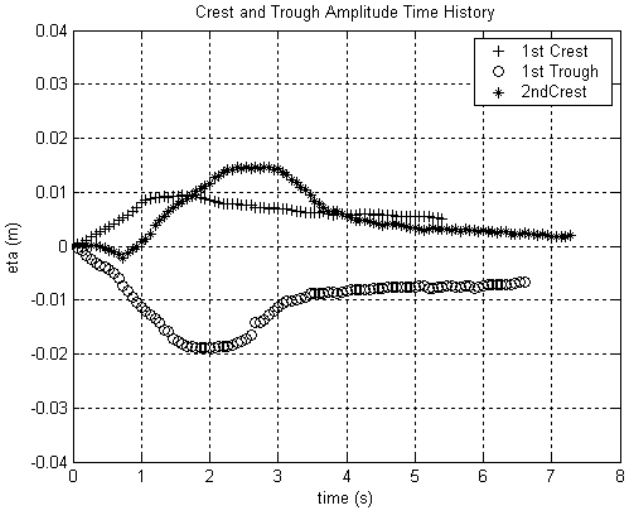

Figure C.64. First crest, first trough, and second crest amplitude time history for the SG5-IS2 test.

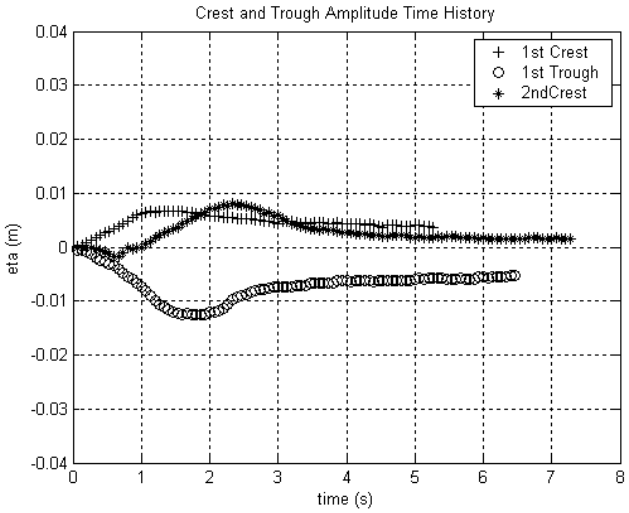

Figure C.65. First crest, first trough, and second crest amplitude time history for the SG5-IS1 test.

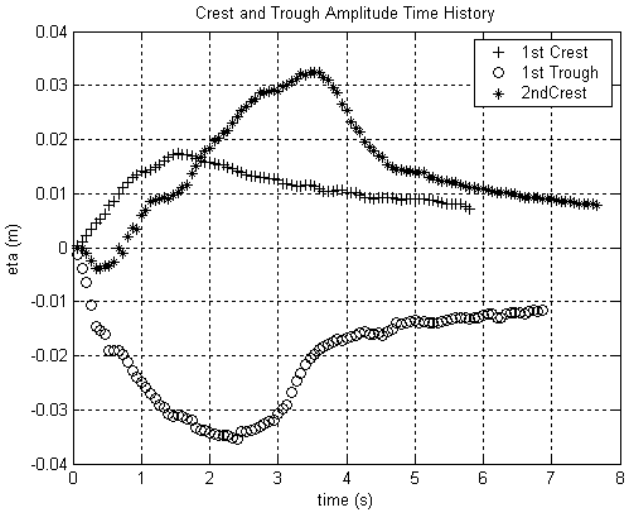

Figure C.66. First crest, first trough, and second crest amplitude time history for the SG4-IS5 test.

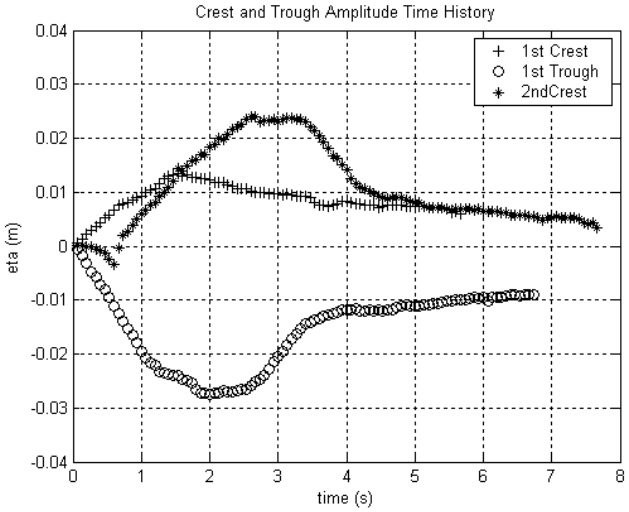

Figure C.67. First crest, first trough, and second crest amplitude time history for the SG4-IS4 test.

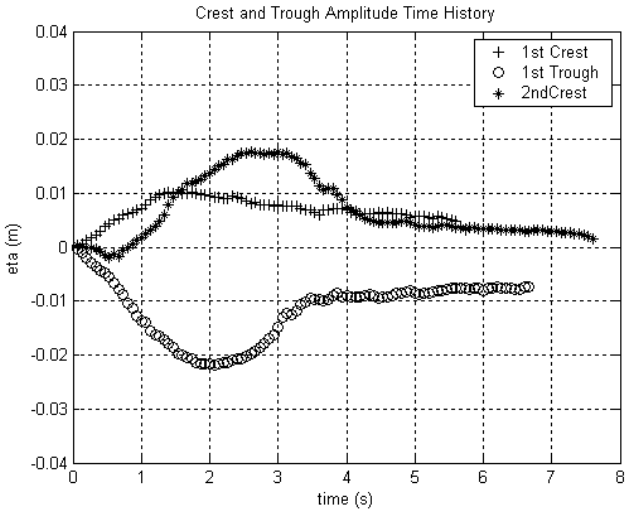

Figure C.68. First crest, first trough, and second crest amplitude time history for the SG4-IS3 test.

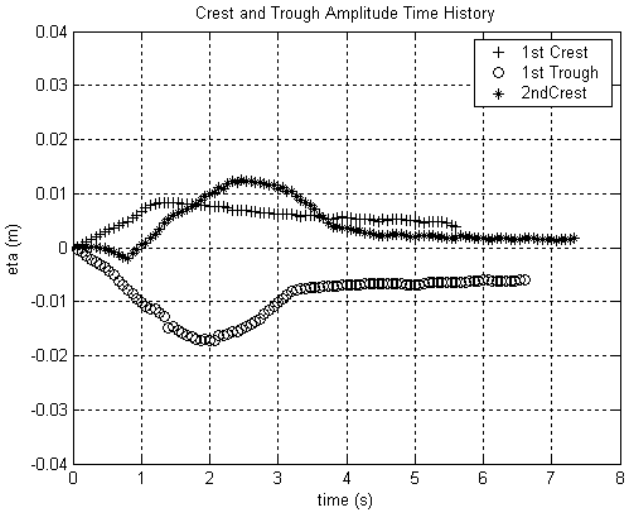

Figure C.69. First crest, first trough, and second crest amplitude time history for the SG4-IS2 test.

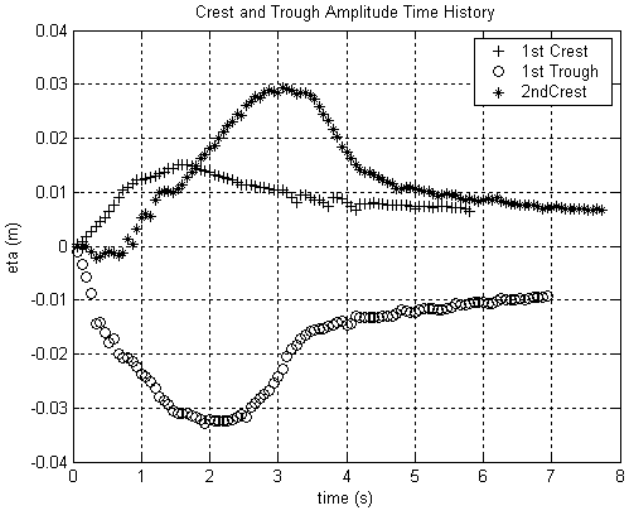

Figure C.70. First crest, first trough, and second crest amplitude time history for the SG3-IS5 test.

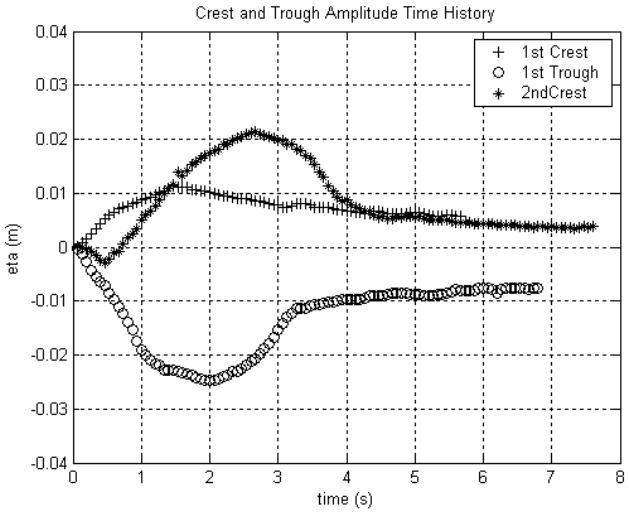

Figure C.71. First crest, first trough, and second crest amplitude time history for the SG3-IS4 test.

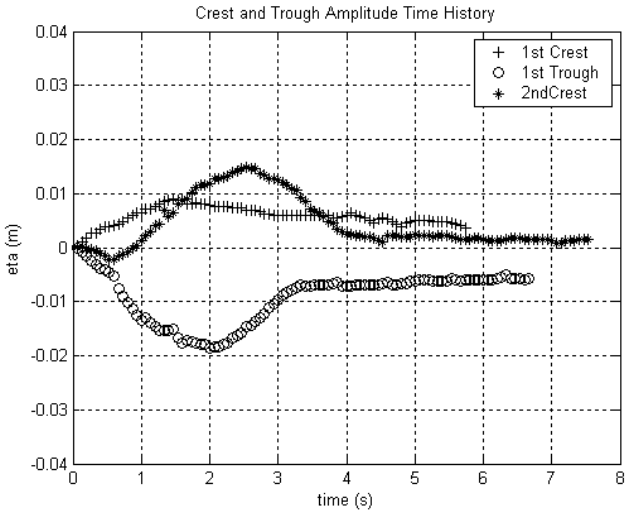

Figure C.72. First crest, first trough, and second crest amplitude time history for the SG3-IS3 test.

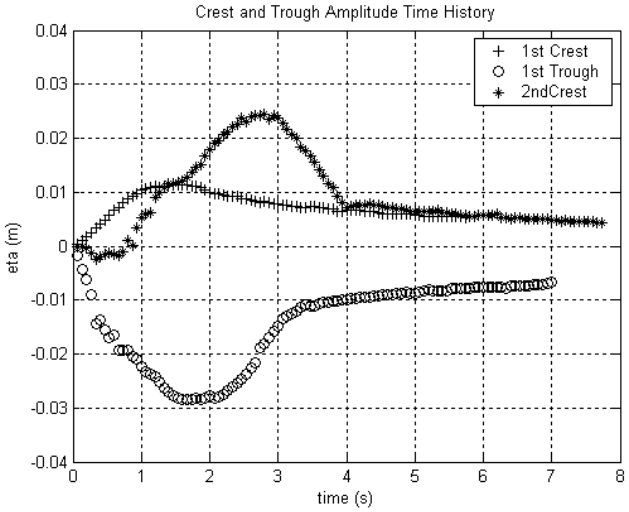

Figure C.73. First crest, first trough, and second crest amplitude time history for the SG2-IS5 test.

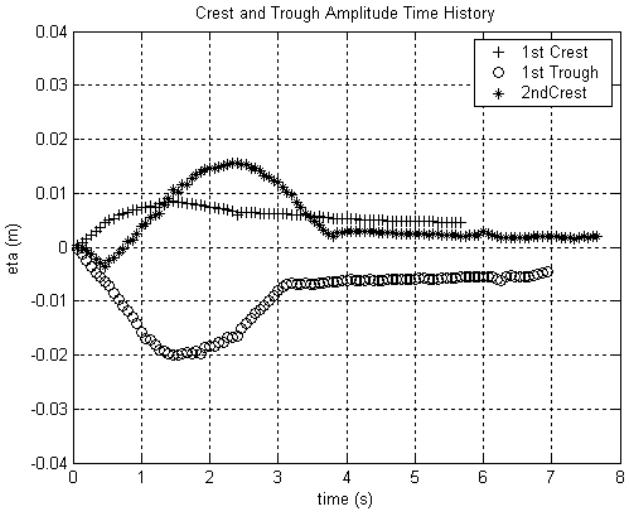

Figure C.74. First crest, first trough, and second crest amplitude time history for the SG2-IS4 test.

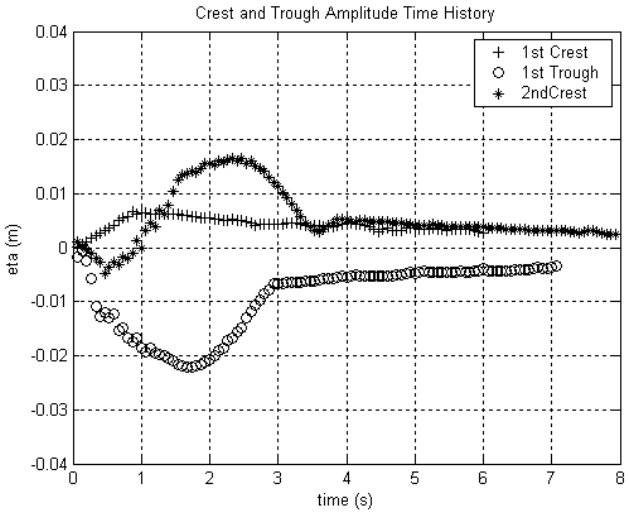

Figure C.75. First crest, first trough, and second crest amplitude time history for the SG1-IS5 test.

C.6 Crest and Trough Length Time History

Plots of the first crest and first trough length time histories, for each of the fifteen specific gravity and initial submergence combinations, are presented in Figures C.76 to C.90.

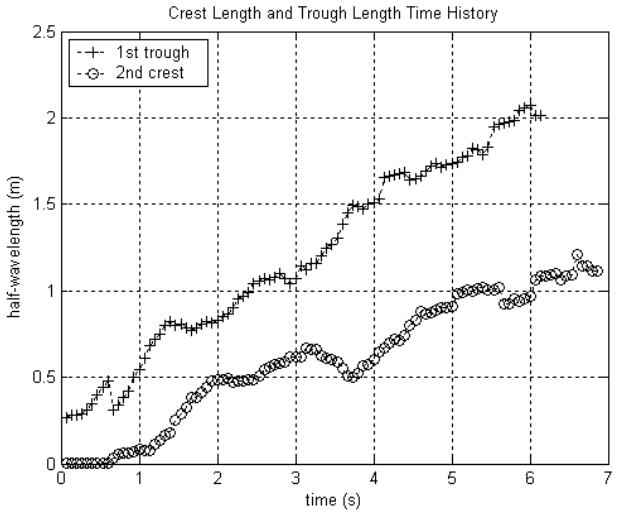

Figure C.76. First crest and first trough length time history for the SG5-IS5 test.

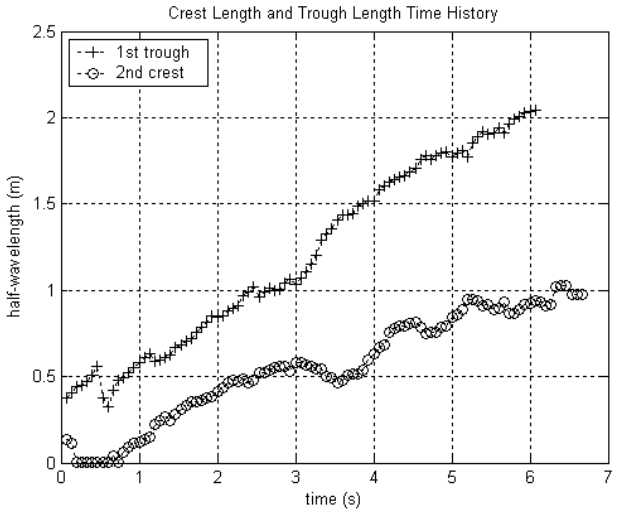

Figure C.77. First crest and first trough length time history for the SG5-IS4 test.

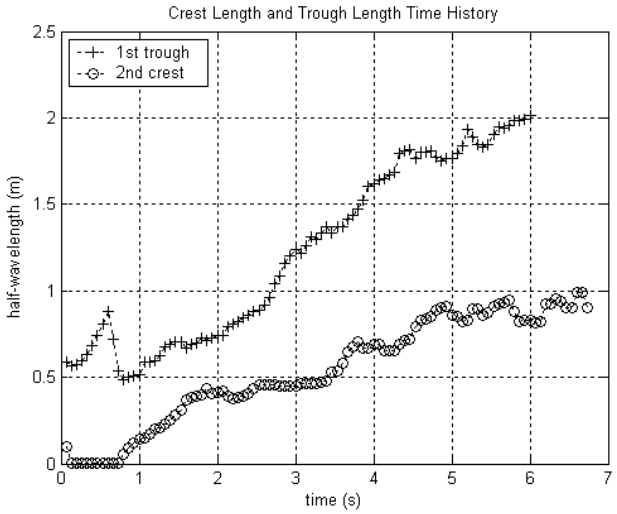

Figure C.78. First crest and first trough length time history for the SG5-IS3 test.

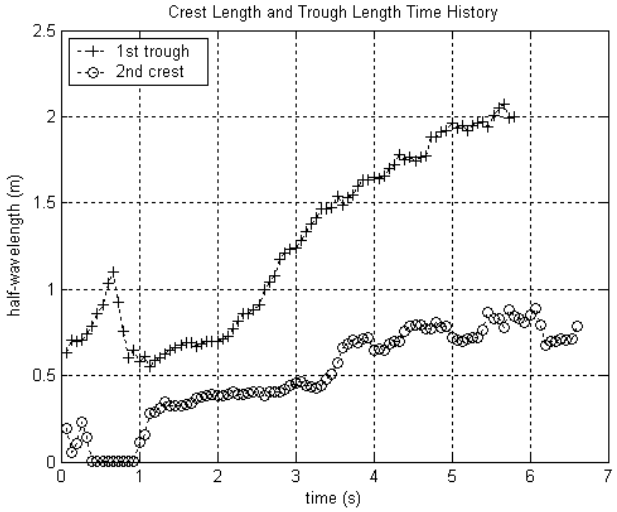

Figure C.79. First crest and first trough length time history for the SG5-IS2 test.

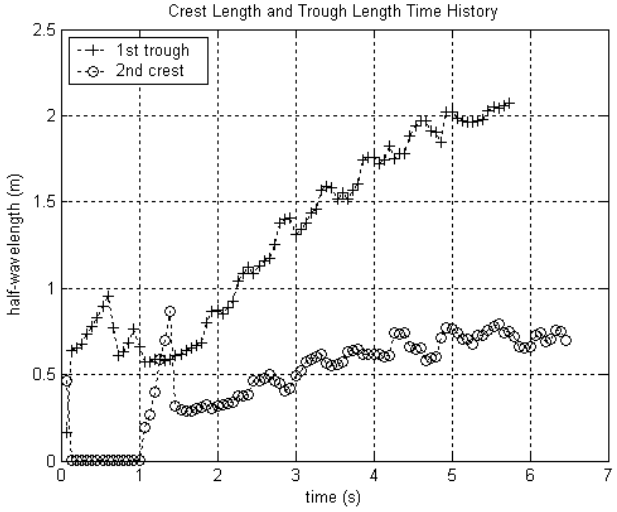

Figure C.80. First crest and first trough length time history for the SG5-IS1 test.

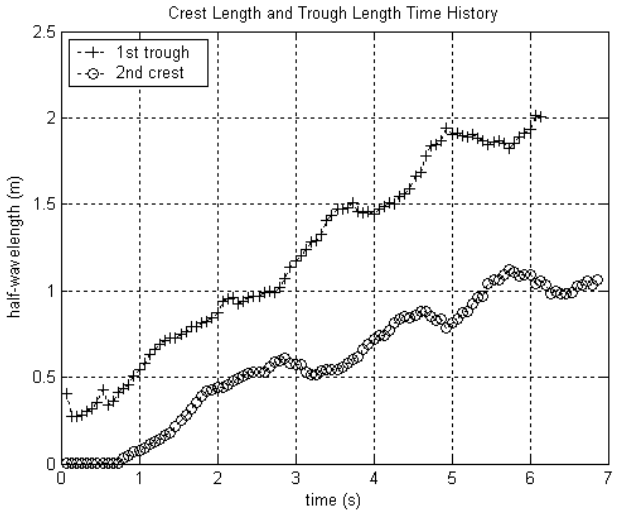

Figure C.81. First crest and first trough length time history for the SG4-IS5 test.

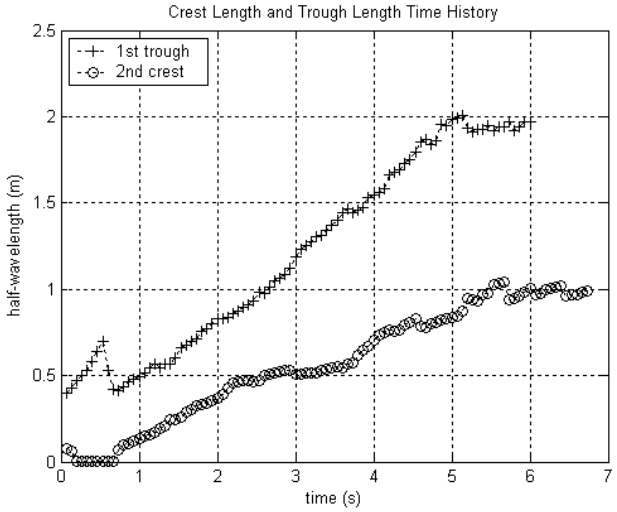

Figure C.82. First crest and first trough length time history for the SG4-IS4 test.

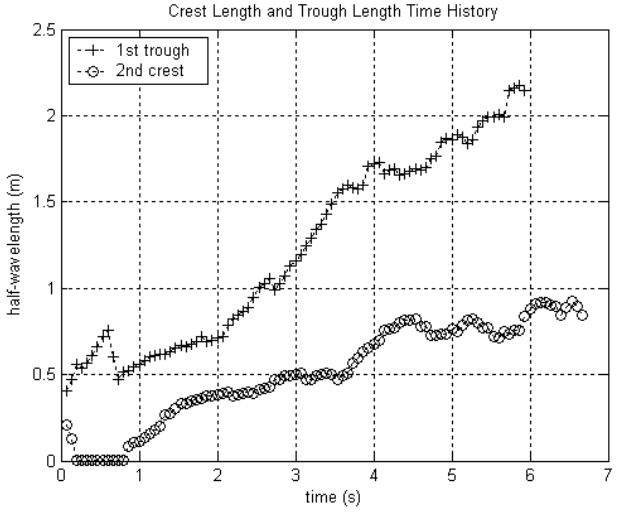

Figure C.83. First crest and first trough length time history for the SG4-IS3 test.

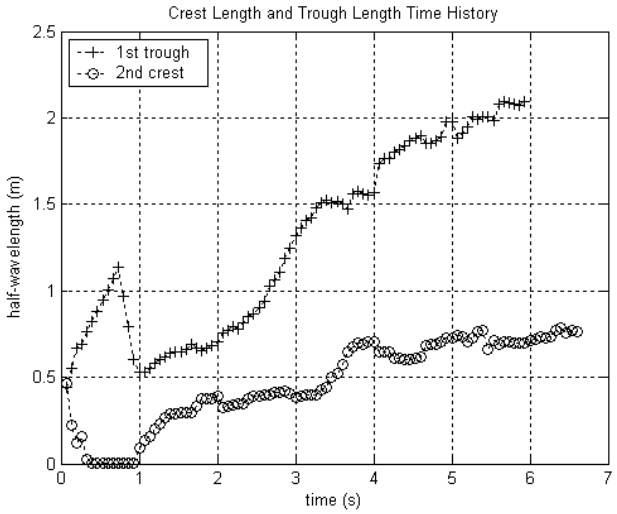

Figure C.84. First crest and first trough length time history for the SG4-IS2 test.

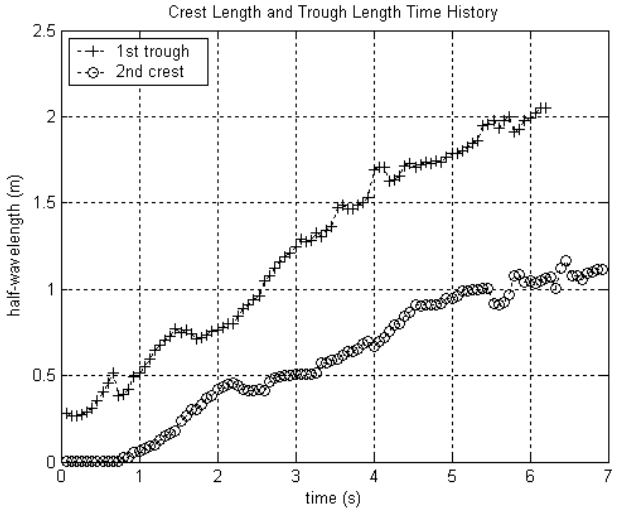

Figure C.85. First crest and first trough length time history for the SG3-IS5 test.

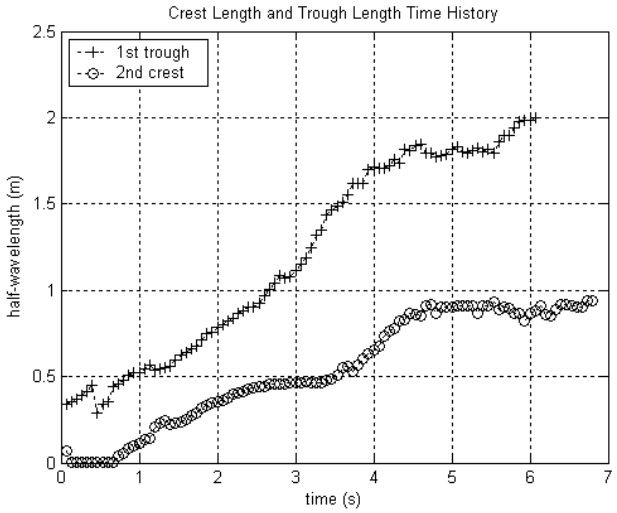

Figure C.86. First crest and first trough length time history for the SG3-IS4 test.

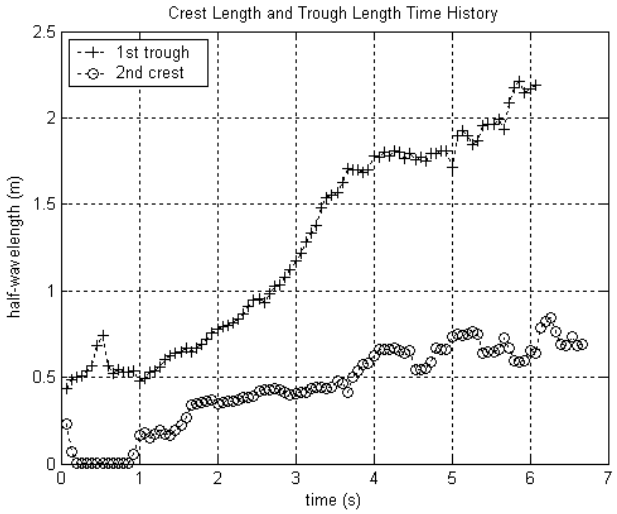

Figure C.87. First crest and first trough length time history for the SG3-IS3 test.

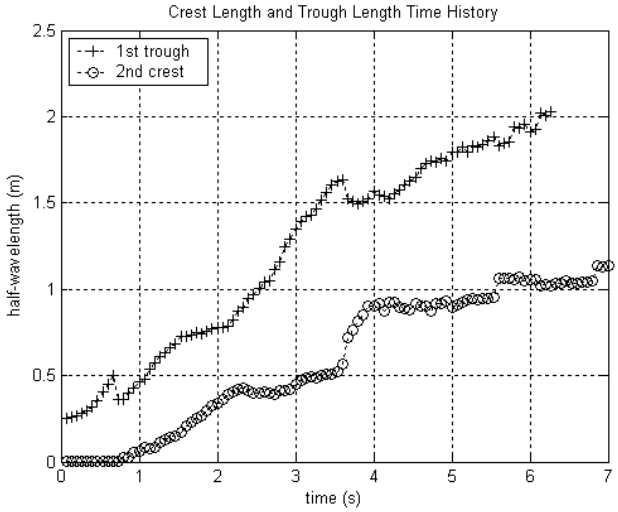

Figure C.88. First crest and first trough length time history for the SG2-IS5 test.

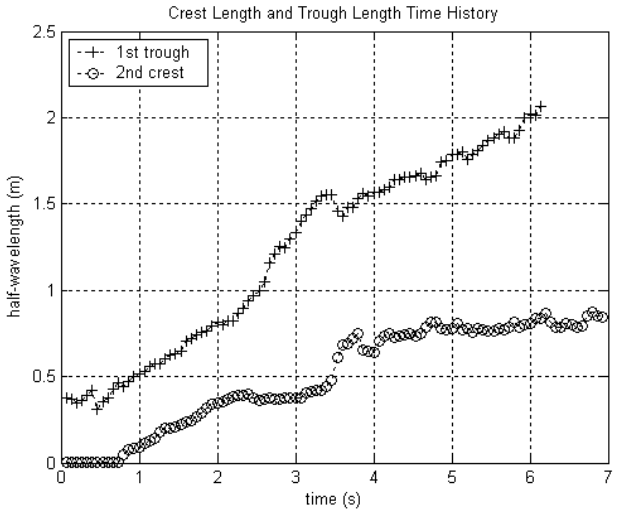

Figure C.89. First crest and first trough length time history for the SG2-IS4 test.

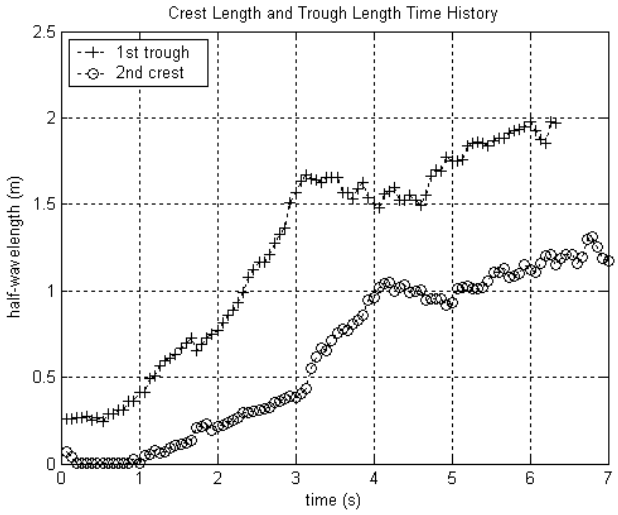

Figure C.90. First crest and first trough length time history for the SG1-IS5 test.

C.7 Crest and Trough Maximum Amplitude

The maximum non-dimensional amplitudes of the first crest, first trough, and second crest, for each specific gravity and initial submergence combination, are presented in Figure C.91

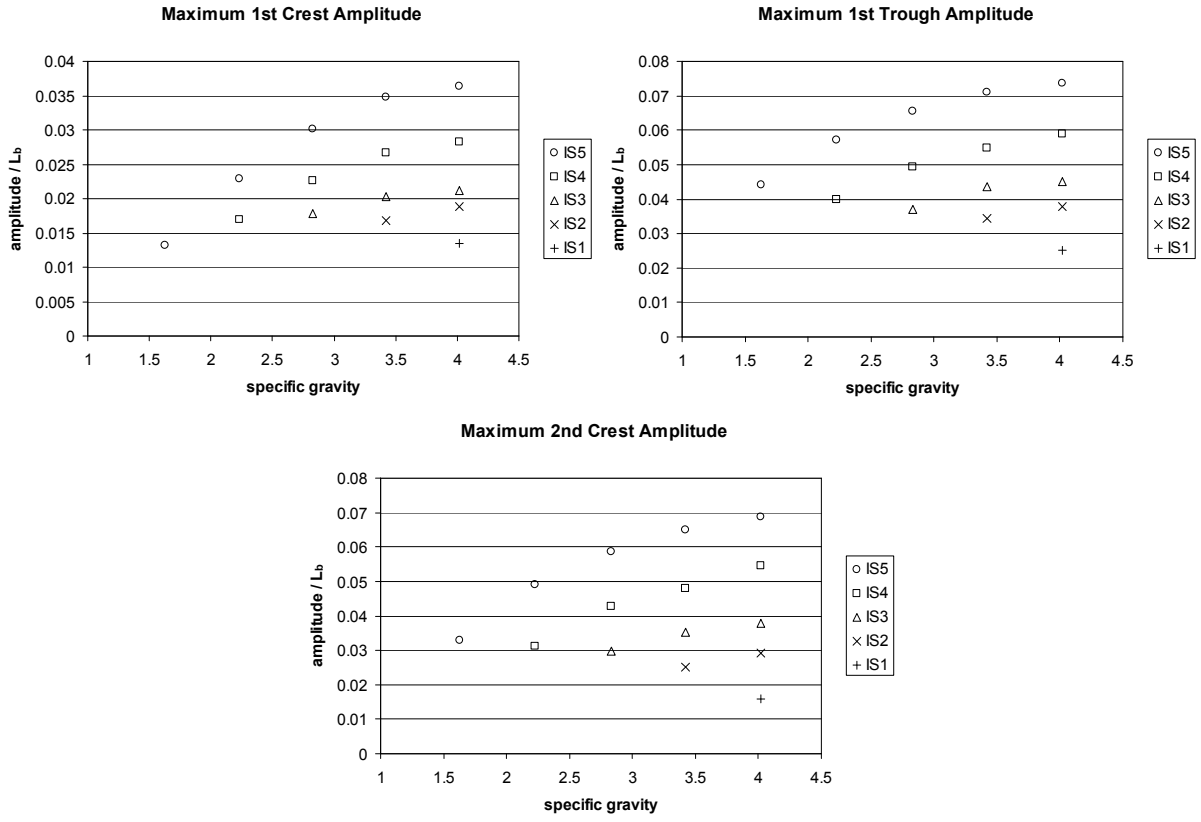

Figure C.91. Maximum non-dimensional amplitude of first crest, first trough, and second crest, for various specific gravities and initial submergences.

C.8 Magnitude, Position, and Time of Maximum Amplitude

Figure C.92 presents data to indicate the non-dimensional downstream position at which the maximum crest and trough amplitude occurred. The maximum amplitudes occurred further downstream for landslides with heavier specific gravities and shallower initial submergences.

The non-dimensional time at which the overall maximum crest and trough amplitude occurred, for the fifteen combinations, are presented in Figure C.93. The maximum amplitudes tended to occur slightly later for landslides with heavier specific gravities and shallower initial submergences.

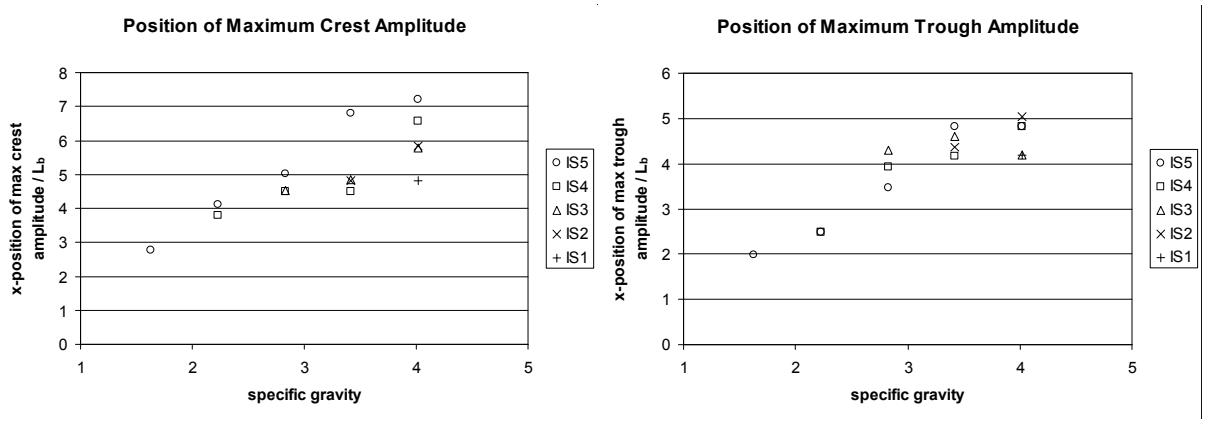

Figure C.92. Horizontal position of maximum crest and trough amplitude for various specific gravities and initial submergences.

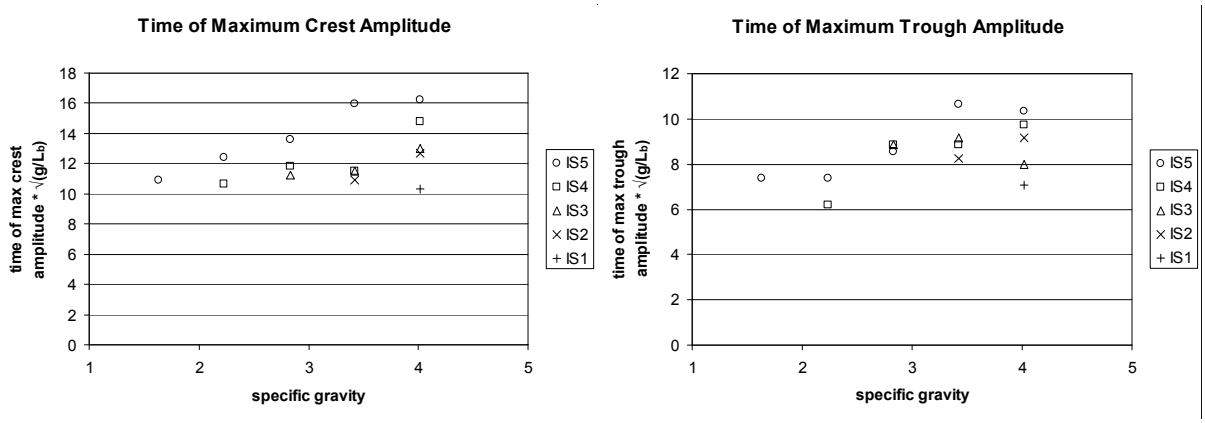

Figure C.93. Time of occurrence of maximum crest and trough amplitude for various specific gravities and initial submergences.

Appendix D: Wave Run-up

Plots of the wave run-up time histories for each of the fifteen specific gravity and initial submergence combinations are presented in Figures D.1 to D.15.

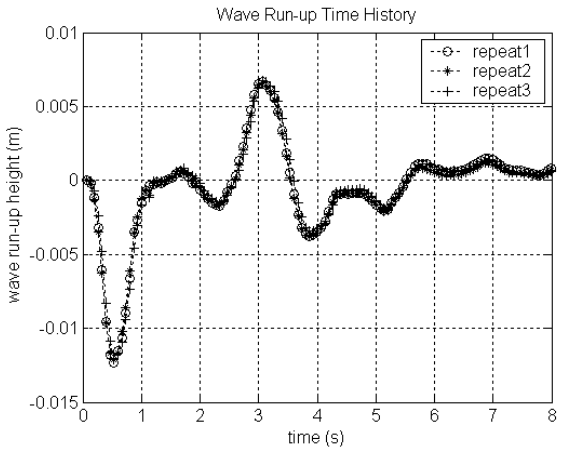

Figure D.1. Wave run-up time history for three repeats of the SG5_IS5 configuration.

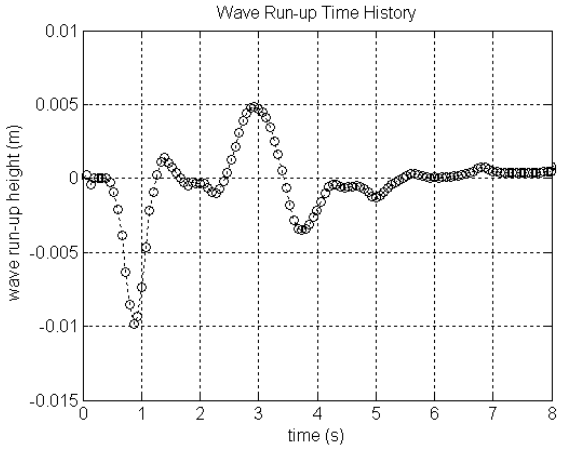

Figure D.2. Wave run-up time history for the SG5_IS4 configuration.

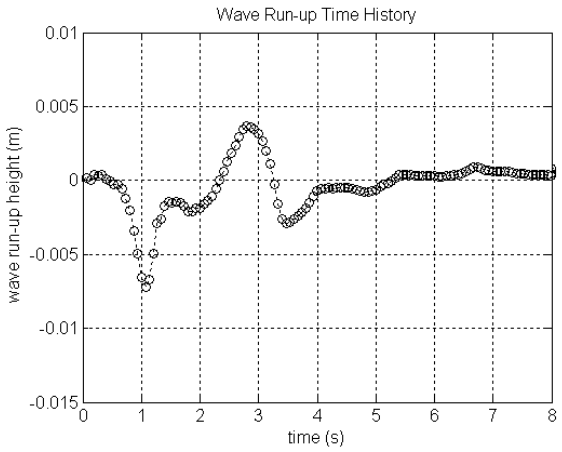

Figure D.3. Wave run-up time history for the SG5_IS3 configuration.

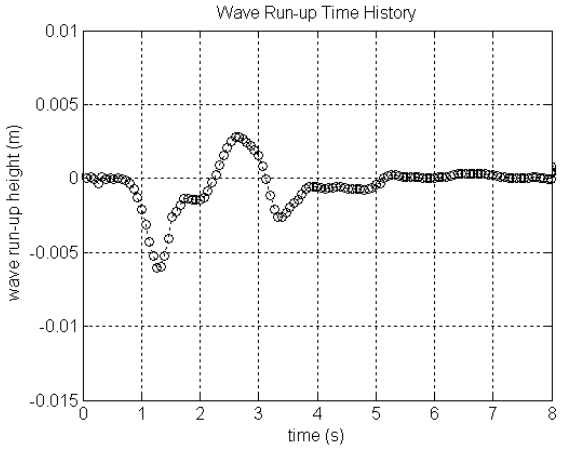

Figure D.4. Wave run-up time history for the SG5_IS2 configuration.

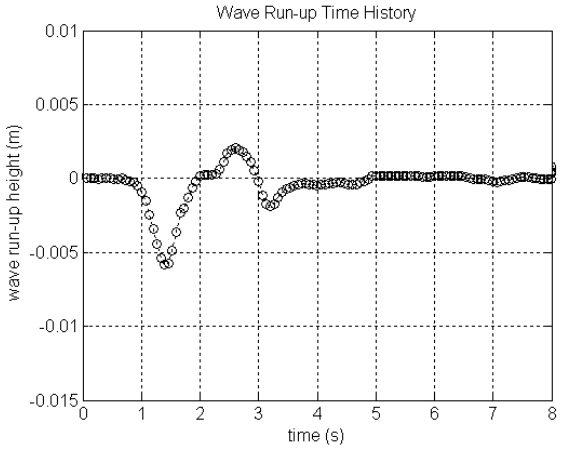

Figure D.5. Wave run-up time history for the SG5_IS1 configuration.

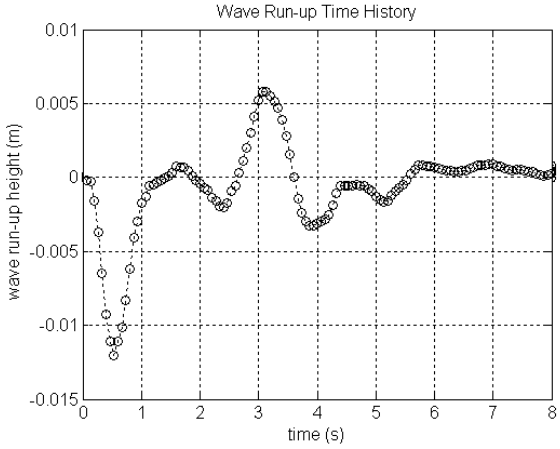

Figure D.6. Wave run-up time history for the SG4_IS5 configuration.

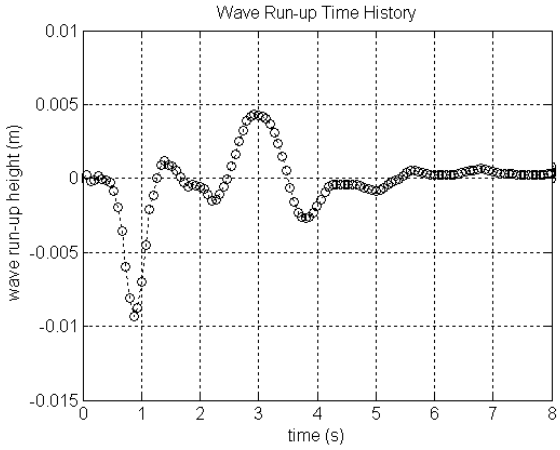

Figure D.7. Wave run-up time history for the SG4_IS4 configuration.

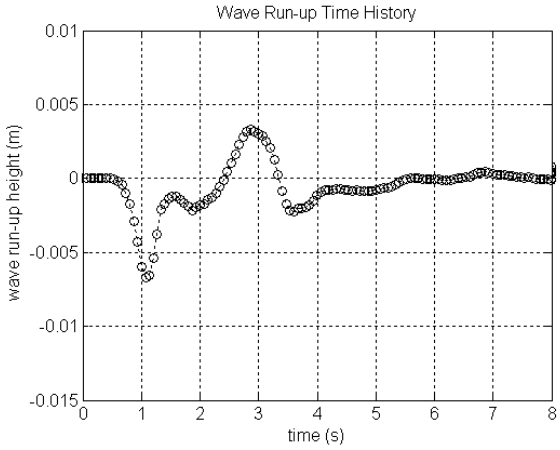

Figure D.8. Wave run-up time history for the SG4_IS3 configuration.

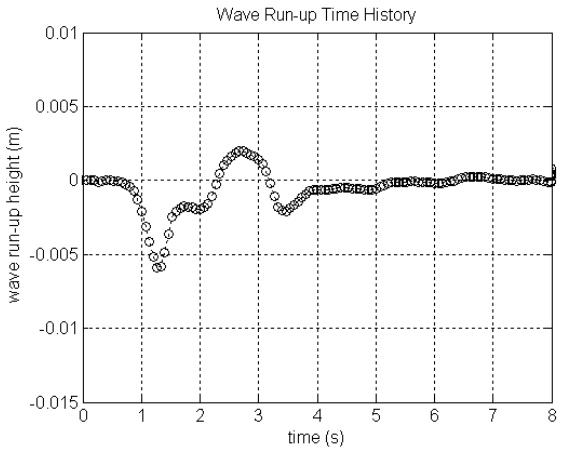

Figure D.9. Wave run-up time history for the SG4_IS2 configuration.

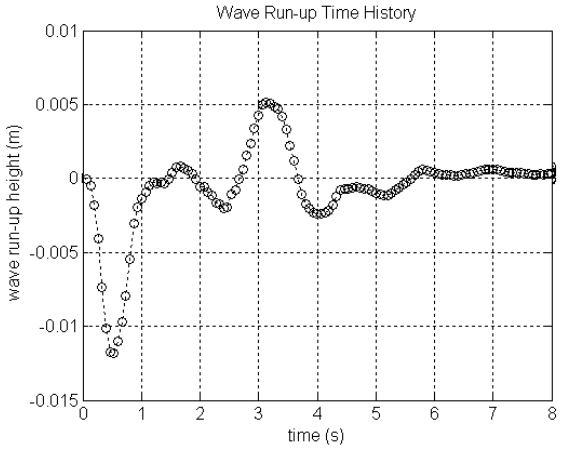

Figure D.10. Wave run-up time history for the SG3_IS5 configuration.

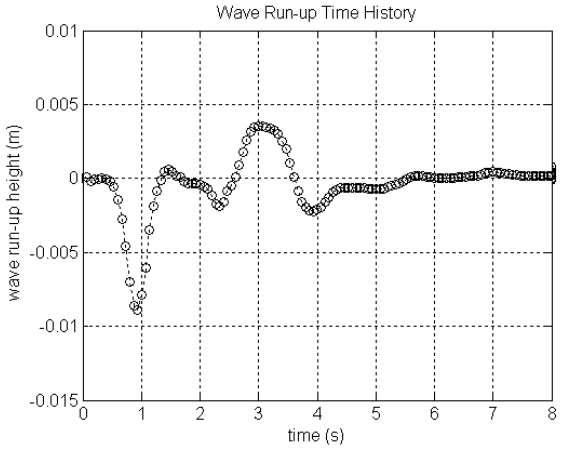

Figure D.11. Wave run-up time history for the SG3_IS4 configuration.

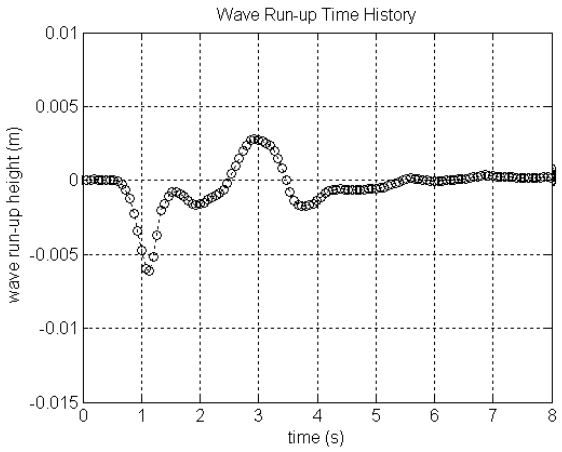

Figure D.12. Wave run-up time history for the SG3_IS3 configuration.

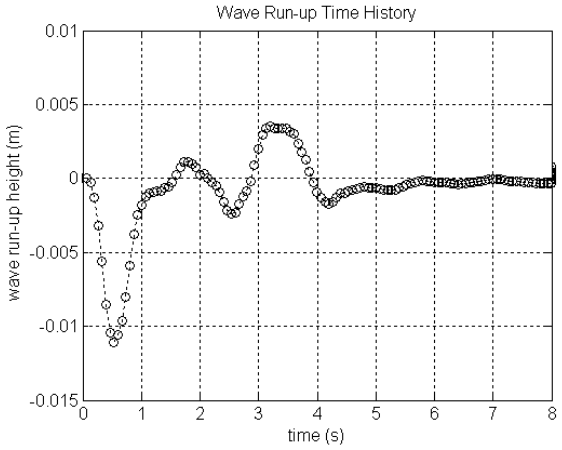

Figure D.13. Wave run-up time history for the SG2_IS5 configuration.

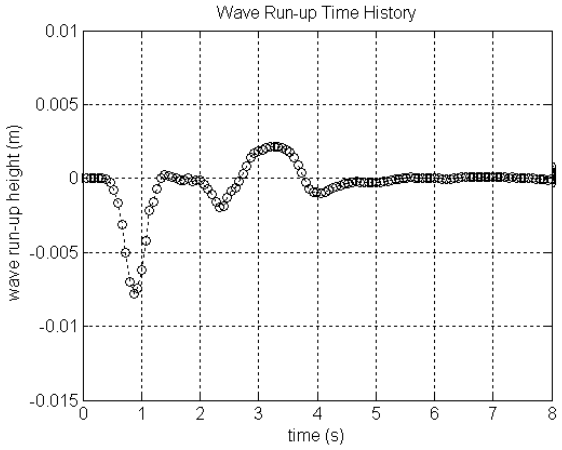

Figure D.14. Wave run-up time history for the SG2_IS4 configuration.

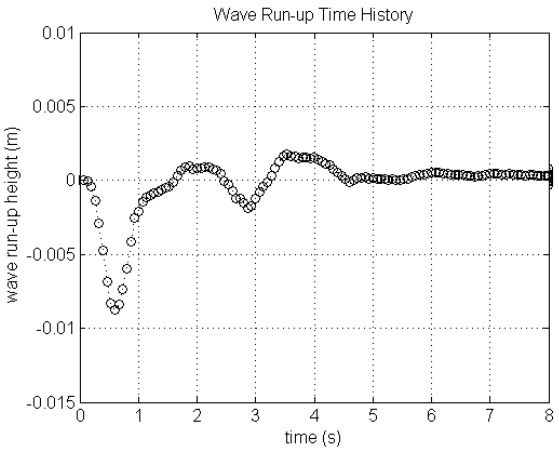

Figure D.15. Wave run-up time history for the SG1_IS5 configuration.

Appendix E: Energy

Plots of the wave potential energy and landslide potential and kinetic energy time histories, for each of the fifteen specific gravity and initial submergence combinations, are presented in Figures E.1 to E.15.

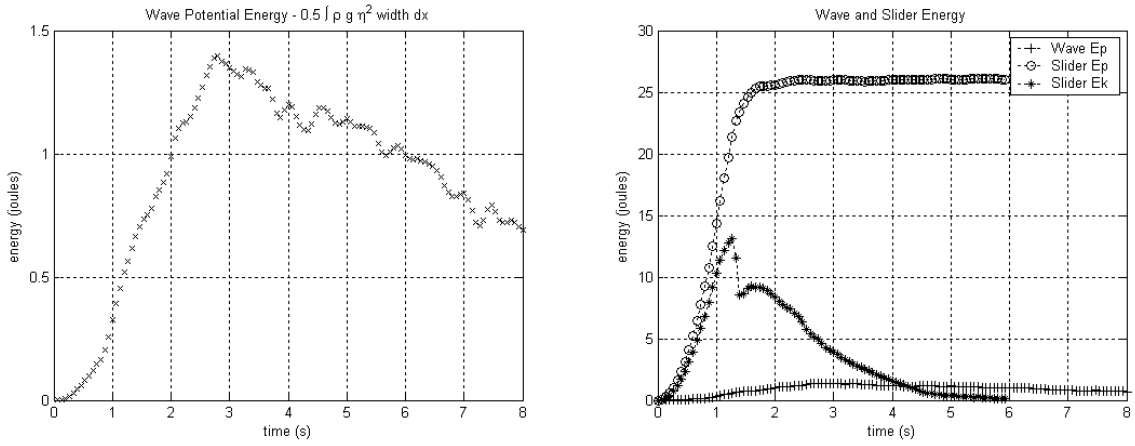

Figure E.1. Wave potential energy and landslide potential and kinetic energy time history for the SG5_IS5 configuration.

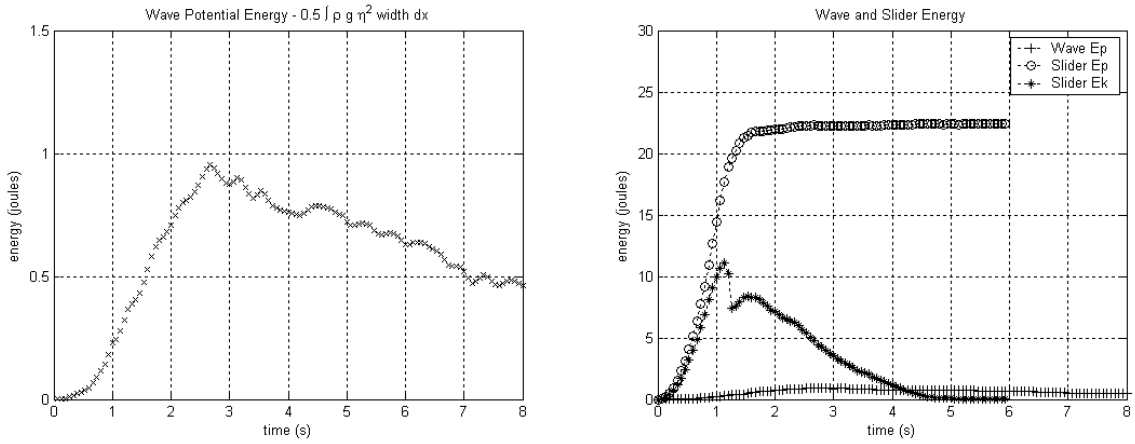

Figure E.2. Wave potential energy and landslide potential and kinetic energy time history for the SG5_IS4 configuration.

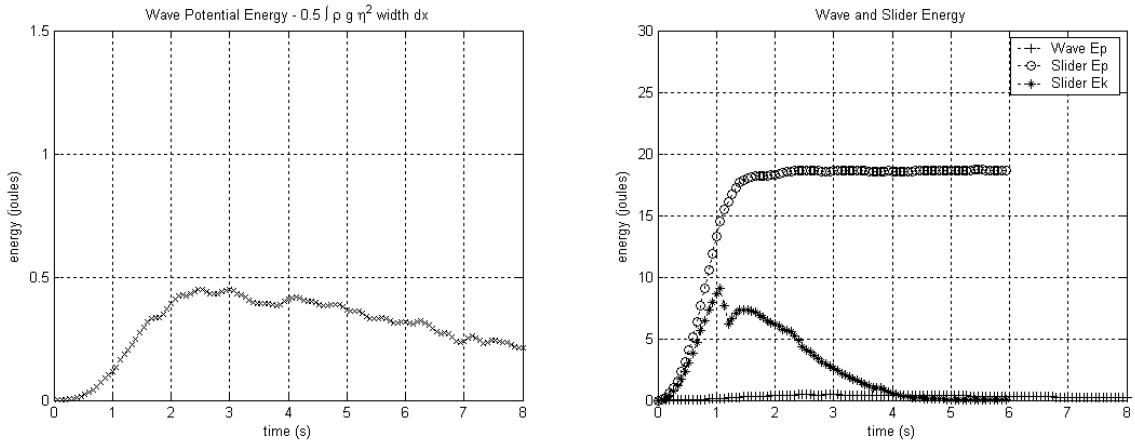

Figure E.3. Wave potential energy and landslide potential and kinetic energy time history for the SG5_IS3 configuration.

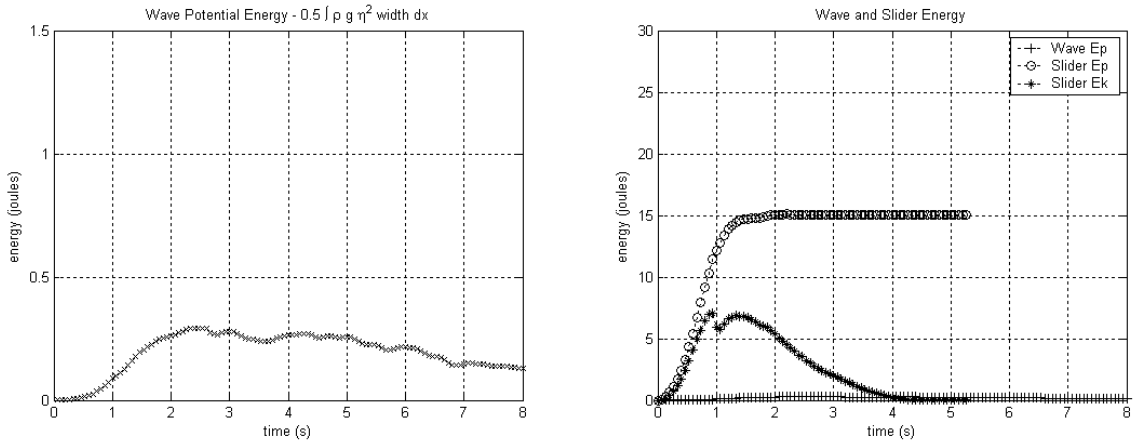

Figure E.4. Wave potential energy and landslide potential and kinetic energy time history for the SG5_IS2 configuration.

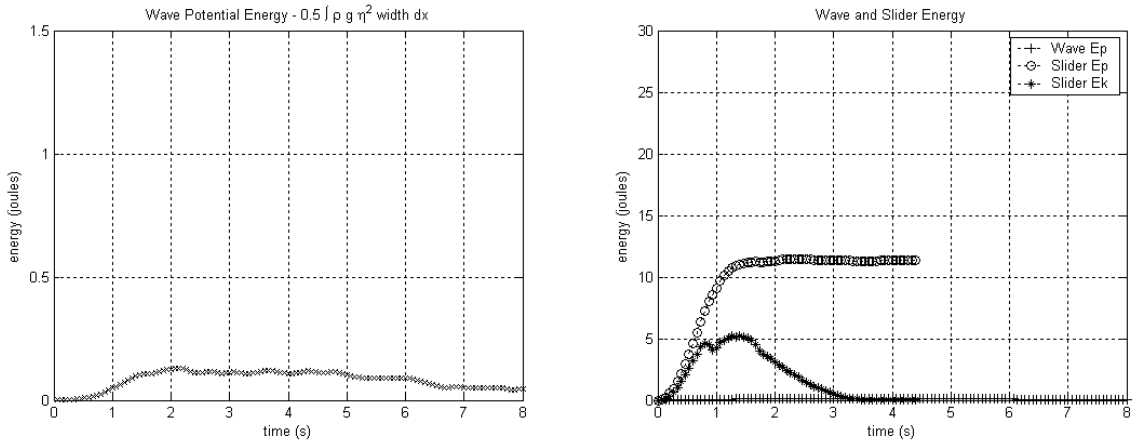

Figure E.5. Wave potential energy and landslide potential and kinetic energy time history for the SG5_IS1 configuration.

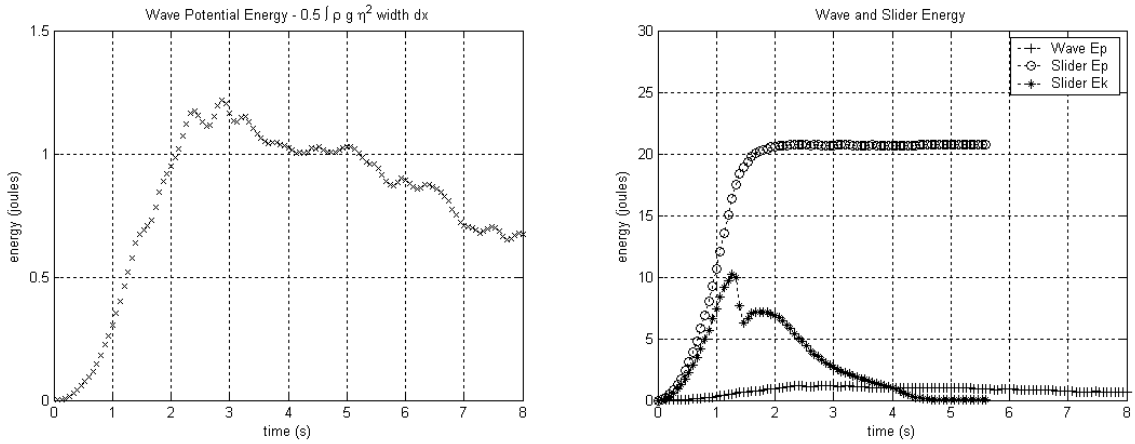

Figure E.6. Wave potential energy and landslide potential and kinetic energy time history for the SG4_IS5 configuration.

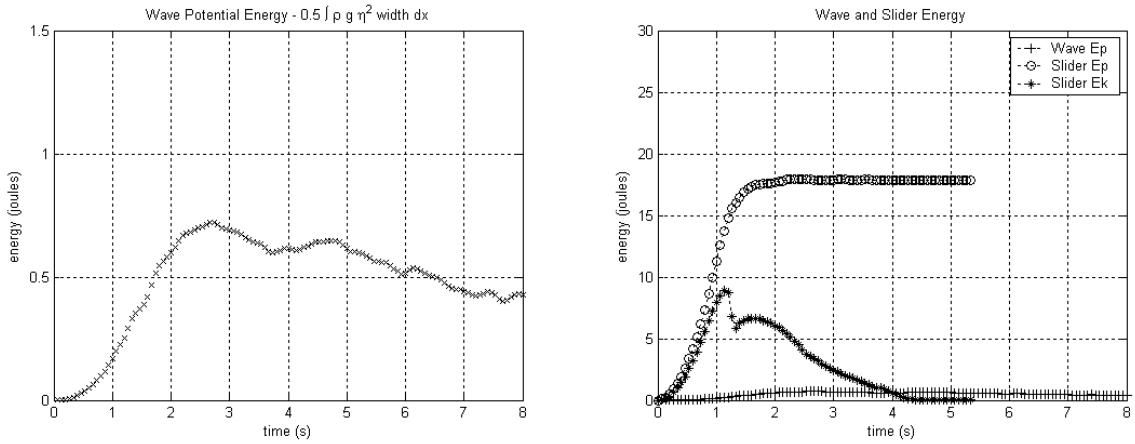

Figure E.7. Wave potential energy and landslide potential and kinetic energy time history for the SG4_IS4 configuration.

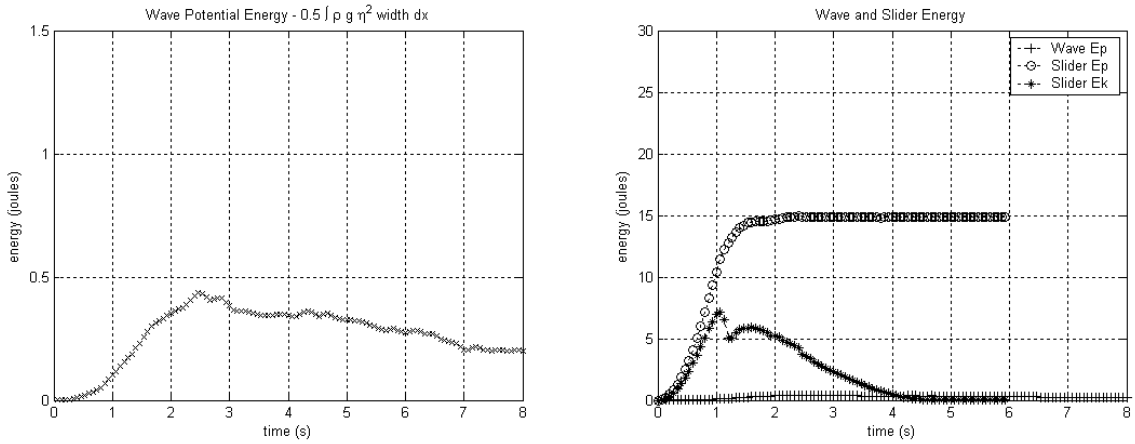

Figure E.8. Wave potential energy and landslide potential and kinetic energy time history for the SG4_IS3 configuration.

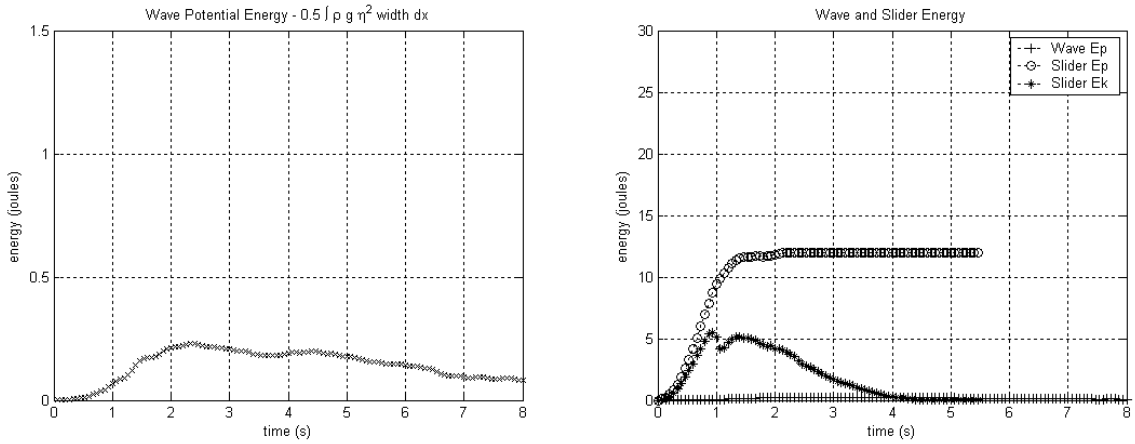

Figure E.9. Wave potential energy and landslide potential and kinetic energy time history for the SG4_IS2 configuration.

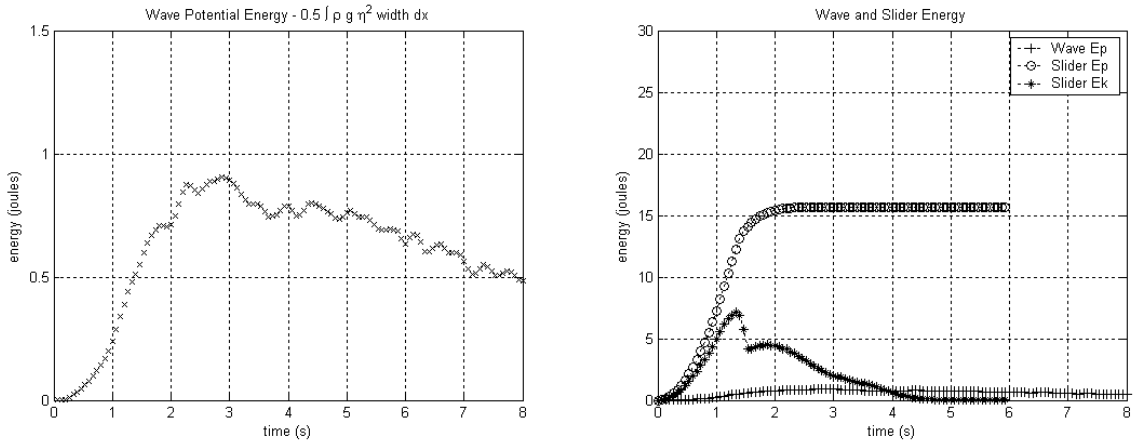

Figure E.10. Wave potential energy and landslide potential and kinetic energy time history for the SG3_IS5 configuration.

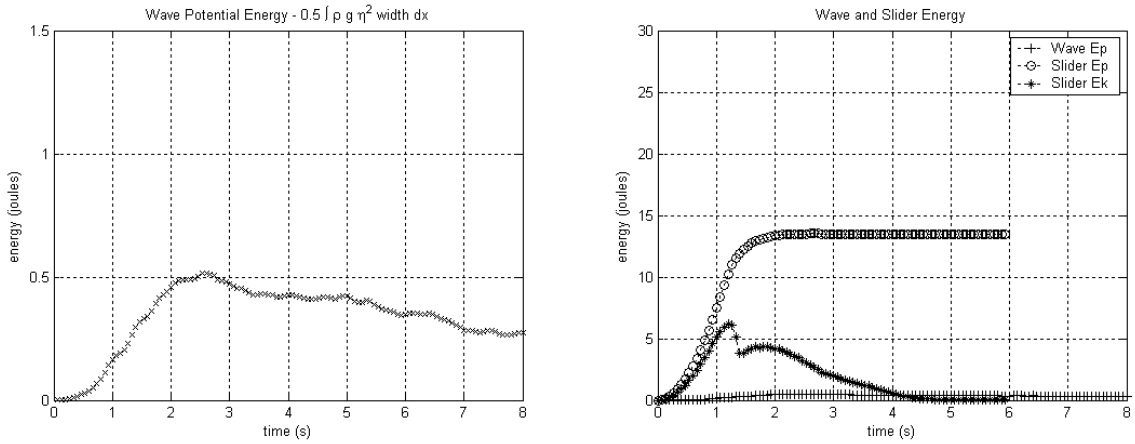

Figure E.11. Wave potential energy and landslide potential and kinetic energy time history for the SG3_IS4 configuration.

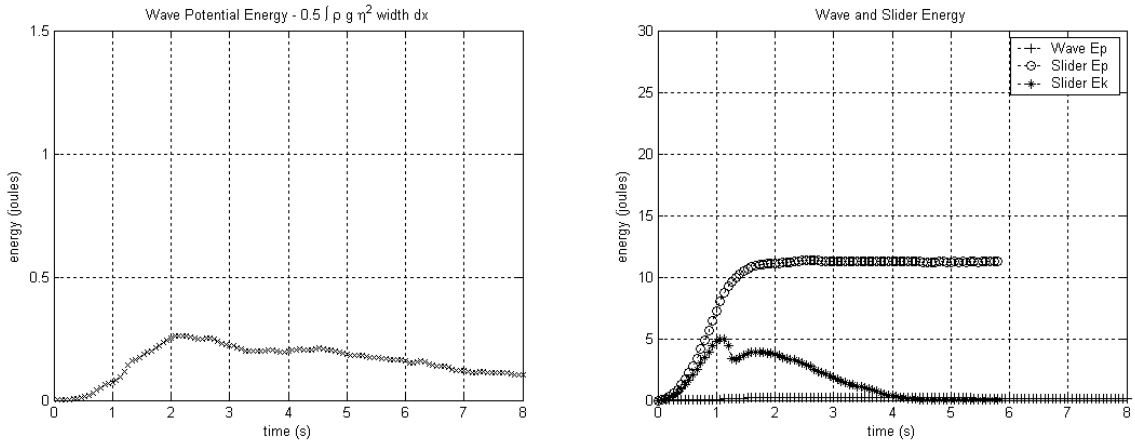

Figure E.12. Wave potential energy and landslide potential and kinetic energy time history for the SG3_IS3 configuration.

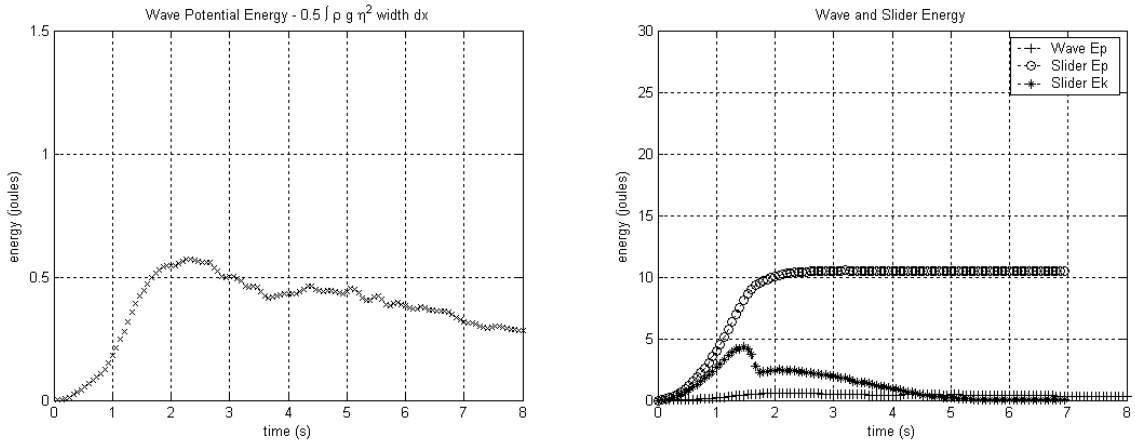

Figure E.13. Wave potential energy and landslide potential and kinetic energy time history for the SG2_IS5 configuration.

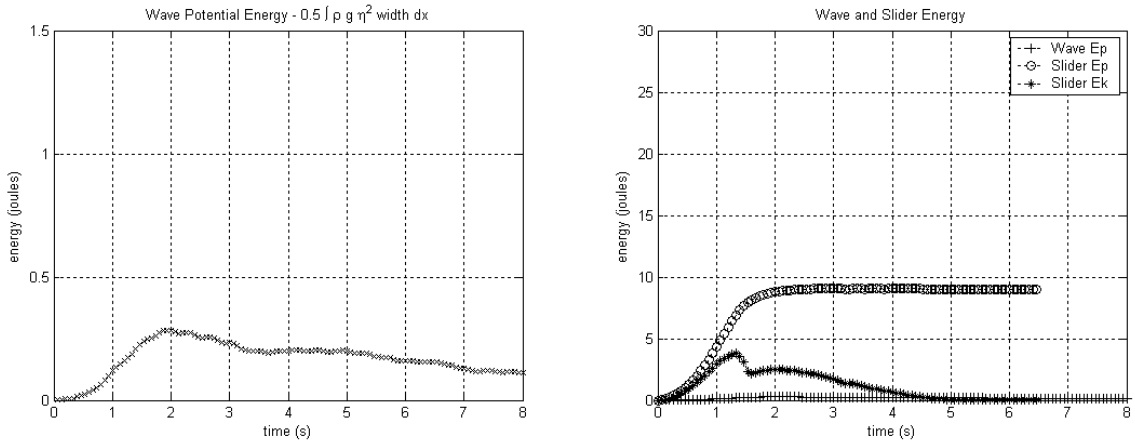

Figure E.14. Wave potential energy and landslide potential and kinetic energy time history for the SG2_IS4 configuration.

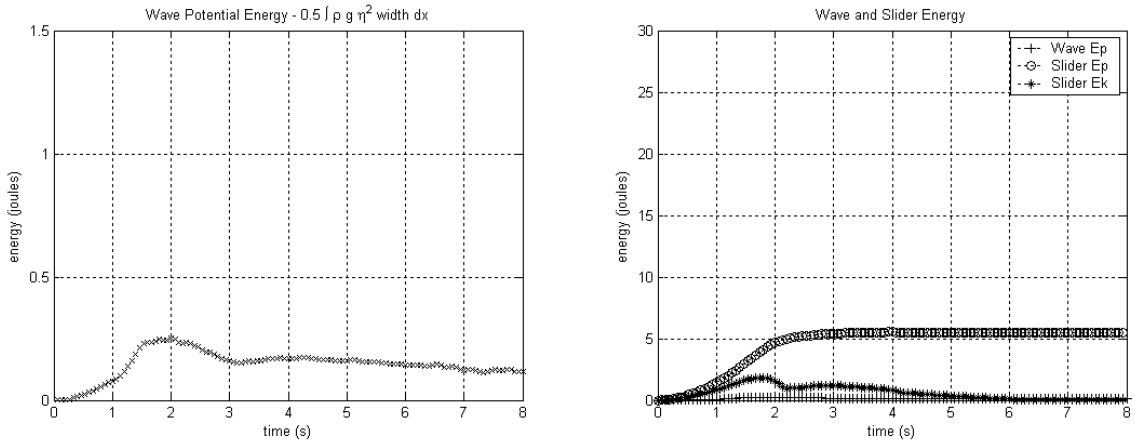

Figure E.15. Wave potential energy and landslide potential and kinetic energy time history for the SG1_IS5 configuration.

Appendix F: Initial Conditions of the Spectral Model Solution

The derivation of the initial conditions given in Equations 6.40 and 6.41 is presented here. The initial conditions of the partial differential equation given in Equation 6.3 are stated in Equations 6.7 and 6.8. Equations 6.8 and 6.19, and linear independence of the $e^{i(kx-\omega t)}$ modes results in

$$c(k,0)=0 \quad for\ all\ k \tag{A.1}$$

The linear independence of Equations 6.7 and 6.26 gives

$$a(k,0)\cosh k\tau(y+1)-\frac{\rho\tau}{k}p(k)e^{-k\tau(y+1)}e^{-ikx_0(0)}\left[\frac{dh_b}{dt}(0)\frac{1}{ik}-h_b(0)\frac{dx_0}{dt}(0)\right]=0 \tag{A.2}$$

Equation A.2 still includes functions of y. However, as the functions of y multiplying the two terms are different and the equality in Equation A.2 can only hold if the other factors are both zero. Therefore

$$a(k,0)=0 \quad for\ all\ k \tag{A.3}$$

Also

$$\frac{dh_b}{dt}(0)=0 \tag{6.42}$$

and

$$\frac{dx_0}{dt}(0)=0 \tag{6.43}$$

Equations 6.42 and 6.43 essentially state that at $t = 0$, the slider cannot be already moving and its size cannot be decaying. Both the acceleration and decay models, presented in Section 6.2.5 and 6.2.6 respectively, satisfy these conditions.

The boundary condition given in Equation 6.13 with $t = 0$ becomes

$$\begin{aligned}\tau^2\left(\frac{\partial c}{\partial t}(k,0)-i\omega c(k,0)/\lambda\right)&\\ =k\tau a(k,0)\sin(k\tau)+\rho\tau^2 p(k)e^{-k\tau}e^{-ikx_0(0)}&\left[\frac{dh_b}{dt}(0)\frac{1}{ik}-h_b(0)\frac{dx_0(0)}{dt}\right]\end{aligned} \tag{A.6}$$

Substituting Equations A.1, A.3, 6.42, and 6.43 into Equation A.6 results in

$$\frac{dc}{dt}(k,0) = 0 \quad for\ all\ k \tag{A.7}$$

Appendix G: BEM Model

G.1 Water Surface Profile

Plots of the simulated and measured water surface profiles at $t(a_0/L)^{0.5}$ = 0.5, 3.5, 6.5, 9.5, and 12.5, for each of the fifteen specific gravity and initial submergence combinations, are presented in Figures G.1 to G.15.

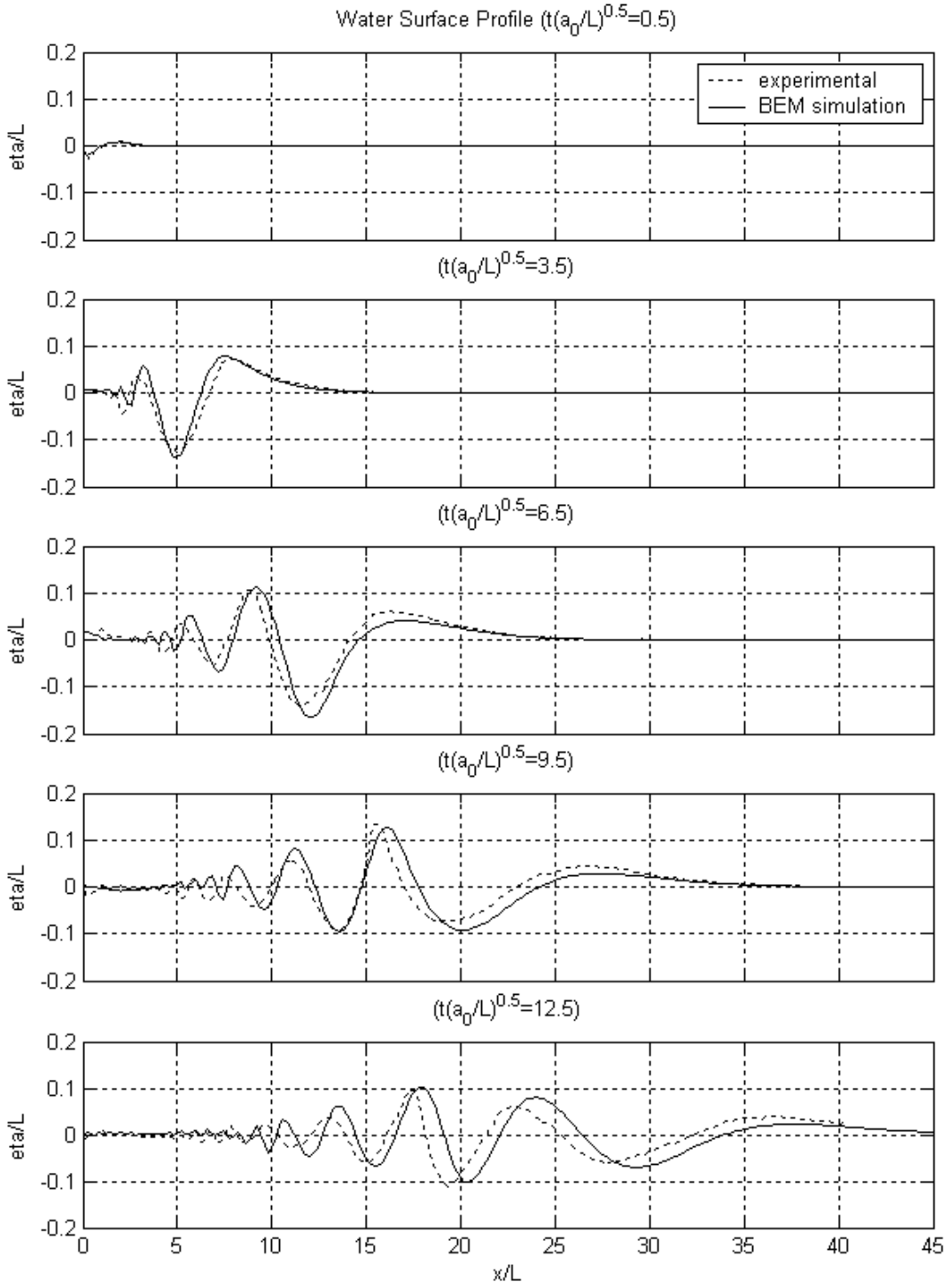

Figure G.1. Simulated and measured water surface profiles at $t(a_0/L)^{0.5}$ = 0.5, 3.5, 6.5, 9.5, and 12.5 for the SG5_IS5 combination.

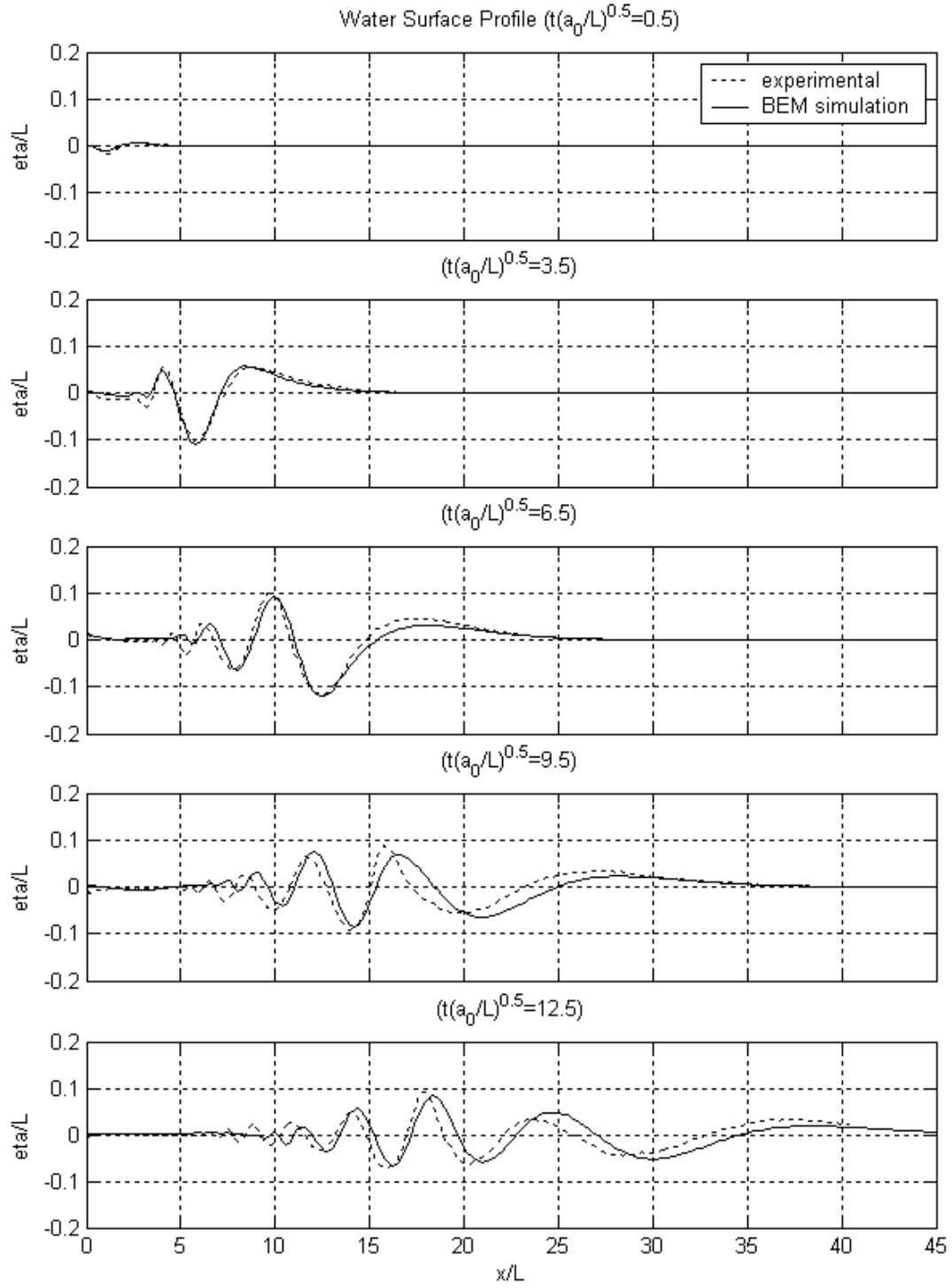

Figure G.2. Simulated and measured water surface profiles at $t(a_0/L)^{0.5}$ = 0.5, 3.5, 6.5, 9.5, and 12.5 for the SG5_IS4 configuration.

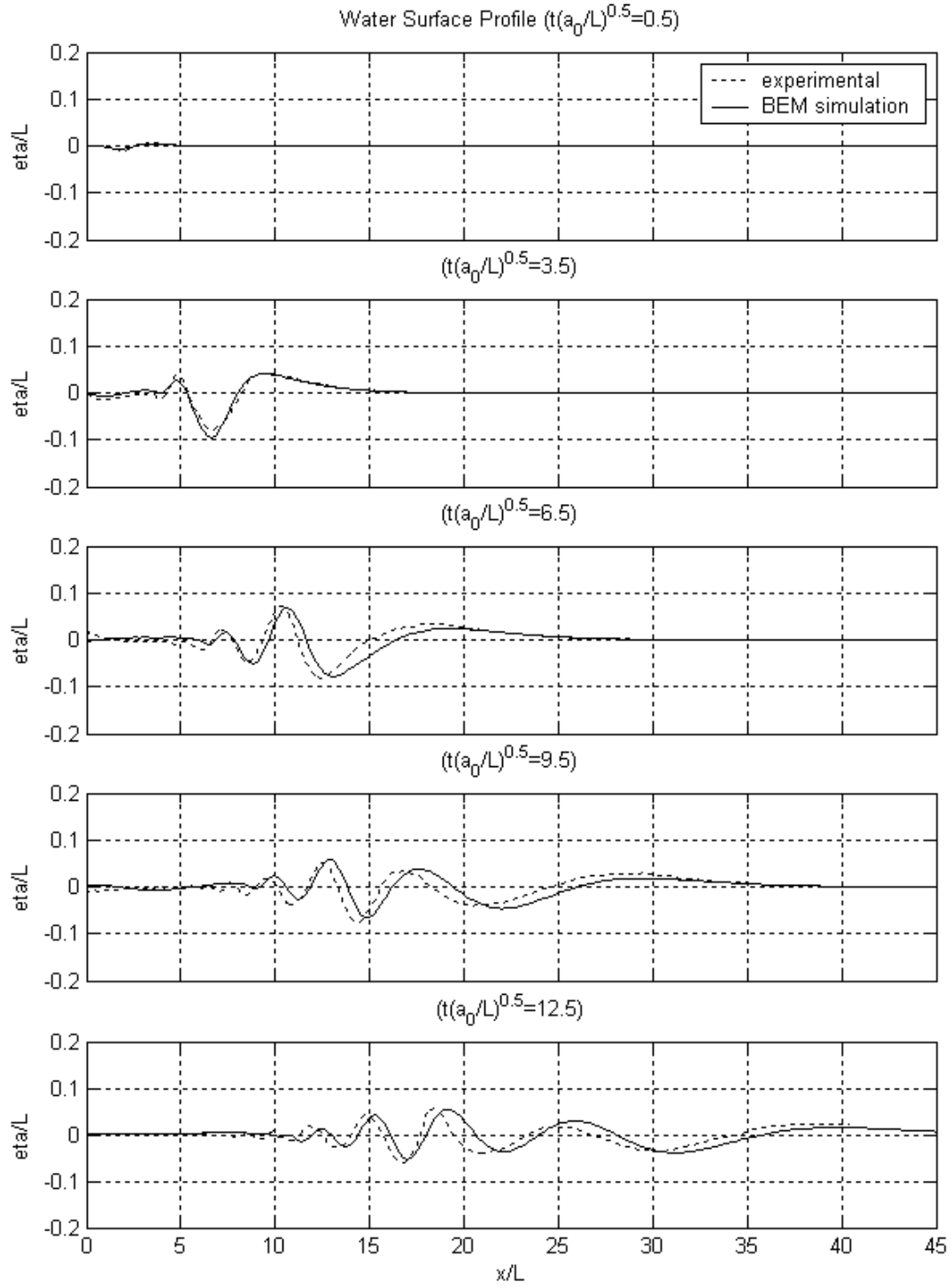

Figure G.3. Simulated and measured water surface profiles at $t(a_0/L)^{0.5}$ = 0.5, 3.5, 6.5, 9.5, and 12.5 for the SG5_IS3 configuration.

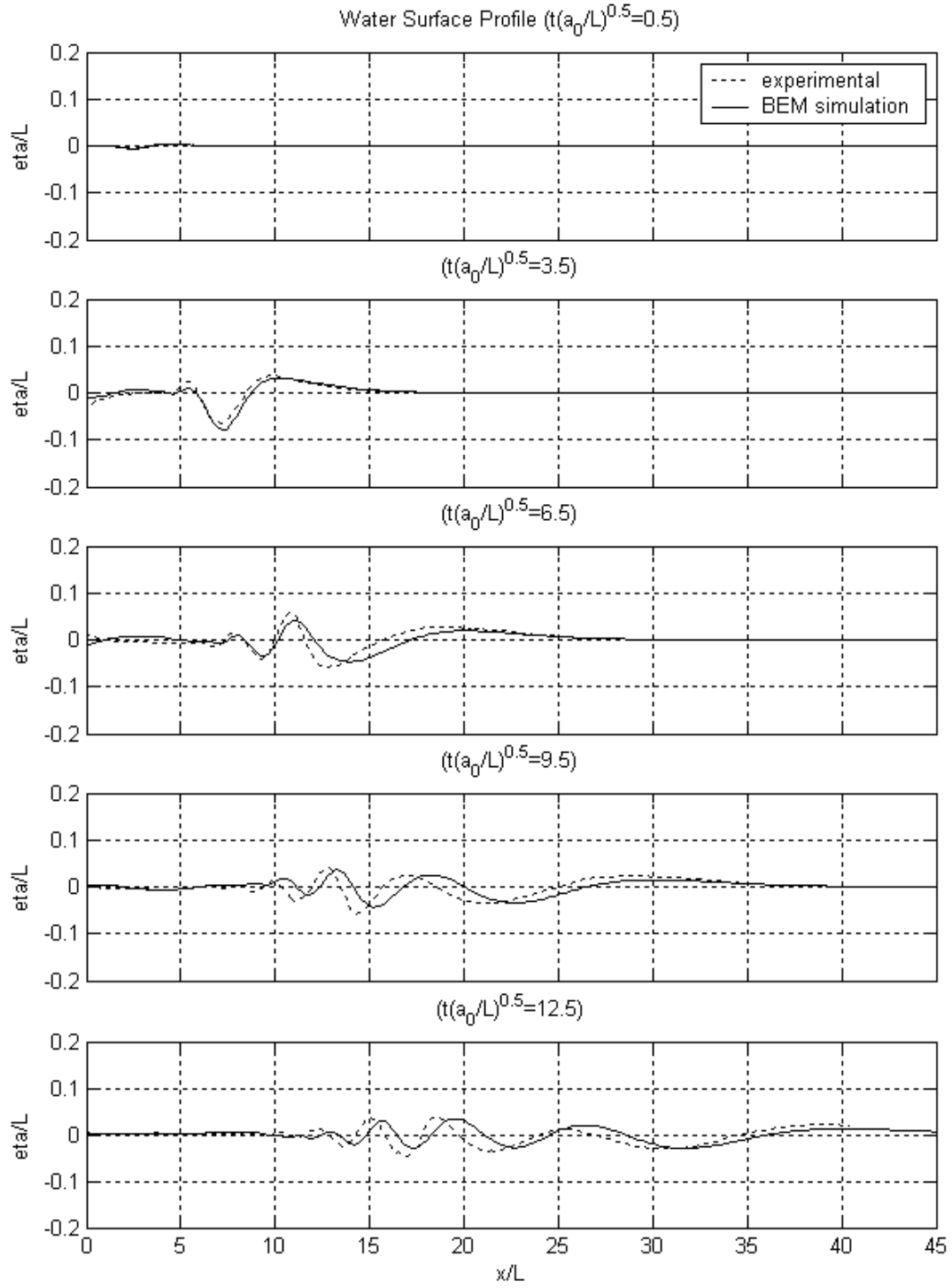

Figure G.4. Simulated and measured water surface profiles at $t(a_0/L)^{0.5}$ = 0.5, 3.5, 6.5, 9.5, and 12.5 for the SG5_IS2 configuration.

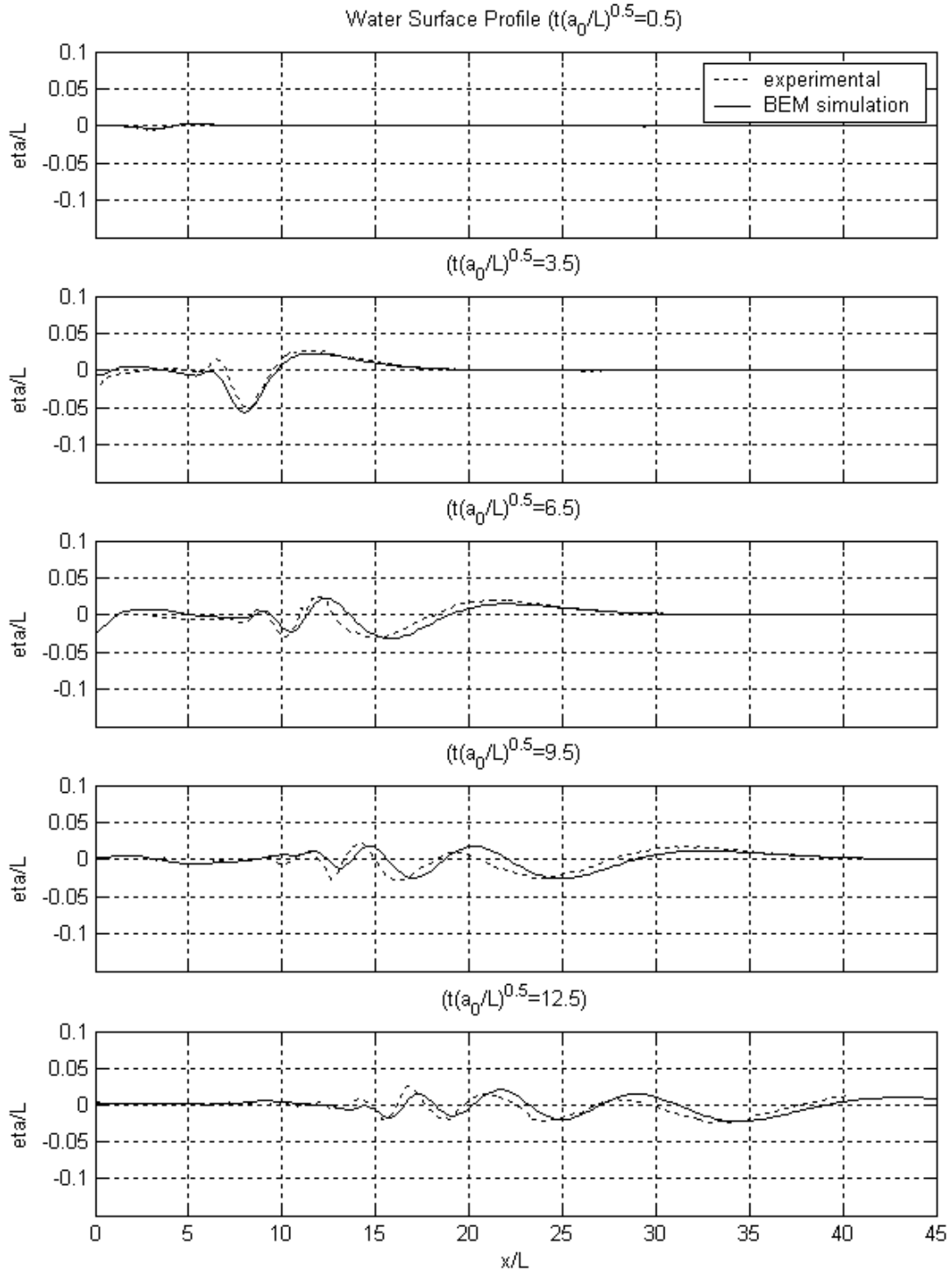

Figure G.5. Simulated and measured water surface profiles at $t(a_0/L)^{0.5}$ = 0.5, 3.5, 6.5, 9.5, and 12.5 for the SG5_IS1 configuration.

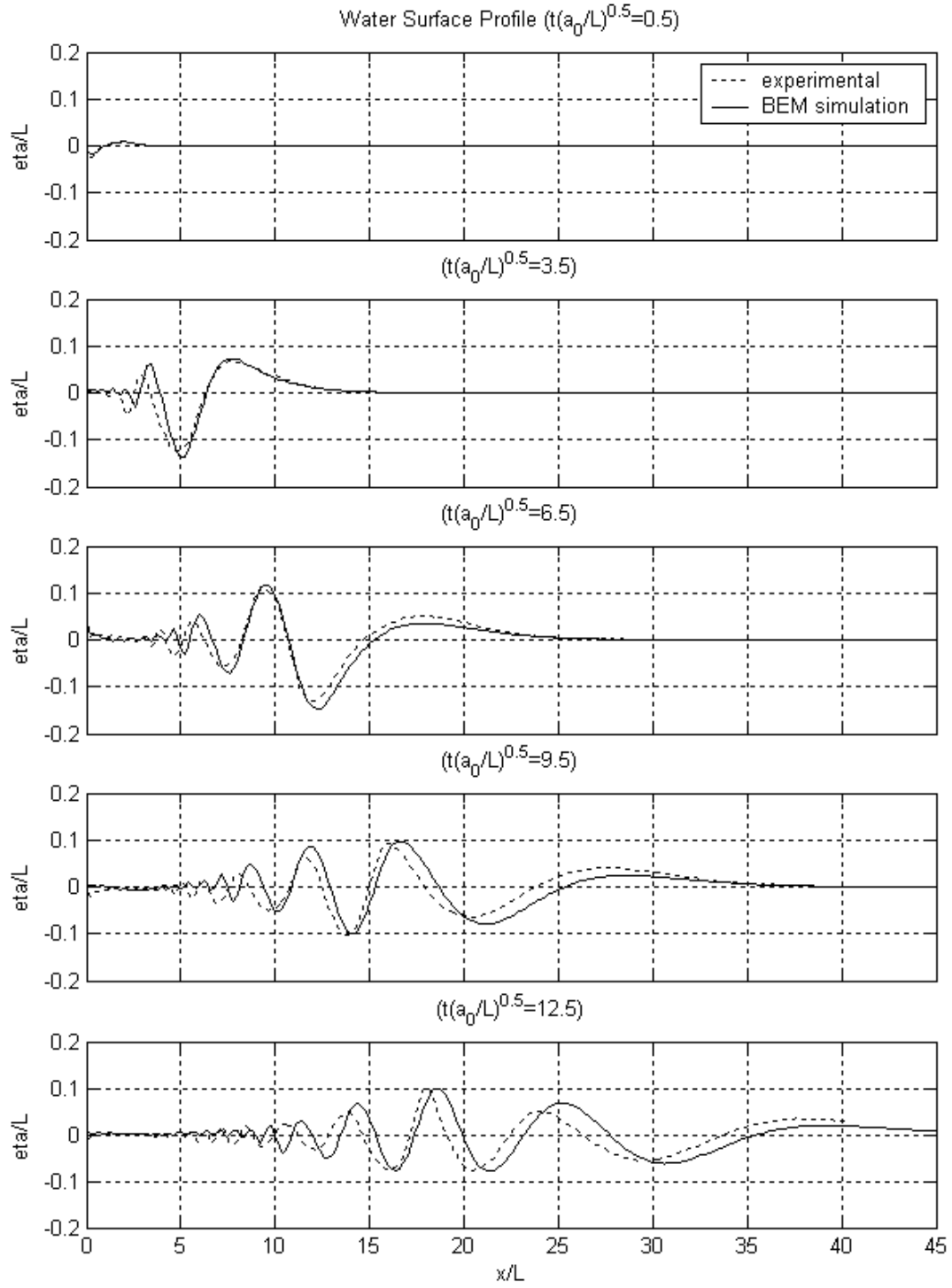

Figure G.6. Simulated and measured water surface profiles at $t(a_0/L)^{0.5}$ = 0.5, 3.5, 6.5, 9.5, and 12.5 for the SG4_IS5 configuration.

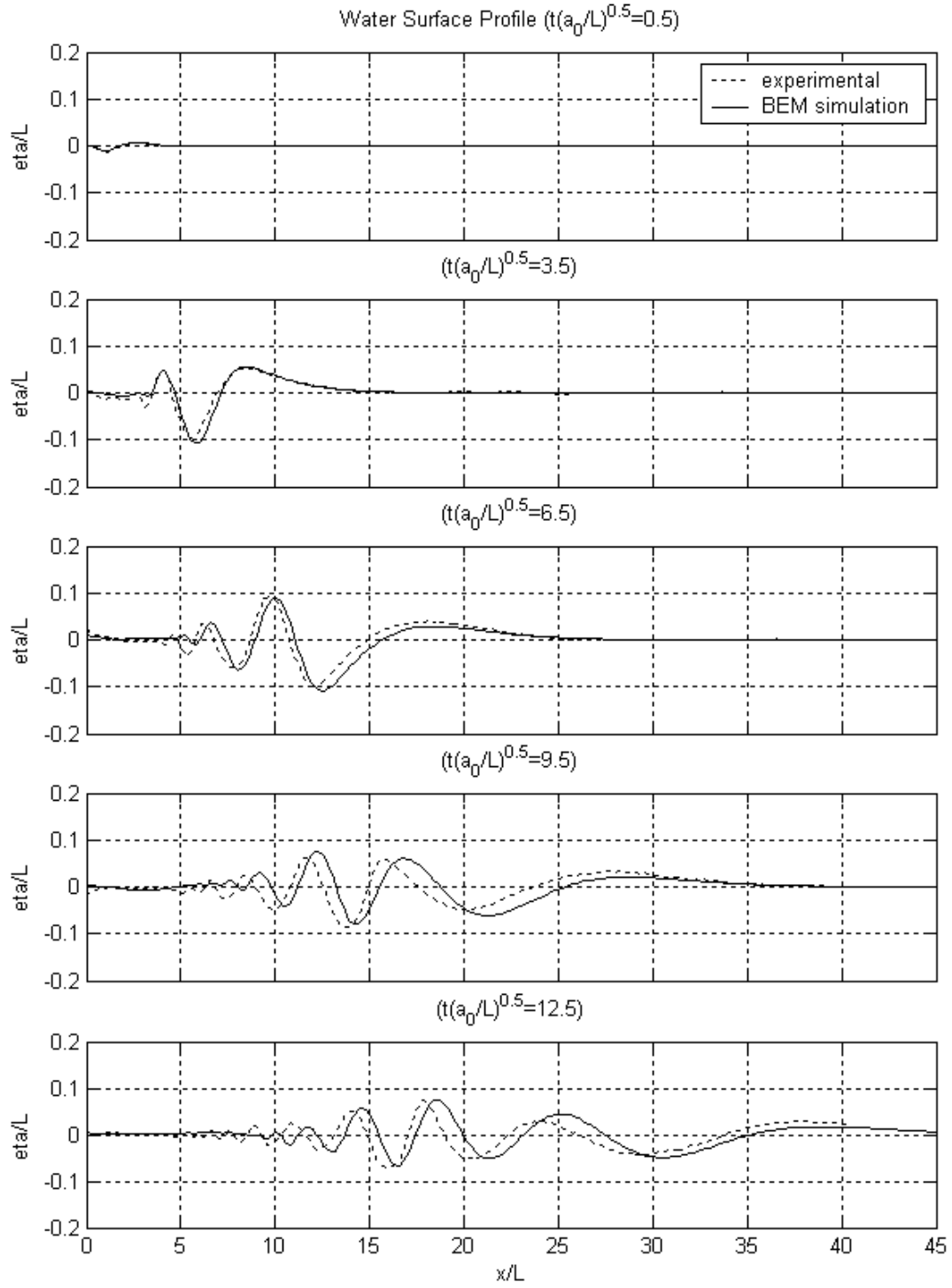

Figure G.7. Simulated and measured water surface profiles at $t(a_0/L)^{0.5}$ = 0.5, 3.5, 6.5, 9.5, and 12.5 for the SG4_IS4 configuration.

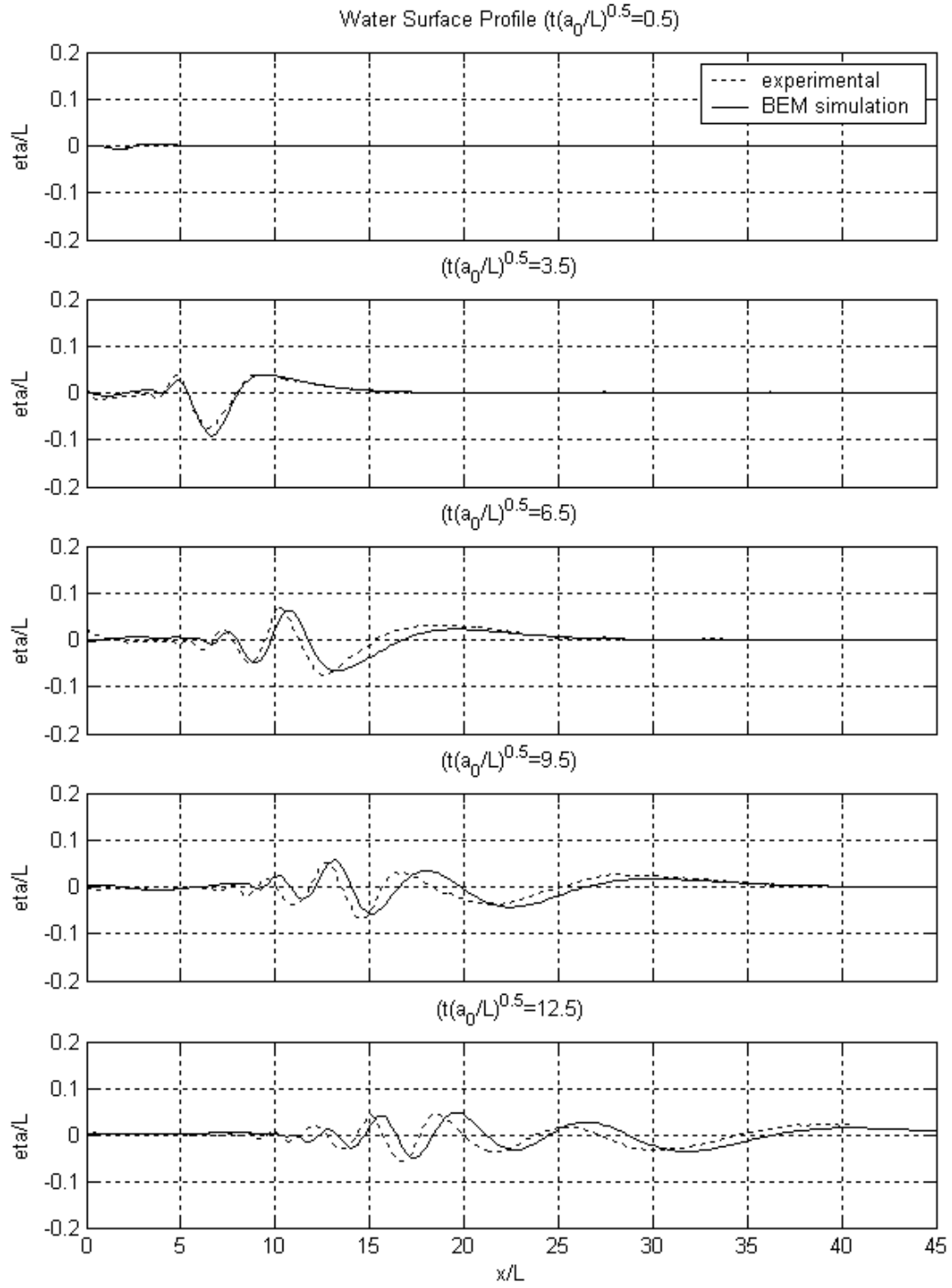

Figure G.8. Simulated and measured water surface profiles at $t(a_0/L)^{0.5}$ = 0.5, 3.5, 6.5, 9.5, and 12.5 for the SG4_IS3 configuration.

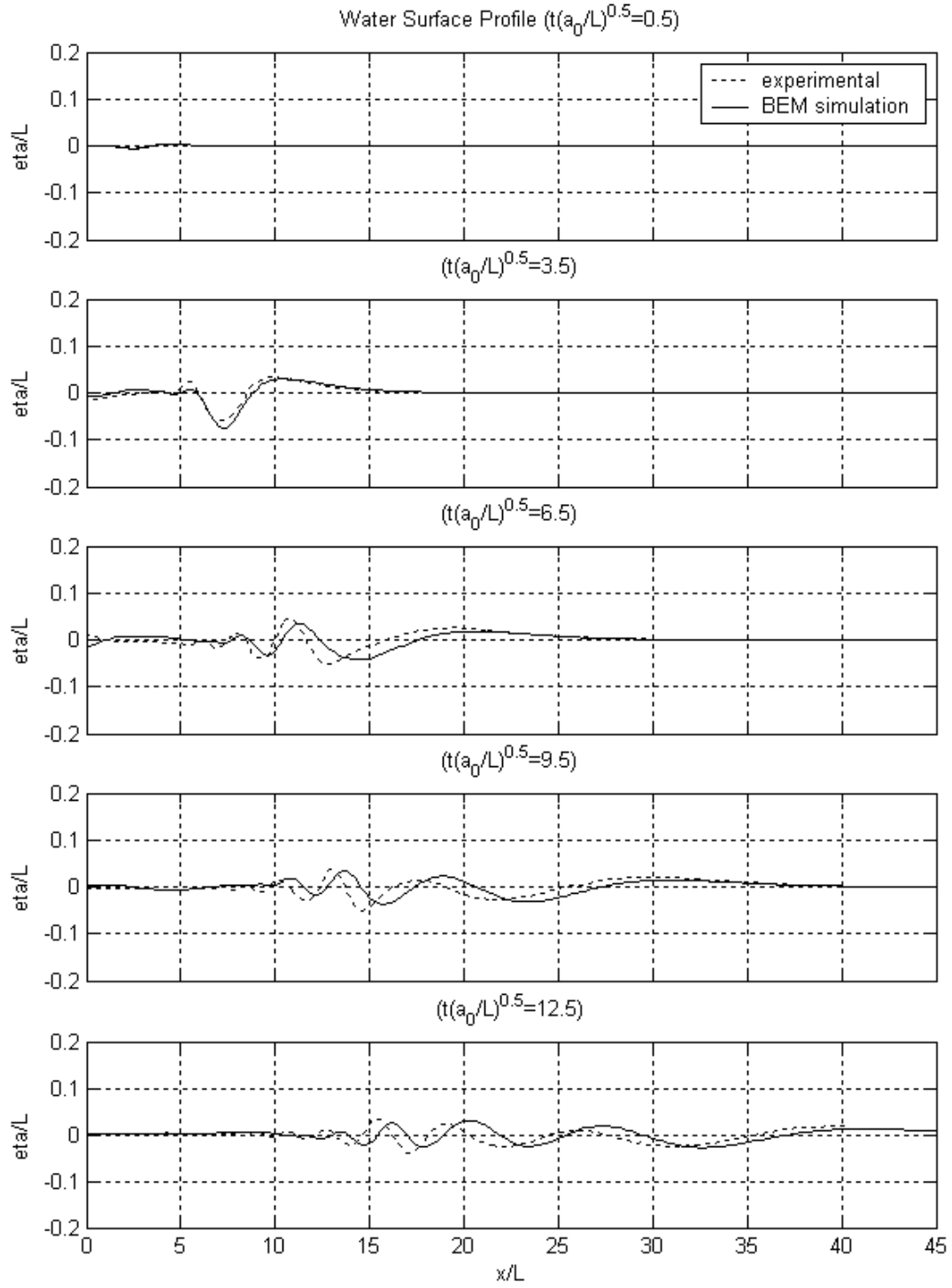

Figure G.9. Simulated and measured water surface profiles at $t(a_0/L)^{0.5}$ = 0.5, 3.5, 6.5, 9.5, and 12.5 for the SG4_IS2 configuration.

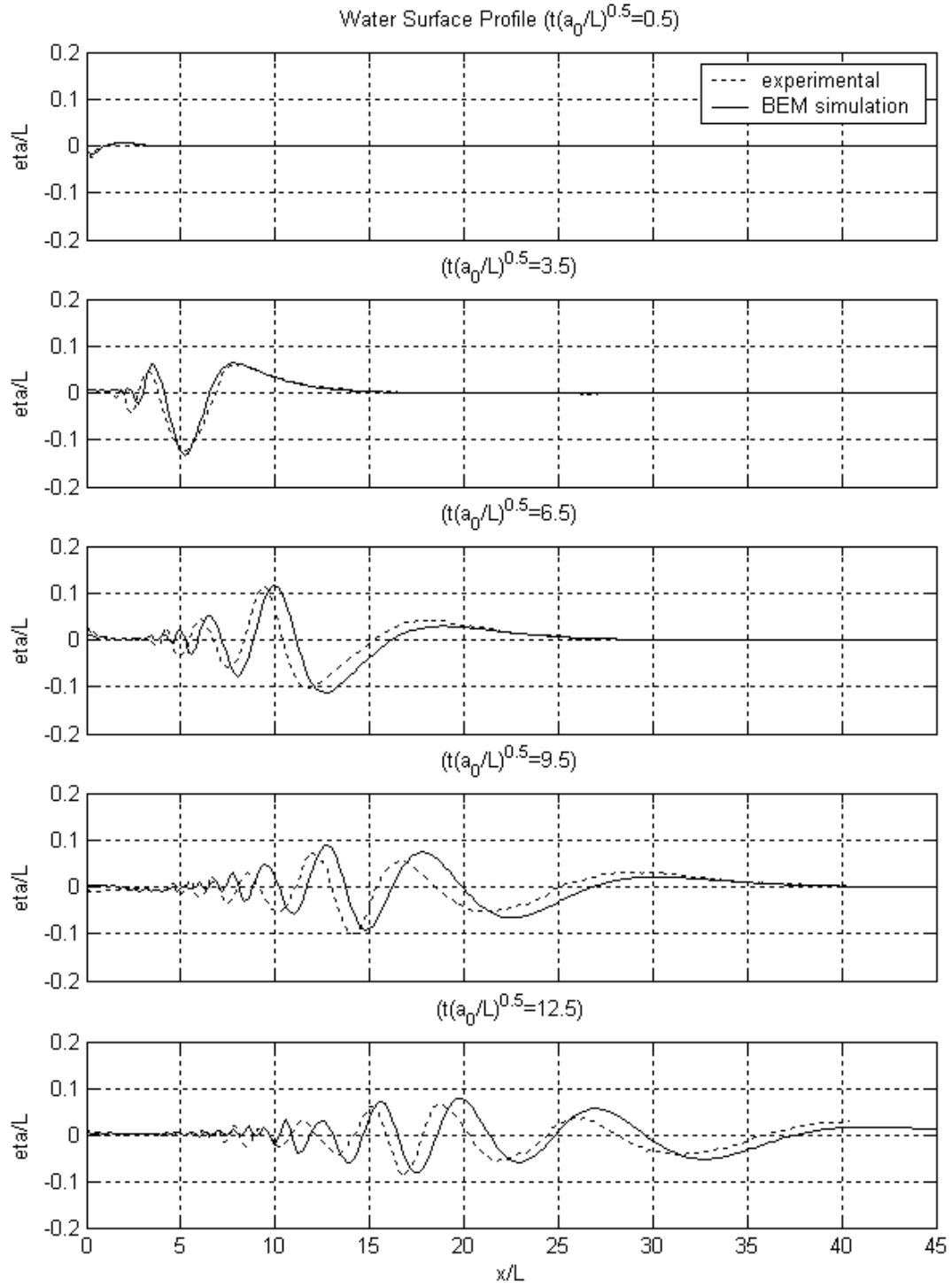

Figure G.10. Simulated and measured water surface profiles at $t(a_0/L)^{0.5}$ = 0.5, 3.5, 6.5, 9.5, and 12.5 for the SG3_IS5 configuration.

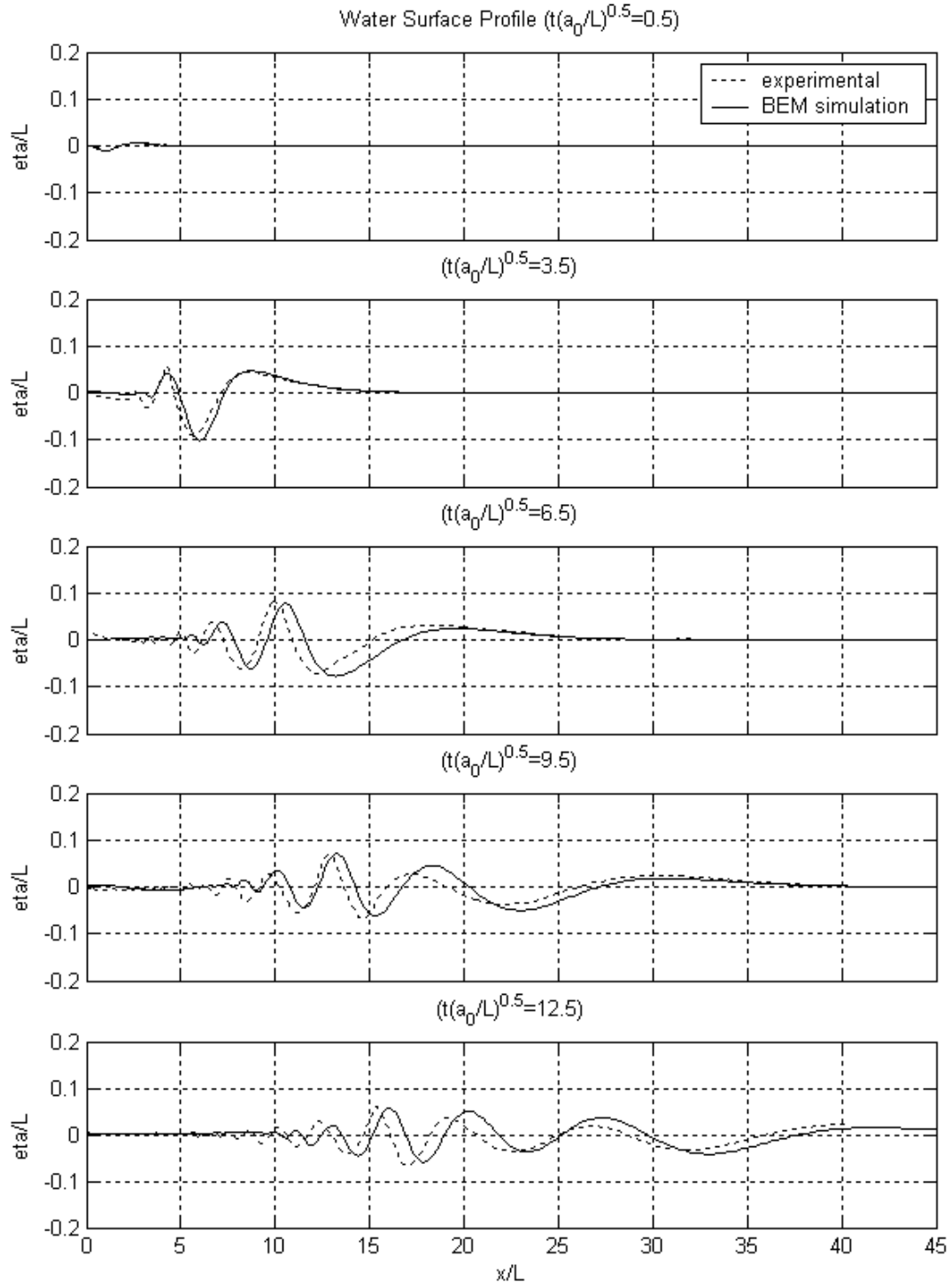

Figure G.11. Simulated and measured water surface profiles at $t(a_0/L)^{0.5}$ = 0.5, 3.5, 6.5, 9.5, and 12.5 for the SG3_IS4 configuration.

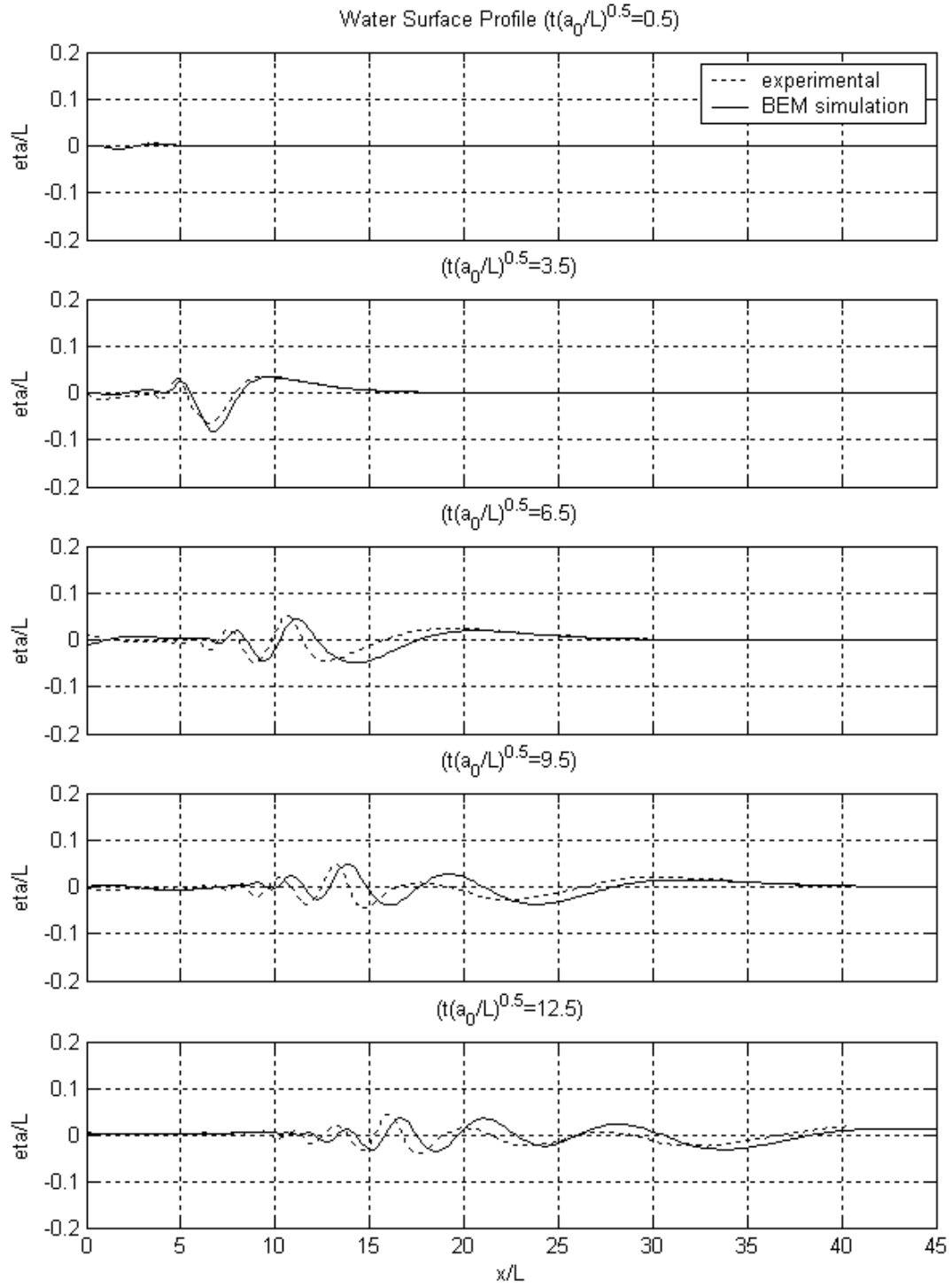

Figure G.12. Simulated and measured water surface profiles at $t(a_0/L)^{0.5}$ = 0.5, 3.5, 6.5, 9.5, and 12.5 for the SG3_IS3 configuration.

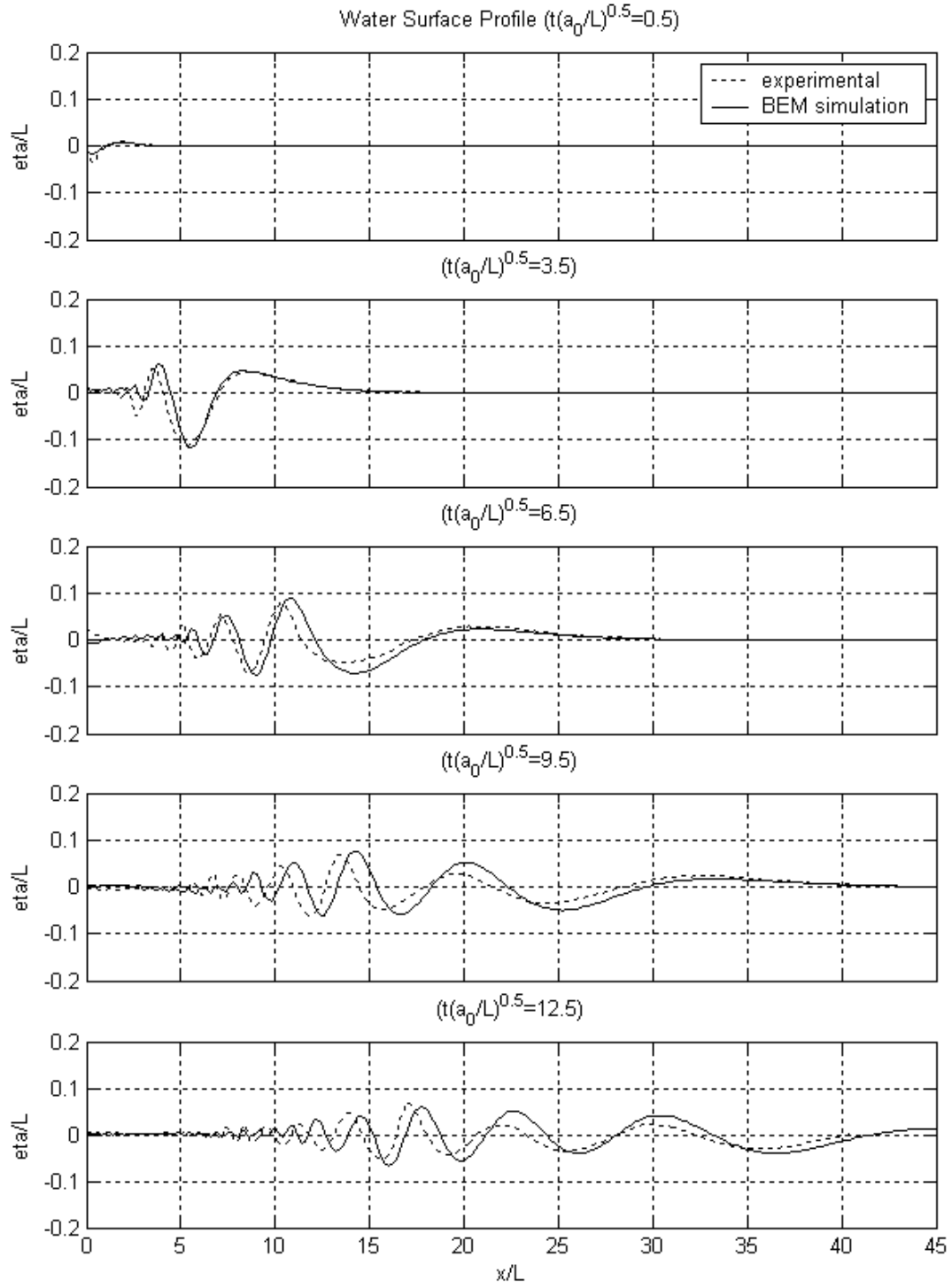

Figure G.13. Simulated and measured water surface profiles at $t(a_0/L)^{0.5}$ = 0.5, 3.5, 6.5, 9.5, and 12.5 for the SG2_IS5 configuration.

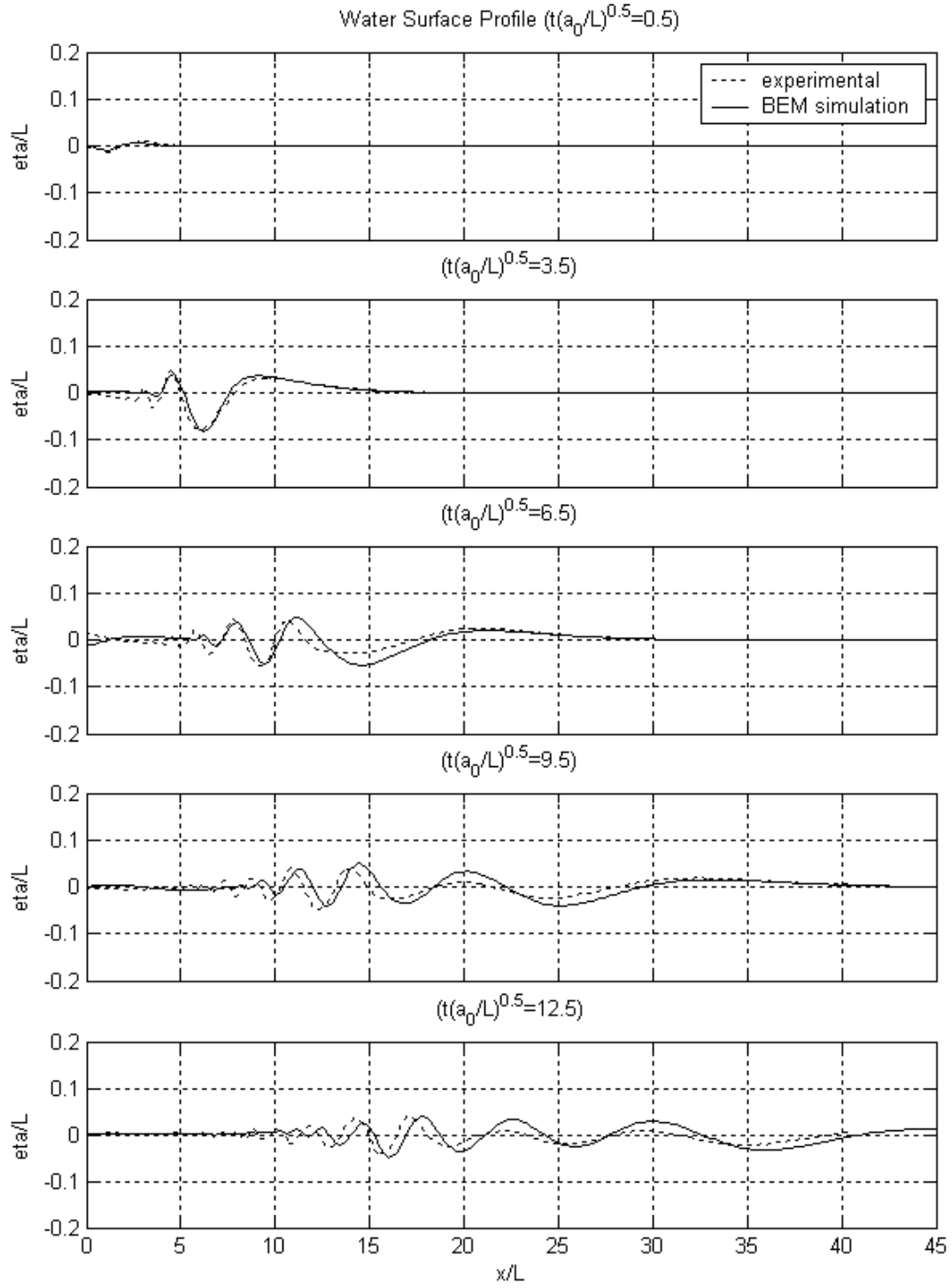

Figure G.14. Simulated and measured water surface profiles at $t(a_0/L)^{0.5}$ = 0.5, 3.5, 6.5, 9.5, and 12.5 for the SG2_IS4 configuration.

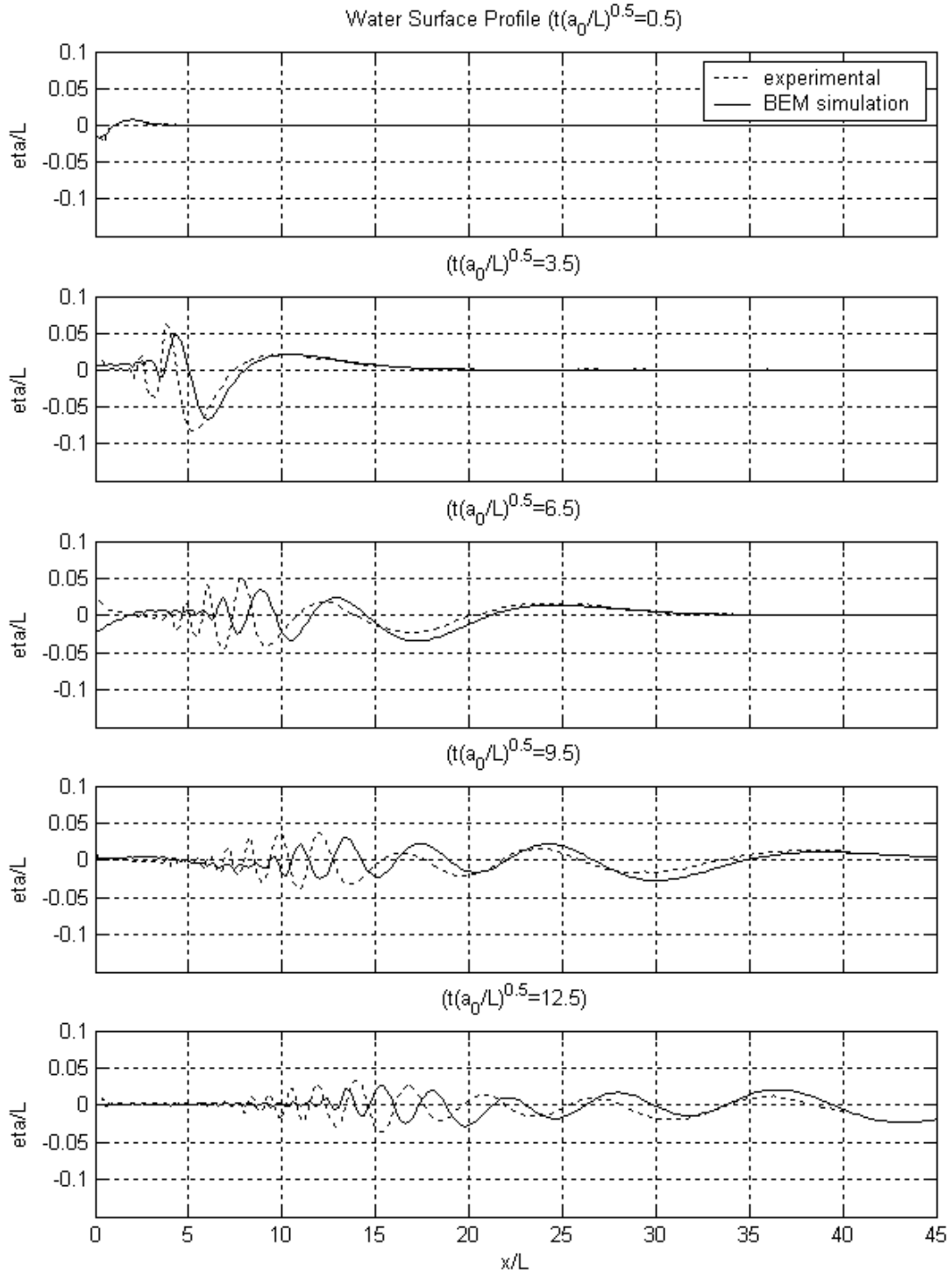

Figure G.15. Simulated and measured water surface profiles at $t(a_0/L)^{0.5}$ = 0.5, 3.5, 6.5, 9.5, and 12.5 for the SG1_IS5 configuration.

G.2 Water Surface Time History

Plots of the simulated and measured water level time histories at x/L = 0.2, 10, 20, 30, and 40, for each of the fifteen specific gravity and initial submergence combinations, are presented in Figures G.16 to G.30.

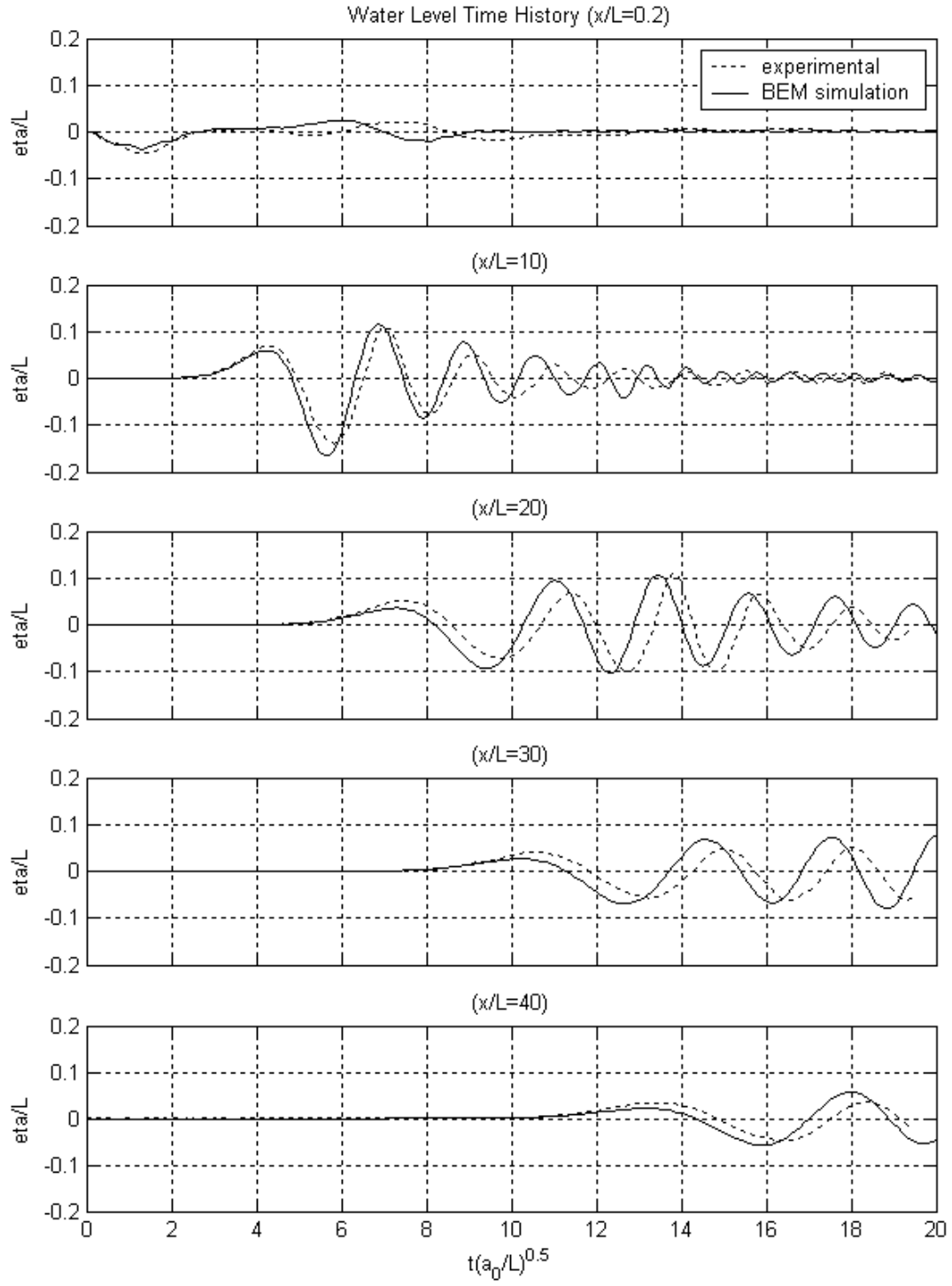

Figure G.16. Simulated and measured water level time histories at x/L = 0.2, 10, 20, 30, and 40 for the SG5_IS5 combination.

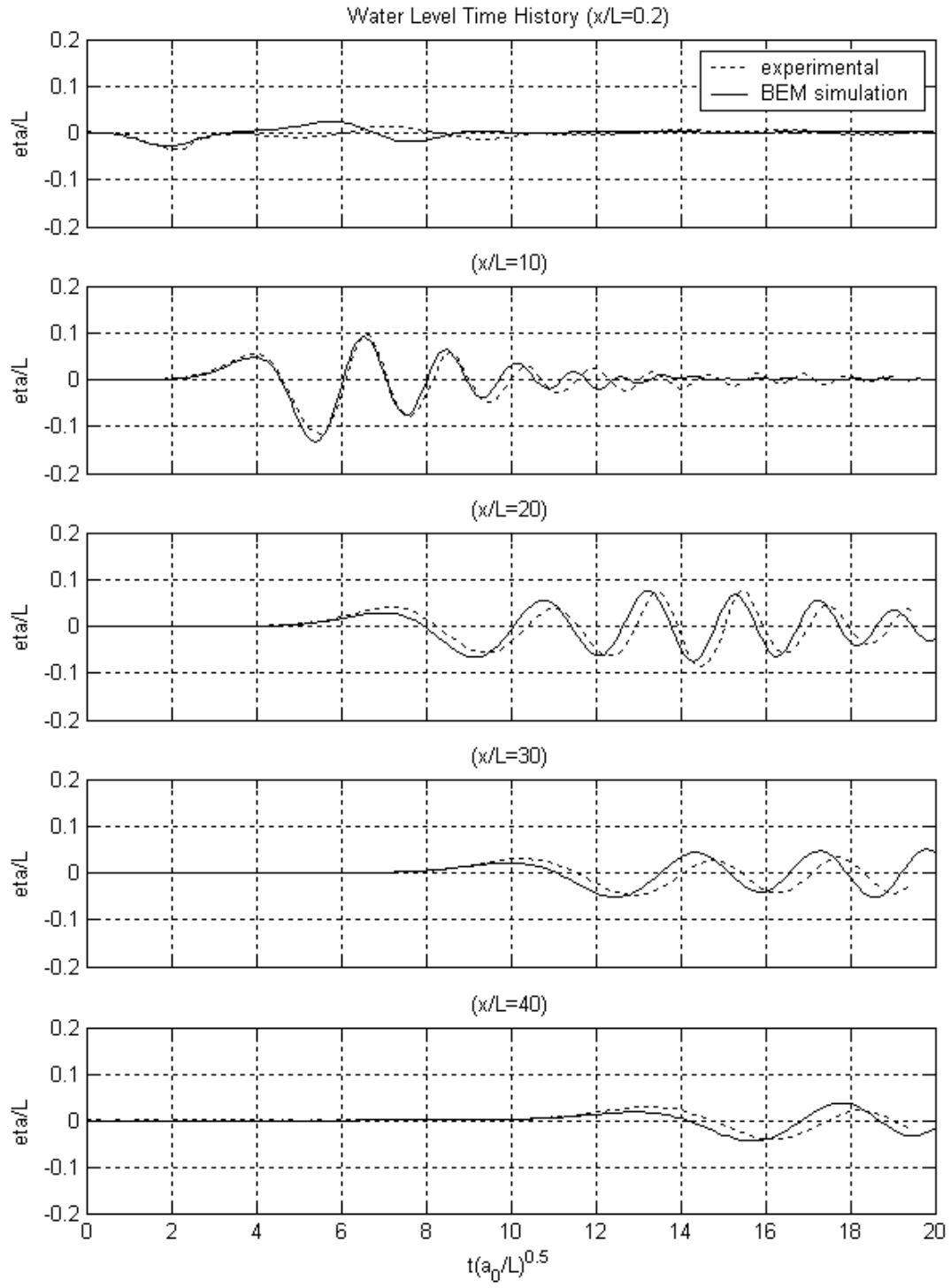

Figure G.17. Simulated and measured water level time histories at x/L = 0.2, 10, 20, 30, and 40 for the SG5_IS4 configuration.

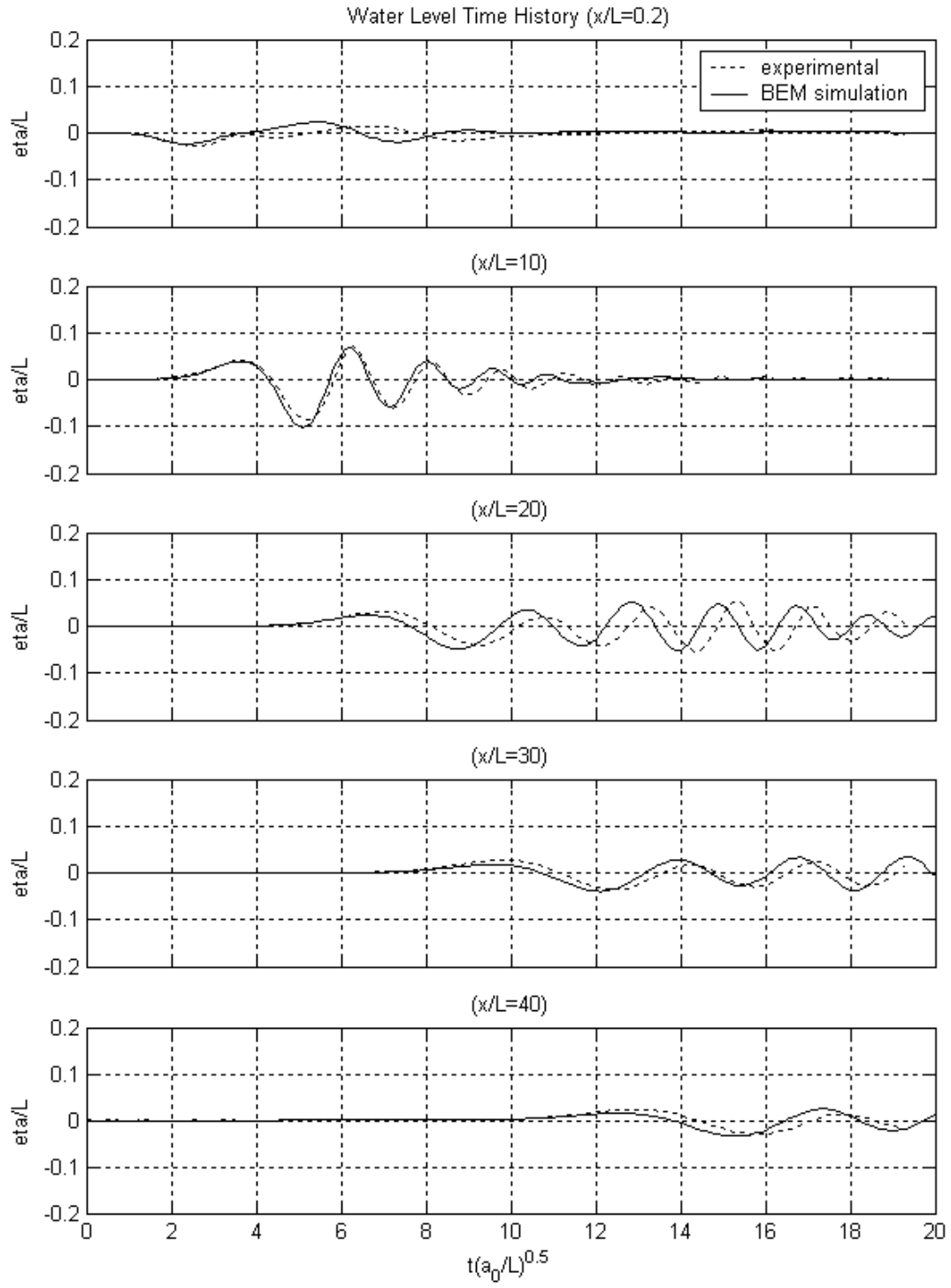

Figure G.18. Simulated and measured water level time histories at x/L = 0.2, 10, 20, 30, and 40 for the SG5_IS3 configuration.

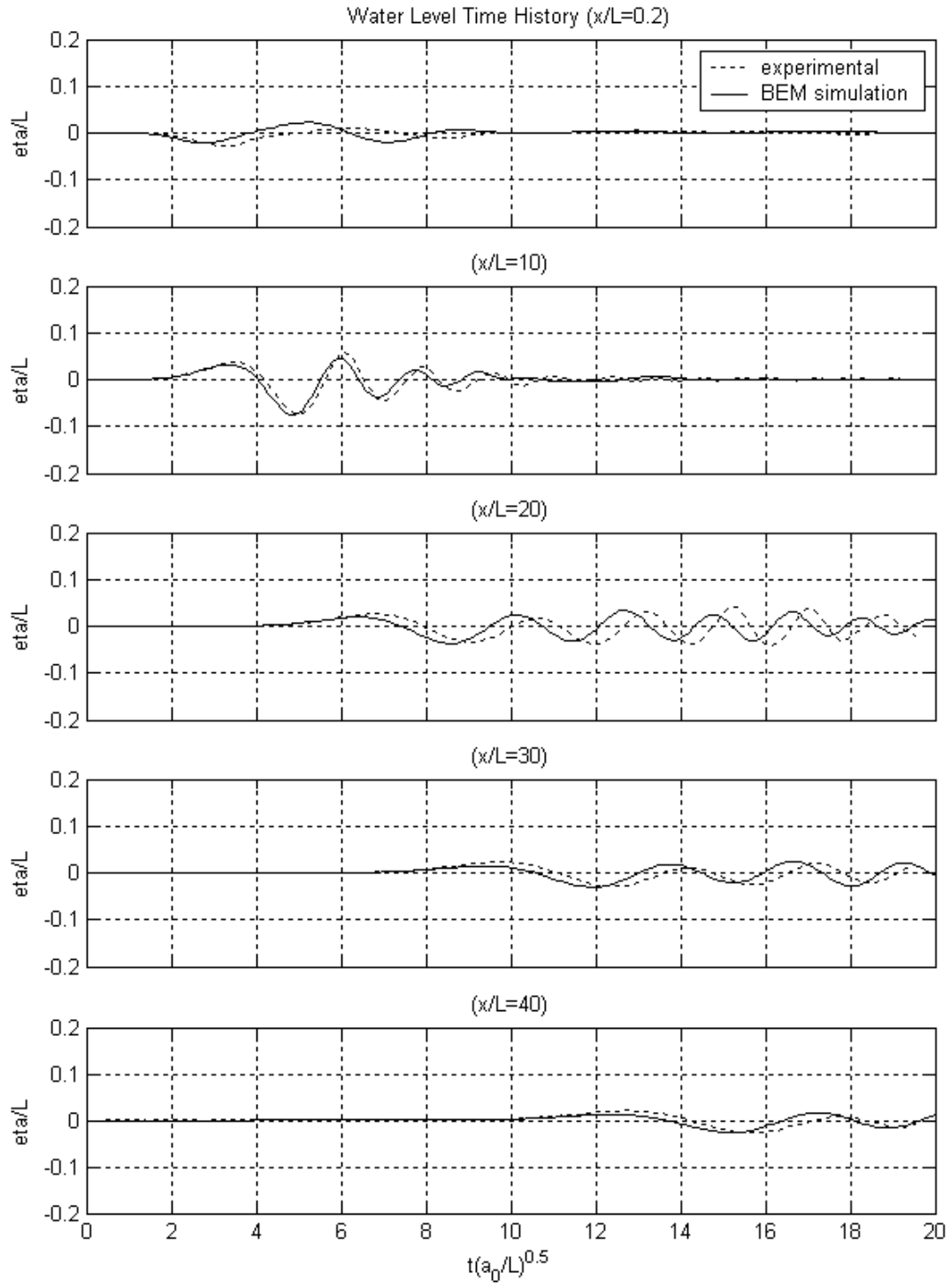

Figure G.19. Simulated and measured water level time histories at x/L = 0.2, 10, 20, 30, and 40 for the SG5_IS2 configuration.

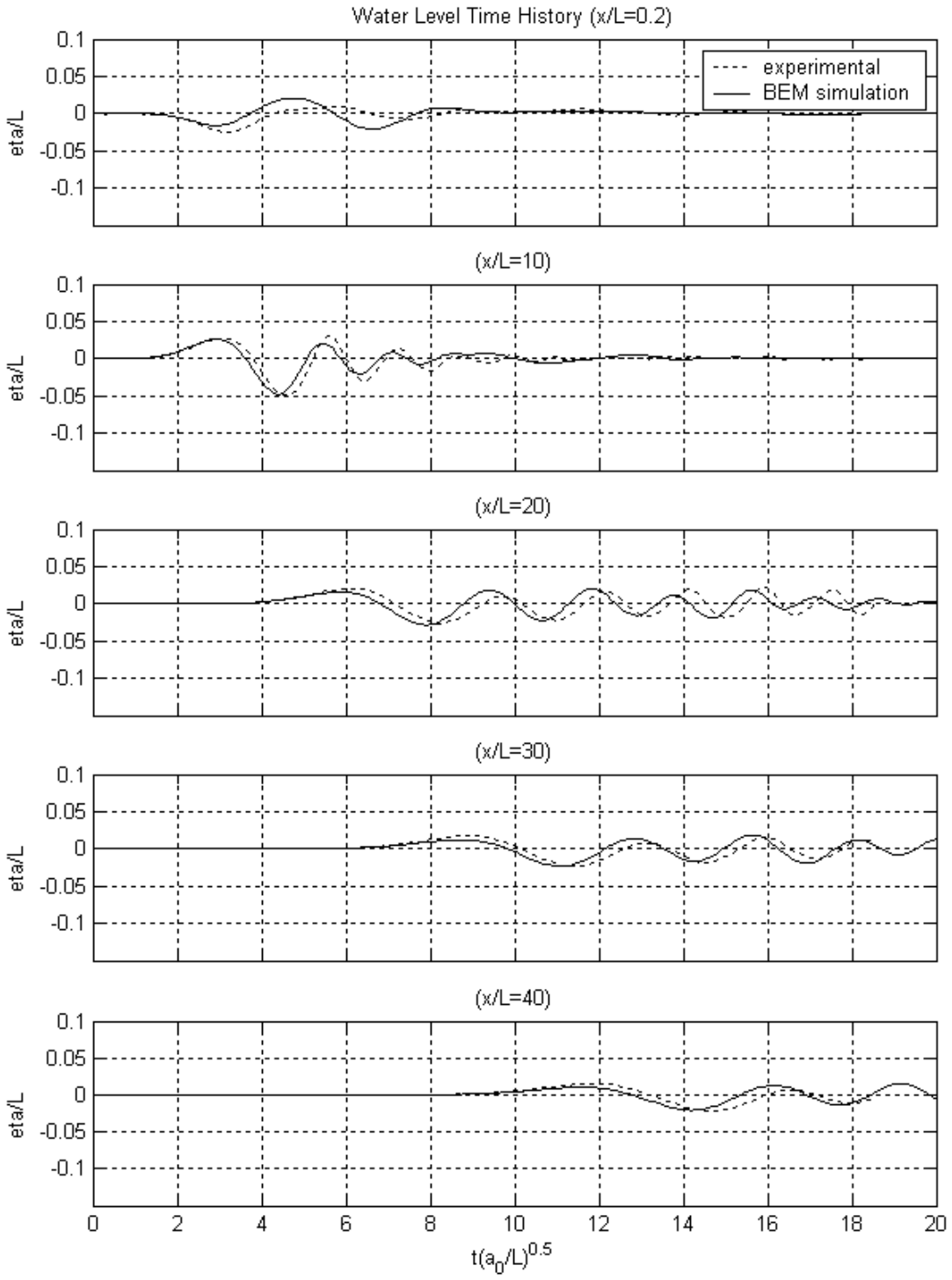

Figure G.20. Simulated and measured water level time histories at x/L = 0.2, 10, 20, 30, and 40 for the SG5_IS1 configuration.

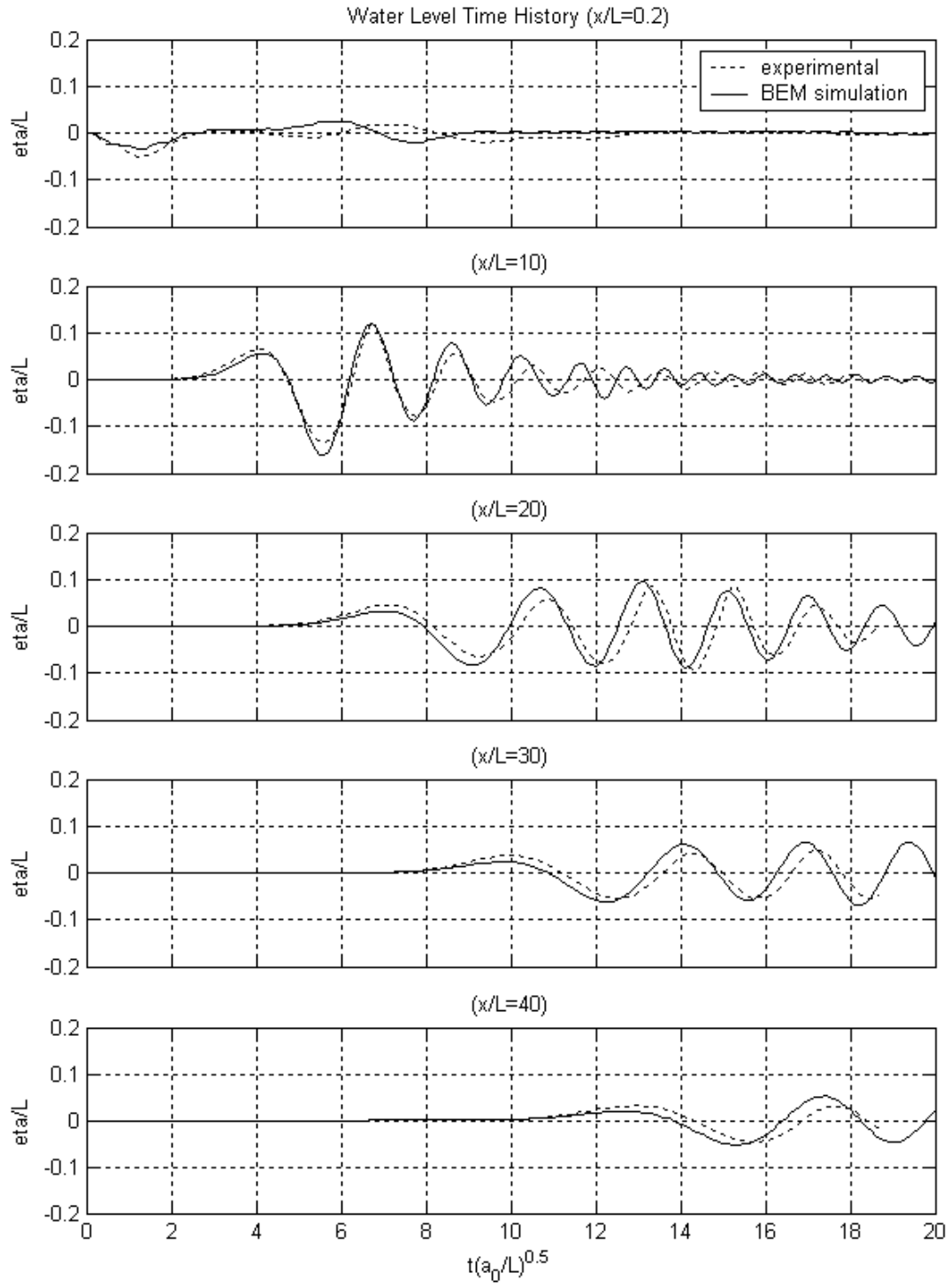

Figure G.21. Simulated and measured water level time histories at x/L = 0.2, 10, 20, 30, and 40 for the SG4_IS5 configuration.

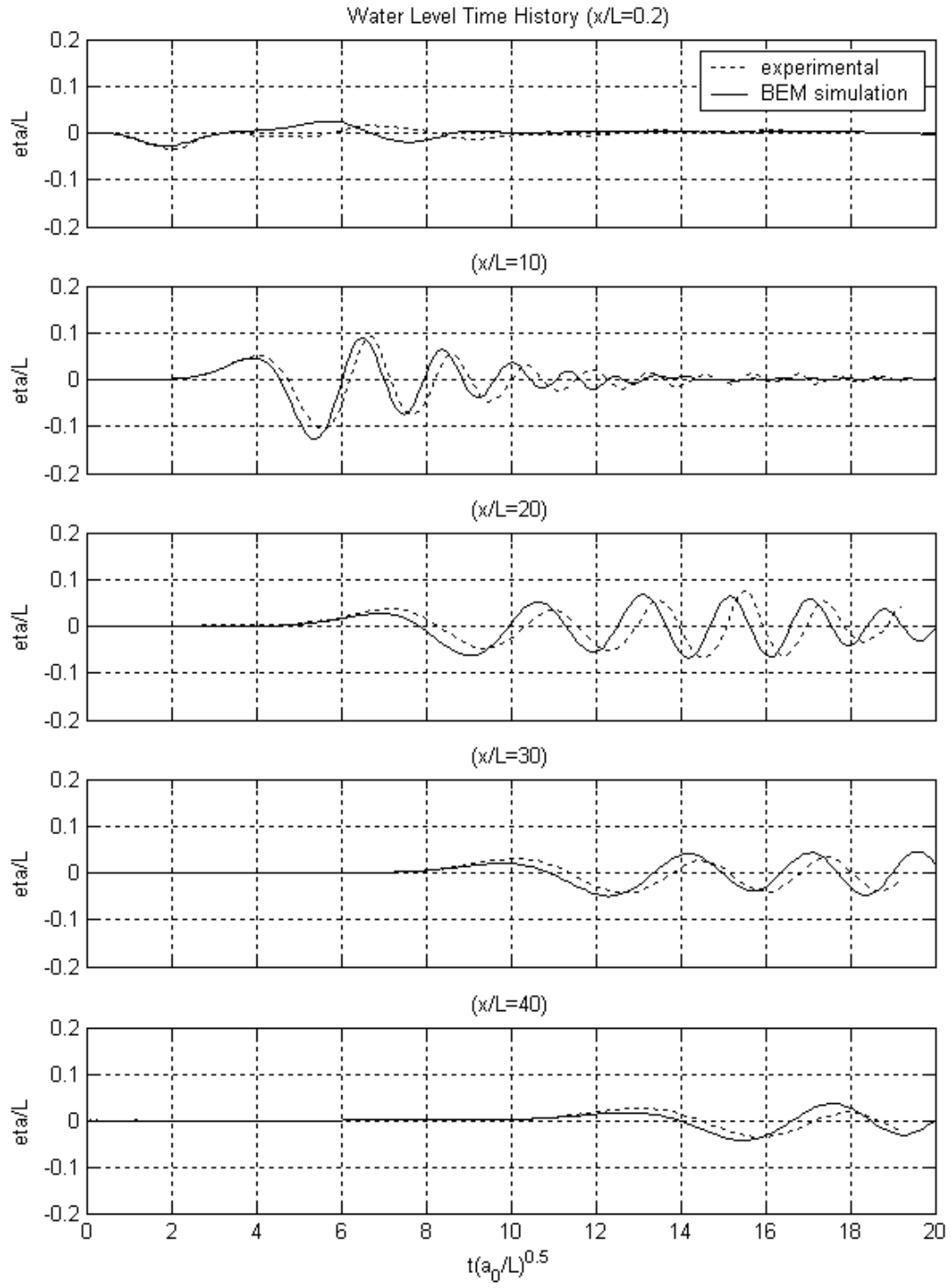

Figure G.22. Simulated and measured water level time histories at x/L = 0.2, 10, 20, 30, and 40 for the SG4_IS4 configuration.

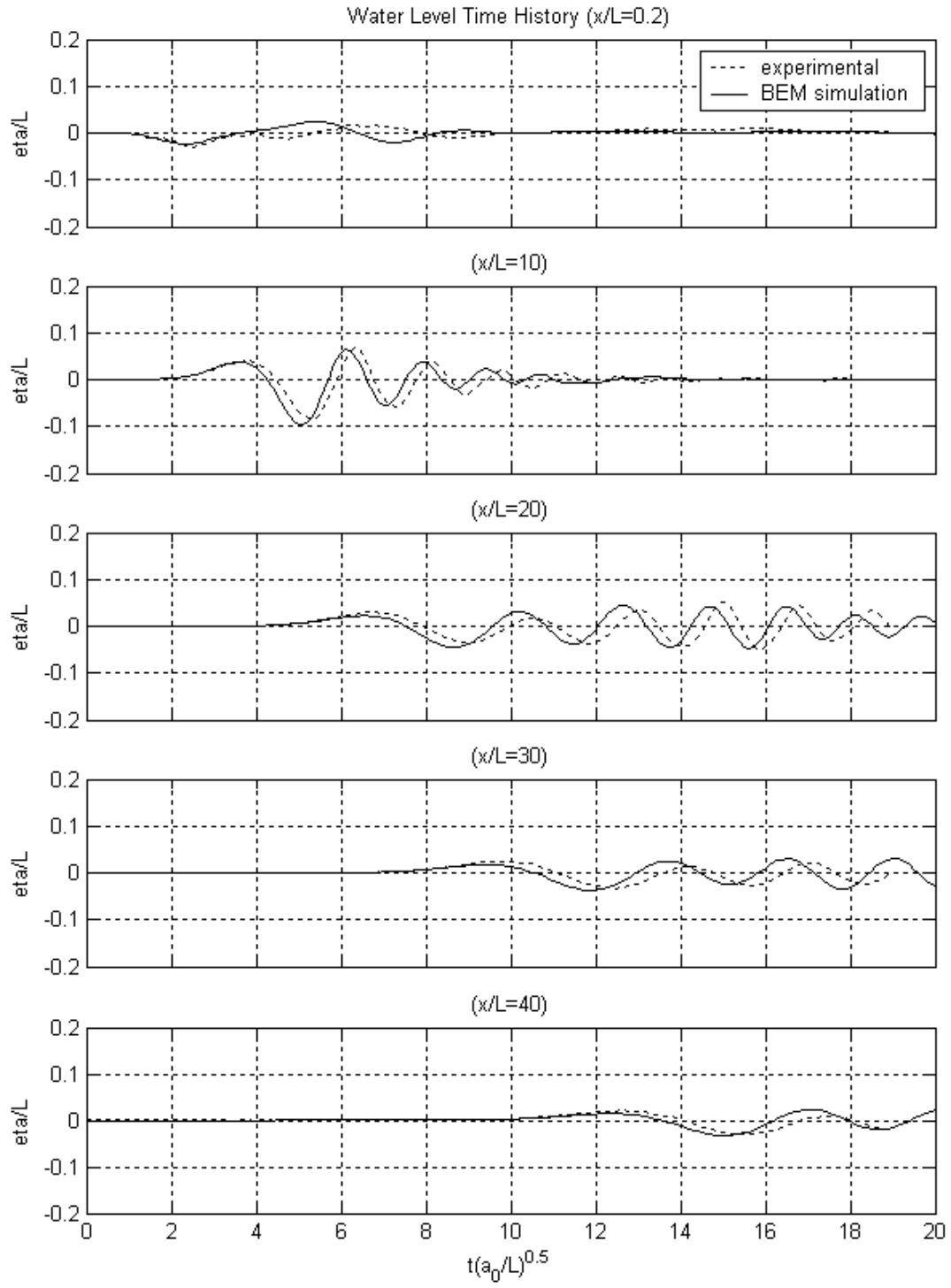

Figure G.23. Simulated and measured water level time histories at x/L = 0.2, 10, 20, 30, and 40 for the SG4_IS3 configuration.

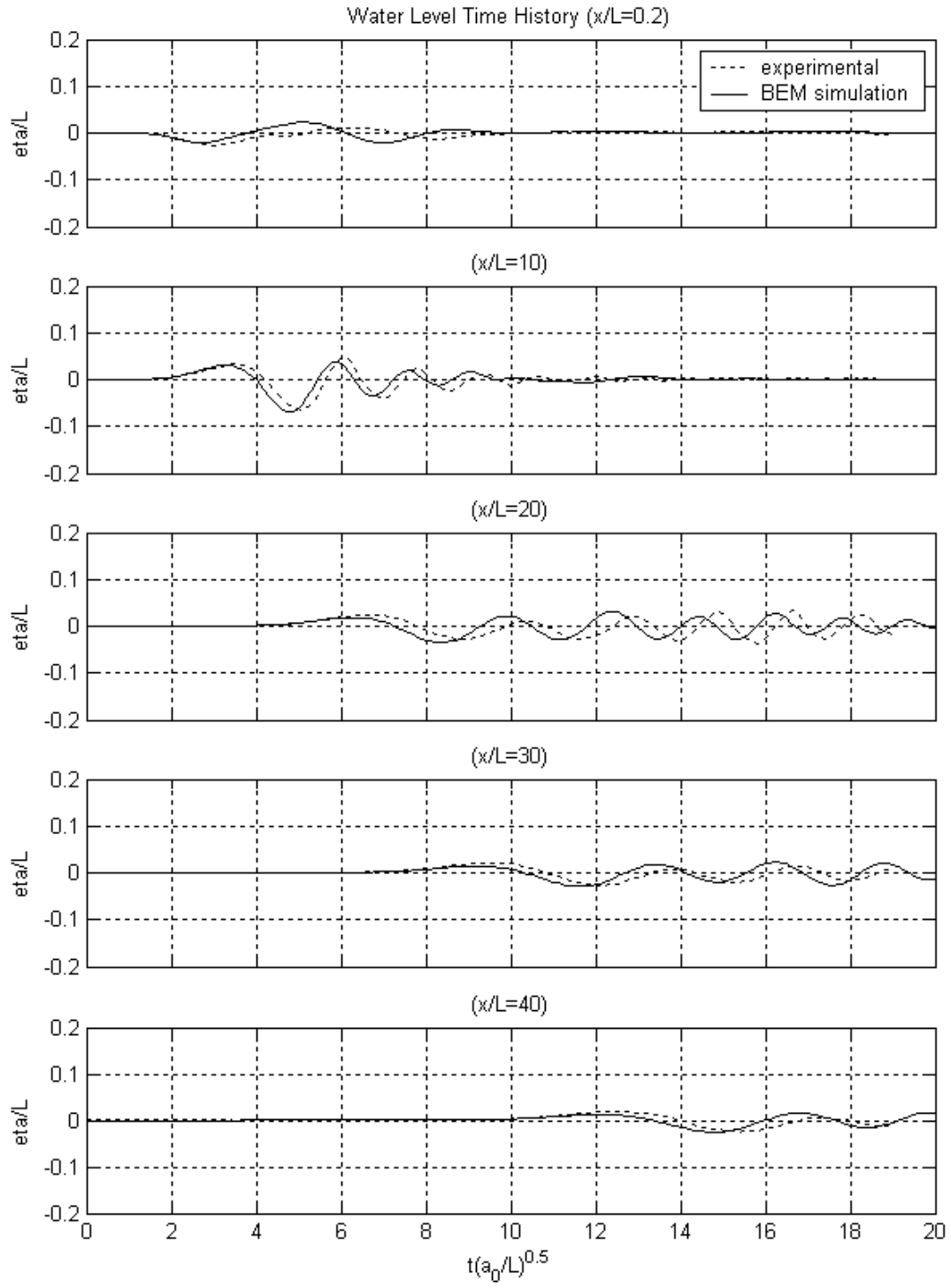

Figure G.24. Simulated and measured water level time histories at x/L = 0.2, 10, 20, 30, and 40 for the SG4_IS2 configuration.

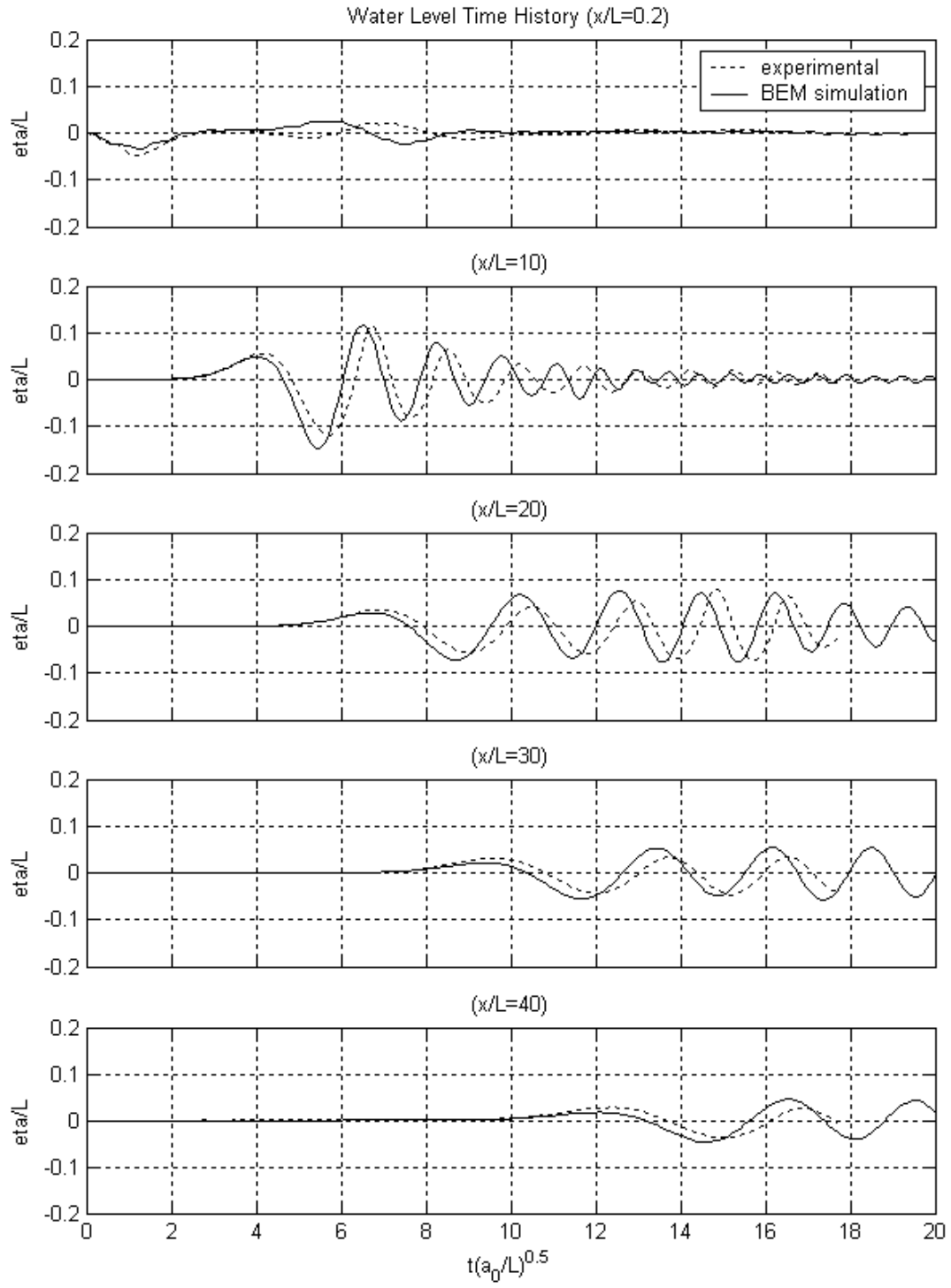

Figure G.25. Simulated and measured water level time histories at x/L = 0.2, 10, 20, 30, and 40 for the SG3_IS5 configuration.

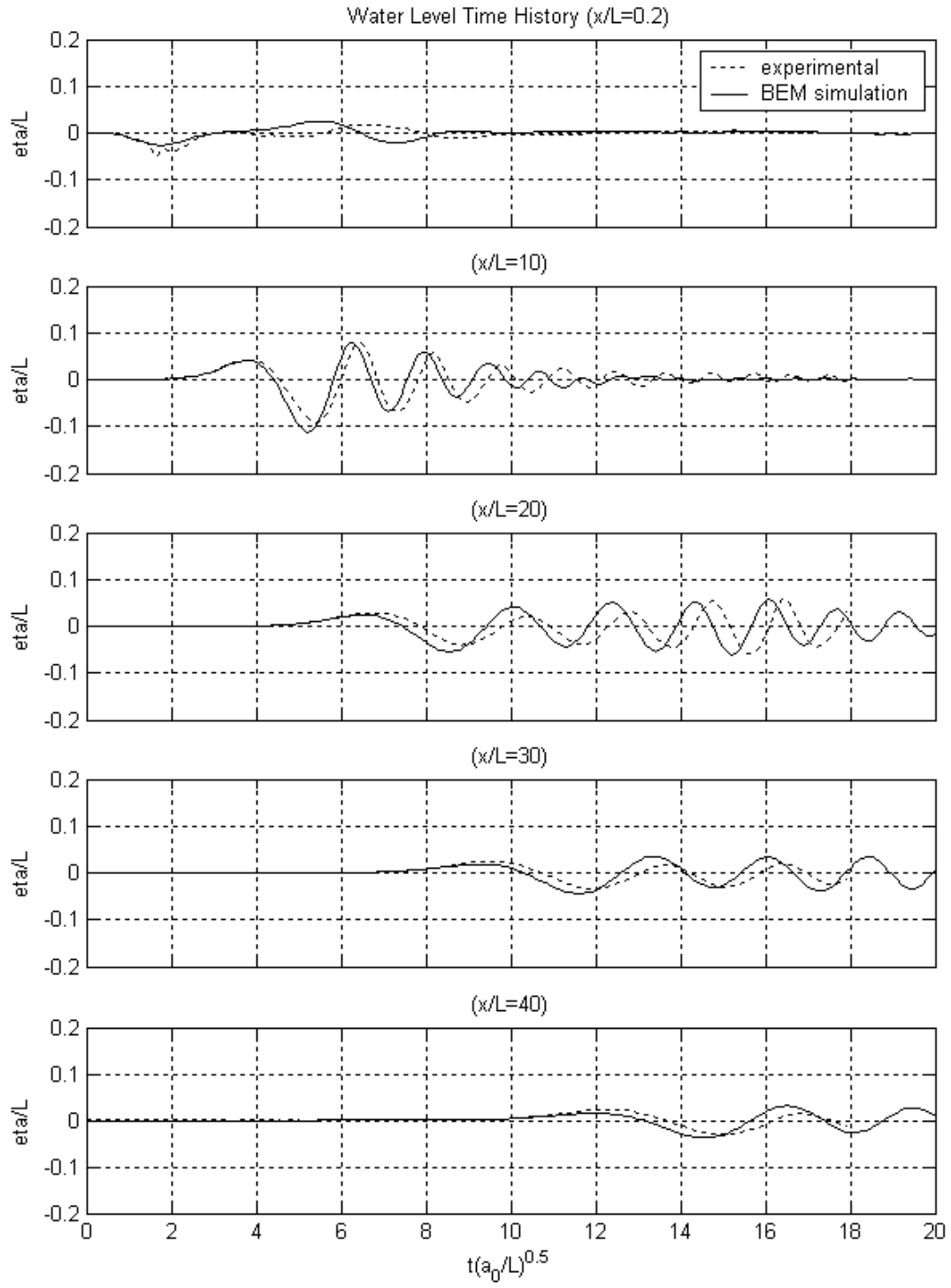

Figure G.26. Simulated and measured water level time histories at x/L = 0.2, 10, 20, 30, and 40 for the SG3_IS4 configuration.

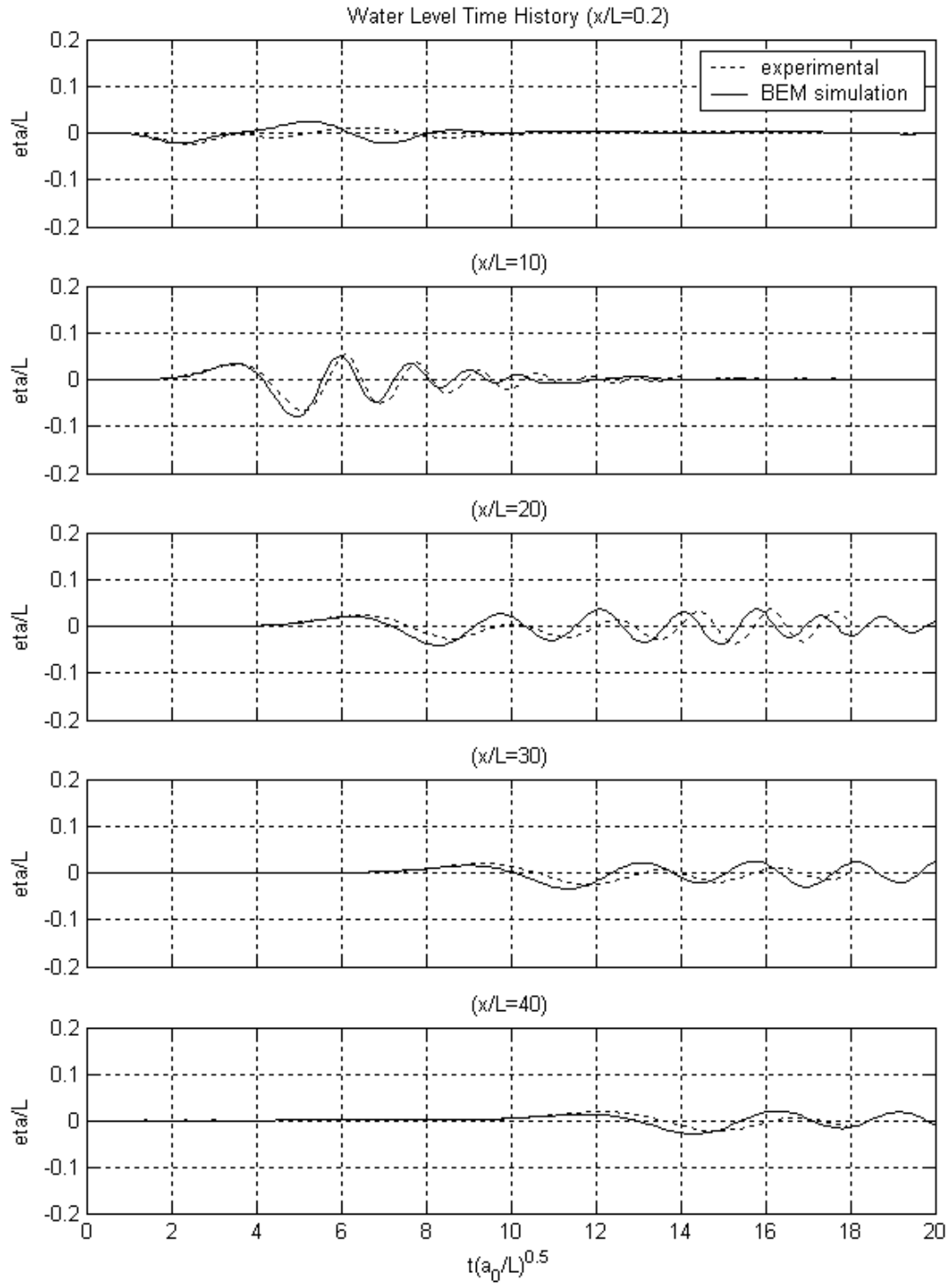

Figure G.27. Simulated and measured water level time histories at x/L = 0.2, 10, 20, 30, and 40 for the SG3_IS3 configuration.

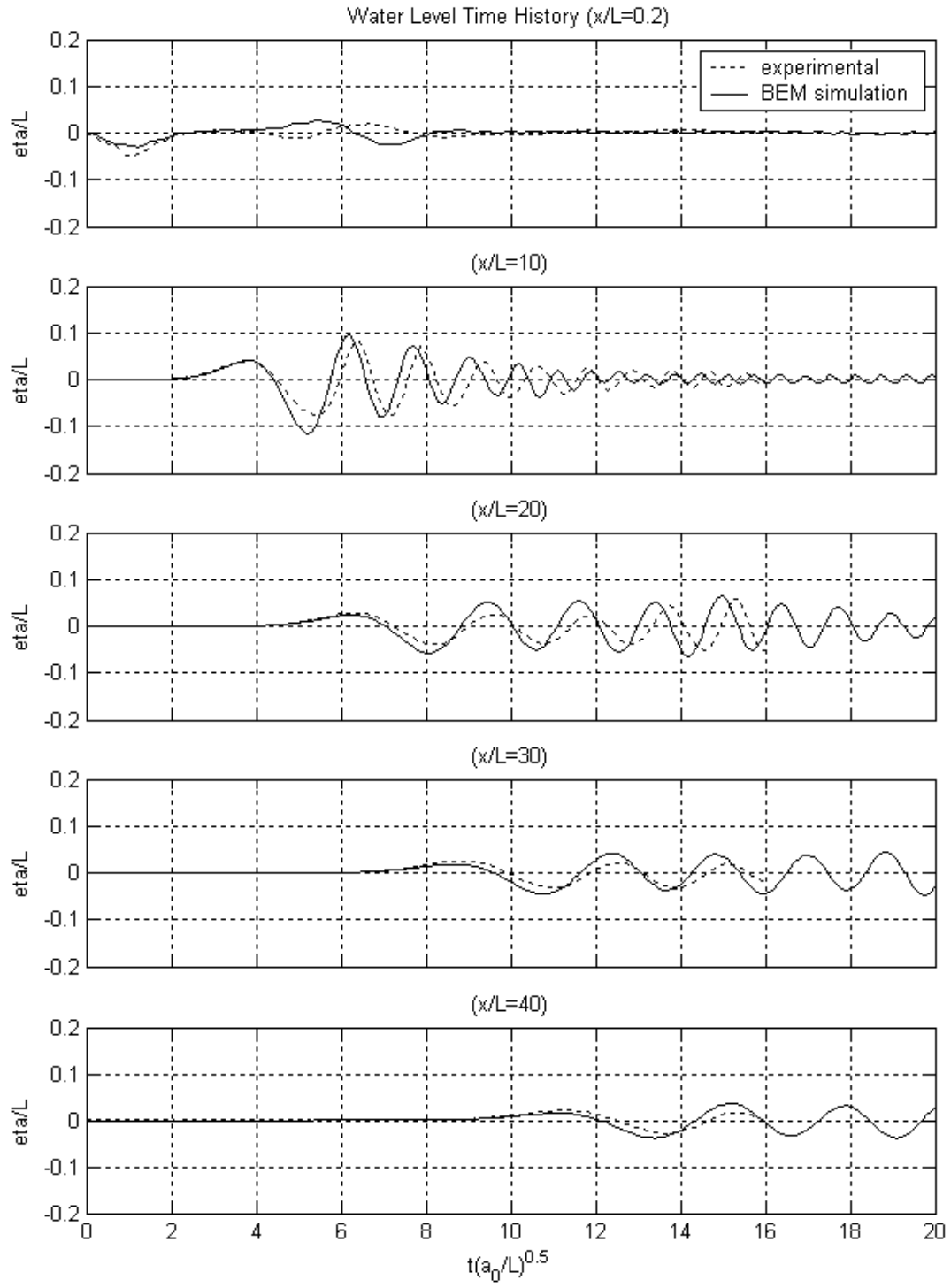

Figure G.28. Simulated and measured water level time histories at x/L = 0.2, 10, 20, 30, and 40 for the SG2_IS5 configuration.

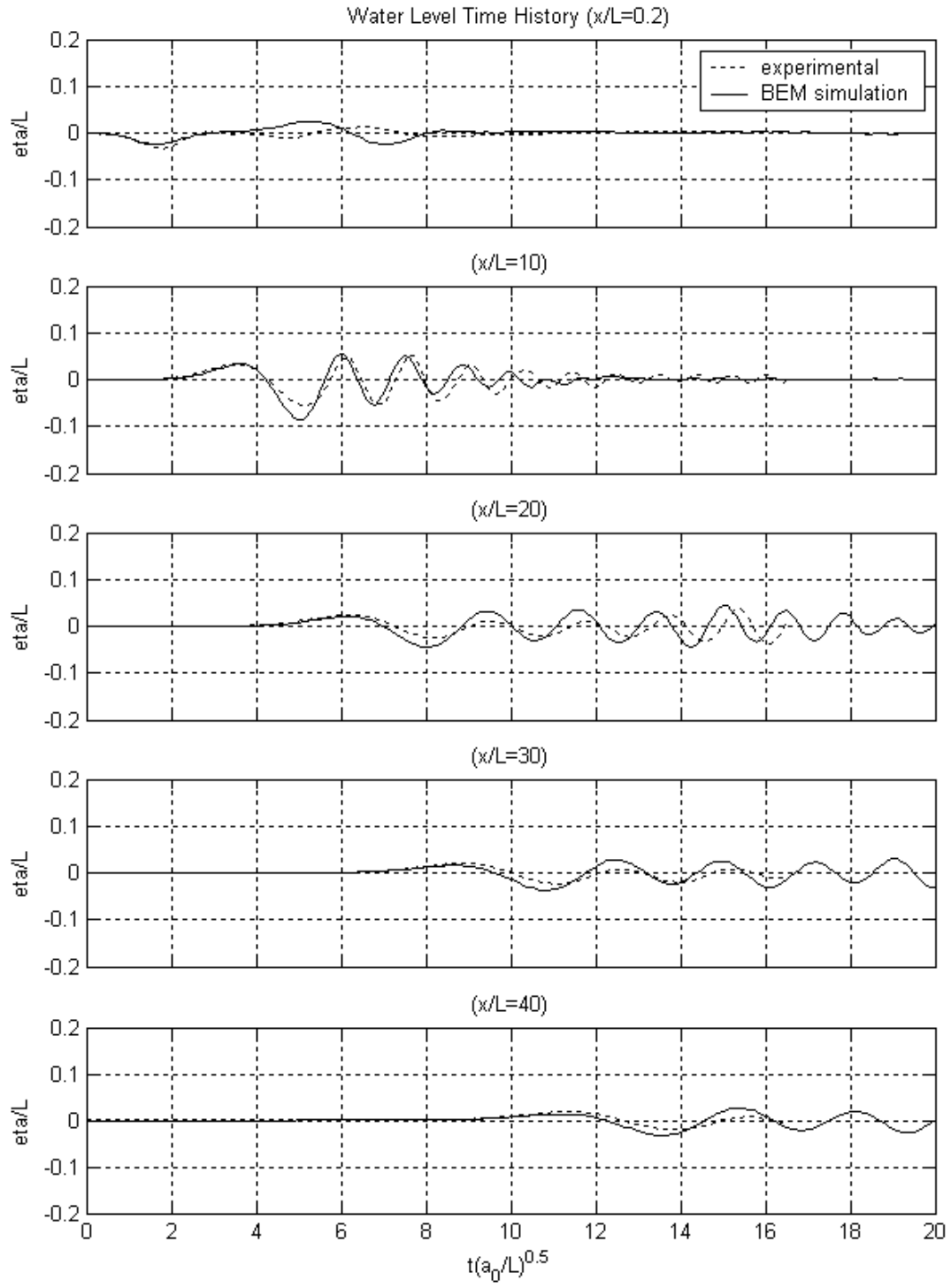

Figure G.29. Simulated and measured water level time histories at x/L = 0.2, 10, 20, 30, and 40 for the SG2_IS4 configuration.

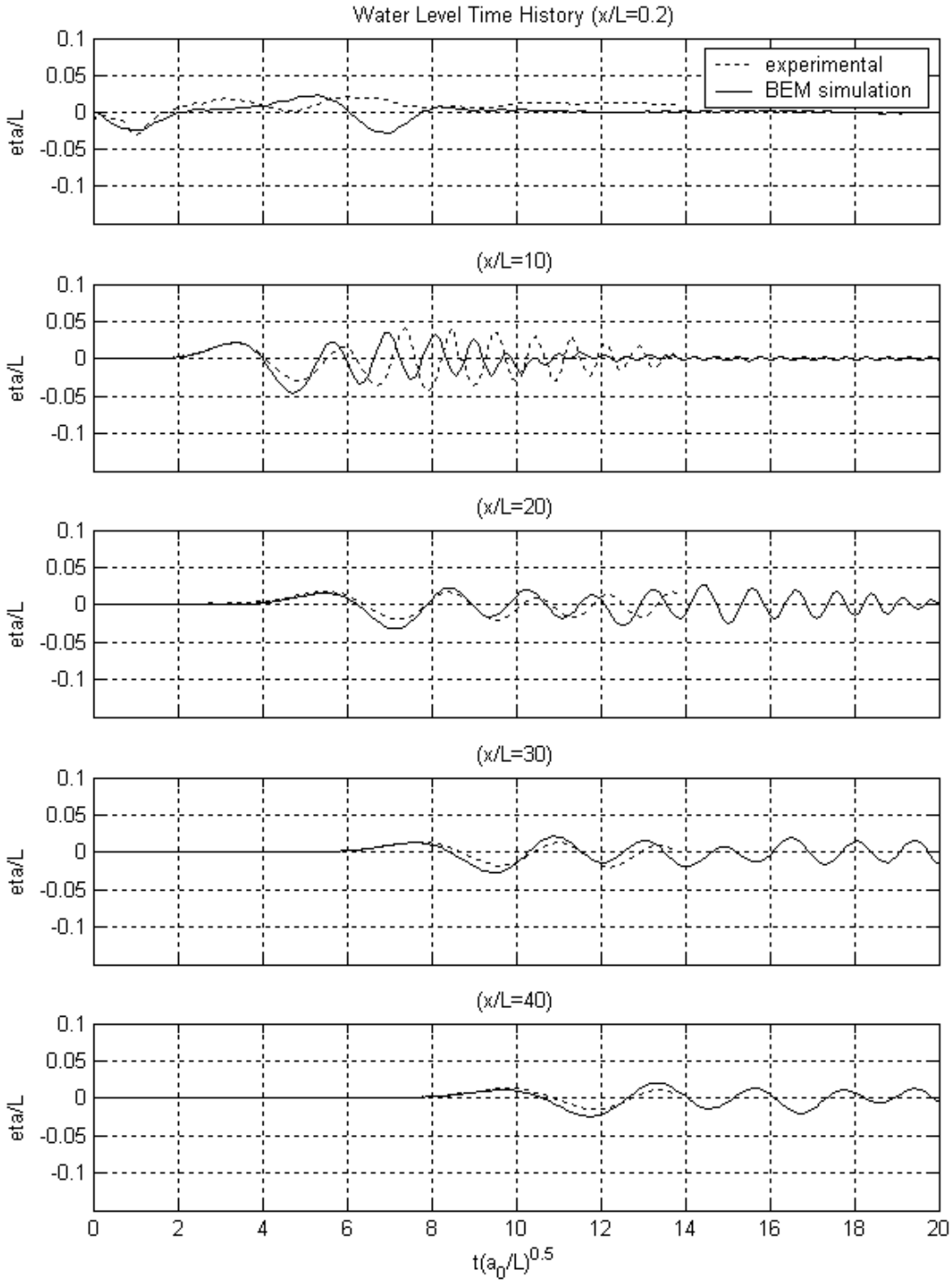

Figure G.30. Simulated and measured water level time histories at x/L = 0.2, 10, 20, 30, and 40 for the SG1_IS5 configuration.

G.3 Maximum Water Level Envelope and Time History

Plots of the simulated and measured spatial and temporal distribution of the maximum crest and trough amplitudes, for each of the fifteen specific gravity and initial submergence combinations, are presented in Figures G.31 to G.45.

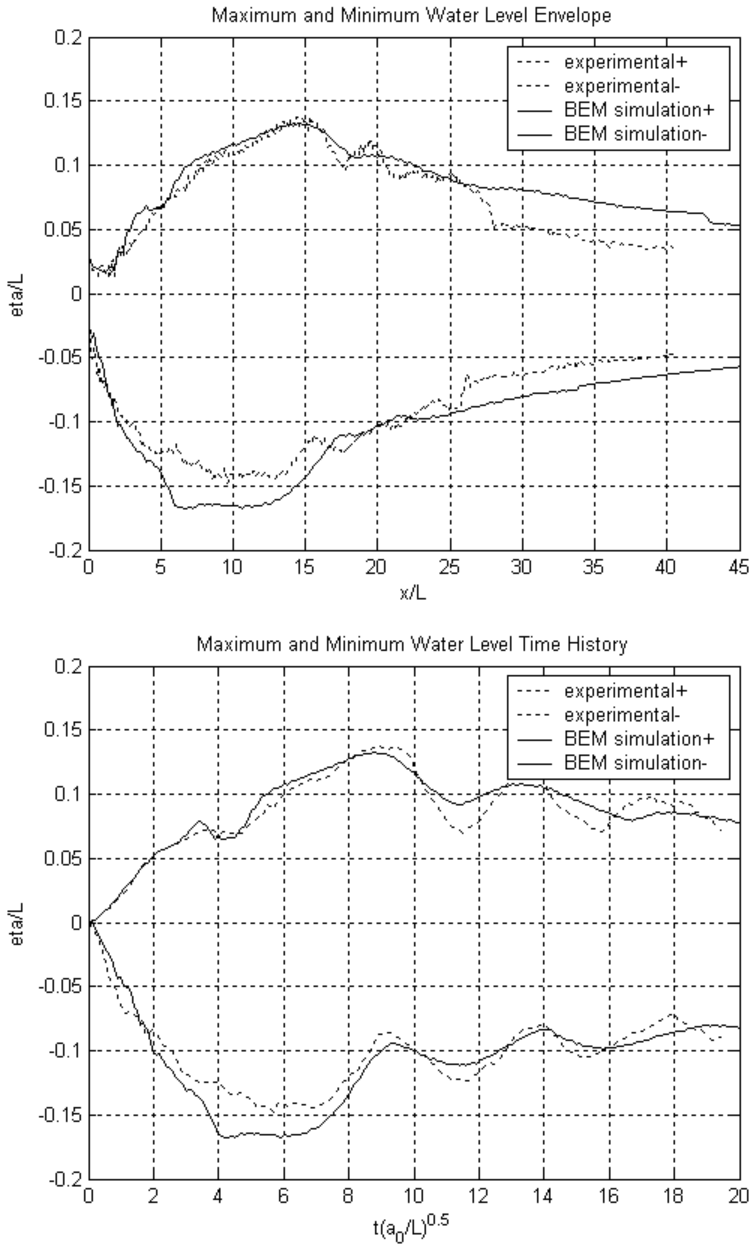

Figure G.31. Simulated and measured spatial and temporal distribution of the maximum crest and trough amplitudes for the SG5_IS5 combination.

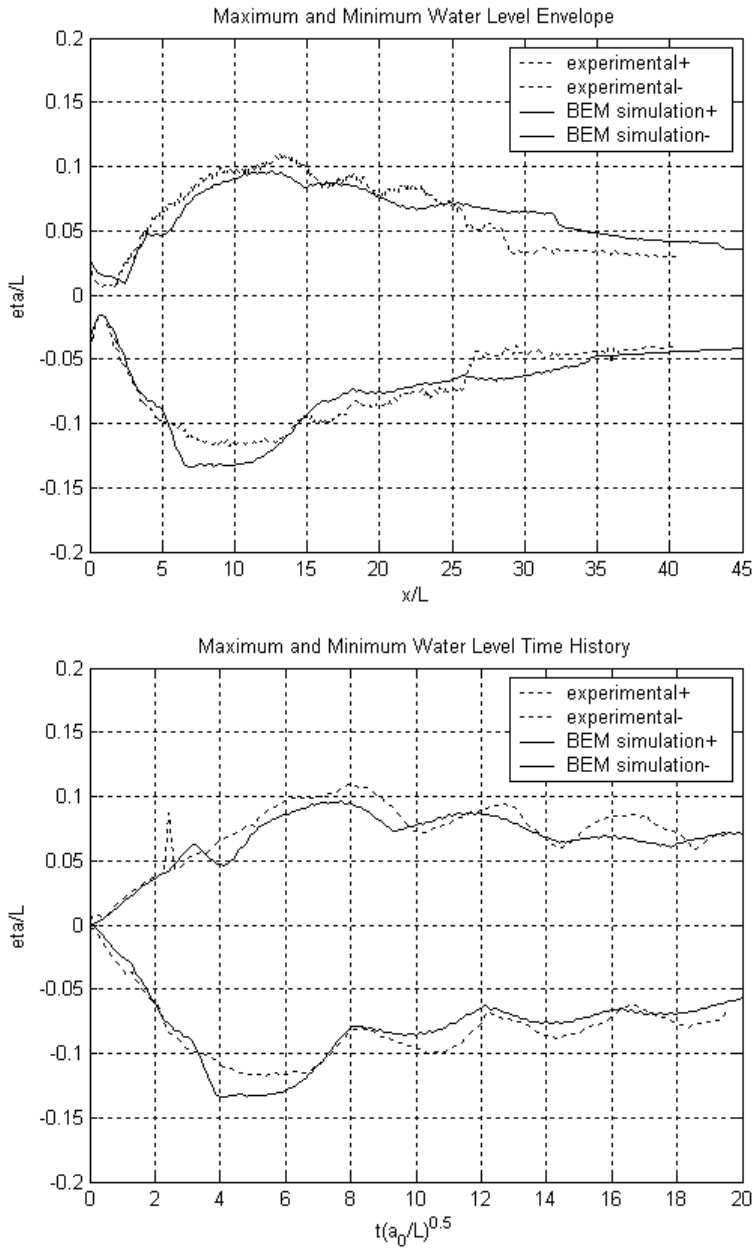

Figure G.32. Simulated and measured spatial and temporal distribution of the maximum crest and trough amplitudes for the SG5_IS4 configuration.

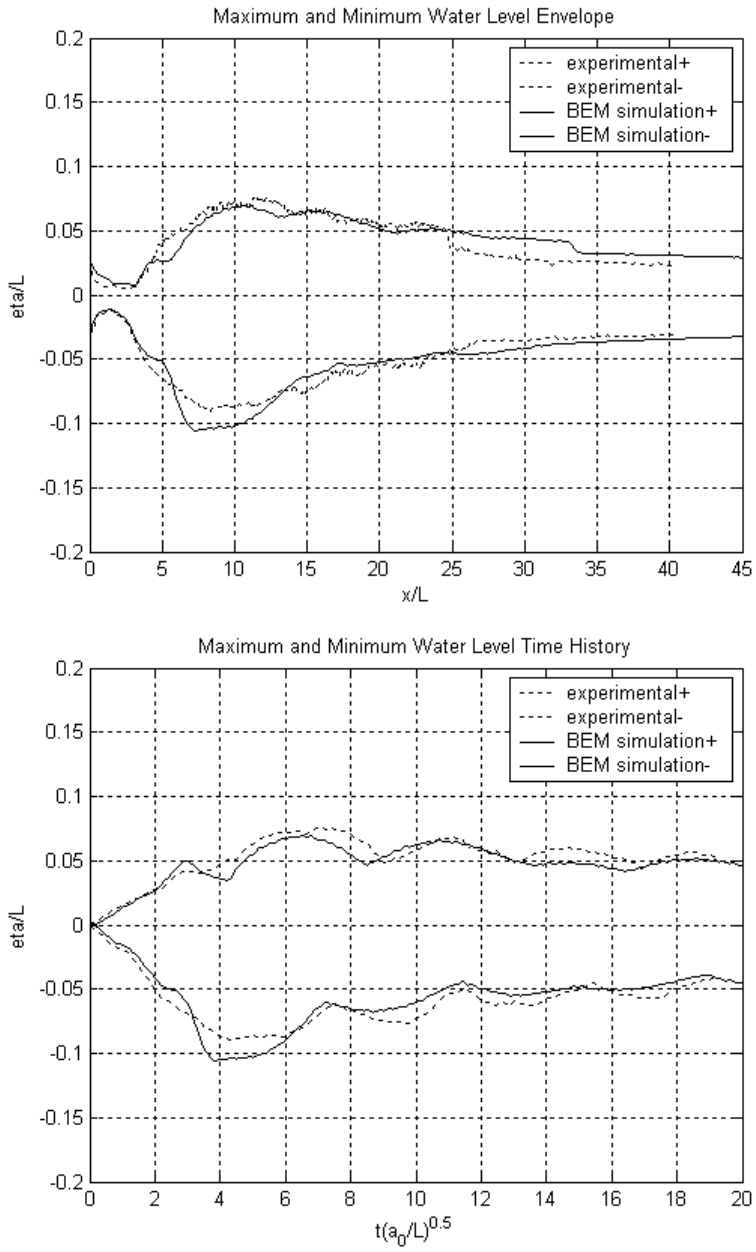

Figure G.33. Simulated and measured spatial and temporal distribution of the maximum crest and trough amplitudes for the SG5_IS3 configuration.

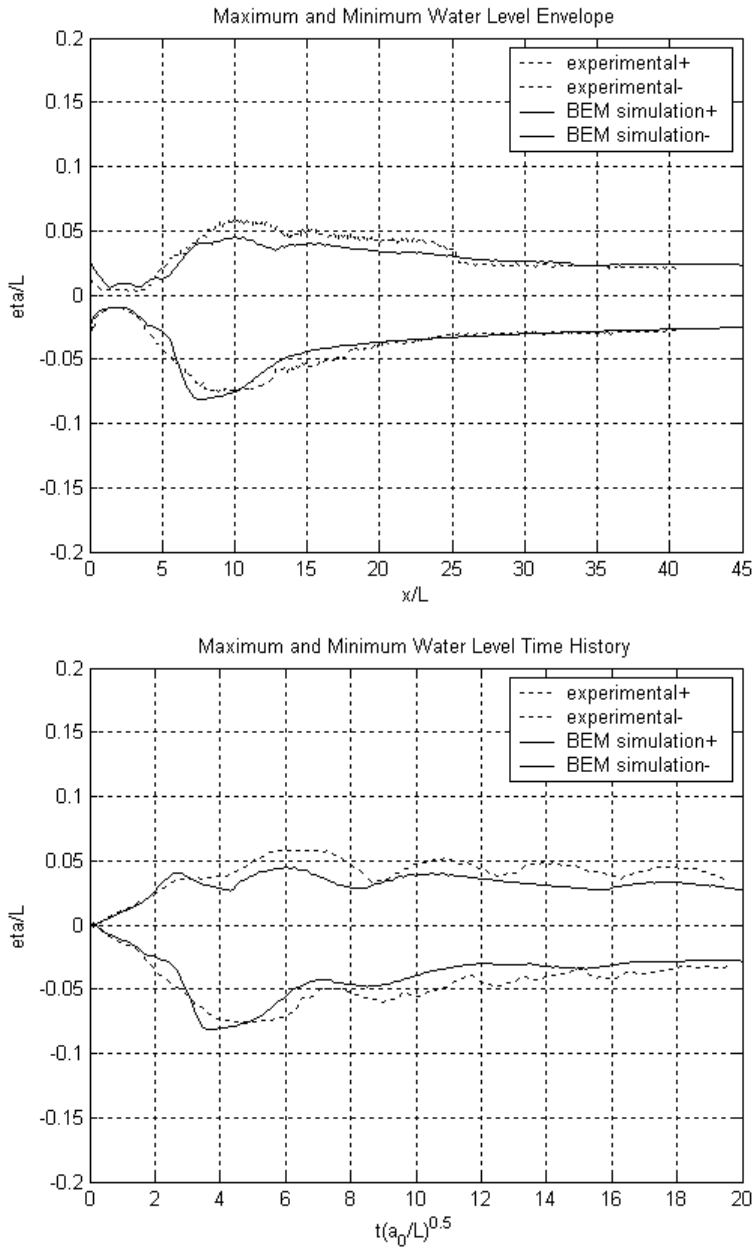

Figure G.34. Simulated and measured spatial and temporal distribution of the maximum crest and trough amplitudes for the SG5_IS2 configuration.

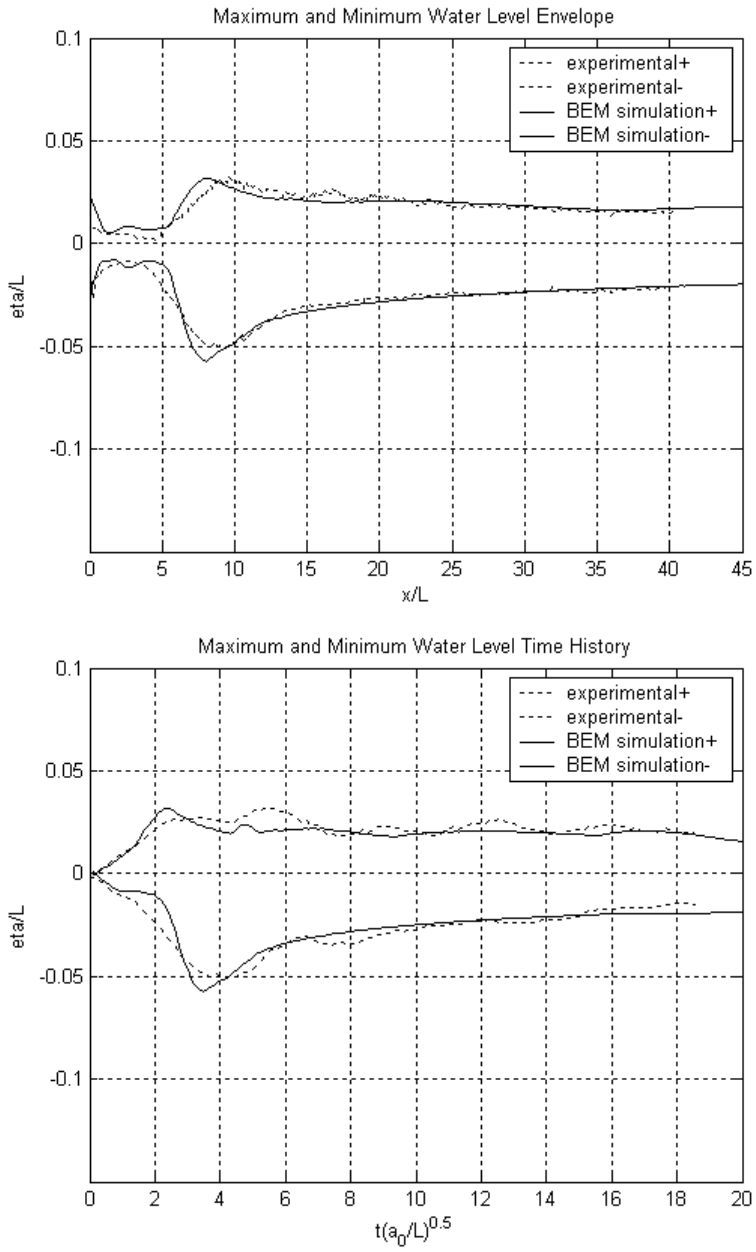

Figure G.35. Simulated and measured spatial and temporal distribution of the maximum crest and trough amplitudes for the SG5_IS1 configuration.

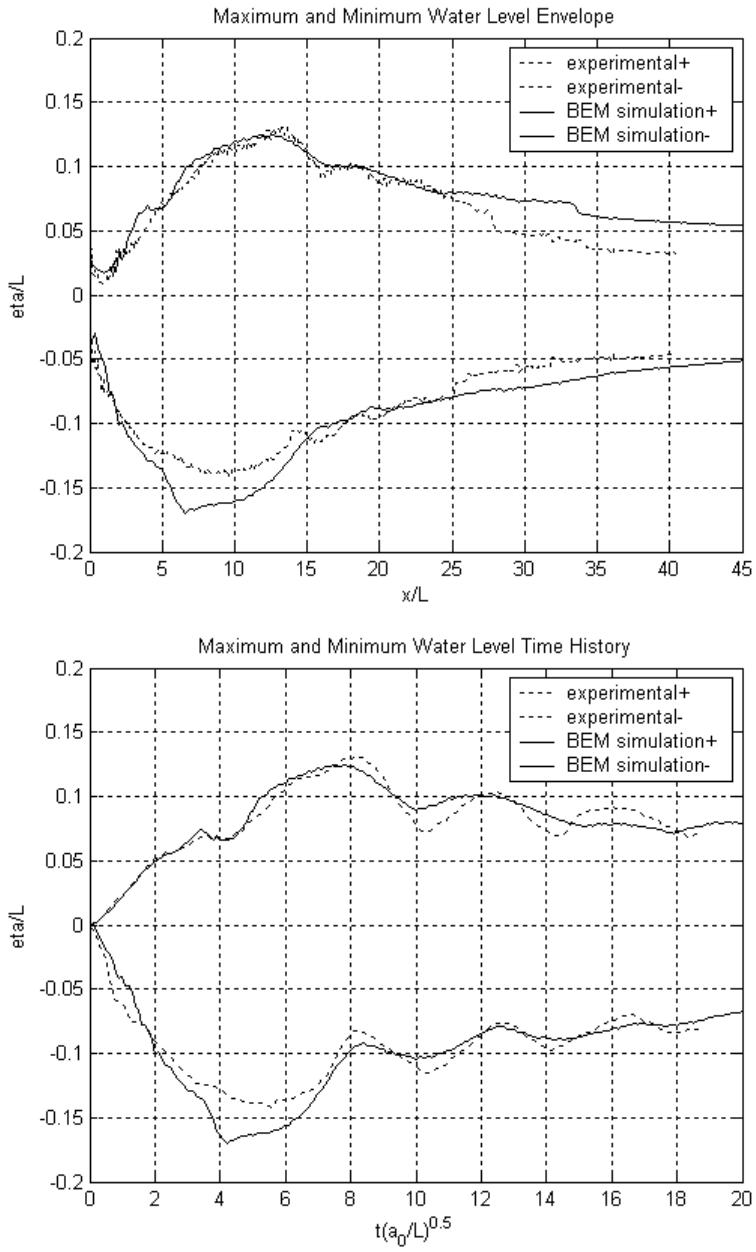

Figure G.36. Simulated and measured spatial and temporal distribution of the maximum crest and trough amplitudes for the SG4_IS5 configuration.

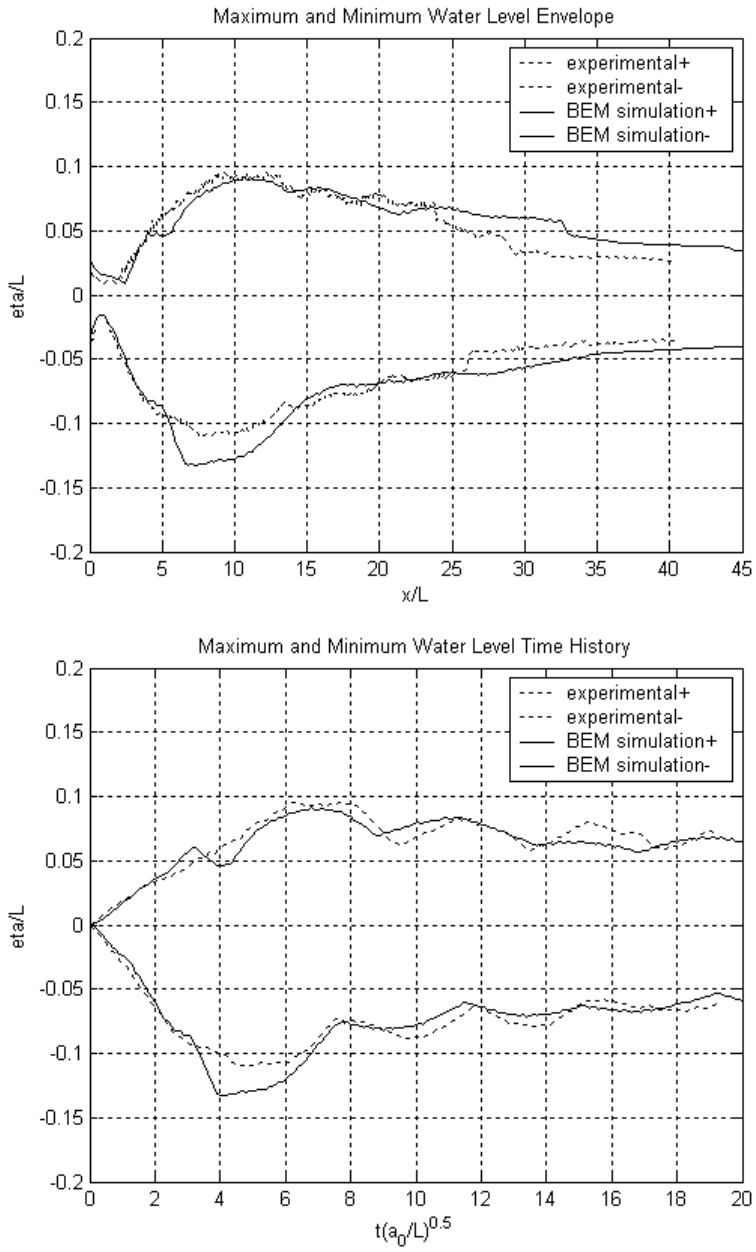

Figure G.37. Simulated and measured spatial and temporal distribution of the maximum crest and trough amplitudes for the SG4_IS4 configuration.

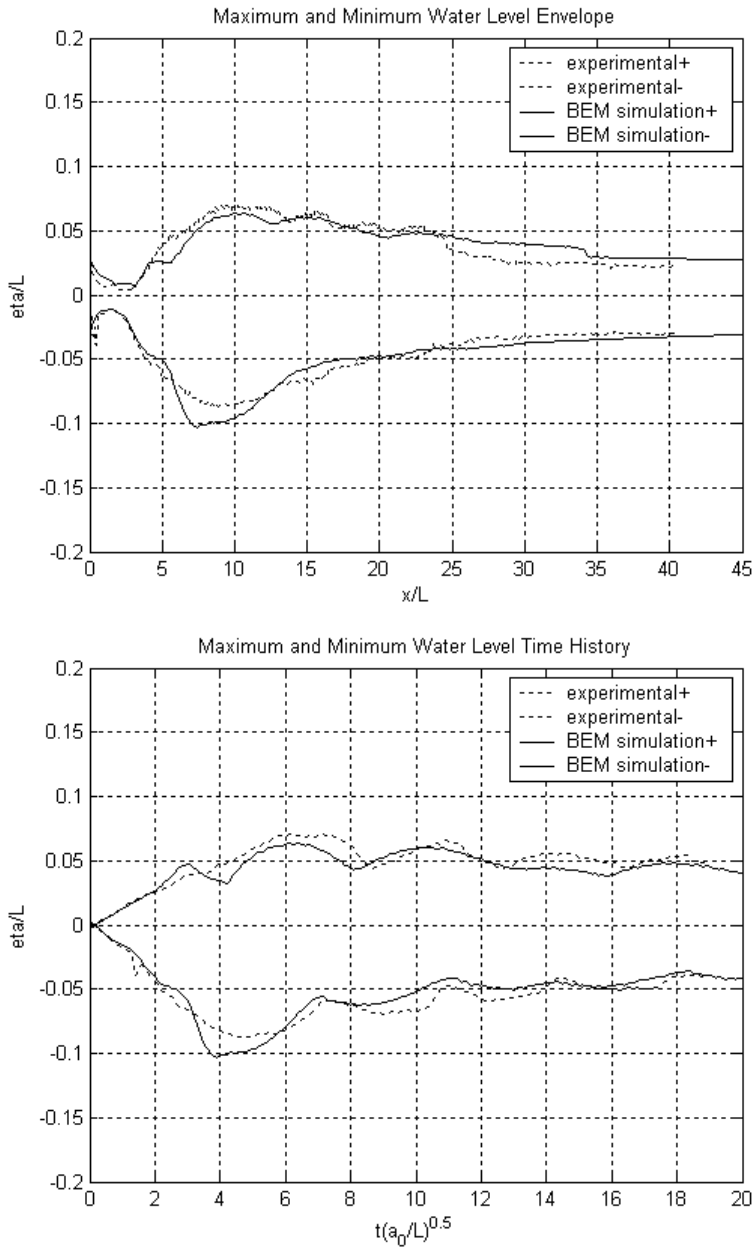

Figure G.38. Simulated and measured spatial and temporal distribution of the maximum crest and trough amplitudes for the SG4_IS3 configuration.

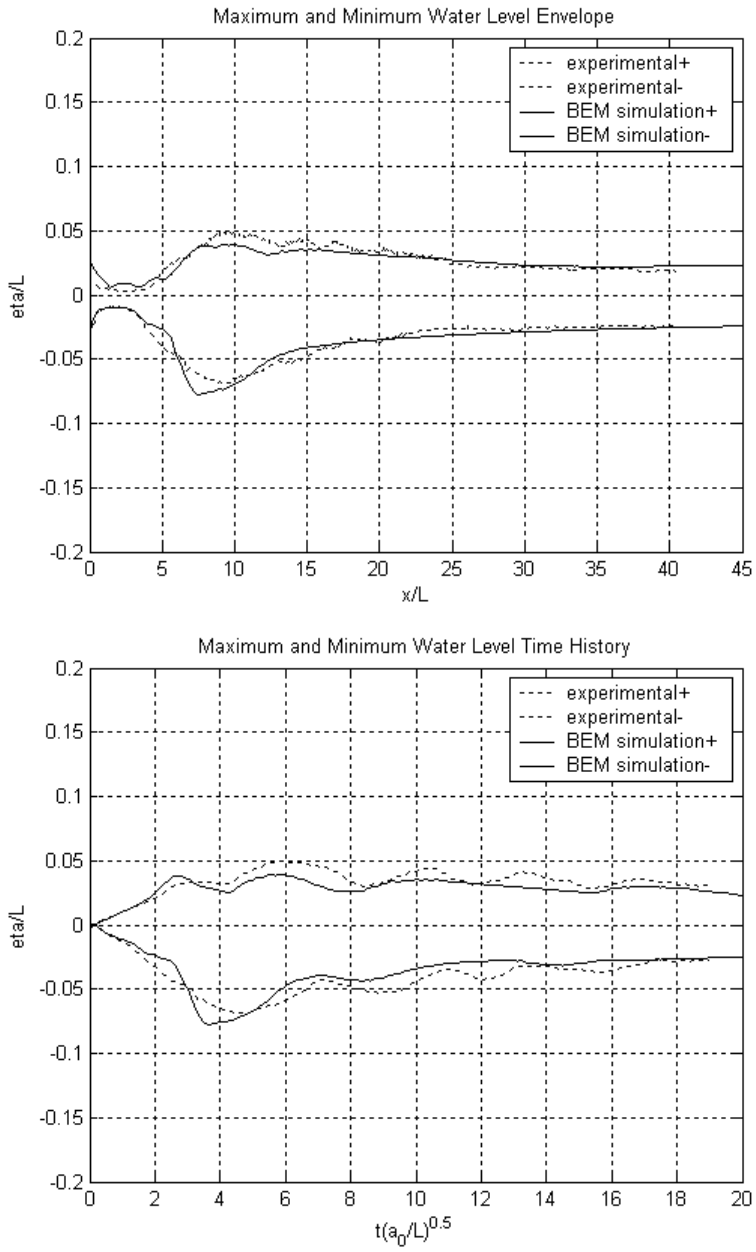

Figure G.39. Simulated and measured spatial and temporal distribution of the maximum crest and trough amplitudes for the SG4_IS2 configuration.

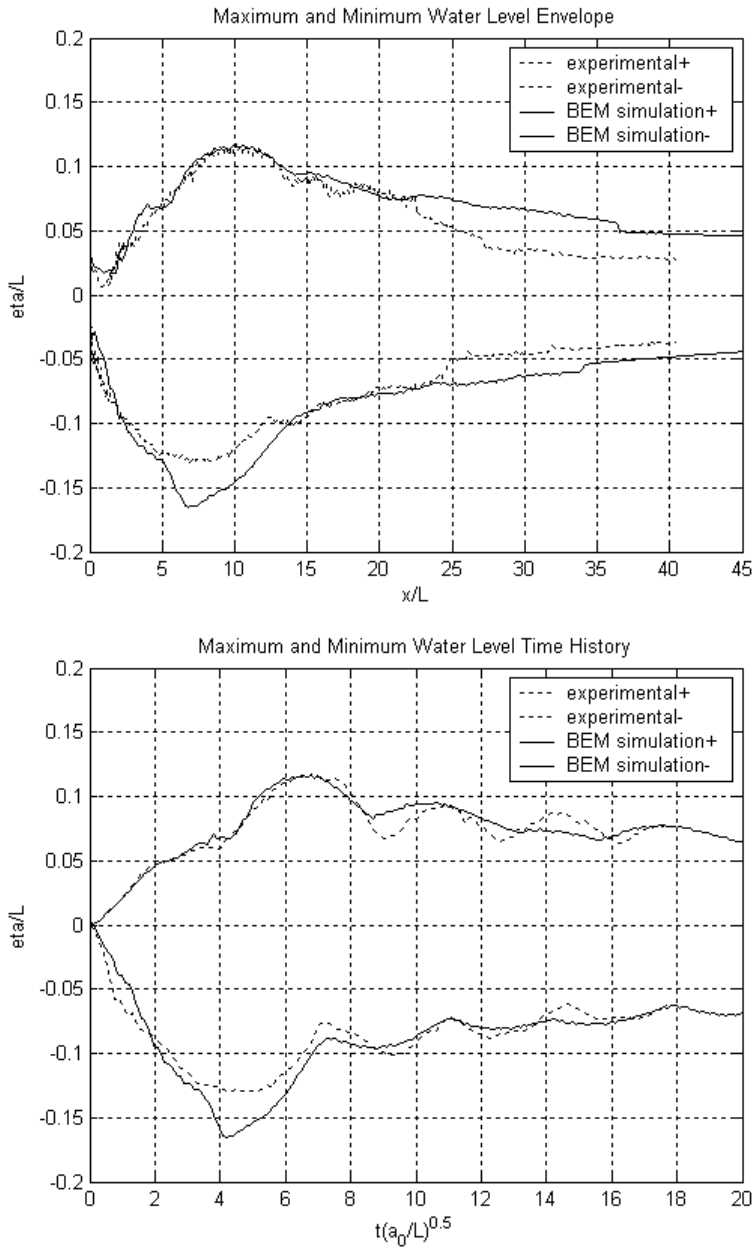

Figure G.40. Simulated and measured spatial and temporal distribution of the maximum crest and trough amplitudes for the SG3_IS5 configuration.

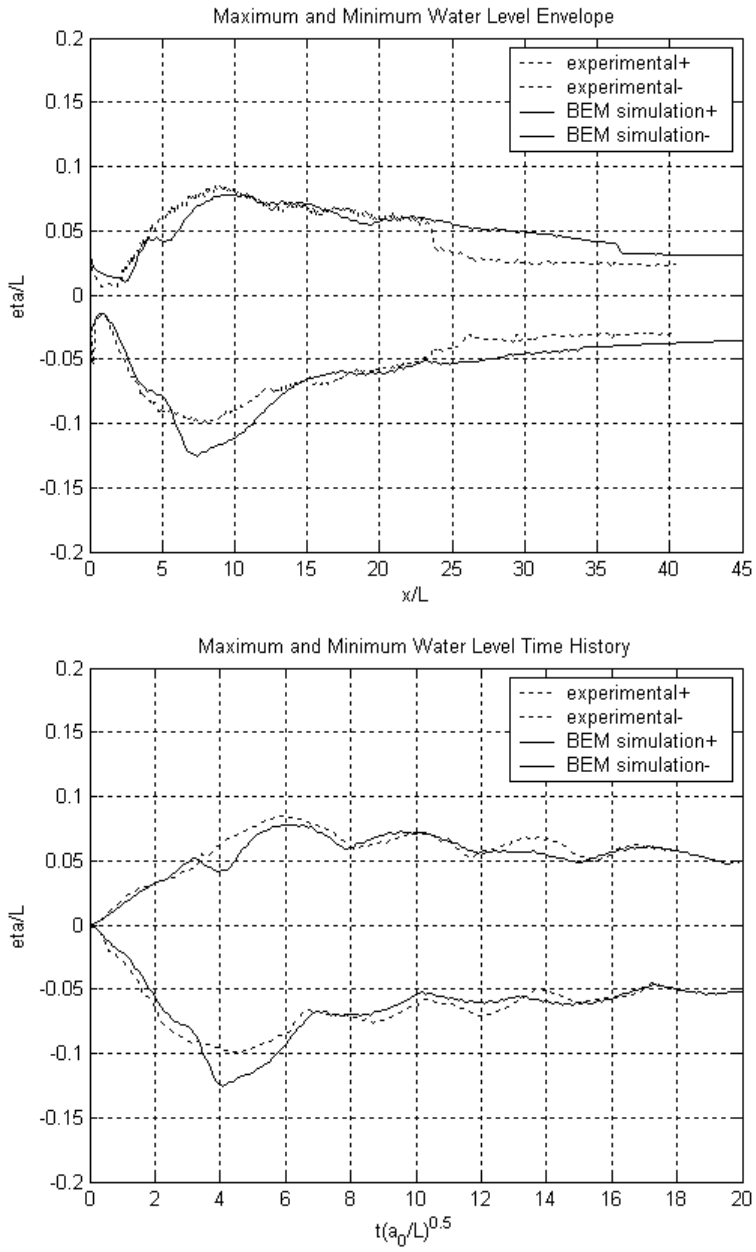

Figure G.41. Simulated and measured spatial and temporal distribution of the maximum crest and trough amplitudes for the SG3_IS4 configuration.

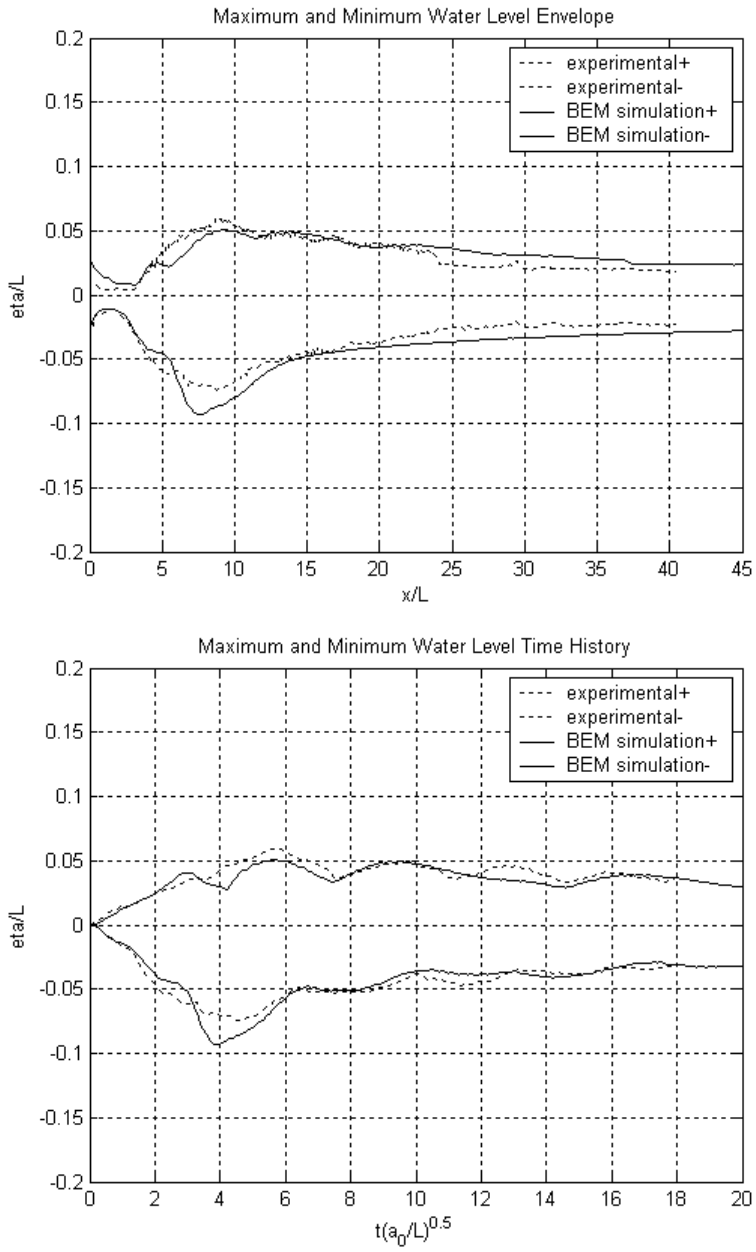

Figure G.42. Simulated and measured spatial and temporal distribution of the maximum crest and trough amplitudes for the SG3_IS3 configuration.

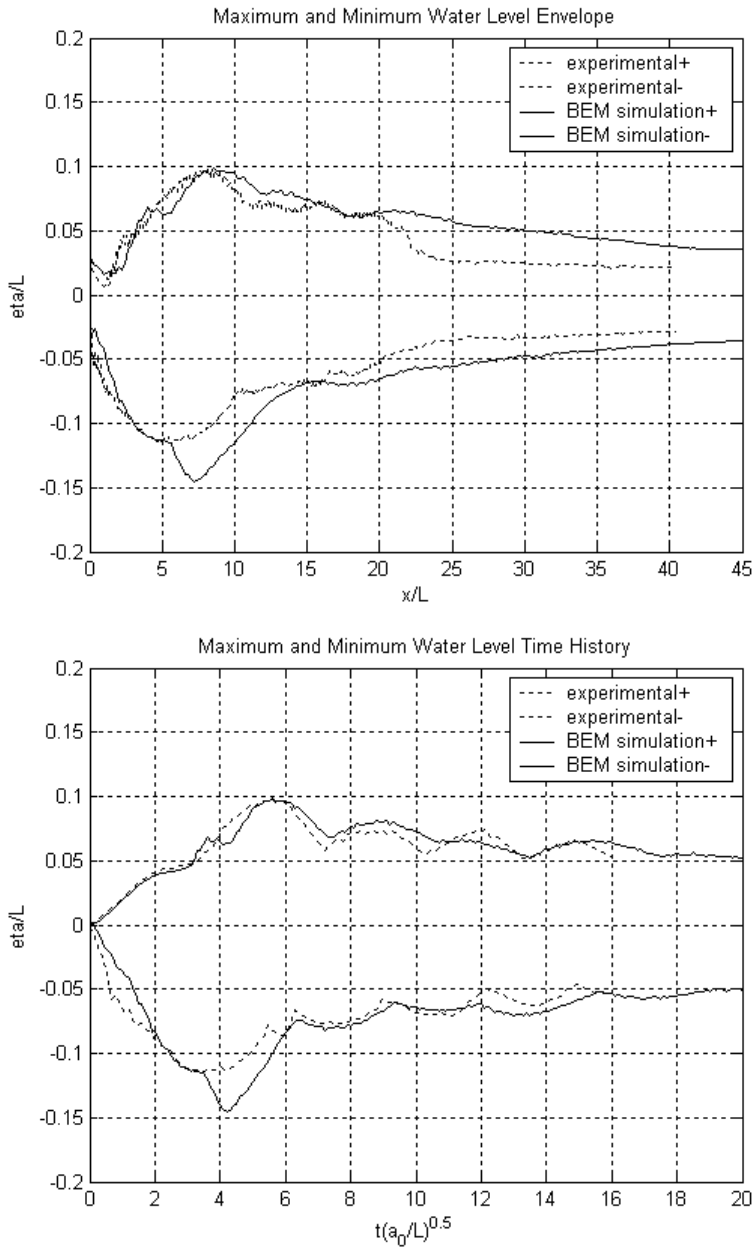

Figure G.43. Simulated and measured spatial and temporal distribution of the maximum crest and trough amplitudes for the SG2_IS5 configuration.

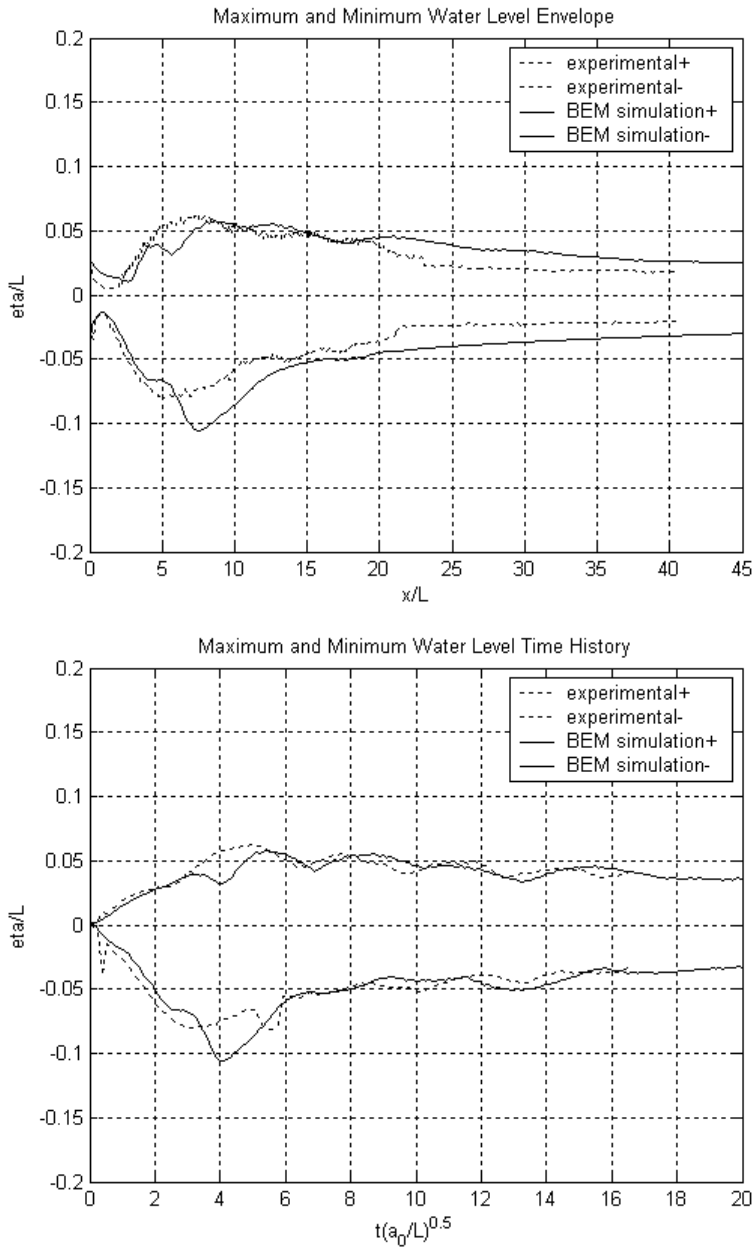

Figure G.44. Simulated and measured spatial and temporal distribution of the maximum crest and trough amplitudes for the SG2_IS4 configuration.

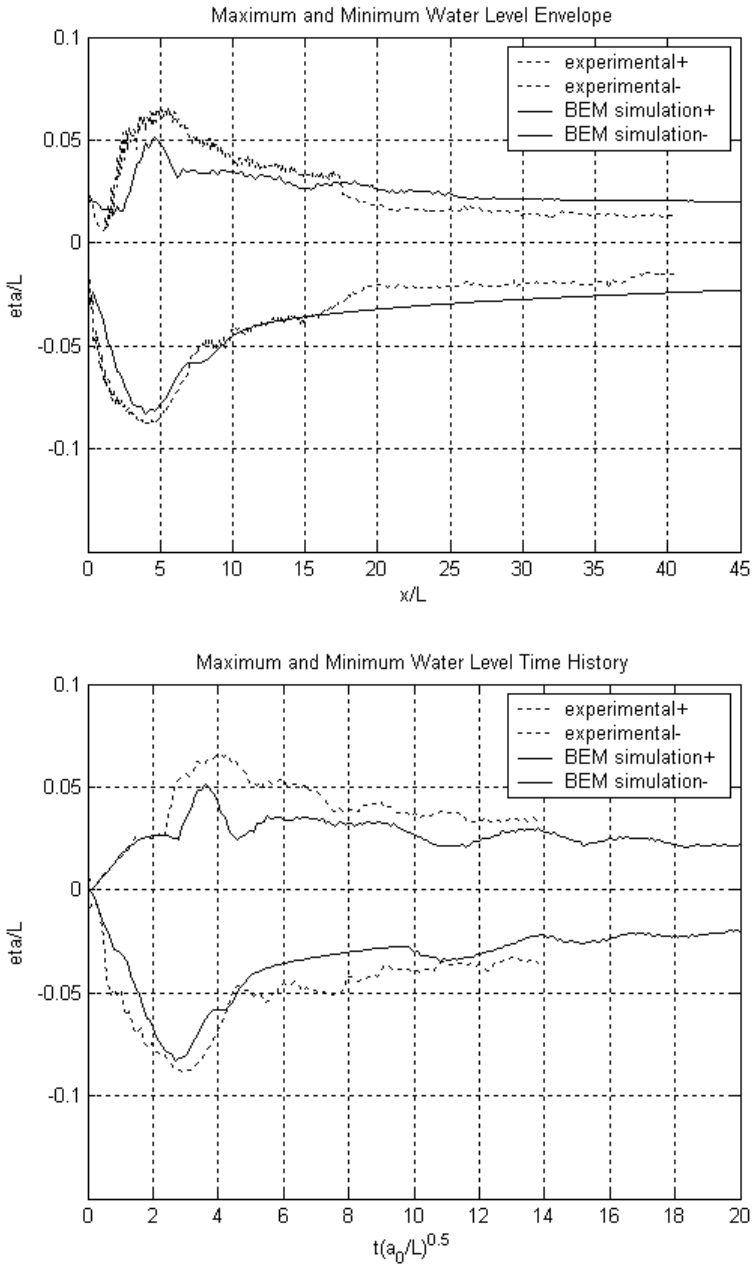

Figure G.45. Simulated and measured spatial and temporal distribution of the maximum crest and trough amplitudes for the SG1_IS5 configuration.

G.4 Wave Potential Energy Time History

Plots of the simulated and measured wave potential energy time history for each of the fifteen specific gravity and initial submergence combinations are presented in Figures G.46 to G.60.

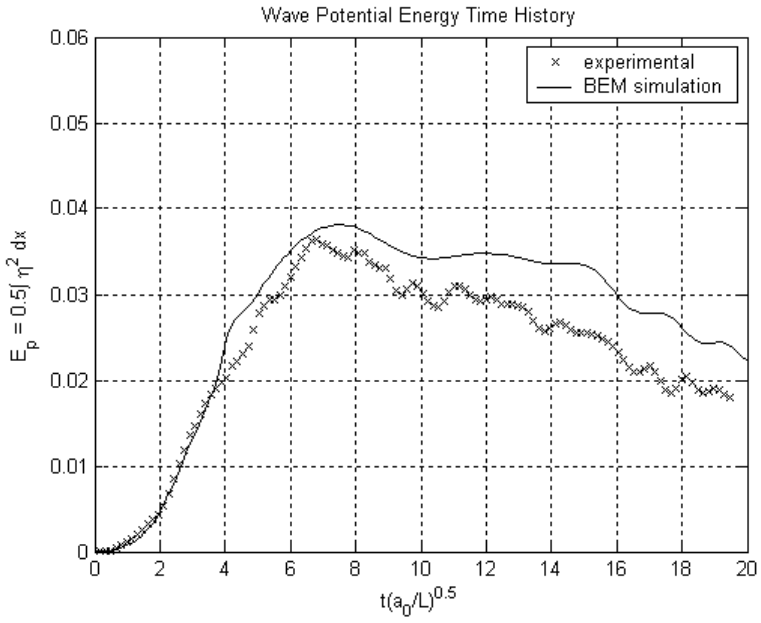

Figure G.46. Simulated and measured wave potential energy time history for the SG5_IS5 combination.

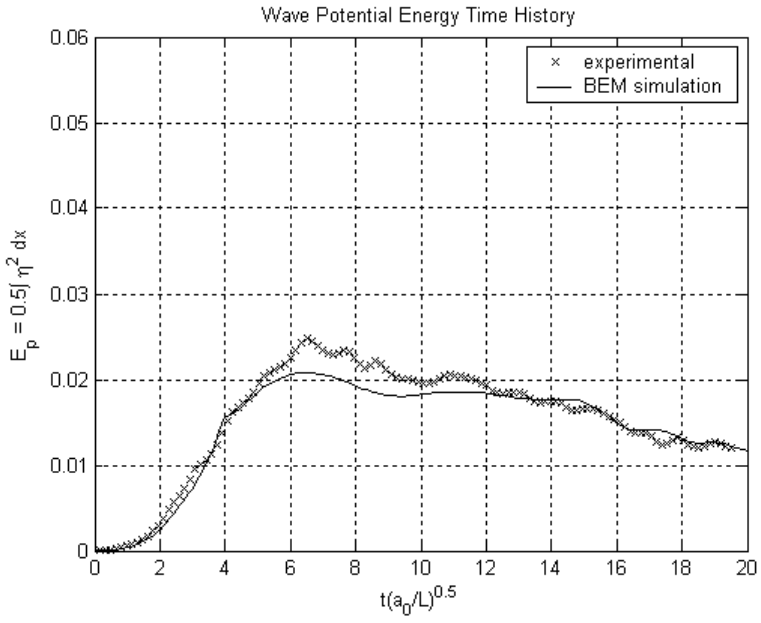

Figure G.47. Simulated and measured wave potential energy time history for the SG5-IS4 combination.

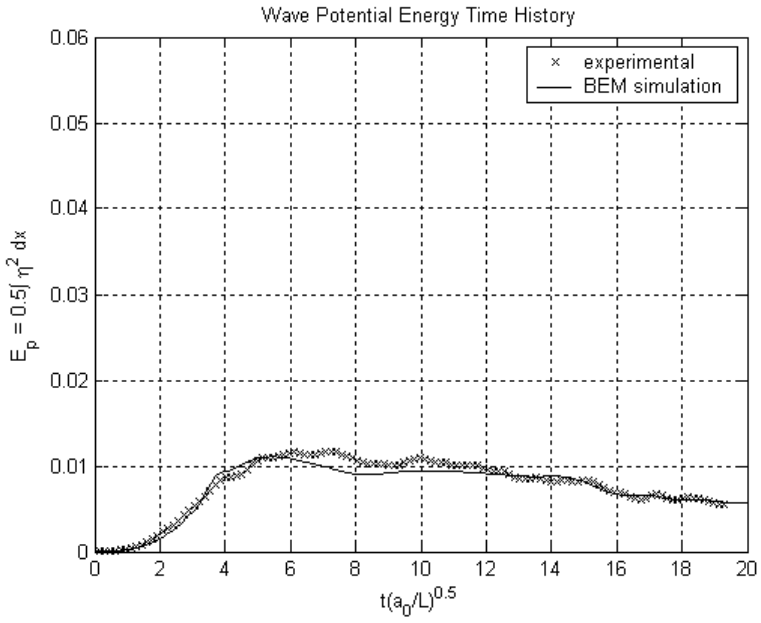

Figure G.48. Simulated and measured wave potential energy time history for the SG5-IS3 combination.

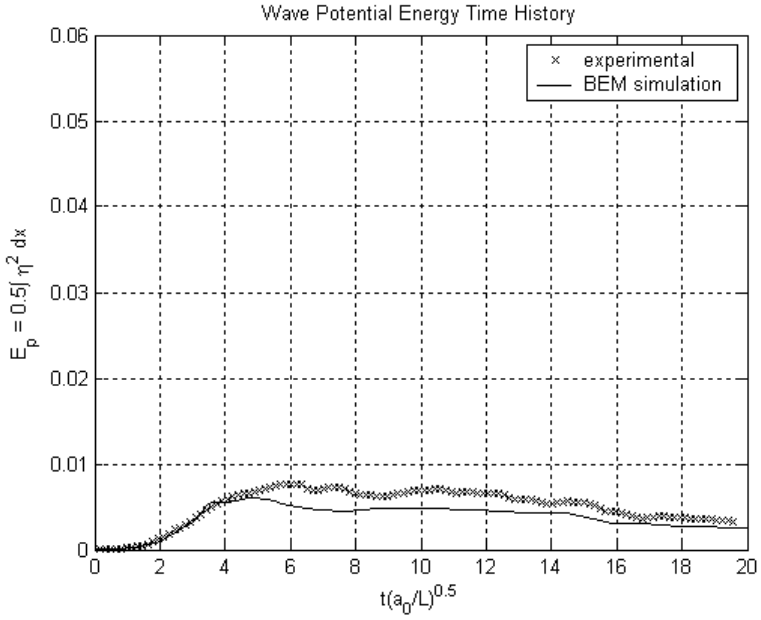

Figure G.49. Simulated and measured wave potential energy time history for the SG5-IS2 combination.

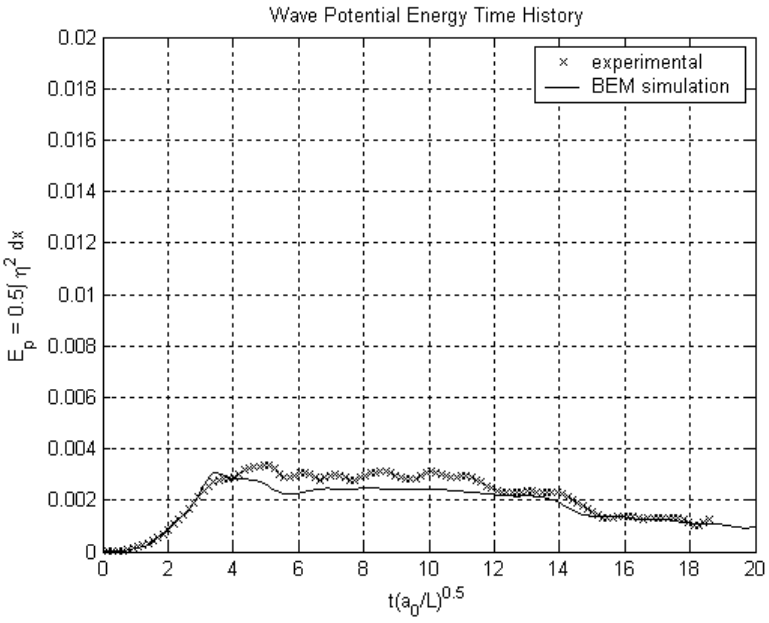

Figure G.50. Simulated and measured wave potential energy time history for the SG5-IS1 combination.

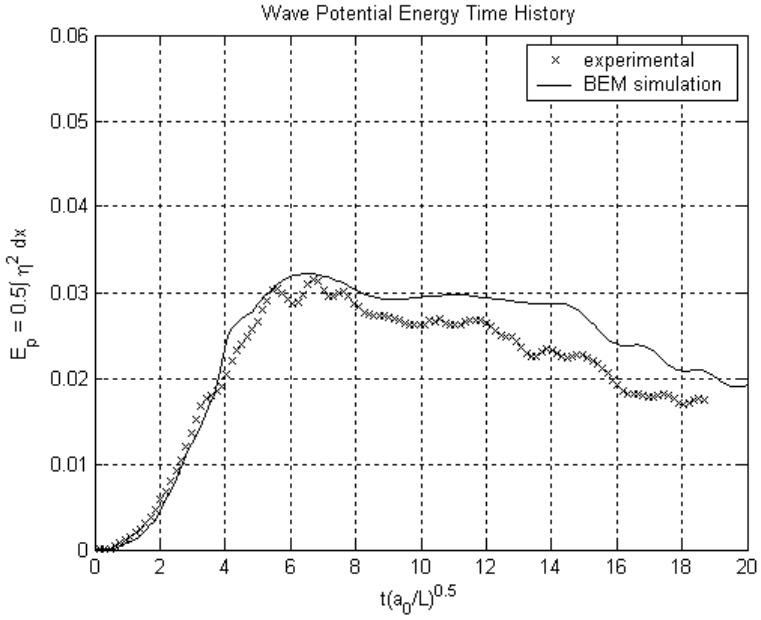

Figure G.51. Simulated and measured wave potential energy time history for the SG4-IS5 combination.

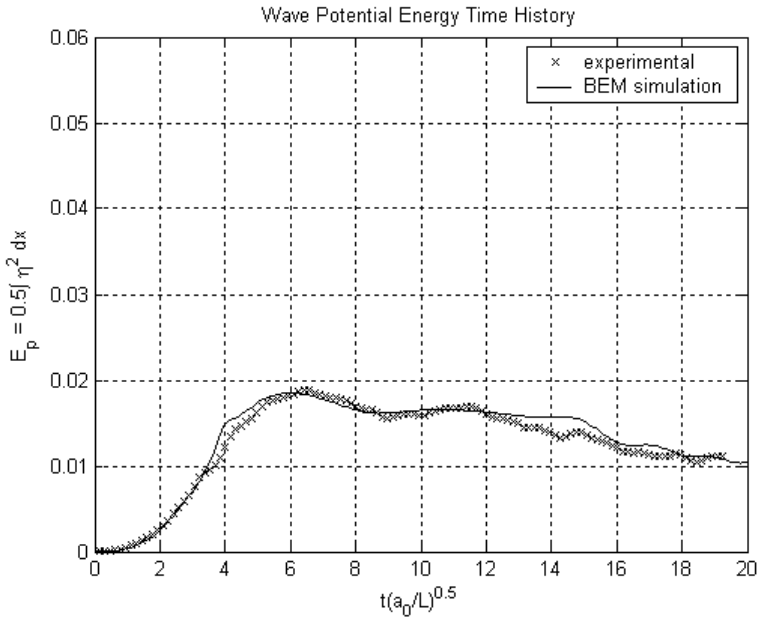

Figure G.52. Simulated and measured wave potential energy time history for the SG4-IS4 combination.

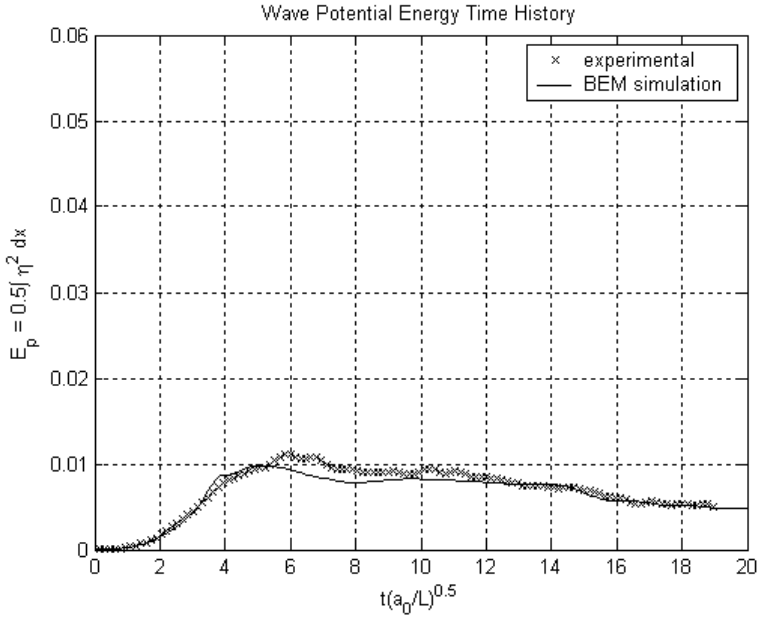

Figure G.53. Simulated and measured wave potential energy time history for the SG4-IS3 combination.

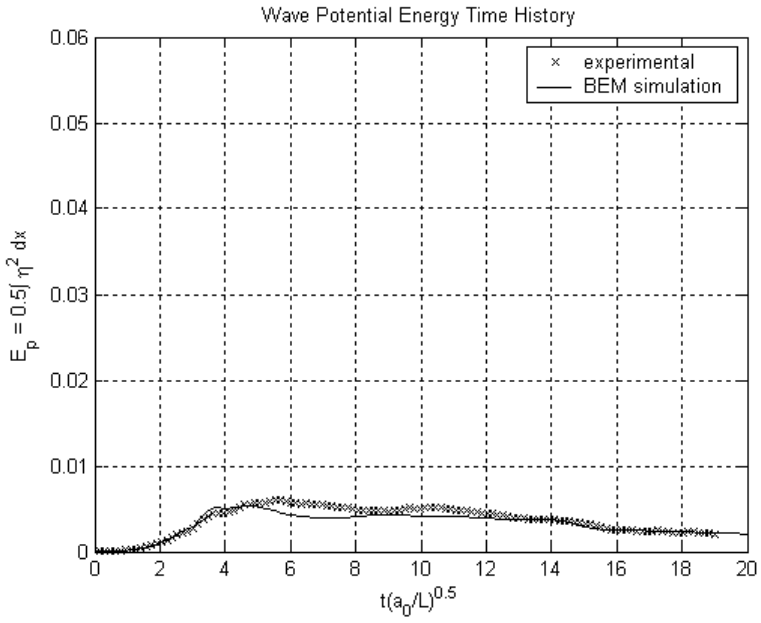

Figure G.54. Simulated and measured wave potential energy time history for the SG4-IS2 combination.

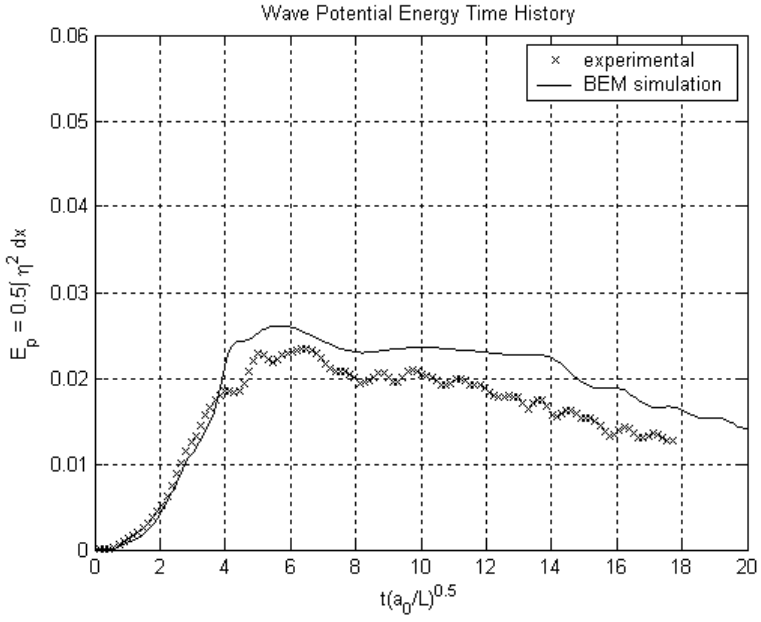

Figure G.55. Simulated and measured wave potential energy time history for the SG3-IS5 combination.

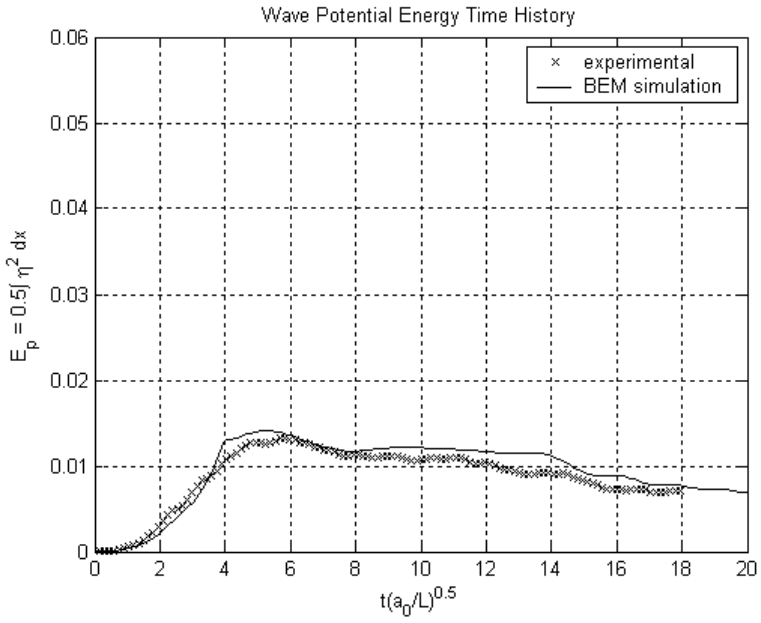

Figure G.56. Simulated and measured wave potential energy time history for the SG3-IS4 combination.

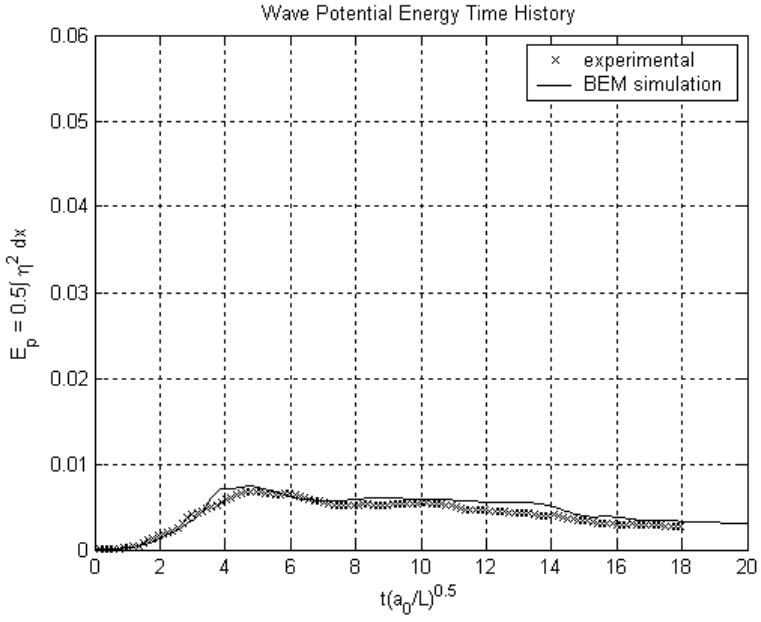

Figure G.57. Simulated and measured wave potential energy time history for the SG3-IS3 combination.

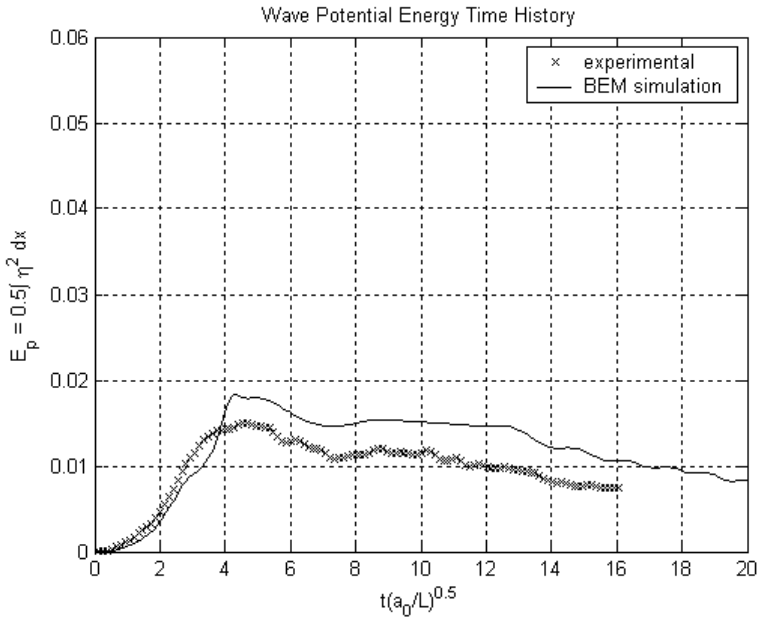

Figure G.58. Simulated and measured wave potential energy time history for the SG2-IS5 combination.

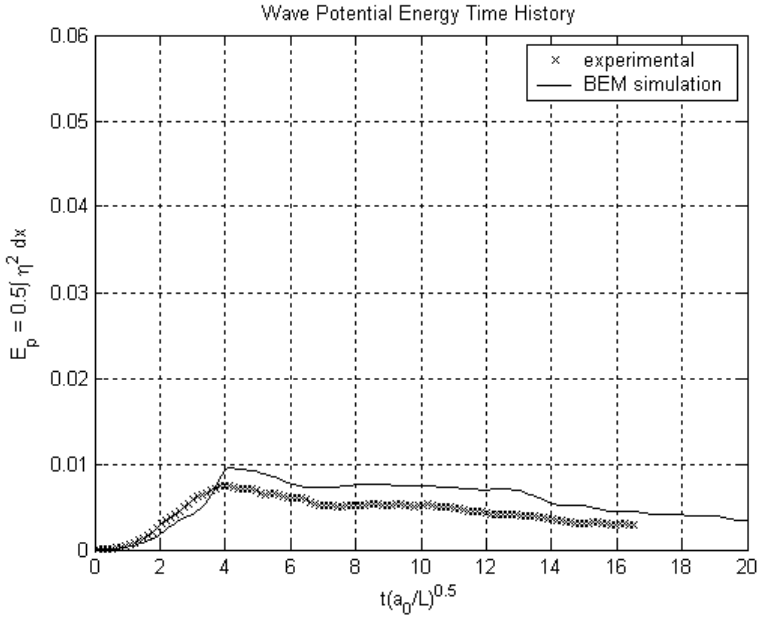

Figure G.59. Simulated and measured wave potential energy time history for the SG2-IS4 combination.

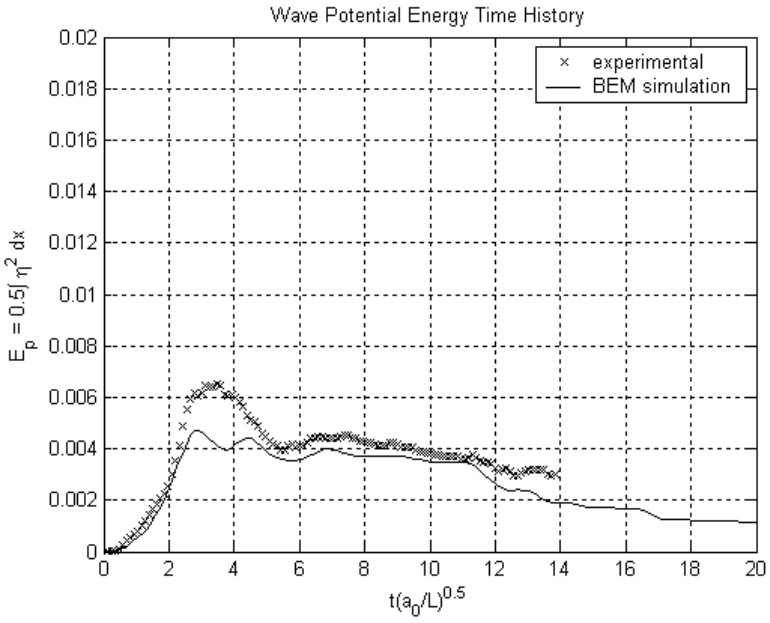

Figure G.60. Simulated and measured wave potential energy time history for the SG1-IS5 combination.